frontiers | Research Topics

Biomechanical and biochemical regulation of the musculoskeletal system

Edited by
Jun Pan, Damien Lacroix and Bin Wang

Published in
Frontiers in Bioengineering and Biotechnology

ISSN 1664-8714
ISBN 978-2-8325-2485-5
DOI 10.3389/978-2-8325-2485-5

About Frontiers

Frontiers is more than just an open access publisher of scholarly articles: it is a pioneering approach to the world of academia, radically improving the way scholarly research is managed. The grand vision of Frontiers is a world where all people have an equal opportunity to seek, share and generate knowledge. Frontiers provides immediate and permanent online open access to all its publications, but this alone is not enough to realize our grand goals.

Frontiers journal series

The Frontiers journal series is a multi-tier and interdisciplinary set of open-access, online journals, promising a paradigm shift from the current review, selection and dissemination processes in academic publishing. All Frontiers journals are driven by researchers for researchers; therefore, they constitute a service to the scholarly community. At the same time, the *Frontiers journal series* operates on a revolutionary invention, the tiered publishing system, initially addressing specific communities of scholars, and gradually climbing up to broader public understanding, thus serving the interests of the lay society, too.

Dedication to quality

Each Frontiers article is a landmark of the highest quality, thanks to genuinely collaborative interactions between authors and review editors, who include some of the world's best academicians. Research must be certified by peers before entering a stream of knowledge that may eventually reach the public - and shape society; therefore, Frontiers only applies the most rigorous and unbiased reviews. Frontiers revolutionizes research publishing by freely delivering the most outstanding research, evaluated with no bias from both the academic and social point of view. By applying the most advanced information technologies, Frontiers is catapulting scholarly publishing into a new generation.

What are Frontiers Research Topics?

Frontiers Research Topics are very popular trademarks of the *Frontiers journals series*: they are collections of at least ten articles, all centered on a particular subject. With their unique mix of varied contributions from Original Research to Review Articles, Frontiers Research Topics unify the most influential researchers, the latest key findings and historical advances in a hot research area.

Find out more on how to host your own Frontiers Research Topic or contribute to one as an author by contacting the Frontiers editorial office: frontiersin.org/about/contact

Biomechanical and biochemical regulation of the musculoskeletal system

Topic editors
Jun Pan — Chongqing University, China
Damien Lacroix — The University of Sheffield, United Kingdom
Bin Wang — Chongqing Medical University, China

Topic Coordinator
Yilu Zhou — University of Pennsylvania, United States

Citation
Pan, J., Lacroix, D., Wang, B., eds. (2023). *Biomechanical and biochemical regulation of the musculoskeletal system*. Lausanne: Frontiers Media SA.
doi: 10.3389/978-2-8325-2485-5

Table of contents

frontiers | Frontiers in Bioengineering and Biotechnology

TYPE Editorial
PUBLISHED 05 May 2023
DOI 10.3389/fbioe.2023.1192638

OPEN ACCESS

EDITED AND REVIEWED BY
Tobias Siebert,
University of Stuttgart, Germany

*CORRESPONDENCE
Jun Pan,
✉ Panj@cqu.edu.cn
Damien Lacroix,
✉ d.lacroix@sheffield.ac.uk
Yilu Zhou,
✉ Yilu.Zhou@pennmedicine.upenn.edu
Bin Wang,
✉ bwang@cqmu.edu.cn

RECEIVED 23 March 2023
ACCEPTED 28 April 2023
PUBLISHED 05 May 2023

CITATION
Pan J, Lacroix D, Zhou Y and Wang B (2023), Editorial: Biomechanical and biochemical regulation of the musculoskeletal system.
Front. Bioeng. Biotechnol. 11:1192638.
doi: 10.3389/fbioe.2023.1192638

Editorial: Biomechanical and biochemical regulation of the musculoskeletal system

Jun Pan[1]*, Damien Lacroix[2]*, Yilu Zhou[3]* and Bin Wang[4]*

[1]Bioengineering College, Chongqing University, Chongqing, China, [2]Department of Mechanical Engineering, The University of Sheffield, Sheffield, United Kingdom, [3]Department of Orthopaedic Surgery, University of Pennsylvania, Philadelphia, PA, United States, [4]Institute of Life Sciences, Chongqing Medical University, Chongqing, China

KEYWORDS

musculoskeletal system, biomechanical regulation, musculoskeletal disorders, computational model, biochemical regulation

Editorial on the Research Topic
Biomechanical and biochemical regulation of the musculoskeletal system

The musculoskeletal system is an essential part of the human body that is responsible for providing support, movement, and protection. The system is composed of bones, muscles, and connective tissues that work together in a complex manner to facilitate the functioning of the body. Over the years, extensive research has been conducted to understand the biomechanical and biochemical regulation of this system, and how these processes are interrelated. The 2017 Global Burden of Disease Study reports that the burden of musculoskeletal disorders accounts for 5.6% of lost years of “healthy” life worldwide (GBD, 2017 DALYs and HALE Collaborators, 2018). This Research Topic in Frontiers in Bioengineering and Biotechnology includes 20 peer-reviewed publications that delve into various aspects of this area of study.

Several factors influence the biomechanical regulation of the musculoskeletal system, including muscle strength, muscle flexibility, joint stability, and joint range of motion (ROM). By understanding these factors, researchers can develop interventions to improve the overall function of the musculoskeletal system. Ching et al. focused on simulating the mechanical and recurrent sprain injuries in chronic ankle instability (CAI) patients, and established a new ankle instability model with multiple ankle injuries using a self-designed machine to sprain the ankle with a controlled inversion angle and speed. This model provided a better understanding of the mechanical factors that contribute to ankle instability, and highlighted that multiple mechanical sprains are a good model for investigating the mechanisms of CAI induced by recurrent sprain injuries. Li et al. explored the biomechanical analysis of oblique-pulling manipulation in treating sacroiliac joint (SIJ) dysfunction. This study showed that pubic symphysis is essential to restrict SIJ motion, and the oblique-pulling manipulation could cause a weak nutation and separation of SIJ. The study highlighted the effects of stretching and loosening of surrounding ligaments in treating SIJ dysfunction. Han et al. performed the biomechanical and clinical study of rod curvature in single-segment posterior lumbar interbody fusion. This study evaluated the effect of rod contouring on single-segment posterior lumbar interbody fusion using the finite element method and retrospective study. The findings of the study have significant implications for the design of spinal implants and the treatment of spinal disorders. Zhang et al. evaluated the biomechanical effects of a novel anatomic titanium mesh cage for single-level anterior cervical corpectomy and fusion using finite element analysis. This study demonstrated the potential benefits of this implant in decreasing the risks of titanium mesh cage subsidence, instrument-related complications, and adjacent segment degeneration after surgery. The study highlighted the importance of biomechanical regulation in the design of cervical spinal implants. Zou et al. focused on the distal humeral trochlear geometry associated with the spatial variation of the dynamic elbow flexion axis. They investigated the relationship between distal humeral trochlear geometry and *in vivo* spatial variation of the dynamic flexion axis. By studying 10 healthy subjects, they found that medial and lateral trochlear sizes could be the key parameters affecting the elbow joint flexion function, highlighting the potential for designing custom implants to improve joint function. Wen et al. explored the relationship between bearing extrusion and postoperative persistent pain in Oxford unicompartmental knee arthroplasty. The study evaluated the biomechanical factors that contribute to bearing extrusion and postoperative pain in patients with knee arthroplasty, highlighting the improvement in bearing movement trajectory in potential beneficial treatment of knee disorders. Wang et al. investigated the biomechanical relationship between posterosuperior rotator cuff tear (PSRCT) size and shoulder abduction function using cadaveric shoulders. These biomechanical testing suggested that the weight-bearing ability of the shoulder significantly decreased as PSRCT progressed. Chang et al. compared the muscle activation patterns and spinal kinematics between the hand-foot kneeling (HFK) position used in the traditional Chinese exercise Wuqinxi and the four-point hand-knee kneeling (HKK) position commonly used for core stabilization exercises. This study suggested that HFK was more effective for strengthening abdominal muscles, while HKK was more effective for strengthening lumbar muscles and increasing spine mobility, providing evidence for selecting specific exercises and developing individualized training programs.

Another exciting area of research that is highlighted in this Research Topic is the use of novel materials and technologies for the treatment of musculoskeletal disorders. For instance, Orth et al. evaluated the use of novel mineral-coated microparticles for spatiotemporal controlled delivery of VEGF and BMP-2, which showed great potential to improve bone healing in atrophic non-unions by promoting angiogenesis and osteogenesis as well as reducing early osteoclast activity. Ran et al. described a new method for bone preparation in total knee arthroplasty using an ultra-pulsed CO_2 laser osteotomy system, which was shown to preserve natural bone structure and improve cell adhesion compared to traditional mechanical saws. This study suggested the promising application of ultra-pulsed CO_2 laser in total knee arthroplasty (TKA) bone preparation, offering non-invasive bone cutting and long-term biological fixation. Besides these original articles, Wang et al. reviewed the application of iron oxide nanoparticles for bone regeneration in recent years, and outlined the mechanisms of iron oxide nanoparticles in bone tissue regeneration in detail based on the physicochemical properties, structural characteristics and safety of iron oxide nanoparticles. This review demonstrated the potential of these nanoparticles in enhancing bone growth and regeneration, highlighting the importance of biochemical regulation in the treatment of bone disorders.

Biochemical regulation, on the other hand, is controlled by various hormones, signaling pathways and growth factors, including VEGF, BMP-2, P1NP, and HbA1c. These substances play a crucial role in regulating the growth, development, and maintenance of the musculoskeletal system. For instance, Zheng et al. demonstrated that activating the Sirt1-autophagy signaling network through the pulsed electromagnetic field (PEMF) therapy can alleviate intervertebral disc degeneration, thereby protecting extracellular matrix (ECM) and reducing intervertebral disc (IVD) degeneration. This finding highlights the critical role of Sirt1-dependent autophagy signaling pathway in ECM protection, and the establishment of therapeutic effect of PEMF on IVD degeneration.

Recent research has focused on the interplay between biomechanical and biochemical regulation of the musculoskeletal system. It has been discovered that mechanical loading can influence the expression of certain genes that regulate muscle growth and repair. Furthermore, biochemical signals can also affect the biomechanical properties of the musculoskeletal system, including the stiffness and strength of bone and connective tissue. For example, Jia et al. focused on the prediction of femoral strength based on bone density and biochemical markers in elderly men with type 2 diabetes mellitus, which illustrated the interplay between biomechanical and biochemical regulation in the treatment of musculoskeletal disorders.

Another fascinating aspect of this Research Topic is the use of computational models to gain insight into the biomechanical and biochemical regulation of the musculoskeletal system. Jeong et al. evaluated the optimal surgical plan for the treatment of extraocular muscle damage in thyroid eye disease patients based on finite element analysis. This study highlighted the potential benefits of using finite element model in designing surgical interventions to reduce damage to the extraocular muscle during treatment strategies. Similarly, Jia et al. focused on the prediction of femoral strength based on bone density and biochemical markers in elderly men with type 2 diabetes mellitus. This study showed how computational models can be used to assess the risk of bone fractures and guide clinical decision-making. Wang et al. investigated the biomechanical effects of medial meniscus radial tears on the knee joint during gait using a finite element model. This study demonstrated that radial tears with larger widths could lead to high stress concentrations, contributing to a better understanding of meniscal tear-induced biomechanical changes during human activities and potential surgical guidance of meniscectomies and the prophylaxis and treatment of OA. Fang et al. used computational kinematic simulations to investigate the effect of different rotational alignments of the tibial component on knee kinematics after total knee arthroplasty. The results showed that moderate external rotation of the tibial component generated more natural knee kinematics than internal rotation or neutral position of the tibial component. Pei et al. investigated the kinematic and biomechanical effects of spinal distraction surgery in children with early onset scoliosis using 3D finite element analysis. This study revealed that traditional bilateral fixation can cause spinal re-imbalance and unexpected cervical lordosis and lateral displacement, and that more attention should be paid to spinal kinematic and biomechanical changes, providing a better understanding of spinal distraction surgery. Wu et al. proposed a principal-strain criterion to evaluate the safety of the fixation construct in cervical kyphosis correction and validates it against a retrospective case of anterior cervical discectomy fusion (ACDF), using finite element model. This study suggested that the ACDF restricted the ROM of cervical segments and lent stability to vertebra fusion, and the shape of the anterior cervical plate conforming to the curvature of the vertebra and screws fully inserted into vertebrae reduced the deformation concentration around the screw trajectories. Zeng et al. used finite element analysis to investigate the stability of internal fixation systems in different subtypes of Schatzker II fracture of the tibial plateau, and found that the use of fillers at the defect site can effectively reduce stress concentration of the implant and loss of the collapsed block, providing good stability for the fracture. This study highlighted finite element analysis as a powerful tool to help improve clinical outcomes.

In conclusion, the articles in this Frontiers Research Topic provide valuable insights into the biomechanical and biochemical regulation of the musculoskeletal system. The studies highlight the mechanical, biochemical factors, and the complex interplay between them in the maintenance of musculoskeletal health and the development of musculoskeletal disorders. The findings of these studies have important implications for the development of new treatments and therapies for musculoskeletal disorders, as well as for the design of prosthetics and orthotics. The use of novel materials, technologies, and computational models is also an exciting area of research that has the potential to revolutionize the field of musculoskeletal biomechanics. Overall, the articles in this Research Topic represent a significant contribution to the field of bioengineering and biotechnology and will be of great interest to researchers, clinicians, and engineers working in this area. The primary challenges within the field of Biomechanical and Biochemical Regulation of the Musculoskeletal System involve deciphering the mechanisms behind musculoskeletal injuries and diseases, enhancing prevention and treatment approaches, and investigating the interplay between mechanical forces and biochemical signaling pathways. In order to tackle these Research Topic, future studies will employ cutting-edge imaging, computational modeling, molecular biology methods, clinical trials, and interdisciplinary partnerships.

Author contributions

All authors listed have made a substantial, direct, and intellectual contribution to the work and approved it for publication.

Funding

The authors acknowledge partial support from the National Natural Science Foundation of China (11602046, 31470902), the Natural Science Foundation of Chongqing, China (CSTB2022NSCQ-MSX0110), the Program for Youth Innovation in Future Medicine, Chongqing Medical University (W0046).

Acknowledgments

The authors wish to thank all the contributors of the Research Topic, reviewers and the Editorial Office of Frontiers in Bioengineering and Biotechnology for the helpful advice during the management of the submitted manuscripts.

Conflict of interest

The authors declare that the research was conducted in the absence of any commercial or financial relationships that could be construed as a potential conflict of interest.

Publisher's note

Reference

GBD 2017 DALYs and HALE Collaborators (2018). Global, regional, and national disability-adjusted life-years (DALYs) for 359 diseases and injuries and healthy life expectancy (HALE) for 195 countries and territories, 1990-2017: A systematic analysis for the global burden of disease study 2017. *Lancet* 392 (10159), 1859–1922. doi:10.1016/S0140-6736(18)32335-3

frontiers in Bioengineering and Biotechnology

ORIGINAL RESEARCH
published: 11 January 2022
doi: 10.3389/fbioe.2021.809397

Local Application of Mineral-Coated Microparticles Loaded With VEGF and BMP-2 Induces the Healing of Murine Atrophic Non-Unions

M. Orth[1,2]*, T. Fritz[1], J. Stutz[1,2], C. Scheuer[2], B. Ganse[1,3], Y. Bullinger[1], J. S. Lee[4], W. L. Murphy[4], M. W. Laschke[2], M. D. Menger[2] and T. Pohlemann[1]

[1]Department of Trauma, Hand and Reconstructive Surgery, Saarland University, Homburg, Germany, [2]Institute for Clinical and Experimental Surgery, Saarland University, Homburg, Germany, [3]Werner Siemens Endowed Chair of Innovative Implant Development (Fracture Healing), Saarland University, Homburg, Germany, [4]Department of Biomedical Engineering, University of Wisconsin-Madison, Madison, WI, United States

Edited by:
Bin Wang,
Chongqing Medical University, China

Reviewed by:
Ramesh Subbiah,
Oregon Health and Science University, United States
Yanfeng Luo,
Chongqing University, China

***Correspondence:**
M. Orth
marcel.orth@uks.eu

Specialty section:
This article was submitted to Biomechanics, a section of the journal Frontiers in Bioengineering and Biotechnology

Received: *04 November 2021*
Accepted: *23 December 2021*
Published: *11 January 2022*

Citation:
Orth M, Fritz T, Stutz J, Scheuer C, Ganse B, Bullinger Y, Lee J, Murphy WL, Laschke MW, Menger MD and Pohlemann T (2022) Local Application of Mineral-Coated Microparticles Loaded With VEGF and BMP-2 Induces the Healing of Murine Atrophic Non-Unions. Front. Bioeng. Biotechnol. 9:809397. doi: 10.3389/fbioe.2021.809397

Deficient angiogenesis and disturbed osteogenesis are key factors for the development of nonunions. Mineral-coated microparticles (MCM) represent a sophisticated carrier system for the delivery of vascular endothelial growth factor (VEGF) and bone morphogenetic protein (BMP)-2. In this study, we investigated whether a combination of VEGF- and BMP-2-loaded MCM (MCM + VB) with a ratio of 1:2 improves bone repair in non-unions. For this purpose, we applied MCM + VB or unloaded MCM in a murine non-union model and studied the process of bone healing by means of radiological, biomechanical, histomorphometric, immunohistochemical and Western blot techniques after 14 and 70 days. MCM-free non-unions served as controls. Bone defects treated with MCM + VB exhibited osseous bridging, an improved biomechanical stiffness, an increased bone volume within the callus including ongoing mineralization, increased vascularization, and a histologically larger total periosteal callus area consisting predominantly of osseous tissue when compared to defects of the other groups. Western blot analyses on day 14 revealed a higher expression of osteoprotegerin (OPG) and vice versa reduced expression of receptor activator of NF-κB ligand (RANKL) in bone defects treated with MCM + VB. On day 70, these defects exhibited an increased expression of erythropoietin (EPO), EPO-receptor and BMP-4. These findings indicate that the use of MCM for spatiotemporal controlled delivery of VEGF and BMP-2 shows great potential to improve bone healing in atrophic non-unions by promoting angiogenesis and osteogenesis as well as reducing early osteoclast activity.

Keywords: non-union, mineral-coated microparticles, VEGF, BMP-2, bone healing, fracture

INTRODUCTION

Despite growing knowledge about the process of bone healing, 5–10% of all fractures still fail to heal (Buza and Einhorn, 2016). The resulting burden for patients and the socioeconomic consequences of non-unions are a major clinical problem (Bishop et al., 2012; Buza and Einhorn, 2016). Key factors for delayed fracture healing and development of non-unions are known to be a deficient angiogenesis and disturbed osteogenesis (Kanczler and Oreffo, 2008). In clinical practice, the gold-standard for the treatment of non-unions is still the transplantation of autologous bone tissue. However, this procedure does not guarantee adequate bone healing and bears the risk of a number of complications, such as donor-site morbidity, infections and additional pain (Pelissier et al., 2003; Yoneda et al., 2005).

To prevent patients from such complications and to improve the fusion rate of not healing fractures, artificial bone substitutes have been developed. Lately, these materials have been optimized by combining osteoconductive and osteoinductive properties in order to support natural bone growth and to induce new bone formation (Fillingham and Jacobs, 2016). Among others, mineral-coated microparticles (MCM) were developed to enable a biomimetic, tunable growth factor delivery (Yu et al., 2014). MCM are biocompatible, can easily be applied to a fracture site by injection, and allow for a controllable binding and spatiotemporal controlled release of growth factors (Yu et al., 2014; Yu et al., 2017). Furthermore, MCM have been analyzed in detail regarding binding and release kinetics for vascular endothelial growth factor (VEGF) and bone morphogenetic protein (BMP)-2 (Yu et al., 2014).

VEGF is a well-known key regulator of physiological angiogenesis during embryogenesis and skeletal growth (Ferrara et al., 2003), whereas BMP-2 promotes differentiation of mesenchymal stem cells and osteoprogenitor cells into osteoblasts and thereby acts osteogenic (Cheng et al., 2003). The application of these growth factors using MCM as a carrier system previously demonstrated improved osseous bone formation in non-unions (Orth et al., 2017; Orth et al., 2019).

Based on these promising previous findings, we herein hypothesized that the combined application of MCM loaded with VEGF and BMP-2 may improve bone healing in atrophic non-unions. To test our hypothesis, we administered MCM loaded with VEGF and BMP-2 with a ratio of 1:2 in a well-established murine non-union model and studied the healing process by means of radiological, biomechanical, histomorphometric and Western blot techniques throughout an observation period of 70 days.

MATERIALS AND METHODS

Preparation of MCM

MCM were prepared by incubating 100 mg hydroxyapatite particles (Biotal LTD., Derbyshire, United Kingdom) in 50 ml modified simulated body fluid (mSBF) at 37°C for 7 days, as described previously (Yu et al., 2014; Orth et al., 2017; Orth et al., 2019). The mSBF contains the similar ionic constituents to human plasma with doubled concentration of calcium and phosphate ions to promote mineral growth. It was prepared by adding the following reagents (Thermo Fisher Scientific, Waltham, United States) into deionized water in the order shown: 141 mM NaCl, 4.0 mM KCl, 0.5 mM $MgSO_4$, 1.0 mM $MgCl_2$, 4.2 mM $NaHCO_3$, 20.0 mM HEPES, 5.0 mM $CaCl_2$, and 2.0 mM KH_2PO_4, and the pH was adjusted to 6.80. During the preparation process, the mSBF was changed daily to maintain consistent ion concentrations for mineral coating growth on the particles. After the incubation period, the coated microparticles were rinsed with deionized water and lyophilized. Morphological and elemental analyses were carried out before and after coating using LEO 1530 field emission scanning microscopy (FE-SEM; Zeiss, Oberkochen, Germany) and energy dispersive spectrometer (EDS) equipped on FE-SEM, respectively. Transmission FT-IR was performed by a Nicolet iS50R FT-IR spectrometer (Thermo Fisher Scientific) to characterize chemical composition, and ImageJ software (National Institutes of Health, Bethesda, United States) was used to determine the size of hydroxyapatite particles and MCM based on SEM images.

Binding of VEGF and BMP-2 to MCM

MCM were either loaded with recombinant human (rh) VEGF or rhBMP-2 (ImmunoTools GmbH, Friesoythe, Germany). For loading with VEGF, 1 mg MCM was incubated in 1 ml PBS containing 21.7 µg VEGF at 37°C for 4 h. This resulted in a VEGF concentration of 10 µg/mg MCM for the *in vivo* experiments (Orth et al., 2019). The applied amount of VEGF was chosen upon previous studies assessing the effect of VEGF on bone healing in rodents (Street et al., 2002; Ogilvie et al., 2012; Amirian et al., 2015; Orth et al., 2019). For loading with BMP-2, 1 mg MCM was incubated in 1 ml PBS containing 34 µg BMP-2 at 37°C for 4 h. This resulted in a BMP-2 concentration of 20 µg/mg MCM for the *in vivo* experiments (Yu et al., 2014; Orth et al., 2017). After binding either VEGF or BMP-2 on separate microparticles, the loaded MCM were centrifuged for 3 min and then washed once with PBS. For the application *in vivo*, 2 mg MCM in total, of which each microparticle was either loaded with VEGF or BMP-2, was used.

Animals

A total of 72 CD-1 mice with a body weight of 30 ± 5 g and an age of 9–14 weeks were used. The animals were bred at the Institute for Clinical and Experimental Surgery, Saarland University, Germany, kept at a regular light and dark cycle and had free access to tap water and standard pellet food (Altromin, Lage, Germany). The study was conducted in accordance with the German legislation on protection of animals and the NIH Guidelines for the Care and Use of Laboratory Animals and was approved by the local governmental animal protection committee (permission number: 53/2013).

Surgical Procedure

For the present study a well-established femoral atrophic non-union model was used, as described previously in detail (Garcia et al., 2008). For the surgical procedure, the mice were anesthetized by an intraperitoneal injection of ketamine (75 mg/kg body weight; Pharmacia, Erlangen, Germany) and xylazine 2% (25 mg/kg body weight; Bayer, Leverkusen, Germany). Briefly, an incision medial to the patella was performed at the right knee and the patella was dislocated laterally. After exposing the intercondylar notch, a hole was drilled between the femoral condyles to insert a distally flattened pin through the intramedullary canal. After implantation of the pin, the diaphysis of the femur was exposed and an approximately 6 mm clip was inserted into the femur. Subsequently, an osteotomy with a gap size of 1.8 mm was created between the two brackets of the metallic clip. Inserting the clip before creation of the gap guaranteed that the gap size was maintained. Finally, the periosteum was stripped 2 mm proximally and distally of the gap.

Animals of the group MCM + VB (n = 24) received 1 mg MCM loaded with a total of 10 μg VEGF and 1 mg MCM loaded with a total of 20 μg BMP-2 by direct injection into the osteotomy gap without any further carrier material. Of interest, we could previously show that MCM without physical support do not dissolve and can still be detected at the site of implantation in our non-union model even after 70 days (Orth et al., 2017). Animals of the group MCM (n = 24) received 2 mg growth factor-free MCM under the same conditions. The animals of the control group (n = 24) received no MCM, leaving the osteotomy gap empty. Finally, wound closure completed the surgical procedure.

Animals were sacrificed on day 14 (n = 12 each group) or 70 (n = 12 each group) postoperatively. Directly prior to sacrifice, X-rays of the operated femurs were taken to exclude secondary dislocation of the metallic implants. Femurs were harvested and used for further analyses.

Biomechanical Analysis

After removal of the pin and the clip as well as the surrounding soft tissue, 3-point-bending stiffness of the osteotomized femurs was measured (*n* = 8 each group; Mini-Zwick Z 2.5, Zwick, Ulm, Germany), as described previously (Orth et al., 2017; Orth et al., 2019). Using this non-destructive approach for biomechanical analyses, the femurs could also be used for subsequent micro-computed tomography (μCT) and histological investigations, resulting in a marked reduction of required animals. To account for differences in bone strength of individual animals, the non-osteotomized left femora were also analyzed and served as internal controls.

μCT

The femurs (n = 8 each group) were scanned (Skyscan 1176, Bruker, Billerica, United States) at a spatial resolution of 9 μm with a standardized setup, as described previously (Orth et al., 2017; Orth et al., 2019). To express gray values as mineral content (bone mineral density; BMD), calcium hydroxyapatite (CaHA) phantom rods with known BMD values were used for calibration. On each transversal slide the region of interest (ROI) was contoured manually defining exclusively novel bone and excluding original cortical bone and the applied MCM. The ROI was processed with a threshold procedure (CTAnalyzer, Bruker), which allowed for differentiation between highly and poorly mineralized bone. The thresholds to distinguish between highly and poorly mineralized bone were based on visual inspection of the images, qualitative comparison with histological sections and other studies investigating bone repair and callus tissue by μCT (Isaksson et al., 2009; Morgan et al., 2009; Bosemark et al., 2013). A BMD with more than 0.642 g/cm^3, resulting in gray values of 98–255, was defined as high mineralized bone. Low mineralized bone was assumed to have a BMD value between 0.410 g/cm^3 and 0.642 g/cm^3, resulting in gray values of 68–97. A BMD with more than 0.41 g/cm^3, resulting in gray values of 68–255, was defined as total mineralized bone.

The following radiological parameters were calculated from the callus region of interest for each specimen: High mineralized bone volume (BV$_{high}$; mm^3), low mineralized bone volume (BV$_{low}$; mm^3) and average bone mineral density for mineralized bone (BMD; g hydroxyapatite(HA)/cm^3). The BMD was calculated by using the voxels within the aforementioned thresholds.

Histology and Histomorphometry

After biomechanical testing and μCT analyses, bones were fixed in 4% phosphate-buffered formalin for 24 h and decalcified in ethylenediaminetetraacetic acid (EDTA) solution for several weeks. After embedding decalcified bones in paraffin, longitudinal sections with a thickness of 5 μm were stained with Safranin-O (n = 8 each group). At a magnification of ×12.5 (Olympus BX60 Microscope, Olympus, Shinjuku, Japan; Zeiss Axio Cam and Axio Vision 3.1, Zeiss, Jena, Germany) structural indices were calculated based on the recommendations of Gerstenfeld et al. (Gerstenfeld et al., 2005). For histomorphometric evaluation the following parameters were measured: 1) total periosteal callus area, 2) bone callus area, 3) cartilaginous callus area and 4) fibrous callus area. The total periosteal callus area was defined as all osseous, cartilaginous and fibrous callus tissue outside of the cortices. Pre-existing cortical bone and endosteal callus formation were excluded as it may have been affected by the intramedullary pin. Each area was marked and calculated using the ImageJ Analysis System.

Additionally, a scoring system was used to evaluate the quality of gap bridging on both postoperative time points, as described previously (Orth et al., 2017). This scoring system allowed a maximum of four points that indicated complete osseous bridging of the non-union, while zero points indicated the absence of osseous or cartilaginous bridging of the gap.

Immunohistochemistry

Longitudinal sections of the femora were co-stained with a monoclonal rat anti-mouse antibody against CD31 (1:100; Abcam, Cambridge, United Kingdom), while a goat anti-rat IgG antibody (Invitrogen, Waltham, United States) served as secondary antibody. Cell nuclei were stained with Hoechst 33342 (2 μg/ml; Sigma-Aldrich, Taufkirchen, Germany). The number of CD31-positive (C31$^+$) microvessels in animals of the groups control, MCM and MCM + VB at 14 and 70 days postoperatively was counted at a magnification of ×400 (Olympus BX60 microscope) in the central healing zone of the periosteal callus using two high-power fields (HPF) per specimen.

Western Blot

Protein expression within the callus tissue was determined by Western blot analyses, including the expression of the osteoclast markers osteoprotegerin (OPG) and receptor activator of NF-κB ligand (RANKL), the angiogenic markers erythropoietin (EPO) and EPO-receptor (EPO-R), the osteogenic marker BMP-4 and the proliferation marker proliferating cell nuclear antigen (PCNA). After harvesting callus tissue on post-operative days

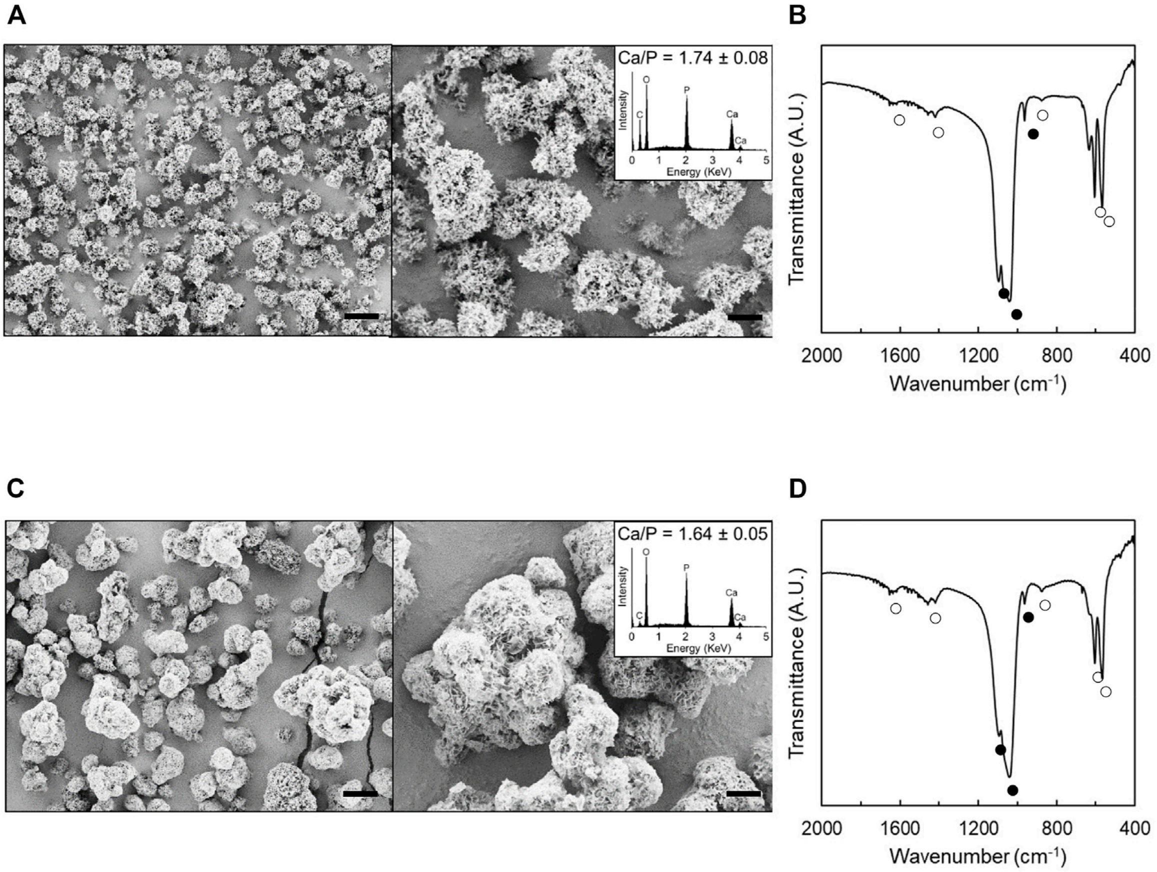

FIGURE 1 | Morphological and compositional analyses of hydroxyapatite particles and MCM. **A, C:** SEM images of hydroxyapatite particles **(A)** and MCM **(C)**. Insets show their EDS spectrum. **B, D:** FT-IR spectra of hydroxyapatite particles **(B)** and MCM **(D)**. ● and ○ denote the peaks associated with phosphate and carbonate, respectively. Scale bars: 5 μm (left images) and 2 μm (right images).

14 (n = 4 each group) and 70 (n = 4 each group), tissue samples were transferred in lysis buffer and stored at −80°C. After saving the whole protein fraction, proteins were separated and transferred to membranes by standard protocols and probed using anti-OPG (Bioss (Biozol), Eching, Germany), anti-RANKL (Abcam), anti-EPO (Santa Cruz Biotechnology, Heidelberg, Germany), anti-EPO-R (Santa Cruz Biotechnology), anti-BMP-4 (Santa Cruz Biotechnology) and anti-PCNA (Dako (Agilent), Hamburg, Germany) antibodies. All antibodies were incubated overnight in concentration of 1: 30 at 4°C and afterwards for 4 h in a concentration of 1:300 at room temperature. The appropriate peroxidase-conjugated anti-IgG antibodies served as secondary antibodies (1:1,000 for 1.5 h, Dako (Agilent)). Protein expression was visualized by means of luminol-enhanced chemiluminescence after exposure of the membrane to the Intas ECL Chemocam Imager (Intas Science Imaging Instrument GmbH, Göttingen, Germany). To correct for unequal loading, signals were normalized to β-actin signals (1: 5,000, Sigma-Aldrich).

Statistics

All data are given as means ± standard error of the mean (SEM). First, data were tested for normal distribution and equal variance. In case of parametric data, comparisons between two experimental groups were performed by an unpaired Student's *t*-test, while analyses of three groups were performed by one-way ANOVA, followed by the Student-Newman-Keuls test for all pairwise comparisons, including the correction of the α-error according to Bonferroni probabilities to compensate for multiple comparisons. In case of non-parametric data, comparisons between two experimental groups were performed by a Mann-Whitney Rank Sum Test, while analyses of three groups were performed by one-way ANOVA on Ranks, followed by a Student-Newman-Keuls test for all pairwise comparisons, which also included the correction of the α-error according to Bonferroni probabilities. The statistical analyses were performed using the SigmaPlot software 13.0 (Systat Software GmbH, Erkrath, Germany). A p-value < 0.05 was considered to indicate significant differences.

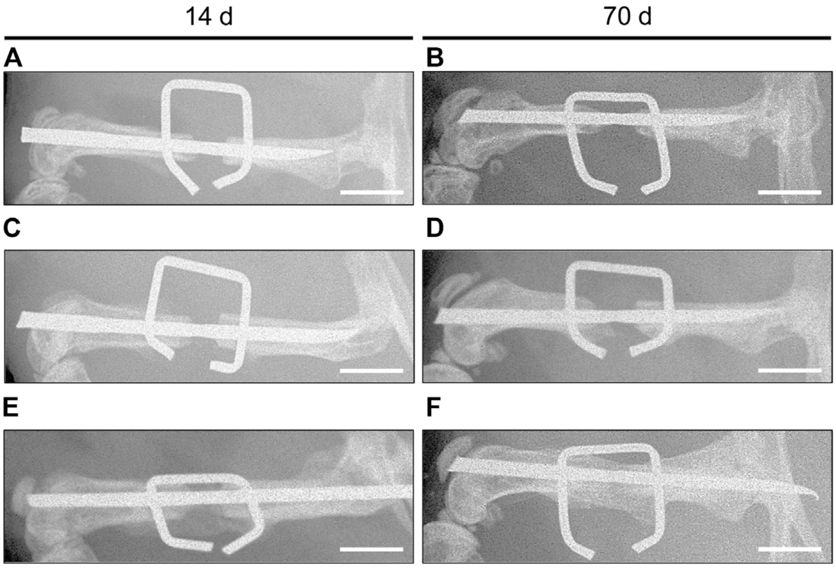

FIGURE 2 | X-ray analysis of mouse femurs. **A-F**: X-rays of osteotomized mouse femurs with a segmental defect of 1.8 mm stabilized by the "pin-clip" technique 14 days **(A, C, E)** and 70 days **(B, D, F)** after osteotomy. Images of control **(A, B)** and MCM **(C, D)** exhibit no osseous bridging with a large persisting gap between the two bone fragments, indicating non-union formation, while images of MCM + VB **(E, F)** show callus formation after 14 days **(E)** and fully osseous bridging after 70 days **(F)**. Note that images of MCM + VB at 70 days **(F)** show signs of remodeling between the brackets of the clip, while images of controls at 70 days **(B)** exhibit that adjoining bone fragments narrowed towards the osteotomy gap as a typical sign for atrophic non-union formation. Scale bars: 2 mm.

RESULTS

MCM Fabrication and Characterization

We created a mineral coating on hydroxyapatite particles by incubation in mSBF. The mineral coating grown on hydroxyapatite particles had a plate-like structure with nanometer scale pores (**Figure 1A,C**). The analysis of SEM images revealed that MCM have an average diameter of 5.5 ± 2.6 μm, which is about 2 μm larger than that of hydroxyapatite particles before coating (3.4 ± 1.0 μm). It is speculated that the mineral coating is ~1 μm in thickness. This result is in agreement with our previous observation by SEM (Yu et al., 2017). The elemental analysis by EDS showed that the calcium to phosphorus ratio (Ca/P) of hydroxyapatite particles (1.74 ± 0.08) is similar to that of MCM (1.64 ± 0.05) (insets, **Figure 1A,C**). FT-IR spectra of uncoated hydroxyapatite particles and MCM showed characteristic peaks associated with phosphate (560–610, 930–1150 cm^{-1}) and carbonate (850–890, 1410–1480, 1640–1700 cm^{-1}) (**Figure 1B,D**) (Lee et al., 2010). The intensity of carbonate peaks from MCM was slightly more prominent compared to those of uncoated hydroxyapatite particles. Taken together, these results demonstrate that the coating of the MCM is plate-like, nanoporous, carbonate-substituted hydroxyapatite.

X-Ray Analysis

X-rays of animals of the control and MCM group showed no osseous bridging with a large persisting gap between the two bone fragments (**Figure 2A–D**), whereas X-rays taken prior to sacrificing showed a radiopaque callus formation after 14 days and fully osseous bridging after 70 days in animals of the MCM + VB group (**Figure 2E,F**). Of interest, X-rays of animals of the MCM + VB group showed a dense and streamlined callus as radiological signs of bone remodeling and indicator of progressive bone healing at 70 days (**Figure 2F**). In contrast X-rays of the control group demonstrated that the form of the adjoining bone fragments narrowed towards the osteotomy gap as a typical sign for atrophic non-union formation (**Figure 2B**).

Biomechanical Analysis

Femurs of the MCM and control group presented practically with no bending stiffness at both time points, which indicates non-union formation in these groups (**Figure 3**). In contrast, femurs of the MCM + VB group exhibited a significantly higher bending stiffness when compared to femurs of the MCM and control group at 14 and 70 days postoperatively (**Figure 3A,B**). Moreover, femurs of the MCM + VB group showed a significant increase of bending stiffness over the study time, indicating bone healing of the non-unions (**Figure 3B**). At 70 days after surgery, bending stiffness of femurs in the MCM + VB group reached approximately 65.8% of that measured for unfractured femurs.

μCT Analysis

μCT analyses revealed a significantly higher formation of high and low mineralized bone tissue on day 14 and 70 in the osteotomy gaps of MCM + VB animals when compared to those of MCM and control animals (**Figure 4A–J**). Of interest, the fraction of high mineralized bone in animals of the MCM + VB group at 14 days was still low and significantly increased over time (**Figure 4G,H**), whereas the fraction of low mineralized bone

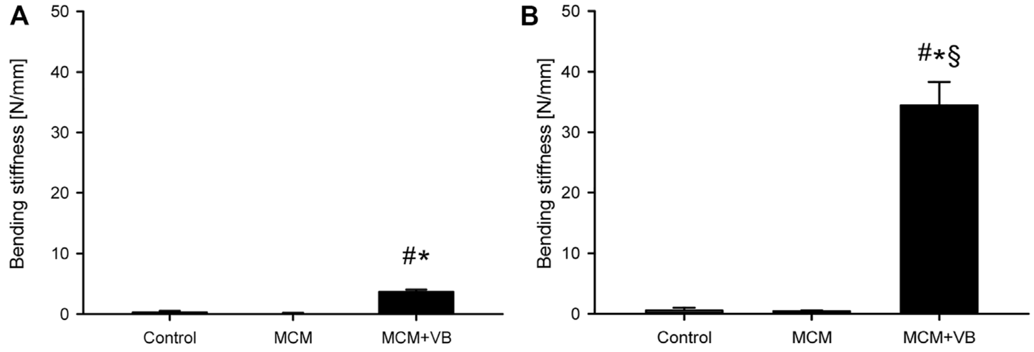

FIGURE 3 | Biomechanical analysis of mouse femurs. **A, B:** Bending stiffness of control ($n = 8$), MCM (n = 8) and MCM + VB (n = 8) femurs 14 days **(A)** and 70 days **(B)** after osteotomy. Mean ± SEM; $^{\#}p < 0.05$ vs control; $^{*}p < 0.05$ vs MCM; $^{\S}p < 0.05$ vs MCM + VB at day 14.

in these animals did not increase in the same period (**Figure 4I,J**). As a sign for mineralization and, thus, remodeling of the callus, the BMD increased in animals of the MCM + VB group during the study period (**Figure 4K,L**).

Histomorphometric Analysis

The histomorphometric analysis on days 14 and 70 after osteotomy demonstrated that the total periosteal callus area of animals of the MCM + VB group was significantly larger than that of animals of the MCM and control group (**Figure 5A–H**). Intergroup comparisons showed no significant difference between the callus area of MCM animals compared to that of controls (**Figure 5G,H**).

Further evaluation of the callus composition revealed at 14 days after osteotomy a significantly increased fraction of osseous tissue and vice versa a reduced fraction of fibrous tissue in animals of the MCM + VB group (**Figure 5A,C,E,I**). This difference in callus composition between the three study groups could also be detected at 70 days after osteotomy (**Figure 5B,D,F,J**). These results indicate an endochondral bone formation process in the MCM + VB group, while the MCM group and controls revealed typical histological signs of atrophic non-unions.

Accordingly, the osseous bridging score after osteotomy was higher in animals of the MCM + VB group than that in animals of the MCM and control group at 14 days (MCM + VB: 2.8 ± 0.7; MCM: 0.0 ± 0.0; control: 0.0 ± 0.0; $p < 0.05$) as well as at 70 days (MCM + VB: 3.7 ± 0.3; MCM: 0.3 ± 0.3; control: 0.0 ± 0.0; $p < 0.05$).

Immunohistochemical Analysis

The immunohistochemical detection of CD31^{+} microvessels in the periosteal callus at 14 and 70 days after surgery revealed significantly more vessels in MCM + VB animals when compared to MCM and control animals (**Figure 6**). This indicates that angiogenesis was improved in MCM + VB animals throughout the study period.

Western Blot Analysis

The Western blot analysis revealed a significantly higher expression of OPG in callus tissue of MCM + VB when compared to callus tissue of MCM and control animals on day 14 after osteotomy (**Figure 7A,C**). On day 70 after surgery, no differences in expression of OPG between the groups could be observed (**Figure 7B,C**). The expression of RANKL was significantly reduced in the callus of MCM + VB animals when compared to that of MCM and controls at 14 days after surgery (**Figure 7A,D**), but did not show significant differences at 70 days (**Figure 7B,D**). The expression of EPO showed no differences between the study groups at day 14 after surgery (**Figure 7A,E**). In contrast, the expression of EPO increased in callus tissue of MCM + VB animals and showed an approximately 8-fold higher expression at day 70 after surgery when compared to callus tissue of MCM and control animals (**Figure 7B,E**). The expression of EPO-R did not show differences between the study groups at 14 days (**Figure 7A,F**). In contrast, its expression was significantly higher in the callus of MCM + VB animals compared to that of MCM and control animals at day 70 after surgery (**Figure 7B,F**). Similar to EPO, the expression of BMP-4 was not different between the groups on day 14 after surgery (**Figure 7A,G**), but demonstrated a significant increase in callus of MCM + VB animals at the late time point and thereby exhibited a significantly higher expression compared to callus tissue of MCM and controls (**Figure 7B,G**). The expression of the proliferation marker PCNA was increased in callus tissue of MCM + VB compared to MCM and controls at both time points (**Figure 7A,B,H**). These findings indicate an expression profile in animals of the groups MCM + VB typical for significantly reduced osteoclast activity at 14 days after surgery and improved vascularization and also enhanced osteogenic activity at 70 days after surgery.

DISCUSSION

The present study demonstrates for the first time the use of MCM as carriers for therapeutic delivery of VEGF and BMP-2 in atrophic non-unions. Our results confirm the hypothesis that the combination of VEGF- and BMP-2-loaded MCM are capable of improving bone repair in a well-established non-union model in mice. This was indicated by radiological signs of osseous

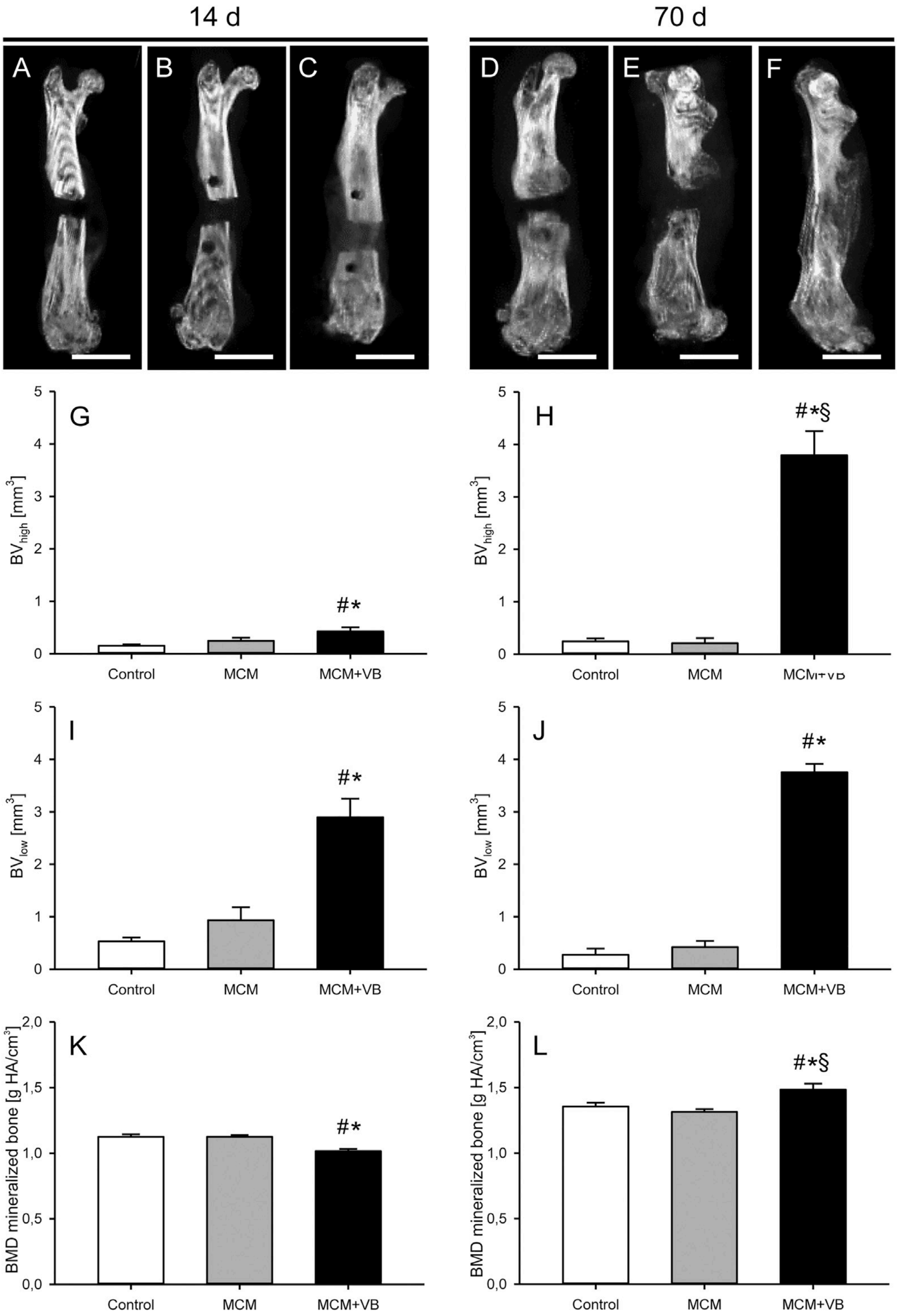

FIGURE 4 | µCT analysis of mouse femurs. **A-F:** µCT images of femurs at 14 days **(A-C)** and 70 days **(D-F)** after surgery of control **(A, D)**, MCM **(B, E)** and MCM + VB **(C, F)** animals. Scale bars: 2 mm. **G, H:** Volume of high mineralized bone (BV$_{high}$) at 14 days **(G)** and 70 days **(H)** after osteotomy within the callus of control (n = 8), MCM (n = 8) and MCM + VB (n = 8) femurs. **I, J**: Volume of low mineralized bone (BV$_{low}$) at 14 days **(I)** and 70 days **(J)** after osteotomy within the callus of control (n = 8), MCM (n = 8) and MCM + VB (n = 8) femurs. **K, L**: BMD of total mineralized bone volume at 14 days **(K)** and 70 days **(L)** after osteotomy within the callus of control (n = 8), MCM (n = 8) and MCM + VB (n = 8) femurs. Mean ± SEM; $^{\#}p < 0.05$ vs control; $^{*}p < 0.05$ vs MCM. $^{§}p < 0.05$ vs MCM + VB at day 14.

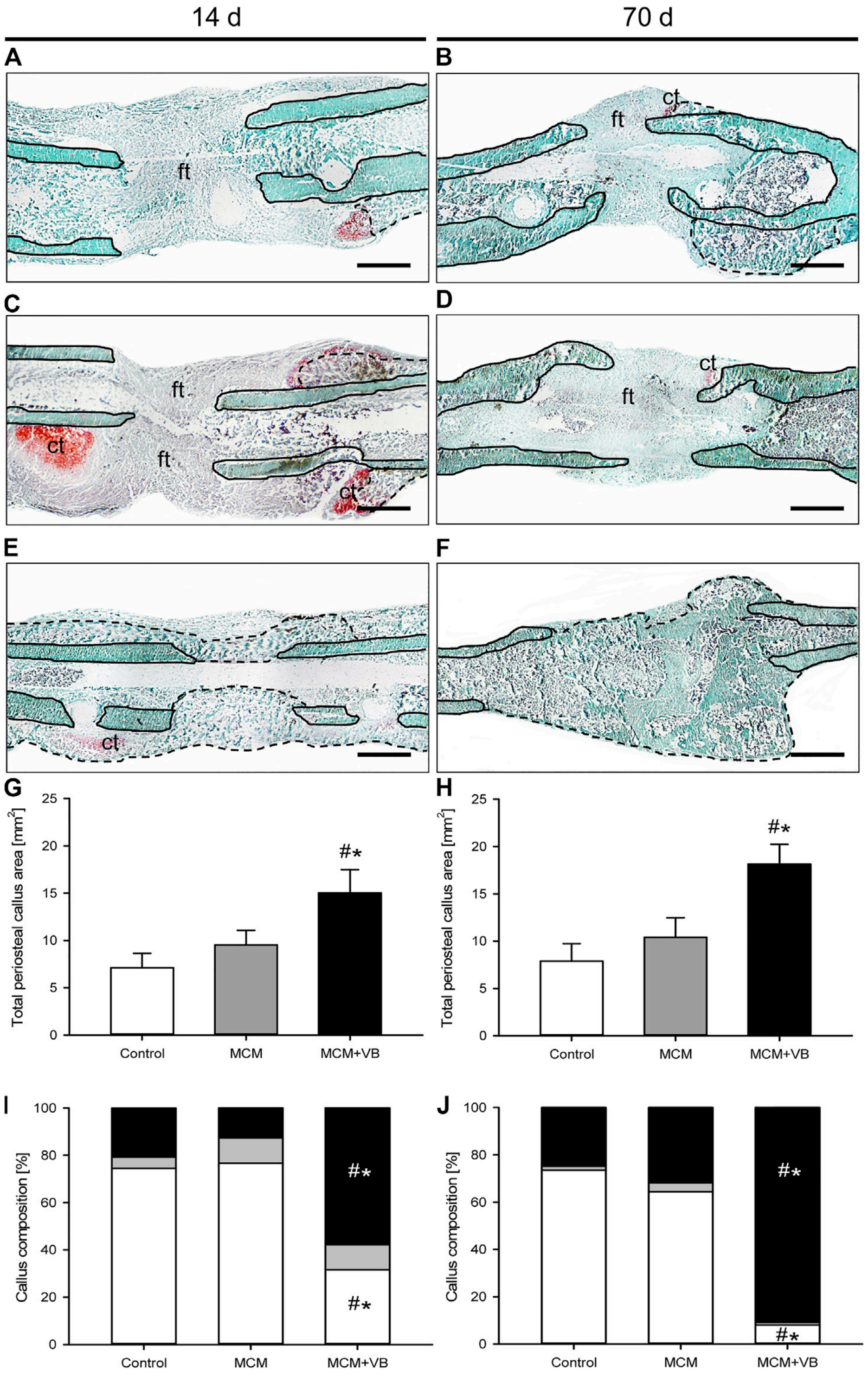

FIGURE 5 | Histomorphometric analysis of mouse femurs. **A-F:** Representative histological images of Safranin-O-stained femurs at 14 days **(A, C, E)** and 70 days **(B, D, F)** after osteotomy of control **(A, B)**, MCM **(C, D)** and MCM + VB **(E, F)** animals. Fibrous tissue (ft), cartilage tissue (ct), native bone (borders marked by solid line), and regenerated bone (borders marked by dashed line) are indicated. Scale bars: 500 µm. **G, H**: Total periosteal callus area of control (n = 8), MCM (n = 8) and MCM + VB (n = 8) femurs at 14 days **(G)** and 70 days **(H)** after osteotomy. **I, J**: Callus composition including fibrous tissue (white), cartilaginous tissue (gray) and osseous tissue (black) of control (n = 8), MCM (n = 8) and MCM + VB (n = 8) femurs at 14 days **(I)** and 70 days **(J)** after osteotomy. Mean ± SEM; $^{\#}p < 0.05$ vs control; $^{*}p < 0.05$ vs MCM.

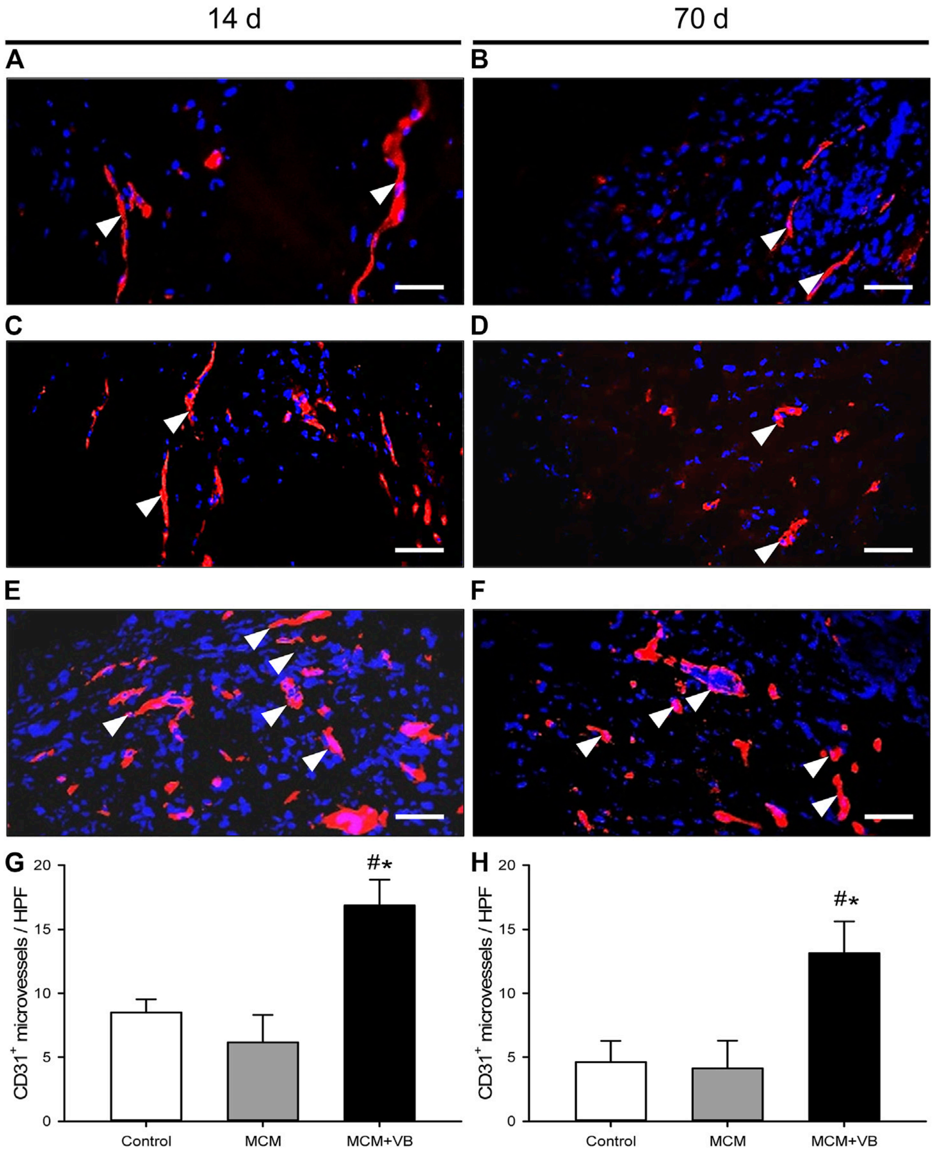

FIGURE 6 | Immunohistochemical analysis of microvessels in the central healing zone of the periosteal callus. **A-F**: Immunohistochemical detection of CD31$^+$ microvessels (arrowheads) within the callus tissue of osteotomized femurs of control **(A, B)**, MCM **(C, D)** and MCM + VB **(E, F)** animals at 14 days **(A, C, E)** and 70 days **(B, D, F)** after osteotomy. Bars represent 50 µm. **G, H:** Number of CD31$^+$ microvessels per HPF of control (n = 4), MCM (n = 4) and MCM + VB (n = 4) femurs at 14 days **(G)** and 70 days **(H)** after osteotomy. Mean ± SEM; $^\#p < 0.05$ vs control; $^*p < 0.05$ vs MCM.

bridging of the osteotomy, an improved biomechanical stiffness, an increased bone volume within the callus, including ongoing mineralization of the new bone during the study period, and a histologically larger total periosteal callus area. These effects can be explained by a reduced osteoclast activity at an early time point and a pro-angiogenic and pro-osteogenic protein expression profile at a late time point, as shown by Western blot analyses of the callus tissue. In fact, the resulting bone formation 70 days after surgery showed nearly full bone healing in MCM + VB animals, as indicated by radiological signs of remodeling, a callus composition consisting predominantly of osseous tissue and a high histological bridging score of the non-unions.

The delivery of growth factors and other bioactive agents by biocompatible carrier systems is difficult due to the susceptibility to denaturation and degradation as well as the heterogenous requirements during binding, cargo and release of the loaded proteins (Yu et al., 2017; Orth et al., 2019). We have developed MCM as a carrier for the controlled protein delivery. MCM were coated by a hydroxyapatite layer having nanostructured porosity (Yu et al., 2017). They have previously been shown to enable robust protein binding by electrostatic interactions between hydroxyapatite mineral surface and the side chains of the loaded proteins. Especially, the large surface area of MCM enables the efficient binding even

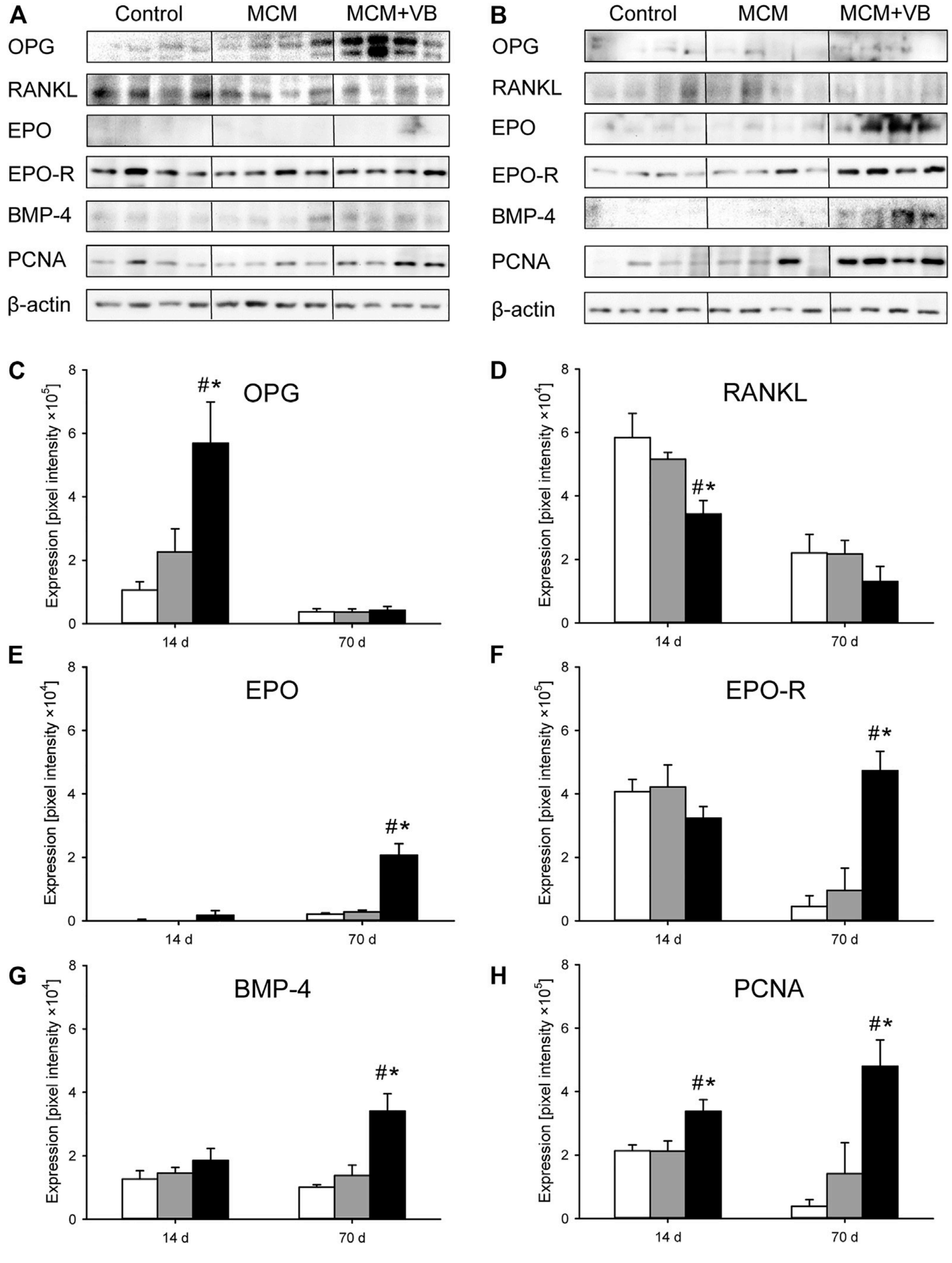

FIGURE 7 | Western blot analysis of callus tissue. **A, B:** Representative Western blots of OPG, RANKL, EPO, EPO-R, BMP-4, PCNA and β-actin expression within the callus tissue of control, MCM and MCM + VB femurs at 14 days **(A)** and 70 days **(B)** after osteotomy. **C-H:** Expression of OPG **(C)**, RANKL **(D)**, EPO **(E)**, EPO-R **(F)**, BMP-4 **(G)** and PCNA **(H)** within the callus tissue of control (white; n = 4), MCM (gray; n = 4) and MCM + VB (black; n = 4) femurs at 14 and 70 days after osteotomy. Mean ± SEM; $^{\#}p < 0.05$ vs control; $^{*}p < 0.05$ vs MCM.

of high amounts of the deliverable protein. We could further systematically modulate the physicochemical properties of mineral coating (e.g., pore size, porosity and dissolution rate) by varying the concentrations of ionic constituents or adding dopants in the mSBF used for the coating solution, which, in turn, dictates the release kinetics of delivered proteins for an extended time period (Lee et al., 2010; Lee et al., 2011; Suárez-González et al., 2012; Yu et al., 2014). In addition, the nanostructured mineral coating of MCM can enhance the stability of bound proteins against external stressors during formulation, storage and release, including organic solvents, proteases, and ethylene oxide gas sterilization (Yu et al., 2017).

Accordingly, MCM allow the controllable binding and spatiotemporal controlled release of a defined quantity of growth factors, and have proved their therapeutic efficacy in various animal models (Yu et al., 2014; Dang et al., 2016; Dang et al., 2016b; Orth et al., 2017; Yu et al., 2017; Clements et al., 2018; Hellenbrand et al., 2019; Orth et al., 2019; Hellenbrand et al., 2021). In particular, our previous studies showed that MCM can bind VEGF and BMP-2 with high affinity and release them over 50 days in a sustained manner (Orth et al., 2017; Orth et al., 2019).

The modulation of bone healing to prevent or to treat non-unions represents a major challenge. In fact, the effect of additional application of VEGF to BMP-2 on bone healing is discussed controversially in the literature. It has recently been shown that the simultaneous or tunable co-delivery of low-dose BMP-2 and VEGF fails to fully restore the mechanics of bone in a bone defect model (Subbiah et al., 2020). Moreover, Samee et al. (2008) found that human periosteum-derived cells transfected with BMP-2 and VEGF *in vitro* do not show more bone formation at 8 weeks after implantation than human periosteum-derived cells transfected only with BMP-2. On the other hand, several studies could demonstrate that the co-application of VEGF and BMP-2 significantly improves bone regeneration when compared to single application of BMP-2 (Luo et al., 2012; Çakır-Özkan et al., 2017; Liu et al., 2020). The application of MCM loaded only with VEGF has been demonstrated to improve bone healing in a previous study using the identical murine non-union model (Orth et al., 2019). However, bone healing was still incomplete 70 days after surgery, as indicated by low values of bending stiffness, a low osseous bridging score and limited osseous tissue within the callus (Orth et al., 2019). The application of MCM loaded only with BMP-2 also resulted in improved bone healing with a high osseous bridging rate and increased osseous tissue fraction within the bone defects (Orth et al., 2017). However, the bending stiffness of the treated bones exhibited only 36% of that measured for unfractured femurs. Furthermore, there were no signs of bone remodeling in X-ray analyses, as observed in the present study. We have previously demonstrated that a hydrogel loaded with microvascular fragments as a potent angiogenic biomaterial may have beneficial effects on angiogenesis during the course of bone healing (Orth et al., 2018). However, we could show that sole support of angiogenesis may even lead to impaired bone healing (Orth et al., 2018). Therefore, the local application of a biomaterial to a non-union needs to respect the diverse interplay of all protagonists within the callus *in vivo* and should address both, angiogenesis and osteogenesis, in order to have a beneficial effect on the healing course (Orth et al., 2018; Orth et al., 2019; Muire et al., 2020). In line with this view, the combined application of VEGF and BMP-2 by MCM herein resulted in an improved bone healing and vascularization of the callus, as demonstrated by radiological signs of remodeling, high absolute and relative bending stiffness, a callus composition consisting predominantly of osseous tissue, and an increased number of microvessels in the callus tissue.

Based on these promising results, it may be speculated that the ratio of VEGF to BMP-2 applied to the defect site plays a crucial role for the healing process. Of interest, Peng et al. demonstrated that a lower ratio of VEGF to BMP-2 promotes bone regeneration (Peng et al., 2005). In line with these findings, we herein demonstrated that a ratio of VEGF to BMP-2 of 1:2 is beneficial for the healing of non-unions. Other studies analyzing the ratio of VEGF- to BMP-2-transfected adipose stem cells on bone healing reported that an even greater shift of 1:9 towards BMP-2 enhances osteogenesis and angiogenesis (Lee et al., 2019). Therefore, we feel that the ratio of VEGF to BMP-2 is of pivotal importance and should be analyzed in more detail in future studies to find an optimal stimulation of angiogenesis and osteogenesis for the treatment of non-unions.

Angiogenesis and osteogenesis are essential for a successful bone healing process and are tightly coupled (Kanczler and Oreffo, 2008; Rather et al., 2019). Angiogenesis is regulated by hypoxia-inducible transcription factors as a physiological response to hypoxic conditions. VEGF itself can act as a hypoxic-like signal during normoxia and serves to induce the expression of EPO (Bellomo et al., 2006; Orth et al., 2019). EPO is a cytokine that is known to improve endochondral ossification and mechanical strength via EPO-R signaling (Holstein et al., 2007). Moreover, VEGF has further direct osteoanabolic effects and induces a chemotactic response by binding on VEGF-receptor one on osteoblasts and serves to secrete osteoanabolic factors by stimulating endothelial cells (Wang et al., 1997; Bouletreau et al., 2002; Beamer et al., 2010). Among others, osteogenesis is further regulated by BMPs, which are well-known to exert an osteogenic effect (Cheng et al., 2003; Chen et al., 2004; Mandal et al., 2016). Of interest, the effect of BMPs and VEGF seems to be reciprocally reinforcing. According to previous studies, VEGF application has shown to potentiate the healing response of BMPs (Cui et al., 2013; Hankenson et al., 2015). BMP-4, in turn, increases the secretion of VEGF (Rivera et al., 2013). Of interest, Western blot analyses in the present study indicated that VEGF and BMP-2 upregulates pro-angiogenic EPO and EPO-R as well as pro-osteogenic BMP-4 at 70 days after surgery. Hence, it may be speculated that the application of MCM loaded with VEGF and BMP-2 synergistically stimulate angiogenesis and osteogenesis with respect to the events during the healing course and promote the substantiated positive effect on bone healing in this challenging non-union model.

Despite angiogenesis and osteogenesis, osteoclast activity is also important during the process of bone healing. As described previously, RANKL is a potent stimulator of bone resorption by binding receptor activator of NF-κB (RANK) in the cell membrane of osteoclasts (Boyce and Xing, 2008). It has been shown that an increased number of osteoclasts may impair bone healing due to a shift of the RANKL/OPG ratio within the callus during the early phase of bone healing (Orth et al., 2018). In contrast, in the present study the expression of

OPG was increased, while the expression of RANKL was low at an early time point after surgery and, thus, shifting the ratio of RANKL to OPG towards OPG. As described elsewhere, this ratio is similarly modified with anti-RANKL treatment by OPG and leads to improved implant fixation and stability in bone (Bernhardsson et al., 2015). Moreover, the application of OPG as a systemic RANKL inhibitor together with BMP-2 enhances bone healing compared to BMP-2 treatment alone in a murine critical-sized femoral defect model (Bougioukli et al., 2016). In line with these findings, the shift of the RANKL/OPG ratio in the present study may have supported the osseous tissue formation by reducing the osteoclast activity during the early phase of bone healing.

In conclusion, the use of MCM for delivery of VEGF and BMP-2 shows a great potential to improve bone healing in atrophic non-unions. In the present study, the combined application of these angiogenic and osteogenic growth factors improved bone healing better than the application of one of these growth factors alone. We found that the ratio of VEGF to BMP-2 seems to be of pivotal importance and that a ratio of 1:2 locally applied to the defect site is beneficial for bone healing in non-unions. This result was most probably due to a synergistic effect of the applied angiogenic and osteogenic growth factors during the course of bone healing and a reduced osteoclast activity in the early phase of bone healing. Therefore, MCM as a carrier and spatiotemporal controlled release system for VEGF and BMP-2 should also be of interest for the treatment of delayed fracture healing and non-unions in clinical practice.

DATA AVAILABILITY STATEMENT

The original contributions presented in the study are included in the article/supplementary material, further inquiries can be directed to the corresponding author.

ETHICS STATEMENT

The animal study was reviewed and approved by Landesamt für Verbraucherschutz Abt. C “Lebensmittel und Veterinärwesen” Zentralstelle Konrad-Zuse-Strasse 11, 66115 Saarbrücken Germany.

AUTHOR CONTRIBUTIONS

MO, TF, JS, CS, YB, JL, WM, ML, MM and TP: Substantial contributions to research design, or the acquisition, analysis or interpretation of data. MO, CS, BG, ML, MM and TP: Drafting the paper or revising it critically. All authors have read and approved the submitted and final version of the manuscript.

ACKNOWLEDGMENTS

We thank Annika Pieper for her excellent contribution during surgical procedure, data acquisition and data analysis. We also thank Janine Becker and Julia Parakenings for their outstanding technical assistance.

REFERENCES

Amirian, J., Linh, N. T. B., Min, Y. K., and Lee, B.-T. (2015). Bone Formation of a Porous Gelatin-Pectin-Biphasic Calcium Phosphate Composite in Presence of BMP-2 and VEGF. *Int. J. Biol. Macromol.* 76, 10–24. doi:10.1016/j.ijbiomac.2015.02.021

Beamer, B., Hettrich, C., and Lane, J. (2010). Vascular Endothelial Growth Factor: an Essential Component of Angiogenesis and Fracture Healing. *HSS Jrnl* 6, 85–94. doi:10.1007/s11420-009-9129-4

Bellomo, M., Marini, H., Adamo, E. B., Catania, M. A., Mannucci, C., Squadrito, F., et al. (2006). Vascular Endothelial Growth Factor Induces Brain Erythropoietin Expression? *Funct. Neurol.* 21, 87–91.

Bernhardsson, M., Sandberg, O., and Aspenberg, P. (2015). Anti-RANKL Treatment Improves Screw Fixation in Cancellous Bone in Rats. *Injury* 46, 990–995. doi:10.1016/j.injury.2015.02.011

Bishop, J. A., Palanca, A. A., Bellino, M. J., and Lowenberg, D. W. (2012). Assessment of Compromised Fracture Healing. *J. Am. Acad. Orthop. Surg.* 20, 273–282. doi:10.5435/JAAOS-20-05-273

Bosemark, P., Isaksson, H., McDonald, M. M., Little, D. G., and Tägil, M. (2013). Augmentation of Autologous Bone Graft by a Combination of Bone Morphogenic Protein and Bisphosphonate Increased Both Callus Volume and Strength. *Acta Orthop.* 84, 106–111. doi:10.3109/17453674.2013.773123

Bougioukli, S., Jain, A., Sugiyama, O., Tinsley, B. A., Tang, A. H., Tan, M. H., et al. (2016). Combination Therapy with BMP-2 and a Systemic RANKL Inhibitor Enhances Bone Healing in a Mouse Critical-Sized Femoral Defect. *Bone* 84, 93–103. doi:10.1016/j.bone.2015.12.052

Bouletreau, P. J., Warren, S. M., Spector, J. A., Steinbrech, D. S., Mehrara, B. J., and Longaker, M. T. (2002). Factors in the Fracture Microenvironment Induce Primary Osteoblast Angiogenic Cytokine Production. *Plast. Reconstr. Surg.* 110, 139–148. doi:10.1097/00006534-200207000-00025

Boyce, B. F., and Xing, L. (2008). Functions of RANKL/RANK/OPG in Bone Modeling and Remodeling. *Arch. Biochem. Biophys.* 473, 139–146. doi:10.1016/j.abb.2008.03.018

Buza, J., and Einhorn, T. (2016). Bone Healing in 2016. *ccmbm* 13, 101–105. doi:10.11138/ccmbm/2016.13.2.101

Çakır-Özkan, N., Eğri, S., Bekar, E., Altunkaynak, B. Z., Kabak, Y. B., Kıvrak, E. G., et al. (2017). The Use of Sequential VEGF- and BMP2-Releasing Biodegradable Scaffolds in Rabbit Mandibular Defects. *J. Oral Maxillofac. Surg.* 75, 221.e1–221.e14. doi:10.1016/j.joms.2016.08.020

Chen, D., Zhao, M., and Mundy, G. R. (2004). Bone Morphogenetic Proteins. *Growth Factors* 22, 233–241. doi:10.1080/08977190412331279890

Cheng, H., Jiang, W., Phillips, F. M., Haydon, R. C., Peng, Y., Zhou, L., et al. (2003). Osteogenic Activity of the Fourteen Types of Human Bone Morphogenetic Proteins (BMPs). *The J. Bone Jt. Surg.-Am. Vol.* 85, 1544–1552. doi:10.2106/00004623-200308000-00017

Clements, A. E. B., Groves, E. R., Chamberlain, C. S., Vanderby, R., and Murphy, W. L. (2018). Microparticles Locally Deliver Active Interleukin-1 Receptor Antagonist *In Vivo. Adv. Healthc. Mater.* 7, 1800263. doi:10.1002/adhm.201800263

Cui, Q., Dighe, A. S., and Irvine Jr, J. N., Jr. (2013). Combined Angiogenic and Osteogenic Factor Delivery for Bone Regenerative Engineering. *Cpd* 19, 3374–3383. doi:10.2174/1381612811319190004

Dang, P. N., Dwivedi, N., Yu, X., Phillips, L., Bowerman, C., Murphy, W. L., et al. (2016). Guiding Chondrogenesis and Osteogenesis with Mineral-Coated Hydroxyapatite and BMP-2 Incorporated within High-Density hMSC Aggregates for Bone Regeneration. *ACS Biomater. Sci. Eng.* 2, 30–42. doi:10.1021/acsbiomaterials.5b00277

Dang, P. N., Dwivedi, N., Phillips, L. M., Yu, X., Herberg, S., Bowerman, C., et al. (2016b). Controlled Dual Growth Factor Delivery from Microparticles Incorporated within Human Bone Marrow-Derived Mesenchymal Stem Cell Aggregates for Enhanced Bone Tissue Engineering via Endochondral Ossification. *Stem Cel. Transl. Med.* 5, 206–217. doi:10.5966/sctm.2015-0115

Ferrara, N., Gerber, H.-P., and LeCouter, J. (2003). The Biology of VEGF and its Receptors. *Nat. Med.* 9, 669–676. doi:10.1038/nm0603-669

Fillingham, Y., and Jacobs, J. (2016). Bone Grafts and Their Substitutes. *Bone Jt. J.* 98-B (1 Suppl. A), 6–9. doi:10.1302/0301-620X.98B.36350

Garcia, P., Holstein, J. H., Maier, S., Schaumlöffel, H., Al-Marrawi, F., Hannig, M., et al. (2008). Development of a Reliable Non-union Model in Mice. *J. Surg. Res.* 147, 84–91. doi:10.1016/j.jss.2007.09.013

Gerstenfeld, L. C., Wronski, T. J., Hollinger, J. O., and Einhorn, T. A. (2005). Application of Histomorphometric Methods to the Study of Bone Repair. *J. Bone Miner Res.* 20, 1715–1722. doi:10.1359/JBMR.050702

Hankenson, K. D., Gagne, K., and Shaughnessy, M. (2015). Extracellular Signaling Molecules to Promote Fracture Healing and Bone Regeneration. *Adv. Drug Deliv. Rev.* 94, 3–12. doi:10.1016/j.addr.2015.09.008

Hellenbrand, D. J., Reichl, K. A., Travis, B. J., Filipp, M. E., Khalil, A. S., Pulito, D. J., et al. (2019). Sustained Interleukin-10 Delivery Reduces Inflammation and Improves Motor Function after Spinal Cord Injury. *J. Neuroinflamm.* 16, 93. doi:10.1186/s12974-019-1479-3

Hanna, A., Hellenbrand, D., Haldeman, C., Lee, J.-S., Gableman, A., Dai, E., et al. (2021). Functional Recovery after Peripheral Nerve Injury via Sustained Growth Factor Delivery from mineral-Coated Microparticles. *Neural Regen. Res.* 16, 871–877. doi:10.4103/1673-5374.297786

Holstein, J. H., Menger, M. D., Scheuer, C., Meier, C., Culemann, U., Wirbel, R. J., et al. (2007). Erythropoietin (EPO) - EPO-Receptor Signaling Improves Early Endochondral Ossification and Mechanical Strength in Fracture Healing. *Life Sci.* 80, 893–900. doi:10.1016/j.lfs.2006.11.023

Isaksson, H., Gröngröft, I., Wilson, W., van Donkelaar, C. C., van Rietbergen, B., Tami, A., et al. (2009). Remodeling of Fracture Callus in Mice Is Consistent with Mechanical Loading and Bone Remodeling Theory. *J. Orthop. Res.* 27, 664–672. doi:10.1002/jor.20725

Kanczler, J., Oreffo, R. O., and Oreffo, R. (2008). Osteogenesis and Angiogenesis: the Potential for Engineering Bone. *eCM* 15, 100–114. doi:10.22203/ecm.v015a08

Lee, J. S., Lu, Y., Baer, G. S., Markel, M. D., and Murphy, W. L. (2010). Controllable Protein Delivery from Coated Surgical Sutures. *J. Mater. Chem.* 20, 8894–8903. doi:10.1039/c0jm01389g

Lee, J. S., Suárez-González, D., and Murphy, W. L. (2011). Mineral Coatings for Temporally Controlled Delivery of Multiple Proteins. *Adv. Mater.* 23, 4279–4284. doi:10.1002/adma.201100060

Lee, E., Ko, J.-Y., Kim, J., Park, J.-W., Lee, S., and Im, G.-I. (2019). Osteogenesis and Angiogenesis Are Simultaneously Enhanced in BMP2-/VEGF-Transfected Adipose Stem Cells through Activation of the YAP/TAZ Signaling Pathway. *Biomater. Sci.* 7, 4588–4602. doi:10.1039/c9bm01037h

Liu, K., Meng, C.-X., Lv, Z.-Y., Zhang, Y.-J., Li, J., Li, K.-Y., et al. (2020). Enhancement of BMP-2 and VEGF Carried by Mineralized Collagen for Mandibular Bone Regeneration. *Regen. Biomater.* 7, 435–440. doi:10.1093/rb/rbaa022

Luo, T., Zhang, W., Shi, B., Cheng, X., and Zhang, Y. (2012). Enhanced Bone Regeneration Around Dental Implant with Bone Morphogenetic Protein 2 Gene and Vascular Endothelial Growth Factor Protein Delivery. *Clin. Oral Impl. Res.* 23, 467–473. doi:10.1111/j.1600-0501.2011.02164.x

Mandal, C. C., Das, F., Ganapathy, S., Harris, S. E., Ghosh Choudhury, G., and Ghosh-Choudhury, N. (2016). Bone Morphogenetic Protein-2 (BMP-2) Activates NFATc1 Transcription Factor via an Autoregulatory Loop Involving Smad/Akt/Ca2+ Signaling. *J. Biol. Chem.* 291, 1148–1161. doi:10.1074/jbc.M115.668939

Morgan, E. F., Mason, Z. D., Chien, K. B., Pfeiffer, A. J., Barnes, G. L., Einhorn, T. A., et al. (2009). Micro-computed Tomography Assessment of Fracture Healing: Relationships Among Callus Structure, Composition, and Mechanical Function. *Bone* 44, 335–344. doi:10.1016/j.bone.2008.10.039

Muire, P. J., Mangum, L. H., and Wenke, J. C. (2020). Time Course of Immune Response and Immunomodulation during Normal and Delayed Healing of Musculoskeletal Wounds. *Front. Immunol.* 11, 1056. doi:10.3389/fimmu.2020.01056

Ogilvie, C. M., Lu, C., Marcucio, R., Lee, M., Thompson, Z., Hu, D., et al. (2012). Vascular Endothelial Growth Factor Improves Bone Repair in a Murine Nonunion Model. *Iowa Orthop. J.* 32, 90–94.

Orth, M., Kruse, N. J., Kruse, N., Braun, B., Scheuer, C., Holstein, J., et al. (2017). BMP-2-Coated mineral Coated Microparticles Improve Bone Repair in Atrophic Non-unions. *eCM* 33, 1–12. doi:10.22203/eCM.v033a01

Orth, M., Altmeyer, M. A. B., Scheuer, C., Braun, B. J., Holstein, J. H., Eglin, D., et al. (2018). Effects of Locally Applied Adipose Tissue-Derived Microvascular Fragments by Thermoresponsive Hydrogel on Bone Healing. *Acta Biomater.* 77, 201–211. doi:10.1016/j.actbio.2018.07.029

Orth, M., Shenar, A. K., Scheuer, C., Braun, B. J., Herath, S. C., Holstein, J. H., et al. (2019). VEGF-loaded mineral-coated Microparticles Improve Bone Repair and Are Associated with Increased Expression of Epo and RUNX-2 in Murine Non-unions. *J. Orthop. Res.* 37, 821–831. doi:10.1002/jor.24267

Pelissier, P., Boireau, P., Martin, D., and Baudet, J. (2003). Bone Reconstruction of the Lower Extremity: Complications and Outcomes. *Plast. Reconstr. Surg.* 111, 2223–2229. doi:10.1097/01.PRS.0000060116.21049.53

Peng, H., Usas, A., Olshanski, A., Ho, A. M., Gearhart, B., Cooper, G. M., et al. (2005). VEGF Improves, whereas sFlt1 Inhibits, BMP2-Induced Bone Formation and Bone Healing through Modulation of Angiogenesis. *J. Bone Miner Res.* 20, 2017–2027. doi:10.1359/JBMR.050708

Rather, H. A., Jhala, D., and Vasita, R. (2019). Dual Functional Approaches for Osteogenesis Coupled Angiogenesis in Bone Tissue Engineering. *Mater. Sci. Eng. C* 103, 109761. doi:10.1016/j.msec.2019.109761

Rivera, J. C., Strohbach, C. A., Wenke, J. C., and Rathbone, C. R. (2013). Beyond Osteogenesis: an *In Vitro* Comparison of the Potentials of Six Bone Morphogenetic Proteins. *Front. Pharmacol.* 4, 125. doi:10.3389/fphar.2013.00125

Samee, M., Kasugai, S., Kondo, H., Ohya, K., Shimokawa, H., and Kuroda, S. (2008). Bone Morphogenetic Protein-2 (BMP-2) and Vascular Endothelial Growth Factor (VEGF) Transfection to Human Periosteal Cells Enhances Osteoblast Differentiation and Bone Formation. *J. Pharmacol. Sci.* 108, 18–31. doi:10.1254/jphs.08036fp

Street, J., Bao, M., deGuzman, L., Bunting, S., Peale, F. V., Jr., Ferrara, N., et al. (2002). Vascular Endothelial Growth Factor Stimulates Bone Repair by Promoting Angiogenesis and Bone Turnover. *Proc. Natl. Acad. Sci.* 99, 9656–9661. doi:10.1073/pnas.152324099

Suárez-González, D., Lee, J. S., Lan Levengood, S. K., Vanderby, R., and Murphy, W. L. (2012). Mineral Coatings Modulate β-TCP Stability and Enable Growth Factor Binding and Release. *Acta Biomater.* 8, 1117–1124. doi:10.1016/j.actbio.2011.11.028

Subbiah, R., Cheng, A., Ruehle, M. A., Hettiaratchi, M. H., Bertassoni, L. E., and Guldberg, R. E. (2020). Effects of Controlled Dual Growth Factor Delivery on Bone Regeneration Following Composite Bone-Muscle Injury. *Acta Biomater.* 114, 63–75. doi:10.1016/j.actbio.2020.07.026

Wang, D. S., Miura, M., Demura, H., and Sato, K. (1997). Anabolic Effects of 1,25-Dihydroxyvitamin D3 on Osteoblasts Are Enhanced by Vascular Endothelial Growth Factor Produced by Osteoblasts and by Growth Factors Produced by Endothelial Cells*. *Endocrinology* 138, 2953–2962. doi:10.1210/endo.138.7.5275

Yoneda, M., Terai, H., Imai, Y., Okada, T., Nozaki, K., Inoue, H., et al. (2005). Repair of an Intercalated Long Bone Defect with a Synthetic Biodegradable Bone-Inducing Implant. *Biomaterials* 26, 5145–5152. doi:10.1016/j.biomaterials.2005.01.054

Yu, X., Khalil, A., Dang, P. N., Alsberg, E., and Murphy, W. L. (2014). Multilayered Inorganic Microparticles for Tunable Dual Growth Factor Delivery. *Adv. Funct. Mater.* 24, 3082–3093. doi:10.1002/adfm.201302859

Yu, X., Biedrzycki, A. H., Khalil, A. S., Hess, D., Umhoefer, J. M., Markel, M. D., et al. (2017). Nanostructured Mineral Coatings Stabilize Proteins for Therapeutic Delivery. *Adv. Mater.* 29, 1701255. doi:10.1002/adma.20170125510.1002/adma.201701255

Conflict of Interest: The authors declare that the research was conducted in the absence of any commercial or financial relationships that could be construed as a potential conflict of interest.

frontiers
in Bioengineering and Biotechnology

ORIGINAL RESEARCH
published: 03 March 2022
doi: 10.3389/fbioe.2022.824688

Biomechanical and Clinical Study of Rod Curvature in Single-Segment Posterior Lumbar Interbody Fusion

Lin Han[1†], *Yongheng Li*[2†], *Zhiyong Li*[2,3], *Hongdao Ma*[1], *Chenfeng Wang*[1], *Qiang Chen*[2*] *and Xuhua Lu*[1*]

[1]Department of Orthopaedics, Shanghai Changzheng Hospital, Second Military Medical University, Shanghai, China, [2]Biomechanics Laboratory, School of Biological Science and Medical Engineering, Southeast University, Nanjing, China, [3]School of Mechanical Medical and Process Engineering, Queensland University of Technology, Brisbane, QLD, Australia

Edited by:
Bin Wang,
Chongqing Medical University, China

Reviewed by:
Chunqiu Zhang,
Tianjin University, China
Shaopeng Pei,
University of Pennsylvania,
United States

***Correspondence:**
Qiang Chen
cq@seu.edu.cn
Xuhua Lu
xuhualu@hotmail.com

†These authors have contributed equally to this work

Specialty section:
This article was submitted to Biomechanics, a section of the journal Frontiers in Bioengineering and Biotechnology

Received: *29 November 2021*
Accepted: *07 February 2022*
Published: *03 March 2022*

Citation:
Han L, Li Y, Li Z, Ma H, Wang C, Chen Q and Lu X (2022) Biomechanical and Clinical Study of Rod Curvature in Single-Segment Posterior Lumbar Interbody Fusion. Front. Bioeng. Biotechnol. 10:824688. doi: 10.3389/fbioe.2022.824688

Objective: Pedicle screw fixation is a common technique used in posterior lumbar interbody fusion (PLIF) surgery for lumbar disorders. During operation, rod contouring is often subjective and not satisfactory, but only few studies focused on the rod-contouring issue previously. The aim of the study was to explore the effect of the rod contouring on the single-segment PLIF by the finite element (FE) method and retrospective study.

Methods: A FE model of the lumbosacral vertebrae was first reconstructed, and subsequently single-segmental (L4/5) PLIF surgeries with four rod curvatures (RCs) were simulated. Herein, three RCs were designed by referring to centroid, Cobb, and posterior tangent methods applied in the lumbar lordosis measurement, and zero RC indicating straight rods was included as well. Clinical data of patients subjected to L4/5 segmental PLIF were also analyzed to verify the correlation between RCs and clinical outcome.

Results: No difference was observed among the four RC models in the range of motion (ROM), intersegmental rotation angle (IRA), and intradiscal pressure (IDP) under four actions. The posterior tangent model had less maximum stress in fixation (MSF) in flexion, extension, and axial rotation than the other RC models. Patients with favorable prognosis had larger RC and positive RC minus posterior tangent angle (RC-PTA) of fused segments with respect to those who had poor prognosis and received revision surgery.

Conclusion: All RC models had similar biomechanical behaviors under four actions. The posterior tangent-based RC model was superior in fixation stress distribution compared to centroid, Cobb, and straight models. The retrospective study demonstrated that moderate RC and positive RC-PTA were associated with better postoperative results.

Keywords: rod curvature, rod contouring, lumbar surgery, finite element analysis, PLIF surgery

INTRODUCTION

Optimal sagittal alignment plays a significant role in improving the spinal sagittal balance, reducing body energy expenditure, and slowing down the disc degeneration of adjacent segments (Makhni et al., 2018). Loss of the spinal sagittal balance can be caused by disc degeneration, spinal deformity, trauma, and surgery, and thus higher muscular force is required to maintain the spinal posture and balance. However,

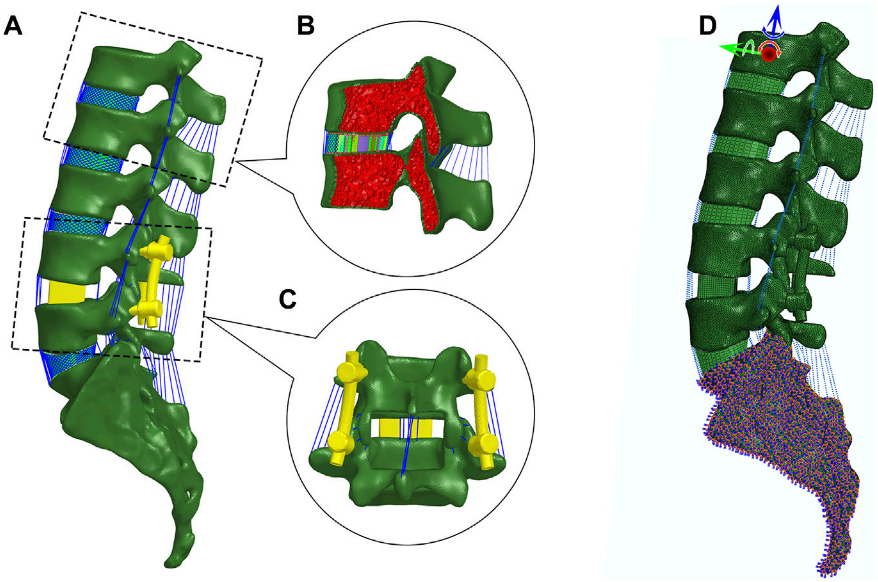

FIGURE 1 | Finite element modeling. **(A)** Lateral view of the lumbosacral model with posterior lumbar interbody fusion in Hypermesh. **(B)** Sagittal section of vertebrae and intervertebral disc. The vertebra is partitioned into cortical and cancellous bone. The disc is composed of nucleus pulposus and annulus ground substance embedded with crossing collagen fibers. **(C)** Posterior view of PLIF. **(D)** Boundary and loading conditions.

the compensatory mechanism may result in adverse effects such as back pain, disability, and decrease in health-related quality of life (HRQOL). In addition, positive sagittal balance indicated by abnormal radiographic parameters is also highly correlated to the adverse outcomes in adult spinal deformity (Glassman et al., 2005).

Restoration of normal sagittal alignment is critical to postoperative outcomes and prognosis (Matsumoto et al., 2017). After spinal fusion, increased stress on the adjacent discs may result in adjacent segment degeneration (ASD). It was reported that the incidences of radiograph ASD and symptomatic ASD were 26.6 and 8.5% in lumbar surgery, respectively (Xia et al., 2013). Sagittal imbalance, such as sagittal vertical axis (SVA) > 50 mm, higher pelvic tilt (PT), decreased lumbar lordosis (LL), and pelvic incidence minus lumbar lordosis (PI-LL) mismatch, is identified as a significant risk factor of ASD after posterior lumbar interbody fusion (PLIF) (Barrey and Darnis, 2015). This pathological change can cause neurologic symptoms which require further medical interventions.

In view of the significance of the normal sagittal alignment, the posterior screw–rod system as the main fixation device and rod curvature (RC) should be consistent with the physiological alignment to achieve satisfactory postoperative outcomes. Otherwise, negative postoperative outcomes can be introduced. For instance, changes in the bending curvature of the implanted rod resulted in overcorrection or undercorrection of the sagittal balance in adolescent idiopathic scoliosis (Salmingo et al., 2014), and the mismatch between RC and normal sagittal alignment correlated to the poor clinical and radiological follow-up (Moufid et al., 2019).

However, perioperative rod contouring or rod bending was rarely studied previously. In clinical practice, French bender is the most commonly used tool for rod contouring. The surgeon uses the device to bend rods according to experience and preference after evaluating the sagittal alignment of patients from the radiography during the operation. Obviously, this experience- or preference-based practice is inevitably subjective and poorly repeatable. Moreover, repetitive rod contouring is likely to cause imprecise fixation, screw loosening, stress concentration, and long operation duration. Therefore, evaluating the rod contouring indicated by RC is necessary. Herein, finite element (FE) analysis was adopted to evaluate the biomechanical effects of four RCs on the single-segment PLIF surgery including three kinds of contoured rods corresponding to three commonly used LL measuring methods (*i.e.*, centroid, Cobb, and posterior tangent) and straight rod. Then, a retrospective clinical study was conducted to discuss whether the RC was correlated with the clinical outcome.

MATERIALS AND METHODS

Finite Element Modeling

A three-dimensional FE model of the lumbosacral vertebrae (**Figure 1**) was first reconstructed through Mimics 16.0 software (Materialise, Leuven, Belgium), based on computed tomography images (CT, Philips Brilliance iCT 256; slice thickness, 1 mm; scanning voxel size, 0.8 × 0.8 × 1.2 mm^3) of a normal male adult without any lumbar disease. The participant was provided a written informed consent prior to the enrollment, and the study protocol was approved by the Institutional Ethics Committee.

Regarding the FE model, the cortical bone, cancellous bone, endplates, and intervertebral disc were created in 3-matic 8.0 (Materialise, Leuven, Belgium) and then meshed in HyperWorks 13.0 (Altair Engineering, Inc., Executive Park, CA, United States). Cortical bone was separated from each vertebra with a thickness of 1 mm (Naserkhaki et al., 2018), and the rest of the vertebra was

TABLE 1 | Material properties of the FE model.

Component	Element type	Young's modulus (Mpa)	Poisson's ratio	Density (g/cm^3)	Cross section (mm^2)	Reference
Bone						
Cortical bone	C3D4	12,000	0.3	1.7e-6		Goel et al. (1994)
Cancellous bone	C3D4	100	0.2	1.1e-6		
Endplate	C3D8H	23.8	0.4	1.2e-6		Ueno and Liu (1987)
Intervertebral disc						
Annulus ground substance	C3D8H	$C_{10} = 0.18$, $C_{01} = 0.045$		1.05e-6		Schmidt et al. (2007)
Nucleus pulpous	C3D8H	$C_{10} = 0.12$, $C_{01} = 0.03$		1.02e-6		
Annulus fiber layers						Polikeit et al. (2003)
Outermost	T3D2	550	0.3	1.0e-6	0.70	
Second	T3D2	495	0.3	1.0e-6	0.63	
Third	T3D2	440	0.3	1.0e-6	0.55	
Fourth	T3D2	420	0.3	1.0e-6	0.49	
Fifth	T3D2	385	0.3	1.0e-6	0.41	
Innermost	T3D2	360	0.3	1.0e-6	0.30	
Fixation devices						
Screw and rod (Ti6Al4V)	C3D4	113,000	0.3			
Cage (PEEK)	C3D8H	3,500	0.3			

Ligaments	Element type	Strain (%)	Stiffness (N/mm)	Strain (%)	Stiffness (N/mm)	Strain (%)	Stiffness (N/mm)	Strain (%)	Stiffness (N/mm)	
Anterior longitudinal ligament	Spring A	$\varepsilon < 0$	0	$0 < \varepsilon < 12.2$	347	$12.2 < \varepsilon < 20.3$	787	$20.3 < \varepsilon$	1864	Rohlmann et al. (2006)
Posterior longitudinal ligament	Spring A			$0 < \varepsilon < 11.1$	29.5	$11.1 < \varepsilon < 23$	61.7	$23 < \varepsilon$	236	
Ligamentum flavum	Spring A			$0 < \varepsilon < 5.9$	7.7	$5.9 < \varepsilon < 49$	9.6	$49 < \varepsilon$	58.2	
Intertransverse ligament	Spring A			$0 < \varepsilon < 18.2$	0.3	$18.2 < \varepsilon < 23.3$	1.8	$23.3 < \varepsilon$	10.7	
Capsular ligament	Spring A			$0 < \varepsilon < 25$	36	$25 < \varepsilon < 30$	159	$30 < \varepsilon$	384	
Interspinous ligament	Spring A			$0 < \varepsilon < 13.9$	1.4	$13.9 < \varepsilon < 20$	1.5	$20 < \varepsilon$	14.7	
Supraspinous ligament	Spring A			$0 < \varepsilon < 20$	2.5	$20 < \varepsilon < 25$	5.3	$25 < \varepsilon$	34	

treated as cancellous bone. The thickness of the endplate was set at 0.5 mm. The element types of vertebrae and endplates were four-node tetrahedral element (C3D4) and eight-node hybrid hexahedral elements (C3D8H), respectively. Intervertebral discs were divided into incompressible nucleus pulposus and annulus ground substance (Guo and Fan, 2018). The nucleus pulposus and annular ground substance were meshed by the C3D8H element with an isotropic, hyper-elastic Mooney–Rivlin material. Six circumferential layers of crossing collagen fibers with different orientations were embedded in the annulus ground substance, and the fibers were meshed by tension-only two-node truss elements (T3D2). A total of seven major ligaments including anterior longitudinal ligament (ALL), posterior longitudinal ligament (PLL), ligamentum flavum (LF), capsular ligament (CL), intertransverse ligament (ITL), interspinous ligament (ISL), and supraspinous ligament (SSL) were meshed by tension-only Spring A elements (Rohlmann et al., 2006). A frictionless surface contact between facet joints was assigned. All material properties of the aforementioned tissues were listed in **Table 1**.

Contouring Methods and Simulation of the Posterior Lumbar Interbody Fusion Procedure

Centroid, Cobb, and posterior tangent methods (**Figure 2**) were applied to measure angles of L4–L5 segment curvatures in

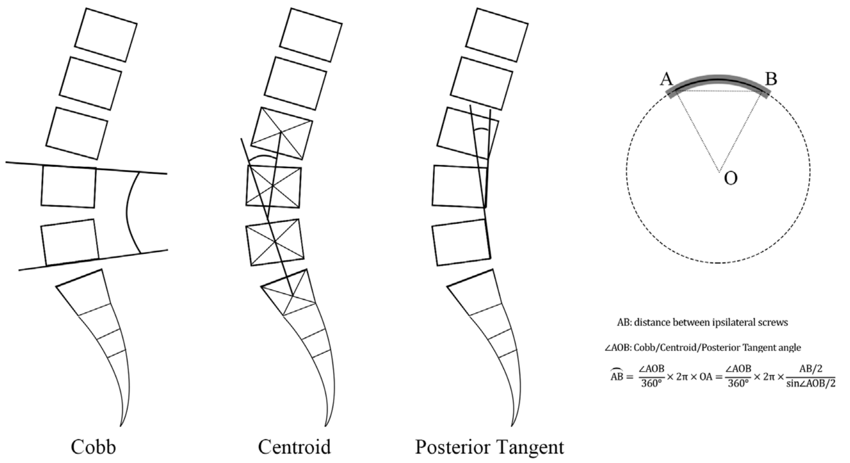

FIGURE 2 | Description of Cobb, centroid, and posterior tangent methods in the rod bending procedure.

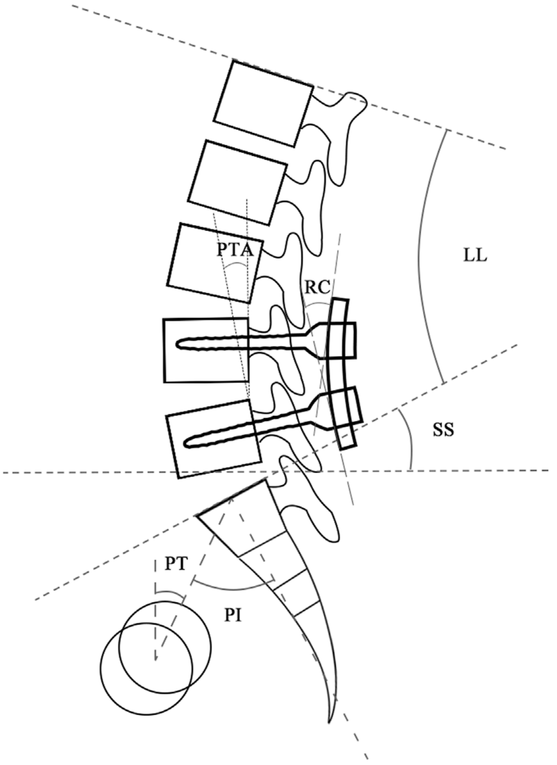

FIGURE 3 | Radiographic parameters measured from lateral radiographs. Abbreviation: LL, lumbar lordosis; PT, pelvic tilt; PI, pelvic incidence; SS, sacral slope; RC, rod curvature; PTA, posterior tangent angle of fused segments.

Mimics (Harrison et al., 2001). Here, the centroid angle was described as the included angle made by two straight lines, which passed through two vertebral centroids at both ends (Chen, 1999). The Cobb angle was defined as the angle between the superior endplate of L4 and the inferior endplate of L5. The posterior tangent angle was defined as the included angle of two lines passing tangentially to posterior wall of the L4 and L5 end vertebrae (Janik et al., 1998). The shape of the contoured rod was simply treated as an arc of a virtual circle. According to the distance between ipsilateral screw tails (*i.e.*, chord length of the arc) and the three previously defined angles, the arc length (*i.e.*, the rod contour) was calculated. The RCs of centroid, Cobb, and posterior tangent models were 33.25°, 18.65°, and 7.99°, respectively. In addition, the straight model (RC = 0°) was also considered. Accordingly, the four types of rods were modeled in SolidWorks 2003 (SolidWorks Corp., Waltham, MA, United States).

PLIF was modeled on L4–L5 segment in 3-matic software. According to the surgical procedure, pedicle screws with a diameter of 6 mm were inserted along the central axis of the pedicle, and two screws in L4 and L5 were parallel to their superior endplates, respectively. Partial spinous processes and laminae (inferior L4 and superior L5) and half of the medial facet joints and three ligaments (LF, ISL, and SSL between L4 and L5) were removed. Then, two cubic cages were inserted into the disc space after removing the inferior endplate of L4 and superior endplate of L5, and this simulated the clinical practice. Finally, rods with four RCs were assembled in each model. All fixation devices were meshed in HyperWorks. Tie constraints were employed to model the contact between vertebrae and screws or cages. All material properties of fixation devices were also reported in **Table 1**.

Boundary and Loading Conditions

The six degrees-of-freedom of the sacrum were constrained. The loading history involved two steps. In the first step, a preload of 500 N as a follower load representing upper body weight and muscle forces was applied according to the force line of the lumber spine (Patwardhan et al., 1999). In the second step, a 7.5 N m moment was applied on the top center of the L1 vertebral body in four actions, *i.e.*, flexion, extension, lateral bending, and axial rotation (Ayturk and Puttlitz, 2011). FE simulation was performed by Abaqus (v6.14, Simulia Inc., Providence, RI, United States).

Model Validation and FE Analysis

To validate the FE model, a normal lumbosacral model was also developed (**Supplementary Figure S1** in Supplementary Materials), and the range of motion (ROM) of the normal lumbosacral model and L4/5 intradiscal pressure (IDP) were compared with a recent FE study and an *in vitro* biomechanical experiment (Rohlmann et al., 2001; Wang et al., 2018). To be consistent with the literature, a follower load of 280 N and increasing moments from 0.0 to 7.5 N m with an interval 2.5 N m were applied on the FE model in flexion, extension, lateral bending, and axial rotation tests. After the validation, ROM, intersegmental rotation angle (IRA) of adjacent levels, IDP in adjacent segmental discs, and maximum von Mises stress in fixation (MSF) of the four RC models were compared (Huang et al., 2021).

Clinical Study

The retrospective study identified patients subjected to L4/5 segmental PLIF surgery for lumbar spinal stenosis from January 2015 to June 2021 with the Institutional Review Board's (IRB) approval. The exclusion criteria were patients with the diagnosis of spinal infection, injury, tumor, apparent deformity, irreducible lumbar spondylolisthesis, and other diseases that caused spinal instability. The normal group included patients with an over two-year satisfactory follow-up, whereas the abnormal group consisted of patients who had poor recovery within two-year follow-up after primary surgery and received revision surgery. Patient demographics (age, gender, and BMI), surgical time, and hospital stay were collected. Radiographic parameters including LL, PT, PI, sacral slope (SS), PI-LL, RC, posterior tangent angle of fused segments (PTA), and the difference between RC and PTA (RC-PTA) were measured from postoperative lateral radiographs (**Figure 3**). The χ^2 test for the parameter of gender and student *t*-test for the remaining parameters were used to determine statistical difference between groups (SPSS Statistics 16.0, IBM Corporation, Somers, NY, United States), and $p < 0.05$ indicated the statistical significance.

RESULTS

Model Validation

The ROM of the normal lumbosacral model was validated against two previous studies (Rohlmann et al., 2001; Wang et al., 2018).

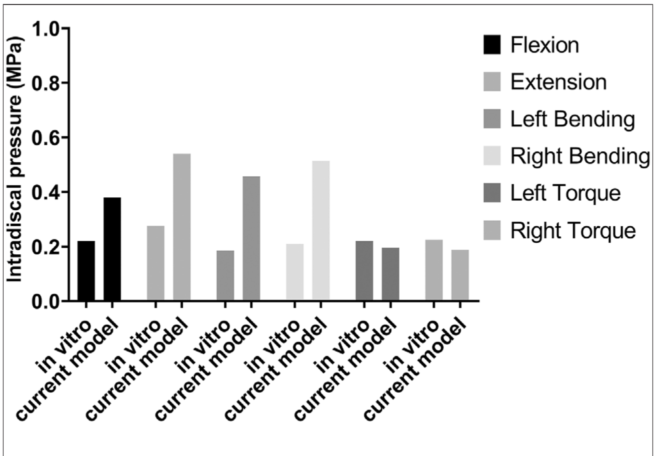

FIGURE 5 | Intradiscal pressure (IDP) of the L4/5 disc for model validation by comparing the *in vitro* study and current model.

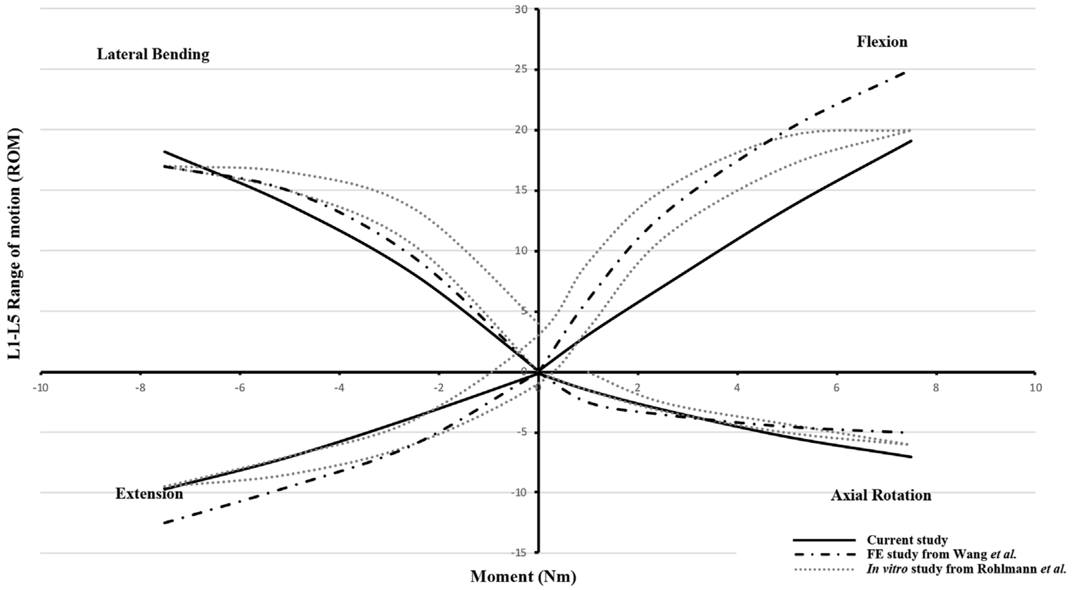

FIGURE 4 | Range of motion (ROM)–moment curvatures for model validation versus the FE study from Wang *et al.* and the *in vitro* study from Rohlmann *et al.*

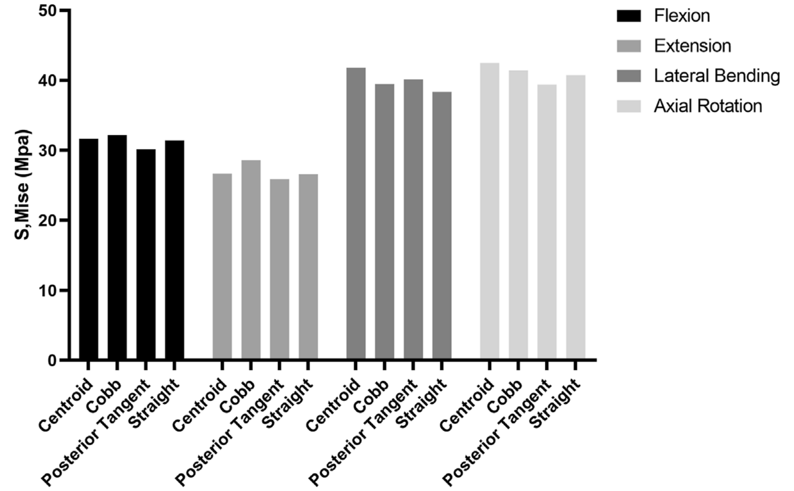

FIGURE 6 | Comparison of maximum stress in fixation (MSF) for four RC models in flexion, extension, lateral bending, and axial rotation.

As shown in **Figure 4**, the ROM–moment curves in the current study agree with the ranges of the *in vitro* study and FE study. The distribution of the IDP in L4/5 is similar to that of the *in vitro* study, *i.e.*, extension > right bending > left bending > flexion > left torque > right torque. However, compared to the axial torsion, the IDPs of flexion, extension, and lateral bending between the present FE result and the *in vitro* experiment show a discrepancy (**Figure 5**). The reason might be that residual muscles or tendons connecting the spine in the *in vitro* study reduced the stress level of the IDP. In any case, IDPs in the current study are still in the acceptable ranges (Dreischarf et al., 2014; Naserkhaki et al., 2018).

Biomechanical Analysis of the Groups

No difference in the ROM of the lumbosacral model in the single-segmental PLIF surgery was observed among four RC models under the four actions of flexion, extension, lateral bending, and axial rotation (**Supplementary Figure S2** in Supplementary Materials). On the neighboring adjacent vertebrae (L3/4 and L5/S1) to the fused L4/5, there was also no substantial difference among four RC models in IRA and IDP with 7.5 N m moment under the four actions (**Supplementary Figure S3** in Supplementary Materials). Stress distributions of the intervertebral discs and vertebrae showed a very weak difference between four RC models (**Supplementary Figures S4, S5** in Supplementary Materials). The stress levels of collagen fibers were higher than those of annulus ground substance. In particular, MSFs under the four actions are illustrated in **Figure 6**. In flexion and extension, the Cobb model had the greatest stress, followed by the centroid model, straight model, and finally posterior tangent model. In the lateral bending and axial rotation, the greatest maximum stresses occurred in the centroid model; however, the posterior tangent model and Cobb model ranked the second and third, respectively, and the straight model was the last in the lateral bending, whereas in axial rotation, Cobb and straight models were in the middle, and posterior tangent had the minimum stress. The stress contours of the screw–rod system in four RC models with the values and locations of MSF under the four actions are shown in **Figure 7**. Overall, MSF in all RC models mainly occurred at the junction of screw and rods, and stress concentration was located at rods and thread run-out. In axial rotation, the screw–rod system experienced larger stress concentration than other actions.

Clinical Results

The analysis for characteristics of patients undergoing L4/5 segmental PLIF surgery were listed in **Table 2**. The primary diagnoses for reoperations were lumbar spinal stenosis at the adjacent level (10 cases) and internal fixation failure (2 cases). No significant differences were found between normal and abnormal groups in aspects of age, gender, BMI, surgical time, hospital stay, LL, PT, PI, SS, PI-LL, and PTA. The normal group had much higher RC (18.87° versus 4.70°, $p < 0.01$) and RC-PTA (6.18° versus −5.23°, $p < 0.01$) than the abnormal group (**Figure 8**).

DISCUSSION

Optimization of spinal alignment measurements could provide guidance to the surgery. However, one question that needs to be answered is whether the rod contouring process should follow the same strategy. In the process of sagittal alignment correction, there is no evaluation on what RC could achieve a better clinical outcome. Thus, basing on three commonly-used LL measurements, we applied an analogy to rod contouring practice in spinal surgery and provided evidence for better rod contouring in single-segmental PLIF surgery by FE simulation. Although the three methods showed similar biomechanical properties under four actions, the posterior tangent method was relevantly superior in the fixation stress distributions of flexion, extension, and axial rotation. The RCs in centroid, Cobb, posterior tangent, and straight models were 33.25°, 18.65°, 7.99°, and 0°. Also, the RC-PTA of the four models were 25.26°, 10.66°, 0°, and −7.99°, respectively. The two variables of the posterior tangent model fell in the middle of the ranges. In the clinical study, it was demonstrated that moderate RC was beneficial for patients who underwent L4/5

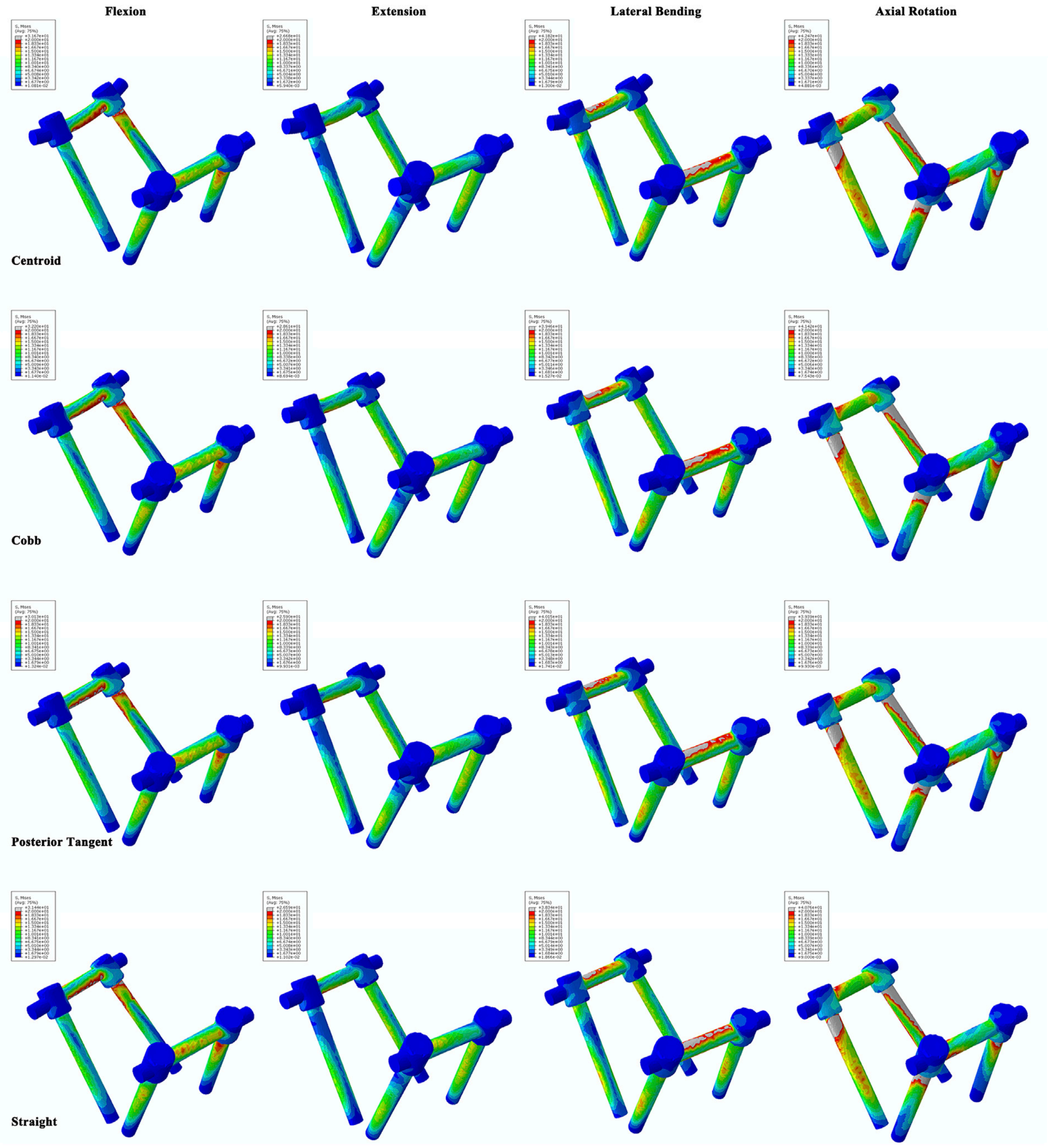

FIGURE 7 | Stress contours of the screw–rod system for four RC models under flexion, extension, lateral bending, and axial rotation tests.

segmental PLIF surgery, and negative RC-PTA was associated with adverse postoperative outcomes. Hence, both FEA and clinical study demonstrated that moderate rod contouring was necessary in L4/5 PLIF surgery. This result was partially consistent with Harrison's finding with respect to algorithm comparison of LL assessment (Harrison et al., 2001). Combined with the analyzing methodologies, the posterior tangent method seemed better to fit normal spinal cord. Thus, we inferred that for the sake of convenience in clinical application, employing the fitting curve of the normal lumbar vertebral posterior edge or centerline of spinal canal to contour rod could be a feasible approach.

To date, improvement of surgical outcome and prevention of ASD-related complications are still the focus and challenge in lumbar surgery. In clinical practice, disappointing postoperative function and mechanical failure have been largely ascribed to inadequate restoration of sagittal alignment. Appropriate LL restoration was beneficial for reducing ASD risk. An *in vitro*

TABLE 2 | Patient demographics and radiographic parameters.

Variable	Normal (*N* = 19)	Revision (*N* = 12)	*p*-value
Age (years)	53.42 ± 10.05	52.71(0.15)	0.42
Gender (male/female)	10/9	9/3	0.27
BMI (kg/m^2)	25.59 ± 3.32	23.49 ± 2.93	0.08
Surgical time (hour)	2.21 ± 0.38	2.46 ± 0.99	0.47
Hospital stay (days)	7.74 ± 3.33	6.67 ± 1.83	0.32
LL	52.62 ± 12.30	48.49 ± 7.97	0.31
PT	15.12 ± 6.95	18.79 ± 4.26	0.11
PI	51.12 ± 6.95	52.74 ± 8.67	0.67
SS	35.99 ± 7.52	33.95 ± 7.90	0.48
PI-LL	−1.51 ± 10.19	4.25 ± 7.84	0.11
RC	18.87 ± 6.16	4.70 ± 3.39	<0.01
PTA	12.68 ± 5.05	9.93 ± 3.09	0.10
RC-PTA	6.18 ± 7.96	−5.23 ± 4.71	<0.01

Abbreviation: LL, lumbar lordosis; PT, pelvic tilt; PI, pelvic incidence; SS, sacral slope; PI-LL, the difference between PI and LL; RC, rod curvature; PTA, posterior tangent angle of fused segments; RC-PTA, the difference between RC and PTA.

biomechanical study reported that hypolordosis in the fused segments could reduce tension behavior of the anterior soft tissues and increase the stress of the posterior column of the adjacent vertebra (Umehara et al., 2000). Meanwhile, high stress of posterior internal fixation might increase risks of screw loosening or rupture. Moreover, decreased LL could increase the ROM and IDP of adjacent segments (Zhao et al., 2018), and excessive LL curvature also increased the IDP of the adjacent intervertebral disc (Wang et al., 2020). These also indicate the potential risk of ASD development. A meta-analysis revealed that post-operative LL was correlated with a significant increase in ASD occurrence after PLIF for degenerative lumbar disease (Wang and Ding, 2020). In this regard, to maintain proper physiologic lordosis at the fusion site, RC should be in accordance with the appropriate LL. This inference supplies the theoretical support for the current study to some extent. In addition, it must be pointed out that proper physiologic lordosis cannot be equated with originally normal lumbar alignment for degenerative lumbar disease. Vertebral osteophyte formation, intervertebral disc degeneration, facet hypertrophy, and compensatory change of surrounding tissues are the reflections of the body's restabilization dealing with the lumbar pathological state in a long-term process. This spontaneous restabilization generates a special biomechanical status distinct from a patient's normal lumbar condition or individuals with normal anatomic structure of lumbar spine. Thus, it requires proper correction of lumbar curvature based on clinical patient-specific conditions, and this challenges surgeons when evaluating spinal balance and planning correction of curvature.

To the best knowledge of the authors, there are few studies on the rod contouring optimization. Wanivenhaus et al. (2019) proposed that augmented reality-assisted rod bending could reduce operation duration by 20% compared with the traditional method and achieve higher accuracy of the rod bending process. Shi et al. (2020) confirmed that the Cobb angle could be used as reference to guide rod bending in thoracolumbar fractures and also reported that 4°–8° greater than the Cobb angle as the RC achieved the best spinal sagittal balance 2 years after the operation. Moufid et al.

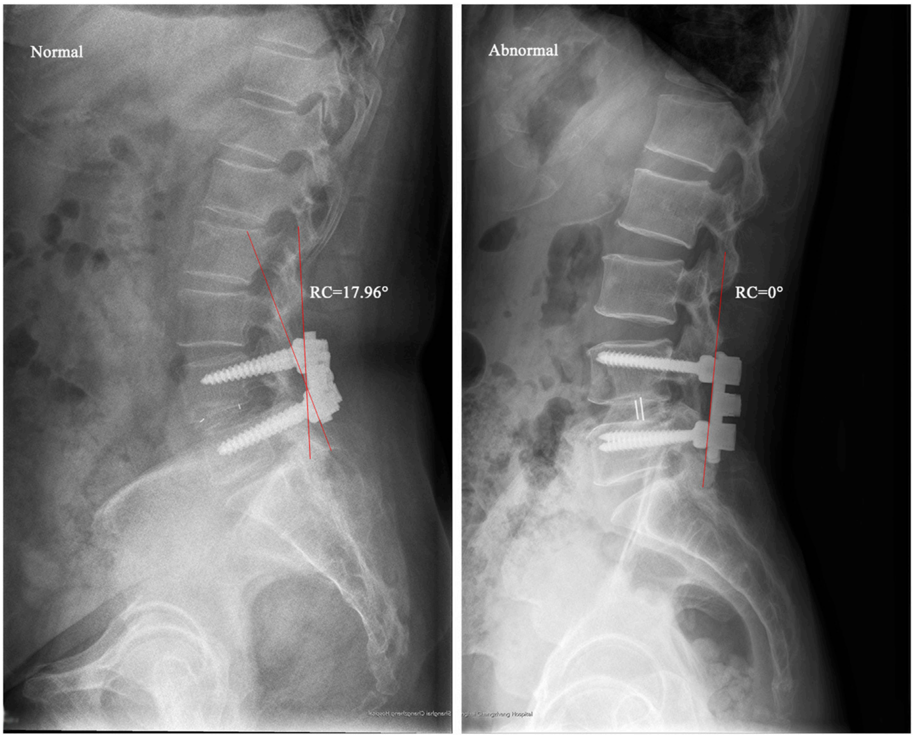

FIGURE 8 | Typical cases showing rod contouring differences between normal and abnormal groups.

(2019) evaluated the mismatch between rod–screw and LL of the fused segment by the concept of the mismatch analysis index (MAI), which was determined by three parameters: the angle between the screw and rod, the angle between the superior endplate and screw, and the distance between the rod and posterior wall of vertebra. In addition, Wang et al. (2016) reported that increasing the bending angle of the concave rod, with respect to the convex rod, could improve the transverse plane correction with advantages in screw pullout forces and kyphosis.

The present study has a certain significance in the practical application of individualized or customized rod contouring before operation. Precise contouring could avoid the reduction of yield strength and stiffness caused by repetitive bending (Demura et al., 2015). It is worth noting that this study made a preliminary exploration on a habitual, pervasive, but subjective surgical procedure that requires standardization in the period of highly developing surgical techniques. Limitations should be acknowledged as well. First, this study did not take into account anatomical variations of the spinal structure. In fact, normal lumbar curvature varies greatly, which may result in different biomechanical performances of rod contouring. Spinal parameters, such as LL, PI, PT, and sacral slope (SS), are also associated with the sagittal balance. Second, the current study computationally modeled three commonly used lumbar lordosis measurements and straight rods to guide rod contouring. However, the modeled RCs should be solidified to have generalizability, interpretability, and clinical applicability by collecting more samples. Third, the clinical observations were patient-specific, and the real mechanical environment corresponding to the model boundary conditions varied, and this might lead to the discrepancy between the model and clinical observations. The patient-specific information should be further included to have exactly consistent results with the clinical observations. Fourth, FEA was a numerical evaluation of the biomechanical effect on the PLIF. The cadaveric study under cyclic loading and multicenter clinical studies with sound evidence should be conducted to verify the results. The accuracy of the radiographic parameter measurement could also be optimized by digital image processing and other analysis techniques. Nevertheless, there is no denying that the current study strongly controlled variables that inevitably occurred in clinical studies such as differences from patients and fixation placement.

CONCLUSION

The present study studied the biomechanical effects of different RCs determined by centroid, Cobb, and posterior tangent methods on the single-segment PLIF surgery. The findings were that four RC models showed similar biomechanical behaviors under four actions, but the posterior tangent mode was relevantly superior to other three RC models in the aspect of fixation stress distribution. Moreover, the retrospective study further revealed that moderate RC and positive RC-PTA were associated with favorable prognosis.

DATA AVAILABILITY STATEMENT

The original contributions presented in the study are included in the article/**Supplementary Material**, further inquiries can be directed to the corresponding authors.

ETHICS STATEMENT

The studies involving human participants were reviewed and approved by Medical Ethics Committee of Shanghai Changzheng Hospital. The patients/participants provided their written informed consent to participate in this study.

AUTHOR CONTRIBUTIONS

LH and XL designed the research. LH and YL conducted the study. ZL, HM, and CW performed data collection and analysis. LH wrote the draft of this manuscript. QC, ZL, and XL revised the article critically. QC and XL were the guarantors.

FUNDING

This study was supported by the Pyramid Talent Project (No. 0910) and the Project of Shanghai Science and Technology Committee (No. 19140901400), and was partially supported by the National Natural Science Foundation of China (No. 32171307).

SUPPLEMENTARY MATERIAL

The Supplementary Material for this article can be found online at: https://www.frontiersin.org/articles/10.3389/fbioe.2022.824688/full#supplementary-material

REFERENCES

Ayturk, U. M., and Puttlitz, C. M. (2011). Parametric Convergence Sensitivity and Validation of a Finite Element Model of the Human Lumbar Spine. *Comput. Methods Biomech. Biomed. Eng.* 14 (8), 695–705. doi:10.1080/10255842.2010.493517

Barrey, C., and Darnis, A. (2015). Current Strategies for the Restoration of Adequate Lordosis during Lumbar Fusion. *World J. Orthop.* 6 (1), 117–126. doi:10.5312/wjo.v6.i1.117

Chen, Y.-L. (1999). Vertebral Centroid Measurement of Lumbar Lordosis Compared with the Cobb Technique. *Spine (Phila Pa 1976)* 24 (17), 1786–1790. doi:10.1097/00007632-199909010-00007

Demura, S., Murakami, H., Hayashi, H., Kato, S., Yoshioka, K., Yokogawa, N., et al. (2015). Influence of Rod Contouring on Rod Strength and Stiffness in Spine Surgery. *Orthopedics* 38 (6), e520–523. doi:10.3928/01477447-20150603-61

Dreischarf, M., Zander, T., Shirazi-Adl, A., Puttlitz, C. M., Adam, C. J., Chen, C. S., et al. (2014). Comparison of Eight Published Static Finite Element Models of the Intact Lumbar Spine: Predictive Power of Models Improves when Combined Together. *J. Biomech.* 47 (8), 1757–1766. doi:10.1016/j.jbiomech.2014.04.002

Glassman, S. D., Berven, S., Bridwell, K., Horton, W., and Dimar, J. R. (2005). Correlation of Radiographic Parameters and Clinical Symptoms in Adult Scoliosis. *Spine (Phila Pa 1976)* 30 (6), 682–688. doi:10.1097/01.brs.0000155425.04536.f7

Goel, V. K., Park, H., and Kong, W. (1994). Investigation of Vibration Characteristics of the Ligamentous Lumbar Spine Using the Finite Element Approach. *J. Biomech. Eng.* 116 (4), 377–383. doi:10.1115/1.2895787

Guo, L.-X., and Fan, W. (2018). Dynamic Response of the Lumbar Spine to Whole-Body Vibration under a Compressive Follower Preload. *Spine (Phila Pa 1976)* 43 (3), E143–E153. doi:10.1097/BRS.0000000000002247

Harrison, D. E., Harrison, D. D., Cailliet, R., Janik, T. J., and Holland, B. (2001). Radiographic Analysis of Lumbar Lordosis: Centroid, Cobb, TRALL, and Harrison Posterior tangent Methods. *Spine (Phila Pa 1976)* 26 (11), E235–E242. doi:10.1097/00007632-200106010-00003

Huang, H., Liu, J., Wang, L., and Fan, Y. (2021). A Critical Review on the Biomechanical Study of Cervical Interbody Fusion Cage. *Med. Novel Technol. Devices* 11, 100070. doi:10.1016/j.medntd.2021.100070

Janik, T. J., Harrison, D. D., Cailliet, R., Troyanovich, S. J., and Harrison, D. E. (1998). Can the Sagittal Lumbar Curvature Be Closely Approximated by an Ellipse? *J. Orthop. Res.* 16 (6), 766–770. doi:10.1002/jor.1100160620

Makhni, M. C., Shillingford, J. N., Laratta, J. L., Hyun, S.-J., and Kim, Y. J. (2018). Restoration of Sagittal Balance in Spinal Deformity Surgery. *J. Korean Neurosurg. Soc.* 61 (2), 167–179. doi:10.3340/jkns.2017.0404.013

Matsumoto, T., Okuda, S., Maeno, T., Yamashita, T., Yamasaki, R., Sugiura, T., et al. (2017). Spinopelvic Sagittal Imbalance as a Risk Factor for Adjacent-Segment Disease after Single-Segment Posterior Lumbar Interbody Fusion. *J. Neurosurg. Spine* 26 (4), 435–440. doi:10.3171/2016.9.SPINE16232

Moufid, A. Y., Cloche, T., Ghailane, S., Ounajim, A., Vendeuvre, T., and Gille, O. (2019). Mismatch between Rod Bending and Actual Post-Operative Lordosis in Lumbar Arthrodesis with Poly Axial Screws. *Orthop. Traumatol. Surg. Res.* 105 (6), 1143–1148. doi:10.1016/j.otsr.2019.03.003

Naserkhaki, S., Arjmand, N., Shirazi-Adl, A., Farahmand, F., and El-Rich, M. (2018). Effects of Eight Different Ligament Property Datasets on Biomechanics of a Lumbar L4-L5 Finite Element Model. *J. Biomech.* 70, 33–42. doi:10.1016/j.jbiomech.2017.05.003

Patwardhan, A. G., Havey, R. M., Meade, K. P., Lee, B., and Dunlap, B. (1999). A Follower Load Increases the Load-Carrying Capacity of the Lumbar Spine in Compression. *Spine (Phila Pa 1976)* 24 (10), 1003–1009. doi:10.1097/00007632-199905150-00014

Polikeit, A., Ferguson, S. J., Nolte, L. P., and Orr, T. E. (2003). Factors Influencing Stresses in the Lumbar Spine After the Insertion of Intervertebral Cages: Finite Element Analysis. *Eur. Spine J.* 12 (4), 413–420. doi:10.1007/s00586-002-0505-8

Rohlmann, A., Bauer, L., Zander, T., Bergmann, G., and Wilke, H.-J. (2006). Determination of Trunk Muscle Forces for Flexion and Extension by Using a Validated Finite Element Model of the Lumbar Spine and Measured *In Vivo* Data. *J. Biomech.* 39 (6), 981–989. doi:10.1016/j.jbiomech.2005.02.019

Rohlmann, A., Neller, S., Claes, L., Bergmann, G., and Wilke, H.-J. (2001). Influence of a Follower Load on Intradiscal Pressure and Intersegmental Rotation of the Lumbar Spine. *Spine (Phila Pa 1976)* 26 (24), E557–E561. doi:10.1097/00007632-200112150-00014

Salmingo, R. A., Tadano, S., Abe, Y., and Ito, M. (2014). Influence of Implant Rod Curvature on Sagittal Correction of Scoliosis Deformity. *Spine J.* 14 (8), 1432–1439. doi:10.1016/j.spinee.2013.08.042

Schmidt, H., Heuer, F., Drumm, J., Klezl, Z., Claes, L., and Wilke, H. J. (2007). Application of a Calibration Method Provides More Realistic Results for a Finite Element Model of a Lumbar Spinal Segment. *Clin Biomech.* 22 (4), 377–384. doi:10.1016/j.clinbiomech.2006.11.008

Shi, Z., Wang, G., Jin, Z., Wu, T., Wang, H., Sun, J., et al. (2020). Use of the Sagittal Cobb* Angle to Guide the Rod Bending in the Treatment of Thoracolumbar Fractures: A Retrospective Clinical Study. *J. Orthop. Surg. Res.* 15 (1), 574. doi:10.1186/s13018-020-02115-5

Ueno, K., and Liu, Y. K. (1987). A Three-Dimensional Nonlinear Finite Element Model of Lumbar Intervertebral Joint in Torsion. *J. Biomech. Eng.* 109 (3), 200–209. doi:10.1115/1.3138670

Umehara, S., Zindrick, M. R., Patwardhan, A. G., Havey, R. M., Vrbos, L. A., Knight, G. W., et al. (20001976). The Biomechanical Effect of Postoperative Hypolordosis in Instrumented Lumbar Fusion on Instrumented and Adjacent Spinal Segments. *Spine* 25 (13), 1617–1624. doi:10.1097/00007632-200007010-00004

Wang, K., Jiang, C., Wang, L., Wang, H., and Niu, W. (2018). The Biomechanical Influence of Anterior Vertebral Body Osteophytes on the Lumbar Spine: A Finite Element Study. *Spine J.* 18 (12), 2288–2296. doi:10.1016/j.spinee.2018.07.001

Wang, T., and Ding, W. (2020). Risk Factors for Adjacent Segment Degeneration after Posterior Lumbar Fusion Surgery in Treatment for Degenerative Lumbar Disorders: A Meta-Analysis. *J. Orthop. Surg. Res.* 15 (1), 582. doi:10.1186/s13018-020-02032-7

Wang, W., Pei, B., Pei, Y., Li, H., Lu, S., Wu, X., et al. (2020). Biomechanical Effects of over Lordotic Curvature after Spinal Fusion on Adjacent Intervertebral Discs under Continuous Compressive Load. *Clin. Biomech.* 73, 149–156. doi:10.1016/j.clinbiomech.2020.01.002

Wang, X., Boyer, L., Le Naveaux, F., Schwend, R. M., and Aubin, C.-E. (2016). How Does Differential Rod Contouring Contribute to 3-dimensional Correction and Affect the Bone-Screw Forces in Adolescent Idiopathic Scoliosis Instrumentation? *Clin. Biomech.* 39, 115–121. doi:10.1016/j.clinbiomech.2016.10.002

Wanivenhaus, F., Neuhaus, C., Liebmann, F., Roner, S., Spirig, J. M., and Farshad, M. (2019). Augmented Reality-Assisted Rod Bending in Spinal Surgery. *Spine J.* 19 (10), 1687–1689. doi:10.1016/j.spinee.2019.06.019

Xia, X.-P., Chen, H.-L., and Cheng, H.-B. (2013). Prevalence of Adjacent Segment Degeneration after Spine Surgery. *Spine* 38 (7), 597–608. doi:10.1097/BRS.0b013e318273a2ea

Zhao, X., Du, L., Xie, Y., and Zhao, J. (2018). Effect of Lumbar Lordosis on the Adjacent Segment in Transforaminal Lumbar Interbody Fusion: a Finite Element Analysis. *World Neurosurg.* 114, e114–e120. doi:10.1016/j.wneu.2018.02.073

Conflict of Interest: The authors declare that the research was conducted in the absence of any commercial or financial relationships that could be construed as a potential conflict of interest.

frontiers in Bioengineering and Biotechnology

ORIGINAL RESEARCH
published: 21 March 2022
doi: 10.3389/fbioe.2022.853872

Pulsed Electromagnetic Field Alleviates Intervertebral Disc Degeneration by Activating Sirt1-Autophagy Signaling Network

Yi Zheng[1], Liangwei Mei[1†], Shengyou Li[1†], Teng Ma[1], Bing Xia[1], Yiming Hao[1], Xue Gao[2], Bin Wei[1], Yitao Wei[1], Da Jing[3*], Zhuojing Luo[1*] and Jinghui Huang[1*]

[1]Department of Orthopedics, Xijing Hospital, Fourth Military Medical University, Xi'an, China, [2]Faculty of Life Sciences, Northwest University, Xi'an, China, [3]Department of Biomedical Engineering, Fourth Military Medical University, Xi'an, China

Edited by:
Jun Pan,
Chongqing University, China

Reviewed by:
Fengxuan Han,
Soochow University, China
Harry M. C. Choi,
University of Maryland School of Medicine, United States

***Correspondence:**
Da Jing
jingdaasq@163.com
Zhuojing Luo
zhuojingl@163.com
Jinghui Huang
huangjh@fmmu.edu.cn

†These authors have contributed equally to this work

Specialty section:
This article was submitted to Biomechanics,
a section of the journal Frontiers in Bioengineering and Biotechnology

Received: 13 January 2022
Accepted: 07 March 2022
Published: 21 March 2022

Citation:
Zheng Y, Mei L, Li S, Ma T, Xia B, Hao Y, Gao X, Wei B, Wei Y, Jing D, Luo Z and Huang J (2022) Pulsed Electromagnetic Field Alleviates Intervertebral Disc Degeneration by Activating Sirt1-Autophagy Signaling Network.
Front. Bioeng. Biotechnol. 10:853872.
doi: 10.3389/fbioe.2022.853872

Intervertebral disc (IVD) degeneration is regarded as a major contributor to low back pain (LBP), causing serious economic burden on individuals and society. Unfortunately, there are limited effective treatment for IVD degeneration. Pulsed electromagnetic field (PEMF) is an economical and effective physical therapy method, with reduced side-effects. It offers certain protection to a number of degenerative diseases. Therefore, understanding the underlying mechanism of PEMF on IVD is important for improving the PEMF therapeutic efficiency. In this study, PEMF up-regulated extracellular matrix (ECM) related genes in degenerated nucleus pulposus (NP) cells. It also increased SIRT1 expression and promoted autophagy in degenerated NP cells. In contrast, the autophagy suppressor 3-methyladenine (3-MA) reversed the beneficial effect of PEMF on ECM production. Similarly, the SIRT1 enzyme activity suppressor EX 527 also inhibited the effect of PEMF on autophagy and ECM production in NP cells, thereby suggesting that PEMF regulated ECM related genes expression through SIRT1-autophagy signaling pathway. Lastly, PEMF significantly reduced IVD degeneration in a rat model of IVD degeneration *in vivo*. In summary, our study uncovers a critical role of SIRT1-dependent autophagy signaling pathway in ECM protection and thus in the establishment of therapeutic effect of PEMF on IVD degeneration.

Keywords: pulsed electromagnetic fields, intervertebral disc degeneration, autophagy, SIRT1, extracellular matrix (ECM)

INTRODUCTION

Low back pain (LBP) is an age-related condition, the prevalence and impact of which are increasing year by year (Cashin et al., 2021; Knezevic et al., 2021). In a recent global survey involving 50 chronic diseases, LBP ranked the first cause of disability in the elderly (Cieza et al., 2021). Although LBP has multifactorial etiology, intervertebral disc (IVD) degeneration is believed to be the main contributor of LBP pathology (Foster et al., 2018; Liu et al., 2021). IVD consists of three distinct regions, namely, the central nucleus pulposus (NP), which is a gel-like tissue rich in aggrecan; the annulus fibrosus (AF), which is mainly composed of collagen fibers; and the cartilage endplate (CEP), which is connected to vertebral bodies. Existing studies revealed that alterations in extracellular matrix (ECM), inflammation, enhanced catabolism, and cellular aging and death promote IVD degeneration (Tu et al., 2021; Francisco et al., 2022). Despite global prevalence of IVD degeneration, there are no effective treatments available for IVD degeneration and its related pathologies.

Pulsed electromagnetic field (PEMF), as an economical and non-invasive form of physical therapy, with reduced side-effects. It has been used in clinical practice since the 1970s, mainly for the treatment of delayed fracture healing, nonunion, and osteonecrosis (Caliogna et al., 2021; Varani et al., 2021). Numerous studies confirmed that PEMF possesses anti-inflammatory and anti-aging properties, and it promotes ECM synthesis both *in vitro* and *in vivo* (Kavand et al., 2016; Zhi et al., 2016; Parate et al., 2017; Bloise et al., 2020). Recent evidences revealed that PEMF serves a certain function in inhibiting IVD degeneration in a short-term treatment. Miller et al., for instance, reported that PEMF lowers levels of inflammatory factors and catabolites, while enhancing anabolism *in vitro* (Miller et al., 2016). In addition, Chan, AK et al. validated that PEMF suppresses levels of inflammatory factors and accelerates ECM production in a rat tail-puncture induced IVD degeneration model in a 7-day treatment (Chan et al., 2019). Although existing studies demonstrated certain clinical benefits of PEMF, the mechanism whereby PEMF regulates IVD degeneration remains unknown.

Interestingly, recent studies have uncovered that PEMF show a potential role in regulating silent information regulator 1 (SIRT1), a NAD + -dependent deacetylase, which might activate autophagy in several tissues (Jeong et al., 2017; Patruno et al., 2020). Autophagy serves an essential function in cell homeostasis by removing non-functional cellular components and organelles. During aging process, autophagy related genes dramatically decrease in IVD tissues (Kritschil et al., 2021). Prior studies have revealed that autophagy protects against IVD degeneration (Hu J. et al., 2021; Dai et al., 2021; Zhong et al., 2021). Hence, activating autophagy may be an effective treatment against IVD degeneration. Emerging evidences have confirmed that PEMF exerts therapeutic effects by activating autophagy (Jiang et al., 2016; Zielinski et al., 2020). However, the role of autophagy in the beneficial effect of PEMF on IVD degeneration is currently unknown, and underlying mechanisms have not yet been fully clarified. Therefore, the present study aimed to evaluate whether PEMF alleviate IVD degeneration *via* SIRT1-mediated autophagy in cellular and animal models.

MATERIALS AND METHOD

PEMF Stimulators

The PEMF stimulation system (GHY-III, Airforce Military Medical University (AMMU), Xi'an, China; China Patent no. ZL02224739.4) consisted of a PEMF generator and Helmholtz coils (**Figure 1**). In cellular experiments, we employed Helmholtz coils with 200 mm diameters and an interval distance of 100 mm. Each coil was composed of 0.8 mm diameter enameled coated copper wire. The PEMF waveform comprised of a pulsed burst (burst width 5 ms; pulse width, 0.2 ms; pulse wait, 0.02 ms; burst wait, 60 ms; pulse rise and fall times: 0.3 μs, 2.0 μs), which was frequented at 15 Hz. This waveform is known to exert a therapeutic effect on nerve injury and osteoporosis, as is evidenced in our prior investigations (Jing et al., 2010; Zhu et al., 2017). A compact 2 Ω resistor was introduced in series connection, accompanying coils. The wave shape and frequency were assessed with an oscilloscope (6,000 series; Agilent Technologies, United States), and a Gaussmeter (Model 455 DSP; Lake Shore Cryotronics) was employed to monitor the precision of PEMF output. NP cells received PEMF stimulation for 4 h/day. In animal experiments, different Helmholtz coils were used, carrying an interval distance of 304, and diameter of 800 mm but the PEMF output was the same in *in vitro* and *in vivo* studies, which was confirmed by the oscilloscope and Gaussmeter test.

NP Cells Isolation, Culture, and Treatment

Our work received ethical approval from the Xijing Hospital, and we received informed consent from all eligible participants. Human intervertebral disc tissue was obtained from patients with lumbar disc herniation (n = 8, age 59.0 ± 0.5 years, range 55–74 years) and fresh NP tissue samples were obtained during the surgery. Samples were washed thrice with normal saline, and cut into 2 mm^3, before digestion for 30 min in 0.2% pancreatin. They were then rinsed thrice in PBS and incubated in 0.25% type II collagenase for 4 h, with shaking every half an hour, before terminating digestion. Any undigested tissue was then filtered with a 70-micron filter, before resuspending the digested tissue in DMEM/F12 medium with 10% fetal bovine serum and antibiotics, prior to culture in a 5% CO_2 humidified incubator at 37°C. Cells received PEMF treatment 4 h per day, and samples were collected at 0, 24, 48, and 96 h to test apoptosis rate. In order to examine PEMF-mediated autophagy *via* SIRT1, cells were pretreated with either 10 mM 3-MA (an autophagy suppressor) or EX-527 (a SIRT1 enzymatic activity suppressor) for 2 h before the first PEMF stimulation and then maintained in the same media for the entire experiment. All experiments were repeated thrice for good measure.

Cell Viability Assay

NP cells were seeded to the 96-well plate (density: 5×10^4/ml). In 24, 48, and 96 h timepoint, each well was washed with PBS and then treated using 10-μl of Cell Counting Kit 8 (CCK8; Dojindo, Kumamoto, Japan) for1 h at 37°C. The optical density was then evaluated *via* a microplate reader (BioTek, United States) at 450 nm absorbance.

RNA Extraction and Quantitative Real-Time Polymerase Chain Reaction (qRT-PCR)

Total RNA was extracted from NP cells using the Total RNA Mini Kit (QIAGEN, Germany), following kit directions, then converted to cDNA, prior to qPCR analysis *via* SYBR Green PCR Master Mix (TAKARA, Japan) and a BioRad CFX96 PCR System (BioRad, Australia). GAPDH served as an endogenous control. The primers used for qRT-PCR reactions were as follows: collagen II (F)5′-CGAGGCAGACAGTACCTTGA-3′, (R) 5′-TGCTCTCGATCTGGTTGTTC-3'; MMP3 (F) 5′-GCTCAT

CCTACCCATTGCAT-3′, (R) 5′-GCTTCCCTGTCATCTTCA GC-3'; GAPDH (F) 5′-GGCACAGTCAAGGCTFAGAATG-3′, (R) 5′-GGTGGTGAAGACGCCAGTA-3'.

Western Blot Assay

NP cells were thrice rinsed in PBS, before harvest using RIPA buffer and centrifugation at 12,000 g for 15 min. Protein quantification was done with a BCA analysis kit. Proteins were electrophoresized *via* SDS-PAGE, before transfer to PVDF membranes (Thermo Fisher Scientific). Next, they were blocked using 5% non-fat milk in TBS-Tween (TBST) at room temperature (RT) for 1 h, before exposure to primary antibodies (namely, p62, SIRT1, LC3B, collagen II, MMP-3, and GAPDH (all from abcam and has a dilution of 1:1,000)) at 4°C overnight (O/N). They were next exposed to secondary HRP-linked antibodies, either goat anti-rabbit or goat anti-mouse secondary antibodies (Cwbiotech, Beijing, China) at a 1:2,000 dilution for 1 h, before protein band detection using chemiluminescence (Bio-Rad).

Immunofluorescence Staining

NP cells underwent fixation in 4% paraformaldehyde for 10–15 min, and permeabilization in 0.2% Triton X-100 for 20 min, before blocking in 10% normal goat serum at RT for 1h, and O/N incubation in antibodies against collagen II (1:200) and MMP-3 (1:150) at 4°C. Then, they were thrice washed in PBS before exposure to secondary antibodies (FITC or Cy-3, 1:200) for 1 h at RT, and to DAPI for 10 min. Cells underwent three PBS washes for 15 min after every step. Lastly, they were visualized under a fluorescence microscope and analyzed using the ImageJ software.

Transmission Electron Microscopy

A TEM (H-7650; Hitachi, Tokyo, Japan) was employed for calculating autophagic vesicles within NP cells. In short, NP cells underwent O/N fixation in 2.5% glutaraldehyde, followed by a 1 h post-fixation in 2% OsO_4, before receiving gradient dehydration in acetone, followed by embedding, and slicing into 70 nm ultrathin sections using LKB-V ultrathin microtome. Subsequently, they were post-stained with uranyl acetate and lead citrate, and visualized with TEM (H-7650; Hitachi, Tokyo, Japan).

Surgical Procedure

All animal experiments abided by the Institutional Ethical Committee of Fourth Military Medical University guidelines. Fifteen rats were arbitrarily separated into three groups: control (n = 5); needle puncture (n = 5); and needle puncture and PEMF treatment (n = 5). All rats were intraperitoneally anesthetized with pentobarbital solution (1%, 40 mg/kg). As described in previous studies, following tail skin disinfection with iodophor and alcohol, a 20-gauge needle was used to fully puncture the tail disc from Co6-Co8 levels, including two IVDs (Co6-Co7 and Co7-Co8) (Sun et al., 2020; Mei et al., 2021). The needle was then rotated 180 and left for 1 min before removal. Following the operation, all the animals were placed back in their cages and provided with ample food and water. The rats in the experimental group were provided with PEMF treatment (8:00–12:00, 4 h/d) immediately after surgery. Rats were housed in a climate-controlled facility (24 ± 1°C, 35–60% humidity; 12 h light/dark cycle).

Magnetic Resonance Imaging

MRI images were captured 8 weeks after treatment, using an MRI system (Siemens 3 T Magnetom Trio Tim scanner, Munich, Germany). The IVD degeneration score was computed by two independent spinal surgeons, based on the Pfirrmann grading system, ranging from grade I to grade V.

Histopathologic Analysis

Upon fixation in 4% paraformaldehyde, the IVD tissue was decalcified, paraffin-embedded, and sliced into 7 μm thick sagittal sections, then stained with Hematoxylin and Eosin (H&E), Safranin O-Fast Green (SOFG), and Sirius Red. The histological scores, including NP morphology and cellularity, AF organization, matrix structure and CEP integrity, were determined by independent researchers who were blinded to the study, as reported previously (Sobajima et al., 2005; Chan et al., 2019).

Statistical Analysis

All data were analyzed using one-way ANOVA from the SPSS 13.0 software (IBM, IL, United States) and expressed as means ± standard deviations (SDs). Tukey's post hoc and Dunnett's tests were employed for significance comparisons (GraphPad Prism 7.0; GraphPad Software, CA, United States). $p < 0.05$ was deemed significant.

RESULTS

The Effect of PEMF on the Characterizations and Anti-degeneration of NP Cells

To examine the PEMF-mediated effect on NP cell apoptosis, viability and cell morphology, we stimulated NP cells with PEMF 4 h/day for four consecutive days, and monitored cell apoptosis and viability using flow cytometry and CCK-8 assay at 0, 24, 48, and 96 h. Based on our results, PEMF did not exert any obvious cytotoxicity on NP cells (**Figures 2A-D** and **Supplementary Figure 1A**). Moreover, phase-contrast microscopy results showed that PEMF didn't change cell morphology at 96 h timepoint (**Supplementary Figure 1B and 1C**).

We also assessed the PEMF-mediated regulation of NP cell ECM related genes expression. Following 4 days of treatment, RT-qPCR data revealed that PEMF markedly enhanced collagen II expression, while decreasing Mmp3 levels in NP cells (**Figures 2F,G**). Results from western blot analysis further corroborated the RT-qPCR data (**Figures 2E,H,I**). In addition, using immunofluorescence staining and semi-quantitative analysis, we also revealed that PEMF markedly elevated collagen II expression in NP cells (**Figures 2J,K**).

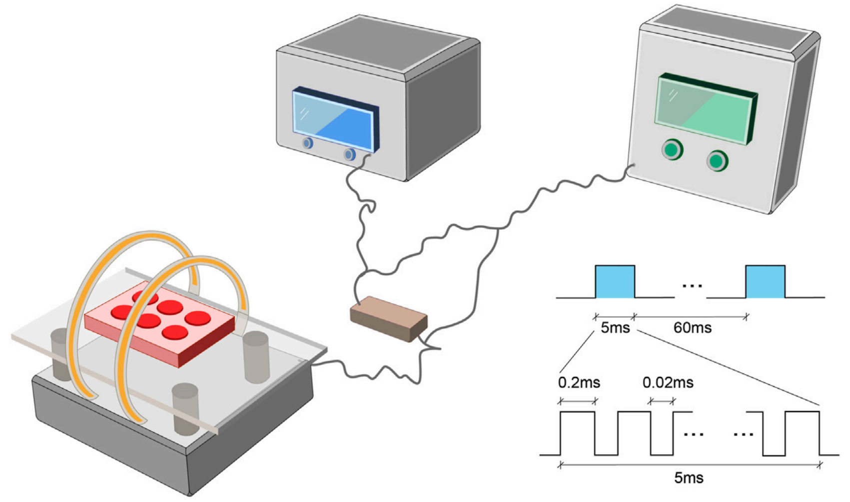

FIGURE 1 | The PEMF exposure system and output waveform. The PEMF device was composed of a signal generator with two Helmholtz coils. A compact 2 Ω resistor was carefully positioned in series with coils. The PEMF waveform was composed of a pulsed burst (burst width, 5 ms; pulse width, 0.2 ms; pulse wait, 0.02 ms; burst wait, 60 ms; pulse rise, 0.3 μs; pulse fall, 2.0 μs), frequented at 15 Hz. PEMF, Pulsed Electromagnetic Fields.

Collectively, these data suggest that PEMF delays the IVD degeneration process *in vitro*.

PEMF Activates Autophagy and Elevates SIRT1 Levels in Degenerated NP Cells

To assess whether PEMF regulates NP cell autophagy, we examined LC3B and p62/SQSTM1 levels in NP cells, using western blot. As depicted in **Figures 3A–D**, after PEMF treatment, the ratio of LC3B-II/LC3B-I increased significantly, whereas, p62 levels dropped significantly. Notably, SIRT1 levels were markedly up-regulated, which is in accordance with autophagic activation. In addition, we evaluated autophagosomes and autophagolysosomes, two key structures associated with autophagy, using TEM. Compared to control cells, the PEMF-treated NP cells displayed more cytoplasmic autophagosomes and autophagolysosomes, thereby confirming autophagic activation in PEMF-treated NP cells (**Figures 3E,F**).

PEMF Regulates ECM Related Makers Expression *via* Autophagy

Next, we examined whether autophagy regulates the PEMF-mediated regulation of ECM related makers expression in NP cells. As illustrated in **Figure 4A**, our western blot data revealed that PEMF treatment markedly reduced MMP3 levels, while increasing type 2 collagen levels, and this effect was reversed by 3-MA exposure (**Figures 4B–E**). In addition, we used immunofluorescence to assess type 2 collagen and MMP3 expressions in PEMF treated and un-treated NP cells. Based on our results, type 2 collagen expression increased remarkably, while MMP3 expression decreased after PEMF treatment. Conversely, the autophagy inhibitor 3-MA reversed this phenomenon (**Figures 4F–I**). Based on these evidences, PEMF regulates degenerative makers expression by inducing autophagic activation.

PEMF Regulates ECM Related Makers Expression *via* SIRT1-Stimulated Autophagic Activation

It is well known that Sirt1 is an upstream regulator of autophagy. Interestingly, we found that PEMF treatment markedly increased Sirt1 expression (**Figures 3G,H**). We, next, examined the relationship between Sirt1, autophagy, and ECM related genes expression in NP cells. We employed EX-527 as a Sirt1 enzyme activity inhibitor, and revealed that EX-527 had no effect on Sirt1 expression. Based on our results, EX-527 treatment inhibited PEMF-induced autophagy, as evidenced by an increase in the LC3-II/LC3-I ratio and p62 levels in the EX 527 group, compared to the PEMF group (**Figures 5A–F**). Our TEM results revealed that the number of autophagosomes and autophagolysosomes in the EX-527 treated NP cells was also significantly reduced, compared to the PEMF treated NP cells (**Figures 5G,H**). Taken together, EX-527 inhibited the PEMF-mediated induction of ECM synthesis in NP cells, as evidenced by the marked decrease in collagen II expression and the simultaneous increase in MMP3 expression. In all, our results suggest that PEMF promotes NP cell ECM synthesis by stimulating the Sirt1-mediated autophagy pathway.

PEMF Improved Rat IVD Degeneration in a Long-Term Treatment

To examine the PEMF-mediated regulation of IVD degeneration *in vivo*, we established an IVD degeneration model by puncturing the IVD of rat tail. Firstly, we

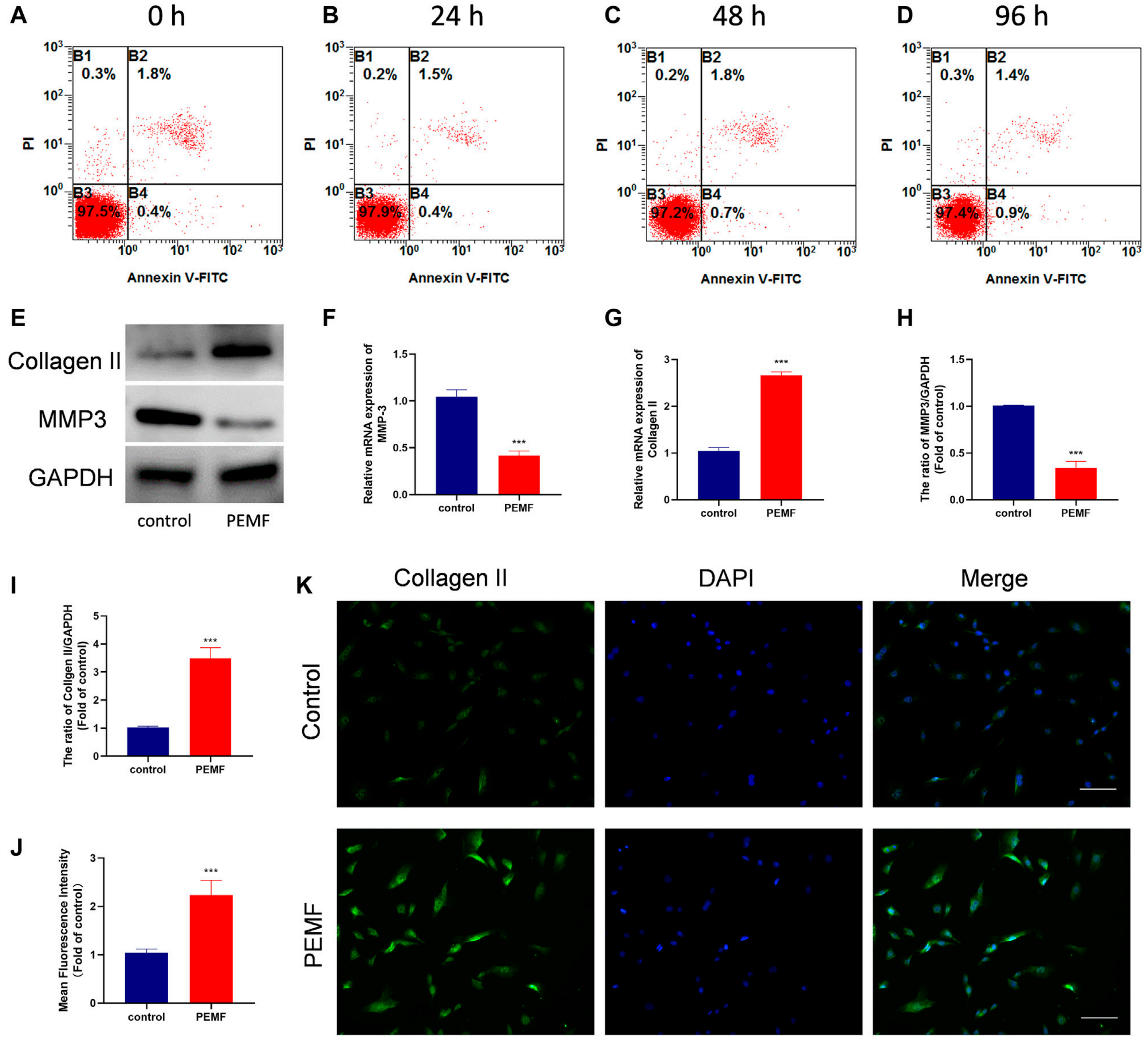

FIGURE 2 | PEMF attenuates cell degeneration in human degenerated NP cells. **(A–D)** The apoptosis ratio of NP cells at time points 24, 48, and 96 h after 4 h/day of PEMF administration. **(E–I)** The qRT-PCR analysis of Collagen II and MMP-3 transcripts (n = 3), western blot and semi-quantitative analyses of Collagen II and MMP-3 protein levels (n = 3). **(J–K)** Representative images of immunofluorescence and semi-quantitative analyses of Collagen II fluorescence intensity in NP cells, imaged by fluorescence microscopy (scale bar = 50 μm). $^{***}p$ < 0.001. Data presented as means ± SD.

measured the changes in the weight of the rats to monitor whether PEMF would affect other tissues in rats. No significance change was observed in the weight of rats in each group at 2w, 4w and 8w timepoint with or without PEMF stimulation, which indicates that PEMF is safe and has no side effects in rats (**Supplementary Figure 2A**). We next assessed IVD degeneration *via* MRI after 8 weeks. Based on our results, the T2-weighted signal intensity of the PEMF rats was stronger, compared to the puncture only rats (**Figure 6A**). Moreover, the Pfirrmann score grading of IVD degeneration showed that the PEMF treatment group had markedly reduced scores, relative to the puncture-only rats (**Figure 6B**). Furthermore, using H&E and Safranin-O staining (**Figures 6C,D**), we revealed that the number of NP tissues in the PEMF treatment group was greater, relative to the puncture-only group, and the integrity of AF and CEP was also significantly better than the puncture-only group. In terms of the histological score, the PEMF-treated rats had markedly reduced scores, compared to the puncture rats (**Figure 6F**). Additionally, based on the Sirius red staining, the amount of collagen I and collagen III in the PEMF-treated rats were markedly reduced, relative to the puncture rats (**Figures 6E,G**). Collectively, the above data indicate that PEMF application attenuates the process of IVD degeneration *in vivo*.

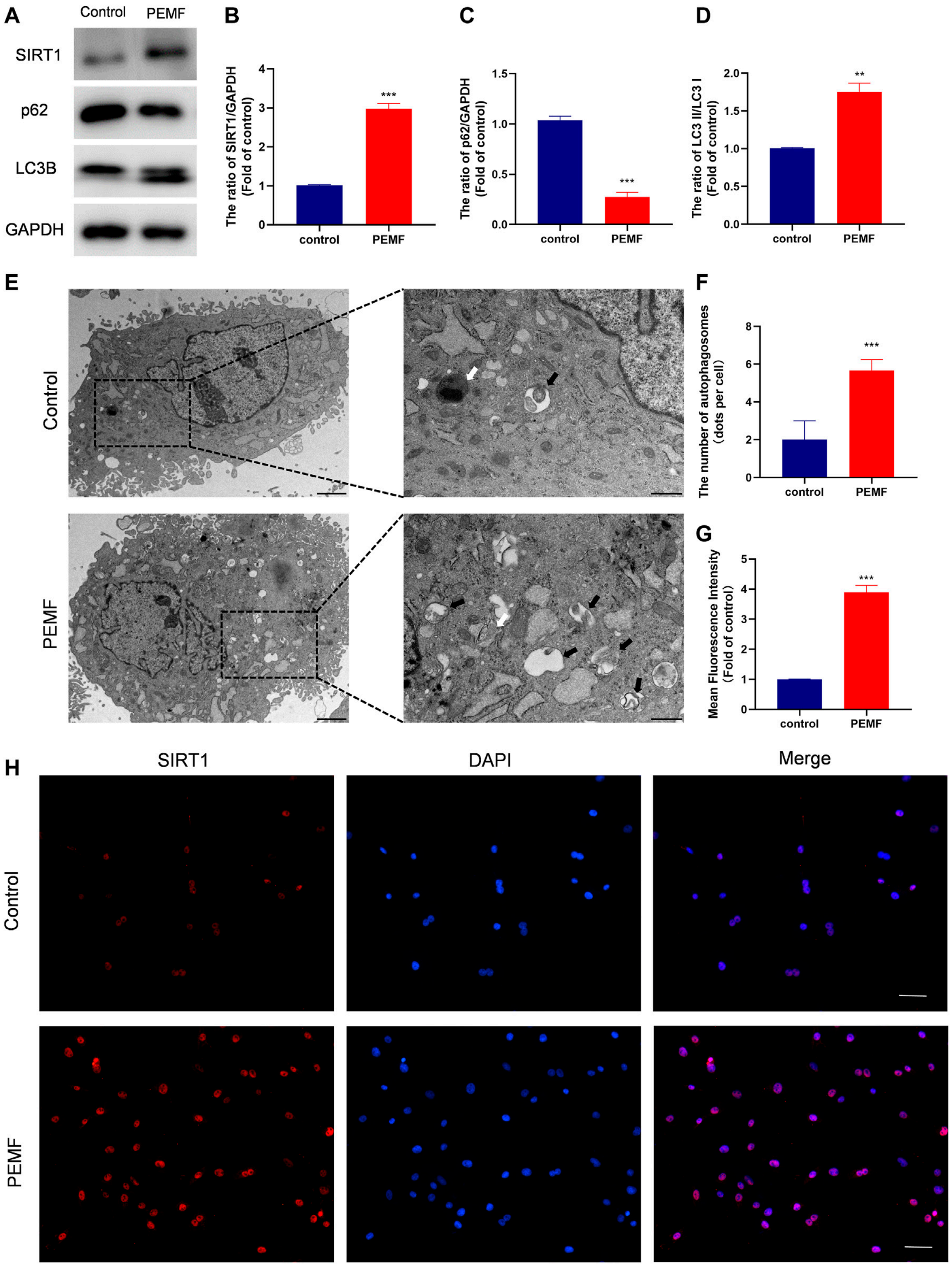

FIGURE 3 | PEMF exposure promotes autophagy and elevates SIRT1 levels and activity in the human degenerated NP cells. **(A–D)** Western blot and semi-quantitative analyses of SIRT1, p62, and LC3B protein levels (n = 3). **(E–F)** Autophagosomes and autophagolysosomes, visualized by transmission electron microscopy (Black arrow, autophagosome; White arrow, autophagolysosome, scale bar:2 μm, 0.5 μm). **(G–H)** Representative images of immunofluorescence and semi-quantitative analyses of SIRT1 fluorescence intensity in NP cells, imaged by fluorescence microscopy (scale bar = 50 μm). $^{**}p < 0.01$, $^{***}p < 0.001$. Data presented as means ± SD.

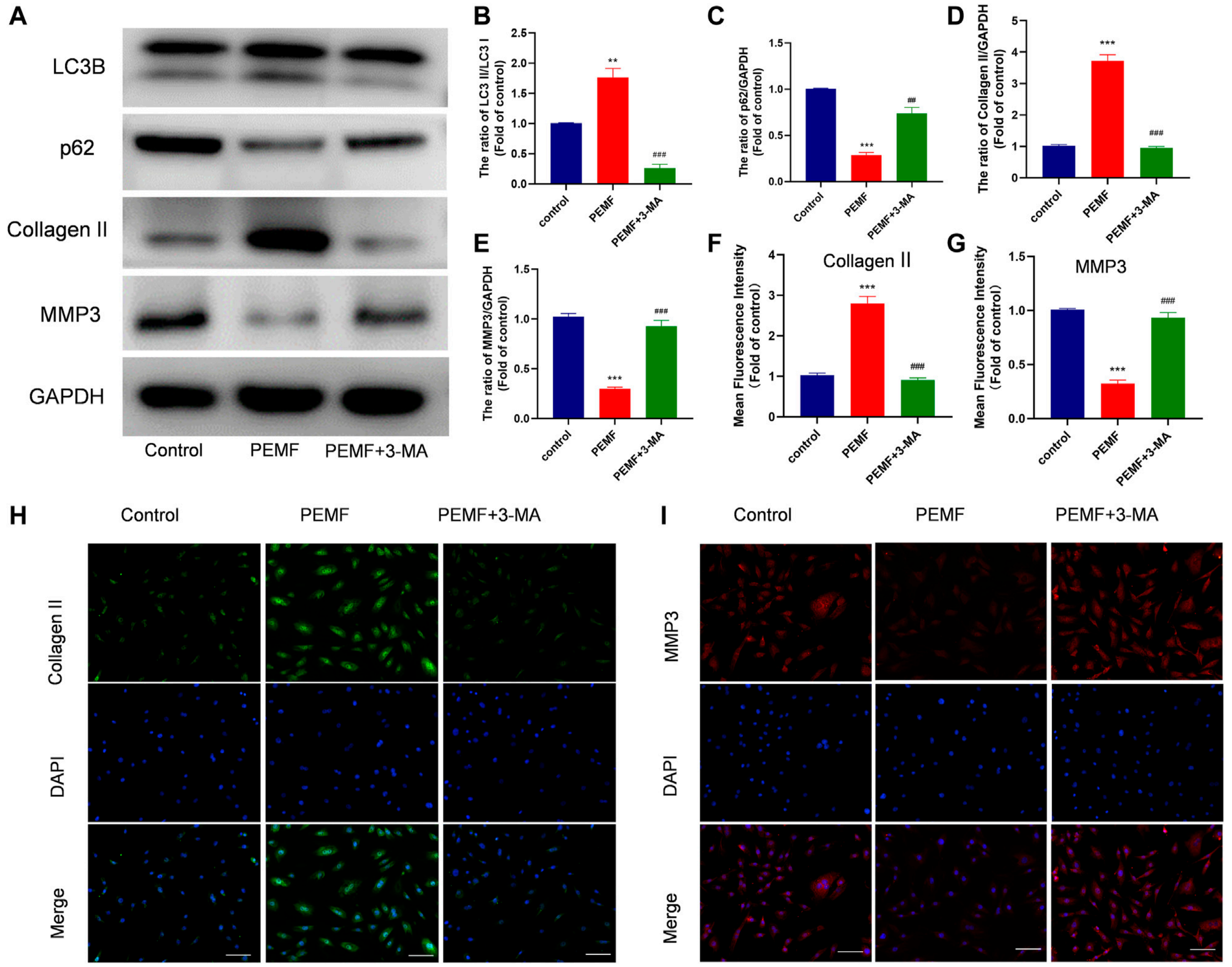

FIGURE 4 | PEMF regulates ECM related makers expression *via* autophagy **(A–E)** Western blot and semi-quantitative analyses of Collagen II, MMP-3, p62, and LC3B protein levels (n = 3). **(F–I)** Representative images of immunofluorescence and semi-quantitative analyses of Collagen II and MMP-3 fluorescence intensity in NP cells, imaged by fluorescence microscopy (scale bar = 50 μm). $^{**}p < 0.01$ vs. control, $^{***}p < 0.001$ vs. control, $^{\#\#}p < 0.01$ vs. PEMF, $^{\#\#\#}p < 0.001$ vs. PEMF. Data presented as means ± SD.

PEMF Induces SIRT1-Mediated Autophagy *in vivo*

We next examined whether PEMF induces the SIRT1-autophagy network *in vivo*. Relative to the puncture only group, immunofluorescence staining revealed that LC3B and SIRT1-positive cells were remarkably enhanced in the PEMF treated rats (**Figures 7A,B**). In addition, based on immunofluorescence staining, Aggrecan and collagen II expressions were also markedly elevated in the PEMF treated rats, relative to the puncture only rats (**Figures 6H–J**). Taken together, our *in vivo* investigation confirmed that PEMF preserve healthy ECM, and limit both collagen II and aggrecan degeneration in NP cells *via* the SIRT1-autophagic network.

DISCUSSION

Herein, we employed the human degenerated NP cells and a rat IVD puncture model to systematically assess the therapeutic outcome of PEMF on IVD degeneration. In our *in vitro* investigation, we revealed that PEMF indeed enhances ECM synthesis *via* the SIRT1-dependent autophagic network. We also assessed PEMF therapeutic efficacy in a rat IVD degeneration model. Based on our research, PEMF indeed delays the progression of IVD degeneration and we confirmed that the PEMF-mediated therapeutic effect on IVD degeneration involves the SIRT1-autophagic network.

Prior investigations revealed that alterations in the ECM metabolism in IVD tissue disrupt ECM structure, thereby

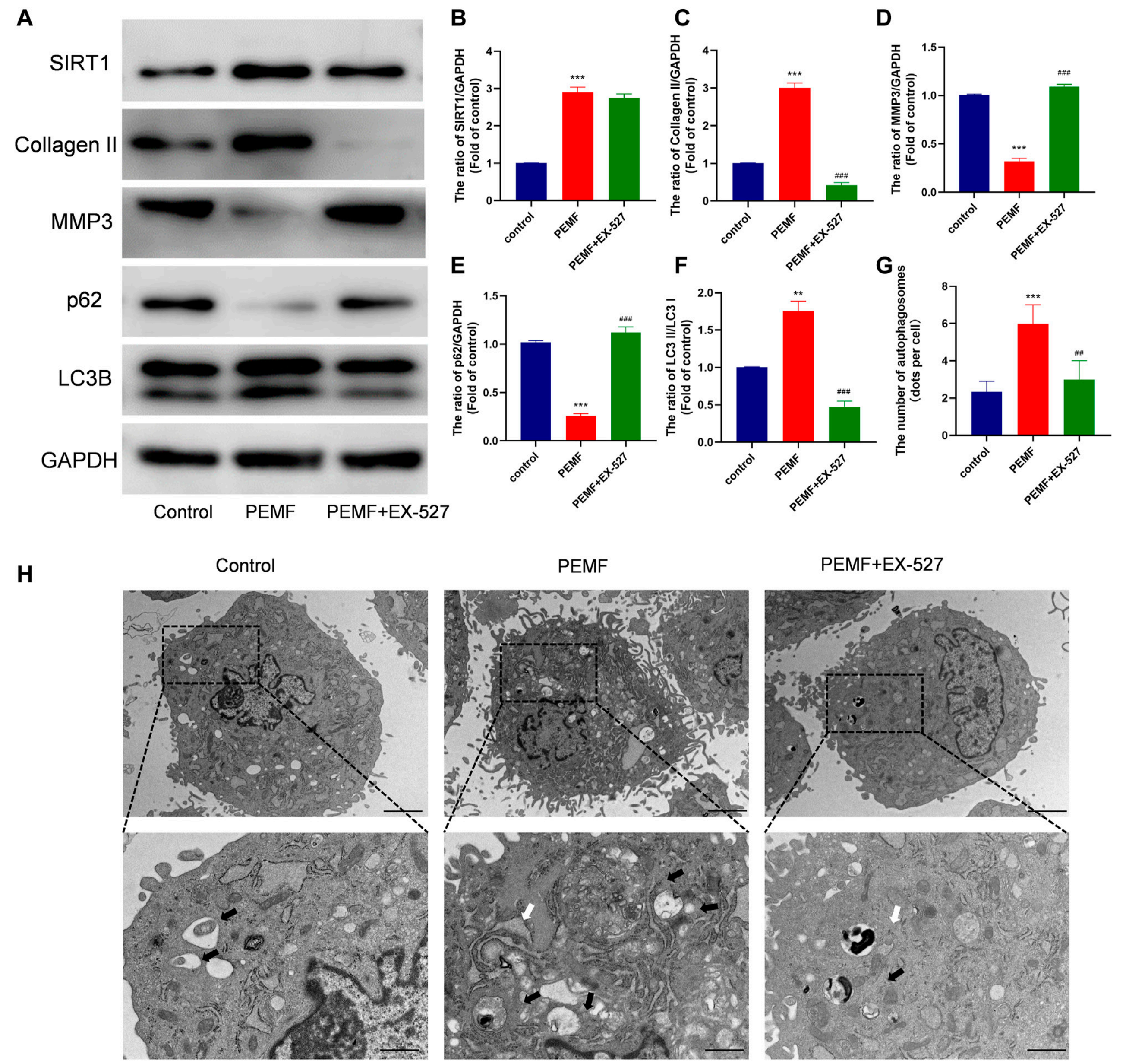

FIGURE 5 | PEMF regulates ECM related makers expression *via* SIRT1-stimulated autophagic activation **(A–F)** Western blot and semi-quantitative analyses of SIRT1, Collagen II, MMP-3, p62 and LC3B protein levels (n = 3). **(G–H)** Autophagosomes and autophagolysosomes, as visualized by transmission electron microscopy (Black arrow, autophagosome; White arrow, autophagolysosome, scale bar:2μm, 0.5 μm). $^{**}p < 0.01$ vs. control, $^{***}p < 0.001$ vs. control, $^{\#\#}p < 0.01$ vs. PEMF, $^{\#\#\#}p < 0.001$ vs. PEMF. Data expressed as means ± SD.

reducing IVD tolerance to mechanical loads (Novais et al., 2021a; Hu S. et al., 2021; Rajasekaran et al., 2021). Generally, reduced ECM production and elevated ECM degradation are characteristic of IVD degeneration. Therefore, developing a treatment method that promotes ECM repair of IVD tissue is essential to treating IVD degeneration.

It is well known that PEMF exerts its therapeutic effect *via* regulation of metabolic pathways (Cadossi et al., 2020). This occurs *via* regulation of cell proliferation, differentiation, and maturation, particularly in the treatment of musculoskeletal diseases (Yang et al., 2021; Liu et al., 2022). PEMF was reported to improve treatment of various bone diseases, such as, cartilage defects, tendon repair, osteoarthritis, osteoporosis, and so on (Reilingh et al., 2016; Wang et al., 2019; Dolkart et al., 2021). In recent years, clinical studies have shown that PEMF also has a significant relieving effect on the pain caused by IVD degeneration (Foley-Nolan et al., 1990; Sutbeyaz et al., 2006; Alvarez et al., 2019). In a placebo-controlled study evaluating the efficacy of PEMF treatment in patients with chronic neck pain, patients who received PEMF showed

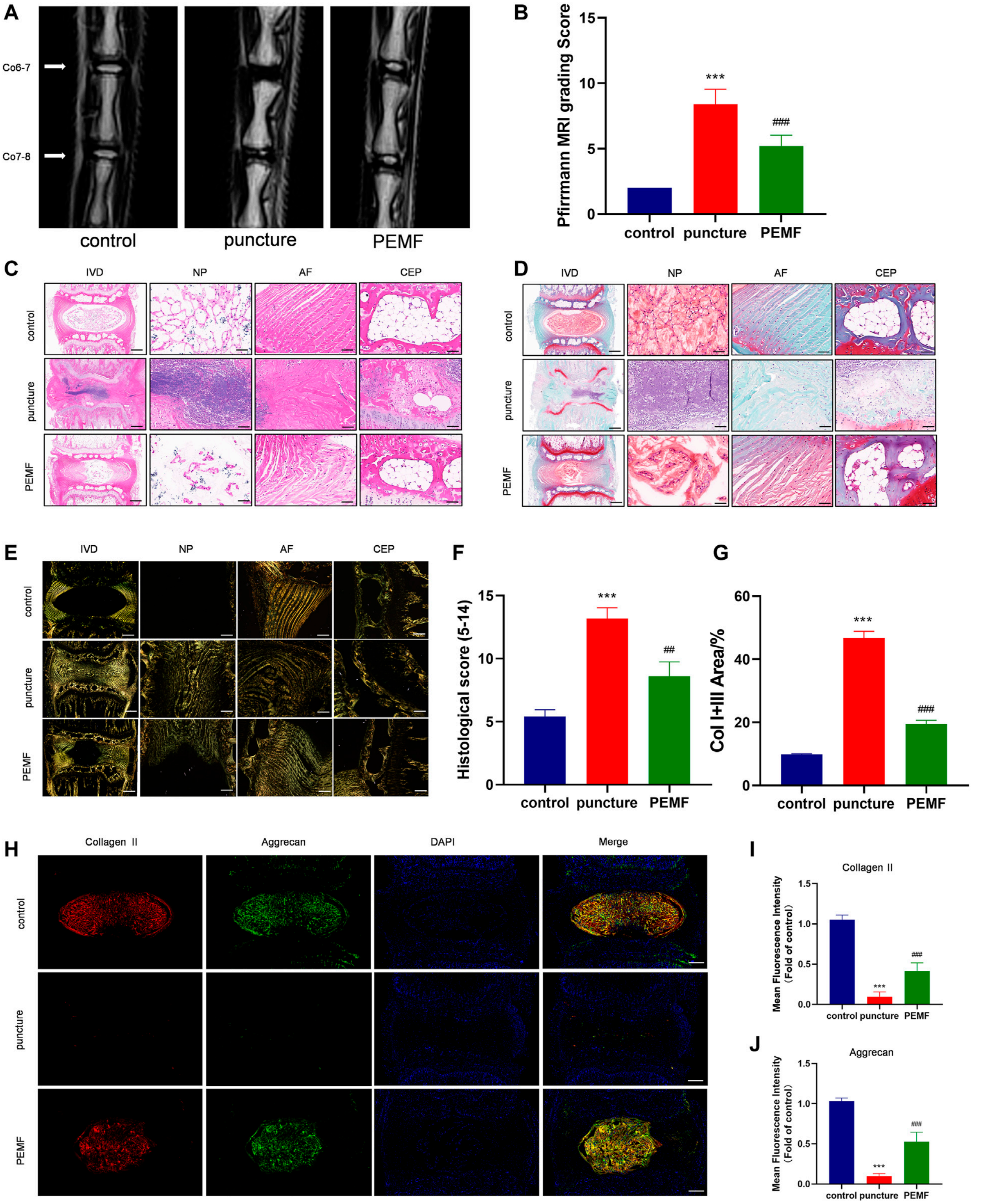

FIGURE 6 | PEMF exposure improved rat IVD degeneration *in vivo*. **(A–B)** Representative images of IVD tissue MRI and Pffirrmann score after 8 weeks of PEMF exposure. **(C–E)** Representative images of IVD tissue HE, S-O staining, and Polarized Sirius Red image (level: Co6-7; sagittal; scale bar: 500 μm, 100 μm). **(F–G)** Corresponding histological score and percentage of type I and type III collagen area. **(H–J)** Representative images of immunofluorescence and semi-quantitative analyses of Collagen II and Aggrecan fluorescence intensity in IVD tissues, imaged by fluorescence microscopy (sagittal; scale bar = 500 μm). ****p* < 0.001 vs. control, ##*p* < 0.01 vs. puncture, ###*p* < 0.001 vs. puncture. Data expressed as means ± SD.

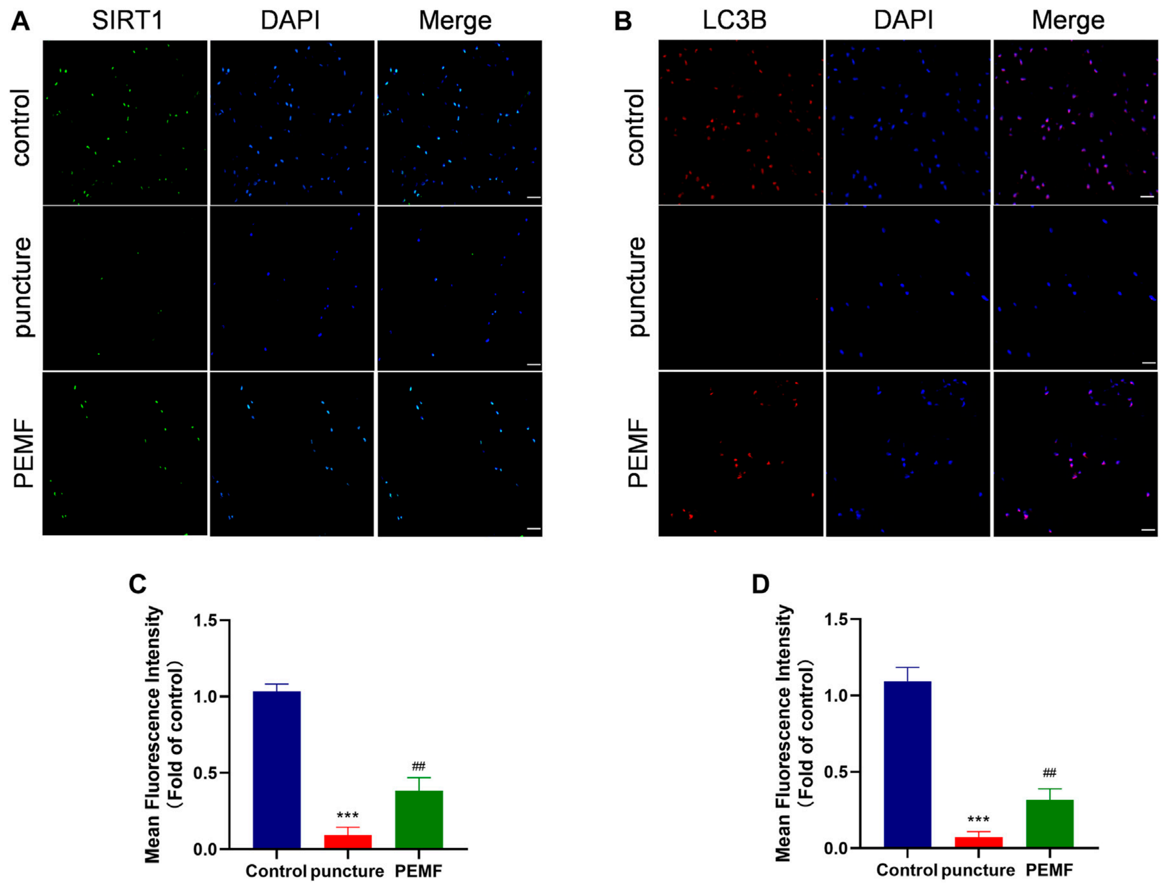

FIGURE 7 | (A–D) Representative images of immunofluorescence and semi-quantitative analyses of SIRT1 and LC3B fluorescence intensity in IVD tissues, imaged by fluorescence microscopy (scale bar = 50 μm). ***p < 0.001 vs. control, ##p < 0.01 vs. puncture. Data expressed as means ± SD.

significant improvements in neck pain and range of motion compared to a control group (Foley-Nolan et al., 1990). In another clinical study evaluating the efficacy of PEMF for pain in patients with cervical disc herniation, patients showed significant improvement in pain scores from pre-treatment to week 12 after treatment compared to control group (Alvarez et al., 2019). In basic science research, since PEMFs can generate oscillating magnetic fields, they are able to affect and alter cellular functions by inducing vibrations of free ions on the cell membrane surface (Ganesan et al., 2009). It has also been suggested that PEMFs can modulate downstream signal transduction pathways and cell surface receptor expression/activation to modulate cellular functions such as proliferation, differentiation, extracellular matrix (ECM) synthesis, and intercellular communication (Delle Monache et al., 2013; Viganò et al., 2016; Furuya-Kanamori et al., 2020). In IVD cells, previous studies demonstrated that PEMF induced upregulation of matrix synthesis through bone morphogenetic protein (BMP) signaling (Schmidt-Rohlfing et al., 2008; Okada et al., 2013). Therefore, in this study, we examined the influence of PEMF on degenerated NP cells and IVD degeneration animal models. In *in vitro* experiments, we demonstrated that PEMF promotes expression of collagen II (related to ECM synthesis), while reducing MMP3 (related to ECM catabolism) levels. However, no significance change was observed in cell characterizations, including cell apoptosis, viability and cell morphology. Even though the positive effect of PEMF in degenerative IVD cells was demonstrated, the role of PEMF in non-degenerated cells remains to be studied. In *in vivo* studies, we successfully constructed a rat tail IVD degeneration model. Then, we applied PEMF systematically to the rats. To better understand the systemic effects of PEMF on rats, we measured body weight of rats at 2w, 4w and 8w timepoint, and no significance change was observed in each group, which confirmed that PEMF might be a safe noninvasive therapy. It has been shown that PEMF modulates biological functions of many tissues under pathological conditions, including injuries in bones, tendons, muscles and nervous system (Gessi et al., 2019; Huegel et al., 2020; Dolkart et al., 2021). In this study we mainly focus on the PEMF effect on disc degeneration induced by tail puncture. Our results suggested that PEMF alleviates IVD degeneration. Moreover, radiographic and histological results showed that no significant change was observed in the tissue surrounding the disc, which indicates that PEMF might be a safe and effective treatment in the future clinical use.

Despite some relatively studies of PEMF in IVD degeneration, little is known about the underlying mechanism of such therapies.

Autophagy is an evolutionarily conserved modulatory behavior that sustains cell homeostasis *via* lysosomal-dependent degradation of nonfunctioning organelles and misfolded proteins (Kitada and Koya 2021). Previous studies reported that autophagy is inhibited in degenerative diseases, including degeneration of IVD (Kim et al., 2021; Valenti et al., 2021). Therefore, autophagy activation can play a protective role. For example, melatonin alleviates IVD degeneration by promoting autophagy (Chen C. G. et al., 2020). Another Studies have shown that activation of autophagy in chondrocytes inhibits MMP activity and exerts a protective effect on chondrocytes, thereby blocking cartilage degeneration (Takayama et al., 2014; Vasheghani et al., 2015). In order to examine whether PEMF plays a protective role by promoting ECM synthesis *via* autophagy in IVD degeneration, we employed the classical autophagy inhibitor 3-MA. According to our analysis, 3-MA treatment markedly inhibited PEMF-mediated autophagy. This was achieved *via* a significant decrease in p62 protein levels and a simultaneous increase in the LC3-II/LC3-I ratio. Conversely, PEMF accelerated ECM synthesis by elevating collagen II levels, and inhibiting the catabolic process (i.e., reducing MMP3 levels). Moreover, these effects were reversed by 3-MA administration. Recently, studies have shown that various matrix molecules, including glycosaminoglycans, collagen, constituting the intervertebral disc and cartilage ECM, regulate autophagy through mTOR signaling (Chen F. et al., 2020; Zhang et al., 2021). Moreover, autophagy can in turn regulate ECM composition, directly or indirectly altering cellular function, i.e., the secretion of ECM molecules (Novais et al., 2021b). Given the complexity of crosstalk between autophagy and ECM, further insights into the molecular effects of crosstalk between ECM and autophagy during disc degeneration will be critical in the future research.

In our earlier work, we demonstrated a negative correlation between SIRT1 expression and IVD degeneration (Wang et al., 2020). In order to elucidate potential associations between SIRT1, autophagy, and IVD degeneration, we employed a classic SIRT1 enzyme activity suppressor EX-527 in our *in vitro* studies. Based on results, EX-527 has no effect on SIRT1 expression, but can severely reduce its enzymatic activity. We demonstrated that EX-527 effectively inhibits PEMF-induced autophagic activation, along with collagen II synthesis and MMP3 decomposition. Using an IVD rat model, we also validated that PEMF successfully improves puncture-stimulated IVD degeneration by elevating SIRT1 levels and activating autophagy. Although previous reports hold varying opinions on PEMF and SIRT1 regulation (Jeong et al., 2017; Patruno et al., 2020; He et al., 2021), our research confirmed that PEMF indeed promotes the expression of SIRT1 and autophagy, and delays the process of IVD degeneration.

CONCLUSION

In conclusion, our research provides evidence that PEMF promotes the SIRT1-autophagic network and reduces IVD degeneration in cells and animal models. These results provide new insights of PEMF in treating IVD degeneration and highlight their therapeutic potential in IVD degeneration. Hence, it is our hope that the present study will promote future application of PEMF as a potential therapeutic treatment for preventing IVD degeneration in clinical use.

DATA AVAILABILITY STATEMENT

The original contributions presented in the study are included in the article/**Supplementary Material**, further inquiries can be directed to the corresponding authors.

ETHICS STATEMENT

The animal study was reviewed and approved by the Animal Experimentation Ethics Committee of The Fourth Military Medical University, People's Republic of China. Written informed consent was obtained from the owners for the participation of their animals in this study. The studies involving human participants were reviewed and approved by the Institutional Review Board of Xijing Hospital of Fourth Military Medical University. Informed consent was obtained from all eligible participants.

AUTHOR CONTRIBUTIONS

YZ, LM and BX designed the experiments. YZ and SL performed most of the experiments and collected results. BW and XG analyzed the data. YZ and LM wrote the manuscript. TM and YH proofread the manuscript and results. All authors contributed to the study and approved the final version of the manuscript.

FUNDING

This work was supported by grants from the National Natural Science Foundation of China (81730065, 81972052, 82020108019, 81802143, 82122043, and 81801216), and the National Key Research and Development Plan (2016YFC1101700).

SUPPLEMENTARY MATERIAL

The Supplementary Material for this article can be found online at: https://www.frontiersin.org/articles/10.3389/fbioe.2022.853872/full#supplementary-material

REFERENCES

Alvarez, L. X., McCue, J., Lam, N. K., Askin, G., and Fox, P. R. (2019). Effect of Targeted Pulsed Electromagnetic Field Therapy on Canine Postoperative Hemilaminectomy: A Double-Blind, Randomized, Placebo-Controlled Clinical Trial. *J. Am. Anim. Hosp. Assoc.* 55, 83–91. doi:10.5326/jaaha-ms-6798

Bloise, N., Patrucco, A., Bruni, G., Montagna, G., Caringella, R., Fassina, L., et al. (2020). *In Vitro* Production of Calcified Bone Matrix onto Wool Keratin Scaffolds via Osteogenic Factors and Electromagnetic Stimulus. *Materials (Basel)* 13, 3052. doi:10.3390/ma13143052

Cadossi, R., Massari, L., Racine-Avila, J., and Aaron, R. K. (2020). Pulsed Electromagnetic Field Stimulation of Bone Healing and Joint Preservation: Cellular Mechanisms of Skeletal Response. *J. Am. Acad. Orthop. Surg. Glob. Res. Rev.* 4, e1900155. doi:10.5435/JAAOSGlobal-D-19-00155

Caliogna, L., Medetti, M., Bina, V., Brancato, A. M., Castelli, A., Jannelli, E., et al. (2021). Pulsed Electromagnetic Fields in Bone Healing: Molecular Pathways and Clinical Applications. *Int. J. Mol. Sci.* 22, 7403. doi:10.3390/ijms22147403

Cashin, A. G., Folly, T., Bagg, M. K., Wewege, M. A., Jones, M. D., Ferraro, M. C., et al. (2021). Efficacy, Acceptability, and Safety of Muscle Relaxants for Adults with Non-specific Low Back Pain: Systematic Review and Meta-Analysis. *Bmj* 374, n1446. doi:10.1136/bmj.n1446

Chan, A. K., Tang, X., Mummaneni, N. V., Coughlin, D., Liebenberg, E., Ouyang, A., et al. (2019). Pulsed Electromagnetic fields Reduce Acute Inflammation in the Injured Rat-Tail Intervertebral Disc. *JOR Spine* 2, e1069. doi:10.1002/jsp2.1069

Chen, C. G., Gubbiotti, M. A., Kapoor, A., Han, X., Yu, Y., Linhardt, R. J., et al. (2020a). Autophagic Degradation of HAS2 in Endothelial Cells: A Novel Mechanism to Regulate Angiogenesis. *Matrix Biol.* 90, 1–19. doi:10.1016/j.matbio.2020.02.001

Chen, F., Liu, H., Wang, X., Li, Z., Zhang, J., Pei, Y., et al. (2020b). Melatonin Activates Autophagy via the NF-Kb Signaling Pathway to Prevent Extracellular Matrix Degeneration in Intervertebral Disc. *Osteoarthritis and Cartilage* 28, 1121–1132. doi:10.1016/j.joca.2020.05.011

Cieza, A., Causey, K., Kamenov, K., Hanson, S. W., Chatterji, S., and Vos, T. (2021). Global Estimates of the Need for Rehabilitation Based on the Global Burden of Disease Study 2019: a Systematic Analysis for the Global Burden of Disease Study 2019. *Lancet* 396, 2006–2017. doi:10.1016/S0140-6736(20)32340-0

Dai, F., Yu, P., Yu, Z., Jiang, H., Ma, Z., and Liu, J. (2021). Yiqi Huoxue Recipe Delayed Intervertebral Disc Degeneration by Activating Autophagy. *Front. Pharmacol.* 12, 705747. doi:10.3389/fphar.2021.705747

Delle Monache, S., Angelucci, A., Sanità, P., Iorio, R., Bennato, F., Mancini, F., et al. (2013). Inhibition of Angiogenesis Mediated by Extremely Low-Frequency Magnetic Fields (ELF-MFs). *PLoS One* 8, e79309. doi:10.1371/journal.pone.0079309

Dolkart, O., Kazum, E., Rosenthal, Y., Sher, O., Morag, G., Yakobson, E., et al. (2021). Effects of Focused Continuous Pulsed Electromagnetic Field Therapy on Early Tendon-To-Bone Healing. *Bone Jt. Res.* 10, 298–306. doi:10.1302/2046-3758.105.bjr-2020-0253.r2

Foley-Nolan, D., Barry, C., Coughlan, R. J., O'Connor, P., and Roden, D. (1990). Pulsed High Frequency (27MHz) Electromagnetic Therapy for Persistent Neck Pain: A Double Blind, Placebo-Controlled Study of 20 Patients. *Orthopedics* 13, 445–451. doi:10.3928/0147-7447-19900401-10

Foster, N. E., Anema, J. R., Cherkin, D., Chou, R., Cohen, S. P., Gross, D. P., et al. (2018). Prevention and Treatment of Low Back Pain: Evidence, Challenges, and Promising Directions. *The Lancet* 391, 2368–2383. doi:10.1016/s0140-6736(18)30489-6

Francisco, V., Pino, J., González-Gay, M. Á., Lago, F., Karppinen, J., Tervonen, O., et al. (2022). A New Immunometabolic Perspective of Intervertebral Disc Degeneration. *Nat. Rev. Rheumatol.* 18, 47–60. doi:10.1038/s41584-021-00713-z

Furuya-Kanamori, L., Xu, C., Lin, L., Doan, T., Chu, H., Thalib, L., et al. (2020). P Value-Driven Methods Were Underpowered to Detect Publication Bias: Analysis of Cochrane Review Meta-Analyses. *J. Clin. Epidemiol.* 118, 86–92. doi:10.1016/j.jclinepi.2019.11.011

Ganesan, K., Gengadharan, A. C., Balachandran, C., Manohar, B. M., and Puvanakrishnan, R. (2009). Low Frequency Pulsed Electromagnetic Field-Aa Viable Alternative Therapy for Arthritis. *Indian J. Exp. Biol.* 47, 939–948.

Gessi, S., Merighi, S., Bencivenni, S., Battistello, E., Vincenzi, F., Setti, S., et al. (2019). Pulsed Electromagnetic Field and Relief of Hypoxia-Induced Neuronal Cell Death: The Signaling Pathway. *J. Cel Physiol* (Epub ahead of print). doi:10.1002/jcp.28149

He, G.-L., Wang, Z.-Z., Yu, X.-T., Shen, T.-T., Luo, Z., Li, P., et al. (2021). The Involvement of Microglial CX3CR1 in Heat Acclimation-Induced Amelioration of Adult Hippocampal Neurogenesis Impairment in EMF-Exposed Mice. *Brain Res. Bull.* 177, 181–193. doi:10.1016/j.brainresbull.2021.09.018

Hu, J., Yan, Q., Jiang, H., Xu, C., Chen, Y., and Yuan, W. (2021a). A Decrease in IL-33 Regulates Matrix Degradation and Apoptosis in Intervertebral Disc Degeneration via HIF-1alpha. *Am. J. Transl Res.* 13, 12724–12733.

Hu, S., Chen, L., Al Mamun, A., Ni, L., Gao, W., Lin, Y., et al. (2021b). The Therapeutic Effect of TBK1 in Intervertebral Disc Degeneration via Coordinating Selective Autophagy and Autophagic Functions. *J. Adv. Res.* 30, 1–13. doi:10.1016/j.jare.2020.08.011

Huegel, J., Boorman-Padgett, J. F., Nuss, C. A., Raja, H. A., Chan, P. Y., Kuntz, A. F., et al. (2020). Effects of Pulsed Electromagnetic Field Therapy on Rat Achilles Tendon Healing. *J. Orthop. Res.* 38, 70–81. doi:10.1002/jor.24487

Jeong, W.-Y., Kim, J.-B., Kim, H.-J., and Kim, C.-W. (2017). Extremely Low-Frequency Electromagnetic Field Promotes Astrocytic Differentiation of Human Bone Marrow Mesenchymal Stem Cells by Modulating SIRT1 Expression. *Biosci. Biotechnol. Biochem.* 81, 1356–1362. doi:10.1080/09168451.2017.1308243

Jiang, D.-P., Li, J.-h., Zhang, J., Xu, S.-L., Kuang, F., Lang, H.-Y., et al. (2016). Long-term Electromagnetic Pulse Exposure Induces Abeta Deposition and Cognitive Dysfunction through Oxidative Stress and Overexpression of APP and BACE1. *Brain Res.* 1642, 10–19. doi:10.1016/j.brainres.2016.02.053

Jing, D., Shen, G., Huang, J., Xie, K., Cai, J., Xu, Q., et al. (2010). Circadian Rhythm Affects the Preventive Role of Pulsed Electromagnetic fields on Ovariectomy-Induced Osteoporosis in Rats. *Bone* 46, 487–495. doi:10.1016/j.bone.2009.09.021

Kavand, H., Haghighipour, N., Zeynali, B., Seyedjafari, E., and Abdemami, B. (2016). Extremely Low Frequency Electromagnetic Field in Mesenchymal Stem Cells Gene Regulation: Chondrogenic Markers Evaluation. *Artif. Organs* 40, 929–937. doi:10.1111/aor.12696

Kim, J. W., Jeon, N., Shin, D. E., Lee, S. Y., Kim, M., Han, D. H., et al. (2021). Regeneration in Spinal Disease: Therapeutic Role of Hypoxia-Inducible Factor-1 Alpha in Regeneration of Degenerative Intervertebral Disc. *Int. J. Mol. Sci.* 22, 5281. doi:10.3390/ijms22105281

Kitada, M., and Koya, D. (2021). Autophagy in Metabolic Disease and Ageing. *Nat. Rev. Endocrinol.* 17, 647–661. doi:10.1038/s41574-021-00551-9

Knezevic, N. N., Candido, K. D., Vlaeyen, J. W. S., Van Zundert, J., and Cohen, S. P. (2021). Low Back Pain. *Lancet* 398, 78–92. doi:10.1016/S0140-6736(21)00733-9

Kritschil, R., Scott, M., Sowa, G., and Vo, N. (2021). Role of Autophagy in Intervertebral Disc Degeneration. *J. Cel Physiol* 237, 1266. doi:10.1002/jcp.30631

Li, Z., Liu, T., Feng, Y., Tong, Y., Jia, Y., Wang, C., et al. (2022). PPARγ Alleviates Sepsis-Induced Liver Injury by Inhibiting Hepatocyte Pyroptosis via Inhibition of the ROS/TXNIP/NLRP3 Signaling Pathway. *Oxidative Med. Cell Longevity* 2022, 1–15. doi:10.1155/2022/1269747

Liu, L., Huang, K., Li, W., Qiu, R., Fang, Y., Huang, Y., et al. (2021). Molecular Imaging of Collagen Destruction of the Spine. *ACS Nano* 15, 19138–19149. doi:10.1021/acsnano.1c07112

Mei, L., Zheng, Y., Ma, T., Xia, B., Gao, X., Hao, Y., et al. (2021). (-)-Epigallocatechin-3-gallate Ameliorates Intervertebral Disc Degeneration through Reprogramming of the Circadian Clock. *Front. Pharmacol.* 12, 753548. doi:10.3389/fphar.2021.753548

Miller, S. L., Coughlin, D. G., Waldorff, E. I., Ryaby, J. T., and Lotz, J. C. (2016). Pulsed Electromagnetic Field (PEMF) Treatment Reduces Expression of Genes Associated with Disc Degeneration in Human Intervertebral Disc Cells. *Spine J.* 16, 770–776. doi:10.1016/j.spinee.2016.01.003

Novais, E. J., Choi, H., Madhu, V., Suyama, K., Anjo, S. I., Manadas, B., et al. (2021a). Hypoxia and Hypoxia-Inducible Factor-1α Regulate Endoplasmic

Reticulum Stress in Nucleus Pulposus Cells. *Am. J. Pathol.* 191, 487–502. doi:10.1016/j.ajpath.2020.11.012

Novais, E. J., Tran, V. A., Johnston, S. N., Darris, K. R., Roupas, A. J., Sessions, G. A., et al. (2021b). Long-term Treatment with Senolytic Drugs Dasatinib and Quercetin Ameliorates Age-dependent Intervertebral Disc Degeneration in Mice. *Nat. Commun.* 12, 5213. doi:10.1038/s41467-021-25453-2

Okada, M., Kim, J. H., Hutton, W. C., and Yoon, S. T. (2013). Upregulation of Intervertebral Disc-Cell Matrix Synthesis by Pulsed Electromagnetic Field Is Mediated by Bone Morphogenetic Proteins. *J. Spinal Disord. Tech.* 26, 167–173. doi:10.1097/bsd.0b013e31823d36cf

Parate, D., Franco-Obregón, A., Fröhlich, J., Beyer, C., Abbas, A. A., Kamarul, T., et al. (2017). Enhancement of Mesenchymal Stem Cell Chondrogenesis with Short-Term Low Intensity Pulsed Electromagnetic fields. *Sci. Rep.* 7, 9421. doi:10.1038/s41598-017-09892-w

Patruno, A., Costantini, E., Ferrone, A., Pesce, M., Diomede, F., Trubiani, O., et al. (2020). Short ELF-EMF Exposure Targets SIRT1/Nrf2/HO-1 Signaling in THP-1 Cells. *Int. J. Mol. Sci.* 21, 7284. doi:10.3390/ijms21197284

Rajasekaran, S., Thangavel, C., Djuric, N., Raveendran, M., Soundararajan, D. C. R., Nayagam, S. M., et al. (2021). Profiling Extra Cellular Matrix Associated Proteome of Human Fetal Nucleus Pulposus in Search for Regenerative Targets. *Sci. Rep.* 11, 19013. doi:10.1038/s41598-021-97620-w

Reilingh, M. L., van Bergen, C. J. A., Gerards, R. M., van Eekeren, I. C., de Haan, R. J., Sierevelt, I. N., et al. (2016). Effects of Pulsed Electromagnetic Fields on Return to Sports after Arthroscopic Debridement and Microfracture of Osteochondral Talar Defects. *Am. J. Sports Med.* 44, 1292–1300. doi:10.1177/0363546515626544

Schmidt-Rohlfing, B., Silny, J., Woodruff, S., and Gavenis, K. (2008). Effects of Pulsed and Sinusoid Electromagnetic fields on Human Chondrocytes Cultivated in a Collagen Matrix. *Rheumatol. Int.* 28, 971–977. doi:10.1007/s00296-008-0565-0

Sobajima, S., Kompel, J. F., Kim, J. S., Wallach, C. J., Robertson, D. D., Vogt, M. T., et al. (2005). A Slowly Progressive and Reproducible Animal Model of Intervertebral Disc Degeneration Characterized by MRI, X-Ray, and Histology. *Spine* 30, 15–24. doi:10.1097/01.brs.0000148048.15348.9b

Sun, Z., Liu, B., Liu, Z.-H., Song, W., Wang, D., Chen, B.-Y., et al. (2020). Notochordal-Cell-Derived Exosomes Induced by Compressive Load Inhibit Angiogenesis via the miR-140-5p/Wnt/β-Catenin Axis. *Mol. Ther. - Nucleic Acids* 22, 1092–1106. doi:10.1016/j.omtn.2020.10.021

Sutbeyaz, S. T., Sezer, N., and Koseoglu, B. F. (2006). The Effect of Pulsed Electromagnetic fields in the Treatment of Cervical Osteoarthritis: a Randomized, Double-Blind, Sham-Controlled Trial. *Rheumatol. Int.* 26, 320–324. doi:10.1007/s00296-005-0600-3

Takayama, K., Kawakami, Y., Kobayashi, M., Greco, N., Cummins, J. H., Matsushita, T., et al. (2014). Local Intra-articular Injection of Rapamycin Delays Articular Cartilage Degeneration in a Murine Model of Osteoarthritis. *Arthritis Res. Ther.* 16, 482. doi:10.1186/s13075-014-0482-4

Tu, J., Li, W., Yang, S., Yang, P., Yan, Q., Wang, S., et al. (2021). Single-Cell Transcriptome Profiling Reveals Multicellular Ecosystem of Nucleus Pulposus during Degeneration Progression. *Adv. Sci. (Weinh)* 9, e2103631. doi:10.1002/advs.202103631

Valenti, M. T., Dalle Carbonare, L., Zipeto, D., and Mottes, M. (2021). Control of the Autophagy Pathway in Osteoarthritis: Key Regulators, Therapeutic Targets and Therapeutic Strategies. *Int. J. Mol. Sci.* 22, 2700. doi:10.3390/ijms22052700

Varani, K., Vincenzi, F., Pasquini, S., Blo, I., Salati, S., Cadossi, M., et al. (2021). Pulsed Electromagnetic Field Stimulation in Osteogenesis and Chondrogenesis: Signaling Pathways and Therapeutic Implications. *Int. J. Mol. Sci.* 22, 809. doi:10.3390/ijms22020809

Vasheghani, F., Zhang, Y., Li, Y.-H., Blati, M., Fahmi, H., Lussier, B., et al. (2015). PPARγ Deficiency Results in Severe, Accelerated Osteoarthritis Associated with Aberrant mTOR Signalling in the Articular Cartilage. *Ann. Rheum. Dis.* 74, 569–578. doi:10.1136/annrheumdis-2014-205743

Viganò, M., Sansone, V., d'Agostino, M. C., Romeo, P., Perucca Orfei, C., and de Girolamo, L. (2016). Mesenchymal Stem Cells as Therapeutic Target of Biophysical Stimulation for the Treatment of Musculoskeletal Disorders. *J. Orthop. Surg. Res.* 11, 163. doi:10.1186/s13018-016-0496-5

Wang, D., He, X., Wang, D., Peng, P., Xu, X., Gao, B., et al. (2020). Quercetin Suppresses Apoptosis and Attenuates Intervertebral Disc Degeneration via the SIRT1-Autophagy Pathway. *Front. Cel Dev. Biol.* 8, 613006. doi:10.3389/fcell.2020.613006

Wang, T., Yang, L., Jiang, J., Liu, Y., Fan, Z., Zhong, C., et al. (2019). Pulsed Electromagnetic fields: Promising Treatment for Osteoporosis. *Osteoporos. Int.* 30, 267–276. doi:10.1007/s00198-018-04822-6

Yang, X., Guo, H., Ye, W., Yang, L., and He, C. (2021). Pulsed Electromagnetic Field Attenuates Osteoarthritis Progression in a Murine Destabilization-Induced Model through Inhibition of TNF-α and IL-6 Signaling. *Cartilage* 13, 1665s–1675S. doi:10.1177/19476035211049561

Zhang, T. W., Li, Z. F., Ding, W., Wang, H. R., Ding, S. L., Han, G. J., et al. (2021). Decorin Inhibits Nucleus Pulposus Apoptosis by Matrix-induced Autophagy via the mTOR Pathway. *J. Orthop. Res.* 39, 1777–1788. doi:10.1002/jor.24882

Zhi, Z., Na, T., Jue, W., Zhihe, Z., and Lijun, T. (2016). Effects of Pulsed Ultrasound and Pulsed Electromagnetic Field on the Extracellular Matrix Secretion of Rat Bone Marrow Mesenchymal Stem Cell Pellets in Chondrogenesis. *Hua Xi Kou Qiang Yi Xue Za Zhi* 34, 291–294. doi:10.7518/hxkq.2016.03.015

Zhong, H., Yang, C., Gao, Y., Cao, P., Tian, Y., Shen, X., et al. (2021). PERK Signaling Activation Restores Nucleus Pulposus Degeneration by Activating Autophagy under Hypoxia Environment. *Osteoarthritis Cartilage* 30, 341. doi:10.1016/j.joca.2021.11.005

Zhu, S., Ge, J., Liu, Z., Liu, L., Jing, D., Ran, M., et al. (2017). Circadian Rhythm Influences the Promoting Role of Pulsed Electromagnetic Fields on Sciatic Nerve Regeneration in Rats. *Front. Neurol.* 8, 101. doi:10.3389/fneur.2017.00101

Zielinski, J., Ducray, A. D., Moeller, A. M., Murbach, M., Kuster, N., and Mevissen, M. (2020). Effects of Pulse-Modulated Radiofrequency Magnetic Field (RF-EMF) Exposure on Apoptosis, Autophagy, Oxidative Stress and Electron Chain Transport Function in Human Neuroblastoma and Murine Microglial Cells. *Toxicol. Vitro* 68, 104963. doi:10.1016/j.tiv.2020.104963

Conflict of Interest: The authors declare that the research was conducted in the absence of any commercial or financial relationships that could be construed as a potential conflict of interest.

frontiers in Bioengineering and Biotechnology

ORIGINAL RESEARCH
published: 28 March 2022
doi: 10.3389/fbioe.2022.855364

Prediction of Femoral Strength Based on Bone Density and Biochemical Markers in Elderly Men With Type 2 Diabetes Mellitus

Shaowei Jia[1], *He Gong*[1]*, *Yingying Zhang*[2], *Hongmei Liu*[1,3], *Haipeng Cen*[1], *Rui Zhang*[2] *and Yubo Fan*[1]*

[1]Key Laboratory for Biomechanics and Mechanobiology of Ministry of Education, Beijing Advanced Innovation Center for Biomedical Engineering, School of Biological Science and Medical Engineering, Beihang University, Beijing, China, [2]Beijing Key Laboratory of Rehabilitation Technical Aids for Old-Age Disability, National Research Center for Rehabilitation Technical Aids, Beijing, China, [3]Rehabilitation Hospital, National Research Center for Rehabilitation Technical Aids, Beijing, China

Purpose: Effects of bone density, bone turnover and advanced glycation end products (AGEs) on femoral strength (FS) are still unclear in patients with type 2 diabetes mellitus (T2DM). This study aims to assess and predict femoral strength and its influencing factors in elderly men with T2DM.

Methods: T2DM patients ($n = 10$, mean age, 66.98 years) and age-matched controls ($n = 8$, mean age, 60.38 years) were recruited. Femoral bone mineral density (BMD) and serum biochemical indices of all subjects were measured. FS was evaluated through finite element analysis based on quantitative computed tomography. Multiple linear regression was performed to obtain the best predictive models of FS and to analyze the ability of predictors of FS in both groups.

Results: FS ($p = 0.034$), HbA1c ($p = 0.000$) and fasting blood glucose ($p = 0.000$) levels of T2DM group were significantly higher than those of control group; however, the P1NP level ($p = 0.034$) was significantly lower. FS was positively correlated with femoral neck T score (FNTS) ($r = 0.794$, $p < 0.01$; $r = 0.881$, $p < 0.01$) in both groups. FS was correlated with age ($r = -0.750$, $p < 0.05$) and pentosidine ($r = -0.673$, $p < 0.05$) in T2DM group. According to multiple linear regression, FNTS and P1NP both contributed to FS in two groups. P1NP significantly improved the prediction of FS in both groups, but significant effect of FNTS on predicting FS was only presented in control group. Furthermore, pentosidine, age and HbA1c all played significant roles in predicting FS of T2DM.

Conclusion: Femoral strength was higher in elderly men with T2DM, which might be caused by higher BMD and lower bone turnover rate. Moreover, besides BMD and bone formation level, AGEs, blood glucose and age might significantly impact the prediction of femoral strength in T2DM.

Keywords: type 2 diabetes mellitus, quantitative computed tomography, finite element analysis, femoral strength, bone turnover

OPEN ACCESS

Edited by:
Bin Wang,
Chongqing Medical University, China

Reviewed by:
Mia M. Thi,
Albert Einstein College of Medicine,
United States
Da Jing,
Air Force Military Medical University,
China

Correspondence:
He Gong
bmegonghe@buaa.edu.cn
Yubo Fan
yubofan@buaa.edu.cn

Specialty section:
This article was submitted to
Biomechanics,
a section of the journal
Frontiers in Bioengineering and
Biotechnology

Received: *15 January 2022*
Accepted: *03 March 2022*
Published: *28 March 2022*

Citation:
Jia S, Gong H, Zhang Y, Liu H, Cen H, Zhang R and Fan Y (2022) Prediction of Femoral Strength Based on Bone Density and Biochemical Markers in Elderly Men With Type 2 Diabetes Mellitus.
Front. Bioeng. Biotechnol. 10:855364.
doi: 10.3389/fbioe.2022.855364

INTRODUCTION

Diabetes mellitus (DM) is one of the most common metabolism diseases. Type 2 diabetes mellitus (T2DM) is complicated and universal, so it has been considered as a health concern (Glovaci et al., 2019). Furthermore, T2DM is often accompanied with high bone fracture risk. Accurate prediction of bone strength could provide important information for preventing bone fracture in T2DM. Previous investigations proved that T2DM had complicated effects on bone because of many factors, including bone metabolism, insulin level, and advanced glycosylation end products (AGEs) (Li et al., 2013). Sufficient understanding of bone strength of T2DM and its influencing factors is necessary for predicting bone strength in clinics.

Strength is one of the most important indices of bone mechanical properties. It reflects the ability of bone to resist deformation and fracture. It could provide important basis for assessing bone quality and protecting bones in patients with T2DM to investigate the relationship between bone strength and its influencing factors. Bone strength was mainly affected by bone mineral density (BMD) and bone quality, and bone quality was determined by bone morphological parameters and material properties (Farr and Khosla, 2016). In clinics, the assessment of bone strength was based on BMD measured *via* clinical dual-energy X-ray (DXA). However, some limitations have been observed. DXA only displayed the 2D projection of 3D complex structures and failed to distinguish soft tissues, cancellous bones, and cortical bones (Kanis et al., 2011). Moreover, BMD measured *via* DXA was insensitive to short-term physical changes in bone strength through certain treatments (Bolotin, 2007). As a noninvasive method to evaluate 3D morphology, quantitative computed tomography (QCT) was widely used to analyze bone morphology and to assess spatial distribution of bone density (Ramamurthi et al., 2012). Moreover, finite element analysis (FEA) based on QCT images was a FDA-approved approach to noninvasively estimate changes in bone strength. QCT-based FEA has been successfully applied to assessing bone strength in previous studies (Keaveny et al., 2014; Knowles et al., 2021). Therefore, QCT-based FEA was reasonable and effective in examining bone strength with changed bone material properties in elderly men with T2DM.

Bone turnover continuously occurred to maintain bone dynamic balance, and it could replace damaged bone. This process consisted of bone formation and bone resorption. Many studies have indicated that the bone turnover rate in patients with T2DM was lower than that in individuals without T2DM (Shu et al., 2012; Farr et al., 2014; Wang et al., 2019). Histomorphometry has confirmed that low bone turnover and formation rates with reduced osteoclast activity were due to a low degree of matrix accumulation instead of abnormal bone mineralization (Krakauer et al., 1995). Therefore, it might be worth further verifying whether a low bone turnover rate could lead to reductions in bone quality and strength. In contrast, a previous study indicated that bone turnover markers (BTMs) and bone turnover rate did not differ between patients with T2DM and control subjects (Starup-Linde and Vestergaard, 2016). Thus, characteristics of bone turnover should be further clarified, and the ability of bone turnover on predicting bone strength in T2DM should also be investigated.

AGEs are composite products formed *via* the Maillard reaction after proteins are modified by aldose sugars *via* nonenzymatic chemical modification. AGEs are also considered as a factor of increasing bone fragility. A high AGEs level was found in patients with T2DM, moreover, a previous study indicated that high AGEs concentration could increase bone stiffness and bone fragility and reduce bone formation because of the suppression of osteoblast activity by AGEs (Ogawa et al., 2007). Pentosidine was a typical AGEs marker, it was significantly increased in non-diabetic patients with hip fracture compared with non-diabetic patients without fracture in the clinical setting, which indicated that increase in the non-enzymatic crosslinked type of AGEs might be a cause of deterioration of bone strength (Yamamoto and Sugimoto, 2016). Due to the difficulty of assessing bone strength *in vivo*, there was still no convinced explanation on the relationship between AGEs and bone strength. In consideration of the accuracy of assessing bone strength *via* QCT-based FEA, investigation of the effect and predictive ability of AGEs on simulated bone strength might be valuable for explaining the relationship between AGEs and bone strength.

In this study, subject-specific femoral strength was evaluated through FEA based on QCT images, and differences in body indices, serum biochemical markers, and femoral strength were compared between T2DM and control groups to investigate the influences of BMD, bone turnover, and serum biochemical markers on the femoral strength of the elderly men with T2DM. The relationships of femoral strength with BMD, bone turnover, and serum biochemical markers were analyzed. Moreover, the best predictive models of femoral strength of T2DM and control groups were obtained by multiple linear regression. In this study, the significant predictors of femoral strength could be found out, and it could provide sufficient evidence for assessing femoral strength of the elderly men with T2DM in clinics.

MATERIALS AND METHODS

Subjects

This study was approved by the ethics committee of the affiliated hospital of the National Research Center for Rehabilitation Technical Aids and conformed to the Declaration of Helsinki. Patients with T2DM ($n = 10$) and control subjects without T2DM ($n = 8$) were recruited in this hospital. All the subjects signed informed consent form. The specific recruitment criteria of control and T2DM subjects were as follows: male subjects; age ≥50 years; no bone diseases and no metal implants in their bodies; and the subjects of T2DM with a duration of T2DM of more than 5 years. Subjects with any of the following conditions were excluded: 1) those taking bone-affecting drugs, including hormone therapy, calcitonin, selective estrogen receptor modulators, parathyroid hormone, and bisphosphonates in the past 1 year; 2) long-term treatment with systemic glucocorticoid (3 months, dose ≥2.5 mg/day); 3) metastatic tumor in the past 5 years; 4) Paget's syndrome; 5) untreated malabsorption

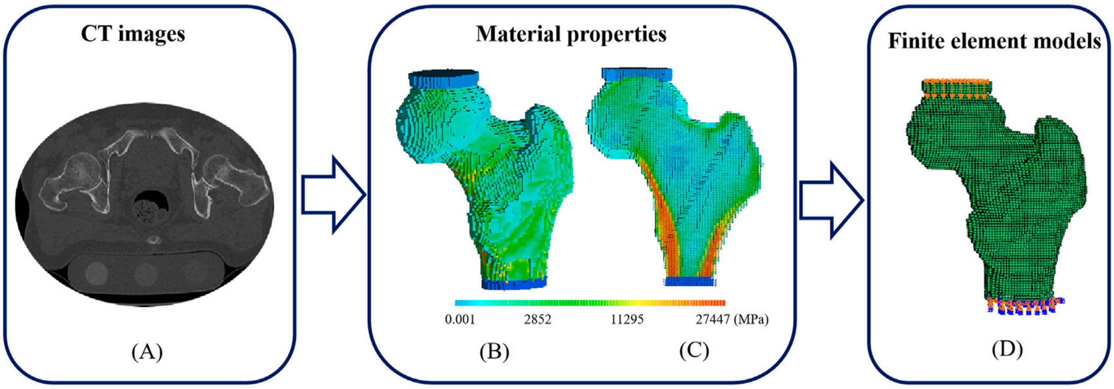

FIGURE 1 | A typical CT image, distributions of elastic modulus and the corresponding FE model with loads and boundary conditions. **(A)** A transverse CT image of a proximal femur **(B)** Elastic modulus distribution of a proximal femur **(C)** Elastic modulus distribution of a proximal femur in cross-section **(D)** FE model with compressive deformation on the top surface of polymethylmethacrylate (PMMA) pad for femoral head and fixed bottom surface of PMMA pad for distal femur.

syndrome; 6) hyperparathyroidism or hypoparathyroidism; and 7) history of renal injury (Pritchard et al., 2012).

DXA Assessment

The femoral BMD and femoral neck T score of the left femur of the subjects were obtained *via* a DXA scanner (Norland X800, Norland Inc. United States).

Imaging the Proximal Femurs

All images of the proximal femurs were collected using a clinical CT scanner (Optima CT680, GE medical system, Milwaukee, WI, United States). The scanning parameters were as follows: 140 kVp, intelligent scanning current (automatically selected on the basis of the thickness of different parts of the human body), 512 × 512 matrix, scanning thickness of 1.25 mm, and reconstructed slice thickness of 0.625 mm. During the scanning, a calibration phantom (QRM, Germany) containing calibration cells with 0.05, 0.1, and 0.2 g/cm^3 equivalent concentrations of calcium hydroxyapatite was placed under the hip joint of the subjects. The calibration phantom and the subjects were scanned simultaneously. A typical transverse CT image was shown in **Figure 1A**.

Biochemical Measurements

The fasting blood samples (before 9 a.m.) of all subjects were collected for measuring the following indices, such as blood routine indices including glycated hemoglobin (HbA1c), fasting plasma glucose (FPG), calcium (Ca), phosphorus (P), magnesium (Mg), C-peptide and Creatinine, BTMs including type I N-terminal propeptide (P1NP), β C-terminal cross-linked telopeptide of type I collagen (β-CTX), osteocalcin (OCN), bone alkaline phosphatase (BALP) and tartrate-resistant acid phosphatase 5b (TRAP5b), AGEs including total AGEs and pentosidine, and other regulating hormones of bone metabolism including intact parathyroid hormone (iPTH), 25-hydroxyvitamin D (25(OH) D), and sclerostin. Blood routine indices were determined *via* the photoelectric method, and BTMs and AGEs were measured using ELISA kits (Cusabio, Wuhan, China).

Establishment of FE Models

Mimics 17.0 software (Materialise Inc. Leuven, Belgium) was used to establish 3D models of the left proximal femurs. Femoral models were meshed with 1.5 mm hexahedral elements. PMMA pads (E = 2,500 MPa, v = 0.3) having elements with the same size as those of the femurs were used to simulate the PMMA pads in mechanical tests (Crawford et al., 2003; Keaveny et al., 2014).

For femoral material assignment, apparent density ($\rho_{apparent}$) was obtained from the relationship between the density of calibration phantom and the Hounsfiled Unit (HU) value, and ash density (ρ_{ash}) was calculated using the following equation: $\rho_{ash} = 1.22\rho_{apparent} + 0.0526$ (Mirzaei et al., 2015). The elastic modulus (E) and yield strength (σ) of the femoral voxel were calculated on the basis of an empirical formula, as shown in **Table 1**. The femurs were set with 120 kinds of materials, and Poisson's ratio was 0.4 (Gong et al., 2012). A typical distribution of femoral materials was shown in **Figures 1B,C**. After material assignment, the femoral models were imported into ABAQUS 6.14 (SIMULIA Inc. United States). In a compressive experiment, tie constraints were set between PMMA pads and femoral models, and all the degrees of freedom were fixed at the bottom surface of the PMMA pads for distal femurs, as shown in **Figure 1D**. Femoral strength was defined as the reaction force at a 4% compressive deformation (compressive displacement divided by femoral height) (Keaveny et al., 2014).

Statistics

Nonparametric tests were used when the parameters were not met normal distribution, small size was mostly the main reason for nonnormal distribution of parameters (Ramachandran and Tsokos, 2015). Moreover, nonparametric tests were widely accepted and used to conduct the statistics analyses with small size samples (Pett, 1997). Therefore, the Mann-Whitney *U* test of nonparametric independent samples was conducted to compare the differences in the femoral BMD, femoral neck T score, femoral strength, and biochemical markers of T2DM group ($n = 10$) and control group ($n = 8$). The measured parameters were presented as quartiles. Moreover, nonparametric Spearman correlation analysis was carried out to

TABLE 1 | Material properties of femur (Gong et al., 2012).

Material properties of femur				
ρ_{ash} (g/cm^3)	$\rho_{ash} = 0$	$0<\rho_{ash} \le 0.27$	$0.27<\rho_{ash} \le 0.6$	$0.6<\rho_{ash}$
Elastic modulus (MPa)	0.001	$33900\rho^{2.2}$	$5307\rho+469$	$10200\rho^{2.01}$
ρ_{ash} (g/cm^3)	$\rho_{ash} < 0.317$	$\rho_{ash} \ge 0.317$	—	—
Yield strength (MPa)	$\sigma = 137{\rho_{ash}}^{1.88}$	$\sigma = 114{\rho_{ash}}^{1.72}$	—	—

TABLE 2 | All parameters of subjects and the differences of parameters between T2DM and control groups.

Basic body parameters	T2DM group (n = 10)	Control group (n = 8)	*p* value
Age (years)	68 (53.75, 71.00)	62 (56.25, 63.75)	0.101
Height (cm)	172 (169, 175)	172 (166, 175)	0.868
Weight (kg)	75 (70, 82.75)	69 (62.75, 72.5)	0.055
BMI (kg/cm^2)	25.69 (24.74, 26.9)	23.72 (21.25, 25.32)	0.068
Duration (year)	10 (7.25, 16.25)	—	—
Treatment	Metformin (*n* = 4); Insulin (*n* = 2); Non-treatment (*n* = 4)	—	—
Femoral BMD (mg/cm^2)	1,016.5 (869.5,1149.0)	935 (885, 965.87)	0.829
Femoral neck T score	0.66 (-2.56, 0.038)	-1.79 (-2.10, -0.98)	0.616
Femoral strength (N)	8,945 (6,339.25, 10211.75)	6,867 (6,222.7,7497.5)	0.034*
Biochemical indexes			
HbA1c (%)	7.95 (7.22, 9.3)	5.6 (5.4, 5.9)	0.000*
FPG (mmol/L)	8.45 (7.1, 11.5)	4.99 (4.59, 5.1)	0.000*
P1NP (ng/ml)	33.28 (30.82, 35.06)	54.3 (34.8, 78.92)	0.034*
β-CTX (ng/ml)	0.11 (0.05, 0.12)	0.15 (0.07, 0.26)	0.408
OCN (ng/ml)	14.9 (11.42, 17.02)	18.3 (14.8, 23.35)	0.101
BALP (μg/L)	10.48 (8.96, 14.92)	7.51 (4.99, 13.38)	0.122
TRAP5b (U/l)	0.9 (0.83, 1.03)	1.44 (0.89, 2.2)	0.101
Total AGEs (ug/ml)	0.805 (0.34, 2.08)	0.56 (0.36, 1.56)	0.696
Pentosidine (pmol/ml)	574.5 (460.7, 634.9)	616.9 (412.1,841.7)	0.762
Sclerostin (pg/ml)	679.4 (491.5,813.7)	829.7 (662.2,1161.9)	0.408
iPTH (pg/ml)	37.91 (24.52, 44.11)	41.28 (30.73, 50.93)	0.515
25(OH)D (ug/ml)	13.72 (10.18, 23.33)	14.88 (13.8, 26.98)	0.515
Ca (mmol/L)	2.13 (2.10, 2.22)	2.14 (2.09, 2.19)	0.460
P (mmol/L)	1.01 (0.84, 1.12)	0.95 (0.93, 1.03)	0.633
Mg (mmol/L)	0.79 (0.76, 0.83)	0.82 (0.79, 0.84)	0.173
C-peptide (ng/ml)	1.17 (0.83, 1.54)	1.64 (1.03, 1.93)	0.068
Creatinine (umol/l)	66.5 (58.5, 69.75)	66 (61.25, 72.5)	0.897

$p < 0.05$; Statistically significant p values are shown in bold; BMI: body mass index. Median (1st quartile, 3rd quartile) was used to show all data of both groups.

analyze the correlations of all the parameters associated with femoral strength of both groups. Multiple linear regression analysis was used to obtain the best models of control and T2DM groups for predicting femoral strength and to analyze the main predictors of femoral strength.

RESULTS

Differences Analysis

Differences in all the parameters of T2DM and control groups were listed in **Table 2**. Bone formation marker P1NP level, HbA1c level, fasting blood glucose (FBG) level, and femoral strength significantly differed between the two groups. The HbA1c level (p = 0.000), FBG level (p = 0.000), and femoral strength (p = 0.034) of T2DM group were significantly higher than those of control group. However, the P1NP level (p = 0.034) of T2DM group was significantly lower than that of control group.

Correlation Analysis

Correlations Between Femoral BMD and Serum Biochemical Makers, and Femoral Neck T Score

The relationships of the femoral BMD with C-peptide level and pentosidine level were illustrated in **Figures 2A,B**. The femoral BMD was negatively correlated with C-peptide (r = –0.697, $p < 0.05$) and pentosidine (r = –0.806, $p < 0.01$) levels and positively correlated with femoral T score (r = 0.818, $p < 0.01$) in T2DM group. However, the femoral BMD was not associated with C-peptide and pentosidine levels in control group. In addition, the femoral BMD was not related to other biochemical markers and basic body parameters in both groups.

Correlations Between Femoral Strength and Femoral BMD, Femoral Neck T Score, Pentosidine, and Age

The relationships of femoral strength with femoral BMD, femoral neck T score, pentosidine level, and age were presented in **Figures 2C–F**. Femoral strength was positively correlated with femoral

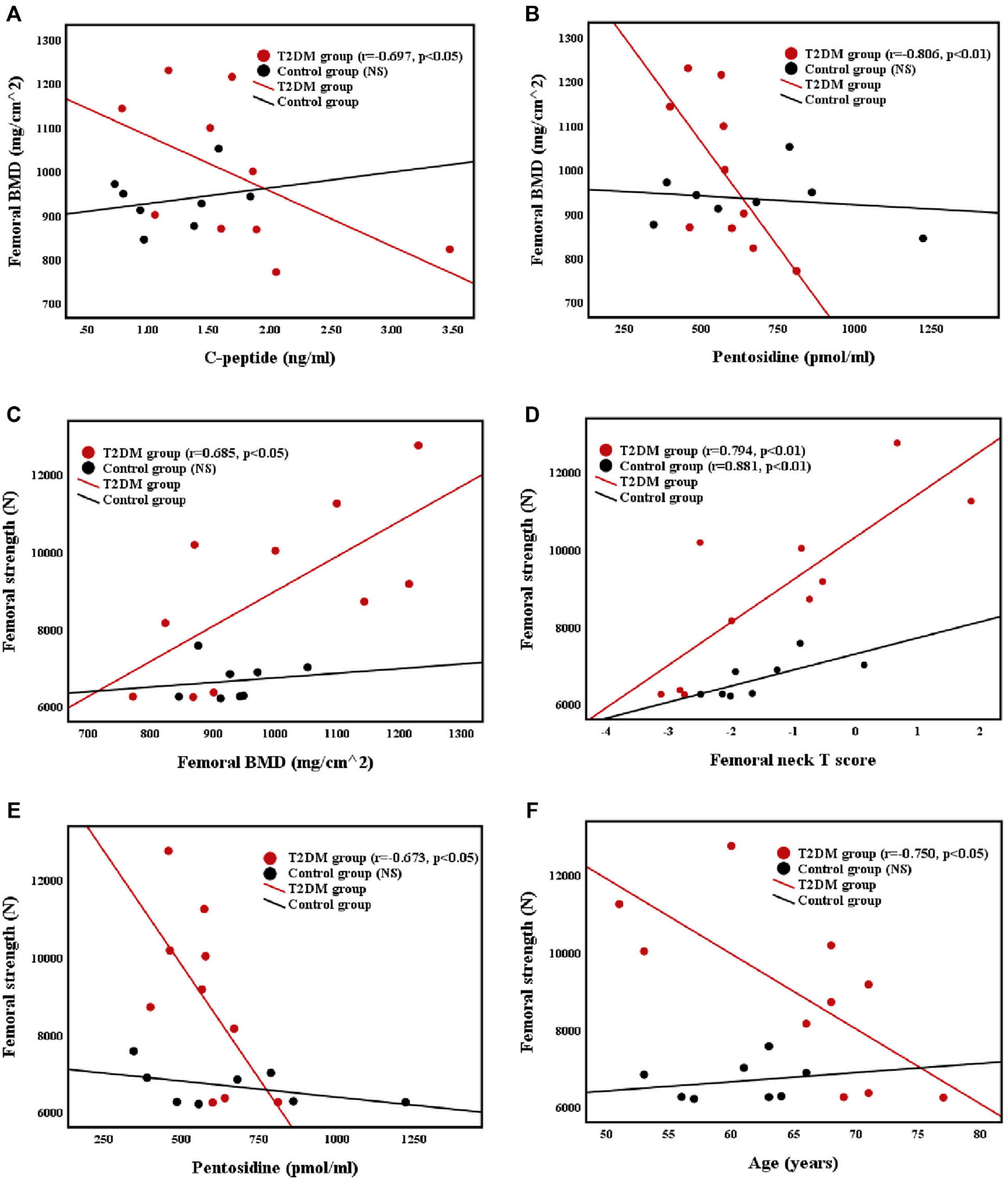

FIGURE 2 | Correlations between **(A)** femoral BMD and C-peptide level **(B)** femoral BMD and pentosidine level **(C)** femoral strength and femoral BMD **(D)** femoral strength and femoral neck T score **(E)** femoral strength and pentosidine level, and **(F)** femoral strength and age in T2DM and control groups.

BMD ($r = 0.685, p < 0.05$) and femoral neck T score ($r = 0.794, p < 0.01$), and negatively correlated with pentosidine level ($r = -0.673$, $p < 0.05$) and age ($r = -0.750$, $p < 0.05$) in T2DM group. Nevertheless, the femoral strength of control group was positively correlated with femoral neck T score ($r = 0.881$, $p < 0.05$), but was not related to femoral BMD or age. Furthermore,

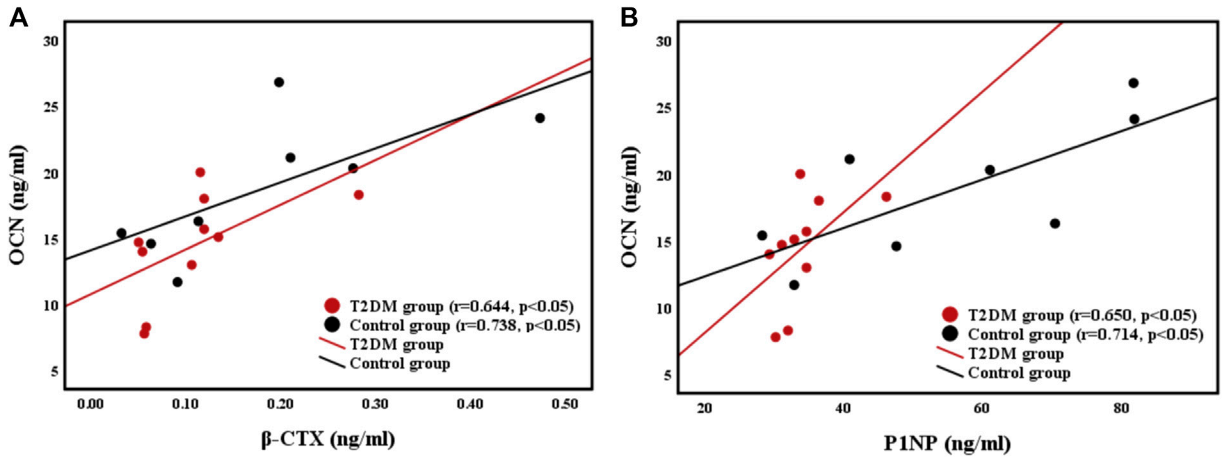

FIGURE 3 | Relationships between **(A)** bone resorption marker β-CTX level and bone formation marker OCN level, and **(B)** bone formation maker P1NP level and OCN level.

femoral strength was not related to other biochemical markers and basic body parameters in both groups.

Correlations Between Femoral Strength and BTMs

The relationships of the OCN (bone formation marker) level with the β-CTX (bone resorption marker) level and P1NP level were shown in **Figure 3**. Femoral strength was not related to BTMs in both groups. However, the OCN level was positively correlated with the CTX level (r = 0.644, $p < 0.05$; r = 0.738, $p < 0.05$) and the P1NP level (r = 0.650, $p < 0.05$; r = 0.714, $p < 0.05$) in both groups.

Multiple Linear Regression

Based on the analyses of difference and correlation, the parameters that were significantly related to femoral strength ($p < 0.05$) were selected as the independent variables of multiple linear regression. In addition, the parameters of significant differences ($p < 0.05$, HbA1c and P1NP) or potential significant differences ($0.05 < p < 0.07$, BMI and C-peptide) between T2DM and control groups were also involved, and femoral strength was the dependent variable of multiple linear regression. For the selection of parameters, although femoral BMD and femoral neck T score were both positively related to femoral strength, femoral neck T score was more related to femoral strength than femoral BMD. In order to avoid collinearity of the independent variables, only femoral neck T score was involved in the multiple linear regression.

Femoral neck T score was the common independent variable that was significantly related to femoral strength in both groups, thus it was used as the independent variable of the basic model. The selected independent variables were added into the models. Goodness-of-fit in the models was characterized by adjusted R-squared, as shown in **Table 3**.

Comparison of the adjusted R-squared values of multiple linear regression models in **Table 3** showed that the model (femoral neck T score + pentosidine + age + HbA1c + P1NP) of T2DM group (adjusted R-squared = 0.961) and model (femoral neck T score + P1NP + BMI) of control group (adjusted R-squared = 0.930) were the best models for predicting femoral strength. The best multiple linear regression models and their coefficients of the best models were shown in **Table 4**. Femoral neck T score and P1NP were the common predictors of femoral strength in two groups. Pentosidine, age and HbA1c played significant roles in predicting femoral strength of T2DM group, but BMI only presented a certain predictive effect on femoral strength of control group.

DISCUSSION

Elderly male patients with T2DM and the age-matched control group were recruited in this study. Femoral strength was obtained *via* FEA method based on QCT images of the hip. Comprehensive biochemical measurements, including blood routine, trace elements, BTMs, and AGEs, were performed. Higher BMD (Nilsson et al., 2017), higher HbA1c (Karim et al., 2018), and lower bone turnover rate (Manavalan et al., 2012; Shu et al., 2012) in patients with T2DM were also confirmed in this study. Femoral strength in T2DM group was significantly higher than that in control group. Furthermore, multiple linear regression analysis was conducted to find out the best models for predicting femoral strength and the main influencing factors of femoral strength for T2DM and control groups.

BMD is regarded as one of the crucial factors in determining bone strength. No significant differences in femoral BMD and femoral neck T score were observed in T2DM and control groups. Some studies have indicated that BMI was higher in patients with T2DM than that in healthy subjects. High BMI was not completely beneficial to preventing bone loss. Although it played a role in protecting bone, the bone was not protected when BMI was in the overweight zone (BMI ≥25 kg/m^2) (Cortet et al., 2019). Medians of BMI and BMD in T2DM group were high in our study, but the differences in BMD and BMI between

TABLE 3 | Multiple linear regression models of the T2DM and control groups.

Linear regression models	Adjusted R-squared	
	T2DM group	Control group
Femoral neck T score	0.632	0.661
Femoral neck T score + Pentosidine	**0.672**	0.618
Femoral neck T score + Pentosidine + Age	**0.733**	0.546
Femoral neck T score + Pentosidine + Age + HbA1c	0.896	0.397
Femoral neck T score + Pentosidine + Age + HbA1c + P1NP	**0.961**	**0.773**
Femoral neck T score + Pentosidine + Age + P1NP + HbA1c + BMI	0.958	**0.798**
Femoral neck T score + Pentosidine + Age + P1NP + HbA1c + BMI + C-peptide	0.942	—
Femoral neck T score + PINP	0.597	**0.888**
Femoral neck T score + P1NP + BMI	0.702	**0.930**

"-" implied that there were no outputs due to the problem of data structure. Independent variables with significant improvement of adjusted R-squared were marked in bold.

TABLE 4 | The best models for predicting femoral strength of T2DM and control groups.

Models		Unstandardized coefficient B	Standardized coefficient β	Sig	95% confidential interval for B	
					Lower bound	Upper bound
T2DM group	Constant	29240.848	—	0.000	21403.464	37078.232
	Femoral neck T score	315.404	0.235	0.121	−131.132	761.940
	Pentosidine	−14.118	−0.754	0.003	−20.102	−8.135
	Age	−153.863	−0.572	0.007	−236.221	−71.505
	HbA1c	−879.085	−0.484	0.004	−1,279.626	−478.543
	P1NP	161.406	0.347	0.037	15.401	307.411
Control group	Constant	9,584.833	—	0.000	8,099.800	11069.867
	Femoral neck T score	745.051	1.083	0.001	528.312	961.790
	BMI	−40.206	−0.200	0.117	−96.163	15.750
	P1NP	−13.840	−0.508	0.011	−22.431	−5.250

the two groups were not statistically significant. Nevertheless, the femoral strength in T2DM group was significantly higher than that in control group, and femoral strength was positively correlated with the femoral BMD and femoral neck T score. Bone strength is mainly determined by the combination of BMD and bone quality. First, BMD was generally considered as the decisive factor of bone strength, as it could determine 70% of bone strength (National Institutes of Health Consensus Development Conference Statement, 2000). BMD of T2DM has always been controversial. In previous studies, reduced bone strength of T2DM was associated with low BMD (Tanaka et al., 2018; Hunt et al., 2019). T2DM group in the present study showed a higher BMD than control group. Therefore, high BMD causing high bone strength in T2DM group did not contradict with previous studies (Tanaka et al., 2018; Hunt et al., 2019), and it was highly reasonable. Second, bone quality is mainly determined by bone material properties and structure. In previous studies, low bone strength in T2DM patients derived from mechanical tests was associated with deterioration of bone microstructure (Karim et al., 2018; Hunt et al., 2019). T2DM could lead to deterioration of cancellous bone structure (Zeitoun et al., 2019). In this study, femoral strength based on QCT image and FEA simulation could not fully reflect bone microstructure characteristics, including decrease in trabecular thickness, increases in rod-trabecular and trabecular separation caused by T2DM (Karim et al., 2018; Hunt et al., 2019). It might be that the effects of impaired cancellous bone microstructure in T2DM group were weakened in the FEA simulation, so as to result in a high dependence of femoral strength on BMD. Therefore, the medians of BMD and femoral neck T score in patients with T2DM were higher than those of the control subjects, implying that femoral strength of T2DM patients is greater than that of individuals without T2DM.

In this study, the femoral BMD was negatively correlated with C-peptide in T2DM group. The absence of insulin leads to metabolic disorders and glucose metabolic barrier, and patients with T2DM presented a high glucose level. C-peptide was a product secreted by pancreatic β-cells, and it was used to represent insulin level (Li et al., 2013). In combination with the significantly high glucose and the negative correlation of glucose and C-peptide of T2DM group in this study, it was confirmed that the absence of insulin might lead to high glucose level. Similar to a previous finding (Li et al., 2013), our results showed that the femoral BMD was negatively correlated with C-peptide. This result indicated that the absence of C-peptide might lead to increase in femoral BMD. Although no significant difference was observed in C-peptide of both groups, the C-peptide level of T2DM group was lower than that of control group. Therefore, decreased C-peptide level might be a potential factor that helped increase femoral BMD and strength in T2DM group.

No differences in the total AGEs, pentosidine and sclerostin levels were observed between T2DM and control groups in the present study. Pentosidine was a typical AGEs, and serum pentosidine level was regarded as a valid marker of AGEs level because the formation of pentosidine required glycosylation and oxidation (Wang et al., 2002). Glycosylation could also affect bone strength (Saito et al., 2006). In our study, no significant difference in the serum pentosidine level was observed between both groups possibly because of metformin and insulin injection in patients with T2DM (Lapolla et al., 2005; Kanazawa et al., 2011). However, similar to a previous result (Wang, et al., 2002), the present study showed that the femoral strength and femoral BMD of T2DM group were both negatively correlated with pentosidine level. In addition, the pentosidine level was positively associated with the C-peptide level in T2DM group, and C-peptide level was used to represent insulin level (Li et al., 2013), thus decreased insulin secretion might lead to lower pentosidine level in T2DM group than that in control group. A previous study indicated that accumulation of AGEs in bone resulted in impairment of bone mineralization (Al-Khateeb et al., 2018). It might be the reason of low pentosidine level and high femoral BMD of T2DM group in the present study. In sum, our findings implied that low pentosidine level might be a cause of high femoral BMD in T2DM, consequently increasing femoral strength. Furthermore, although there was no significant difference in sclerostin level between two groups in the present study, the median of sclerostin level in control group was a little higher than that in T2DM group. A previous study had shown that the sclerostin level in diabetic rats decreased with aging and the deterioration of glycemic control, which indicated that sclerostin level might be related to the glycemic control and age of rats (Pereira et al., 2017). Therefore, a higher sclerostin level of control group than T2DM group in the present study might be related to the stable glycemic control and younger age.

Aging was considered an important factor of bone loss and decreased bone strength (Lang et al., 2012). The present study showed that age was negatively correlated with femoral strength in T2DM group. This result implied that the bone strength of T2DM might decline with aging and it agreed with the finding that both men and women lose their bone strength with aging (Lang et al., 2012). However, age had no significant correlations with the femoral BMD and femoral strength in control group. A previous research revealed that DM could change bone microstructure and bone spatial distribution (Burghardt et al., 2010), which affected bone mechanical properties. Therefore, the correlation between age and femoral strength in T2DM group might be due to the combined contribution of age and bone structure. The specific mechanism of the combined contribution should be confirmed in further studies.

A previous study reported that increasing BTMs in old people could lead to exacerbation of hip bone loss (Bauer et al., 2009). In the present study, the P1NP level in T2DM group was strongly lower than that in control group, and the medians of β-CTX and OCN levels in T2DM group were lower than those in control group, but they did not have statistical significance. Moreover, bone resorption and formation markers were positively correlated in both groups, as shown in **Figure 3**. Similar to previous results (Shu et al., 2012; Farr et al., 2014), our findings indicated that the bone turnover rate in T2DM group was lower than that in control group, and **Figure 3** showed that bone turnover was balanced in both groups. Uncoupled or unbalanced bone turnover could cause severe changes in bone mass (Stein et al., 2010), thus balanced bone turnover might prevent loss of bone mass. The bone turnover rate in T2DM group was lower than that in control group possibly because high glucose level suppresses the functions of osteoclasts and osteoblasts (Wittrant et al., 2008). Although low bone turnover rate could reduce the bone loss rate, it also increased bone fragility because of the irreparable accumulation of microdamage. Nevertheless, a previous study suggested that rapid bone turnover might cause younger and less dense mineralized bone to replace more dense mineralized bone; thus, bone stiffness and strength could be reduced (Seeman and Delmas, 2006). In addition, OCN and β-CTX had a positive correlation in both groups, implying that bone turnover was balanced in both groups. In summary, bone turnover was balanced in both groups, and the femoral BMD and strength of T2DM group were higher than those of control group likely because of a low bone turnover rate.

Multiple linear regression analysis showed that the best predictive models of T2DM and control groups could accurately predict the femoral strength. Femoral neck T score and P1NP were the common predictors of femoral strength in both groups, which indicated that BMD and bone formation level played important roles in predicting femoral strength. Furthermore, pentosidine, age and HbA1c presented significant effects on predicting femoral strength in T2DM group, which implied that AGEs, age and blood glucose might be the important influencing factors on bone strength of T2DM. However, blood glucose and AGEs were not significantly related to the predication of femoral strength, which might be caused by the normal blood glucose level in control group due to increase in AGEs level with high blood glucose level (Farlay et al., 2016). Age was only associated with the prediction of bone strength in T2DM group, which suggested that age played a more significant role in the change of bone mass in T2DM patients than that in controls. In addition, BMI only showed a certain predictive potential in control group. Higher BMI could decrease bone loss (Cortet et al., 2019), thus BMI as a predictor of femoral strength of control group might be reasonable in the present study. For T2DM group, high glucose could cause some complicated situation of bone tissue, such as metabolic disorders and the accumulation of pentosidine, which might weaken the effect of BMI on femoral strength. Above results indicated that the predictors of femoral strength for T2DM patients and non-T2DM people were different. Moreover, in all the predictors of the best model for the controls, femoral neck T score presented the strongest predictive ability, which was consistent with a previous study (Keaveny et al., 2010). However, the ability of femoral neck T score for predicting femoral strength was weaker than other predictors of the best model for T2DM group. Multiple regression differed from correlation analysis, and regression model was a result of the interaction and control of independent variables (Gogtay et al., 2017). Thus, other predictors in the predictive model of femoral strength for T2DM could weaken the significance of femoral neck T score in multiple linear regression so as to obtain the optimized predictive model. In sum, multiple linear regression analysis stated that femoral neck T score contributed to predicting femoral strength, and P1NP, pentosidine, age and HbA1c also played important roles in evaluating femoral strength in T2DM. Therefore, in clinical assessment of bone fracture risk of T2DM, besides femoral neck T score, more attention should be paid on P1NP, pentosidine, age and HbA1c.

To date, many studies have indicated that T2DM could lead to increase of bone fragility (Napoli et al., 2017; Acevedo et al., 2018). Although there was a higher femoral strength in T2DM group than control group in the present study, it did not contradict with the high bone fracture risk in T2DM. Increase in bone fragility of T2DM might be one cause of high bone fracture risk. Bone fragility could be defined by biomechanical parameters, including ultimate force, ultimate displacement and work to failure (energy absorption or toughness) (Turner, 2002). Bone elasticity and plasticity both contributed to fracture (Seeman, 2008). Toughness derived from bone plasticity could compensate bone fragility. A previous study showed that accumulation of AGEs in T2DM bone could reduce bone plasticity and toughness, which led to decrease in bone ductility and increase in bone fragility (Tang and Vashishth, 2011). Furthermore, bone strength and stiffness increased with the increase in BMD, but bone toughness decreased with the increase in BMD (Seeman and Delmas, 2006). It implied that bone strength and fragility could both increase with the increase of BMD. Therefore, when bone strength is high, increased bone fracture risk may result from the significant decrease in bone plasticity and increase in bone fragility. In addition, there were many factors that may be related to the high bone fracture risk of T2DM (Schwartz and Sellmeyer, 2007; Isidro and Ruano, 2010; Moseley, 2012). Compared to the non-diabetes, the fall risk of T2DM patients was higher. Moreover, the complications of T2DM could increase the fall risk of patients, such as syncope directly caused by hypoglycemia, falls caused by autonomic neuropathy, orthostatic hypotension, peripheral neuropathy, and retinopathy, thus increase in fall risk might be an important factor of high bone fracture risk of T2DM (Schwartz et al., 2008; Moseley, 2012). Taken together, increase in bone fracture risk of T2DM is not only related to the intrinsic mechanical properties of bone, but also associated with the high fall risk of T2DM patients. Furthermore, high bone strength and increased bone fragility might both exist at the same time in T2DM bone.

This study has some limitations. First, the number of subjects was less than our expectation because of the strict recruitment criteria and the absence of several volunteers in some processes. Small sample size might lead to undervalued differences in data between two groups. In addition, this study was unable to assess the roles of drug therapies in predicting femoral strength due to the small sample size and the different drugs taken by T2DM patients. It was expected that future studies with a large sample size study could overcome the difficulties faced by investigations of drug therapies for T2DM patients, so as to conduct a detailed and comprehensive analysis on the effects of different drug therapies and treatment duration on the prediction of bone strength in T2DM. Second, bone microstructure played a certain role in predicting bone strength. Although our study found out the significant influencing factors of femoral strength, it lacked femoral microstructure analysis due to the limitation of clinical CT scanner for imaging femoral microstructure. Investigation of femoral microstructure *via* high resolution magnetic resonance imaging in patients with T2DM might be valuable for evaluating femoral strength (Chang et al., 2017). Third, the results of the present study suggested that AGEs, blood glucose and age were all the important predictors of femoral strength in T2DM, but the detailed and in-depth mechanism research of predicting femoral strength was absent in this study. Therefore, further molecular and compositional investigations in femurs might contribute to the understanding of deep predictive mechanism of the predictors.

In conclusion, femoral strength was significantly higher in elderly men with T2DM than those without T2DM (range of age: 51–77 years), and this finding might be related to higher BMD and lower bone turnover rate in T2DM. C-peptide, pentosidine, and age had harmful effects on the femoral BMD and strength of patients with T2DM. Furthermore, besides femoral neck T score and P1NP, pentosidine, age and HbA1c all played significant roles in predicting femoral strength in T2DM. This study provided important references for predicting femoral strength and evaluating bone fracture risk in clinics.

DATA AVAILABILITY STATEMENT

The raw data supporting the conclusion of this article will be made available by the authors, without undue reservation.

ETHICS STATEMENT

The studies involving human participants were reviewed and approved by the Ethics committee of the affiliated hospital of the National Research Center for Rehabilitation Technical Aids. The patients/participants provided their written informed consents to participate in this study. Written informed consent was obtained from the individual(s) for the publication of any potentially identifiable images or data included in this article.

AUTHOR CONTRIBUTIONS

Conceptualization: HG; Methodology: SJ and HG; Formal analysis and investigation: SJ, YZ, RZ and HC; Writing—original draft preparation: SJ; Writing—review and editing: HG; Funding acquisition: HG and YF; Resources: HL; Supervision: HG.

FUNDING

This work was supported by the National Natural Science Foundation of China (grant numbers 11872095, 11902090, and 11802067).

ACKNOWLEDGMENTS

We gratefully acknowledge the funds from National Natural Science Foundation of China (grant numbers 11872095, 11902090, and 11802067), the immense help received from Ning Zhao (equipment operator) and Wei Liu (diabetes nurse) of the Rehabilitation Hospital, National Research Center for Rehabilitation Technical Aids, who assisted to collect data for this study.

REFERENCES

Acevedo, C., Sylvia, M., Schaible, E., Graham, J. L., Stanhope, K. L., Metz, L. N., et al. (2018). Contributions of Material Properties and Structure to Increased Bone Fragility for a Given Bone Mass in the UCD-T2DM Rat Model of Type 2 Diabetes. *J. Bone Miner Res.* 33 (6), 1066–1075. doi:10.1002/jbmr.3393

Al-Khateeb, A. R., Shaari, N. M., Muid, S. A., and Froemming, G. R. (2018). A Critical Link between Advanced Glycation End Products, Osteoporosis and Type 2 Diabetes Mellitus. *Regen. Res.* 6, 1–9.

Bauer, D. C., Garnero, P., Harrison, S. L., Cauley, J. A., Eastell, R., Ensrud, K. E., et al. (2009). Biochemical Markers of Bone Turnover, Hip Bone Loss, and Fracture in Older Men: the MrOS Study. *J. Bone Mineral Res.* 24, 2032–2038. doi:10.1359/jbmr.090526

Bolotin, H. H. (2007). DXA *In Vivo* BMD Methodology: an Erroneous and Misleading Research and Clinical Gauge of Bone mineral Status, Bone Fragility, and Bone Remodelling. *Bone* 41, 138–154. doi:10.1016/j.bone.2007.02.022

Burghardt, A. J., Issever, A. S., Schwartz, A. V., Davis, K. A., Masharani, U., Majumdar, S., et al. (2010). High-resolution Peripheral Quantitative Computed Tomographic Imaging of Cortical and Trabecular Bone Microarchitecture in Patients with Type 2 Diabetes Mellitus. *J. Clin. Endocrinol. Metab.* 95, 5045–5055. doi:10.1210/jc.2010-0226

Chang, G., Boone, S., Martel, D., Rajapakse, C. S., Hallyburton, R. S., Valko, M., et al. (2017). MRI Assessment of Bone Structure and Microarchitecture. *J. Magn. Reson. Imaging* 46, 323–337. doi:10.1002/jmri.25647

Cortet, B., Lucas, S., Legroux-Gerot, I., Penel, G., Chauveau, C., and Paccou, J. (2019). Bone Disorders Associated with Diabetes Mellitus and its Treatments. *Jt. Bone Spine* 86, 315–320. doi:10.1016/j.jbspin.2018.08.002

Crawford, R. P., Cann, C. E., and Keaveny, T. M. (2003). Finite Element Models Predict *In Vitro* Vertebral Body Compressive Strength Better Than Quantitative Computed Tomography. *Bone* 33, 744–750. doi:10.1016/s8756-3282(03)00210-2

Farlay, D., Armas, L. A., Gineyts, E., Akhter, M. P., Recker, R. R., and Boivin, G. (2016). Nonenzymatic Glycation and Degree of Mineralization Are Higher in Bone from Fractured Patients with Type 1 Diabetes Mellitus. *J. Bone Miner. Res.* 31 (1), 190–195. doi:10.1002/jbmr.2607

Farr, J. N., and Khosla, S. (2016). Determinants of Bone Strength and Quality in Diabetes Mellitus in Humans. *Bone* 82, 28–34. doi:10.1016/j.bone.2015.07.027

Farr, J. N., Drake, M. T., Amin, S., Melton, L. J., Iii, Mccready, L. K., and Khosla, S. (2014). *In Vivo* assessment of Bone Quality in Postmenopausal Women with Type 2 Diabetes. *J. Bone Miner. Res.* 29, 787–795. doi:10.1002/jbmr.2106

Glovaci, D., Fan, W., and Wong, N. D. (2019). Epidemiology of Diabetes Mellitus and Cardiovascular Disease. *Curr. Cardiol. Rep.* 21, 21. doi:10.1007/s11886-019-1107-y

Gogtay, N. J., Deshpande, S. P., and Thatte, U. M. (2017). Principles of Regression Analysis. *J. Assoc. Physicians India* 65, 48–52.

Gong, H., Zhang, M., Fan, Y., Kwok, W. L., and Leung, P. C. (2012). Relationships between Femoral Strength Evaluated by Nonlinear Finite Element Analysis and BMD, Material Distribution and Geometric Morphology. *Ann. Biomed. Eng.* 40, 1575–1585. doi:10.1007/s10439-012-0514-7

Hunt, H. B., Torres, A. M., Palomino, P. M., Marty, E., Saiyed, R., Cohn, M., et al. (2019). Altered Tissue Composition, Microarchitecture, and Mechanical Performance in Cancellous Bone from Men with Type 2 Diabetes Mellitus. *J. Bone Mineral Res.* 34, 1191–1206. doi:10.1002/jbmr.3711

Isidro, M. L., and Ruano, B. (2010). Bone Disease in Diabetes. *Curr. Diabetes Rev.* 6, 144–155. doi:10.2174/157339910791162970

Kanazawa, I., Yamamoto, M., Yamaguchi, T., and Sugimoto, T. (2011). Effects of Metformin and Pioglitazone on Serum Pentosidine Levels in Type 2 Diabetes Mellitus. *Exp. Clin. Endocrinol. Diabetes* 119, 362–365. doi:10.1055/s-0030-1267953

Kanis, J. A., Hans, D., Hans, D., Cooper, C., Baim, S., Bilezikian, J. P., et al. (2011). Interpretation and Use of FRAX in Clinical Practice. *Osteoporos. Int.* 22, 2395–2411. doi:10.1007/s00198-011-1713-z

Karim, L., Moulton, J., Van Vliet, M., Velie, K., Robbins, A., Malekipour, F., et al. (2018). Bone Microarchitecture, Biomechanical Properties, and Advanced Glycation End-Products in the Proximal Femur of Adults with Type 2 Diabetes. *Bone* 114, 32–39. doi:10.1016/j.bone.2018.05.030

Keaveny, T. M., Kopperdahl, D. L., Melton, L. J., Hoffmann, P. F., Amin, S., Riggs, B. L., et al. (2010). Age-dependence of Femoral Strength in white Women and Men. *J. Bone Miner. Res.* 25, 994–1001. doi:10.1359/jbmr.091033

Keaveny, T. M., Mcclung, M. R., Genant, H. K., Zanchetta, J. R., Kendler, D., Brown, J. P., et al. (2014). Femoral and Vertebral Strength Improvements in Postmenopausal Women with Osteoporosis Treated with Denosumab. *J. Bone Miner. Res.* 29, 158–165. doi:10.1002/jbmr.2024

Knowles, N. K., Whittier, D. E., Besler, B. A., and Boyd, S. K. (2021). Proximal Tibia Bone Stiffness and Strength in HR-pQCT- and QCT-Based Finite Element Models. *Ann. Biomed. Eng.* 49, 2389–2398. doi:10.1007/s10439-021-02789-w

Krakauer, J. C., Mckenna, M. J., Buderer, N. F., Rao, D. S., Whitehouse, F. W., and Parfitt, A. M. (1995). Bone Loss and Bone Turnover in Diabetes. *Diabetes* 44, 775–782. doi:10.2337/diab.44.7.775

Lang, T. F., Sigurdsson, S., Karlsdottir, G., Oskarsdottir, D., Sigmarsdottir, A., Chengshi, J., et al. (2012). Age-related Loss of Proximal Femoral Strength in Elderly Men and Women: The Age Gene/Environment Susceptibility Study - Reykjavik. *Bone* 50, 743–748. doi:10.1016/j.bone.2011.12.001

Lapolla, A., Reitano, R., Baccarin, L., Sartore, G., Plebani, M., and Fedele, D. (2005). Pentosidine Plasma Levels and Relation with Metabolic Control in Diabetic Patients. *Horm. Metab. Res.* 37, 252–256. doi:10.1055/s-2005-861413

Li, Y., Liu, H., and Sato, Y. (2013). The Association between the Serum C-Peptide Level and Bone mineral Density. *PLoS One* 8, e83107. doi:10.1371/journal.pone.0083107

Manavalan, J. S., Cremers, S., Dempster, D. W., Zhou, H., Dworakowski, E., Kode, A., et al. (2012). Circulating Osteogenic Precursor Cells in Type 2 Diabetes Mellitus. *J. Clin. Endocrinol. Metab.* 97, 3240–3250. doi:10.1210/jc.2012-1546

Mirzaei, M., Keshavarzian, M., Alavi, F., Amiri, P., and Samiezadeh, S. (2015). QCT-based Failure Analysis of Proximal Femurs under Various Loading Orientations. *Med. Biol. Eng. Comput.* 53, 477–486. doi:10.1007/s11517-015-1254-2

Moseley, K. F. (2012). Type 2 Diabetes and Bone Fractures. *Curr. Opin. Endocrinol.* 19 (2), 128–135. doi:10.1097/med.0b013e328350a6e1

Napoli, N., Chandran, M., Chandran, M., Pierroz, D. D., Abrahamsen, B., Schwartz, A. V., et al. (2017). Mechanisms of Diabetes Mellitus-Induced Bone Fragility. *Nat. Rev. Endocrinol.* 13 (4), 208–219. doi:10.1038/nrendo.2016.153

National Institutes of Health Consensus Development Conference Statement (2000). Osteoporosis Prevention, Diagnosis, and Therapy. Available at: https://consensus.nih.gov/2000/2000osteoporosis111.html (Accessed March 27–29, 2000) 17 (1), 1–45.

Nilsson, A. G., Sundh, D., Johansson, L., Nilsson, M., Mellström, D., Rudäng, R., et al. (2017). Type 2 Diabetes Mellitus Is Associated with Better Bone Microarchitecture but Lower Bone Material Strength and Poorer Physical Function in Elderly Women: A Population-Based Study. *J. Bone Miner. Res.* 32, 1062–1071. doi:10.1002/jbmr.3057

Ogawa, N., Yamaguchi, T., Yano, S., Yamauchi, M., Yamamoto, M., and Sugimoto, T. (2007). The Combination of High Glucose and Advanced Glycation End-Products (AGEs) Inhibits the Mineralization of Osteoblastic MC3T3-E1 Cells through Glucose-Induced Increase in the Receptor for AGEs. *Horm. Metab. Res.* 39, 871–875. doi:10.1055/s-2007-991157

Pereira, M., Gohin, S., Lund, N., Hvid, A., Smitham, P. J., Oddy, M. J., et al. (2017). Sclerostin Does Not Play a Major Role in the Pathogenesis of Skeletal Complications in Type 2 Diabetes Mellitus. *Osteoporos. Int.* 28 (1), 309–320. doi:10.1007/s00198-016-3718-0

Pett, M. A. (1997). *Nonparametric Statistics for Health Care Research: Statistics for Small Samples and Unusual Distributions*, 307. California: SAGE Publications.

Pritchard, J. M., Giangregorio, L. M., Atkinson, S. A., Beattie, K. A., Inglis, D., Ioannidis, G., et al. (2012). Association of Larger Holes in the Trabecular Bone at the Distal Radius in Postmenopausal Women with Type 2 Diabetes Mellitus Compared to Controls. *Arthritis Care Res.* 64, 83–91. doi:10.1002/acr.20602

Ramachandran, K. M., and Tsokos, C. P. (2015). "Nonparametric Tests," in *Mathematical Statistics with Applications in R*. Second Edition. Amsterdam: Elsevier, 2, 589–637. doi:10.1016/b978-0-12-417113-8.00012-6

Ramamurthi, K., Ahmad, O., Engelke, K., Taylor, R. H., Zhu, K., Gustafsson, S., et al. (2012). An *In Vivo* Comparison of Hip Structure Analysis (HSA) with Measurements Obtained by QCT. *Osteoporos. Int.* 23, 543–551. doi:10.1007/s00198-011-1578-1

Saito, M., Fujii, K., Mori, Y., and Marumo, K. (2006). Role of Collagen Enzymatic and Glycation Induced Cross-Links as a Determinant of Bone Quality in

Spontaneously Diabetic WBN/Kob Rats. *Osteoporos. Int.* 17, 1514–1523. doi:10.1007/s00198-006-0155-5

Schwartz, A. V., and Sellmeyer, D. E. (2007). Diabetes, Fracture, and Bone Fragility. *Curr. Osteoporos. Rep.* 5, 105–111. doi:10.1007/s11914-007-0025-x

Schwartz, A. V., Vittinghoff, E., Sellmeyer, D. E., Feingold, K. R., Rekeneire, N. d., Strotmeyer, E. S., et al. (2008). Diabetes-Related Complications, Glycemic Control, and Falls in Older Adults. *Diabetes Care* 31 (3), 391–396. doi:10.2337/dc07-1152

Seeman, E., and Delmas, P. D. (2006). Bone Quality - the Material and Structural Basis of Bone Strength and Fragility. *N. Engl. J. Med.* 354, 2250–2261. doi:10.1056/nejmra053077

Seeman, E. (2008). Bone Quality: The Material and Structural Basis of Bone Strength. *J. Bone Miner Metab.* 26 (1), 1–8. doi:10.1007/s00774-007-0793-5

Shu, A., Yin, M. T., Stein, E., Cremers, S., Dworakowski, E., Ives, R., et al. (2012). Bone Structure and Turnover in Type 2 Diabetes Mellitus. *Osteoporos. Int.* 23, 635–641. doi:10.1007/s00198-011-1595-0

Starup-Linde, J., and Vestergaard, P. (2016). Biochemical Bone Turnover Markers in Diabetes Mellitus - A Systematic Review. *Bone* 82, 69–78. doi:10.1016/j.bone.2015.02.019

Stein, E. M., Compston, J., and Shane, E. (2010). "Transplantation Osteoporosis - ScienceDirect," in *Osteoporosis in Men*. Second Edition, 443–452. doi:10.1016/B978-0-12-374602-3.00037-7

Tanaka, H., Yamashita, T., Yoneda, M., Takagi, S., and Miura, T. (2018). Characteristics of Bone Strength and Metabolism in Type 2 Diabetic Model Tsumura, Suzuki, Obese Diabetes Mice. *Bone Rep.* 9, 74–83. doi:10.1016/j.bonr.2018.07.004

Tang, S. Y., and Vashishth, D. (2011). The Relative Contributions of Non-enzymatic Glycation and Cortical Porosity on the Fracture Toughness of Aging Bone. *J. Biomech.* 44 (2), 330–336. doi:10.1016/j.jbiomech.2010.10.016

Turner, C. H. (2002). Biomechanics of Bone: Determinants of Skeletal Fragility and Bone Quality. *Osteoporos. Int.* 13 (2), 97–104. doi:10.1007/s001980200000

Wang, X., Shen, X., Li, X., and Mauli Agrawal, C. (2002). Age-related Changes in the Collagen Network and Toughness of Bone. *Bone* 31, 1–7. doi:10.1016/s8756-3282(01)00697-4

Wang, L., Li, T., Liu, J., Wu, X., Wang, H., Li, X., et al. (2019). Association between Glycosylated Hemoglobin A1c and Bone Biochemical Markers in Type 2 Diabetic Postmenopausal Women: a Cross-Sectional Study. *BMC Endocr. Disord.* 19, 31–39. doi:10.1186/s12902-019-0357-4

Wittrant, Y., Gorin, Y., Woodruff, K., Horn, D., Abboud, H. E., Mohan, S., et al. (2008). High D(+)glucose Concentration Inhibits RANKL-Induced Osteoclastogenesis. *Bone* 42, 1122–1130. doi:10.1016/j.bone.2008.02.006

Yamamoto, M., and Sugimoto, T. (2016). Advanced Glycation End Products, Diabetes, and Bone Strength. *Curr. Osteoporos. Rep.* 14, 320–326. doi:10.1007/s11914-016-0332-1

Zeitoun, D., Caliaperoumal, G., Bensidhoum, M., Constans, J. M., Anagnostou, F., and Bousson, V. (2019). Microcomputed Tomography of the Femur of Diabetic Rats: Alterations of Trabecular and Cortical Bone Microarchitecture and Vasculature-A Feasibility Study. *Eur. Radiol. Exp.* 3 (17), 17–19. doi:10.1186/s41747-019-0094-5

Conflict of Interest: The authors declare that the research was conducted in the absence of any commercial or financial relationships that could be construed as a potential conflict of interest.

frontiers | Frontiers in Bioengineering and Biotechnology

ORIGINAL RESEARCH
published: 29 April 2022
doi: 10.3389/fbioe.2022.858862

Ultra-Pulsed CO_2 Laser Osteotomy: A New Method for the Bone Preparation of Total Knee Arthroplasty

Tianfei Ran[1], Chuanchuan Lin[2], Tianying Ma[1], Yinyin Qin[1], Jie Li[1], Yuan Zhang[1], Yuan Xu[1], Changqing Li[1] and Min Wang[1]*

[1]Department of Orthopedics, Xinqiao Hospital, Third Military Medical University, Chongqing, China, [2]Department of Blood Transfusion, Xinqiao Hospital, Amy Medical University (Third Military Medical University), Chongqing, China

Cementless total knee arthroplasty (TKA) can achieve long-term biological fixation, but its application is limited by the risk of early aseptic loosening. One of the important reasons for early aseptic loosening is that mechanical osteotomy tools cannot achieve ideal bone preparation because of poor accuracy and serious bone tissue damage produced by them. Therefore, we designed an ultra-pulsed CO_2 laser osteotomy system to solve these problems. To reveal the safety at the tissue and cell levels of the ultra-pulsed CO_2 laser osteotomy system, a series of experiments on distal femur osteotomy in animals were performed. Then, the bone surface characteristics were analyzed through scanning electron microscopy, and the bone thermal and mechanical damage was evaluated *via* histological analysis. Finally, mesenchymal stem cells (MSCs) were inoculated on the bone surfaces prepared by the two osteotomy tools, and the effect of cell adhesion was analyzed through a confocal laser scanning microscope (CLSM). We successfully achieved TKA bone preparation of animal knees with the ultra-pulsed CO_2 laser osteotomy system. Moreover, the biological evaluation results indicated that compared with the traditional mechanical saw, the laser can preserve the natural bone structure and cause no thermal damage to the bone. In addition, CLSM examination results showed that the laser-cut bone surface was more conducive to cell adhesion and infiltration than the bone surface cut by a mechanical saw. Overall, these results indicate that ultra-pulsed CO_2 laser can achieve non-invasive bone cutting, which can be a new option for TKA bone preparation and has the potential to lead in the future.

Keywords: CO_2 laser osteotomy, total knee arthroplasty, cementless, thermal damage, bone preparation, adhesion

Edited by:
Jun Pan,
Chongqing University, China

Reviewed by:
Zhongli Li,
First Affiliated Hospital of the General Hospital of PLA, China
Qiujian Zheng,
Guangdong Provincial People's Hospital, China

***Correspondence:**
Min Wang
xqwangmin@163.com

Specialty section:
This article was submitted to Biomechanics, a section of the journal Frontiers in Bioengineering and Biotechnology

Received: *20 January 2022*
Accepted: *31 March 2022*
Published: *29 April 2022*

Citation:
Ran T, Lin C, Ma T, Qin Y, Li J, Zhang Y, Xu Y, Li C and Wang M (2022) Ultra-Pulsed CO_2 Laser Osteotomy: A New Method for the Bone Preparation of Total Knee Arthroplasty. Front. Bioeng. Biotechnol. 10:858862. doi: 10.3389/fbioe.2022.858862

INTRODUCTION

Total knee arthroplasty (TKA) is the most effective treatment for degenerative diseases of the knee (Lotke et al., 1976; Katz et al., 2021). In TKA, cemented or cementless implants or a hybrid of the two is fixed to the bone surface. The cemented fixation can achieve rapid stability between the implants and bone surface but cannot achieve the integration between the bone and implants, raising concerns about the long-term durability of cemented fixation (Miller et al., 2013). Theoretically, the advantage of cementless biological implants is that it can achieve permanent biological fixation between bone and implants (Dalury, 2016; Behery et al., 2017). However, limited application of cementless TKA has been reported in studies (Parker et al., 2001; Nakama et al., 2012; List et al., 2017), and defects in traditional bone osteotomy methods are one of the key reasons.

We believe that the defects of traditional bone osteotomy lie in the following aspects: first, it is difficult to achieve accurate bone cutting with traditional mechanical osteotomy tools (Macdonald et al., 2004). The inevitable shaking perpendicular to the osteotomy plane during mechanical cutting will eventually increase the gap and micro motion at the junction between the implant and bone surface (Kamath et al., 2021), which may lead to prosthesis failure. Second, the preparation of dense sclerotic bone can cause the saw blade to skive, and this adversely affects flush surface cutting. In addition, the sclerotic bone may further generate excessive heat during mechanical osteotomy, which may lead to thermal necrosis (Eriksson et al., 1984). Third, the saw will also cause mechanical damage to the bone, destroy the microstructure of bone tissue, and produce a significant amount of bone debris. This debris is bone sequestra, a cause of aseptic necrosis, which will then retard bone regeneration by increasing the time for the macrophages to cleanse the wound (Giraud et al., 1991). Therefore, it is important to find a new way of osteotomy in TKA.

Recently, laser, as the most promising technology to replace traditional mechanical osteotomy tools such as electric saws and drills to achieve bone cutting, has attracted the attention of researchers (Baek et al., 2015). Laser has unique advantages such as non-contact, non-vibration (Berrocal et al., 2007), high-precision, and arbitrary-geometry cutting. This is especially true when the laser beam with a diameter of only micron order is combined with advanced computer control, and it can cut bones more accurately (Baek et al., 2015; Marcello et al., 2018).

Theoretically, the advantages of laser can perfectly suit the needs of TKA bone preparation. However, the thermal damage of laser has always puzzled researchers (Gunaratne et al., 2016). With the improvement in laser design, the heat has been effectively controlled. To test that laser osteotomy can achieve ideal TKA bone preparation, we designed a new ultra-pulsed CO_2 laser osteotomy system. Then, this system and the traditional mechanical saw were used to perform distal femur osteotomy in animals for comparison. We analyzed the osteotomy surface structure, evaluated the thermal effect on bone and bone cells, and studied the biological characteristics of bone surface to reveal the safety of the ultra-pulsed CO_2 laser osteotomy system.

MATERIALS AND METHODS

Materials

4% paraformaldehyde, Triton X-10, and 10% EDTA solution were provided by Biosharp (Anhui, China). The Hematoxylin–Eosin (HE) Staining Kit and DAPI were purchased from Beyotime (Chongqing, China). A Calcein/PI Live/Dead Cell Viability Kit was supplied by Sigma Chemical Co. (St. Louis, MO, United States). Rhodamine phalloidin, Alexa Fluor 488, and anti-paxillin antibody were supplied by Abcam (Shanghai). Sprague–Dawley (SD) rats aged 12 weeks (400 ± 40 g) were provided by Hunan SJA Laboratory Animal Co.. LTD. (Hunan, China).

TABLE 1 | Parameters of the ultra-pulsed CO_2 laser osteotomy system.

Parameters	
Wavelength	9.3 μm
Average power	5 W
Peak power	500 W
Beam waist diameter	2.2 mm
Full divergence angle	6.2 mrad
Rise time	<10 μs
Fall time	<15 μs
Pulse repetition frequency	500 Hz

Laser System and Animal TKA Osteotomy

The parameters of the ultra-pulsed CO_2 laser osteotomy system (Shenzhen KBF Laser Technology Co., Ltd., China) are shown in **Table 1**. In this study, the pulse duration is 25 μs, the single pulse energy is 25 mJ, and the focal spot diameter after the beam passes through the galvanometer is 60 μm. The galvanometer (AxialScAN-20-30, Germany) can dynamically control the working position of the laser focus on X, Y, and Z-axes through the software Marking Mate 3D (Version 2.7). All cutting processes in this study are performed by line filling cutting, with a line width of 1 mm (the course of the laser beam is shown in **Figure 1A**). After completing a scanning filling, the galvanometer controls the focus to drop 0.05 mm along the *Z*-axis, and the cutting speed is 80 mm/s. The model of the laser osteotomy system is shown in **Figure 1**.

We used this system to perform TKA osteotomy on the isolated knee of sheep aged one year and weighing 40 kg (the shape of the femoral condyle in the sheep is similar to that in humans). The experiments were performed in accordance with the protocols approved by the Ethics Committee of TMMU (Approval Number: 20170002). Before cutting, the femur was fixed on the super-light clay, which could be shaped quickly. Then, laser osteotomy was performed in accordance with the TKA osteotomy method. After each resection, the position of the femur was manually adjusted. The distal femur, anterior cortex, anterior bevel, posterior condyle, and posterior bevel were sequentially sectioned, and finally, box resection was performed. The whole process was sprayed with a self-made water sprayer, 1 ml/min (Kuttenberger et al., 2008). Water acts as a coolant to reduce thermal injury, and the micro explosion of water irradiated by the laser can accelerate cutting (Zhang et al., 2012). The distal femur after laser cutting is shown in **Figure 1C**.

Surface Characterization and Thermal Analysis

Specimen and Grouping

For animal protection and subsequent bioactivity analysis of the osteotomy surface, the experimental animal model was changed to an SD rat. The specimens were the femurs of rats dissected immediately after cardiac injection of excessive anesthesia. The experimental group was the laser osteotomy group (L group), and the control group was the mechanical saw group (S group).

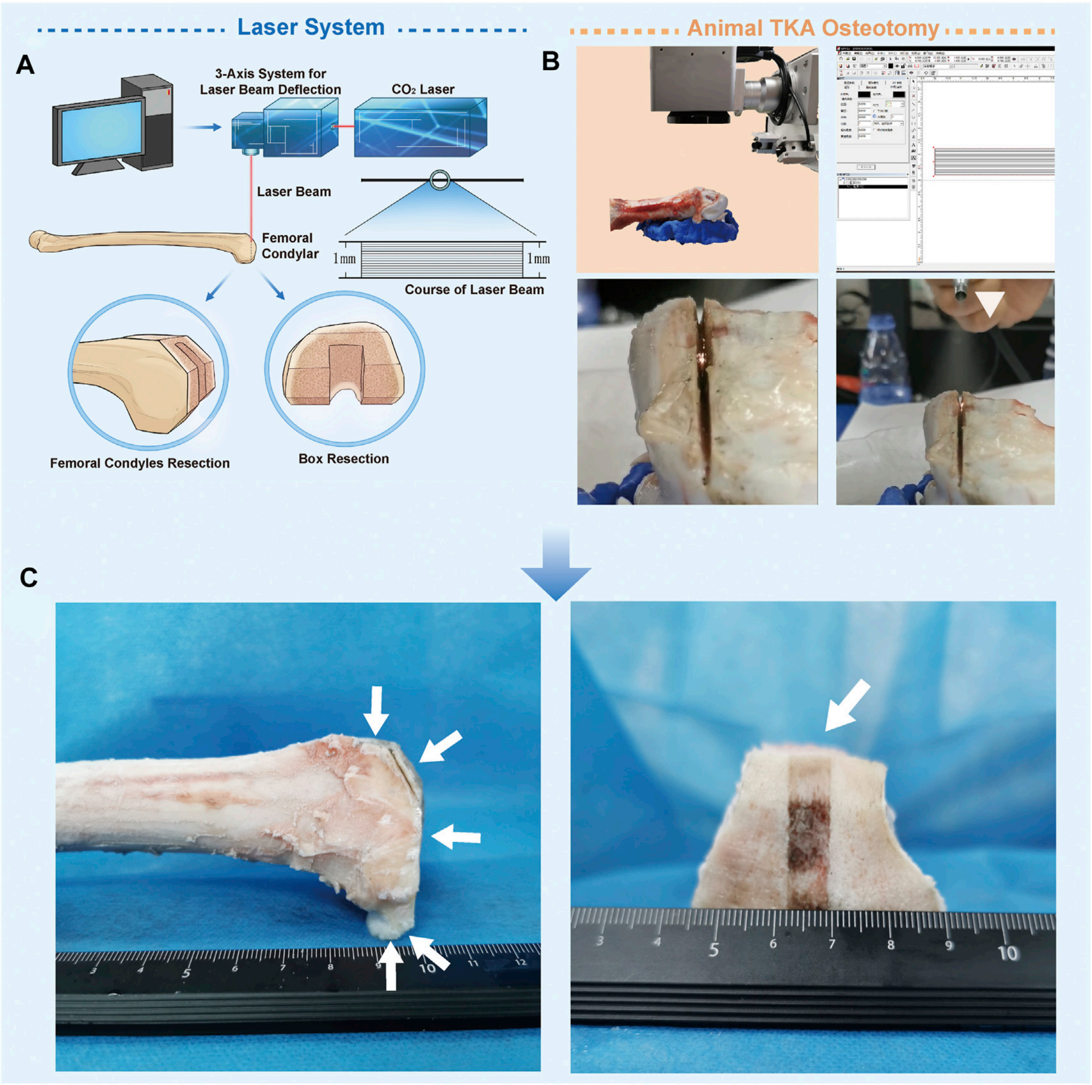

FIGURE 1 | Ultra-pulsed CO_2 laser osteotomy of the distal femur of sheep. **(A)** Schematic chart of the ultra-pulsed laser CO_2 laser osteotomy system **(B)** Operational process of the sheep distal femur bone-cutting surface in total knee replacement using this system; the white triangle indicates the self-made water spray device **(C)** Distal femur after laser cutting.

Femoral Osteotomy

Osteotomy was performed at the distal femur to analyze the cancellous bone and performed in the middle of the femur to analyze the cortical bone. In the L group, the aforementioned laser system was used for cutting. Briefly, after fixing the femur, it was completely resected at 5 mm from the distal femur to obtain the cancellous bone specimen, and then, the femur was cut in the middle section to obtain the cortical bone specimen. A water spray (1 ml/min) was used during cutting. In the S group, a mechanical saw (saw blade thickness 1mm, UNIVERSAL, American) was used to cut the femur at the same site. To minimize interference, each cut was performed at a maximum round-trip frequency with water spraying (1 ml/min). Finally, the specimens were collected. There were 18 samples of cancellous bone and 18 samples of cortical bone from 18 rats, half of which were used for surface characterization and half for histological analysis.

Surface Characterization.

The specimens were gently rinsed with normal saline at room temperature and then freeze-dried. Briefly, the samples were sequentially refrigerated at 4°C for 30 min, −20°C for 12 h, and −80°C for 7 days. The freeze-drying apparatus (FD-1A-50, BiLon, Beijing) was used to prepare the samples for 24 h. After spraying gold, the morphology of the cutting surface was observed by scanning electron microscopy (SEM) (S-3400N, HITACHI, Japan). The surface roughness of the samples was examined by using a 3D laser confocal scanning microscope (OLS5000, Olympus, Japan), and the results were analyzed by multifile analyzer software. The

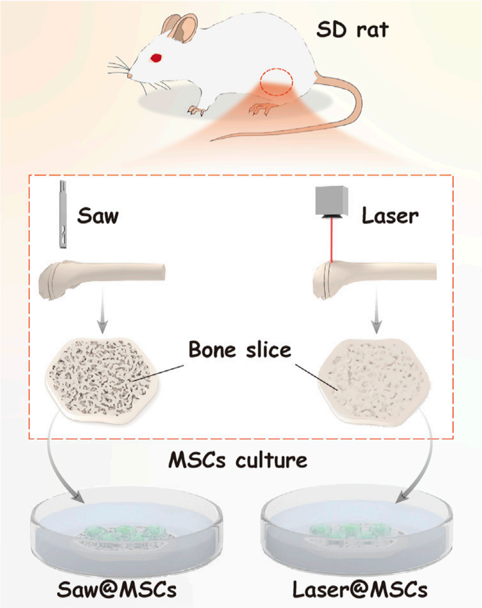

FIGURE 2 | Preparation of bone slices and cell culture.

surface roughness was measured for six different specimens, and the average values were recorded.

Histological Analysis

The samples were fixed by immersion in 4% paraformaldehyde for 48 h and decalcified in 10% EDTA solution for 1 week. Then, the samples were washed repeatedly and gently with normal saline to eliminate the effect of the decalcification solution on tissue staining. The samples were embedded in paraffin and then, serial sections were made perpendicular to the osteotomy surface and stained with the Hematoxylin–Eosin (HE) Staining Kit. After the sections were prepared, a microscope (Olympus, Japan) was used to observe and photograph the sections. ImageJ was used to calculate the depth of the mechanical damage and the thermal damage to the bone. The numbers of bone lacunae with cells and empty bone lacunae within 200 μm of the cutting edge were counted, and the rate of empty bone lacunae was calculated (Yin et al., 2016; Palaia et al., 2020).

Biological Characteristics of the Osteotomy Surface.

Preparation of Bone Slices

To observe the biological characteristics of the osteotomy surface prepared by the two cutting methods, a laser and mechanical saw were used to cut the distal femur to prepare the bone slices. Briefly, after the femur specimen was fixed, a laser (the mechanical saw was used in the S group) was used to cut the distal femur into 3-mm-thick slices. Twelve rats were used to prepare bone slices. Since two bone slices could be prepared from one femur, 48 bone slices were prepared and used for all cell experiments. The preparation schematic chart of the bone slice is shown in **Figure 2**. Then, the samples were soaked in 75% alcohol for 24 h for disinfection.

Cell Culture

Rat mesenchymal stem cells (MSCs) were isolated from three rats aged 2 weeks (100 ± 10 g) and cultured as previously reported (Mandal and Kundu, 2009). The MSCs were cultured in Dulbecco's modified Eagle medium (DMEM) supplemented with 10% (v/v) fetal bovine serum (FBS) and 1% penicillin–streptomycin solution at 37 °C in an incubator containing 5% CO_2, and the culture medium was replaced every second day. The identification of MSC was shown in **Supplementary Materials**. The MSCs at the 3rd passage were used in all subsequent *in vitro* studies. The cell density of all cell experiments was 2×10^4 cells/well.

Cell Infiltration

The sterilized samples (six in each group) were placed at the bottom of a 24-well plate and then, the MSCs were inoculated. To allow the cells to settle uniformly on the surface of the bone slice, the cells were suspended during inoculation. The cells were cultured in an incubator containing 5% CO_2 at 37°C with 100% relative humidity, and the medium was changed every 2 days.

After 2 and 5 days of culture, the culture medium was discarded, and the cells were flushed gently with sterile PBS three times. The cells were stained using the Calcein/PI Live/Dead Cell Viability Kit according to the instructions for use. The fluorescence solution Calcein can make living cells appear green at 494 μm wavelength, and PI can make dead cells appear red at 617 μm wavelength. After staining, a laser confocal scanning microscope (LSCM, LSM900, ZEISS, German) was used to observe and photograph the MSCs adhered to the surface of the bone slices. High-resolution images of Z-stacks were obtained and confocal Z-stacks of the images were processed and reconstructed with ZEN blue edition software (Version 3.3, ZEISS, German). Then, the cells attached to the bone slices were counted, the survival rate was calculated (Lin et al., 2021), and the depth of cell infiltration was measured with the image reconstructed on the *Z*-axis (Zhao et al., 2016).

Cytoskeleton Staining and Scanning Electron Microscopy

The method of cell inoculation was the same as mentioned previously. There were three samples in each group. After culturing for 48 h, the medium was removed and the samples (half for staining and half for SEM) were flushed with PBS. After that, 4% paraformaldehyde solution and 0.1% Triton X-100 were added sequentially. Finally, the samples were incubated with Rhodamine-phalloidin (1: 500) solution at room temperature for 2 h. After washing with PBS, DAPI was used to stain the nuclei. All samples were imaged *via* the CLSM. The fractal dimension of the cytoskeleton was calculated with ImageJ software. Before SEM, the samples were fixed with 4% paraformaldehyde and subjected to dehydration using graded

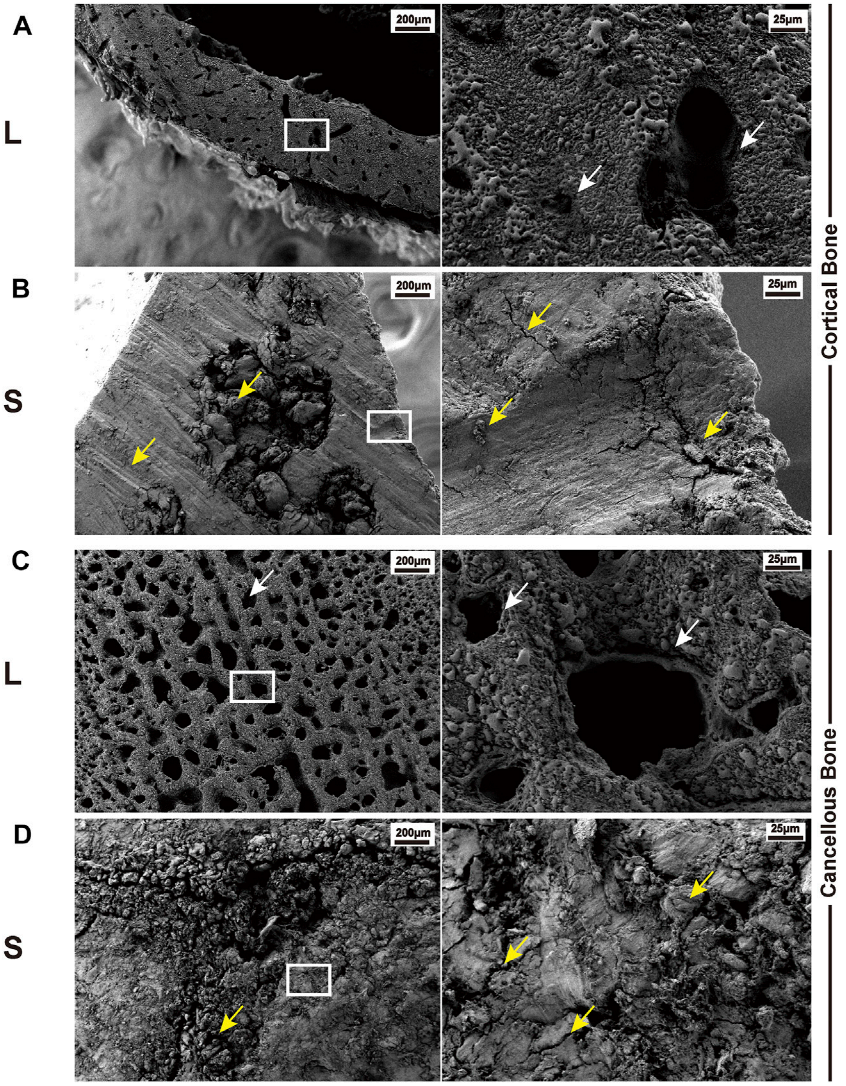

FIGURE 3 | Typical SEM images of bone surface cutting by the laser and mechanical saw. **(A)** Cortical bone surface produced by laser osteotomy; white arrows indicate the trophoblast vascular lumen and Haversian canal. **(B)** Cortical bone surface produced by mechanical saw osteotomy; yellow arrows indicate abrasion marks, cracks, and bone chips caused by the saw blade. **(C)** Cancellous bone surface produced by laser osteotomy; white arrows indicate the trabecular bone and the space between the trabecular bones. **(D)** Cancellous bone surface produced by mechanical saw osteotomy; yellow arrows indicate cracks and bone chips. White boxes indicate the cut-out after the subsequent magnification.

ethanol, and then the samples were coated with a thin sputtered gold layer.

Focal Adhesion Staining Analysis

The method of cell inoculation was the same as that of cell infiltration, with three samples in each group. After fixing the samples with the aforementioned method, the cells were incubated with paxillin (rabbit pAb; 1:50) at 4°C overnight. Then, they were incubated with secondary antibodies coupled to Alexa Flour 488 for 1 h and with rhodamine phalloidin (1: 500) solution for 2 h at 37°C. After that, the samples were washed with PBS and the cell nuclei were stained with DAPI. Fluorescence images were obtained using CLSM. Profiles of F-actin (red) and p-paxillin (green) were extracted from the images of CLSM using ImageJ.

Statistical Analysis

All experiments were performed at least in triplicate. Data are presented as the mean ± standard deviation (SD). Statistical calculations were performed by Student's *t*-test using SPSS ver.22 software (United States of America). Statistical significance was set to $^*p < 0.05$, $^{**}p < 0.01$, and $^{***}p < 0.001$.

RESULTS

Ultra-Pulsed CO_2 Laser Osteotomy System Complete Animal TKA Bone Cutting

The laser successfully realized the osteotomy of the distal femur of sheep, and no carbonizations were found on the bone. There was

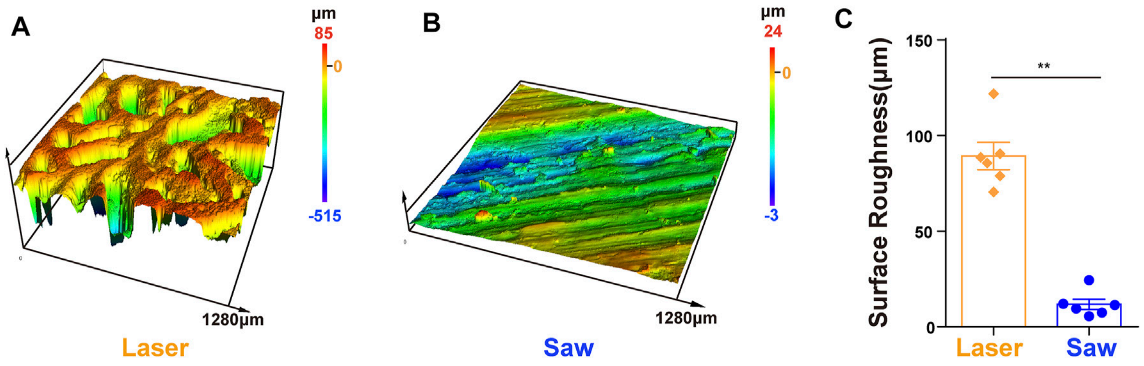

FIGURE 4 | Surface roughness. **(A,B)** 3D height distribution images of the bone surface which were taken with the laser confocal scanning microscope after laser and mechanical saw cutting. **(C)** Surface roughness, **, $p < 0.01$.

a crackling sound during cutting, with the smell of protein burning, and white debris flew out of the incision (**Figure 1**).

Laser Osteotomy Preserves the Intact Structure of the Bone Surfaces and Has Better Surface Roughness than Mechanical Saw Osteotomy

L group: The osteotomy surface retained the original physical structure of the bone, with smooth sections and no mechanical damage. The typical images are shown in **Figure 3**. An open trophoblast lumen and a Haversian canal were observed on the cortical bone surface (**Figure 3A**). In addition, on the cancellous bone surface, intact trabeculae and a large number of interlacing pores formed by the trabeculae were observed (**Figure 3C**).

S group: The surface was severely damaged, showing fragmentary and no porous structure. There were several large cracks on the cortical bone and wear marks caused by saw blade grinding (**Figure 3B**). Furthermore, the trabeculae could not be distinguished on the cancellous bone surface, and a large number of cracks and bone debris appeared on the surface. The holes between the trabeculae were filled with the bone debris generated by the saw blade (**Figure 3D**).

The surface roughness of the L group is significantly higher than that of the S group as shown in **Figure 4**.

Laser Osteotomy Does Not Cause Thermal and Mechanical Damage to Bone Tissue and Cells

L group: The sections were uniformly stained, and it was observed that in the cancellous bone sections, all the bone trabeculae at the cutting edge were intact without thermal or mechanical damage, and the cells remained intact. Typical images are shown in **Figure 5**. In addition, the cortical bone had a neat cutting edge without mechanical cracks. The cell morphology near the cutting edge was consistent without thermal damage, and there were even intact cells on the cutting edge (**Figure 5B**).

S group: In the cancellous bone, the bone tissue and cells were seriously damaged, the bone trabeculae were fragmented, and the pores between the bone trabeculae were filled with a large amount of bone debris (**Figure 5C**). A large number of empty bone lacunae left after the cells cracked and disappeared. The damage also occurred in the cortical bone with more pronounced thermal damage (**Figure 5D**). In the S group, the mechanical damage depth was 243 ± 44 μm (**Figure 5E**), the thermal damage depth was 44 ± 10 μm (**Figure 5F**), and the empty bone lacunae rate was 55.6 ± 7% (**Figure 5G**), which were significantly higher than those in the L group.

Osteotomy Surface Biological Studies: Infiltration, Cytoskeleton, and Focal Adhesion Analysis

MSCs were evenly distributed on the surface of the samples. It was observed that more MSCs adhered in the L group than in the S group on day 2. The same results were also observed on day 5, and the differences were statistically significant ($p < 0.001$). More importantly, in the L group, the infiltration depth of the MSCs was greater than that in the S group, and the difference was statistically significant ($p < 0.001$). There was no difference in the survival rate of the MSCs between the two groups. Typical images are shown in **Figure 6**.

A typical comparison of MSC cytoskeleton staining images in the L and S groups is shown in **Figure 7**. It shows that the cells were well spread out in the L group, having a tendency to extend along the trabecular direction, and the cytoskeleton polarization was obvious. However, in the S group, the cells were randomly adhered on the bone surface, and the cytoskeleton polarization appeared only at the cell edge. Moreover, the fractal dimension of the cells in the L group is better than that in the S group. The SEM images further indicate that the cells in the L group were more spread out than those in the S group.

To better understand how cell adhesion was altered in the two groups, MSCs were immunostained with F-actin and paxillin to examine FA dynamics. The paxillin and the cytoskeleton co-located showed focal adhesion. Typical images are shown in **Figure 8**. MSCs in the L group developed numerous, larger FAs. In contrast, we noted that the S group only exhibited a dot-like staining pattern near the cell periphery.

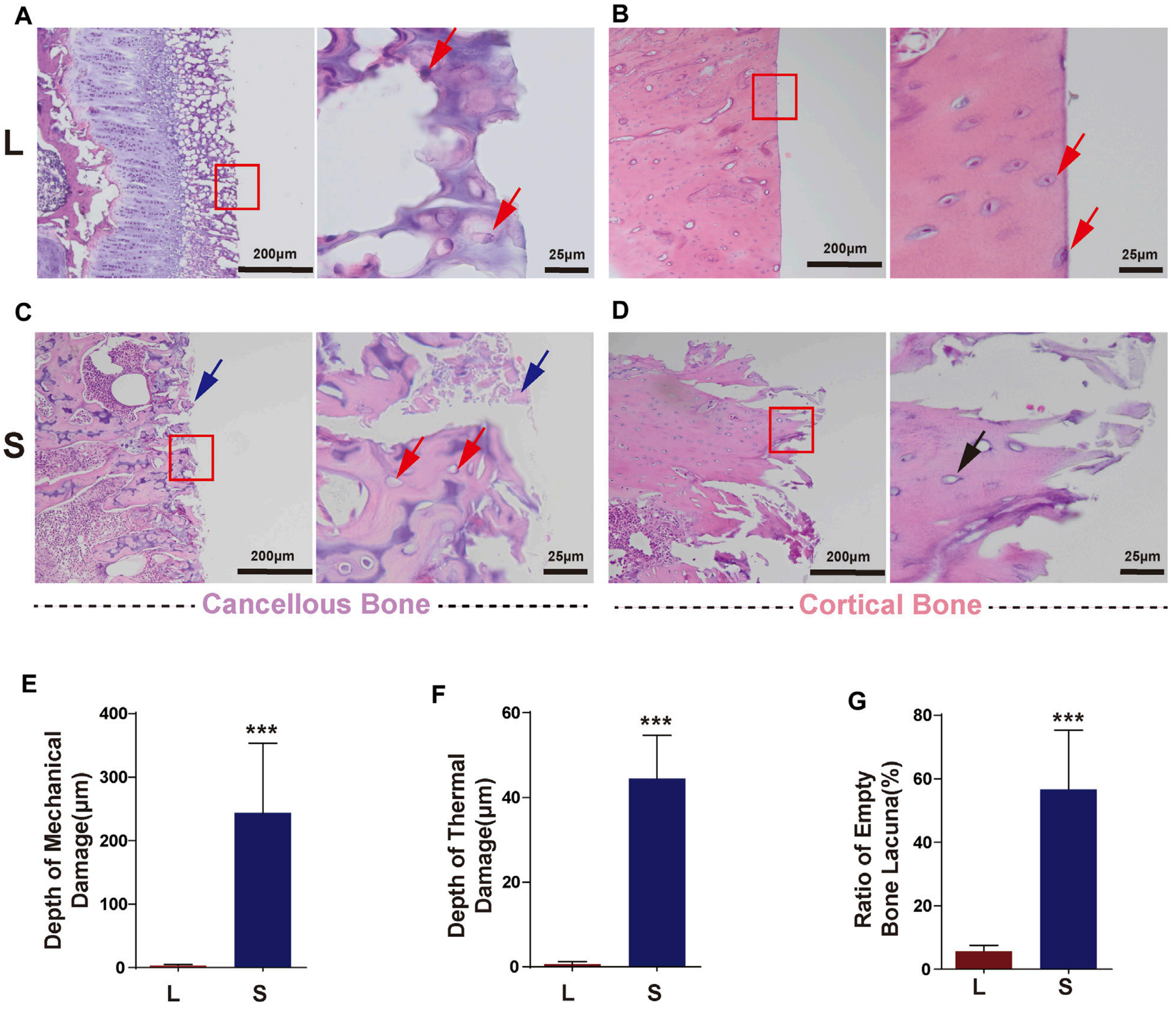

FIGURE 5 | Typical histology images after laser and mechanical saw osteotomy. **(A)** HE images of laser-cut cancellous bone, with intact cells at the cutting edge indicated by red arrows. **(B)** HE images of laser-cut cortical bone with neat cutting edges and intact cells. Red arrows indicate cells on the cutting edge. **(C)** Images of the cancellous bone cut by mechanical sawing, with blue arrows indicating bone chips filled with cutting edges and red arrows indicating empty lacunae and crushed trabeculae. **(D)** HE images of the cortical bone cut by mechanical sawing. Black arrows indicate the destroyed margin bone tissue and empty lacunae. **(E)** Depth of mechanical damage. **(F)** Depth of thermal damage. Boxes indicate cutout after subsequent magnification. **(G)** Empty bone lacunae rate. HE, Hematoxylin–Eosin staining. *** $p < 0.001$.

DISCUSSION

In this study, we used an improved ultra-pulsed CO_2 laser osteotomy system to successfully achieve the five facial and box osteotomy of TKA in sheep knees, and no thermal damage such as carbonization occurred during the experiment (**Figure 1C**). At present, laser has been successfully applied in medical treatment, such as in ophthalmology and oral surgery (Sugar and Alan, 2002; Liu et al., 2006; Zhang et al., 2011). Theoretically, lasers are the most promising alternative to conventional mechanical tools for performing accurate osteotomy. Furthermore, laser has the advantages of non-contact, non-vibration (Berrocal et al., 2007), high-precision, and arbitrary-geometric-shape cutting (Baek et al., 2015; Marcello et al., 2018). Moreover, improved laser cutting methods and the newly developed laser can perform osteotomy with controlled thermal impact. Ivanenko et al. (2005) and Kuttenberger et al. (2010) successfully performed pulsed CO_2 laser osteotomy without thermal damage to animals. However, so far, there are few reports describing the characteristics of the bone surface after laser cutting. The bone surface is very important, especially in operations that require complete contact between the bone surface and the implant to achieve bone integration, such as TKA. Therefore, we further analyzed the bone surface structure and biological characteristics after laser cutting and compared them with traditional mechanical osteotomy tools.

To better protect animals and conduct subsequent cytological experiments, the animal model was adjusted to SD rats. The

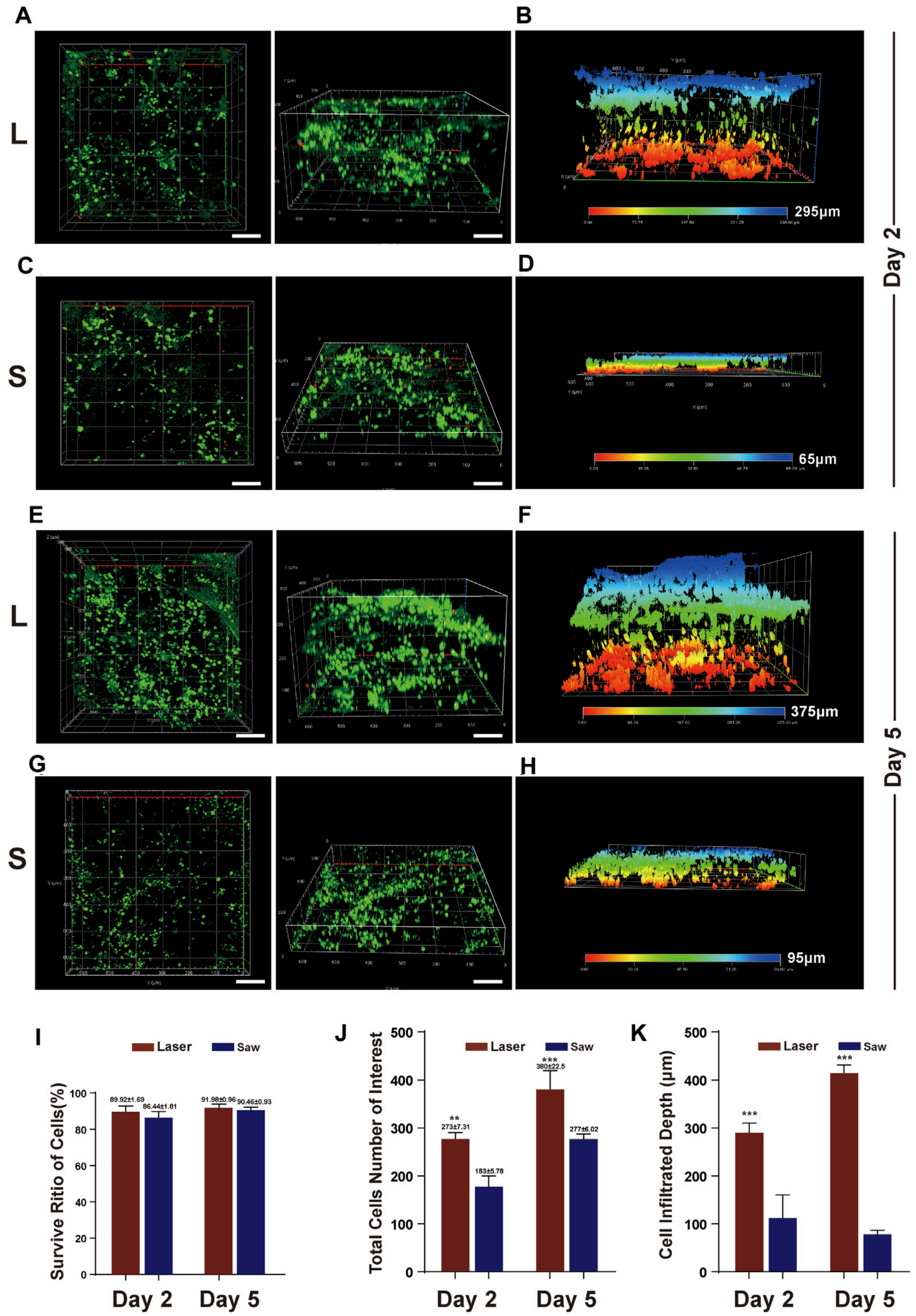

FIGURE 6 | MSC infiltration into bone surface. **(A)** Typical images of z-axis reconstruction of adhesive MSCs on bone slices at Day 2 after the cell inoculation (culture) in L group, **(B)** infiltration depth at Day 2 after the cell inoculation in L group. **(C)** Typical images of z-axis reconstruction of adhesive MSCs on bone slices at Day 2 after the cell inoculation in S group, **(D)** infiltration depth at Day 2 after the cell inoculation in S group. **(E&G)** Typical images at Day 5 after the cell inoculation in the two groups. live = green, red =dead and scale bar = 100 μm. **(F&H)** infiltration depth at Day 2 after the cell inoculation in the two groups. **(I)** Quantification of viable cell percentage in five scopes in L and S group. **(J)** Quantification of total number of MSCs in five scopes in L and S group. **(K)** Quantification of MSCs infiltration depth in five scopes in L and S group. **, $p < 0.01$, ***, $p < 0.001$.

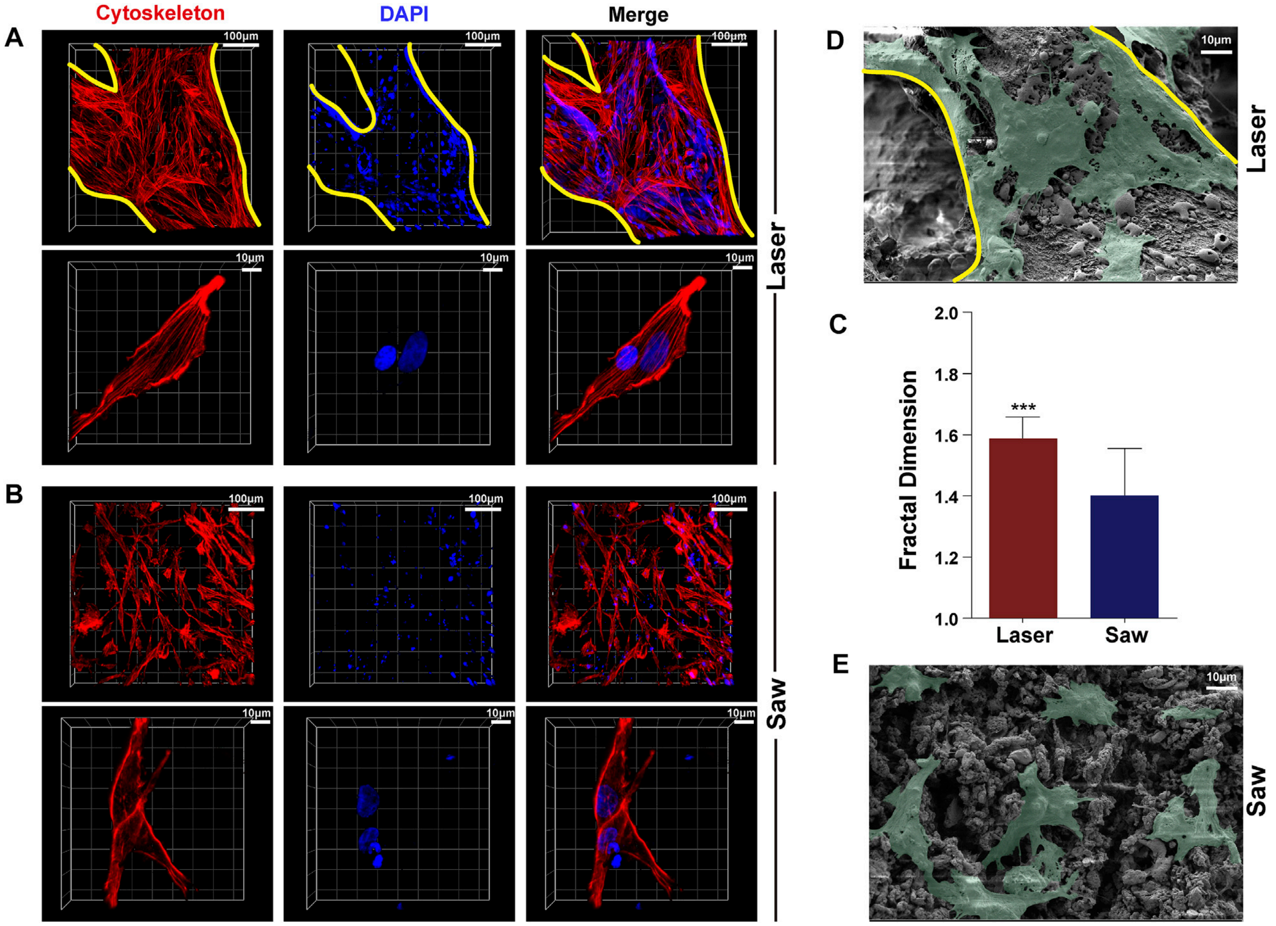

FIGURE 7 | Typical images of adhesion of MSCs. **(A)** is the laser group, **(B)** is the mechanical saw group, photographed by using a laser confocal scanning microscope, and red represents the cytoskeleton, blue represents the nucleus, and the yellow line represents the trabecular boundary. **(C)** Statistics of the fractal dimension of a single MSC cytoskeleton of the two groups (*n* = 50) **(D,E)** are scanning electron microscopy images of MSC adhesion to the bone surface of the two groups (green).

results of scanning electron microscopy (SEM) on the osteotomy surface of rat femur showed that mechanical sawing could seriously damage the bone structure, whereas laser could completely preserve the topological structure of the bone. Mechanical saw cutting led to severe damage of the bone trabeculae, producing a large amount of bone debris filling the pores and resulting in the complete destruction of the bone trabecula structure. In addition, many cracks and abrasion marks after sawing appeared in the cortical bone. Studies have shown that bone debris will increase aseptic inflammatory response, resulting in prolonged bone healing time (Giraud et al., 1991). Such results may have an adverse effect when cementless prostheses are used. On the contrary, laser can cut into a completely different bone surface. In the cancellous bone, the trabecular bone on the osteotomy surface remains intact with a large number of pores in it. At the same time, the cortical bone in the middle part of the femur has a smooth bone surface and many complete open Haversian canals. The surface roughness analysis shows that the laser-cut surface has better performance in roughness. Combined with the SEM images, we believe that laser can achieve ideal osteotomy while maintaining the complete natural topological structure of the bone, which may be conducive to the early stabilization of cementless prostheses and the realization of long-term bone integration.

Previous studies have shown that a micromotion larger than 150 μm can inhibit bone ingrowth onto porous surfaces and consequently lead to implant failure (Justy, 1997). While it is difficult to achieve the desired bone cutting with traditional mechanical cutting tools, Macdonald et al. (2004) reported an error of more than 2 mm when using traditional mechanical cutting tools during TKA bone preparation. Apparently, laser cutting has no such concerns. The laser can greatly reduce the incision width to 100 μm. The specific width depends on the focal spot diameter. In this study, the focal spot diameter is 60 μm. In addition, the cutting geometry is not restricted and arbitrary and complex cutting shapes in the geometry are available. Of course, laser must be combined with computer and robot tools to achieve accurate osteotomy (Burgner et al., 2010).

Significantly, the laser osteotomy system used in this study can further reduce thermal damage to the bone. By performing H–E

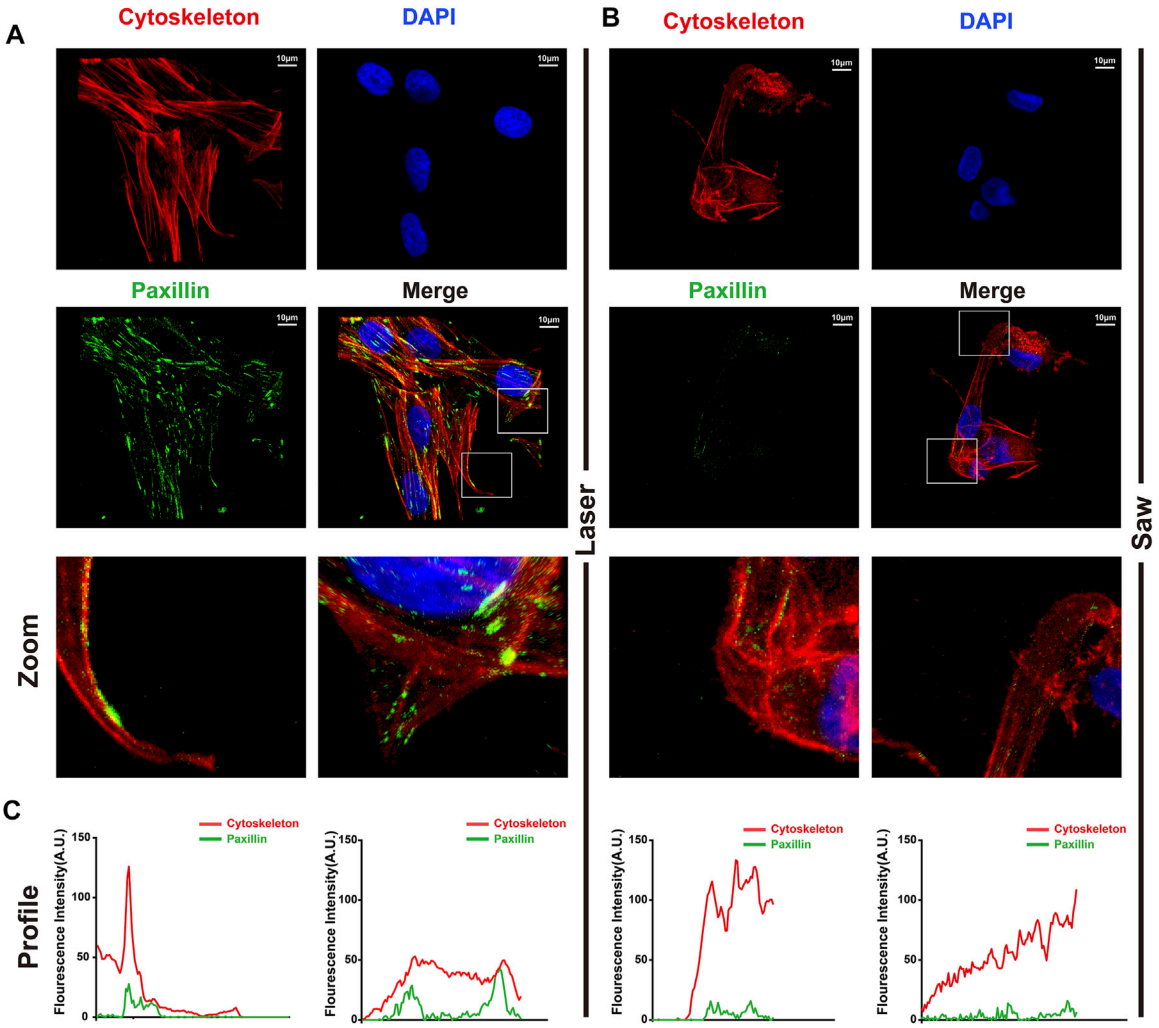

FIGURE 8 | Typical images of laser cutting bone surface promoting the formation of focal adhesion. **(A)** The laser group and **(B)** the mechanical saw group were photographed by laser confocal microscope. The red is the cytoskeleton, the green is the paxillin, and the blue is the nucleus. **(C)** Profiles of F-actin (red) and p-paxilin (green) were extracted from images (white segments) using ImageJ software.

staining, we found that intact cells were preserved at the cutting edge of laser-cut bone tissue. In contrast, mechanical sawing resulted in severe mechanical damage to bone tissue (cracks up to 500 μm deep) and thermal damage (incomplete damage to cells within 200 μm of the cutting edge). The previous research on CO_2 laser osteotomy has ever been plagued by thermal damage. In the early studies, a continuous CO_2 laser was used for bone cutting experiments, which resulted in severe carbonization of bone tissues (Panossian et al., 1984). Later, Frentzen et al. (2003) used a pulsed CO_2 laser to cut pig ribs with a water jet. They reported thermal damage to the bone tissue only within10 μm near the cutting edge and incomplete damage to bone tissue cells within 50 μm of the edge.

We can analyze these results by the following mechanisms of action of laser osteotomy. 1) First, laser parameters determine the effect of laser irradiation on the tissues [34]. When laser energy reaches the surface of the bone, it can be reflected, scattered, absorbed, or transmitted to the surrounding tissues. The 9.3-μm wavelength laser we used has high absorption in bone tissue. Since bones mainly comprise water and inorganic calcium salts, a rapid phase transformation from water to gas will result in the micro-rupture and micro-explosive removal of bone mineral phases (Gunaratne et al., 2016). However, the removal only occurred in the bone tissue irradiated by the laser (the focus diameter of the beam in this study was 60 microns), so there was little mechanical damage to the nearby bone tissue. 2) The second mechanism is that the laser can transmit the required energy in a short time (rise time 10 μs, fall time 15 μs, and pulse duration 25 μs), and the energy has little time to diffuse into the surrounding tissues. 3) At the same time, water acts as a coolant to reduce thermal injury (Zhang et al., 2012), so almost no heat damage was found in the tissues, while mechanical tools, cutting with strong mechanical forces, will inevitably damage nearby bone tissues and the repeated grinding of the saw blade will also raise the temperature and cause tissue and cell damage.

Cell adhesion is an important factor affecting the ability of bone integration (Zhao et al., 2013; Taale et al., 2018; Kelly et al., 2021). Therefore, we further studied the adhesion of MSCs to the bone surface prepared by the two cutting tools. The results showed that both the number of cells adhered to the bone surface, and the infiltration depth in the laser group was greater than that in the control group. The cells adhered to the bone surface prepared by laser reside in a comfortable environment, while the cells adhered to the bone surface cut by the mechanical saw seem to be damaged. Judging from those results, we believe that laser cutting retains the original topological structure of the bone surface, which is more conducive to the adhesion of MSCs. In addition, the porous bone surface obtained by laser cutting means that the surface area of the bone surface is increased. The results may be beneficial for bone integration.

Limitations

There are also limitations in this study, and further research is still needed. First, the width of the incision for laser osteotomy is 1 mm, which greatly reduces the efficiency of laser cutting. The reason is that the optical transmission design is insufficient and the optical path design needs to be further optimized. Second, the average power of the laser used in the system is low, which limits the speed of laser cutting.

CONCLUSION

In this study, we realized the designed laser TKA osteotomy of animal knee joints and found that the laser-cut bone surface can retain the natural topology of the bone, which is conducive to cell adhesion and infiltration and may promote the bone integration of prosthesis.

DATA AVAILABILITY STATEMENT

The raw data supporting the conclusion of this article will be made available by the authors, without undue reservation.

ETHICS STATEMENT

The animal study was reviewed and approved by the Animal Care and Use Ethics Committee of Army Medical University (Third Military Medical University).

AUTHOR CONTRIBUTIONS

MW: conceived the study and editing. TR: experiments and writing—original draft. CcL: software and formal analysis. SK and TM: data curation. YQ and JL: statistical analysis. YZ and YX: methodology, supervision of the project, administration, and funding acquisition. All authors read and approved the manuscript.

FUNDING

This work was supported by grants from the Science and Technology Innovation and Application Development Project of Chongqing (Grant number 2021MSXM197), the accurate knee surgery system based on intraoperative real-time CT and navigation assistance (2018JCLC0035), and the medical pre-research project (2019D010).

ACKNOWLEDGMENTS

The authors would like to thank the Shenzhen KBF Laser Technology Co., Ltd. for debugging the laser system and supporting the optical instruments.

SUPPLEMENTARY MATERIAL

The Supplementary Material for this article can be found online at: https://www.frontiersin.org/articles/10.3389/fbioe.2022.858862/full#supplementary-material

REFERENCES

Baek, K.-w., Deibel, W., Marinov, D., Griessen, M., Dard, M., Bruno, A., et al. (2015). A Comparative Investigation of Bone Surface after Cutting with Mechanical Tools and Er:YAG Laser. *Lasers Surg. Med.* 47 (5), 426–432. doi:10.1002/lsm.22352

Behery, O. A., Kearns, S. M., Rabinowitz, J. M., and Levine, B. R. (2017). Cementless vs Cemented Tibial Fixation in Primary Total Knee Arthroplasty. *The J. Arthroplasty* 32 (5), 1510–1515. doi:10.1016/j.arth.2016.12.023

Burgner, J., Müller, M., Raczkowsky, J., and Wörn, H. (2010). *Ex Vivo* accuracy Evaluation for Robot Assisted Laser Bone Ablation. *Int. J. Med. Robotics Comput. Assist. Surg.* 6 (4), 489–500. doi:10.1002/rcs.366

Dalury, D. F. (2016). Cementless Total Knee Arthroplasty. *Bone Jt. J.* 98-B (7), 867–873. doi:10.1302/0301-620x.98b7.37367

Eriksson, R. A., Albrektsson, T., and Magnusson, B. (1984). Assessment of Bone Viability after Heat Trauma: A Histological, Histochemical and Vital Microscopic Study in the Rabbit. *Scand. J. Plast. Reconstr. Surg.* 18 (3), 261–268. doi:10.3109/02844318409052849

Frentzen, M., Gtz, W., Ivanenko, M., Afilal, S., Werner, M., and Hering, P. (2003). Osteotomy with 80-?s CO2 Laser Pulses ? Histological Results. *Lasers Med. Sci.* 18 (2), 119–124. doi:10.1007/s10103-003-0264-8

Giraud, J.-Y., Villemin, S., Darmana, R., Cahuzac, J.-P., Autefage, A., and Morucci, J.-P. (1991). Bone Cutting. *Clin. Phys. Physiol. Meas.* 12 (1), 1–19. doi:10.1088/0143-0815/12/1/001

Ivanenko, M., Sader, R., Afilal, S., Werner, M., Hartstock, M., von Hänisch, C., et al. (2005). *In Vivo* animal Trials with a Scanning CO2 Laser Osteotome. *Lasers Surg. Med.* 37 (2), 144–148. doi:10.1002/lsm.20207

Justy, M. (1997). *In Vivo* skeletal Responses to Porous-Surfaced Implants Subjected to Small Induced Motions. *J. Bone Jt. Surg. Am.* 79, 707–714. doi:10.2106/00004623-199705000-00010

Kamath, A. F., Siddiqi, A., Malkani, A. L., and Krebs, V. E. (2021). Cementless Fixation in Primary Total Knee Arthroplasty: Historical Perspective to Contemporary Application. *J. Am. Acad. Orthop. Surg.* 29 (8), e363–e379. doi:10.5435/jaaos-d-20-00569

Katz, J. N., Arant, K. R., and Loeser, R. F. (2021). Diagnosis and Treatment of Hip and Knee Osteoarthritis. *Jama* 325 (6), 568–578. doi:10.1001/jama.2020.22171

Kelly, C. N., Wang, T., Crowley, J., Wills, D., Pelletier, M. H., Westrick, E. R., et al. (2021). High-strength, Porous Additively Manufactured Implants with

Optimized Mechanical Osseointegration. *Biomaterials* 279, 121206. doi:10.1016/j.biomaterials.2021.121206

Kuttenberger, J. J., Stübinger, S., Waibel, A., Werner, M., Klasing, M., Ivanenko, M., et al. (2008). Computer-guided CO2-laser Osteotomy of the Sheep Tibia: Technical Prerequisites and First Results. *Photomed. Laser Surg.* 26 (2), 129–136. doi:10.1089/pho.2007.2139

Kuttenberger, J. J., Waibel, A., Stübinger, S., Werner, M., Klasing, M., Ivanenko, M., et al. (2010). Bone Healing of the Sheep Tibia Shaft after Carbon Dioxide Laser Osteotomy: Histological Results. *Lasers Med. Sci.* 25 (2), 239–249. doi:10.1007/s10103-009-0714-z

Leco Berrocal, M. I., Martínez González, J. M., and Donado Rodríguez, M. (2007). Clinical and Radiological Course in Apicoectomies with the Erbium:YAG Laser. *Med. Oral Patol Oral Cir Bucal* 12 (1), E65–E69.

Lin, C., He, Y., Feng, Q., Xu, K., Chen, Z., Tao, B., et al. (2021). Self-renewal or Quiescence? Orchestrating the Fate of Mesenchymal Stem Cells by Matrix Viscoelasticity via PI3K/Akt-CDK1 Pathway. *Biomaterials* 279, 121235. doi:10.1016/j.biomaterials.2021.121235

Liu, J.-F., Lai, Y.-L., Shu, W.-Y., and Lee, S.-Y. (2006). Acceptance and Efficiency of Er:YAG Laser for Cavity Preparation in Children. *Photomed. Laser Surg.* 24 (4), 489–493. doi:10.1089/pho.2006.24.489

Lotke, P. A., Ecker, M. L., Mccloskey, J., and Steinberg, M. E. (1976). Early Experience with Total Knee Arthroplasty. *JAMA J. Am. Med. Assoc.* 236 (21), 2403–2406. doi:10.1001/jama.236.21.2403

Macdonald, W., Styf, J., Carlsson, L. V., and Jacobsson, C. M. (2004). Improved Tibial Cutting Accuracy in Knee Arthroplasty. *Med. Eng. Phys.* 26 (9), 807–812. doi:10.1016/j.medengphy.2004.06.006

Mandal, B. B., and Kundu, S. C. (2009). Osteogenic and Adipogenic Differentiation of Rat Bone Marrow Cells on Non-mulberry and mulberry Silk Gland Fibroin 3D Scaffolds. *Biomaterials* 30 (28), 5019–5030. doi:10.1016/j.biomaterials.2009.05.064

Marcello, A., Waldemar, D., and Katja, N. (2018). Comparative Microstructural Analysis of Bone Osteotomies after Cutting by Computer-Assisted Robot-Guided Laser Osteotome and Piezoelectric Osteotome: an *In Vivo* Animal Study. *Lasers Med. Sci.* 33 (7), 1471–1478. doi:10.1007/s10103-018-2502-0

Miller, M. A., Goodheart, J. R., Izant, T. H., Rimnac, C. M., Cleary, R. J., and Mann, K. A. (2014). Loss of Cement-Bone Interlock in Retrieved Tibial Components from Total Knee Arthroplasties. *Clin. Orthop. Relat. Res.* 472 (1), 304–313. doi:10.1007/s11999-013-3248-4

Nakama, G. Y., Peccin, M. S., Almeida, G. J., Lira Neto, Ode. A., Queiroz, A. A., and Navarro, R. D. (2012). Cemented, Cementless or Hybrid Fixation Options in Total Knee Arthroplasty for Osteoarthritis and Other Non-traumatic Diseases. *Cochrane Database Syst. Rev.* 10 (10), CD006193. doi:10.1002/14651858.CD006193.pub2

Palaia, G., Impellizzeri, A., Tenore, G., Caporali, F., Visca, P., Del Vecchio, A., et al. (2020). Ex Vivo *Histological Analysis of the thermal Effects Created by a 445-nm Diode Laser in Oral Soft Tissue Biopsy*. *Clin. oral investig.* 24 (8), 2645–2652. doi:10.1007/s00784-019-03123-4

Panossian, B., Lacau Saint-Guily, J., Brasnu, D., Brocheriou, C., Marsan, J., Voreaux, P., et al. (1984). Effects of the CO2 Laser on Mandibular Bone. Preliminary Study. *Ann. Otolaryngol. Chir Cervicofac* 101 (8), 653–655.

Parker, D. A., Rorabeck, C. H., and Bourne, R. B. (2001). Long-term Followup of Cementless versus Hybrid Fixation for Total Knee Arthroplasty. *Clin. Orthopaedics Relat. Res.* 388, 68–76. doi:10.1097/00003086-200107000-00011

Rajitha Gunaratne, G. D., Khan, R., Fick, D., Robertson, B., Dahotre, N., and Ironside, C. (2016). A Review of the Physiological and Histological Effects of Laser Osteotomy. *J. Med. Eng. Techn.* 41, 1–12. doi:10.1080/03091902.2016.1199743

Sugar, A. (2002). Ultrafast (Femtosecond) Laser Refractive Surgery. *Curr. Opin. Ophthalmol.* 13 (4), 246–249. doi:10.1097/00055735-200208000-00011

Taale, M., Schütt, F., Zheng, K., Mishra, Y. K., Boccaccini, A. R., Adelung, R., et al. (2018). Bioactive Carbon-Based Hybrid 3D Scaffolds for Osteoblast Growth. *ACS Appl. Mater. Inter.* 10, 43874–43886. doi:10.1021/acsami.8b13631

van der List, J. P., Sheng, D. L., Kleeblad, L. J., Chawla, H., and Pearle, A. D. (2017). Outcomes of Cementless Unicompartmental and Total Knee Arthroplasty: A Systematic Review. *The Knee* 24 (3), 497–507. doi:10.1016/j.knee.2016.10.010

Yin, C., Ruzzante, S. W., and Fraser, J. M. (2016). Automated 3D Bone Ablation with 1,070 Nm Ytterbium-doped Fiber Laser Enabled by Inline Coherent Imaging. *Lasers Surg. Med.* 48 (3), 288–298. doi:10.1002/lsm.22459

Zhang, X., Zhan, Z., Liu, H., Zhao, H., Xie, S., and Ye, Q. (2012). Influence of Water Layer Thickness on Hard Tissue Ablation with Pulsed CO2 Laser. *J. Biomed. Opt.* 17, 038003. doi:10.1117/1.JBO.17.3.038003

Zhang, Z.-H., Jin, H.-Y., Suo, Y., Patel, S. V., Montés-Micó, R., Manche, E. E., et al. (2011). Femtosecond Laser versus Mechanical Microkeratome Laser *In Situ* Keratomileusis for Myopia: Metaanalysis of Randomized Controlled Trials. *J. Cataract Refractive Surg.* 37 (12), 2151–2159. doi:10.1016/j.jcrs.2011.05.043

Zhao, X., Sun, X., Yildirimer, L., Lang, Q., William Lin, Z. Y., Zheng, R., et al. (2016). Cell Infiltrative Hydrogel Fibrous Scaffolds for Accelerated Wound Healing. *Acta Biomater.* 49, 66–77. doi:10.1016/j.actbio.2016.11.017

Zhao, Y., Wong, H. M., Wang, W., Li, P., Xu, Z., Chong, E. Y. W., et al. (2013). Cytocompatibility, Osseointegration, and Bioactivity of Three-Dimensional Porous and Nanostructured Network on Polyetheretherketone. *Biomaterials* 34 (37), 9264–9277. doi:10.1016/j.biomaterials.2013.08.071

Conflict of Interest: The authors declare that the research was conducted in the absence of any commercial or financial relationships that could be construed as a potential conflict of interest.

frontiers | Frontiers in Bioengineering and Biotechnology

ORIGINAL RESEARCH
published: 24 June 2022
doi: 10.3389/fbioe.2022.850198

Distal Humeral Trochlear Geometry Associated With the Spatial Variation of the Dynamic Elbow Flexion Axis

Diyang Zou[1,6†], *Xiangjun Hu*[5†], *Kai-Nan An*[3], *Kerong Dai*[1,2,6], *Xiaowei Yu*[4], *Weihua Gong*[2*] *and Tsung-Yuan Tsai*[1,2,6*]

[1]School of Biomedical Engineering & Med-X Research Institute, Shanghai Jiao Tong University, Shanghai, China, [2]Department of Orthopaedic Surgery, Shanghai Ninth People s Hospital, Shanghai Key Laboratory of Orthopaedic Implants & Clinical Translation R&D Center of 3D Printing Technology, Shanghai Jiao Tong University School of Medicine, Shanghai, China, [3]Department of Biomechanics, Mayo Clinic, Rochester, MN, United States, [4]Department of Orthopaedic Surgery, Shanghai Jiao Tong University Affiliated Sixth People's Hospital, Shanghai, China, [5]Department of Rehabilitation Medicine, Zhongshan Hospital, Fudan University, Shanghai, China, [6]Engineering Research Center of Digital Medicine and Clinical Translation, Ministry of Education, Shanghai, China

Background: The complexity of the spatial dynamic flexion axis (DFA) of the elbow joint makes the elbow prosthesis design and humeral component alignment challenging. This study aimed to 1) investigate the variations of the spatial DFA during elbow flexion and 2) investigate the relationship between the distal humeral trochlear geometry and the *in vivo* spatial variation of the DFA.

Methods: Ten healthy subjects participated in this study. Each subject performed a full elbow extension to maximum flexion with hand supination under dual fluoroscopic imaging system (DFIS) surveillance. The 2D fluoroscopic images and the 3D bone models were registered to analyze the *in vivo* elbow kinematics and DFAs. The spatial DFA positions were defined as inclination with the medial and lateral epicondyle axes (MLA) in the transverse and coronal planes. The range of the DFA positions was also investigated during different flexion phases. The Spearman correlation method was used to analyze the relationship between the distal humeral trochlear's morphological parameters and the position of DFAs during different flexion phases.

Results: The pathway of the DFAs showed an irregular pattern and presented individual features. The medial trochlear depth (MTD) ($r = 0.68$, $p = 0.03$) was positively correlated with the range of the DFA position (2.8° ± 1.9°) in the coronal plane from full extension to 30° of flexion. Lateral trochlear height (LTH) ($r = -0.64$, $p = 0.04$) was negatively correlated with the DFA position (–1.4° ± 3.3°) in the transverse plane from 30° to 60° of flexion. A significant correlation was found between LTH with the DFA position in the coronal ($r = -0.77$, $p = 0.01$) and transverse planes ($r = -0.76$, $p = 0.01$) from 60° to 90° of flexion.

Conclusion: This study showed that the pathway of the dynamic flexion axis has an individual pattern. The medial and lateral trochlear sizes were the key parameters that might affect the elbow joint flexion function. When recovering complex distal humeral fractures or considering the implant design of total elbow arthroplasty, surgeons should

Edited by:
Jun Pan,
Chongqing University, China

Reviewed by:
Ding Jian,
Shanghai Jiao Tong University, China
Jay Trivedi,
Rhode Island Hospital, United States

Correspondence:
Weihua Gong
gwh1124@sina.com
Tsung-Yuan Tsai
tytsai@sjtu.edu.cn

†These authors have contributed equally to this work

Specialty section:
This article was submitted to Biomechanics,
a section of the journal
Frontiers in Bioengineering and Biotechnology

Received: *07 January 2022*
Accepted: *13 May 2022*
Published: *24 June 2022*

Citation:
Zou D, Hu X, An K-N, Dai K, Yu X, Gong W and Tsai T-Y (2022) Distal Humeral Trochlear Geometry Associated With the Spatial Variation of the Dynamic Elbow Flexion Axis. Front. Bioeng. Biotechnol. 10:850198. doi: 10.3389/fbioe.2022.850198

pay more attention to the medial and lateral trochlea's geometry, which may help restore normal elbow kinematics.

Keywords: humeroulnar joint, elbow flexion axis, flexion–extension movement, morphology, distal humeral trochlea

INTRODUCTION

Total elbow arthroplasty (TEA) is an effective treatment to replace damaged elbow articular surfaces for patients with rheumatoid arthritis, osteoarthritis, serious distal humeral fracture, or bone tumors (Sanchez-Sotelo, 2011; Mansat et al., 2013b; Krukhaug et al., 2018). Although TEA can relieve the symptoms and restore the elbow's function for the patient, many postoperative complications such as aseptic loosening, infection, postoperative instability, and periprosthetic fractures were recorded (Schoch et al., 2017; Pham et al., 2018; Geurts et al., 2019). Recent clinical studies have reported a high revision rate of 25% and a high complication rate of 27%–43% after TEA within 10 years (Mansat et al., 2013a; Schoch et al., 2017; Pham et al., 2018; Geurts et al., 2019). Several studies have suggested that the elbow flexion axis mismatch during TEA surgery may lead to high complications (Brownhill et al., 2012). Therefore, it is crucial to determine the axis position accurately when performing TEA surgery.

Accurate identification of the elbow flexion axis during the TEA surgery remains challenging. In clinical practices, the trochlea central axis (TCA) is usually considered as the anatomical elbow flexion axis (Brownhill et al., 2006; McDonald et al., 2010; Wiggers et al., 2014). Traditionally, the position of the TCA is well identified by using lateral X-ray imaging. Surgeons aim to overlap the capitalism and the trochlear contour until they create concentric circles with their centers representing the elbow rotation axis (Wiggers et al., 2017). However, the anatomical bow of the distal humerus and the limb's position may cause an imperfect lateral X-ray projection and errors in identifying the flexion axis (Dos Santos et al., 2017). Previous studies have demonstrated that these errors could reach up to 10° in the coronal and transverse planes (Brownhill et al., 2006; Wiggers et al., 2014). The mean flexion axis (MFA), known as the functional rotation axis, was another conception for the description of the joint movement (Ehrig et al., 2007; Gordon and Dapena, 2013). The humeral side was fixed while the forearm was flexed freely so that the MFA of the elbow joint was calculated using a motion capture system (Stokdijk et al., 1999; Song et al., 2018). Some researchers recommended MFA as a more appropriate way for rotation axis alignment than the intraoperative X-ray imaging method (Song et al., 2018). However, most MFA calculations rely on image-based navigation or motion capture systems, which are not available in every hospital. Besides, there is no consensus on which referencing method is the best for determining the elbow flexion axis for TEA.

The helical axis theory proposed by Woltring et al. (1985) was commonly used to calculate the dynamic flexion axis (DFA) of joints from acquired kinematics data in biomechanical or clinical studies (Song et al., 2018; Ehrig and Heller, 2019). Previous studies have reported that the DFA during elbow flexion was not fixed but moved like a twist around an axis (Bottlang et al., 2000; Goto et al., 2004). Most of the studies about DFA were based on cadaveric specimens (Duck et al., 2003a; Duck et al., 2003b; Muriuki et al., 2012). It cannot reproduce the flexion motion without muscle activation. The *in vivo* continuous flexion motion measurement plays an essential role in understanding the elbow flexion movement pattern. Studies have shown that various factors would affect elbow motion, including the integrity of the ligament, the employing load, the effect of forearm rotation (pronation or supination), the active or passive motions, and geometrical characters (Duck et al., 2003a; Duck et al., 2003b; Hua et al., 2020). Morphologic studies about the distal elbow showed that the articular shape might vary among people, including the capitellum or trochlear diameters, articular width, and anatomic bow (Brownhill et al., 2007; Desai et al., 2014; Lenoir et al., 2015a). However, the current elbow prosthesis design does not reproduce the complicated distal humeral anatomical structure. This could be another reason which leads to a higher failure rate of TEA (Geurts et al., 2019). The relationship between distal humeral anatomical features with a spatial DFA position is still unclear. Understanding the characteristics of DFA can provide an insight into the elbow prosthesis design and help surgeons determine which anatomic parameters are critical when reconstructing a severely damaged distal humeral trochlear.

The purposes of the present study were to 1) investigate the variations of DFA during *in vivo* elbow flexion–extension movement, and 2) investigate the relationship between the anatomical parameters of the distal humerus with the variation of the DFA in different ranges of flexion. We hypothesized that the DFA of each subject might have an individual movement pattern. The individual height and diameter of the trochlear might correlate with the position of the DFA.

MATERIALS AND METHODS

Subjects and Image Protocol

Ten healthy subjects were recruited in this study (six men and four women, with 10 right elbows). The study was approved by the Institution's Review Board, and all subjects signed and informed consent before participating in the experiment. The average age was 21.1 ± 0.8 years. The average height and body weights were 171.9 ± 5.4 cm and 65.2 ± 14.6 kg, respectively, and the average BMI was 21.8 ± 4.1. Each subject filled out the American Shoulder and Elbow Surgeons Shoulder Score (ASES) questionnaires with 100 points scored. The dominant hand of all subjects was the right. All subjects included in this research had no history of elbow injury or other musculoskeletal and neural diseases.

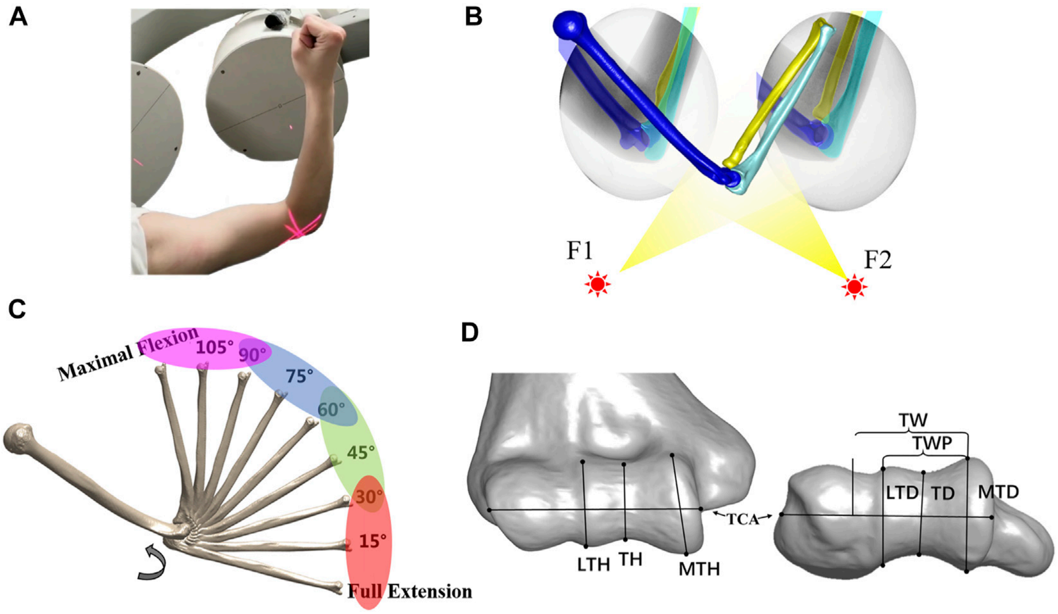

FIGURE 1 | Experimental workflow. **(A)** Each subject performed a full extension to maximal flexion under a biplane fluoroscopic imaging system. **(B)** Virtual experiment environment of 3D–2D registration for acquiring the *in vivo* elbow flexion kinematics. **(C)** Range of the flexion was divided into four phases at full extension to 30°, 30°–60°, 60°–90°, and 90° to maximal flexion. The helical axis theory was applied to calculate the dynamic flexion axis (DFA) at each phase. **(D)** Measurement of distal humeral trochlea morphology. Lateral trochlear height (LTH), trochlear height (TH), and medial trochlear height (MTH) in the coronal plane. Trochlear width (TW), trochlear width proper (TWP), lateral trochlear depth (LTD), trochlear groove depth (TD), and medial trochlear depth (MTD) in the transverse plane.

All subjects received computed tomography (CT) scans (SOMATOM Definition AS, Siemens, Germany) from the wrist to the humeral head. We set the scan voltage and current to 100 KV and 65 mA with an image resolution of 512 × 512 pixels and a voxel size of 0.4 mm^3 × 0.4 mm^3 × 0.6 mm^3. A software platform for three-dimensional (3D) data visualization, Amira (v.6.7.0, Thermo Fisher Scientific, Waltham, MA, United States), was used to generate the 3D model of the humerus, ulna, and radius from the CT images. All subjects completed a full extension to maximum flexion elbow movement with hand supination under a dual fluoroscopic imaging system (DFIS) (BV Pulsera, Philips, Dutch) at a 30 Hz sampling rate. The average time from extension to flexion was 2 s. Two static images of the elbow at full extension and maximum flexion positions with hand supination were also captured for all subjects to calculate the elbow's range of motion (**Figure 1A**).

Registration Procedure

After the experiment, a series of fluoroscopic images were imported into a custom modeling software application MATLAB (MATLAB, MathWorks, Natick, MA, United States). The CT-based bone 3D surface model was introduced into the software for translation and rotation until the projection of the surface model matched the contour of the bone captured on the selected perspective image. The process was repeated every 0.1 s (every three frames) from the maximum straightening position (0 s) to the maximum flexion position (2 s) to complete the registration of the entire moving process (**Figure 1B**).

Definition of the Elbow Coordinate System

To describe the spatial movement of elbow flexion in clinically relevant terms, we defined the local anatomic coordinate system of the humerus and ulna using three orthogonal vectors (Wu et al., 2005). The origin of the humeral coordinate system was determined at the medial point of the humeral medial–lateral epicondyle axis (MLA). The medial and lateral epicondyles were located by finding the center of their bony protrusion. The *Y-axis* was from the origin to the center of the best fit sphere of the humeral head, indicating the proximal-distal (PD) direction. The *X-axis* was defined as the vector cross product of the PD-axis and medial–lateral epicondyle axis, showing the anterior–posterior (AP) direction. The *Z-axis* was defined as the cross product of *Y-axis* and *Z-axis*, indicating the medial–lateral (ML) direction. The coordinate system of the ulna was defined with the origin of the ulnar notch center. The *Y-axis* pointed proximally from the distal ulnar styloid to the origin. The *X-axis* was defined as the line perpendicular to the plane formed by the ulnar styloid, humeral lateral epicondyle, and humeral medial epicondyle, pointing to the front. The *Z-axis* was defined as the cross product of the *Y-axis* and *Z-axis*, pointing laterally. The six-degree-of-freedom (6-DOF) kinematics of the elbow was calculated using the Euler angle with a *Z-X-Y* sequence based on the registered bone positions. The average errors of this technique applied in elbow kinematics evaluation were less than ±1.0 mm and ±1.0° (McDonald et al., 2012).

Rotation Axis Calculation

We used a Gaussian filter to smooth kinematic data by assuming that the noise follows the Gaussian distribution. First, the original transformation matrix was converted to the 6-DOF kinematic data. Second, the 6-DOF kinematic data were smoothed by using a Gaussian filter (The window width of the Gaussian filter was 10 points). The filter parameters were optimized by minimizing the difference between the smoothed data and the raw kinematic data. Finally, the smoothed kinematic data were converted to transformation matrices for calculating the DFA for each subject. *In vivo* kinematics was measured at every interval of 1° from full extension to maximal elbow flexion for the comparison of the results with those presented in the previous study (Ericson et al., 2003; Goto et al., 2004). The finite helical axis method was used to calculate the DFA with a 30° interval and 5° increasing step (Woltring et al., 1985; Ericson et al., 2003; Goto et al., 2004), i.e., the screw axis calculated from 0° to 30° represented the DFA at 0°, while the next screw axis calculated from 5° to 35° represented the DFA at 5°. The TCA was defined as the fitted cylinder centerline on the surface of the humeral trochlear. The elbow motion was divided into four phases with a full-extension (FE)–30°, 30°–60°, 60°–90°, and 90°–maximal flexion (MF) (**Figure 1C**). The MFA was defined as taking the average position of all DFAs. The average DFA at each phase was calculated as the average of the screw axes in each phase, and its position was defined as the inclination with the MLA in the transverse and coronal planes. The range of DFA was also revealed at a different phase of motion in coronal and transverse views. The intercept point of DFA with the medial and lateral sagittal planes, perpendicular to TCA, illustrates its continual dynamic process of elbow flexion. The coronal plane was defined as the plane determined by the humeral long axis and MLA. The DFA intercept sagittal plane of each subject was normalized to the average articular width of 39.2 mm (from the most lateral circle on the capitellum to the most medial circle on the trochlea).

Measurement of Elbow Morphological Parameters

The 3D bone models were imported into Amira (v.6.7.0, Thermo Fisher Scientific, Waltham, MA, United States) to measure the morphological parameters of the distal humerus, following the method in the article of Desai et al. (2014) in the anterior–posterior plane and the axis plane. In total, eight parameters (**Figure 1D**) were obtained, namely, the lateral trochlear height (LTH), trochlear height (TH), medial trochlear height (MTH), trochlear width (TW), trochlear width proper (TWP), lateral trochlear depth (LTD), trochlear groove depth (TD), and medial trochlear depth (MTD). Some parameters (LTH and LTD) were repeatedly measured by the same observer (DY-Z) and co-author (XJ-H) to test our reliability. The intraclass correlation coefficients (ICC) of inter-observer and intra-observer reliabilities were 0.98 and 0.96 for the LTH measurement and were 0.97, and 0.98 for the LTD measurement.

Statistical Analysis

A *post hoc* power analysis was performed to estimate the statistical power (1-β), with a medium effect size and a = 0.05, using statistical power analysis software (G*Power version 3.1). The Mann–Whitney *U* test was performed to compare the difference in morphology parameters. The Spearman correlation analysis was used to calculate the relationship between distal humeral morphology parameters and DFA changes at different ranges. A statistical analysis was performed by numeral calculation software MATLAB (MATLAB, MathWorks, Natick, MA, United States). The significance level was set at 0.05 for all statistical analyses.

RESULTS

Mean Flexion Axis and Trochlear Central Axis

The average orientation of MFA was 3.1° ± 1.9° varus (range, 5.4° varus–1.0° valgus) relative to the TCA in the coronal plane among all the subjects (**Figure 2A**). The angle between the MFA and TCA was 1.3° ± 3.0° (range, 4.7° internal rotation–4.8° external rotation) in the transverse plane (**Figure 2B**). Also, the 3D spatial angle between MFA and TCA was 5.2° ± 1.4° (3.4°–7.3°).

The MFA was located in 0.3 ± 0.3 mm (range −0.2 to 0.8 mm) anterior and 0.2 ± 0.4 mm (range −0.2 to 1.1 mm) distal related to the center of the trochlear on the medial sagittal plane (**Figure 3A**). The MFA was located in 0.8 ± 1.3 mm (range −1.7 to 2.3 mm) anterior and −0.8 ± 1.0 mm (range −1.9 to 1.4 mm) distal related to the lateral trochlear center on the lateral sagittal plane (**Figure 3B**; **Table 1**).

Dynamic Flexion Axis of the Ulna Relative to the Humerus

The pathway of the intercept points of the DFA did not show a regular pattern during the flexion for all the subjects (**Figure 4**). On the lateral sagittal plane, the trajectory of the intercepts twined around the lateral trochlear center within an area of 4.4 mm × 3.7 mm. On the medial sagittal plane, the trajectory of the intercepts moved above the medial trochlear center and was laid within an area of 3.1 mm × 2.1 mm. The positions and range of an average DFA at the difference flexion phase are shown in **Table 2**. At the coronal plane, the average DFA showed the valgus to medial–lateral epicondyle axis at all flexion phases. At the transverse plane, the average DFA showed an external rotation relative to the medial–-lateral epicondyle axis except during the flexion phase from 90° to maximal flexion.

Distal Humeral Morphological Parameters

The sagittal diameters of the medial trochlear, lateral trochlear, and trochlear were 21.4 ± 1.8 mm, 19.0 ± 1.7 mm, and 15.2 ± 1.3 mm. The mean MTH (range 18.6–24.8 mm) was significantly (p = 0.0071) larger than LTH. The LTH (range 16.3–22.5 mm) was significantly ($p < 0.0001$) larger than TH (range 13.3–17.2 mm) amount subjects (MTH > LTH > TH). Likewise, the MTD was significantly larger than LTD (p = 0.0011), and LTD was significantly larger than TD ($p <$ 0.0001) (MTD > LTD > TD). The depth values of MTD, LTD, and TD were 22.5 ± 1.7 mm, 19.8 ± 1.3 mm, and 16.2 ± 1.1 mm, respectively (**Table 3**).

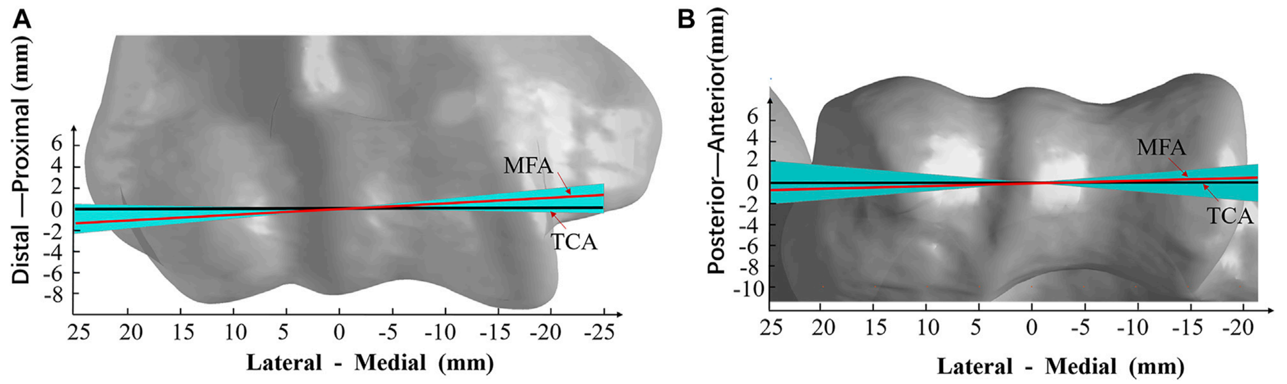

FIGURE 2 | Varus–valgus and internal rotation–external rotation range of the mean flexion axis (MFA). **(A)** Varus–valgus (coronal plane view) and **(B)** internal rotation–external rotation (transverse plane view) of the MFA from all trials of the subject are shown. The solid red line is the mean position of MFA (3.1° varus and 1.3° internal rotation); the black line is the trochlea central axis (TCA). The light blue area represents the deviation of MFA within all subjects (5.4° varus maximum to 1.0° valgus minimum, and 4.8° external rotation to 4.7° internal rotation); the models of the humerus are all normalized to the average TCA length of 39.2 mm.

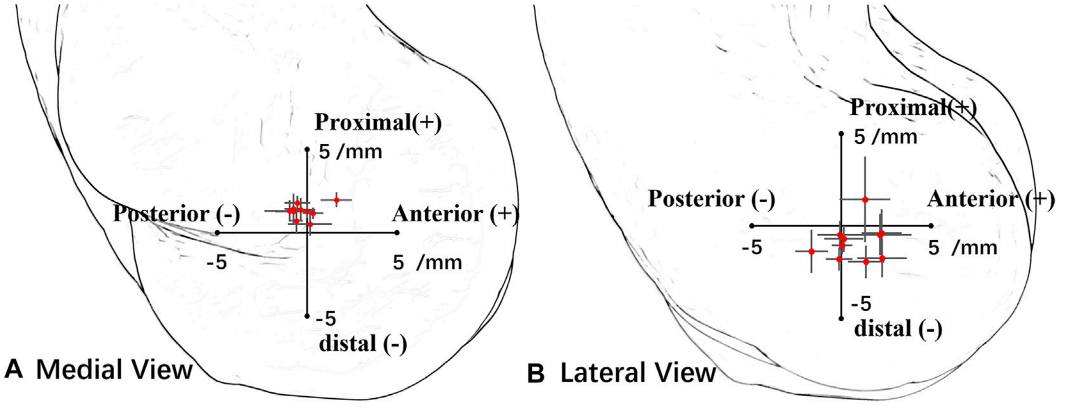

FIGURE 3 | Position of all subjects' mean flexion axis (MFA) intersection points in the lateral plane and medial plane. Red points represent the average center, and the horizontal and vertical lines represent the standard deviation of the axis in the anterior–posterior direction and the distal–proximal direction. **(A)** In the medial view, the origin point is the medial trochlear center. **(B)** In the lateral view, the origin point is the lateral trochlear center.

TABLE 1 | Mean flexion axis (MFA) position in the coronal, transverse, lateral sagittal, and medial sagittal planes. Positive inclination indicated that MFA was varus and internally rotated to the medial–lateral epicondyle axis (MLA). In the lateral and medial planes, positive values indicated that the MFA was anterior and proximal to the center of the trochlea.

Subject	Coronal plane/°	Transverse plane/°	Lateral plane (mm)		Medial plane (mm)	
			Lateral X	Lateral Y	Medial X	Medial Y
1	−4.0 ± 1.5	0.0 ± 2.4	0.1 ± 1.1	−0.7 ± 0.7	0.3 ± 0.6	1.2 ± 0.3
2	1.6 ± 1.9	1.4 ± 2.4	1.4 ± 1.0	−1.9 ± 0.9	−0.5 ± 0.7	1.8 ± 0.5
3	−3.2 ± 3.1	−2.8 ± 2.2	2.3 ± 1.1	−0.4 ± 1.3	−0.8 ± 0.5	1.4 ± 0.9
4	−4.9 ± 1.7	3.1 ± 2.1	−0.1 ± 0.7	−1.8 ± 0.6	−0.4 ± 0.8	1.4 ± 0.7
5	−9.0 ± 4.4	0.8 ± 2.2	1.3 ± 1.4	1.4 ± 2.3	−0.6 ± 0.4	0.7 ± 0.8
6	−4.5 ± 2.3	−6.9 ± 2.3	−1.7 ± 0.9	−1.4 ± 1.2	1.6 ± 0.9	2.0 ± 0.5
7	1.8 ± 1.1	−2.8 ± 1.1	0.0 ± 0.6	−1.0 ± 0.5	0.0 ± 0.3	1.3 ± 0.4
8	−0.4 ± 1.4	3.4 ± 2.5	2.3 ± 1.4	−1.7 ± 1.0	−0.8 ± 1.0	1.3 ± 0.7
9	−6.6 ± 1.1	−1.3 ± 3.5	−0.1 ± 1.3	−0.5 ± 0.8	0.2 ± 1.2	0.5 ± 0.7
10	−9.0 ± 1.7	−0.8 ± 4.4	2.2 ± 1.8	−0.5 ± 1.1	−1.0 ± 1.4	1.3 ± 0.6

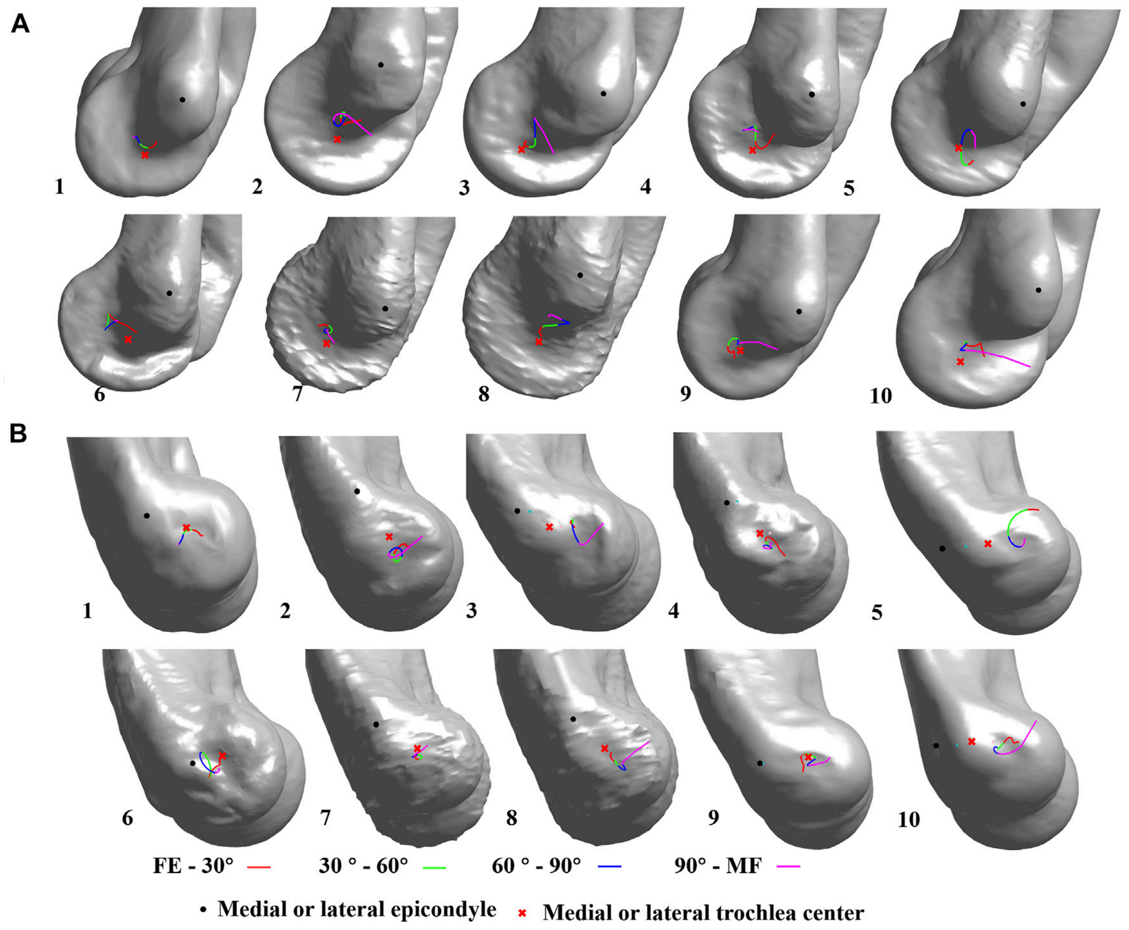

FIGURE 4 | Dynamic flexion axis (DFA) change among all subjects. The continuous change in the DFA is represented by four colors which indicate four flexion–extension phases. FE, full-extension; MF, maximum flexion; **(A)** medial view; **(B)** lateral view.

TABLE 2 | Values representing the angle between the average rotation axis and medial–lateral epicondyle axis in the coronal plane and transverse plane at different phases of flexion. Positive values indicate the average rotation axis was varus and internally rotated to the medial–lateral epicondyle axis (MLA) (FE–30, full extension to 30° flexion; 30–60, 30° flexion to 60° flexion; 60–90, 60° flexion to 90° flexion; 90–max, 90° flexion to max flexion; FE–MF, full extension to max flexion).

	Coronal plane (°)				Transverse plane(°)			
	Mean/std	Max/std	Min/std	ROM/std	Mean/std	Max/std	Min/std	Range/std
FE–30	−5.2/5.1	1.2/3.8	−6.6/5	2.8/1.9	−0.8/3.5	3.2/4.1	−2.4/3.3	3.6/2.4
30–60	−4.2/4.8	−2.7/4.3	−5.7/5.3	3.0/2.3	−1.4/3.3	−0.2/3.7	−2.5/3.5	2.3/1.2
60–90	−3/3.5	−1.7/3.6	−4.3/3.7	2.6/2	−1.3/4.2	0/4.1	−2.5/4.0	2.5/1.3
90–MF	−2.9/3.6	−2.7/4.3	−5.8/4.3	4.1/3.0	1.0/3.5	−0.2/3.7	−1.4/3.2	6.0/5.6
FE–MF	−3.8/3.8	−1.2/3.8	−7.9/4.7	6.7/2.5	−0.6/3.1	−5.9/4.3	−4.0/2.8	9.9/4.1

TABLE 3 | Result of all morphological parameters.

	MTD	TD	LTD	TWP	TW	MTH	TH	LTH
Average (mm)	22.5	16.2	19.8	18.4	22.8	21.4	15.2	19.0
STD (mm)	1.7	1.1	1.3	2.1	2.3	1.8	1.3	1.7
Max/min	25.7/19.7	17.5/14.5	22.0/17.3	20.9/13.5	25.5/18.0	24.8/18.6	17.2/13.3	22.5/16.3

TABLE 4 | Correlation between the morphological parameters with the position of average DFA and range of DFA in different phases of flexion (FE, full extension; MF, maximal flexion).

Variable	Descriptive data/mm		Range of the DFA in the coronal plane (FE–30°)					
	Means ± SD	Range	Means ± SD/°	*r*	*p*	Means ± SD/°	*r*	*p*
MTD	22.5 ± 1.7	19.7–25.7	2.8 ± 1.9	0.68	0.03	—	—	—
MTH	21.4 ± 1.8	18.6–24.8		0.69	0.03	—	—	—
			Position of the average DFA in the transverse plane (30°–60°)	Range of the DFA in the coronal plane (30°–60°)				
LTH	19.0 ± 1.7	16.3–22.5	−1.4 ± 3.3	−0.64	0.04	3.0 ± 2.3	0.71	0.02
			Position of the average DFA in the coronal plane (30°–60°)	Position of the average DFA in the transverse plane (30°–60°)				
LTH	19.0 ± 1.7	16.3–22.5	−3.0 ± 3.5	−0.77	0.01	−1.3 ± 4.2	−0.76	0.01
			Range of the DFA in the transverse plane (60°–90°)	—				
TW	22.8 ± 2.3	18.0–25.5	6.0 ± 5.6	−0.66	0.04	—	—	—
TWP	18.4 ± 2.1	13.5–20.9	6.0 ± 5.6	−0.67	0.04	—	—	—
			Position of the average DFA in the coronal plane (FE–MF)	Position of the average DFA in the transverse plane (FE–MF)				
LTH	19.0 ± 1.7	16.3–22.5	−3.8 ± 3.8	−0.64	0.04	−0.6 ± 3.1	−0.71	0.02

Correlation Between Morphological Parameters and DFA

The different morphological parameters were correlated with the positions and ranges of the DFA at different phases. From full extension to a 30° flexion, MTD ($r = 0.68$ and $p = 0.03$) and MTH ($r = 0.69$ and $p = 0.03$) were all positively correlated with the range of DFA (2.8° ± 1.9°) in the coronal plane. From flexion of 30° to 60°, LTH ($r = -0.64$ and $p = 0.04$) was negatively correlated with the position of average DFA (−1.4° ± 3.3°) in the transverse plane. LTH ($r = 0.71$ and $p = 0.02$) was positively correlated with the range of DFA (3.0 ± 2.3°) in the coronal plane. From flexion of 60° to 90°, a significant correlation was found between LTH with the position of average DFA in the coronal ($r = -0.77$ and $p = 0.01$) and transverse planes ($r = -0.76$ and $p = 0.01$). From a flexion of 90° to maximal flexion, TW ($r = 0.66$ and $p = 0.04$) and TWP ($r = 0.67$ and $p = 0.04$) were all positively correlated with the range of DFA (6.0° ± 5.6°) in the transverse plane. During the whole range of flexion motion, significant correlation was found among LTH with the position of the average DFA in the coronal ($r = -0.64$ and $p = 0.04$) and transverse planes ($r = -0.71$ and $p = 0.01$) (**Table 4**).

DISCUSSION

This study quantified the difference between the MFA and TCA, investigated the *in vivo* continuous position of the DFA of the healthy human elbow joint during extension to flexion, and evaluated its relationship with distal humeral morphological parameters. First, we found that the MFA showed a mean angle of 3.1° ± 1.9° varus and an external rotation of 1.3° ± 3.0° relative to TCA. Also, MFA was closer to the trochlear center on the medial side but more away from the trochlear center on the lateral side. Second, the pathway of the DFA presented individual patterns. Finally, the widths of the lateral and medial trochlea were strongly correlated with the position of the DFA, while the size of the trochlear grove was not. These results indicated that the lateral and medial sizes of the trochlea were the key parameters that may affect the elbow joint function.

The position of MFA was varus and externally rotated to the TCA in the coronal and transverse planes, suggesting that the TCA may not be suitable to represent the elbow flexion axis. *In vivo* (Ericson et al., 2003; Ericson et al., 2008) and *in vitro* (Bottlang et al., 2000; Duck et al., 2003a) studies about the optimum elbow flexion axis have also been published. Bottlang et al. (2000) reported the range of MFA was 2.6° ± 1.0° in the coronal plane and 5.7° ± 2.2° in the transverse plane in a passive movement by using the electromagnetic motion tracking method. Ericson et al. (2003) found greater variations in the coronal plane (6.2° varus to 6.5° valgus) than in the transverse plane (2.4 ° internal rotation to 2.2 ° external rotation) in an *in vivo* active elbow movement situation. Those variations were close to our result (coronal plane: 5.4° varus to 1.0° valgus, transverse plane: 4.7° internal rotation to 4.8° external rotation). Bottlang et al. (2000) reported that the DFA intersection has the smallest distribution near the medial trochlea, located 2.0 ± 0.6 mm away from the longitudinal axis of the humerus in the frontal plane. Goto et al. (2004) reported that the DFA intersection distribution tended to be scattered on the lateral trochlea than on the medial trochlea. Our study quantified the MFA intersection located on the medial trochlea (0.3 ± 0.3 mm anterior and 0.2 ± 0.4 mm distal) and the lateral trochlea (0.8 ± 1.3 mm anterior and −0.8 ± 1.0 mm distal), which showed a similar pattern that the distribution was more scattered on the lateral side and more concentrated on the medial side (**Figure 3**). The previous study has shown that the MCL provided a primary stabilizer to resist valgus stress and constrained the internal rotation of the forearm at the elbow (Labott et al., 2018). These results may explain the constrained function of the MCL on the medial side of the elbow.

Accurately aligning the implant or external fixation with the elbow is still a challenge for surgeons. Although the TCA is easy to recognize through the humeral trochlear feature, there is still a high alignment error. According to Wiggers et al. (2014), the mean errors of identifying the TCA were 8° of the mean rotation and 2 mm of the mean translation with a large inter-observer variability. The humeral stem loading will increase after humeral component mal-alignment, according to an *in vitro* study (Brownhill et al., 2012). For extra fixation mal-alignment conditions, increasing stresses might be transferred to the fixator pins and the pin–bone interface. They were potential factors that lead to clinical issues of pin loosening, pin breaking, or persistent instability (Stavlas et al., 2007). A more accurate alignment can be obtained through the computer navigation technology. McDonald et al. (2010) improved the implant alignment errors to below 2° and 2 mm in total elbow arthroplasty, according to the reference of TCA by applying the image-based navigation system. However, the MFA could represent the elbow flexion better than the TCA. An accurate alignment of TCA could still cause abnormal stress at the implant–bone interface during flexion. According to our result, the MFAs showed individual positions, which complicated the alignment of the MFA. Surgeons could get an individual and accurate MFA alignment by combining the MFA calculation algorithm and computer navigation technology (Song et al., 2018).

Previous studies have reported that the DFA pathway is a roller configuration during elbow flexion (Bottlang et al., 2000; Goto et al., 2004). Those studies using electromagnetic tracking and passive or simulative active cadaveric elbow might reproduce high repeatability of regular movement, which leads to a regular pattern of the axis. The only study reported by Ericson et al. (2003) revealed an irregular DFA pattern during *in vivo* elbow flexion, which was similar to our finding. The variation in the subjects' muscle activity, joint laxity, and geometry may influence the movement that results in an individual pattern of DFA and differ from those *in vitro* studies. It has been proven that the DFA movement pattern would be affected by various factors such as ligament, forearm position, or muscle force (Duck et al., 2003a; Duck et al., 2003b). Duck et al. (2003a) reported that a division of an elbow ligament led to the deviation of DFA displacement and active movement of the elbow by simulating the muscle force provided more stability of the axis than passive motion. Duck et al. (2003b) also reported that the mean DFA was more externally rotated by 1° with the forearm held supinated rather than pronated. These results may suggest the movement pattern of DFA may reflect the biomechanical condition of the elbow.

Geometry variation, as one of the biomechanical factors, should be considered in the TEA implant design and treatment of distal humerus fracture (Shiba et al., 1988; Desai et al., 2014; Lapner et al., 2014). Few studies had analyzed the distal humerus morphologic sizes based on CT/MRI models or cadavers (Desai et al., 2014; Giannicola et al., 2017). Desai et al. (2014) showed that the mean MTH and LTD were 29.9 and 21.6 mm, which are both significantly larger than the TH's 17.8 mm. Our study revealed that the distal humeral articular surface had a concave barrel-shaped trochlea with a circular concavity and showed similar sizes of the trochlea with MTH, LTH, and TH which were 21.4, 19.0, and 15.2 mm, respectively. A new kind of an implant that followed this relationship was proved to have significantly better ulnohumeral contact (Lapner et al., 2014; Willing et al., 2014). It might reduce the contact pressure and increase survival time. However, Kamineni et al. (2005) suggested that the implant design, which does not precisely match the elbow, does not significantly affect the elbow function. Thus, the information about the geometry and the function of the elbow requires further investigation.

Some other research had evaluated the effects of the anatomical variation on the biomechanical changes of the joint. Lenoir et al. (2015b) revealed that the anterior angulation of the humerus led to a humeral component lateral offset, which was associated with pain intensity. Some studies revealed that the articular geometry changes reflected the knee kinematics and the moment arm (Bull et al., 2008; Gray et al., 2021). Our study showed a strong correlation between humeral trochlear morphological features and the position of the DFA in the different phases of flexion. 1) At the early stage of flexion, our study found the shape of the medial trochlear, which means that MTH and MTD were correlated with the DFA range from full extension to 30° flexion. Goto et al. (2004) reported that the contact area of the humeroulnar joint was mainly concentrated on the medial trochlea during early flexion. When the height or depth of the medial trochlea increases, it may cause a change in the joint contact pattern, which might explain the range of the DFA change at the early flexion phase. 2) During the phase of flexion, from 30° to 90° of flexion, the LTH was considered an important feature that would affect the position of the average DFA in the transverse or coronal planes. Giannicola et al. (2016) found that there were significant individual differences in the trochlear notch angle. The increasing size of the lateral side of the trochlea would directly decrease the angle of the trochlear notch, thereby causing the inherent position of the humeroulnar joint to change, leading to changes in the DFA position. 3) During the phase of flexion from 90° to the maximum flexion angle, the TW and the TWP were the essential factors that would affect the range of the DFA. 4) Our study also found that TH or TD did not correlate with the DFA position or range at all phases of flexion. According to the research by Lapner et al. (2014), when the anatomical shaping humeral prosthesis was applied to the specimen, a significant edge wearing was visited from the humeral spool on the proximal ulna surface after simulation testing. At the same time, the trochlear groove did not show noticeable wearing on the ulna. It was also evident that the feature of the trochlear groove was not as essential as the size of the medial or lateral trochlea. Therefore, this information implies that doctors or engineers when repairing the articular surface of the humerus or designing the distal humerus prosthesis, should pay more attention as the medial and lateral sizes of the trochlea were important characteristic factors.

The present study should be interpreted in light of its potential limitations. First, we only recruited 10 subjects, so it was impossible to compare the effects of gender, age, and other factors on the rotation axis of the elbow joint. The result of the *post hoc* power analysis (0.97, which is higher than 0.8) proved that the sample size was sufficient to reflect statistical differences. Second, all the subjects were healthy and could not evaluate the relationship between the shape of the trochlea and the DFA after the elbow joint's repair. Further studies of cadaveric specimens might be used to verify our findings.

CONCLUSION

In summary, the current study investigated the relationship between the *in vivo* elbow dynamic flexion axis location and the distal humeral trochlear geometry. The inclination of MFA was found to be 3.1° varus and 1.3° external rotation to the TCA. Significant inter-individual differences in the pattern of the dynamic *in vivo* DFA were observed in our study. The lateral and medial sizes of the trochlea were significantly correlated with the position and range of the DFA, which indicated that they were the key parameters that might affect the elbow joint flexion function. When recovering complex distal humeral fractures or considering the TEA implant design, surgeons should pay more attention to the lateral and medial trochlear geometry.

DATA AVAILABILITY STATEMENT

DZ and XH made substantial contributions to the conception and design, acquisition and analysis, and interpretation of the data, were involved in drafting the article, and gave final approval of the version to be published. K-NA and KD each partially helped in the article revision, and all gave final approval of the version to be published. XY provided some suggestions and helped in article revise during article review time. WG and T-YT made contributions to the conception and design, were involved in revising it critically for important intellectual content, and gave final approval of the version to be published. All authors contributed to the article and approved the submitted version.

ETHICS STATEMENT

The studies involving human participants were reviewed and approved by Shanghai Ninth People's Hospital: SH9H-2019-T5-2. The patients/participants provided their written informed consent to participate in this study.

AUTHOR CONTRIBUTIONS

DZ and XH made substantial contributions to the conception and design, acquisition and analysis, and interpretation of the data, were involved in drafting the manuscript, and gave final approval of the version to be published. K-NA and KD each partially helped in the manuscript revision, and all gave final approval of the version to be published. WG and T-YT made contributions to the conception and design, were involved in revising it critically for important intellectual content, and gave final approval of the version to be published. All authors contributed to the manuscript and approved the submitted version.

FUNDING

This work was supported by National Key R&D Program of China (2019YFC0120600), the National Natural Science Foundation of China (31972924), Shanghai Jiao Tong University (YG2021QN68, ZH2018QNA06), and Shanghai Institute of Rehabilitation with Integrated Western and Chinese Traditional Medicine (YJS-099-1), the Clinical Science and Technology Innovation Project of Shanghai Hospital Development Center (SHDC12019X24).

REFERENCES

Bottlang, M., Madey, S. M., Steyers, C. M., Marsh, J. L., and Brown, T. D. (2000). Assessment of Elbow Joint Kinematics in Passive Motion by Electromagnetic Motion Tracking. *J. Orthop. Res.* 18 (2), 195–202. doi:10.1002/jor.1100180206

Brownhill, J. R., Furukawa, K., Faber, K. J., Johnson, J. A., and King, G. J. W. (2006). Surgeon Accuracy in the Selection of the Flexion-Extension axis of the Elbow: an *In Vitro* Study. *J. Shoulder Elb. Surg.* 15 (4), 451–456. doi:10.1016/j.jse.2005.09.011

Brownhill, J. R., King, G. J. W., and Johnson, J. A. (2007). Morphologic Analysis of the Distal Humerus with Special Interest in Elbow Implant Sizing and Alignment. *J. Shoulder Elb. Surg.* 16 (3 Suppl. l), S126–S132. doi:10.1016/j.jse.2006.01.018

Brownhill, J. R., Pollock, J. W., Ferreira, L. M., Johnson, J. A., and King, G. J. W. (2012). The Effect of Implant Malalignment on Joint Loading in Total Elbow Arthroplasty: an *In Vitro* Study. *J. Shoulder Elb. Surg.* 21 (8), 1032–1038. doi:10.1016/j.jse.2011.05.024

Bull, A. M. J., Kessler, O., Alam, M., and Amis, A. A. (2008). Changes in Knee Kinematics Reflect the Articular Geometry after Arthroplasty. *Clin. Orthop. Relat. Res.* 466 (10), 2491–2499. doi:10.1007/s11999-008-0440-z

Desai, S. J., Deluce, S., Johnson, J. A., Ferreira, L. M., Leclerc, A. E., Athwal, G. S., et al. (2014). An Anthropometric Study of the Distal Humerus. *J. Shoulder Elb. Surg.* 23 (4), 463–469. doi:10.1016/j.jse.2013.11.026

Wiggers, J. K., Dobbe, J. G. G., Streekstra, G. J., Schep, N. W. L., Snijders, R. M., and den Hartog, D. (2017). Accuracy in Identifying the Elbow Rotation axis on Simulated Fluoroscopic Images Using a New Anatomical Landmark. *Strateg. Trauma Limb Reconstr.* 12 (3), 133–139. doi:10.1007/s11751-017-0289-3

Dos Santos, A., Creze, M., Begin, M., Laemmel, E., Assabah, B., and Soubeyrand, M. (2017). Cadaveric Assessment of a 3D-Printed Aiming Device for Implantation of a Hinged Elbow External Fixator. *Eur. J. Orthop. Surg. Traumatol.* 27 (3), 405–414. doi:10.1007/s00590-016-1889-1

Duck, T. R., Dunning, C. E., Armstrong, A. D., Johnson, J. A., and King, G. J. W. (2003a). Application of Screw Displacement Axes to Quantify Elbow Instability. *Clin. Biomech.* 18 (4), 303–310. doi:10.1016/s0268-0033(03)00021-4

Duck, T. R., Dunning, C. E., King, G. J. W., and Johnson, J. A. (2003b). Variability and Repeatability of the Flexion axis at the Ulnohumeral Joint. *J. Orthop. Res.* 21 (3), 399–404. doi:10.1016/s0736-0266(02)00198-5

Ehrig, R. M., and Heller, M. O. (2019). On Intrinsic Equivalences of the Finite Helical axis, the Instantaneous Helical axis, and the SARA Approach. A Mathematical Perspective. *J. Biomechanics* 84, 4–10. doi:10.1016/j.jbiomech.2018.12.034

Ehrig, R. M., Taylor, W. R., Duda, G. N., and Heller, M. O. (2007). A Survey of Formal Methods for Determining Functional Joint Axes. *J. Biomechanics* 40 (10), 2150–2157. doi:10.1016/j.jbiomech.2006.10.026

Ericson, A., Arndt, A., Stark, A., Wretenberg, P., and Lundberg, A. (2003). Variation in the Position and Orientation of the Elbow Flexion axis. *J. Bone Jt. Surg. Br. volumeBritish volume* 85-B (4), 538–544. doi:10.1302/0301-620x.85b4.13925

Ericson, A., Stark, A., and Arndt, A. (2008). Variation in the Position of the Elbow Flexion axis after Total Joint Replacement with Three Different Prostheses. *J. Shoulder Elb. Surg.* 17 (5), 760–767. doi:10.1016/j.jse.2008.03.003

Geurts, E. J., Viveen, J., van Riet, R. P., Kodde, I. F., and Eygendaal, D. (2019). Outcomes after Revision Total Elbow Arthroplasty: a Systematic Review. *J. Shoulder Elb. Surg.* 28 (2), 381–386. doi:10.1016/j.jse.2018.08.024

Giannicola, G., Scacchi, M., Sedati, P., and Gumina, S. (2016). Anatomical Variations of the Trochlear Notch Angle: MRI Analysis of 78 Elbows. *Musculoskelet. Surg.* 100 (Suppl. 1), 89–95. doi:10.1007/s12306-016-0407-2

Giannicola, G., Spinello, P., Scacchi, M., and Gumina, S. (2017). Cartilage Thickness of Distal Humerus and its Relationships with Bone Dimensions: Magnetic Resonance Imaging Bilateral Study in Healthy Elbows. *J. Shoulder Elb. Surg.* 26 (5), e128–e136. doi:10.1016/j.jse.2016.10.012

Gordon, B. J., and Dapena, J. (2013). A Method to Determine the Orientation of the Upper Arm about its Longitudinal axis during Dynamic Motions. *J. Biomechanics* 46 (1), 97–101. doi:10.1016/j.jbiomech.2012.10.011

Goto, A., Moritomo, H., Murase, T., Oka, K., Sugamoto, K., Arimura, T., et al. (2004). *In Vivo* elbow Biomechanical Analysis during Flexion: Three-Dimensional Motion Analysis Using Magnetic Resonance Imaging. *J. Shoulder Elb. Surg.* 13 (4), 441–447. doi:10.1016/j.jse.2004.01.022

Gray, H. A., Guan, S., Thomeer, L. T., and Pandy, M. G. (2021). Moment Arm of the Knee-Extensor Mechanism Measured *In Vivo* across a Range of Daily Activities. *J. Biomechanics* 123, 110484. doi:10.1016/j.jbiomech.2021.110484

Hua, K., Ji, S., Li, T., Chen, C., Zha, Y., Gong, M., et al. (2020). Correlation between Modified Trochleocapitellar Index and Post-traumatic Elbow Stiffness in Type C2-3 Distal Humeral Fractures Among Adults. *J. Shoulder Elb. Surg.* 29 (9), 1876–1883. doi:10.1016/j.jse.2020.02.016

Kamineni, S., O'Driscoll, S. W., Urban, M., Garg, A., Berglund, L. J., Morrey, B. F., et al. (2005). Intrinsic Constraint of Unlinked Total Elbow Replacements-The Ulnotrochlear Joint. *J. Bone & Jt. Surg.* 87 (9), 2019–2027. doi:10.2106/jbjs.C.00983

Krukhaug, Y., Hallan, G., Dybvik, E., Lie, S. A., and Furnes, O. N. (2018). A Survivorship Study of 838 Total Elbow Replacements: a Report from the Norwegian Arthroplasty Register 1994-2016. *J. Shoulder Elb. Surg.* 27 (2), 260–269. doi:10.1016/j.jse.2017.10.018

Labott, J. R., Aibinder, W. R., Dines, J. S., and Camp, C. L. (2018). Understanding the Medial Ulnar Collateral Ligament of the Elbow: Review of Native Ligament Anatomy and Function. *Wjo* 9 (6), 78–84. doi:10.5312/wjo.v9.i6.78

Lapner, M., Willing, R., Johnson, J. A., and King, G. J. W. (2014). The Effect of Distal Humeral Hemiarthroplasty on Articular Contact of the Elbow. *Clin. Biomech.* 29 (5), 537–544. doi:10.1016/j.clinbiomech.2014.03.010

Lenoir, H., Chammas, M., Micallef, J. P., Lazerges, C., Waitzenegger, T., and Coulet, B. (2015a). The Effect of the Anatomy of the Distal Humerus and Proximal Ulna on the Positioning of the Components in Total Elbow Arthroplasty. *Bone & Jt. J.* 97-b (11), 1539–1545. doi:10.1302/0301-620x.97b11.36071

Lenoir, H., Micallef, J. P., Djerbi, I., Waitzenegger, T., Lazerges, C., Chammas, M., et al. (2015b). Total Elbow Arthroplasty: Influence of Implant Positioning on Functional Outcomes. *Orthop. Traumatology Surg. Res.* 101 (6), 721–727. doi:10.1016/j.otsr.2015.07.008

Mansat, P., Bonnevialle, N., Rongières, M., Mansat, M., and Bonnevialle, P. (2013a). Results with a Minimum of 10 Years Follow-Up of the Coonrad/Morrey Total Elbow Arthroplasty. *Orthop. Traumatology Surg. Res.* 99 (6), S337–S343. doi:10.1016/j.otsr.2013.07.002

Mansat, P., Nouaille Degorce, H., Bonnevialle, N., Demezon, H., and Fabre, T. (2013b). Total Elbow Arthroplasty for Acute Distal Humeral Fractures in Patients over 65 Years Old - Results of a Multicenter Study in 87 Patients. *Orthop. Traumatology Surg. Res.* 99 (7), 779–784. doi:10.1016/j.otsr.2013.08.003

McDonald, C. P., Johnson, J. A., Peters, T. M., and King, G. J. W. (2010). Image-based Navigation Improves the Positioning of the Humeral Component in Total Elbow Arthroplasty. *J. Shoulder Elb. Surg.* 19 (4), 533–543. doi:10.1016/j.jse.2009.10.010

McDonald, C. P., Moutzouros, V., and Bey, M. J. (2012). Measuring Dynamic *In-Vivo* Elbow Kinematics: Description of Technique and Estimation of Accuracy. *J. Biomech. Eng.* 134 (12), 124502. doi:10.1115/1.4007951

Muriuki, M. G., Mohagheh-Motlagh, A., Smolinski, P. J., and Miller, M. C. (2012). Elbow Helical Axes of Motion Are Not the Same in Physiologic and Kinetic Joint Simulators. *J. Biomechanics* 45 (13), 2289–2292. doi:10.1016/j.jbiomech.2012.06.021

Pham, T. T., Delclaux, S., Huguet, S., Wargny, M., Bonnevialle, N., and Mansat, P. (2018). Coonrad-Morrey Total Elbow Arthroplasty for Patients with Rheumatoid Arthritis: 54 Prostheses Reviewed at 7 years' Average Follow-Up (Maximum, 16 years). *J. Shoulder Elb. Surg.* 27 (3), 398–403. doi:10.1016/j.jse.2017.11.007

Sanchez-Sotelo, J. (2011). Total Elbow Arthroplasty. *Toorthj* 5, 115–123. doi:10.2174/1874325001105010115

Schoch, B., Wong, J., Abboud, J., Lazarus, M., Getz, C., and Ramsey, M. (2017). Results of Total Elbow Arthroplasty in Patients Less Than 50 Years Old. *J. Hand Surg.* 42 (10), 797–802. doi:10.1016/j.jhsa.2017.06.101

Shiba, R., Sorbie, C., Siu, D. W., Bryant, J. T., Cooke, T. D. V., and Wevers, H. W. (1988). Geometry of the Humeroulnar Joint. *J. Orthop. Res.* 6 (6), 897–906. doi:10.1002/jor.1100060614

Song, J., Ding, H., Han, W., Wang, J., and Wang, G. (2018). An X-ray-free Method to Accurately Identify the Elbow Flexion-Extension axis for the Placement of a Hinged External Fixator. *Int. J. CARS* 13 (3), 375–387. doi:10.1007/s11548-017-1680-8

Stavlas, P., Jensen, S. L., and Søjbjerg, J. O. (2007). Kinematics of the Ligamentous Unstable Elbow Joint after Application of a Hinged External Fixation Device: a Cadaveric Study. *J. Shoulder Elb. Surg.* 16 (4), 491–496. doi:10.1016/j.jse.2006.07.012

Stokdijk, M., Meskers, C. G. M., Veeger, H. E. J., de Boer, Y. A., and Rozing, P. M. (1999). Determination of the Optimal Elbow axis for Evaluation of Placement of Prostheses. *Clin. Biomech.* 14 (3), 177–184. doi:10.1016/s0268-0033(98)00057-6

Wiggers, J. K., Streekstra, G. J., Kloen, P., Mader, K., Goslings, J. C., and Schep, N. W. L. (2014). Surgical Accuracy in Identifying the Elbow Rotation axis on Fluoroscopic Images. *J. Hand Surg.* 39 (6), 1141–1145. doi:10.1016/j.jhsa.2014.03.008

Willing, R., Lapner, M., King, G. J. W., and Johnson, J. A. (2014). *In Vitro* assessment of the Contact Mechanics of Reverse-Engineered Distal Humeral Hemiarthroplasty Prostheses. *Clin. Biomech.* 29 (9), 990–996. doi:10.1016/j.clinbiomech.2014.08.015

Woltring, H. J., Huiskes, R., de Lange, A., and Veldpaus, F. E. (1985). Finite Centroid and Helical axis Estimation from Noisy Landmark Measurements in the Study of Human Joint Kinematics. *J. Biomechanics* 18 (5), 379–389. doi:10.1016/0021-9290(85)90293-3

Wu, G., van der Helm, F. C. T., Veeger, H. E. J., Makhsous, M., Van Roy, P., Anglin, C., et al. (2005). ISB Recommendation on Definitions of Joint Coordinate Systems of Various Joints for the Reporting of Human Joint Motion-Part II: Shoulder, Elbow, Wrist and Hand. *J. Biomechanics* 38 (5), 981–992. doi:10.1016/j.jbiomech.2004.05.042

Conflict of Interest: The authors declare that the research was conducted in the absence of any commercial or financial relationships that could be construed as a potential conflict of interest.

The reviewer DJ declared a shared parent affiliation, with several of the authors DZ, KD, WG, and TYT to the handling editor at the time of the review.

frontiers | Frontiers in Bioengineering and Biotechnology

ORIGINAL RESEARCH
published: 24 June 2022
doi: 10.3389/fbioe.2022.881979

Biomechanical Effects of a Novel Anatomic Titanium Mesh Cage for Single-Level Anterior Cervical Corpectomy and Fusion: A Finite Element Analysis

Ke-rui Zhang[1†], Yi Yang[1†], Li-tai Ma[1], Yue Qiu[2], Bei-yu Wang[1], Chen Ding[1], Yang Meng[1], Xin Rong[1], Ying Hong[3] and Hao Liu[1]*

[1]Department of Orthopedic West China Hospital, Sichuan University, Chengdu, China, [2]Department of Applied Mechanics, Sichuan University, Chengdu, China, [3]Department of Operation Room, West China Hospital, Sichuan University, Chengdu, China

Edited by:
Bin Wang,
Chongqing Medical University, China

Reviewed by:
Xiaogang Wu,
Taiyuan University of Technology, China
Luigi La Barbera,
Politecnico di Milano, Italy

****Correspondence:***
Hao Liu
liuhao6304@126.com

†These authors have contributed equally to this work

Specialty section:
This article was submitted to Biomechanics, a section of the journal Frontiers in Bioengineering and Biotechnology

Received: *23 February 2022*
Accepted: *05 May 2022*
Published: *24 June 2022*

Citation:
Zhang K-r, Yang Y, Ma L-t, Qiu Y, Wang B-y, Ding C, Meng Y, Rong X, Hong Y and Liu H (2022) Biomechanical Effects of a Novel Anatomic Titanium Mesh Cage for Single-Level Anterior Cervical Corpectomy and Fusion: A Finite Element Analysis. Front. Bioeng. Biotechnol. 10:881979. doi: 10.3389/fbioe.2022.881979

Background: The traditional titanium mesh cage (TTMC) has become common as a classical instrument for Anterior Cervical Corpectomy and Fusion (ACCF), but a series of complications such as cage subsidence, adjacent segment degeneration (ASD), and implant-related complications by using the TTMC have often been reported in the previous literature. The aim of this study was to assess whether a novel anatomic titanium mesh cage (NTMC) could improve the biomechanical condition after surgery.

Methods: The NTMC model consists of two spacers located on both sides of the TTMC which match the anatomic structure between the endplates by measuring patient preoperative cervical computed tomography (CT) data. The ranges of motion (ROMs) of the surgical segments and the stress peaks in the C6 superior endplates, titanium mesh cage (TMC), screw–bone interface, anterior titanium plate, and adjacent intervertebral disc were compared.

Results: Compared with the TTMC, the NTMC reduced the surgical segmental ROMs by 89.4% postoperatively. The C6 superior endplate stress peaks were higher in the TTMC (4.473–23.890 MPa), followed by the NTMC (1.923–5.035 MPa). The stress peaks on the TMC were higher in the TTMC (47.896–349.525 MPa), and the stress peaks on the TMC were lower in the NTMC (17.907–92.799 MPa). TTMC induced higher stress peaks in the screw–bone interface (40.0–153.2 MPa), followed by the NTMC (14.8–67.8 MPa). About the stress peaks on the anterior titanium plate, the stress of TTMC is from 16.499 to 58.432 MPa, and that of the NTMC is from 12.456 to 34.607 MPa. Moreover, the TTMC induced higher stress peaks in the C3/4 and C6/7 intervertebral disc (0.201–6.691 MPa and 0.248–4.735 MPa, respectively), followed by the NTMC (0.227–3.690 MPa and 0.174–3.521 MPa, respectively).

Abbreviations: ACCF, anterior cervical corpectomy and fusion; ASD, adjacent segment degeneration; CT, computed tomography; FE, finite element; IDP, intradiscal pressure; NTMC, novel anatomic titanium mesh cage; ROM, range of motion; TTMC, traditional titanium mesh cage; TMC, titanium mesh cage.

Conclusion: First, the application of the NTMC can effectively decrease the risks of TMC subsidence after surgery. Second, in the NTMC, the stresses at the anterior screw-plate, bone–screw, and TMC interface are much less than in the TTMC, which decreased the risks of instrument-related complications after surgery. Finally, increases in IDP at adjacent levels are associated with the internal stresses of adjacent discs which may lead to ASD; therefore, the NTMC can effectively decrease the risks of ASD.

Keywords: novel anatomic titanium mesh cage, traditional titanium mesh cage, cage subsidence, implant-related complications, anterior cervical corpectomy and fusion, adjacent segment degeneration, finite element analysis

INTRODUCTION

Anterior cervical corpectomy and fusion (ACCF) is an effective treatment method for various cervical disorders, including cervical spondylosis myelopathy, ossified posterior longitudinal ligaments (OPLL), trauma, tumors, and rheumatoid arthritis.(Ji, Yu, Yan, Wang, Hou, Hou and Cai 2020, Missori, Domenicucci and Marruzzo 2018; Zeng, Duan, Yang, Wang, Hong, Lou, Ning and Liu 2018). ACCF has been widely accepted with satisfactory postoperative prognosis because of removing the direct decompression of the spinal cord and offering immediate stabilization of the surgical segments (Fengbin, Jinhao, Xinyuan, Xinwei, Yu and Deyu 2013; Yang, Chen, Liu, Song, Kong, Zeng, Xue and Ren 2013).

The use of the traditional titanium mesh cage (TTMC) has become the main method for cervical reconstruction during ACCF surgery (Fehlings, Smith, Kopjar, Arnold, Yoon, Vaccaro, Brodke, Janssen, Chapman, Sasso, Woodard, Banco, Massicotte, Dekutoski, Gokaslan, Bono and Shaffrey 2012). Although this method maintains immediate anterior column stability with good biocompatibility after surgery and has a relatively high bone fusion rate, the incidence of postoperative titanium mesh cage (TMC) subsidence reported in the previous literature is as high as 90% (Fengbin, Jinhao, Xinyuan, Xinwei, Yu and Deyu 2013; Yang, Chen, Liu, Song, Kong, Zeng, Xue and Ren 2013). TMC subsidence may be correlated with poor clinical efficacy or poor neurological recovery and can even lead to symptom recurrence, deterioration of nerve function, failure of internal fixation, and revision surgery (Mo, Li, Jia, Yang, Wong and Fan 2017; Wu, Meng, Wang, Rong, Hong, Ding, Chen and Liu 2019). Moreover, an instrument-related complication is a more serious type of complication, which includes plate fracture, broken screw, or TMC dislodgement, and may lead to a more serious set of consequences. Although there are many risk factors related to TMC subsidence and instrument-related complications, the structural improvement of the TMC is one of the most important methods to solve the problem in clinical practice.

For ACCF using the TTMC, the contact area between the TMC and endplate is limited. The upper and lower endplates are all characterized by irregular anatomical shapes. After TMC implantation, contact with the endplate through the edge of the titanium mesh and the match is poor. The contact area between the TMC and endplate is small, which is point-to-point contact. Moreover, this kind of point contact causes relatively concentrated stress, which easily leads to TMC subsidence and instrument-related complications after surgery. Therefore, it is of great importance to find a novel anatomic titanium mesh cage (NTMC) consisting of two spacers located on both sides of the TMC which match the anatomic structure between the endplates and change point-to-point contact into face-to-face contact, which can avoid uneven stress distribution and decrease the incidence of postoperative TMC subsidence and instrument-related complications.

For this purpose, an NTMC was designed, whose ends possessed enlarged spacers which match the anatomic shape between the endplates by measuring patient preoperative cervical CT data. The mechanical properties were analyzed by using a three-dimensional finite element (FE) analysis to analyze whether this NTMC could effectively improve the biomechanical performance in ACCF.

MATERIALS AND METHODS

Finite Element Model of the Intact Lower Cervical Spine

An intact C2-7 FE model was constructed with the following steps. Computed tomography (CT) images (SOMATOM Definition AS+, Siemens, Germany) of the C2-7 cervical spine were obtained from a young healthy volunteer (37 years of age; height, 172 cm; weight, 65 kg) and were then imported into Mimics 17.01 (Materialise Corporation, Belgium) to reconstruct the surface model of each vertebra. Solid models of the cortical shell, cancellous bone, and intervertebral disk were constructed in Geomagic Studio 2015 (Raindrop Geomagio Inc. United States). Meshes of the bones, intervertebral discs, and ligaments were constructed using Hypermesh 14.0 (Atair Corporation. United States) and imported into Abaqus 6.14 (Dassault System. France) for material property definitions, model assembly, and FE analysis (Liu, Lu, Wang, Sun, Li and He 2019).

Figure 1 shows the FE model of the intact C2-7 cervical spine, which consisted of six vertebrae, five intervertebral disks, the anterior longitudinal ligament, the posterior longitudinal ligament, the capsular ligament, the interspinous ligament, the supraspinous ligament, and the ligamentum flavum. A 0.5-mm-thick shell consisting of cortical bone (Denoziere and Ku 2006) and the nucleus pulposus was modeled as an incompressible inviscid fluid, and the intervertebral disc was divided into the

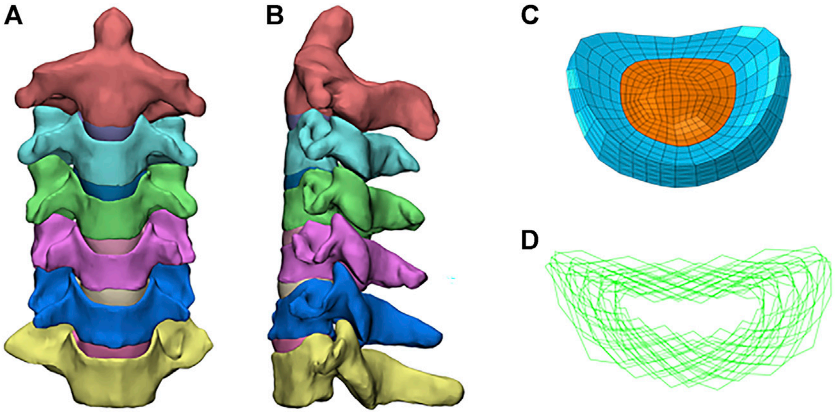

FIGURE 1 | Finite element model of the intact C2–C7 cervical spine: **(A)** front view; **(B)** sagittal view; **(C)** annulus fiber; **(D)** intact intervertebral disk.

TABLE 1 | Material properties assigned to the finite element model.

component	Element type	Young's modulus (MPa)	Poisson ratio	Cross-sectional area (mm^2)
Cortical bone	C3D4	12,000	0.29	
Cancellous bone	C3D4	450	0.29	
Nucleus pulpous	C3D8H	1	0.49	
Anterior longitudinal	T3D2	30	0.3	6.1
Posterior longitudinal	T3D2	20	0.3	5.4
Capsular	T3D2	20	0.3	46.6
Ligamentum flavum	T3D2	1.5	0.3	5.0
Interspinous	T3D2	1.5	0.3	13.1
Supraspinous ligament	T3D2	1.5	0.3	5.0
Facet joint cartilage	C3D4	10.4	0.4	
Titanium alloy	C3D4	110,000	0.3	
Screws	C3D4	110,000	0.3	
Cages	C3D4	110,000	0.3	
Spacers	C3D4	110,000	0.3	
Endplates	C3D4	5.6	0.3	
Annulus fibers	T3D2	110	0.3	

PEEK, polyetheretherketone.

annulus fibrosus and nucleus pulposus, with a volume ratio of 7:3 (Kallemeyn, Gandhi, Kode, Shivanna, Smucker and Grosland 2010). The annulus fibrosus was modeled as an annulus ground substance embedded with annulus fibers. Annulus fibers surrounded the ground substance with an inclination to the transverse plane between 15° and 45° (Mo, Li, Jia, Yang, Wong and Fan 2017). Hypoelastic material properties were assigned to the ligament according to the stress–strain curves that were published previously (Kallemeyn, Gandhi, Kode, Shivanna, Smucker and Grosland 2010). A convergence analysis was performed to ensure that the maximum changes in the strain energy were <5% (Ayturk and Puttlitz 2011; Jones and Wilcox 2008). The element types and material properties used in the FE model are shown in **Table 1**, which is based on previous publications (Kallemeyn, Gandhi, Kode, Shivanna, Smucker and Grosland 2010; Wu, Meng, Wang, Rong, Hong, Ding, Chen and Liu 2019).

FE Model of the ACCF Procedures

Figures 2A,B show the FE models of ACCF at C4-6. The corpectomy of C5 was simulated by removing the C4-5 and C5-6 intervertebral disks; two-thirds of the vertebral body in C5; and the corresponding anterior and posterior longitudinal ligaments (Liu, Lu, Wang, Sun, Li and He 2019). After the corpectomies, a TTMC (Johnson & Johnson, United States) with a 12-mm diameter was trimmed into a suitable length and implanted into the intervertebral space. Both ends of the TTMC were ensured to be in close contact with the corresponding endplates. The contact area in the cage-endplate interface end was 0.27 cm^2. An anterior plate-screw system was placed at C4-6 to further stabilize the surgical segment. The length and width of the anterior titanium plate were 36 and 12 mm, respectively, and the length and diameter of the screws were 12 and 3 mm, respectively (TTMC internal fixation system).

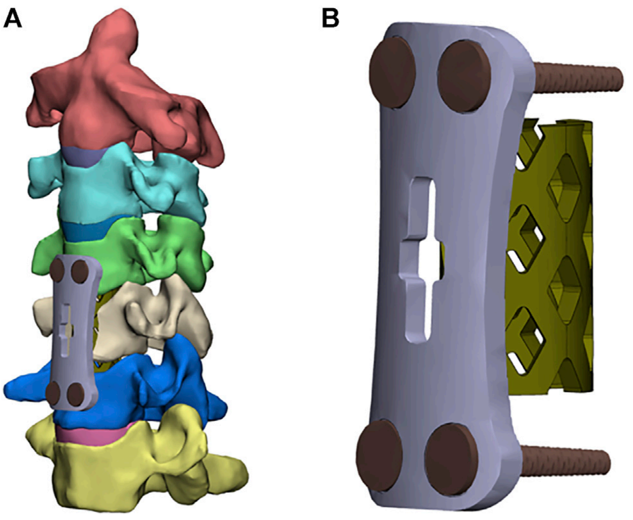

FIGURE 2 | Finite element models of the surgical procedures: **(A)** front view of ACCF using the TTMC; **(B)** the structure of the TTMC.

Figures 3A,B show the FE model of ACCF using the NTMC for interbody fusion. After the corpectomies, an NTMC with a 12-mm diameter was implanted into the space. Both ends of the NTMC were enlarged by adding a spacer to each end, which matches the shapes between the endplates by measuring the patient preoperative CT scan data, and the TMC was fixed to the spacer by the slot structure (**Figure 3C**). Satisfactory matching between the endplate and spacer was achieved using the Boolean calculation to remove the portion that overlapped with the vertebral body. The contact area in the spacer–endplate interface was 3.63 cm^2. For all surgical models, the interfaces at the cage endplate and screw bone were defined as a tied contact condition to simulate a complete fusion status (Zhao, Chen, Liu, Elsamaloty, Liu, Li, Elgafy, Zhang and Wang 2018).

Loading and Boundary Conditions

The FE model of intact C2–C7 segments was fixed at the inferior endplate of C7. Follower loads of 75 N were used to simulate muscle force and head weight. A 1.0-Nm moment and a 75-N follower load were applied to the odontoid of the C2 vertebrae to produce flexion, extension, lateral bending, and axial rotation (Wu, Meng, Liu, Wang, Hong, Rong, Ding and Chen 2019). The surgical segment ranges of motion (ROMs), the stress of the C6 superior endplates, TMC, screw–bone interface, anterior titanium plate, and adjacent intervertebral disc were compared between the constructs of ACCF using the TTMC and ACCF using the NTMC. Based on previous studies and literature data, C4/5 and C5/6 were chosen as the implanted levels because they are the most frequently involved levels in clinical practice (Ouyang, Lu, He, Gao, Cai and Jin 2019).

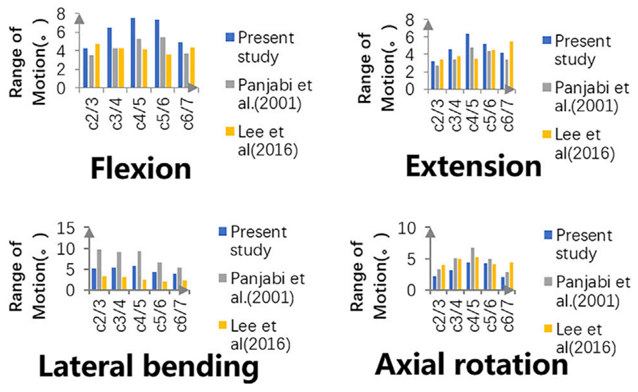

FIGURE 4 | Intersegmental ROMs of the intact model are compared with those of previously published studies, and validity has been proven.

RESULTS

Model Validation

The intersegmental ROMs at C2-3, C3-4, C4-5, C5-6, and C6-7 were 4.29°, 6.49°, 7.45°, 7.35°, and 4.89°, respectively, in flexion; 3.16°, 4.57°, 6.32°, 5.22°, and 4.21°, respectively, in extension; 5.14°, 5.42°, 5.67°, 4.21°, and 3.85°, respectively, in bending; and 2.14°, 3.15°, 4.36°, 3.60°, and 2.08°, respectively, in rotation. As shown in **Figure 4**, the intersegmental ROMs in each motor direction showed good agreement with the outcomes of previous publications, where the consistency can be as high from 61.3 to 95.1% (Panjabi, Crisco, Vasavada, Oda, Cholewicki, Nibu and

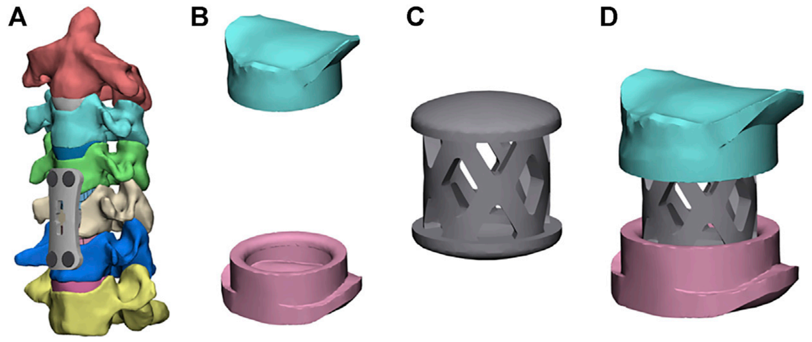

FIGURE 3 | Finite element models of the surgical procedures: **(A)** front view of ACCF using the NTMC, **(B)** the structure of spacers, **(C)** the structure of the TMC, and **(D)** TMC and the spacer are connected by the slot structure.

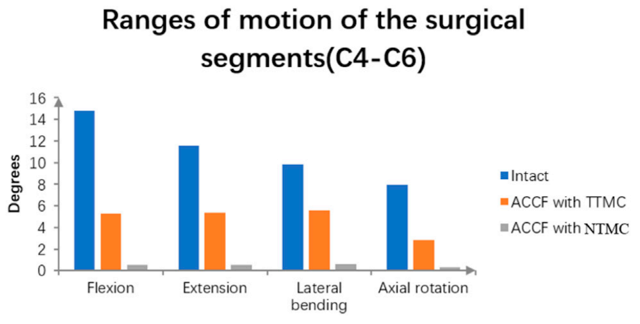

FIGURE 5 | Using the intact model as a reference, comparisons of the ROMs of the surgical segments (C4–C6) between the TTMC and NTMC models has been performed.

Shin 2001; Lee, Park, Kim and Jahng 2016). Moreover, in the study of cadaver specimens *in vitro*, the intersegmental ROMs at C2-3, C3-4, C4-5, C5-6, and C6-7 were 3.90°, 7.05°, 6.02°, 7.93°, and 5.33°, respectively, in flexion; 2.21°, 4.97°, 5.32°, 7.81°, and 5.61°, respectively, in extension; 4.32°, 6.54°, 4.07°, 4.28°, and 2.79°, respectively, in bending; and 2.37°, 3.97°, 5.13°, 6.22°, and 3.63°, respectively, in rotation, where the consistency is up to 98.4% and can prove the validity of the model to a certain extent (Kallemeyn, Gandhi, Kode, Shivanna, Smucker and Grosland 2010).

ROMs of the Surgical Segments

As shown in **Figure 5**, the ROMs of the intact C4-6 model in flexion, extension, bending, and rotation were 14.8°, 11.55°, 9.86°, and 7.96°, respectively. Postoperatively, the surgical segment ROMs of ACCF using a TTMC and ACCF using the NTMC were 5.28° and 0.56°, respectively, in flexion; 5.38° and 0.52°, respectively, in extension; 5.55° and 0.59°, respectively, in bending; and 2.85° and 0.31°, respectively, in rotation. The differences in the surgical segment ROMs between the TTMC and NTMC can be as much as 90.3%, and the differences were significant between the two groups, which is similar to previous literature (La Barbera, Larson, Rawlinson and Aubin 2021).

Cortical Endplate Stresses

Figure 6A shows the maximum stresses in the C6 superior endplates. The endplate stress peaks were higher in the construct of ACCF using a TTMC, wherein the stresses were 4.47, 21.27, 14.35, and 23.89 MPa in flexion, extension, bending, and rotation, respectively. In the same direction of movement, the endplate stress peaks were lower by using the NTMC in ACCF, which reduced to 1.92, 5.04, 3.81, and 3.97 MPa, respectively. The stress distributions in the C6 superior endplates are shown in **Figure 6B**.

Stress at the TMC

The maximum von Mises stresses in the TMC are shown in **Figure 7**. In the ACCF using a TTMC model, the stresses at the TMC interface in flexion, extension, lateral bending, and axial rotation were 47.90, 285.45, 252.04, and 349.53 MPa, respectively. In the ACCF using an NTMC model, the stresses at the TMC interfacial in flexion, extension, lateral bending, and axial rotation were 17.91, 92.80, 34.73, and 59.01 MPa, respectively.

Stress at the Bone–Screw Interface

The maximum von Mises stresses in the C6 screw interface are shown in **Figure 8A**. In the ACCF using a TTMC model, the stresses at the bone–screw interface in flexion, extension, lateral bending, and axial rotation were 40.04, 153.18, 134.83, and 103.57 MPa, respectively. In the ACCF using an NTMC model, the stresses at the bone-screw interface in flexion, extension, lateral bending, and axial rotation were 14.82, 65.49, 28.17, and 63.44 MPa, respectively. The stress cloud map in the C6 screw–bone interfacial stresses between two models is shown in **Figure 8B**.

Fixation Systems Stresses

The maximum von Mises stresses of the fixation systems are shown in **Figure 9**. In the ACCF using a TTMC model, the stresses at the anterior titanium plate in flexion, extension, lateral bending, and axial rotation were 16.51, 16.47, 44.49, and 32.54 MPa, respectively. In the ACCF using an NTMC model, the stresses at the anterior titanium plate in flexion, extension, lateral bending, and axial rotation were 12.48, 15.17, 27.93, and 30.02 MPa, respectively.

Stress on the C3/4 Intervertebral Disc

Intradiscal pressure (IDP) measures at the supra-adjacent (C3/4) segment are presented in **Figure 10**. Compared with the TTMC model, the stress on the upper (C3/4) adjacent intervertebral disc in the NTMC model was lower during flexion, extension, lateral bending, and rotation. In the TTMC model, the maximum von Mises stresses on the C3/4 intervertebral disc were 0.20 MPa during flexion; 4.55 MPa during extension; 4.53 MPa during lateral bending; and 6.96 MPa during rotation. In the NTMC

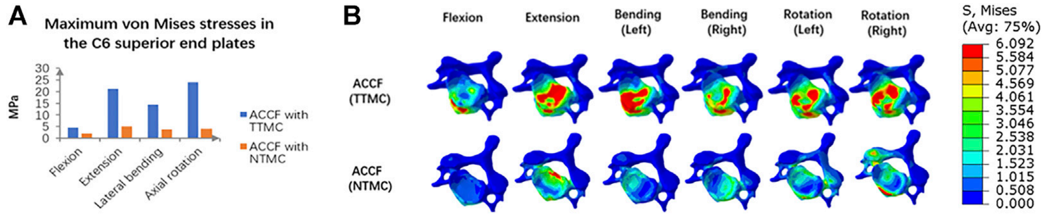

FIGURE 6 | (A) Comparisons of the maximum von Mises stresses in the C6 superior endplate between the TTMC and NTMC models; **(B)** Stress cloud map of the C6 superior endplates between TTMC and NTMC models.

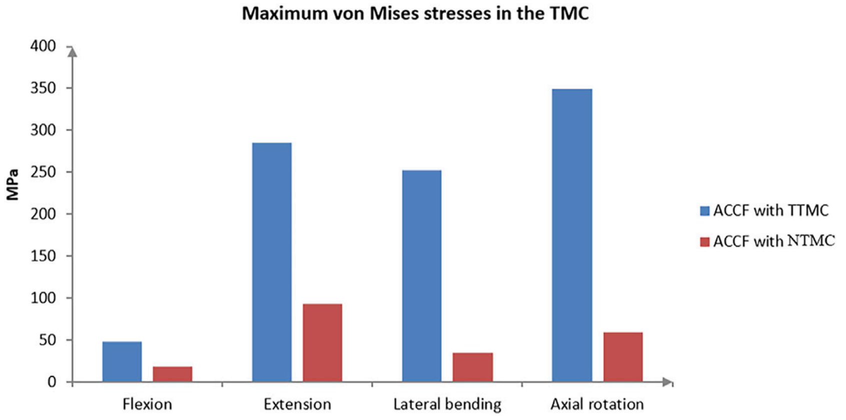

FIGURE 7 | Comparisons of the maximum von Mises stresses in the TMC between TTMC and NTMC models.

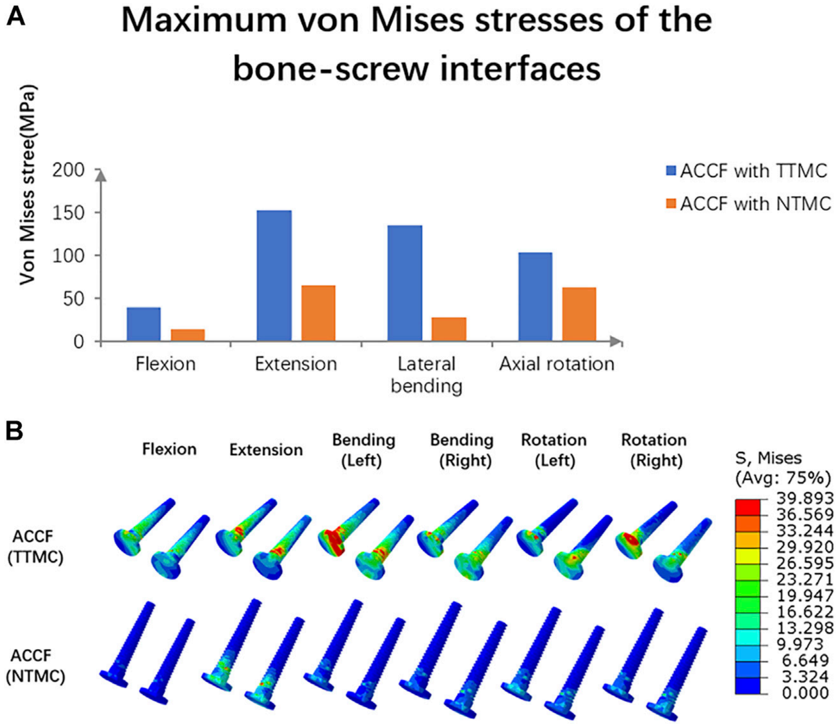

FIGURE 8 | (A) Comparisons of the maximum von Mises stresses in the C6 screw–bone interface between TTMC and NTMC models; **(B)** Stress cloud map of the C6 screw–bone interface between TTMC and NTMC models.

model, the maximum von Mises stresses on the C3/4 intervertebral disc were 0.23 MPa during flexion; 3.69 MPa during extension; 2.87 MPa during lateral bending; and 3.27 MPa during rotation; and in the intact model, the maximum von Mises stresses on the C3/4 intervertebral disc were 0.19 MPa during flexion; 0.32 MPa during extension; 0.37 MPa during lateral bending; and 0.36 MPa during rotation. The stress distributions on the C3/4 intervertebral disc are shown in **Figure 10B**.

Stress on the C6/7 Intervertebral Disc

IDP measures at the infra-adjacent (C6/7) segment are presented in **Figure 11**. In these two models, the NTMC group had lower stress on the intervertebral disc than the TTMC group. In the TTMC group, the maximum von Mises stresses on the C6/7 intervertebral disc were 0.25 MPa during flexion; 4.00 MPa during extension; 4.37 MPa during lateral bending; and 4.74 MPa during rotation. In the NTMC group, the maximum von Mises stresses on the C6/7 intervertebral

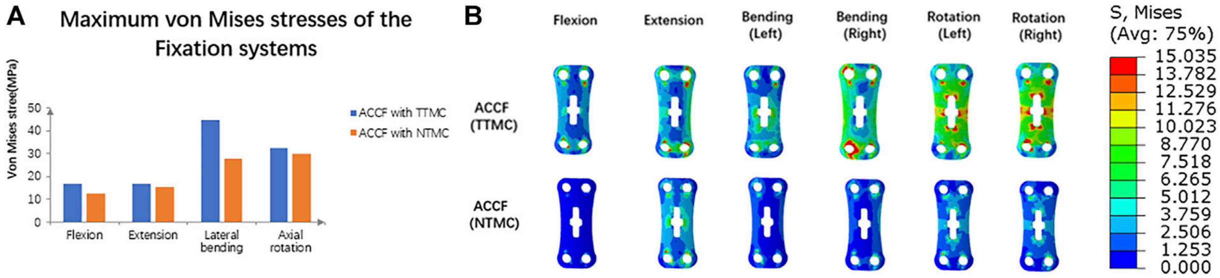

FIGURE 9 | (A) Comparisons of the maximum von Mises stresses of the fixation systems between TTMC and NTMC models; **(B)** Stress cloud map of the anterior titanium plate between TTMC and NTMC models.

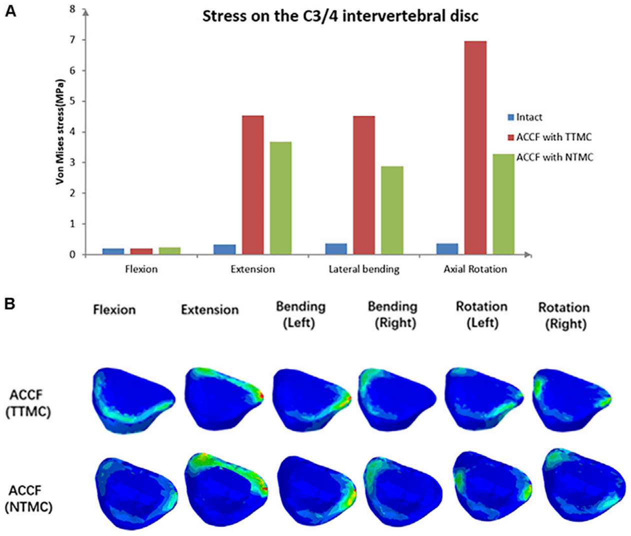

FIGURE 10 | (A) Comparisons of the maximum von Mises stresses in the IDP of the C3/4 segment among the intact model, TTMC model and NTMC model; **(B)** Stress cloud map of IDP of the C3/4 segment between TTMC and NTMC models.

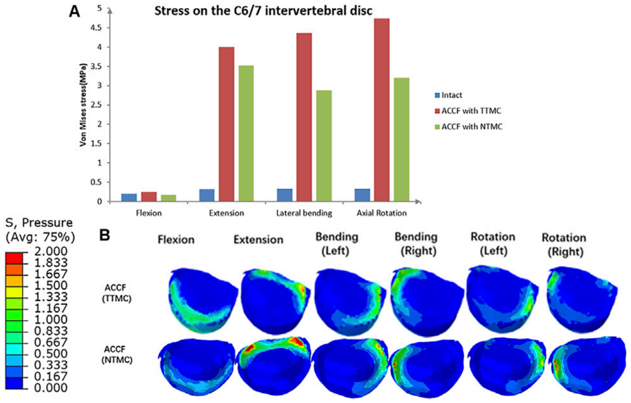

FIGURE 11 | (A) Comparisons of the maximum von Mises stresses in the IDP of the C6/7 segment among the intact model, TTMC model, and NTMC model; **(B)** Stress cloud map of IDP of the C6/7 segment between TTMC and NTMC models.

disc were 0.17 MPa during flexion; 3.52 MPa during extension; 2.88 MPa during lateral bending; and 3.20 MPa during rotation, and in the intact model, the maximum von Mises stresses on the C6/7 intervertebral disc were 0.21 MPa during flexion; 0.32 MPa during extension; 0.33 MPa during lateral bending; and 0.33 MPa during rotation. The stress distributions on the C6/7 intervertebral disc are shown in **Figure 11B**.

DISCUSSION

Construct Stability

This study comprehensively compared the biomechanical stabilities provided by ACCF with the TTMC model and NTMC model. As shown in the results, both models could significantly reduce the ROMs in the surgical segments compared with the intact model. Therefore, the ACCF with the TTMC model and NTMC model both can achieve strong construct stability in the surgical segments.

According to the result of the ROMs of the surgical segments, compared with the TTMC model, the ACCF with the NTMC model has smaller ROMs in the surgical segments, which means that the NTMC model has better stability. In the present study, similar to previous studies, the boundary conditions of the spacer–bone interfaces were assigned to be tied contacts to simulate the status of bony fusion (Wu, Meng, Wang, Rong, Hong, Ding, Chen and Liu 2019). Compared with the cage–bone interfaces in the TTMC model, the spacer–bone interfaces have a larger area in contact with the whole endplate, which is more beneficial to increasing anterior column stability immediately after surgery and bone fusion during the process of follow-up. As the bony fusion at the endplate space, the stiffness of the anterior column increases, which further improves the stability of the construct. A recent study found that compared with immediately after surgery, the ROMs of the surgical level were further reduced by 11.5% when bony fusion was achieved at the intervertebral space (Li, Wu, Chu, Liu, Hou, Yu and Hou 2018). In general, the NTMC model can not only improve the stability immediately after surgery but also maintain long-term stability after the operation.

Subsidence Resistance

TMC subsidence is one of the common postoperative complications in ACCF (Wen, Lu, Wang, Liang, Gao and He 2018). The relatively high endplate interfacial stress concentration is an important factor that facilitates the cage penetrating into the endplate and inducing cage subsidence (Lu, Liang, Liu, Guo, Zhang, Yang and He 2017; Wen, Lu, Wang, Liang, Gao and He 2018). In some literature, bony endplate strain/stress threshold is also reported (Ottardi, La Barbera, Pietrogrande and Villa 2016; La Barbera, Cianfoni, Ferrari, Distefano, Bonaldi and Villa 2019; La Barbera, Cianfoni, Ferrari, Distefano, Bonaldi and Villa 2019).

Although cage subsidence has little influence on the clinical outcomes in some patients, some severe cases may induce kyphosis, neurologic deterioration, and instrumental-related complications because of the significant decrease in intervertebral height and the subsequent increase in stress load within the anterior titanium plate (Takase, Murata, Sato, Tanaka, Miyazaki, Yoshizumi, Tateishi, Kawahara and Yamamoto 2018).

To address these issues, the NTMC model consisting of two spacers located on both sides of the TMC that match the shapes of the upper and lower endplate was developed, where the contact area in the spacer–endplate interface was 3.57 cm^2. The outcomes of endplate stresses showed that ACCF using the TTMC for vertebral body construction induced approximately 3 to 5-fold greater stress peaks on the C6 endplate than the NTMC model (4.5–23.9 vs. 1.9–5.0 MPa, respectively). For the TTMC model, the contact area between the TMC end and the endplate is small (the contact area was 0.31 cm^2), which results in a large stress concentration and leads to cage subsidence.

The present study concluded that the larger the spacer–endplate interface contact area, the lower the subsidence rate of the TMC. In addition, some new cages also have been reported to support this viewpoint. These new cages offered larger contact areas with the endplate by enlarging the surface area and simulating the endplate shapes in the cage end to prevent excessive stress concentration, which effectively dispersed the stress distribution and reduced the subsidence rate (Fengbin, Jinhao, Xinyuan, Xinwei, Yu and Deyu 2013; Shamji, Zhang, Quan, Zhao, Luo, Tang, Li, Zhou and Jiang 2014). Due to the anatomical structure of the cervical spine among patients being different, it is difficult to achieve perfect anatomical matching with the endplates by using new cages (Lou, Liu, Rong, Li, Wang and Gong 2016). However, the postoperative results found that these new cages are still in close contact with the endplates, effectively increasing the contact area, rebuilding the intervertebral height, and dispersing the endplate stress. By simulating the shape of the endplate, these new cages significantly decreased the interval between the spacer and the endplate compared with the conventional TMC with a flat end (Fengbin, Jinhao, Xinyuan, Xinwei, Yu and Deyu 2013; Shamji, Zhang, Quan, Zhao, Luo, Tang, Li, Zhou and Jiang 2014). Therefore, the reduction of the interval leads to a significant increase in the contact area, which further reduces the stress concentration and decreases the risk of postoperative subsidence (Ordway, Rim, Tan, Hickman and Fayyazi 2012).

It can be seen from the endplate stress nephograms that due to the limited interface contact area between the TMC and endplate, the stress distribution of using the TTMC in ACCF is mainly concentrated on the anterior and lateral parts of the endplate. By using the NTMC in ACCF, due to the spacer simulated the shape of the endplate, the contact area at the cage endplate significantly expanded, and the stress distribution on the endplate became homogeneous, which reduced the concentration of stress and decreased the subsidence rate of the TMC.

Risks of Instrument-Related Complications

Instrument-related complications include plate fracture, broken screw, or TMC dislodgement, which can lead to risks such as neck pain, compression of the esophagus, compression of the spinal cord, and even paralysis after surgery, and most of them even require revisions. Therefore, the NTMC model was designed to decrease the risks of instrument-related complications.

A previous study found that the lowest maximum load to identify an endplate failure event by using the conventional TMC is about 1300 N, and the contact area between the endplate and the TMC is about 30.5 mm^2. From this, we can conclude that the stress threshold of the endplate is about 42.6 Mpa. For another, the lowest maximum load to identify an endplate failure event by using the novel TMC is about 2100 N (Lu, Liang, Liu, Guo, Zhang, Yang and He 2017). However, the present methods for a reasonable estimation of the stress threshold for subsidence are limited, and because the physiological curvature of the cervical spine is lordotic, the load on the anterior spine would be eccentric with respect to the posterior spine. Therefore, any compressive load is not only pure axial translation but also involves a rotation. As mentioned above, since the spine rotation is not taken into account, our previous stress applied at the interface between the cage and the endplate cannot lead to a reasonable estimation of the stress threshold for subsidence. In addition, due to the subsidence failure being also associated with huge shear loads and bending moments, even if the load was following the spine curvature (follower load), we would not be sure that the load would be uniformly distributed across the cage–endplate interface. Accordingly, we would make relevant targeted optimizations in future research.

Compared with the ACCF using a TTMC model, the stresses at the anterior screw–plate interface, bone–screw interface, and TMC in the NTMC model are much less. According to the load-shared results, we found that the NTMC model can effectively reduce the stress load on the TMC. The reasons for the lower stress loads at the anterior screw–plate interface, bone–screw interface, and TMC by implanting the NTMC were attributed to the increase in the contact area at the spacer–endplate interface and the dispersion of the stress distribution, which offered greater stability for the anterior column (Fengbin, Jinhao, Xinyuan, Xinwei, Yu and Deyu 2013; Lu, Liang, Liu, Guo, Zhang, Yang and He 2017) and decreased the risks of instrument-related complications in ACCF.

Risks of the Degeneration at Adjacent Discs

It is of great importance to evaluate the changes in internal stresses at adjacent levels of surgical segments by measuring the IDP (Barrey, Campana, Persohn, Perrin and Skalli 2012). Increases in IDP at adjacent levels may lead to adjacent segment degeneration (ASD), which affected patient postoperative recovery and quality of life (Zeng, Duan, Yang, Wang, Hong, Lou, Ning and Liu 2018). Increases in IDP at adjacent levels after surgery may be relevant to many reasons, such as discogenic pathology, changes in cervical curvature, and subsequent pain (Eck, Humphreys, Lim, Jeong, Kim, Hodges and An 2002). The present study found that the insufficient stability of the anterior column can also lead to increases in IDP. In addition, the stress load led to the intervertebral disc cells being stimulated by stresses such as compressive stress and tensile stress, which not only increased the change of ROM but also damaged the intervertebral disc to a large extent. Because of offering a better fixation method to improve the stabilities of the cervical spine, the adjacent IDP in the NTMC model was less than that in the TTMC model in all directions, which agreed with the changes of ROM, suggesting that the new model had the ability to delay the degeneration at adjacent discs. It can be seen from the IDP nephograms that the stress distribution of using the TTMC in ACCF is consistent with the NTMC model, and both are aligned with the direction of motion. This indicates that the stress distribution of the adjacent intervertebral disc is related to the motion direction of the cervical spine.

Moreover, the paravertebral muscle strength played a crucial role in regulating IDP. Therefore, for daily activities, patients should pay attention to the muscle strength of their neck through exercise to decrease the IDP at adjacent levels after surgery.

Limitations

FE analysis is a traditional style for judging the diagnosis after different surgical strategies and offering treatment options. However, there are still some limitations of the current study. First, we idealized some situations within an acceptable range. The frictionless contact in the facet joint surfaces may lead to potential errors (Panzer and Cronin 2009; Li, Fogel, Liao, Tyagi and Liu 2018). Any possible micromotion among the TMC-spacers, bone-implant, and screw–bone interface was ignored, which were modeled as a tie. Second, although we operated on an *in vitro* model for surgical simulation and inserted a device in the surgical models, simplified *in vitro* models may not simulate the actual biomechanical environment during the process of surgery, especially for endplates and ligaments at the surgical segments. Third, in this research, we performed the finite element model analysis based on CT data from a 37-year-old young healthy man, which might not take the impact of degenerative pathology into account on the biomechanical properties of the spine. Finally, various types of NTMCs have different structural and biomechanical features, and the results of the current study have certain limitations and may not be applicable to other devices. Thus, the FE model may not be the best representation of the real state, and the main purpose of this research is to provide a trend rather than actual data.

CONCLUSION

First, the application of the NTMC that possessed two enlarged spacers and matched the anatomic structure between the endplates seems to suggest a decreased risk of TMC subsidence in ACCF by dispersing stress, which can be proved by the stress cloud map. Second, in the ACCF with the NTMC, the stresses at the anterior screw–plate interface, bone–screw interface, and TMC are much less than those at the TTMC, which might decrease the risks of instrument-related complications after surgery and enhance the speed of postoperative bone healing so as to improve the prognosis of patients. Finally, increases in IDP at adjacent levels are associated with the internal stresses of adjacent discs which may lead to ASD; therefore, the NTMC has the potential to decrease the risks of ASD.

DATA AVAILABILITY STATEMENT

The original contributions presented in the study are included in the article/Supplementary Material; further inquiries can be directed to the corresponding author.

AUTHOR CONTRIBUTIONS

K-RZ and YY contributed to the design of the study. K-RZ drafted the manuscript with help from L-TM. HL and YQ helped in the statistical analyses. Statistical analyses were discussed with K-RZ and L-TM. K-RZ and YH contributed to the revision. All authors have read and approved the final manuscript.

FUNDING

This study was supported by the National Natural Science Foundation of China (82172522), Sichuan Province Science and Technology Support Program of China (NO.2020YFS0089), Sichuan Province Science and Technology Support Program of China (NO.2020YFS0077), Post-Doctor Research Project, West China Hospital, Sichuan University (NO. 2019HXBH063), and the Postdoctoral Science Foundation of China (NO. 2020M673240).

REFERENCES

Ayturk, U. M., and Puttlitz, C. M. (2011). Parametric Convergence Sensitivity and Validation of a Finite Element Model of the Human Lumbar Spine. *Comput. Methods Biomechanics Biomed. Eng.* 14, 8, 695–705. doi:10.1080/10255842.2010.493517

Barrey, C., Campana, S., Persohn, S., Perrin, G., and Skalli, W. (2012). Cervical Disc Prosthesis versus Arthrodesis Using One-Level, Hybrid and Two-Level Constructs: An *In Vitro* Investigation. *Eur. Spine J.* 21, 3, 432–442. doi:10.1007/s00586-011-1974-4

Denozière, G., and Ku, D. N. (2006). Biomechanical Comparison between Fusion of Two Vertebrae and Implantation of an Artificial Intervertebral Disc. *J. Biomechanics* 39, 4, 766–775. doi:10.1016/j.jbiomech.2004.07.039

Eck, J. C., Humphreys, S. C., Lim, T.-H., Jeong, S. T., Kim, J. G., Hodges, S. D., An, H. S., et al. (2002). Biomechanical Study on the Effect of Cervical Spine Fusion on Adjacent-Level Intradiscal Pressure and Segmental Motion, *Spine*, 27, 22, 2431-2434. doi:10.1097/00007632-200211150-00003

Fehlings, M. G., Smith, J. S., Kopjar, B., Arnold, P. M., Yoon, S. T., Vaccaro, A. R., et al. (2012). Perioperative and Delayed Complications Associated with the Surgical Treatment of Cervical Spondylotic Myelopathy Based on 302 Patients from the Aospine North america Cervical Spondylotic Myelopathy Study. *Spi* 16, 5, 425–432. doi:10.3171/2012.1.spine11467

Fengbin, Y., Jinhao, M., Xinyuan, L., Xinwei, W., Yu, C., and Deyu, C. (2013). Evaluation of a New Type of Titanium Mesh Cage versus the Traditional Titanium Mesh Cage for Single-Level, Anterior Cervical Corpectomy and Fusion. *Eur. Spine J.* 22, 12, 2891–2896. doi:10.1007/s00586-013-2976-1

Jones, A. C., and Wilcox, R. K. (2008). Finite Element Analysis of the Spine: Towards a Framework of Verification, Validation and Sensitivity Analysis. *Med. Eng. Phys.* 30, 10, 1287–1304. doi:10.1016/j.medengphy.2008.09.006

Kallemeyn, N., Gandhi, A., Kode, S., Shivanna, K., Smucker, J., and Grosland, N. (2010). Validation of a C2-C7 Cervical Spine Finite Element Model Using Specimen-specific Flexibility Data. *Med. Eng. Phys.* 32, 5, 482–489. doi:10.1016/j.medengphy.2010.03.001

La Barbera, L., Cianfoni, A., Ferrari, A., Distefano, D., Bonaldi, G., and Villa, T. (2019a). Stent Screw–Assisted Internal Fixation (SAIF) of Severe Lytic Spinal Metastases: A Comparative Finite Element Analysis of the SAIF Technique. *World Neurosurg.* 128. 291-301. doi:10.1016/j.wneu.2019.04.154

La Barbera, L., Cianfoni, A., Ferrari, A., Distefano, D., Bonaldi, G., and Villa, T. (2019b). Stent-screw Assisted Internal Fixation of Osteoporotic Vertebrae: A Comparative Finite Element Analysis on Saif Technique. *Front. Bioeng. Biotechnol.* 7, 291. doi:10.3389/fbioe.2019.00291

La Barbera, L., Larson, A. N., Rawlinson, J., and Aubin, C.-E. (2021) .In Silico patient-specific Optimization of Correction Strategies for Thoracic Adolescent Idiopathic Scoliosis, *Clin Biomech.*, 81, 105200, doi:10.1016/j.clinbiomech.2020.105200

Lee, J. H., Park, W. M., Kim, Y. H., and Jahng, T.-A. (2016). A Biomechanical Analysis of an Artificial Disc with a Shock-Absorbing Core Property by Using Whole-Cervical Spine Finite Element Analysis, *Spine* 41, E893-E901. doi:10.1097/brs.0000000000001468

Li, Y., Fogel, G. R., Liao, Z., Tyagi, R., and Liu, W. (2018b). Prosthesis and Hybrid Strategy Consideration for Treating Two-Level Cervical Disc Degeneration in Hybrid Surgery, *Spine*, 43, 6, 379–387. doi:10.1097/brs.0000000000002316

Li, Z., Wu, H., Chu, J., Liu, M., Hou, S., Yu, S., Hou, T., et al. (2018a). Motion Analysis of Dynamic Cervical Implant Stabilization versus Anterior Discectomy and Fusion: A Retrospective Analysis of 70 Cases. *Eur. Spine J.* 27, 11, 2772–2780. doi:10.1007/s00586-018-5755-1

Liu, N., Lu, T., Wang, Y., Sun, Z., Li, J., and He, X. (2019). Effects of New Cage Profiles on the Improvement in Biomechanical Performance of Multilevel Anterior Cervical Corpectomy and Fusion: A Finite Element Analysis. *World Neurosurg.* 129, e87-e96. doi:10.1016/j.wneu.2019.05.037

Lou, J., Liu, H., Rong, X., Li, H., Wang, B., and Gong, Q. (2016). Geometry of Inferior Endplates of the Cervical Spine. *Clin. Neurology Neurosurg.* 142, 132–136. doi:10.1016/j.clineuro.2016.01.027

Lu, T., Liang, H., Liu, C., Guo, S., Zhang, T., Yang, B., He, X., et al. (2017). Effects of Titanium Mesh Cage End Structures on the Compressive Load at the Endplate Interface: A Cadaveric Biomechanical Study. *Med. Sci. Monit.* 23, 2863–2870. doi:10.12659/msm.905466

Missori, P., Domenicucci, M., and Marruzzo, D. (2018). Clinical Effects of Posterior Longitudinal Ligament Removal and Wide Anterior Cervical Corpectomy for Spondylosis. *World Neurosurg.* 113, e761-e768. doi:10.1016/j.wneu.2018.02.144

Mo, Z., Li, Q., Jia, Z., Yang, J., Wong, D. W.-C., and Fan, Y. (2017). Biomechanical Consideration of Prosthesis Selection in Hybrid Surgery for Bi-level Cervical Disc Degenerative Diseases. *Eur. Spine J.* 26, 4, 1181–1190. doi:10.1007/s00586-016-4777-9

Ordway, N. R., Rim, B. C., Tan, R., Hickman, R., and Fayyazi, A. H. (2012). Anterior Cervical Interbody Constructs: Effect of a Repetitive Compressive Force on the Endplate. *J. Orthop. Res.* 30, 4, 587–592. doi:10.1002/jor.21566

Ottardi, C., La Barbera, L., Pietrogrande, L., and Villa, T. (2016). Vertebroplasty and Kyphoplasty for the Treatment of Thoracic Fractures in Osteoporotic Patients: A Finite Element Comparative Analysis. *J. Appl. Biomater. Funct. Mater* 14, 2, 197–204. doi:10.5301/jabfm.5000287

Ouyang, P., Lu, T., He, X., Gao, Z., Cai, X., and Jin, Z. (2019). Biomechanical Comparison of Integrated Fixation Cage versus Anterior Cervical Plate and Cage in Anterior Cervical Corpectomy and Fusion (Accf): A Finite Element Analysis. *Med. Sci. Monit.* 25, 1489–1498. doi:10.12659/msm.913630

Panjabi, M. M., Crisco, J. J., Vasavada, A., Oda, T., Cholewicki, J., Nibu, K., Shin, E., et al. (2001). Mechanical Properties of the Human Cervical Spine as Shown by Three-Dimensional Load-Displacement Curves, *Spine*, 26, 2692–2700. doi:10.1097/00007632-200112150-00012

Panzer, M. B., and Cronin, D. S. (2009). C4-c5 Segment Finite Element Model Development, Validation, and Load-Sharing Investigation. *J. Biomechanics* 42, 4, 480–490. doi:10.1016/j.jbiomech.2008.11.036

Takase, H., Murata, H., Sato, M., Tanaka, T., Miyazaki, R., Yoshizumi, T., Yamamoto, T., et al. (2018). Delayed C5 Palsy after Anterior Cervical Decompression Surgery: Preoperative Foraminal Stenosis and Postoperative Spinal Cord Shift Increase the Risk of Palsy. *World Neurosurg.* 120. e1107-e1119. doi:10.1016/j.wneu.2018.08.240

Wen, Z., Lu, T., Wang, Y., Liang, H., Gao, Z., and He, X. (2018). Anterior Cervical Corpectomy and Fusion and Anterior Cervical Discectomy and Fusion Using Titanium Mesh Cages for Treatment of Degenerative Cervical Pathologies: A Literature Review. *Med. Sci. Monit.* 24, 6398–6404. doi:10.12659/msm.910269

Wu, T.-k., Meng, Y., Liu, H., Wang, B.-y., Hong, Y., Rong, X., Chen, H., et al. (2019b). Biomechanical Effects on the Intermediate Segment of Noncontiguous Hybrid Surgery with Cervical Disc Arthroplasty and Anterior Cervical Discectomy and Fusion: a Finite Element Analysis. *Spine J.* 19, 7, 1254–1263. doi:10.1016/j.spinee.2019.02.004

Wu, T.-k., Meng, Y., Wang, B.-y., Rong, X., Hong, Y., Ding, C., Liu, H., et al. (2019a). Biomechanics Following Skip-Level Cervical Disc Arthroplasty versus Skip-Level Cervical Discectomy and Fusion: A Finite Element-Based Study. *BMC Musculoskelet. Disord.* 20, 49. doi:10.1186/s12891-019-2425-3

Yang, X., Chen, Q., Liu, L., Song, Y., Kong, Q., Zeng, J., Ren, C., et al. (2013). Comparison of Anterior Cervical Fusion by Titanium Mesh Cage versus Nano-Hydroxyapatite/polyamide Cage Following Single-Level Corpectomy. *Int. Orthop. (SICOT)* 37, 12, 2421–2427. doi:10.1007/s00264-013-2101-4

Zeng, J., Duan, Y., Yang, Y., Wang, B., Hong, Y., Lou, J., Liu, H., et al. (2018). Anterior Corpectomy and Reconstruction Using Dynamic Cervical Plate and Titanium Mesh Cage for Cervical Spondylotic Myelopathy. *Baltim.* 97, e9724–e9729. doi:10.1097/md.0000000000009724

Zhang, Y., Quan, Z., Zhao, Z., Luo, X., Tang, K., Li, J., Jiang, D., et al. (2014). Evaluation of Anterior Cervical Reconstruction with Titanium Mesh Cages versus Nano-Hydroxyapatite/polyamide66 Cages after 1- or 2-level Corpectomy for Multilevel Cervical Spondylotic Myelopathy: A Retrospective Study of 117 Patients. *PLoS ONE* 9, S68–74. doi:10.1371/journal.pone.0096265

Zhao, L., Chen, J., Liu, J., Elsamaloty, L., Liu, X., Li, J., Wang, L., et al. (2018). Biomechanical Analysis on of Anterior Transpedicular Screw-Fixation after Two-Level Cervical Corpectomy Using Finite Element Method. *Clin. Biomech.* 60, 76–82. doi:10.1016/j.clinbiomech.2018.09.008

Conflict of Interest: The authors declare that the research was conducted in the absence of any commercial or financial relationships that could be construed as a potential conflict of interest.

frontiers | Frontiers in Bioengineering and Biotechnology

ORIGINAL RESEARCH
published: 13 July 2022
doi: 10.3389/fbioe.2022.910311

Moderate External Rotation of Tibial Component Generates More Natural Kinematics Than Internal Rotation After Total Knee Arthroplasty

Chaohua Fang[1,2,3†], Yichao Luan[4†], Zhiwei Wang[5], Long Shao[1], Tiebing Qu[6,7] and Cheng-Kung Cheng[2,3]*

[1]Department of Joint Surgery, Ningbo No. 6 Hospital, Ningbo, China, [2]School of Biomedical Engineering, Shanghai Jiao Tong University, Shanghai, China, [3]Engineering Research Center of Digital Medicine, Ministry of Education, Shanghai, China, [4]School of Biological Science and Medical Engineering, Beihang University, Beijing, China, [5]Department of Orthopaedics, Beijing Chaoyang Hospital, Beijing, China, [6]Department of Orthopaedics, Beijing Boai Hospital, Beijing, China, [7]The Center of Diagnosis and Treatment for Joint Disease, China Rehabilitation Research Center, Beijing, China

Edited by:
Bin Wang,
Chongqing Medical University, China

Reviewed by:
Zhongmin Jin,
University of Leeds, United Kingdom
Wenxin Niu,
Tongji University, China

***Correspondence:**
Cheng-Kung Cheng
ckcheng2020@sjtu.edu.cn

†These authors have contributed equally to this work and share first authorship

Specialty section:
This article was submitted to Biomechanics, a section of the journal Frontiers in Bioengineering and Biotechnology

Received: 01 April 2022
Accepted: 13 June 2022
Published: 13 July 2022

Citation:
Fang C, Luan Y, Wang Z, Shao L, Qu T and Cheng C-K (2022) Moderate External Rotation of Tibial Component Generates More Natural Kinematics Than Internal Rotation After Total Knee Arthroplasty.
Front. Bioeng. Biotechnol. 10:910311.
doi: 10.3389/fbioe.2022.910311

This study aimed to investigate the influence of tibial malrotation on knee kinematics after total knee arthroplasty (TKA). A symmetric fixed-bearing posterior-stabilized prosthesis was implanted in the validated knee model with different rotational alignments of the tibial component (neutral, 3° external rotation, 5° external rotation, 3° internal rotation, and 5° internal rotation). Computational kinematic simulations were used to evaluate the postoperative kinematics of the knee joint including anteroposterior translation femoral condyles and axial rotation of tibial component during 0°–135° knee flexion. The results revealed that the neutral position of the tibial component was not the closest kinematics to the intact knee, the model with 5° external rotation of the tibial component showed the closest lateral condyle translation and tibial axial rotation, and moderate external rotation could improve the kinematics after TKA.

Keywords: computational simulation, total knee arthroplasty, tibial component, rotational alignment, kinematics

INTRODUCTION

Total knee arthroplasty (TKA) has been the most common treatment for severe arthritis of knee joints for the past several decades with high survival rates; however, nearly 20% of patients were still not satisfied postoperatively because of knee pain or restricted function (Bourne et al., 2010). Rotational malalignment between the femoral and tibial components is one of the reasons, and the proportion of tibial component malrotation beyond 3° can reach 57% according to a research study using 3D-CT measurement (Cerquiglini et al., 2018). Malrotation of knee components influenced the mechanical behaviors of the knee joint, including the ligament tension, patella force, and contact stress on the polyethylene liner (Kuriyama et al., 2014), and caused patellofemoral maltracking, femoral–insert interface, anterior knee pain, patellar subluxation, excessive polyethylene wear, and even early failure of the tibial liner (Cerquiglini et al., 2018).

Abbreviations: FEA, flexion–extension axis; FFC, flexion facet center; LCL, lateral collateral ligament; MCL, medial collateral ligament; PS, posterior-stabilized; PLCL, posterolateral corner-locked; TEA, transepicondylar axis; TKA, total knee arthroplasty.

As for the rotational alignment in TKA, the transepicondylar axis (TEA) is universally accepted as the gold standard of femoral rotational alignment. This is partly because the TEA can represent the best approximation of the actual flexion–extension axis (FEA) of the knee (Churchill et al., 1998). However, it is still controversial with regard to the tibial rotational alignment. The correct tibial rotational alignment is usually regarded, as with the anterior–posterior axis of the tibial component, as being perpendicular to TEA at the full leg extension position. It is considered the neutral position or internal or external rotation (Akagi et al., 2004; Kim et al., 2017). The positions of the femur and tibia in the primary knee joint are changeable during gait cycles, and the tibia plateau aligns with slight external rotation compared to the femoral condyle in full leg extension (Duparc et al., 2014). Until now, there has been no TKA that can replicate the kinematics of the living knee, and the main abnormal kinematics includes decreased posterior femoral rollback, paradoxical anterior femoral translation, and reverse axial rotation of the tibia (Dennis et al., 1998). For the posterior-stabilized (PS) prosthesis of TKA, the cam-post mechanism was designed to avoid paradoxical anterior femoral translation (Arnout et al., 2015). However, the rotation between femoral and tibial components was limited because of this mechanism, which resulted in complications, such as impingement, wear, and even fracture of the post (Callaghan et al., 2002; Dolan et al., 2011; Diamond et al., 2018). Therefore, it is crucial for rotational alignment when PS prostheses are used in TKA. Moreover, the few studies focusing on knee kinematics after TKA with different tibial rotational alignment show inconsistent results (Harman et al., 2012; Hutter et al., 2013; Nakahara et al., 2015). No study has evaluated how the degree of tibial component malrotation affects the kinematics of the knee joint after TKA.

The current study aimed to investigate the effect of tibial component rotation on knee kinematics after TKA. We hypothesized that external rotational alignment of the tibial component results in kinematics closer to the intact knee.

MATERIALS AND METHODS

An intact kinematic knee model which was validated in a previous study was used (Wang et al., 2012; Fang et al., 2015). This model was built according to CT data from a healthy female volunteer with informed consent before scanning, and was approved by the local institutional review board (approval number: 12-S-70). The model included the proximal tibial bone, distal femoral bone, patella, cartilage, and meniscus. Three-dimensional solid models of a symmetric fixed-bearing PFC Sigma PS prosthesis (DePuy; Johnson & Johnson, Warsaw, IN) were constructed using reverse engineering, including a femoral component, tibial component, and tibial insert.

The bone-cutting was performed using Pro/ENGINEER Wildfire 5.0 (Parametric Technology Corp) with the techniques of mechanical alignment and measured resection in TKA (Daines and Dennis, 2014). On the coronal and sagittal planes, the distal femoral and proximal tibia were resected perpendicular to their mechanical axes. The femoral mechanical axis was defined as the line that connected the center of the intercondylar notch and the center of the femoral head; the tibial mechanical axis was defined as the line that connected the center of the tibial plateau and the center of the talus (Wu et al., 2002). On the transverse plane, the femoral component was implanted with its transverse axis parallel to the TEA, and the tibial component was implanted depending on the medial angle of its anterior–posterior axis (the line connected the midpoints of anterior and posterior edges) and projection of the TEA on the tibial cutting surface at the full leg extension position. It was regarded as internal rotation if the angle was less than 90°, otherwise, as external rotation. Model A has an angle of 90° that was regarded as the neutral rotational alignment of the tibial component (Akagi et al., 2004; Kim et al., 2017); the other four models (Model B–E) were established with 5° internal rotation, 3° internal rotation, 3° external rotation, and 5° external rotation, respectively (**Figure 1**).

The model was assembled by placing the most distal points of the femoral condyles on the lowest points of the polyethylene tibial insert in MSC.ADAMS_R3 (MSC Software, Santa Ana, CA). The medial collateral ligament (MCL), lateral collateral ligament (LCL), cruciate ligaments, patella tendon, quadriceps, and hamstrings were simulated as nonlinear force elements to calculate knee kinematics. The origin and insertion points of ligaments and tendons were referenced from relevant literature (Ikeuchi et al., 2007; Tao et al., 2014) and confirmed by the senior surgeon (TB Qu). The flexion facet center (FFC) was generated by the circular fitting of the condyles of the femoral component (Iwaki et al., 2000). The line connecting the medial and lateral FFC was regarded as the *x*-axis, the mechanical axis was designed as the *z*-axis, and the *y*-axis was generated automatically according to the *x*-axis and *z*-axis. A Cartesian coordinate system was constructed on the original position (Grood and Suntay, 1983). During knee flexion, the displacements of medial and lateral FFCs in the *y*-direction were used to represent the anteroposterior translation of medial and lateral condyles, respectively, and tibial rotation (internal–external rotation of the tibia) was defined as the angular displacement in the *z*-direction (**Figure 2**).

In this model, the contact properties of tibiofemoral articulation and patellofemoral articulation were set as “solid to solid,” and the friction of these two articulations were 0.04 and 0, respectively (Godest et al., 2002). A ground reaction force (1.5 bodyweights = 750 N) was applied to the center of mass of the tibial component (D’Lima et al., 2007). The femoral component was only permitted to move in the flexion–extension direction, but the tibial component was only constrained in the flexion–extension direction and unconfined in all other directions.

All the five models were simulated with the knee flexion from 0° to 135°; the kinematics data, including femoral anteroposterior translation and tibial rotation, were acquired every 15° during knee flexion and visualized in Microsoft Excel (Version 2016; Microsoft, Redmond, WA, United States). In addition, Model A with the neutral alignment of the tibial component was used for validating the TKA model against the results of an *in vivo*

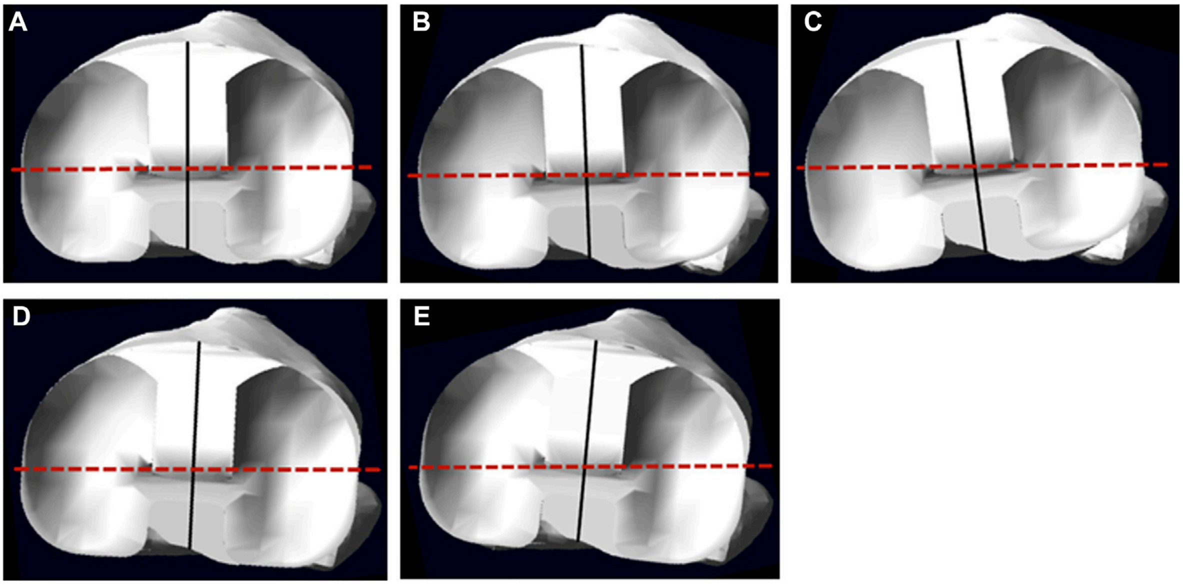

FIGURE 1 | The superior view of the tibial component on the tibia; the solid line indicates the anterior–posterior axis of the tibial component, and the dotted line indicates the projection of the TEA. **(A–E)** show models A, B, C, D, and E, respectively.

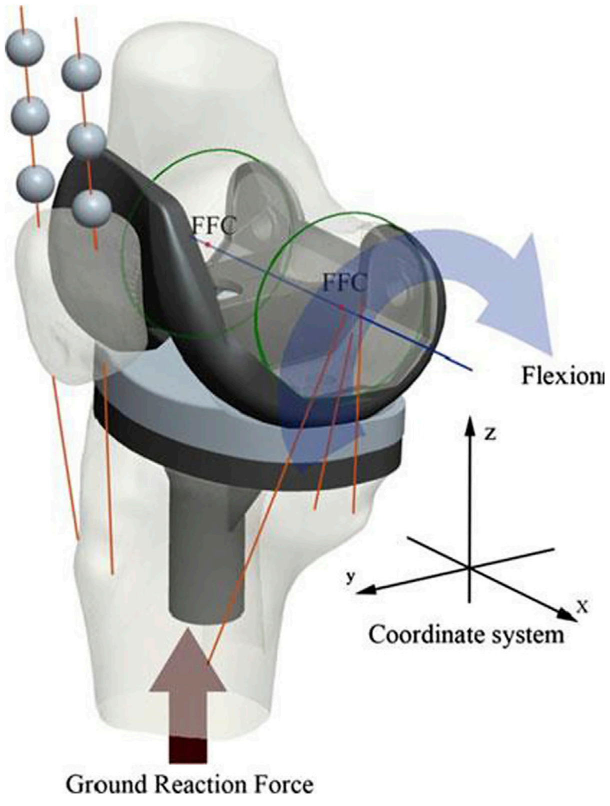

FIGURE 2 | The TKA model and the coordinate system in ADAMS.

kinematic study using the same prostheses and surgical techniques (Ranawat et al., 2004).

RESULTS

The TKA model (Model A) was validated by comparing the simulated results and *in vivo* data. The difference in both medial and lateral femoral condylar contact positions was less than 2 mm at any angle of knee flexion from 0° to 90° (Wang et al., 2012; Steinbrück et al., 2016).

The data of femoral anteroposterior translation and tibial rotation were acquired from intact knee and TKA models. Different kinematic results were generated from the intact knee model and all TKA models, especially for the lateral femoral condyle translation in the full flexion process and tibia axial rotation beyond 60° flexion.

The TKA models showed less posterior translation of the lateral femoral condyle and internal tibial rotation. As for the kinematics among the TKA models with different rotational alignments, the femoral condyle translation and tibial axial rotation were proportional to the external rotation of the tibial component. However, the overall trends of translation and rotation were similar. Compared with the neutral position, the internal rotation of the tibial component decreased the anterior translation of medial condyle, but increased the anterior translation of lateral femoral condyle, and decreased the internal rotation of the tibia during flexion. External malalignment showed contrary results. Moreover, the kinematic results of Model E with 5° external malrotation were the closest to the intact knee model including lateral

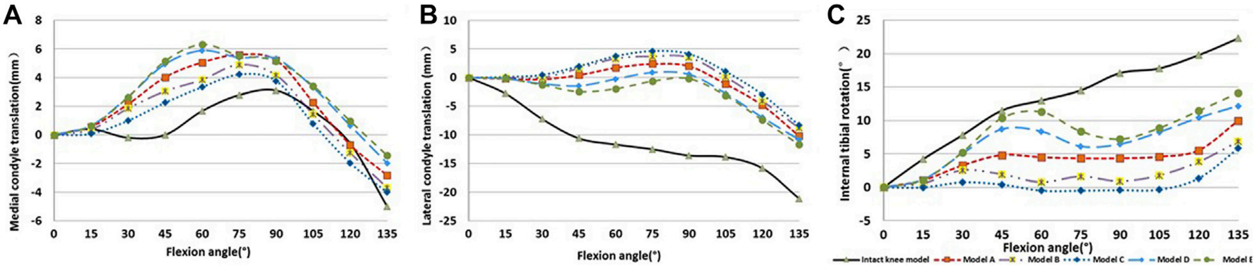

FIGURE 3 | The kinematics of TKA models and intact knee model. **(A)** Medial condyle translation, **(B)** lateral condyle translation, and **(C)** internal tibial rotation. Positive means anterior translation or tibia internal rotation against the femur. Negative indicates the opposite.

femoral condyle translation and tibial axial rotation (**Figure 3**).

DISCUSSION

To investigate the influence of tibial rotational alignment on the kinematics of TKA, dynamic simulations of TKA models with different tibial rotational alignments were used to calculate the femoral condylar translation and tibial rotation. The key finding of this study is that the external rotational alignment of the tibial component can restore the lateral femoral condyle translation and tibial axial rotation, which was closer to a normal knee joint than the neutral position. For the medial femoral condyle translation, the internal rotational alignment is most similar to that of a normal knee. Considering the posterior translation of the lateral condyle is greater than the anterior translation of the medial condyle, the whole femoral condyle slides more posteriorly at external 5° rotational alignment than that at internal 5° rotation during flexion. However, anterior translation of the medial condyle was decreased because of internal malrotation that leads to paradoxical tibial axial rotation. Overall, the external 5° rotational alignment is better than the neutral position because it is closer to the normal joint in femoral condyle translation and tibial axial rotation. The reason for this might be that the tibia was externally rotated to the femur at full extension of the intact knee joint, and it is the tibial component implanted with a moderate external rotation that mostly aids recovery in this situation.

The goal of TKA is not only to alleviate pain and improve function but also to help the patient regain normal kinematics of the knee joint. Recovering the optimal rotational alignment of the tibial component is helpful to achieve this goal, but it still requires further research. Previous studies revealed internal malrotation can lead to many complications such as stiffness, anterior knee pain, and extensor mechanism deficiency (Bédard et al., 2011; Steinbrück et al., 2016; Abdelnasser et al., 2020). Recently, a systematic review confirmed that excessive internal rotation (>10° of internal rotation demonstrated the common value) of the tibial component was a significant risk for knee pain and inferior functional outcomes after TKA, although external rotation does not affect the results (Panni et al., 2018). External rotation might be helpful. A retrospective study of 1,696 consecutive patients (3,048 knees), with a mean follow-up duration of 15.8 years (range, 11–18 years), found that the risk factors for failure of the components involved <2° external rotational alignment of the tibial components and recommended that the tibial component be placed with the rotational alignment of 2–5° external rotation (Kim et al., 2014).

The altered postoperative kinematics might be responsible for postoperative complications and patients' subjective dissatisfaction. The kinematics of TKA was affected by a variety of factors, such as the prosthesis design and surgery procedure (Koh et al., 2019; Wang et al., 2019). However, only a few cadaveric and computational simulation studies have investigated the influence of tibial rotational alignment. A cadaveric study recorded the kinematics of the femorotibial joint with an ultrasonic-based motion analysis system using the tibial component with 3° internal rotation, neutral, or 3° external rotation. With the regression coefficients from the mixed-effects model analysis, we found that the mean anterior translation of the femur was −0.9, 0, and 0.4 mm at the tibial component with 3° internal rotation, neutral, or 3° external rotation position, respectively, and the internal femorotibial rotation was 1.2°, 0°, and 0.2°, respectively (Steinbrück et al., 2016). These results are consistent with those of our current study, where the femoral component anterior translation increased and internal tibial axial rotation decreased if the tibial component was internally rotated. Another cadaveric study compared the preoperative and postoperative tibiofemoral kinematics from 0° to 90° of flexion with the tibial components self-adapted, 6° internal rotation, 6° external rotation and with the femoral component ligament balanced, 3° external rotation, 6° external rotation, or 6° internal rotation. The largest kinematic differences between knees were found from the combination of femoral component internal and tibial component external rotation. The tibial component with 6° external rotation can restore a tibial longitudinal rotation most similar to that of the preoperative one with the femoral component of balanced ligament, 6° external rotation. The femoral component rotation was referenced with the posterior condylar line, which is internally rotated concerning both the surgical and anatomic TEA, with mean angles between 3° and 7° in the study (Maderbacher et al., 2017). Consequently, a 6° external rotation of the femoral component might result in a neutral rotation similar to the femoral rotational alignment in the current study. It is consistent with the current study that the tibial component with 5° external rotation regains the tibial axial rotation closest to the normal knee joint. According to the literature we retrieved, only one computational simulation investigated the influence of tibial rotational alignment on tibiofemoral kinematics. For the PS implant, an externally rotated 15° tibial component permitted greater anterior femoral translation than an internally rotated 15° tibial component, and the anterior translations of the medial condyle appeared to be increased in the cases of external tibial component rotation, which is also consistent with the result in the current study (Thompson et al., 2011).

Increased MCL force resulting from the internal rotational alignment of the tibial component might be one of the possible reasons for the decreased anterior translation of the medial condyle, but MCL force also increased slightly with external rotational alignment; the orientation of the MCL might induce this discrepancy. As proven by MRI studies, the tibial attachment to the MCL is located more anteriorly than the femoral attachment in knee extension (Thompson et al., 2011). So, an internally rotated tibial component results in an internally rotated femur and posterior translational femoral medial condyle relative to the tibia, which lengthens the MCL and increases the tensile force. On the contrary, an externally rotated tibial component leads to the anterior translation of the medial femoral condyle; the length of MCL might be shortened slightly or unchanged; moreover, the MCL force would not change significantly. Meanwhile, the LCL is less affected by malrotation of the tibial component because of its lower stiffness value and is modeled as a single bundle compared to the MCL with anterior, deep, and oblique bundles. In addition, the orientation of LCL was almost straight from the beginning to the end, which was different from the MCL, so the length was less influenced by malrotation of the tibial component (Kuriyama et al., 2014).

However, there are still some limitations in the current simulation. First, only five rotational alignments were simulated. The influence of tibial malalignment on kinematics might be more specific with more simulations of different alignments. The value of malrotation was set according to a previous work in which the degree of tibial malrotation was measured referencing the Akagi line, medial 1/3 tibia tubercle, or the posterolateral corner-locked (PLCL) technique in the normal Chinese population (Fang et al., 2020). According to a retrospective cohort study with 3,048 knees, 2–5° external rotation of the tibial component accounted for 2,490 knees, which was shown as the main rotational alignment in clinical practice (Kim et al., 2014). In addition, the prosthesis used in the current study is the PFC Sigma fixed-bearing prosthesis, which is a PS prosthesis with a cam-post mechanism. Excessive internal rotation (10° internal rotation) of the tibial insert resulted in impingement between the cam-post and higher stress on the post (Huang et al., 2006). Thus, moderate malrotation alignment (5°) was used in this study, but the cutoff was not determined in the current study. Another limitation is that the results of the current study may not apply to other commercial prostheses because the posterior cruciate-retaining and insert conformity design may affect the kinematics as well. Finally, the bone model was constructed according to data from an individual, which cannot reflect on all patients because of anatomical differences.

CONCLUSION

The tibial component rotational alignment can alter the kinematics after TKA, and the neutral position is not the optimal tibial rotational alignment. Moderate external rotation (5°) can restore the lateral femoral condyle translation and tibial axial rotation to a state closest to the normal knee joint compared with external 3°, internal 3°, internal 5° rotation, and neutral position. More studies that focus on the optimal rotational alignment of the tibial component, rather than the accuracy of rotational alignment, need to be conducted in the future.

DATA AVAILABILITY STATEMENT

The raw data supporting the conclusions of this article will be made available by the authors, without undue reservation.

ETHICS STATEMENT

The studies involving human participants were reviewed and approved by Medical Ethics Committee, Beijing Chaoyang Hospital, Capital Medical University. The patients/participants provided their written informed consent to participate in this study. Written informed consent was obtained from the individual(s) for the publication of any potentially identifiable images or data included in this article.

AUTHOR CONTRIBUTIONS

CF and C-KC conceived and designed the study. YL, ZW, and TQ validated the knee model. YL and LS completed the simulation and collected the data. CF, YL, and C-KC interpreted the data. All authors participated in the preparation, revision, and approval of the version to be published.

FUNDING

This research was supported by the Medical and Health Technology Plan of Zhejiang Province (No. 2022RC068) and Ningbo Public Welfare Science and Technology Project (No. 2022S064).

ACKNOWLEDGMENTS

We would like to thank Colin McClean for his assistance with editing this manuscript.

REFERENCES

Abdelnasser, M. K., Adi, M. M., Elnaggar, A. A., and Tarabichi, S. (2020). Internal Rotation of the Tibial Component in Total Knee Arthroplasty Can Lead to Extension Deficit. *Knee Surg. Sports Traumatol. Arthrosc.* 28 (9), 2948–2952. doi:10.1007/s00167-019-05695-w

Akagi, M., Oh, M., Nonaka, T., Tsujimoto, H., Asano, T., and Hamanishi, C. (2004). An Anteroposterior axis of the Tibia for Total Knee Arthroplasty. *Clin. Orthop. Relat. Res.* 420, 213–219. doi:10.1097/00003086-200403000-00030

Arnout, N., Vanlommel, L., Vanlommel, J., Luyckx, J. P., Labey, L., Innocenti, B., et al. (2015). Post-cam Mechanics and Tibiofemoral Kinematics: a Dynamic *In Vitro* Analysis of Eight Posterior-Stabilized Total Knee Designs. *Knee Surg. Sports Traumatol. Arthrosc.* 23 (11), 3343–3353. doi:10.1007/s00167-014-3167-2

Bédard, M., Vince, K. G., Redfern, J., and Collen, S. R. (2011). Internal Rotation of the Tibial Component Is Frequent in Stiff Total Knee Arthroplasty. *Clin. Orthop. Relat. Res.* 469 (8), 2346–2355. doi:10.1007/s11999-011-1889-8

Bourne, R. B., Chesworth, B. M., Davis, A. M., Mahomed, N. N., and Charron, K. D. J. (2010). Patient Satisfaction after Total Knee Arthroplasty: Who Is Satisfied and Who Is Not? *Clin. Orthop. Relat. Res.* 468 (1), 57–63. doi:10.1007/s11999-009-1119-9

Callaghan, J. J., O???Rourke, M. R., Goetz, D. D., Schmalzried, T. P., Campbell, P. A., and Johnston, R. C. (2002). Tibial Post Impingement in Posterior-Stabilized Total Knee Arthroplasty. *Clin. Orthop. Relat. Res.* 404, 83–88. doi:10.1097/00003086-200211000-00014

Cerquiglini, A., Henckel, J., Hothi, H., Rotigliano, N., Hirschmann, M. T., and Hart, A. J. (2018). 3D Patient Imaging and Retrieval Analysis Help Understand the Clinical Importance of Rotation in Knee Replacements. *Knee Surg. Sports Traumatol. Arthrosc.* 26 (11), 3351–3361. doi:10.1007/s00167-018-4891-9

Churchill, D. L., Incavo, S. J., Johnson, C. C., and Beynnon, B. D. (1998). The Transepicondylar axis Approximates the Optimal Flexion axis of the Knee. *Clin. Orthop. Relat. Res.* 356, 111–118. doi:10.1097/00003086-199811000-00016

Daines, B. K., and Dennis, D. A. (2014). Gap Balancing vs. Measured Resection Technique in Total Knee Arthroplasty. *Clin. Orthop. Surg.* 6 (1), 1–8. doi:10.4055/cios.2014.6.1.1

Dennis, D. A., Komistek, R. D., Colwell, C. E., Jr., Ranawat, C. S., Scott, R. D., Thornhill, T. S., et al. (1998). *In Vivo* Anteroposterior Femorotibial Translation of Total Knee Arthroplasty. *Clin. Orthop. Relat. Res.* 356, 47–57. doi:10.1097/00003086-199811000-00009

Diamond, O. J., Howard, L., and Masri, B. (2018). Five Cases of Tibial Post Fracture in Posterior Stabilized Total Knee Arthroplasty Using Prolong Highly Cross-Linked Polyethylene. *Knee* 25 (4), 657–662. doi:10.1016/j.knee.2018.05.005

D'Lima, D. D., Patil, S., Steklov, N., Chien, S., and Colwell, C. W., Jr. (2007). *In Vivo* knee Moments and Shear after Total Knee Arthroplasty. *J. Biomechanics* 40 (Suppl. 1), S11–S17. doi:10.1016/j.jbiomech.2007.03.004

Dolan, M. M., Kelly, N. H., Nguyen, J. T., Wright, T. M., and Haas, S. B. (2011). Implant Design Influences Tibial Post Wear Damage in Posterior-Stabilized Knees. *Clin. Orthop. Relat. Res.* 469 (1), 160–167. doi:10.1007/s11999-010-1515-1

Duparc, F., Thomine, J. M., Simonet, J., and Biga, N. (2014). Femoral and Tibial Bone Torsions Associated with Medial Femoro-Tibial Osteoarthritis. Index of Cumulative Torsions. *Orthop. Traumatology Surg. Res.* 100 (1), 69–74. doi:10.1016/j.otsr.2013.12.014

Fang, C.-H., Chang, C.-M., Lai, Y.-S., Chen, W.-C., Song, D.-Y., McClean, C. J., et al. (2015). Is the Posterior Cruciate Ligament Necessary for Medial Pivot Knee Prostheses with Regard to Postoperative Kinematics? *Knee Surg. Sports Traumatol. Arthrosc.* 23 (11), 3375–3382. doi:10.1007/s00167-014-3249-1

Fang, C.-H., Cheng, C.-K., Qu, T.-B., Zhang, J.-H., Zhang, B., Hua, Q., et al. (2020). The Posterolateral Corner-Locked Technique Is Applicable in a Chinese Population Regarding the Tibial Component Rotation Alignment in Total Knee Arthroplasty. *J. Knee Surg.* 33 (5), 466–473. doi:10.1055/s-0039-1678536

Godest, A. C., Beaugonin, M., Haug, E., Taylor, M., and Gregson, P. J. (2002). Simulation of a Knee Joint Replacement during a Gait Cycle Using Explicit Finite Element Analysis. *J. Biomechanics* 35 (2), 267–275. doi:10.1016/s0021-9290(01)00179-8

Grood, E. S., and Suntay, W. J. (1983). A Joint Coordinate System for the Clinical Description of Three-Dimensional Motions: Application to the Knee. *J. Biomech. Eng.* 105 (2), 136–144. doi:10.1115/1.3138397

Harman, M. K., Banks, S. A., Kirschner, S., and Lützner, J. (2012). Prosthesis Alignment Affects Axial Rotation Motion after Total Knee Replacement: a Prospective *In Vivo* Study Combining Computed Tomography and Fluoroscopic Evaluations. *BMC Musculoskelet. Disord.* 13, 206. doi:10.1186/1471-2474-13-206

Huang, C.-H., Liau, J.-J., Huang, C.-H., and Cheng, C.-K. (2006). Influence of Post-cam Design on Stresses on Posterior-Stabilized Tibial Posts. *Clin. Orthop. Relat. Res.* 450, 150–156. doi:10.1097/01.blo.0000218739.76871.28

Hutter, E. E., Granger, J. F., Beal, M. D., and Siston, R. A. (2013). Is There a Gold Standard for TKA Tibial Component Rotational Alignment? *Clin. Orthop. Relat. Res.* 471 (5), 1646–1653. doi:10.1007/s11999-013-2822-0

Ikeuchi, M., Yamanaka, N., Okanoue, Y., Ueta, E., and Tani, T. (2007). Determining the Rotational Alignment of the Tibial Component at Total Knee Replacement. *J. Bone Jt. Surg. Br. volume* 89-B (1), 45–49. doi:10.1302/0301-620x.89b1.17728

Iwaki, H., Pinskerova, V., and Freeman, M. A. R. (2000). Tibiofemoral Movement 1: the Shapes and Relative Movements of the Femur and Tibia in the Unloaded Cadaver Knee. *J. Bone Jt. Surg. Br. volume* 82-B (8), 1189–1195. doi:10.1302/0301-620x.82b8.1071710.1302/0301-620x.82b8.0821189

Kim, J. I., Jang, J., Lee, K. W., Han, H. S., Lee, S., and Lee, M. C. (2017). Anterior Tibial Curved Cortex Is a Reliable Landmark for Tibial Rotational Alignment in Total Knee Arthroplasty. *BMC Musculoskelet. Disord.* 18 (1), 252. doi:10.1186/s12891-017-1609-y

Kim, Y.-H., Park, J.-W., Kim, J.-S., and Park, S.-D. (2014). The Relationship between the Survival of Total Knee Arthroplasty and Postoperative Coronal, Sagittal and Rotational Alignment of Knee Prosthesis. *Int. Orthop. (SICOT)* 38 (2), 379–385. doi:10.1007/s00264-013-2097-9

Koh, Y.-G., Son, J., Kwon, O.-R., Kwon, S. K., and Kang, K.-T. (2019). Tibiofemoral Conformity Variation Offers Changed Kinematics and Wear Performance of Customized Posterior-Stabilized Total Knee Arthroplasty. *Knee Surg. Sports Traumatol. Arthrosc.* 27 (4), 1213–1223. doi:10.1007/s00167-018-5045-9

Kuriyama, S., Ishikawa, M., Furu, M., Ito, H., and Matsuda, S. (2014). Malrotated Tibial Component Increases Medial Collateral Ligament Tension in Total Knee Arthroplasty. *J. Orthop. Res.* 32 (12), 1658–1666. doi:10.1002/jor.22711

Maderbacher, G., Keshmiri, A., Springorum, H. R., Maderbacher, H., Grifka, J., and Baier, C. (2017). Influence of Component Rotation in Total Knee Arthroplasty on Tibiofemoral Kinematics-A Cadaveric Investigation. *J. Arthroplasty* 32 (9), 2869–2877. doi:10.1016/j.arth.2017.03.055

Nakahara, H., Okazaki, K., Hamai, S., Kawahara, S., Higaki, H., Mizu-uchi, H., et al. (2015). Rotational Alignment of the Tibial Component Affects the Kinematic Rotation of a Weight-Bearing Knee after Total Knee Arthroplasty. *Knee* 22 (3), 201–205. doi:10.1016/j.knee.2015.01.002

Panni, A. S., Ascione, F., Rossini, M., Braile, A., Corona, K., Vasso, M., et al. (2018). Tibial Internal Rotation Negatively Affects Clinical Outcomes in Total Knee Arthroplasty: a Systematic Review. *Knee Surg. Sports Traumatol. Arthrosc.* 26 (6), 1636–1644. doi:10.1007/s00167-017-4823-0

Ranawat, C. S., Komistek, R. D., Rodriguez, J. A., Dennis, D. A., and Anderle, M. (2004). *In Vivo* kinematics for Fixed and Mobile-Bearing Posterior Stabilized Knee Prostheses. *Clin. Orthop. Relat. Res.* 418, 184–190. doi:10.1097/00003086-200401000-00030

Steinbrück, A., Schröder, C., Woiczinski, M., Müller, T., Müller, P. E., Jansson, V., et al. (2016). Influence of Tibial Rotation in Total Knee Arthroplasty on Knee Kinematics and Retropatellar Pressure: an *In Vitro* Study. *Knee Surg. Sports Traumatol. Arthrosc.* 24 (8), 2395–2401. doi:10.1007/s00167-015-3503-1

Tao, K., Cai, M., Zhu, Y., Lou, L., and Cai, Z. (2014). Aligning the Tibial Component with Medial Border of the Tibial Tubercle-Is it Always Right? *Knee* 21 (1), 295–298. doi:10.1016/j.knee.2012.06.007

Thompson, J. A., Hast, M. W., Granger, J. F., Piazza, S. J., and Siston, R. A. (2011). Biomechanical Effects of Total Knee Arthroplasty Component Malrotation: a Computational Simulation. *J. Orthop. Res.* 29 (7), 969–975. doi:10.1002/jor.21344

Wang, X.-H., Song, D.-Y., Dong, X., Suguro, T., and Cheng, C.-K. (2019). Motion Type and Knee Articular Conformity Influenced Mid-flexion Stability of a Single Radius Knee Prosthesis. *Knee Surg. Sports Traumatol. Arthrosc.* 27 (5), 1595–1603. doi:10.1007/s00167-018-5181-2

Wang, Z.-W., Liu, Y.-L., Lin, K.-J., Qu, T.-B., Dong, X., Cheng, C.-K., et al. (2012). The Effects of Implantation of Tibio-Femoral Components in Hyperextension on Kinematics of TKA. *Knee Surg. Sports Traumatol. Arthrosc.* 20 (10), 2032–2038. doi:10.1007/s00167-011-1829-x

Wu, G., Siegler, S., Allard, P., Kirtley, C., Leardini, A., Rosenbaum, D., et al. (2002). ISB Recommendation on Definitions of Joint Coordinate System of Various Joints for the Reporting of Human Joint Motion-Part I: Ankle, Hip, and Spine. *J. Biomechanics* 35 (4), 543–548. doi:10.1016/s0021-9290(01)00222-6

Conflict of Interest: The authors declare that the research was conducted in the absence of any commercial or financial relationships that could be construed as a potential conflict of interest.

frontiers | Frontiers in Bioengineering and Biotechnology

TYPE Original Research
PUBLISHED 15 July 2022
DOI 10.3389/fbioe.2022.933341

OPEN ACCESS

EDITED BY
Jun Pan,
Chongqing University, China

REVIEWED BY
Wenxin Niu,
Tongji University, China
Feng Li,
Qingdao University of Science and Technology, China

*CORRESPONDENCE
Xueqing Wu,
xueqingwu@buaa.edu.cn
Shuqin Wu,
wushuqin@nuc.edu.cn

†These authors have contributed equally to this work and share first authorship

SPECIALTY SECTION
This article was submitted to Biomechanics,
a section of the journal
Frontiers in Bioengineering and Biotechnology

RECEIVED 30 April 2022
ACCEPTED 27 June 2022
PUBLISHED 15 July 2022

CITATION
Pei B, Lu D, Wu X, Xu Y, Ma C and Wu S (2022), Kinematic and biomechanical responses of the spine to distraction surgery in children with early onset scoliosis: A 3-D finite element analysis. *Front. Bioeng. Biotechnol.* 10:933341. doi: 10.3389/fbioe.2022.933341

Kinematic and biomechanical responses of the spine to distraction surgery in children with early onset scoliosis: A 3-D finite element analysis

Baoqing Pei[1†], Da Lu[1†], Xueqing Wu[1*], Yangyang Xu[1], Chenghao Ma[1] and Shuqin Wu[2*]

[1]Beijing key laboratory for design and evaluation technology of advanced implantable and interventional medical devices, Beijing Advanced Innovation Center for Biomedical Engineering, School of Biological Science and Medical Engineering, Beihang University, Beijing, China, [2]School of Big Data and Information, Shanxi College of Technology, Shanxi, China

Periodical and consecutive distraction is an effective treatment for severe early onset scoliosis (EOS), which enables the spinal coronal and sagittal plane deformity correction. However, the rate of rod fractures and postoperative complications was still high mainly related to the distraction process. Previous studies have primarily investigated the maximum safe distraction force without a rod broken, neglecting the spinal re-imbalance and distraction energy consumption, which is equally vital to evaluate the operative value. This study aimed to reveal the kinematic and biomechanical responses occurring after spinal distraction surgery, which were affected by traditional bilateral fixation. The spinal models (C6-S1) before four distractions were reconstructed based on CT images and the growing rods were applied with the upward displacement load of 0–25 mm at an interval of 5 mm. Relationships between the distraction distance, the distraction force and the thoracic and lumbar Cobb angle were revealed, and the spinal displacement and rotation in three-dimensional directions were measured. The spinal overall imbalance would also happen during the distraction process even under the safe force, which was characterized by unexpected cervical lordosis and lateral displacement. Additionally, the law of diminishing return has been confirmed by comparing the distraction energy consumption in different distraction distances, which suggests that more attention paid to the spinal kinematic and biomechanical changes is better than to the distraction force. Notably, the selection of fixed segments significantly impacts the distraction force at the same distraction distance. Accordingly, some results could provide a better understanding of spinal distraction surgery.

KEYWORDS

spinal distraction surgery, bilateral fixation, kinematic and biomechanical response, law of diminishing return, traditional growth rod

Introduction

EOS is a progressive spinal deformity that occurs in children before the age of 10 years. Unilateral or bilateral posterior fixation such as the growing rod technique was used to limit the progression of scoliosis without stunting the spinal growth (Stokes et al., 1996; Akbarnia et al., 2005, Akbarnia et al., 2008; Thompson et al., 2007; Villemure and Stokes, 2009; Elsebai et al., 2011). It requires repeat distraction every 6 or more months via open surgery under general anesthesia (Akbarnia et al., 2005, 2008; Sankar et al., 2011). However, the situations such as postoperative complications, rod fractures and second spinal imbalance are still existing. For example, more than 50% of patients treated with growing rods had at least one complication at some point after surgery (Bess et al., 2010). Similarly, rod fractures occured in 15% of patients (Thompson et al., 2005; Bess et al., 2010; Yang et al., 2011), which were perhaps accompanied by screw loosening (Li et al., 2010). Higher or lower force, suboptimal distraction could also lead to poor sagittal contours in juvenile patients (Akbarnia et al., 2005). These conditions are related to the choice of distraction force and distraction frequency, which depends on the patient's growth.

The recent studies contributed to a better understanding of the relationship between distraction force and distraction frequency. A shorter distraction episode can effectively reduce the stress on the rods while patients must undergo more surgical damage (Agarwal, et al., 2014a; Agarwal, et al., 2014b, Agarwal, et al., 2015, Agarwal, et al., 2017; Agarwal, et al., 2017a). Meantime, frequent distractions are more gentle on the soft tissues and may avoid progressive stiffness of auto fusion of the spinal segments (Cheung et al., 2016). On the other hand, a greater distraction force resulted in a significant therapeutic effect in a short time and a reduction of surgical damage, which also meant an increased risk of rod fracture (Agarwal et al., 2017b). However, little attention has been paid to the overall spinal balance and local biomechanical environment changes after distraction surgery.

Agarwal et al. (2017) simulated 6 months of spinal growth under various distraction forces and found that the optimal force existed in all types of scoliotic curves. Optimization of the biomechanical environment could reduce the complications associated with growing rods. The force threshold that the rod can withstand may not be applicable to the bones. They paid more attention to the stress on rods that neglected the biomechanical changes on the spine or vertebrae. Nevertheless, Justin V.C. Lemans et al. (Jvcl et al., 2021) investigated the destructive force by stretching the spine *in vitro* and found the maximum force threshold was 800–1200N (age >5). They did not focus on the issues of spinal coronal or sagittal imbalance. Nail rod system has more stable characteristics than spine. So, it is more effective to focus on the spinal response after distraction surgery.

No prior study has ever systematically investigated the local or global kinematic and biomechanical response after spinal distraction. Therefore, the current study aimed to reveal the spinal biomechanical changes in the cases of growing rods distracting at different distances. In particular, the distraction force, reduction of Cobb angle, spinal movement and rotation in three-dimension, coronal and sagittal balance and intervertebral disc (IVD) stress parameters were measured. The interplay between them is also interpreted to aid in developing and optimizing this technology and its contemporary counterparts.

Materials and methods

Subjects

The research was approved by the Science and Ethics Committee of the School of Biological Science and Medical Engineering at Beihang University (protocol code: BM20220087).

The patient (8 years, 115 cm, 30 kg) underwent the first growing rod implantation in 2015 due to excessive lordosis of the cervicothoracic junction. Three more surgeries for spine distraction followed in 2016, 2017, and 2019 (Figure 1). This patient did not have any other known musculoskeletal disorders. The preoperative X-ray displays a thoracic curve Cobb angle of 62.9°/54.4°/47.3°/29.9° (thoracic apex: T8; thoracic cephalic vertebra: T5; thoracic caudal vertebra: T10) and a lumbar curve Cobb angle of 45.1°/44.1°/37.4°/29.7° (lumbar apex: T12; lumbar cephalic vertebra: T11; lumbar caudal vertebra: L3), which were captured at an interval of 1 mm and a resolution of 512 × 512 px using a CT scanner (model: SOMATAM Definition Edge) from Berlin and Munich, Germany. The CT scanner has a maximum scanning speed of 230 mm/s1, a spatial resolution of 0.3 mm and a single source.

Creating the base model

The modeling process in this study has been shown in Figure 2. The initial and rough models including C6-S1 vertebrae, screws and growing rods were reconstructed based on CT images and MIMICS (version: 17.0; company: Materialise; location: Europe Belgium). After getting point clouds from MIMICS, the operations of further smoothing and surface patches divided were carried on through Geomagic Studio (version: 2013; company: Geomagic; location: Triangle, NC, United States). Then, individual CAD models were imported into a whole in SolidWorks (version: 2019; company: Dassault Systemes SE; location: Paris, France). It's worth noting that IVDs were built by lofting the superior and inferior vertebra surface rather than CT data since IVDs contained less bony material to image on CT. In the fourth step, the rest operations such as mesh division, material properties assignment and ligaments established were finished in Hypermesh (version: 14.0; company: Altair; location: Troy, Michigan, United States). In the fifth step, these assembled models were imported into ABAQUS (version: 2016; company: Dassault SIMULIAL; location: Providence, Rhode Island, United States) for simulation. Finally, the data post-processing was carried out in MATLAB (version: 2018a; company: MathWorks; location: Natick, Massachusetts, United States). The coronal view and sagittal view of reconstructed models with different growth phases and fixed segments was shown in Figure 3.

Adopted mesh and material properties

Bony structures and soft tissues were discretized to tetrahedral (C3D4) element type and hexahedral (C3D8) element type. For the same element size, hexahedral discretization will produce more element nodes than tetrahedral discretization which lead to the time-consuming phenomenon. This phenomenon can be avoided by discretizing some trivial structures using tetrahedral elements. This division method also achieved high accuracy and reliability. And the ligament tissues were modeled with three-dimensional truss elements and discretized in a one-dimensional line grid. These ligament tissues included the anterior longitudinal ligament (ALL), posterior longitudinal ligament (PLL), interosseous transverse ligament (ITL), capsular ligament (CL), interspinous ligament (ISL), supraspinous ligament (SSL), and ligament flavum (LF). Similarly, the IVDs were divided into fibrous annulus (AF), nucleus pulposus (NP) and cartilage endplate. Then, each material property is shown in Table 1.

Bony structures were assumed as linear elastic materials, without considering plastic deformation. Although there is overwhelming evidence that younger immature bone can undergo more plastic deformation prior to fracture than mature bone (Berteau et al., 2015; Szabo and Rimnac, 2022), the yield stress (about 100 MPa reported in (Currey and Pond, 1989) is not likely to be achieved in clinical surgery.

Constraint setting and validation

Many individual components were not combined into a finite element entity. Thus, an illustration of the spinal constraint setting is shown in Figure 4. A complete functional segment unit (FSU) consists of vertebrae, IVD, ligaments and a growing rod system. Among them, the IVD

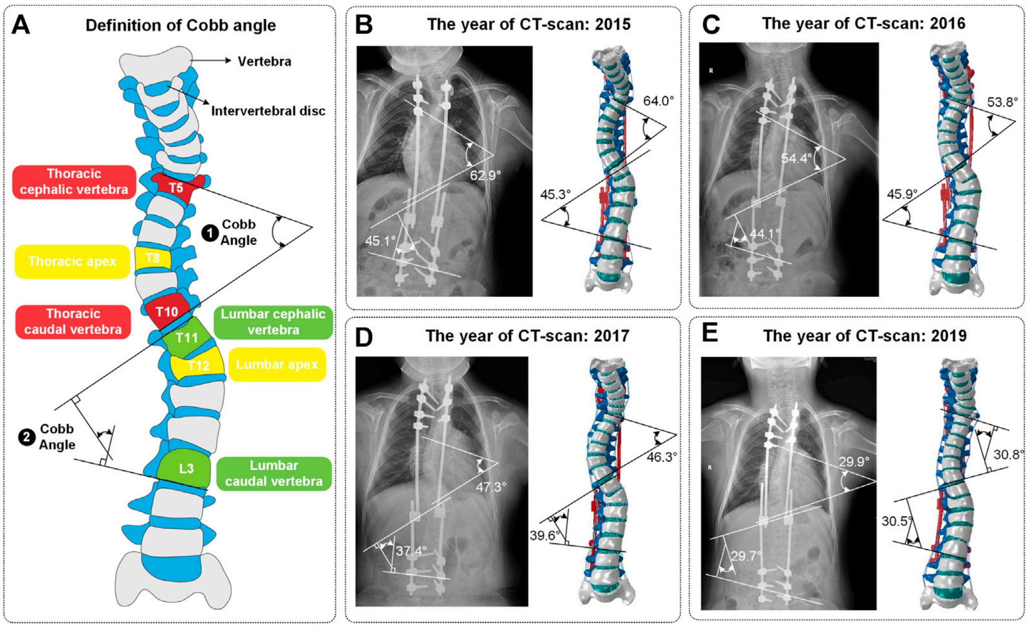

FIGURE 1
(A) Definition of Cobb angle. Cobb angle is the angle of intersection between the vertical of the superior edge of the cephalic vertebra and the vertical of the inferior edge of the caudal vertebra. **(B–E)** The four surgeries included one growing rod implantation and three spinal distractions. These four models were named Model_1, Model_2, Model_3 and Model_4. The Cobb angle of models conformed to the ones of CT images (mean error: 1.08°).

includes nucleus pulposus (NP), annulus fibrosus (AF) and endplates, the growing rod system includes the growing rods, domino connectors and screws (Figures 4A–C).

Additionally, these operations were performed: the vertebrae were connected by ligament, the vertebrae and IVDs were connected by binding, the S1 segment and ground were connected by binding, the facet joints were connected by finite sliding (friction coefficient = 0.01 (Cai et al., 2019)) and the growing rod and domino connector connected by sliding too (Figures 4D–F).

Soft tissues such as muscles are hard to reconstruct while the muscle force has a vital influence on finite element results. Moreover, the characteristics of muscle force are alterability and nonlinear. Here, the way of the follower load was used as an alternative mode to muscle force (Figure 4D). As published by Patwardhan et al. (Patwardhan et al., 2010), using a follower load provided a similar kinematics response as *in vivo*. A thermosensitive truss can transmit force by the principle that expansion with heat and contraction with cold. The thermal expansion effect can transfer the biomechanical load among the elements by assigning a temperature field change to a thermosensitive truss. The expansion coefficient α was defined for the prestressed element, and the unbonded prestress was determined using the following formula (Yoganandan et al., 2000):

$$\delta T = \varepsilon/\alpha \qquad (1)$$

Where δT is the thermal load for the iteration, ε is the thermal strain (growing strains) for the iteration, and α is an arbitrary number representing the thermal expansion coefficient.

The follower load of each vertebra is set based on Pasha's study and is shown in Table 2. Only the T1-S1 vertebral weight was defined in the literature (Pasha et al., 2014) and the percentage of body weight (BW) of the T1 segment was set to (1.1% + 8% of head weight). Thus, the C1-C7 vertebral weight to BW was defined as approximately 1.1%. In other words, the C6 and C7 vertebral weight of BW was set to 6.9 and 1.1%. Additionally, the T3-T5 vertebral weight was larger than T2 and T6 because the weight of superior limbs was taken into account. (El-Rich and Shirazi-Adl, 2005).

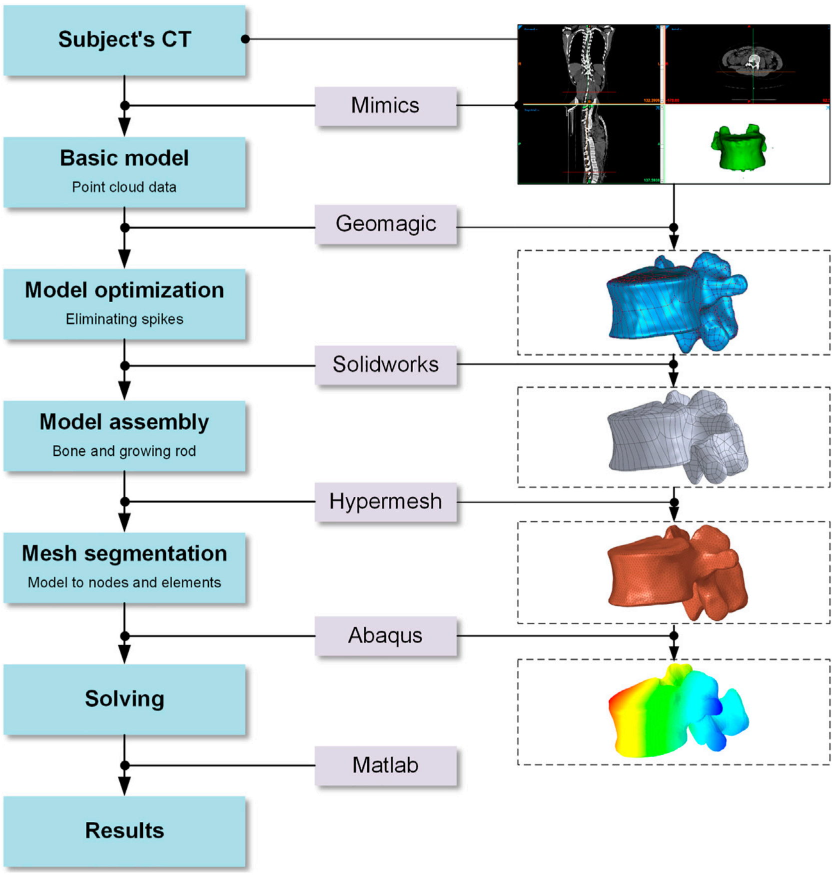

FIGURE 2
Modeling process in this study.

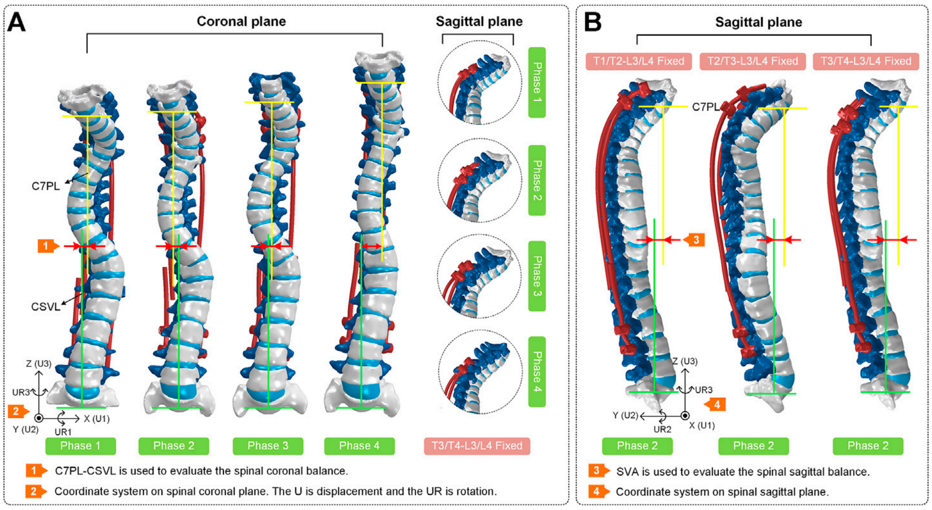

FIGURE 3
(A) Coronal view and sagittal view of the spines at four phases. The T3/T4-L3/L4 segments of each spine are fixed. The coronal balance parameters (C7PL-CSVL) of four models are shown to evaluate the surgical effects. **(B)** Sagittal view of spines in surgical phase 2. The T1/T2-L3/L4, T2/T3-L3/L4 and T3/T4-L3/L4 segments of each spine are fixed separately. The sagittal balance parameters (SVA) of three models are shown to evaluate the surgical effects.

TABLE 1 Material properties in the present finite element models.

Element construction	Element type	Elasticity modulus/ MPa	Poisson ratio	Cross-sectional area/mm^2	Scale factors	References
Cortical bone	Hexahedron	1.344e4	0.30	—	0.805(b)	(Currey, 2004; Berteau et al., 2014)
Cancellous bone	Quadrilateral	2.41e2	0.30	—	0.805(b)	Kopperdahl and Keaveny, (1998)
Posterior	Hexahedron	3.5e3	0.25	—	(a)	Rohlmann et al. (2009)
Endplate cartilage	Quadrilateral	2.38e1	0.40	—	(a)	Kurutz and Oroszváry, (2010)
Nucleus pulposus	Hexahedron	1.0e0	0.49	—	(a)	
Annulus fibrosus	Hexahedron	4.2e0	0.45	—	0.782(b)	
ALL	Three-dimensional truss	7.8e0	0.12	63.7	0.893(b)	Kurutz and Oroszváry, (2010)
PLL		1.0e1	0.11	20.0		
ITL		1.0e1	0.18	1.80		
CL		7.5e0	0.25	30.0		
ISL		8.0e0	0.14	30.0		
SSL		1.0e1	0.20	40.0		
LF		1.5e1	0.062	40.0		
Growing rod	Hexahedron	1.1e5	0.30	—	(a)	(Aakash et al., 2015)

(a) Indicates that the material parameters were the same as the values of an adult. (b) The scale factors were used to scale adult material parameters to child ones (Yoganandan et al., 2000).

Validation is an important step in building the credibility of numerical models (Babuska and Oden, 2004; Henninger et al., 2010). It is mainly used to verify that the material properties and spinal basic structure are correct. The spinal constraint settings used in validation were shown in Figure 4G. The grid cells of the C6 upper surface were coupled and applied a pure torque (0.5, 1.0, 1.5 and 2.0 Nm) in flexion and extension directions. The lower surface of C7 was bound with the ground. Finally, the angular displacement of the C6-C7 segment was achieved and it displayed that the average error between the experiment and simulation in flexion and extension is 5.7%

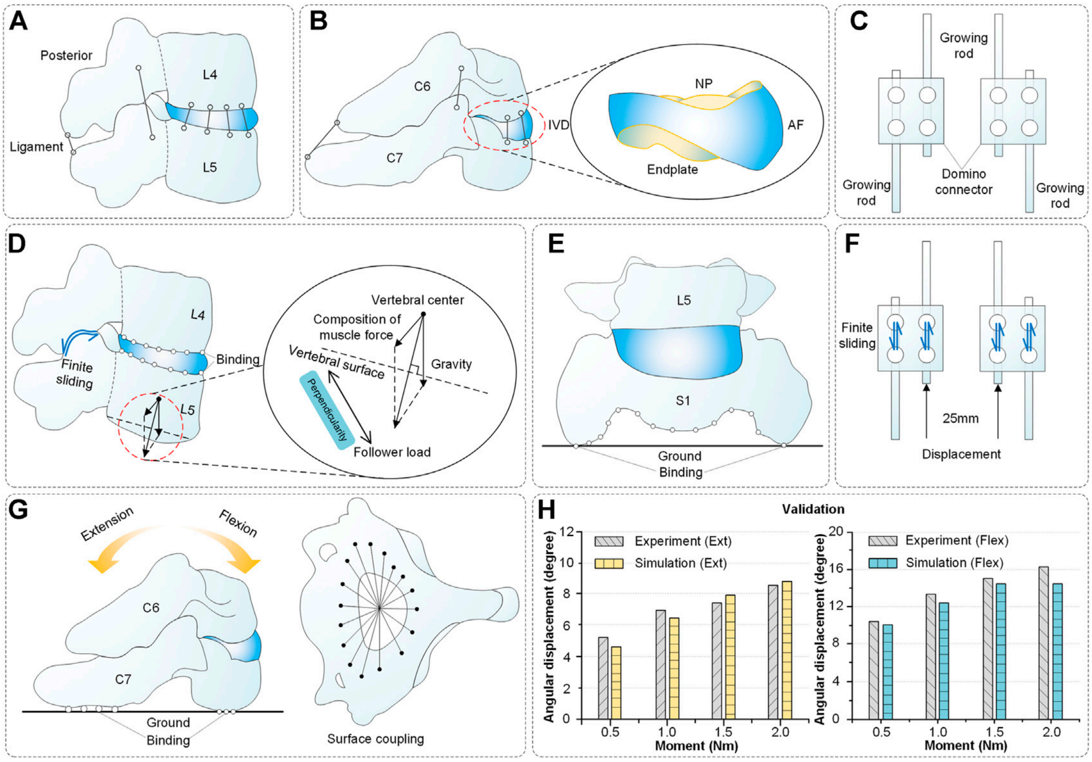

FIGURE 4
Spinal composition, constraint setting and validation. **(A-B)** Components of spinal reconstruction. **(C)** Structure of growing rods and domino connectors. **(D)** Spinal constraint setting (L4-L5 segments as an example) includes finite sliding (facet joints), binding (vertebra and IVD) and follower load (vertebrae). **(E)** Spinal constraint setting: binding (S1 segment and ground). **(F)** Constraint setting: finite sliding (growing rod and domino connector), displacement load (growing rod, 0–25 mm). **(G)** Spinal constraint setting for validation. The superior surface of C6 was coupled and applied a pure torque. The inferior surface of C7 was bound with the ground. **(H)** Validation results of the model.

and 6.9% (Figure 4H) (Li et al., 2019). In addition, as shown in Figure 1, the mean error between the Cobb angles of the reconstructed model and CT images is only 1.08°.

Result

Spinal kinematic and biomechanical response after distraction surgery

Kinematic and biomechanical responses to distraction surgery are shown in Figure 5. In this condition, the distraction distance is significantly correlated with the distraction force and Cobb angle in all four models (Figure 5A). When the distraction distance is 25 mm, the distraction force reaches the maximum (221 N of Model_1, 265 N of Model_2, 343 N of Model_3 and 420 N of Model_4) (Figure 5B). The Cobb angle of thoracic scoliosis and lumbar scoliosis becomes smaller as the distraction distance increases. The slopes of the thoracic curve and lumbar curve are shown (K = −0.46/−0.46/−0.40/−0.29 of the thoracic curve and K = −0.40/−0.40/−0.35/−0.30 of the lumbar curve) (Figures 5C,D).

The spinal rotation in three-dimensional directions is shown in Figure 6. The nephogram illustrated that the spinal middle-upper parts had a higher rotational value and the spinal middle-lower parts had a lower one (Figure 6A). In the UR1 direction, the cervical segment had the largest motion range which characterized cervical lordosis. In the UR2 direction, the thoracic segments and lumbar segments had an opposite and obvious movement which displayed a process of straightening the spine. In the UR3 direction, the positions of maximum rotation on the spine were inconsistent. The mean values of the rotational angle increased almost linearly as the distraction distance increased. The maximum values of rotational angle were recorded at each distraction. The rotational angle is the largest (17.68° in UR1, 9.14° in UR2, and 6.36° in UR3) when the distraction distance is 25 mm. The spine had maximum distraction efficiency in the UR1 direction, followed by UR2 and UR3 (Figures 6B–D).

The spinal displacement of four models in three directions is shown in Figure 7. The nephogram illustrated that the largest deformation occurred in the middle-upper spine (Figure 7A). In the U1 direction, the cervical and thoracic segments had the largest motion range which characterized the C7PL-CSVL getting greater. In the U2 direction, the cervical segment had the largest negative movement value which displayed the process of cervical lordosis. In the U3 direction, there was an obvious movement in the cervical segment which represented the progress of the spine getting straight.

It is noteworthy that the presence of cervical lordosis caused the downward displacement of the spinal topmost segment. The displacement is significantly related to the distraction distance. The displacement value is the largest when the distraction distance is 25 mm (8.29 mm in U1, −23.05 mm in U2 and 3.38 mm in U3). The maximum distraction efficiency occurred in U2, followed by U1 and U3 (Figures 7B–D). The mean values of C7PL-CSVL and SVA of the four models were shown in the subgraph of Figure 7B and Figure 7C. The coronal balance decreased first and then increased (the minimum value is 6.2 mm when distraction distance is 5 mm) and the sagittal balance (SVA) increased reversely (from −2 mm to −22 mm).

Some researchers investigated how the forces increased during every distraction episode (Figure 8). Each distraction force was recorded and the maximum and minimum distraction forces formed the grey shaded area. The maximum distraction force in literature was 644 N (Noordeen et al., 2011) and the one in this paper was 420 N. The trend of mean distraction forces in this paper is consistent with the literature that they increased as the distraction episode increased. The mean distraction forces in this paper are all in the gray shaded area (Noordeen et al., 2011; Teli et al., 2012; Agarwal et al., 2018).

The movement of fixed segments is worth studying to understand the whole spinal movement. Thus, the displacements of T3 and T4 are shown in Figure 9. Significant changes occurred in the anterior and posterior parts of the vertebra. The anterior part had a lower displacement and the posterior part had a larger one. The difference between the highest value and the lowest value represents the middle-part rotation of the vertebra (T3: 12.2/13.2/14.5/16.0 mm in four models; T4: 12.8/14.1/14.5/16.4 mm in four models). The initial Cobb angle is inversely proportional to the difference (Figures 9A,B). The model in late growth phases had the smallest maximum IVD stress at the same distraction distance (Figure 9C). The downward percentage for each period has been shown 40%/33%/17% (5 mm), 14%/33%/17% (10 mm), 10%/30%/11% (15 mm), 13%/26%/3% (20 mm) and 8%/24%/6% (25 mm) (Figure 9C).

Distraction energy consumption is an index that evaluates the distraction force required for each 1° reduction of the Cobb angle. The index of the thoracic curve and lumbar curve is shown in Figure 10. The distraction energy consumption of the four models had the following trend: Model_1 < Model_2 < Model_3 < Model_4 (Figures 10A,B). Every curve had an upward trend, especially with a high slope at the distraction distance of 5–15 mm. The distraction energy consumption was the largest (thoracic curve: 64.28N/° of Model_4, 38.10N/° of Model_3, 26.32N/° of Model_2 and 24.48N/° of Model_1; lumbar curve: 69.23N/° of Model_4, 50.00N/° of

TABLE 2 The follower load of C6-S1 spinal segments (Pasha et al., 2014).

Vertebral	Percentage of BW (%) in Pasha's study	Percentage of BW (%) in this study	Follower load(N) (Patient's BW = 300N)
C6	—	6.9 (Head)	20.7
C7	—	1.1	3.3
T1	1.1 + 8 (Head)	1.1	3.3
T2	1.1		3.3
T3	1.3 + 4.0 (Superior limbs)		15.9
T4	1.3 + 4.0 (Superior limbs)		15.9
T5	1.3 + 4.0 (Superior limbs)		15.9
T6	1.3		3.9
T7	1.4		4.2
T8	1.5		4.5
T9	1.6		4.8
T10	2.0		6.0
T11	2.1		6.3
T12	2.5		7.5
L1	2.4		7.2
L2	2.4		7.2
L3	2.3		6.9
L4	2.6		7.8
L5	2.6		7.8
S1	2.6		7.8

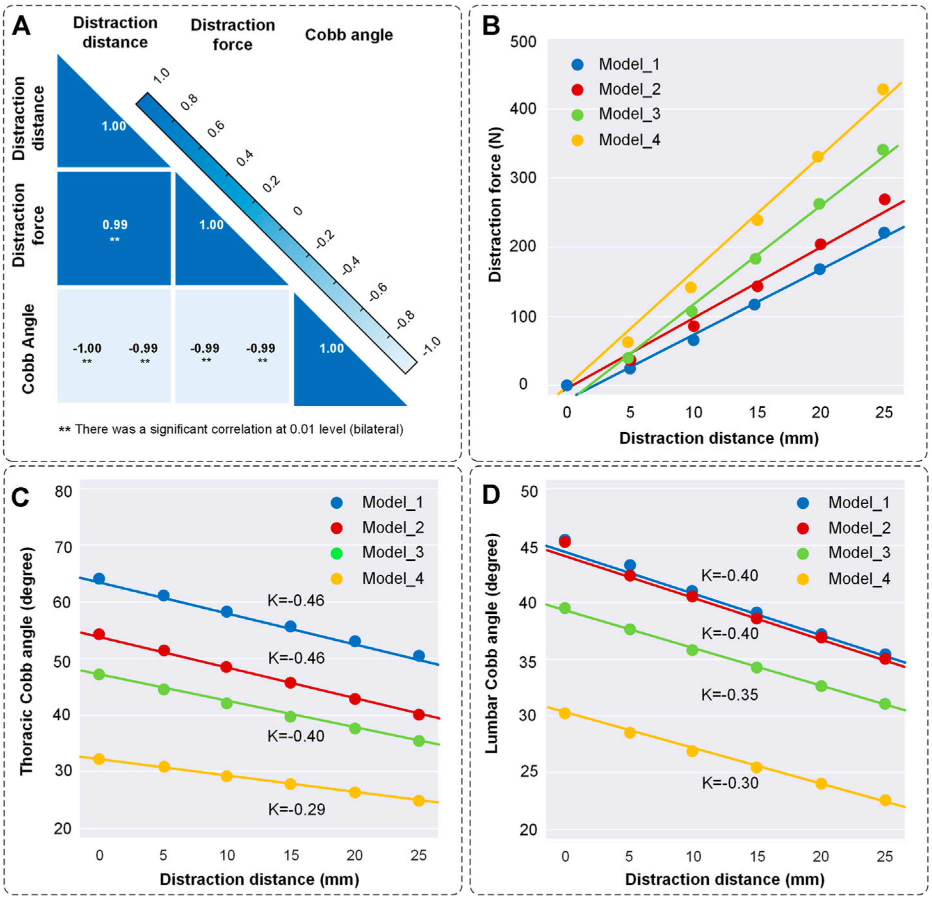

FIGURE 5
Changes of distraction force and the Cobb angle of thoracic and lumbar curves. **(A)** Correlation coefficient heatmap. The liner relations between distraction distance, distraction force and Cobb angle were normally distributed and significantly correlated at 0.01 level according to the Shapiro-Wilk test and Pearson correlation. **(B)** Scatter diagram of distraction distance and distraction force. K represents the slope of the curves. **(C)** Scatter diagram of distraction distance and the Cobb angle of thoracic scoliosis. **(D)** Scatter diagram of distraction distance and the Cobb angle of lumbar scoliosis. The straight was fitted by scatter points.

Model_3, 34.63N/° of Model_2 and 28.56N/° of Model_1) when the distraction distance was 25 mm.

Spinal kinematic and biomechanical responses in different fixed modes are shown in Figure 11. The thoracic and lumbar Cobb angles were all decreased as the distraction distance increased. The Cobb angle of the thoracic and lumbar curve was reduced (12.9°/9.4° in T1/T2-L3/L4 fixed-mode group; 13.5°/10.2° in T2/T3-L3/L4 fixed-mode group; 13.2°/10.4° in T3/T4-L3/L4 fixed-mode group) and the correct rate was increased (24.3%/20.5% in T1/T2-L3/L4 fixed-mode group; 25.5%/22.3% in T2/T3-L3/L4 fixed-mode group; 24.8%/22.6% in T3/T4-L3/L4 fixed-mode group) when the growing rod was extended to 25 mm. No significant differences were seen in the groups. The Cobb angle of the T2/T3-L3/L4 fixed-mode group is slightly lower than the other groups (Figures 11A,B). When the distraction distance was less than 5 mm, there was little difference in the distraction force among the three groups which were all less than 65 N. Subsequently, the difference became greater because the slope increased with every 5 mm distraction. The maximum distraction force in the three groups was 311.5, 354.3 and 420.1 N (Figure 11C). The maximum IVD stress is proportional to the distraction distance in the three groups, in which the maximum stress was located in the lower thoracic segment (T5-T10). No obvious pattern was observed in the three groups (Figure 11D).

Discussion

Periodical and consecutive distraction is an effective treatment for severe EOS, which enables the spinal coronal and sagittal plane deformity correction. The position of each distraction directly determines the rate of rod fracture, which is related to the distraction force. However, more attention has been paid to the growing rod and the spinal biomechanical environment was ignored. Cheung et al. reported complications occur in 60% of patients,

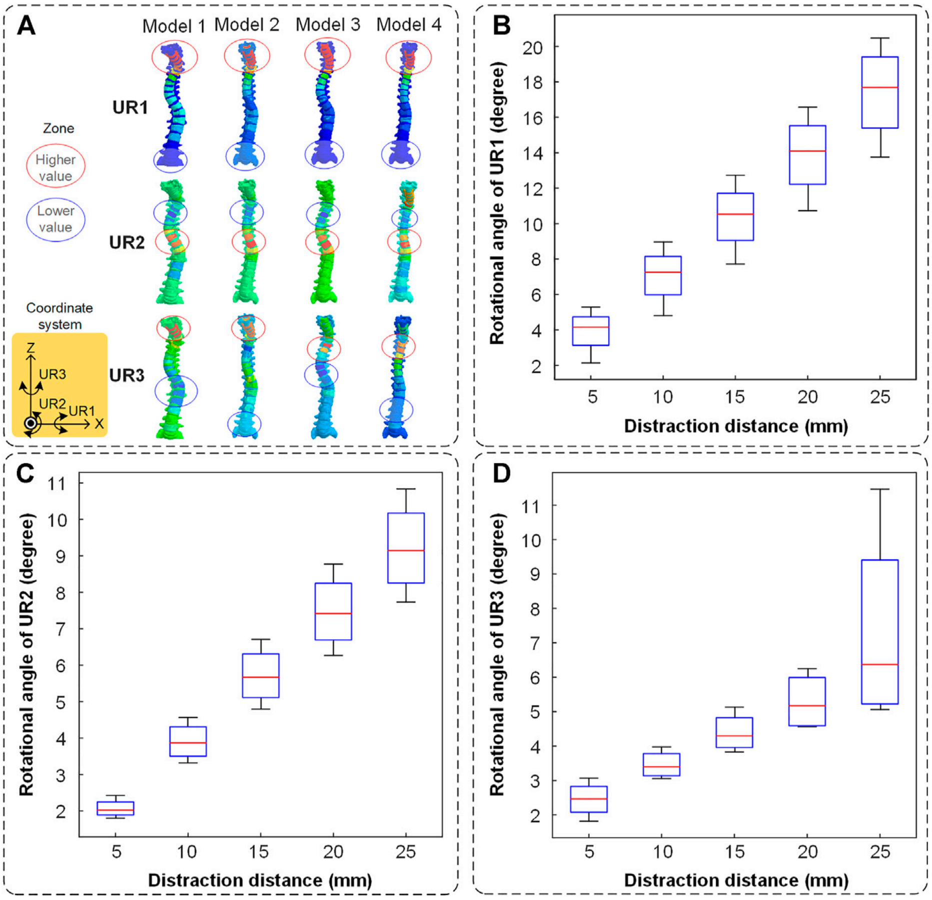

FIGURE 6
The spinal rotation in three directions. **(A)** The nephogram of finite element results (when the distraction distance is 25 mm). The higher value is labeled in a red circle and the lower value is labeled in a blue circle. **(B)** The spinal rotation in the UR1 direction. **(C)** The spinal rotation in the UR2 direction. **(D)** The spinal rotation in the UR3 direction.

including distraction failure, proximal junctional kyphosis (PJK) and implant loosening. These patients all needed reoperation via the extension of the proximal foundation or exchanging larger screws (Cheung et al., 2019). Watanabe et al. performed a retrospective multicenter review of 88 patients with EOS and found that 23% of patients developed PJK (Watanabe et al., 2016). The occurrence of PJK is due to the ossification in fixed segments and motor compensation in unfixed segments. These phenomena cause reoperation that is related to surgical phases and distraction mode. Thus, more attention paid to the kinematic and biomechanical environment in local structure is momentous for understanding complications unrelated to the rod itself.

Many researchers have tried to judge the optimal distraction force by whether the rod is broken or not (Teli et al., 2012; Agarwal et al., 2017a). They ignored whether the spinal coronal and sagittal plane was still balanced. Other researchers also focused on the effect of distraction frequency on the reduction of rod fracture. Agarwal et al.(2015) confirmed the importance of a shorter distraction period in reducing stresses on the rods. But a shorter distraction frequency resulted in multiple operations, which lead to greater injury for patients. Magnetically driven growing rods as an alternative to traditional growing rod technology can increase the distraction frequency and reduce surgical injury at the same time (Agarwal et al., 2014a). It is also not popular because of its limited distraction force and high rod breaking rate (Rushton et al., 2019). Fortunately, Agarwal et al. (2015) mentioned a great sagittal balance of the spine in optimal distraction force and the reduction of Cobb angle. But they have not revealed the law of diminishing returns that the reduction rate of Cobb angle decreased with the increase of distraction times (Sankar et al., 2011). The present study aimed to investigate the kinematic and biomechanical response of the spine after traditional growing rod surgery. To achieve this, distraction force, spinal displacement and rotation in

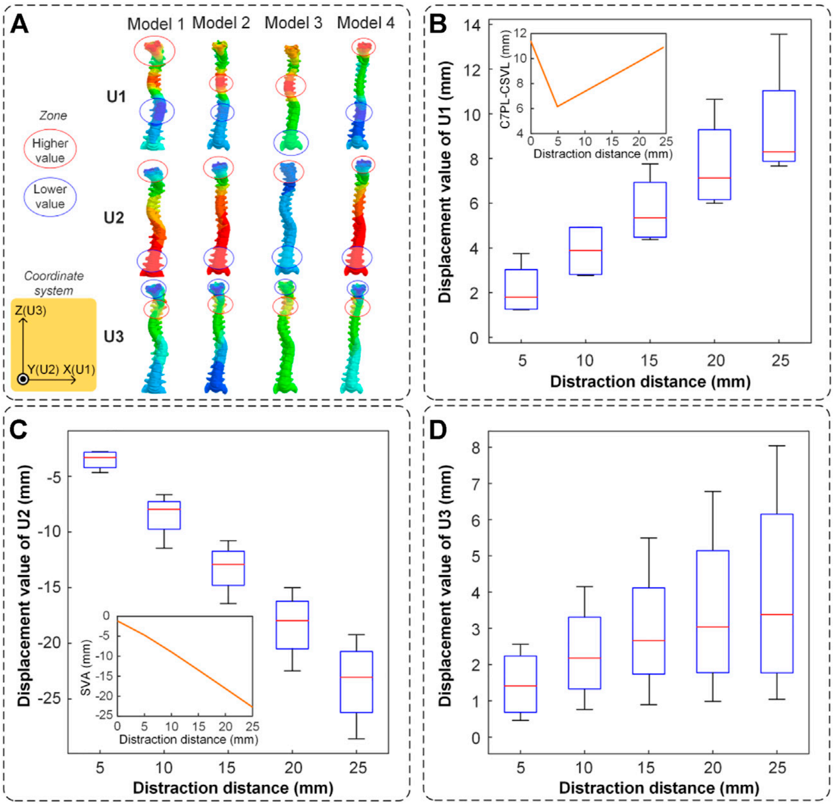

FIGURE 7
The spinal displacement in three directions. **(A)** The nephogram of finite element results (when the distraction distance is 25 mm). The higher value is labeled in a red circle and the lower value is labeled in a blue circle. **(B)** The spinal maximum displacement in the U1 direction. The mean value of C7PL-CSVL was measured and displayed in the subgraph. **(C)** The spinal maximum displacement in the U2 direction. The mean value of SVA was measured and displayed in the subgraph. **(D)** The spinal maximum displacement in the U3 direction.

three-dimensional directions, reduction of thoracic and lumbar Cobb angle and distraction energy consumption were measured.

As an initial factor, distraction distance affected the force on the growing rod and the spinal shape. Model_4 had the minimum initial Cobb angle and the largest distraction force. Understandably, the downward component of the muscle force on the vertebra increases with the decrease of Cobb angle, which made the upward support force smaller (Figure 5B). Some studies had shown that large displacement was achieved with a relatively small distraction force (Noordeen et al., 2011; Shekouhi et al., 2022). This condition commonly occurred in the prophase distraction. However, there is a lack of sufficient statistical data to establish a clear timeline or a threshold of distraction distance. There are various variables that could affect the conclusion, including the initial Cobb angles, number of fixed segments, time of the first implantation and distraction frequency, etc. Although lacking sufficient evidence, it can be considered that a small distraction force is accompanied by a large displacement when the distraction distance is 0–15 mm. Additionally, the spinal stiffness was increased due to the spine growing itself and skeletal maturity, which caused a greater distraction force (Noordeen et al., 2011). The reduction trend of thoracic and lumbar Cobb angle was consistent that Model_4 had the minimal Cobb angle changes. The trend confirmed the law of diminishing returns (Figures 5C,D). These results enlightened us that a reduced distraction distance should be appropriately performed in spine straightening gradually. At the same time, the time interval of distraction should be prolonged to 6–9 months in every distraction.

Positive benefits of spinal distraction should be the rotation of each vertebra in the UR2 direction. Conversely, spinal rotation in the UR1 direction represented cervical lordoses such as flexion or extension, and the one in the UR3 direction represented the left-right torsion of the human body (Figure 6A). The rotational situation exhibited that cervical lordosis had the largest change in the distraction process and self-rotation inevitably occurred. The negative

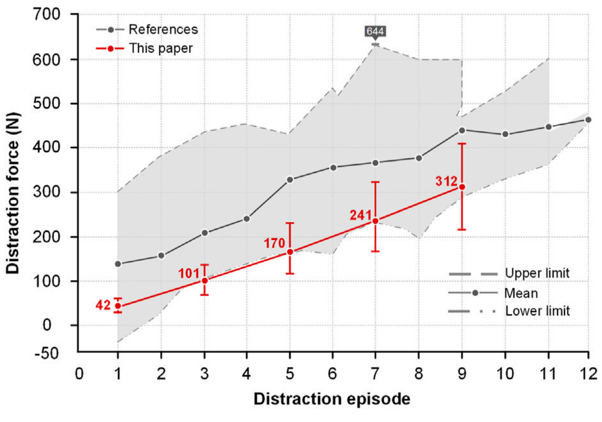

FIGURE 8
Comparison of distraction force between this paper and literature. The maximum and minimum values were recorded from the literature and were merged into a gray region. The upper boundary of the gray region represented the largest distraction force and the lower boundary represented the smallest one. Accordingly, the gray line represents the mean force value in literature. The upper and lower limits of four models were also recorded and the red line was used to display the mean value in this paper.

benefits of rotation basically occurred in the cervical spine, especially the segment unfixed. The thoracic vertebra and lumbar vertebra had an opposite rotational direction and that is why the thoracic and lumbar scoliosis is decreasing (Figure 6). The positive benefits of spinal distraction should be the distance of each vertebra in the U3 direction. Additionally, the spinal movement in the U1 direction represents a horizontal displacement of the cervical thoracic segment in the coronal plane. The coronal balance parameter C7PL-CSVL decreased first and increased (Figures 7A,B). The spinal movement in the U2 direction represents the trend of cervical flexion. The sagittal balance parameter SVA became greater (Figures 7A,C). It reminds us that a single distraction should not be too large, otherwise the coronal and sagittal balance will backfire.

In the movement of the U3 direction, the thoracic segment had a forward displacement and the cervical segment had a reverse displacement. It explained that spinal scoliosis was gradually improving, while the existence of the original cervical curvature caused it to move forward and downward. This phenomenon is consistent with the rotational situation. Another reason for this phenomenon is that the distraction force acted on the posterior vertebra rather than the vertebra center, which caused an additional displacement of the posterior vertebra. The U3 displacement of the T3-T4 anterior and posterior vertebra showed an upward trend and reached the maximum in Model_4 (Figure 9). For the other models, Model_4 has less displaceable space in the +U3 direction and a more displaceable space in the −U3 direction. The maximum IVD stress also has been measured, which was an index that characterized the rate of complications to some extent. The trend showed that later implantation of the growing rod can effectively reduce the maximum IVD stress, or reduce the rate of complication (Figure 9C). Bess

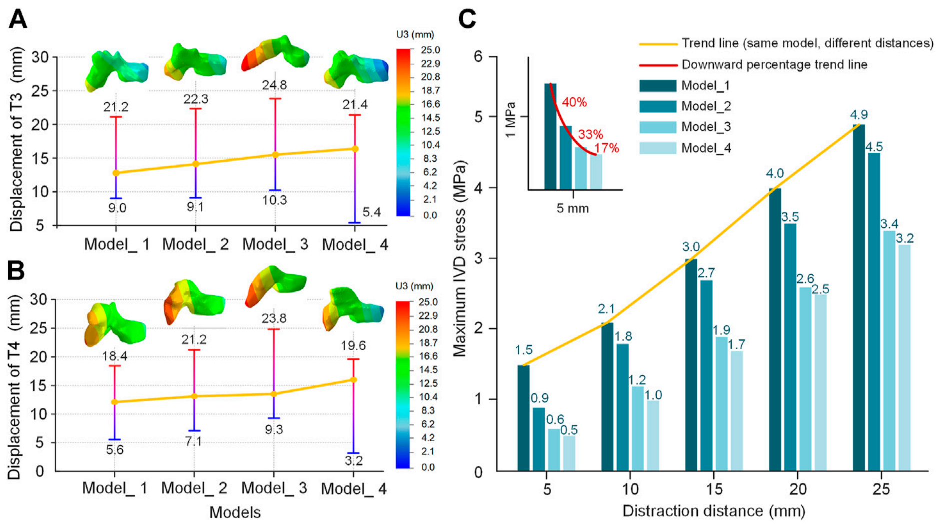

FIGURE 9
The displacement of the T3 and T4 vertebra in the U3 direction (distraction distance is 25 mm). **(A)** Displacement of T3. **(B)** Displacement of T4. **(C)** The maximum IVD stress of four models from different growth phases at different distraction distances. The asymptotes represent changes going from a low value (blue) to a high value (red). The yellow line is the difference between the low value and high value.

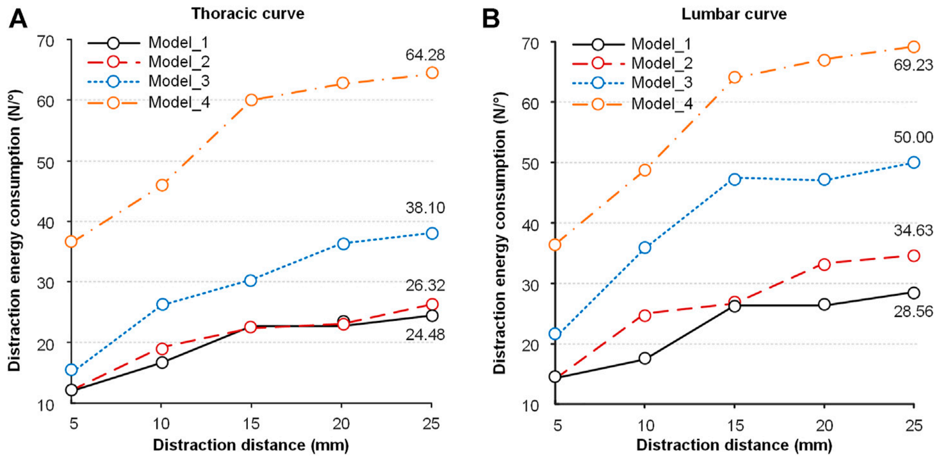

FIGURE 10
Distraction energy consumption of the four models in the process of distraction. **(A)** The distraction energy consumption in the thoracic curve. **(B)** The distraction energy consumption in the lumbar curve.

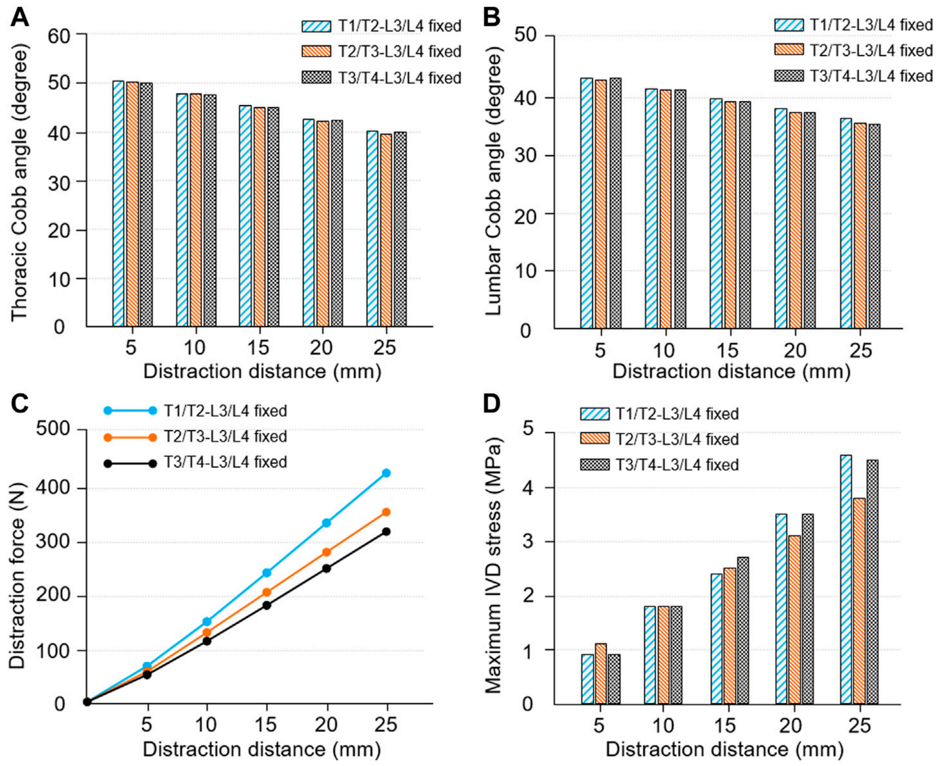

FIGURE 11
Spinal kinematic and mechanical responses in different fixed modes. **(A)** The changes of thoracic Cobb angle as the distraction distance increased. **(B)** The changes of lumbar Cobb angle as the distraction distance increased. **(C)** The relationship between distraction distance and distraction force. **(D)** The relationship between distraction distance and maximum IVD stress.

et al. (2010) demonstrated that rates could be reduced by delaying initial implantation (13% decrease for every additional year of inpatient age at the beginning of treatment).

Distraction energy consumption is very important for understanding the law of diminishing returns (Figure 10). It represents the distraction force needed for each 1° distraction. For all models, the distraction energy of Model_4 is the largest, followed by Model_3, Model_2, and Model_1. This law enlightens us that an optimal distraction distance is accompanied by a lower distraction force and a better correction effect, rather than the largest distraction force. This is why some researchers believe applying less distraction with more frequent surgeries is favorable. However, additional surgeries would increase the risk of complications such as wound infection (Bess et al., 2010; Agarwal et al., 2015, 2019). This risk increased by 24% at each additional surgery, which had been shown by authors (Bess et al., 2010; Mundis et al., 2013).

The influences of fixed segments on the kinematic and biomechanical response have been studied (Figure 11). It exhibited that the intragroup trend was consistent with the trend mentioned above, while the difference between groups is not obvious. Among the results, the curve of distraction force had a gradually rising slope and the T3/T4-L3/L4 fixed model had the largest distraction force (Pei et al., 2022). The spinal structure itself has a stage of easy deformation due to the elasticity of soft tissue, which includes stages of compression and tension. Thus, the more the vertebral numbers in the fixed area, the larger the deformable space.

After understanding the law of diminishing returns, there is some specific advice for surgeons. Although the time interval of distraction has been proposed to be 6 months in early experience with growing rod procedures, more and more surgeons are used to extending the frequency to 9–12 months/time. Because continued forceful distraction in dysplastic spine theoretically includes PJK. More recently, other authors have reported similar experiences. Carbone et al. (2019) reported a 1-year distraction interval in their cohort of NF1 patients. They explained that less frequent lengthening surgeries reduce the psychological burden on their patient. Another reason for the long distraction interval used in this cohort was that the risk of wound infection is minimized by reducing the frequency of distraction. Additionally, a single over-distraction will backfire especially in spine straightening. Thus, decreasing distraction distance and increasing interval may be considered by the surgeons to reduce the rod fracture and complications.

There are a few limitations to this study. First, the distraction amounts of bilateral growing rods were not adjusted according to the initial state of the model, which should be considered during the operation, resulting in additional imbalance. Second, there were no corresponding biomechanical experiments to verify the finite element results. It was very difficult to obtain a long segmental specimen of scoliosis in children. Third, material properties that change with age were not considered. Finally, this paper did not consider other types of scoliosis, which may lead to accidental results. While the distraction distance and distraction frequency are vital to understanding rod fracture, there are other factors that need further investigation such as the patient's age (Bess et al., 2010; Jiang et al., 2011; Upasani et al., 2016) and T1-S1 growth rate (Abolaeha et al., 2012; Agarwal, 2015, 2015).

Conclusion

The kinematic and biomechanical responses of the spine occurring after growing rod distraction surgery were investigated. Compared to previous studies, a more realistic spinal environment was restored, being simulated the postoperative effects of different growth phases and different fixed segments on spinal distraction. Our results show that the process of spinal distraction may be accompanied by the spinal re-imbalance in the coronal sagittal plane. The positive distraction benefits of the spine are inversely proportional to the distraction distance. In addition, there is an optimal distraction force, rather than the maximum one, to ensure lower distraction energy consumption and lower pressure on the rod and IVD. The choice of optimal distraction force depends on the response of the fixed segment and the positive return we obtained. In summary, more attention should be paid to the spinal balance and aesthetic evaluation, rather than relying on whether the rod is broken to set the optimal distraction force. This study can provide a better understanding of the biomechanical response after spinal distraction surgery. The next avenue of future work could be adding more types of the spine to verify our results.

Data availability statement

The raw data supporting the conclusions of this article will be made available by the authors, without undue reservation.

Ethics statement

The studies involving human participants were reviewed and approved by BM20220087. Written informed consent to participate in this study was provided by the participants' legal guardian/next of kin. The animal study was reviewed and approved by BM20220087. Written informed consent was obtained from the minor(s)' legal guardian/next of kin for the publication of any potentially identifiable images or data included in this article.

Author contributions

Conceptualization, BP and XW; methodology, DL; software, YX and CM; validation, YX and CM; investigation, BP; resources, BP; data curation, BP and DL; writing—original draft preparation, BP, DL, and XW; writing—review and editing, BP, DL, and XW; visualization, SW; supervision, SW; project administration, XW; funding acquisition, BP All authors have read and agreed to the published version of the manuscript.

Funding

This research was funded by the National Natural Science Foundation of China (Nos. 11972065), Beijing Natural Science Foundation (L202006) and the Defense Industrial Technology Development Program (JCKY2021601B021).

Conflict of interest

The authors declare that the research was conducted in the absence of any commercial or financial relationships that could be construed as a potential conflict of interest.

Publisher's note

References

Abolaeha, O. A., Weber, J., and Ross, L. T. (2012). Finite element simulation of a scoliotic spine with periodic adjustments of an attached growing rod. Conference proceedings: Annual International Conference of the IEEE Engineering in Medicine and Biology Society. IEEE Engineering in Medicine and Biology Society. Conference: 5781–5785. doi:10.1109/EMBC.2012.6347308

Agarwal, A., Agarwal, A. K., Jayaswal, A., and Goel, V. K. (2014a). Effect of distraction force on growth and Biomechanics of the spine: A finite element study on normal juvenile spine with dual growth rod instrumentation. *Spine Deform.* 2 (4), 260–269. doi:10.1016/j.jspd.2014.03.007

Agarwal, A., Agarwal, A. K., Jayaswal, A., and Goel, V. (2014b). Smaller interval distractions may reduce chances of growth rod breakage without impeding desired spinal growth: A finite element study. *Spine Deform.* 2 (6), 430–436. doi:10.1016/j.jspd.2014.08.004

Agarwal, A., Zakeri, A., Agarwal, A. K., Jayaswal, A., and Goel, V. K. (2015). Distraction magnitude and frequency affects the outcome in juvenile idiopathic patients with growth rods: Finite element study using a representative scoliotic spine model. Toledo, Ohio, USA. *Spine J.* 15 (8), 1848–1855. doi:10.1016/j.spinee.2015.04.003

Agarwal, A., Jayaswal, A. K., Goel, V. K., and Agarwal, A. K. (2017). Letter to the editor concerning "rod fracture and lengthening intervals in traditional growing rods: Is there a relationship?" by P. Hosseini et al. Eur spine J (2016). *Eur. Spine J.* 26, 1696–1697. doi:10.1007/s00586-017-5102-y

Agarwal, A., Agarwal, A. K., Jayaswal, A., and Goel, V. K. (2017a). Outcomes of optimal distraction forces and frequencies in growth rod surgery for different types of scoliotic curves: An in silico and *in vitro* study. *Spine Deform.* 5, 18–26. doi:10.1016/j.jspd.2016.09.047

Agarwal, A., Jayaswal, A., Goel, V. K., and Agarwal, A. K. (2018b). Patient-specific distraction regimen to avoid growth-rod failure. *Spine* 43 (4), E221–E226. doi:10.1097/BRS.0000000000002286

Agarwal, A., Goswami, A., Vijayaraghavan, G. P., Srivastava, A., Kandwal, P., Nagaraja, U. B., et al. (2019). Quantitative characteristics of consecutive lengthening episodes in early-onset scoliosis (EOS) patients with dual growth rods. *Spine (Phila Pa 1976)* 44 (6), 397–403. doi:10.1097/BRS.0000000000002835

Agarwal, A. (2015).Mitigating biomechanical complications of growth rods in juvenile idiopathic scoliosis. Toledo (OH): University of Toledo. *Doctoral dissertation.* Available at: http://rave.ohiolink.edu/etdc/view?acc_num=toledo1429875994.

Akbarnia, B. A., Marks, D. S., Boachie-Adjei, O., Thompson, A. G., and Asher, M. A. (2005). Dual growing rod technique for the treatment of progressive early-onset scoliosis. *Spine* 30, S46–S57. doi:10.1097/01.brs.0000175190.08134.73

Akbarnia, B. A., Breakwell, L. M., Marks, D. S., McCarthy, R. E., Thompson, A. G., Canale, S. K., et al. (2008). Dual growing rod technique followed for three to eleven years until final fusion. *Spine* 33, 984–990. doi:10.1097/BRS.0b013e31816c8b4e

Babuska, I., and Oden, J. T. (2004). Verification and validation in computational engineering and science: Basic concepts. *Comput. Methods Appl. Mech. Eng.* 193 (36-38), 4057–4066. doi:10.1016/j.cma.2004.03.002

Berteau, J.-P., Baron, C., Pithioux, M., Launay, F., Chabrand, P., and Lasaygues, P. (2014). *In vitro* ultrasonic and mechanic characterization of the modulus of elasticity of children cortical bone. *Ultrasonics* 54 (5), 1270–1276. doi:10.1016/j.ultras.2013.09.014

Berteau, J.-P., Gineyts, E., Pithioux, M., Baron, C., Boivin, G., Lasaygues, P., et al. (2015). Ratio between mature and immature enzymatic cross-links correlates with post-yield cortical bone behavior: An insight into greenstick fractures of the child fibula. *Bone* 79, 190–195. doi:10.1016/j.bone.2015.05.045

Bess, S., Akbarnia, B. A., Thompson, G. H., Sponseller, P. D., Shah, S. A., El Sebaie, H., et al. (2010). Complications of growing-rod treatment for early-onset scoliosis. *J. Bone Jt. Surgery-American Volume* 92 (15), 2533–2543. doi:10.2106/JBJS.I.01471

Cai, X.-Y., Sang, D., Yuchi, C.-X., Cui, W., Zhang, C., Du, C.-F., et al. (2020). Using finite element analysis to determine effects of the motion loading method on facet joint forces after cervical disc degeneration. *Comput. Biol. Med.* 116, 103519. doi:10.1016/j.compbiomed.2019.103519

Carbone, M., Vittoria, F., and Del Sal, A. (2019). Treatment of early-onset scoliosis with growing rods in patients with neurofibromatosis-1. *J. Pediatr. Orthop. B* 28 (3), 278–287. doi:10.1097/BPB.0000000000000627

Cheung, J. P. Y., Bow, C., Samartzis, D., Kwan, K., and Cheung, K. M. C. (2016). Frequent small distractions with A magnetically controlled growing rod for early-onset scoliosis and avoidance of the law of diminishing returns. *J. Orthop. Surg. Hong. Kong)* 24 (3), 332–337. doi:10.1177/1602400312

Cheung, J. P. Y., Yiu, K., Kwan, K., and Cheung, K. M. C. (2019). Mean 6-year follow-up of magnetically controlled growing rod patients with early onset scoliosis: A glimpse of what happens to graduates. *Neurosurg.* 84 (5), 1112–1123. doi:10.1093/neuros/nyy270

Currey, J. D., and Pond, C. M. (1989). Mechanical properties of very young bone in the axis deer (*Axis axis*) and humans. *J. Zoology* 218 (1), 59–67. doi:10.1111/j.1469-7998.1989.tb02525.x

Currey, J. D. (2004). Tensile yield in compact bone is determined by strain, post-yield behaviour by mineral content. *J. Biomechanics* 37 (4), 549–556. doi:10.1016/j.jbiomech.2003.08.008

El-Rich, M., and Shirazi-Adl, A. (2005). Effect of load position on muscle forces, internal loads and stability of the human spine in upright postures. *Comput. Methods Biomechanics Biomed. Eng.* 8 (6), 359–368. doi:10.1080/10255840500445630

Elsebai, H. B., Yazici, M., Thompson, G. H., Emans, J. B., Skaggs, D. L., Crawford, A. H., et al. (2011). Safety and efficacy of growing rod technique for pediatric congenital spinal deformities. *J. Pediatr. Orthop.* 31 (1), 1–5. doi:10.1097/BPO.0b013e318202c1f0

Henninger, H. B., Reese, S. P., Anderson, A. E., and Weiss, J. A. (2010). Validation of computational models in Biomechanics. *Proc. Inst. Mech. Eng. H.* 224 (7), 801–812. doi:10.1243/09544119JEIM649

Jiang, Y., Zhao, Y., Wang, Y. P., Qiu, G. X., Weng, X. S., and Li, Y. (2011). Lung function after growing rod surgery for progressive early-onset scoliosis: A preliminary study. *Chin. Med. J. Engl.* 124 (23), 3858–3863. doi:10.3760/cma.j.issn.0366-6999.2011.23.005

Kopperdahl, D. L., and Keaveny, T. M. (1998). Yield strain behavior of trabecular bone. *J. Biomechanics* 31 (7), 601–608. doi:10.1016/S0021-9290(98)00057-8

Kurutz, M., and Oroszváry, L. (2010). Finite element analysis of weightbath hydrotraction treatment of degenerated lumbar spine segments in elastic phase. *J. Biomechanics* 43 (3), 433–441. doi:10.1016/j.jbiomech.2009.10.004

Lemans, J. V. C., Wijdicks, S. P. J., Koutsoliakos, I., Hekman, E. E. G., Agarwal, A., Castelein, R. M., et al. (2021). Distraction forces on the spine in early-onset scoliosis: A systematic review and meta-analysis of clinical and biomechanical literature. *J. Biomechanics* 124, 110571. doi:10.1016/j.jbiomech.2021.110571

Li, Q. Y., Zhang, J. G., Qiu, G. X., Wang, Y. P., Shen, J. X., Zhao, Y., et al. (2010). Primary effect of dual growing rod technique for the treatment of severe scoliosis in young children. *Chin. Med. J. Engl.* 123 (2), 151–155. doi:10.3760/cma.j.issn.0366-6999.2010.02.005

Li, Z., Song, G., Su, Z., and Wang, G. (2020). Development, validation, and application of ligamentous cervical spinal segment C6-C7 of a six-year-old child and an adult. *Comput. Methods Programs Biomed.* 183, 105080. doi:10.1016/j.cmpb.2019.105080

Mundis, G. M., Kabirian, N., and Akbarnia, B. A. (2013). Dual growing rods for the treatment of early-onset scoliosis. *JBJS Essent. Surg. Tech.* 3 (1), e6. doi:10.2106/JBJS.ST.K.00050

Noordeen, H. M., Shah, S. A., Elsebaie, H. B., Garrido, E., Farooq, N., and Al Mukhtar, M. (2011). *In vivo* distraction force and length measurements of growing rods. *Spine* 36 (26), 2299–2303. doi:10.1097/BRS.0b013e31821b8e16

Pasha, S., Aubin, C.-E., Parent, S., Labelle, H., and Mac-Thiong, J.-M. (2014). Biomechanical loading of the sacrum in adolescent idiopathic scoliosis. *Clin. Biomech.* 29 (3), 296–303. doi:10.1016/j.clinbiomech.2013.12.004

Patwardhan, A. G., Havey, R. M., Carandang, G., Simonds, J., Voronov, L. I., Ghanayem, A. J., et al. (2010). Effect of compressive follower preload on the flexion-extension response of the human lumbar spine. *J. Orthop. Res.* 21 (3), 540–546. doi:10.1016/S0736-0266(02)00202-4

Pei, B., Lu, D., Wu, X., Xu, Y., Ma, C., and Wu, S. (2022). Effects of growing rod technique with different surgical modes and growth phases on the treatment outcome of early onset scoliosis: A 3-D finite element analysis. *Ijerph* 19 (4), 2057. doi:10.3390/ijerph19042057

Rohlmann, A., Zander, T., Rao, M., and Bergmann, G. (2009). Applying a follower load delivers realistic results for simulating standing. *J. Biomechanics* 42 (10), 1520–1526. doi:10.1016/j.jbiomech.2009.03.048

Rushton, P. R. P., Smith, S. L., Forbes, L., Bowey, A. J., Gibson, M. J., and Joyce, T. J. (20191976). Force testing of explanted magnetically controlled growing rods. *Spine (Phila. pa.* 44 (4), 233–239. doi:10.1097/BRS.0000000000002806

Sankar, W. N., Skaggs, D. L., Yazici, M., Johnston, C. E., Shah, S. A., Javidan, P., et al. (2011). Lengthening of dual growing rods and the law of diminishing returns. *Spine* 36 (10), 806–809. doi:10.1097/brs.0b013e318214d78f

Shekouhi, N., Kelkar, A., Dick, D., Goel, V. K., and Shaw, D. (2022). Current benchtop protocols are not appropriate for the evaluation of distraction-based growing rods: A literature review to justify a new protocol and its development. *Eur. Spine J.* 31 (4), 963–979. doi:10.1007/s00586-022-07113-1

Stokes, I. A. F., Spence, H., Aronsson, D. D., and Kilmer, N. (1996). Mechanical modulation of vertebral body growth. *Spine* 21, 1162–1167. doi:10.1097/01241398-199611000-0004010.1097/00007632-199605150-00007

Szabo, E., and Rimnac, C. (2022). Biomechanics of immature human cortical bone: A systematic review. *J. Mech. Behav. Biomed. Mater.* 125, 104889. doi:10.1016/j.jmbbm.2021.104889

Teli, M., Grava, G., Solomon, V., Andreoletti, G., Grismondi, E., and Meswania, J. (2012). Measurement of forces generated during distraction of growing-rods in early onset scoliosis. *World J. Orthop.* 3(2): 15–19. doi:10.5312/wjo.v3.i2.15

Thompson, G. H., Akbarnia, B. A., Kostial, P., Poe-Kochert, C., Armstrong, D. G., Roh, J., et al. (2005). Comparison of single and dual growing rod techniques followed through definitive surgery. *Spine* 30 (18), 2039–2044. doi:10.1097/01.brs.0000179082.92712.89

Thompson, G. H., Akbarnia, B. A., and Campbell, R. M. (2007). Growing rod techniques in early-onset scoliosis. *J. Pediatr. Orthop.* 27 (3), 354–361. doi:10.1007/s00299-002-0436-110.1097/bpo.0b013e3180333eea

Upasani, V. V., Parvaresh, K. C., Pawelek, J. B., Miller, P. E., Thompson, G. H., Skaggs, D. L., et al. (2016). Age at initiation and deformity magnitude influence complication rates of surgical treatment with traditional growing rods in early-onset scoliosis. *Spine Deform.* 4, 344–350. doi:10.1016/j.jspd.2016.04.002

Villemure, I., and Stokes, I. A. F. (2009). Growth plate mechanics and mechanobiology. A survey of present understanding. *J. Biomechanics* 42 (12), 1793–1803. doi:10.1016/j.jbiomech.2009.05.021

Watanabe, K., Uno, K., Suzuki, T., Kawakami, N., Tsuji, T., Yanagida, H., et al. (2016). Risk factors for proximal junctional kyphosis associated with dual-rod growing-rod surgery for early-onset scoliosis. *Clin. Spine Surg.* 29 (8), E428–E433. doi:10.1097/bsd.0000000000000127

Yang, J. S., Sponseller, P. D., Thompson, G. H., Akbarnia, B. A., Emans, J. B., Yazici, M., et al. (2011). Growing rod fractures. *Spine* 36 (20), 1639–1644. doi:10.1097/BRS.0b013e31822a982f

Yoganandan, N., Pintar, F. A., Kumaresan, S., and Gennarelli, T. A. (2000). Pediatric and small female neck injury scale factors and tolerance based on 433 human spine biomechanical characteristics. Proceedings of the International Ircobi Conference on the Biomechanics of Impact. Montpellier, France, 20–22. September 2000. Available at: https://trid.trb.org/view/715663.

frontiers | Frontiers in Bioengineering and Biotechnology

TYPE Review
PUBLISHED 25 August 2022
DOI 10.3389/fbioe.2022.937803

Hope for bone regeneration: The versatility of iron oxide nanoparticles

Nan Wang[1]†, Yimin Xie[1]†, Zhipeng Xi[1], Zehua Mi[2], Rongrong Deng[1], Xiyu Liu[1], Ran Kang[1,3]* and Xin Liu[1,3]*

[1]Affiliated Hospital of Integrated Traditional Chinese and Western Medicine, Nanjing University of Chinese Medicine, Nanjing, China, [2]Hospital for Skin Diseases, Institute of Dermatology Chinese Academy of Medical Sciences, Peking Union Medical College, Nanjing, China, [3]Department of Orthopedics, Nanjing Lishui Hospital of Traditional Chinese Medicine, Nanjing, China

Check for updates

OPEN ACCESS

EDITED BY
Jun Pan,
Chongqing University, China

REVIEWED BY
Alessandra Quarta,
Department of Physical Sciences and Technologies of Matter, National Research Council (CNR), Italy
Zuhao Li,
Shanghai Jiao Tong University, China

*CORRESPONDENCE
Ran Kang,
kangran126@126.com
Xin Liu,
liuxin@njucm.edu.cn

†These authors have contributed equally to this work and share first authorship

SPECIALTY SECTION
This article was submitted to Biomechanics, a section of the journal Frontiers in Bioengineering and Biotechnology

RECEIVED 06 May 2022
ACCEPTED 02 August 2022
PUBLISHED 25 August 2022

CITATION
Wang N, Xie Y, Xi Z, Mi Z, Deng R, Liu X, Kang R and Liu X (2022), Hope for bone regeneration: The versatility of iron oxide nanoparticles.
Front. Bioeng. Biotechnol. 10:937803.
doi: 10.3389/fbioe.2022.937803

Abstract: Although bone tissue has the ability to heal itself, beyond a certain point, bone defects cannot rebuild themselves, and the challenge is how to promote bone tissue regeneration. Iron oxide nanoparticles (IONPs) are a magnetic material because of their excellent properties, which enable them to play an active role in bone regeneration. This paper reviews the application of IONPs in bone tissue regeneration in recent years, and outlines the mechanisms of IONPs in bone tissue regeneration in detail based on the physicochemical properties, structural characteristics and safety of IONPs. In addition, a bibliometric approach has been used to analyze the hot spots and trends in the field in order to identify future directions. The results demonstrate that IONPs are increasingly being investigated in bone regeneration, from the initial use as magnetic resonance imaging (MRI) contrast agents to later drug delivery vehicles, cell labeling, and now in combination with stem cells (SCs) composite scaffolds. In conclusion, based on the current research and development trends, it is more inclined to be used in bone tissue engineering, scaffolds, and composite scaffolds.

KEYWORDS

iron oxide nanoparticles, tissue engineering, bone regeneration, scaffolds, stem cells

Introduction

Orthopedic diseases are the second leading cause of disability worldwide, as living conditions improve and people live longer, skeletal diseases are becoming more frequent, and their incidence is increasing every year (Rasker, 1995; Jakob et al., 2013; Weinstein, 2016). Among them, bone defects caused by trauma, tumors, chronic inflammation, infection, osteoporosis and congenital deformities caused great physical, and emotional damage to patients and diminished their quality of life (Gao et al., 2022; Li et al., 2017; Migliorini et al., 2021; Li et al., 2022b). Bone is a living organ that can heal and remodel itself. Nonetheless, extensive defects of bone and cartilage require the necessary interventions. For osteochondral defects that are not self-repairing, autologous or allogeneic osteochondral grafts are currently used as the primary means. However, this has the disadvantages of infection, immune rejection, inflammation, and disease transmission, and these limitations have severely restricted their widespread use in clinical practice (Tang et al., 1998; Kowalczewski and Saul, 2018; Zhang et al., 2019c; Yao et al., 2019; Koons et al., 2020; Xu et al., 2021). Particularly for those with serious irregularities in bone and cartilage, their rational repair and reconstruction can be interesting and challenging (Fazzalari, 2011; Tevlin et al., 2014; Ho-Shui-Ling et al., 2018).

In recent years, magnetic nanoparticles (MNPs) have been widely used in medical research, such as magnetic resonance imaging (MRI), cell labeling, targeted drug delivery, antitumor, thermal therapy, and biosensing (Ferreira et al., 2016). Compared with other materials, MNPs have unique advantages, including low production cost, good biocompatibility, stable physicochemical properties, and low toxicity (Ozbey et al., 2015), and consequently, they are receiving increasing attention in the biomedical field. The magnetic materials currently most used in the medical field are based on iron oxide (IO), such as ferric oxide (Fe_2O_3) and ferroferric oxide (Fe_3O_4) (Ramimoghadam et al., 2014; Shokrollahi, 2017). Iron is an essential trace element in the body, and exogenous IO can be metabolized and degraded through various pathways when it enters the body, and it is relatively non-toxic (Xia et al., 2019c; Liu et al., 2020a). Because IO is more common in nature, easy to synthesise and particularly sensitive to magnetic fields, it has been researched more frequently (Paik et al., 2015; Salehiabar et al., 2018). And mainly due to the mobility in response to magnetic fields (Kitture and Ghosh, 2019), iron oxide nanoparticles (IONPs) have been approved by the FDA and are the most widely studied material in the field of nanomedicine (Bobo et al., 2016). However, due to the easy aggregation of bare iron and the potential toxicity caused by the release of iron ions, most of them are coated with biocompatible ligands, which can affect cell proliferation, adhesion, migration, differentiation, movement, and distribution under the action of an external magnetic field (Vangijzegem et al., 2019). IONPs can be visualized by MRI and can also promote cell differentiation, inhibit osteoclast formation, and enhance osteogenesis (Li et al., 2018a; Xia et al., 2018b; Liu et al., 2018). Overall, IONPs have a strong ability to promote bone regeneration, good biocompatibility and chemical stability, as well as no significant intrinsic toxicity, which is superior to other magnetic nanoparticles, and are widely used in bone regeneration therapy (Paik et al., 2015; Li et al., 2018a; Xia et al., 2018b; Salehiabar et al., 2018).

Consequently, this article summarizes some of the achievements and progress in the use of IONPs in bone regeneration in recent years and provides a summary and perspective of the research hotspots and trends. Specifically, the characteristics of IONPs and their application in bone repair, mechanism studies, and safety were discussed. Furthermore, this article adopts a bibliometric approach to analyze and discuss the hot spots and research trends. Through the above research, it is hoped that this contribution will guide the study of bone regeneration (Figure 1).

Bone regeneration mechanisms

The skeleton is a vital organ that supports the body and remains under stress and weight for the whole life (Zhu et al., 2021). Usually, bone resorption and destruction is a dynamically balanced metabolic process. In the micro-ecological environment of bone, various cells are involved, including a large number of osteocytes, osteoclasts, and immune cells (Mohammadi et al., 2018). Osteocytes and osteoblasts play a key role in bone formation, while osteoclasts are involved in the resorption and regeneration of bone tissue (Torgbo and Sukyai, 2018). In addition, type I collagen, the inorganic minerals calcium (Ca^{2+}), and phosphate (PO_4^{3-}) are still important components of bone structure (Jang et al., 2009). Physiologically, it has a certain degree of self-healing when minor bone defects or bone destruction occurs; however, this ability is limited, especially in the case of trauma, infections, and tumours that result in bone defects worth more than 2 cm (Yang et al., 2018; Zhang W. et al., 2019a; Wagner et al., 2019). More importantly, bone defects can also lead to bone ischaemia, bone loss, and osteonecrosis, which further lead to a failure of bone healing (Loi et al., 2016). When a bone defect cannot heal itself, additional means are essential to achieve the goal of stimulating bone regeneration. How to maximize the optimal repair of bone defects has been a hot topic. The current methods used for bone regeneration consist of five main components depending on the pathogenesis of the bone injury (Figure 2): 1) external stimulation, 2) cells, 3) blood vessels, 4) biomolecules, and 5) biomaterials (Saiz et al., 2013; Hankenson et al., 2015; Lopes et al., 2018). In current studies, several methods are used in combination to enhance the effectiveness of the therapy. External stimulation such as magnetic fields promote bone regeneration (Singh et al., 2014; Zhuang et al., 2018); cellular therapy is currently focused on the use of MSCs (Jia et al., 2019); vascular regeneration is essential to ensure cellular metabolism and nutrition (Xia et al., 2018b); biomolecules include growth factors and bone morphogenetic proteins (Yu et al., 2020); and biomaterials are currently an important modality in the treatment of bone defects, and the development of various scaffolds has extended the effect of osteogenesis. For the study of scaffolds, various requirements need to be met, of which biocompatibility, absorbability, mechanical properties, non-toxic side effects, and bubble structure are the most important, as shown in Table 1.

In response to the mechanisms of bone regeneration, current research focuses on promoting bone healing through the modification of external conditions. There are various methods of bone regeneration, but in order to enhance the effect of bone growth, a combination of methods is usually applied, and this is most noticeable in the case of biological

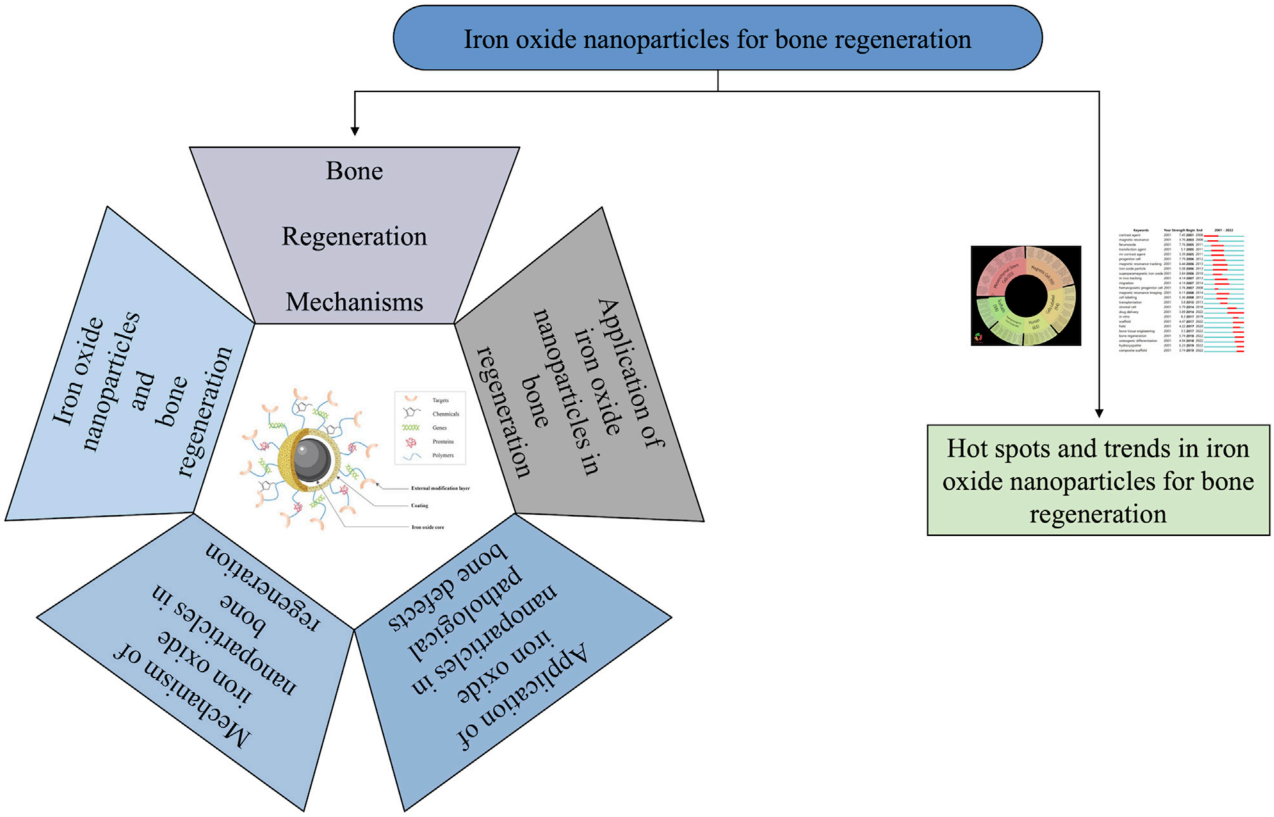

FIGURE 1
General diagram of the core content of the article. This paper contains six main contents, which are respectively bone regeneration mechanisms, iron oxide nanoparticles and bone regeneration, application of iron oxide nanoparticles in bone regeneration, application of iron oxide nanoparticles in pathological bone defects, mechanism of iron oxide nanoparticles in bone regeneration, and hot spots and trends in iron oxide nanoparticles for bone regeneration.

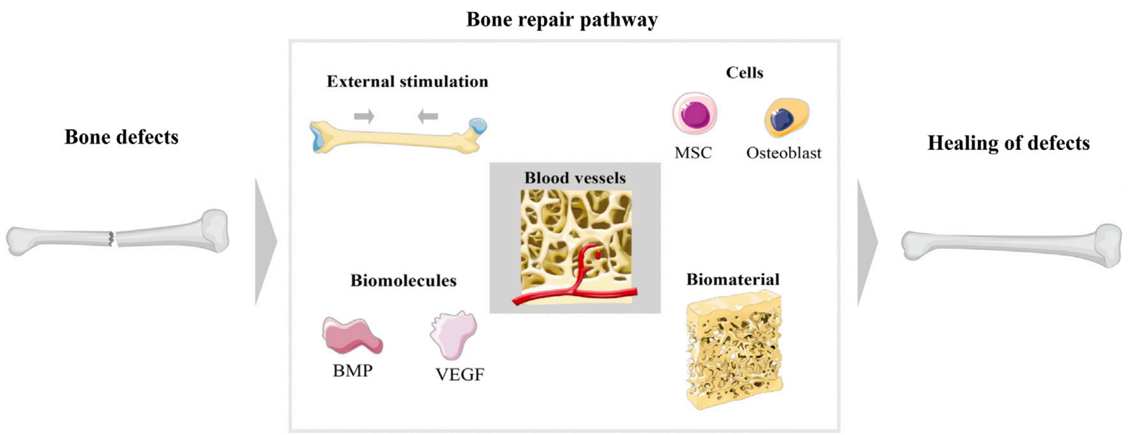

FIGURE 2
Main schematic diagram of bone regeneration. There are five ways to promote bone repair after bone injury, which are external stimulation, cells, blood vessels, biomolecules, and biomaterials.

TABLE 1 Requirements for biomaterial scaffolds in bone regeneration.

Requirements	Purpose	References
Biocompatibility	Supports cellular activity and molecular signalling without causing immune rejection or inflammatory responses	Murphy et al. (2010); Chen et al. (2022)
Absorbability	Provides space for new tissue to grow inwards; allows for controlled degradation *in vivo*	Williams, (2008)
Mechanical properties	Meets mechanical strength needs and provides transfer properties	Yi et al. (2016)
non-toxic side effects	The various properties should be carried out under non-toxic conditions	Mondschein et al. (2017)
Bubble structural	Can provide a reasonable amount of space for bone regeneration	Hou et al. (2019)

scaffolds. If biomolecules, cells, and IONPs are mixed in a scaffold, it retains all the advantages of a scaffold but also has molecular, cellular, and nanoparticle-related characteristics (Ou et al., 2019; Yang et al., 2019; Petretta et al., 2021). Although some results have been reached, the search for the design of scaffolds with ideal loading molecules and cells with good biological effects, suitable mechanical properties, optimized bubble structures with controlled degradability, and non-toxic to tissues are still the direction being pursued.

Iron oxide nanoparticles and bone regeneration

Overview of iron oxide nanoparticles

Among the various nanoparticles, magnetic materials are more attractive to researchers because of their unique responsiveness to magnetic fields (Dhivya et al., 2015). Currently, magnetic materials commonly used in the biomedical field include iron, cobalt, titanium, and nickel metal alloys as well as IO, ferrite ($BaFe_{12}O_{19}$, $CoFe_2O_4$), and nano-magnetic hydroxyapatite, among which magnetic IONPs are the most widely studied because iron is an essential element for the human body and can be sensitive to magnetic fields (Li et al., 2016). It can be combined with growth factors, stem cells (SCs), drugs, and other biologics so that be labeled, imaged, thermally treated, and disease targeted (Ghosh et al., 2015; Accomasso et al., 2016; Rajan et al., 2020). The biomedical applications of IONPs are mainly based on their superparamagnetic properties. Superparamagnetic iron oxide nanoparticles (SPIONs) are a type of IONPs with a diameter of 10–100 nm and can generate strong magnetism in a weak magnetic field, and its magnetism can disappear with the withdrawal of the external magnetic field (Laurent et al., 2008; Kircher et al., 2011). Based on its superparamagnetic properties, IONPs are usually used in MRI examinations and targeted to specific areas under the action of an external magnetic field to achieve targeted therapeutic effects (Radeloff et al., 2020). Maria et al. (Volokhova et al. 2022) made SiO_2-coated magnetic iron oxide nanoparticles into α-Fe@SiO_2 with a cubic morphology, which exhibited higher MRI relaxation than iron oxide alone and could show high-performance contrast effects. Zheng et al. (2022) found that allantoin phosphate can deliver iron oxide nanoparticles precisely to bone tissue for targeted synergistic treatment of osteoporosis. At present, the preparation of IONPs primarily consists of dry and wet methods (Yu et al., 2016; Huang et al., 2018) (Figure 3). The wet methods are more commonly used and include thermal decomposition, chemical co-precipitation, sol-gel, ball milling and atomic layer deposition (Cotin et al., 2022; Kiyani et al., 2022). The co-precipitation method is more commonly used in the synthesis of MNPs and allows for better control of the size and magnetic properties of the material, but the MNPs have a tendency to aggregate due to the small particle size (Lin et al., 2017). The high-temperature pyrolysis method is mainly used to synthesis ultra-fine powders and crystals of different materials, but it cannot obtain NPs smaller than 10 nm in size (Bhavani et al., 2017). Therefore, different extraction methods have their advantages and disadvantages, and researchers should select the appropriate method for generating IONPs according to the specific situation.

Iron oxide nanoparticle physicochemical properties

The physicochemical properties of IONPs include magnetic properties, chemical stability, modifiability, biocompatibility and ease of surface functionalization (Clark et al., 2005) (Figure 4). In particular, the magnetic properties make it multifunctional. IONPs have long been used for MRI contrast for its uniquely magnetic and highly biocompatible (Zhao et al., 2022). Its good biocompatibility allows it to label specific cells without causing damage (Moise et al., 2017). With their biocompatible, magnetic, small size and customised surface coating properties, SPIONs can be used for the delivery and monitoring of small molecules, drugs and cells, particularly in areas of muscle, bone or cartilage (Iyer et al., 2017).

Magnetism is the most important property of IONPs. SPION can sparingly deliver drugs to specific areas under the action of an external magnetic field and can undergo magnetothermal transformation to kill tumour cells which ultimately treats

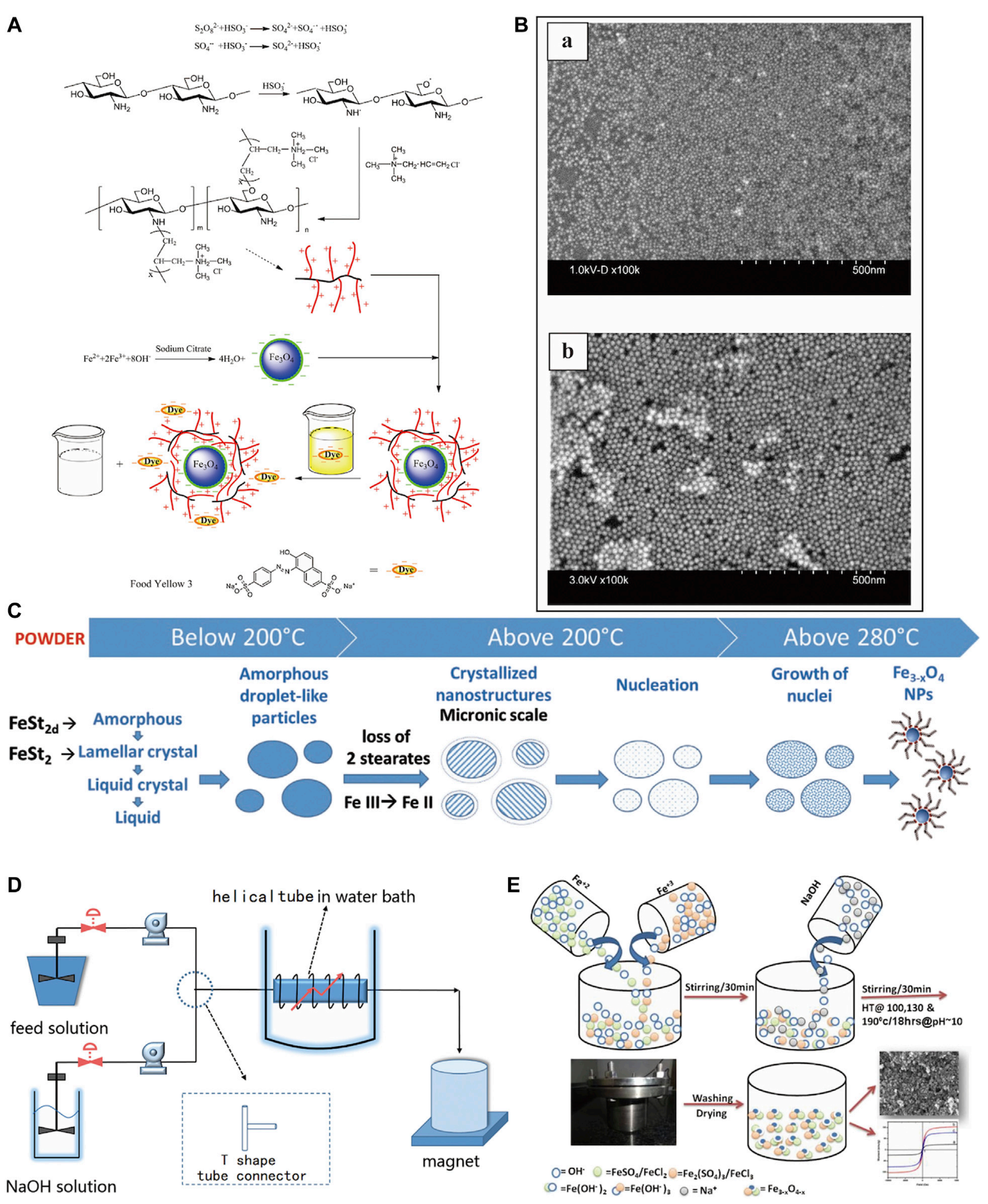

FIGURE 3
Methods for the preparation of IONPs. **(A)** Wet method preparation process of CTS-g-PTMAAC/SC-Fe_3O_4 composite magnetic nanoparticles (Chen et al., 2016); **(B)** Images of IONPs prepared by immunoprecipitation technique under scanning electron microscope (SEM), **(a)** 5 nm, **(b)** 20 nm (Mengesha et al., 2022); **(C)** IONPs obtained by thermal decomposition (Cotin et al., 2022); **(D)** Preparation of IONPs by co-precipitation method in microchannel reactor (Lin et al., 2017); **(E)** Preparation of high saturation magnetic IO nanomaterials (Bhavani et al., 2017).

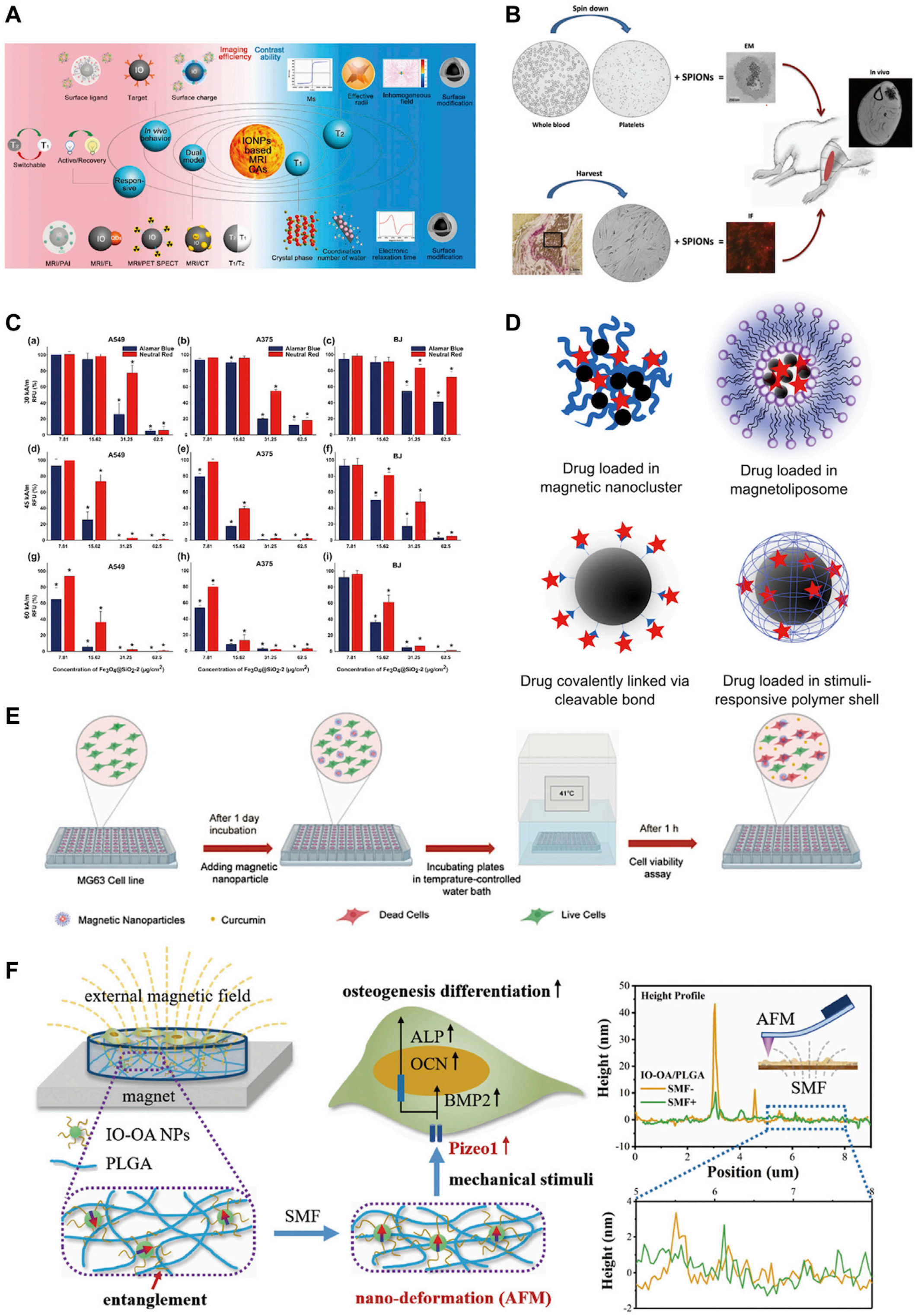

FIGURE 4
Physicochemical properties of iron oxide nanoparticles. **(A)** IONPs are used for MRI examination due to their good magnetic properties and biocompatibility (Zhao et al., 2022); **(B)** IONPs are readily absorbed by cells and can label cells for cell tracking (Iyer et al., 2017); **(C)** IONPs have magnetic heating properties and can substantially promote tumor cell death *in vitro* (Iacoviţă et al., 2021); **(D)** IONPs are used for targeted magnetic drug delivery (Hola et al., 2015); **(E)** CSLM images showing MG-63 cancer cell line stained alive/dead at 41°C (Khodaei et al., 2022); **(F)** IO-OA/PLGA produces mechanical stimulation in the presence of an external magnetic field and promotes osteogenic differentiation of MC3T3-E1 cells (Hao et al., 2019).

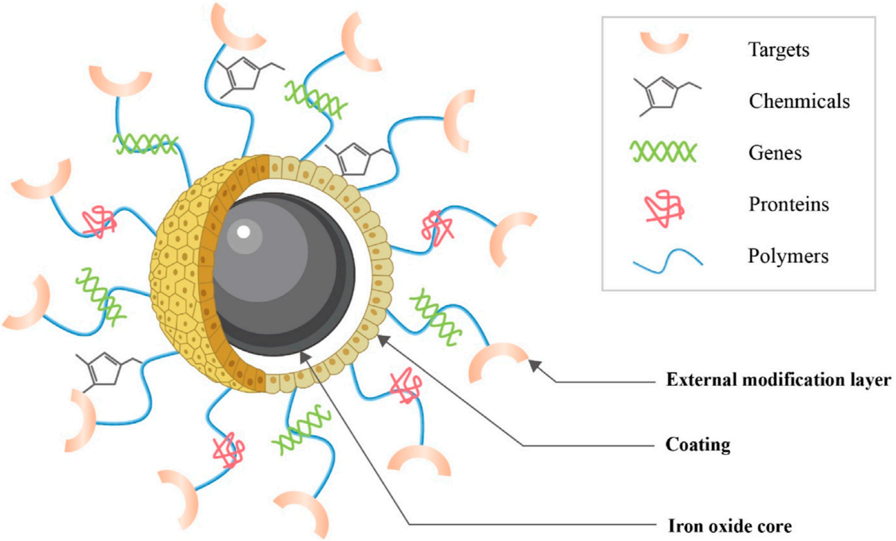

FIGURE 5
Structure of IONPs. IONPs consist primarily of an IO core, a coating and an external modification layer (This diagram is drawn from (Dasari et al., 2022)).

tumours (Iacoviță et al., 2021; Pucci et al., 2022). Additionally, magnetic materials can have mechanical properties that can regulate cell behaviour and promote bone regeneration (Hao et al., 2019). The small particle size of IONPs allow them to overcome the biological barrier for wide distribution in the body, and they can also be excreted from the body by themselves (Hola et al., 2015). Studies have indicated that very small particles with hydrodynamic diameters up to 5 nm–8 nm can be excreted from the kidneys; while larger IONPs are readily captured by the reticuloendothelial system (RES), allowing imaging of the liver and spleen and detection of areas of inflammation; it ranging in size from about 20 to 150 nm may also accumulate in the stomach, bones and kidneys (Dadfar et al., 2019). Thus, the particle nature of the iron oxide nanoparticles is also an important characteristic to ensure its functionality.

Iron oxide nanoparticle structure

IONPs consist primarily of an IO core, a coating, and an external modification layer (Figure 5). The core is a large amount of IO, which ensures that it has a certain magnetism. Uncovered IO is toxic because it tends to collect and react chemically, so an organic or inorganic coating needs to be applied to the surface of the core, which reduces IO oxidation, toxicity, and enhances its biocompatibility (Dadfar et al., 2019). Current coating materials include organic, inorganic, and organic-inorganic composites (Ma et al., 2013). Organic coatings include mainly dextran, chitosan, citrate, agarose, collagen, polylactic acid (PLA), polycaprolactone (PCL), polyglycolic acid (PGA), and polylactic acid-glycolic acid copolymer (PLGA) (Iyer et al., 2017; Marin et al., 2020); the inorganic coating consists mainly of silica, calcium phosphate, calcium silicate, and calcium phosphate cement complexes (Ferrage et al., 2017); organic-inorganic composites such as mineralized collagen, which retain the common properties of both while giving the scaffold good rigidity and toughness (Li et al., 2021b). The main purpose of the coating is generally to restrict particle aggregation and provide hydrophilicity, stability, and biocompatibility to the internal core (Accomasso et al., 2016; Harrison et al., 2017). In order to bind specifically to the receptor, molecular modifications can be applied outside the coating, or the therapeutic agent can be loaded so that the combination can be used for specific targeted therapy (Li et al., 2012).

Iron oxide nanoparticle safety

One of the first things to ensure when IONPs are used for bone regeneration is safety (Figure 6). Studies have indicated that IONPs have superior biocompatibility and stability without significant intrinsic toxicity (Salehiabar et al., 2018). Most studies have demonstrated that low doses of IONPs are non-toxic to organisms (Pariti et al., 2014). In general, the toxicity of nanoparticles depends on their physical and chemical properties, such as particle size, surface properties, and chemical composition (Huang et al., 2017b). Therefore, before evaluating the toxicity of IONPs *in vitro* and *in vivo*, their

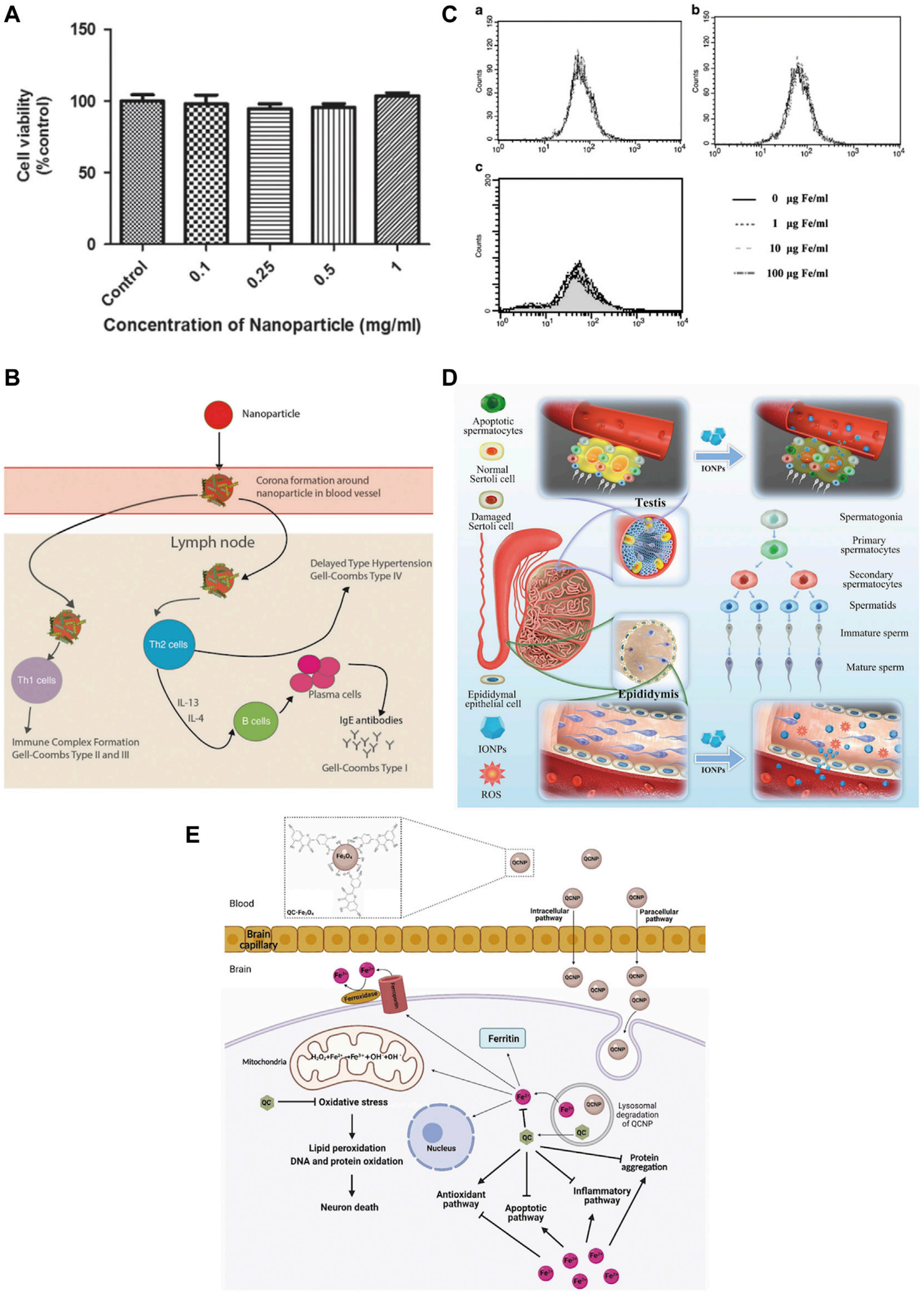

FIGURE 6
Safety of IONPs. **(A)** MTS assay showed that different concentrations of Au-Fe3O4 nanoparticles were not significantly toxic to CHO cells (Pariti et al., 2014); **(B)** USPIO could induce an immune response (Daldrup-Link, 2017); **(C)** Flow cytometry assay showed that SPIO was incubated directly on hMSCs for a long time (72 h) and had no significant effect on ROS(Yang et al., 2011); **(D)** IONPs can cause reversible damage to the reproductive system of male mice without affecting major organs (Yang et al., 2022); **(E)** Quercetin attenuates the neurotoxicity induced by IONPs(Bardestani et al., 2021).

physicochemical properties must be clarified. Various nanoparticles exhibit size-dependent toxicity *in vitro* and *in vivo* (Wu et al., 2022a). Under normal conditions, nanoparticles smaller than 10 nm are eliminated by the kidneys, while nanoparticles larger than 200 nm are phagocytosed (Rajan et al., 2020). The majority of IONPs are engulfed by hepatocytes, which on the one hand, facilitates their usefulness in liver imaging and, on the other hand, is a potential hazard to the body (Daldrup-Link, 2017). Although IONPs can stay in the body for a long time, they are biodegradable, can be metabolised from the circulation through a variety of pathways (Ventola, 2012). However, some IONPs are still non-degradable and it is not known whether there are serious effects on the body. It is also considered that IONPs can induce some toxic side effects in the body. IONPs have been found to cause significant toxicity in rats when kept in the body for long periods, causing reduced body weight, significant liver damage, and mild splenic toxicity (Verma et al., 2021). The interaction of the surface charge of IONPs between nanoparticles and biological components also substantially affects their toxic response (Woo et al., 2021). Toxic reactions are mainly manifested by impaired mitochondrial activity, membrane leakage, and morphological changes that negatively affect cell viability, proliferation, and metabolic activity, significantly weakening its therapeutic efficiency (Yang et al., 2011). Nanoparticle-treated cells may trigger immune-inflammatory reactions and other side effects if they migrate in tissues or accumulate at specific sites over time (Mahmoudi et al., 2010; Mahmoudi et al., 2012). IONPs were discovered to cause reversible damage to the reproductive system of male mice without affecting major organs (Yang et al., 2022). There are some solutions to these risks. For example, IONPs may damage neural tissue through free iron accumulation, protein aggregation, and oxidative stress, but quercetin may reduce neurotoxicity in clinical applications (Bardestani et al., 2021). The effect of IONPs on the inflammatory response is size-dependent, with smaller IONPs weakening the inflammatory response; this inflammatory response can also be attenuated by blocking actin polymerization, endoplasmic reticulum (ER) stress, or oxidative stress (Ying et al., 2022). New predictive models have also been developed as a method of toxicity screening to provide a safety profile for the clinical use of IONPs. Coccini et al. (2019) have developed a model for assessing human stem cells-based Fe_3O_4 NP toxicity screening and support using this approach to improve the safety of NPs to predict health outcomes with confidence. Hence, when utilizing IONPs, it is essential to understand their physicochemical properties. IO itself is toxic, but by choosing a suitable surface coating, reducing the dosage, reducing the diameter of the particles, and avoiding long-term aggregation in the same location, the toxic reaction can be effectively reduced. Measures should be taken in advance for different side effects, and extracts of some herbs can be used in synergy with IONPs to reduce toxicity. Models for predicting toxicity and safety assessment are also necessary for the rational use of nanoparticles.

Effect of iron oxide nanoparticles on bone regeneration

IONPs, as a special magnetic particle, have a multifaceted effect on bone regeneration. Its function of promoting bone regeneration is closely related to its physicochemical properties. Among them, magnetism is an important prerequisite for the action of IONPs on bone regeneration. It has been demonstrated that IONPs not only respond to external magnetic fields, but also act as a magnetic domain themselves on the nanoscale, with nanoparticles forming magnetic fields to generate a number of biochemical reactions (Xie et al., 2019). When an external magnetic field is applied to bone defects, it promotes fracture healing and tissue repair, even without the intervention of IONPs(Shan et al., 2013; Thrivikraman et al., 2014). When IONPs are used to treat bone defects, a magnetic field is applied externally, which further enhances their magnetic effect, and this magnetism stimulates osteoblast-associated cells, activating the osteogenic pathway and exerting a bone regeneration effect (Jia et al., 2019). In addition, mechanical stimulation was found to promote osteogenic differentiation of stem cells (Meng et al., 2021). IONPs are mechanically stimulated by the effect of a magnetic field, which acts on the cells to generate internal biochemical signals and enhance bone regeneration (Wang et al., 2016; Zhuang et al., 2018). Furthermore, IONPs can generate magnetothermal conversion with the intervention of an alternating magnetic field (AMF), which is delivered to deep lesions to generate heat for the treatment of bone tumours and post-operative bone defects (Guo et al., 2017; Lee et al., 2018; Albarqi et al., 2019). The production of blood vessels is still essential for the regeneration of bone tissue. IONPs were identified to improve angiogenic properties and promote the formation of new blood vessels in bone defects, which was present in the presence or absence of static magnetic field (SMF) intervention (Singh et al., 2014; Xia et al., 2018b; Hu et al., 2018). It can be absorbed by cells through endocytosis (Kolosnjaj-Tabi et al., 2013), so it is used for cell tracking and targeting (Zhang and Zhang, 2005; Shen et al., 2013). This can detect the location of cells in bone regeneration and migration of SCs(Liao et al., 2022). Cells labelled with these nanoparticles are non-toxic and easily reach the desired effect. Note that for those IONPs that are smaller in size and have a longer half-life in the blood stream, it has significant bone targeting properties (Arami et al., 2015). In particular, it can remove reactive oxygen species from the body to regulate bone metabolism and improve post-menopausal bone loss (Yu et al., 2020). It has also been found that IONPs can inhibit osteoclast production and

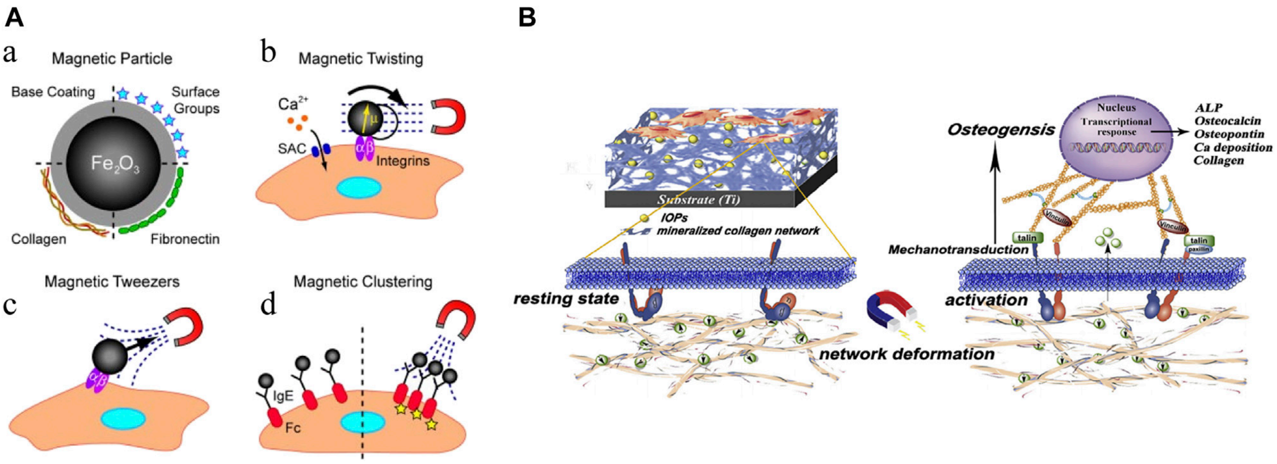

FIGURE 7
Mechanical stimulation of IONPs. **(A)** Mechanical activation of IONPs stimulates cellular receptors (Sniadecki, 2010); **(B)** Fe_3O_4/mineralized collagen coating promotes osteogenic differentiation of MC3T3-E1 cells (Zhuang et al., 2018).

differentiation (Zheng et al., 2022). Its multifaceted action promotes the occurrence of bone regeneration.

Application of iron oxide nanoparticles in bone regeneration

The multifaceted properties of IONPs have led to a wide range of research and applications in bone regeneration. The main directions of application include direct action (Figure 7), action on stem cells (differentiation, migration, homing, tracking) (Figure 8), targeted drug delivery, combined use with scaffolds, and composite scaffolds.

Direct action

IONPs have a direct effect on cells. Various physical forces can affect cell activation, and studies have demonstrated that magnetic and mechanical stimulation can promote SCs proliferation and differentiation (Sniadecki, 2010; Schwartz et al., 2018). Magnetic forces can be converted into mechanical forces, and when cells are mechanically stimulated, they can generate a series of biochemical signals that induce a biological response to the organism (Ingber, 2006; Martino et al., 2018). Research has revealed that a composite coating formed by IONPs with a mineralized collagen coating under a static magnetic field can promote osteogenic differentiation through mechanical stimulation (Zhuang et al., 2018). Studies have also indicated that SIONPs themselves can strengthen bone regeneration without external magnetic fields (Hu et al., 2018). Proven research has also been conducted on the effects of the state of nanoparticles on cells, finding that direct delivery of colloidal ferromagnetic fluids is more desirable than the administration of powdered particles (Uskoković et al., 2019). Evidently, IONPs can stimulate cells directly with or without external magnetic field intervention and promote osteogenesis.

Action on stem cells

SCs are an important tool in the treatment of bone defects. It holds great promise in treating many diseases and conditions (Daneshmandi et al., 2017; Česen Mazič et al., 2018). SCs are a particularly important group of cells in bone tissue engineering, which can differentiate into different cells under certain conditions. SCs are primarily derived from bone marrow, adipose tissue, muscle, umbilical cord, cord blood, placenta, Wharton's glue, and amniotic fluid, all of which can differentiate into osteoblasts, of which the most studied are bone marrow mesenchymal stem cells (BMSCs) (Kangari et al., 2020). When bone damage occurs, MSCs migrate from the bone marrow or other adjacent tissues to the site of injury and secrete growth factors such as BMP and VEGF to promote the bone healing process (Schreivogel et al., 2019; Wasnik et al., 2019; McNeill et al., 2020). At the same time, MSCs are also involved in regulating inflammation and repairing bone damage together with progenitor cells, stromal cells and macrophages (Grayson et al., 2015; Xue et al., 2022; Yin et al., 2023). MSCs are also capable of differentiating into bone tissue and have favourable immunomodulatory properties (Safarova et al., 2020).

In recent years, SCs therapy has provided a strategy for bone regeneration, particularly in repairing large bone defects (Watanabe et al., 2016). As Hao et al. (2022) constructed

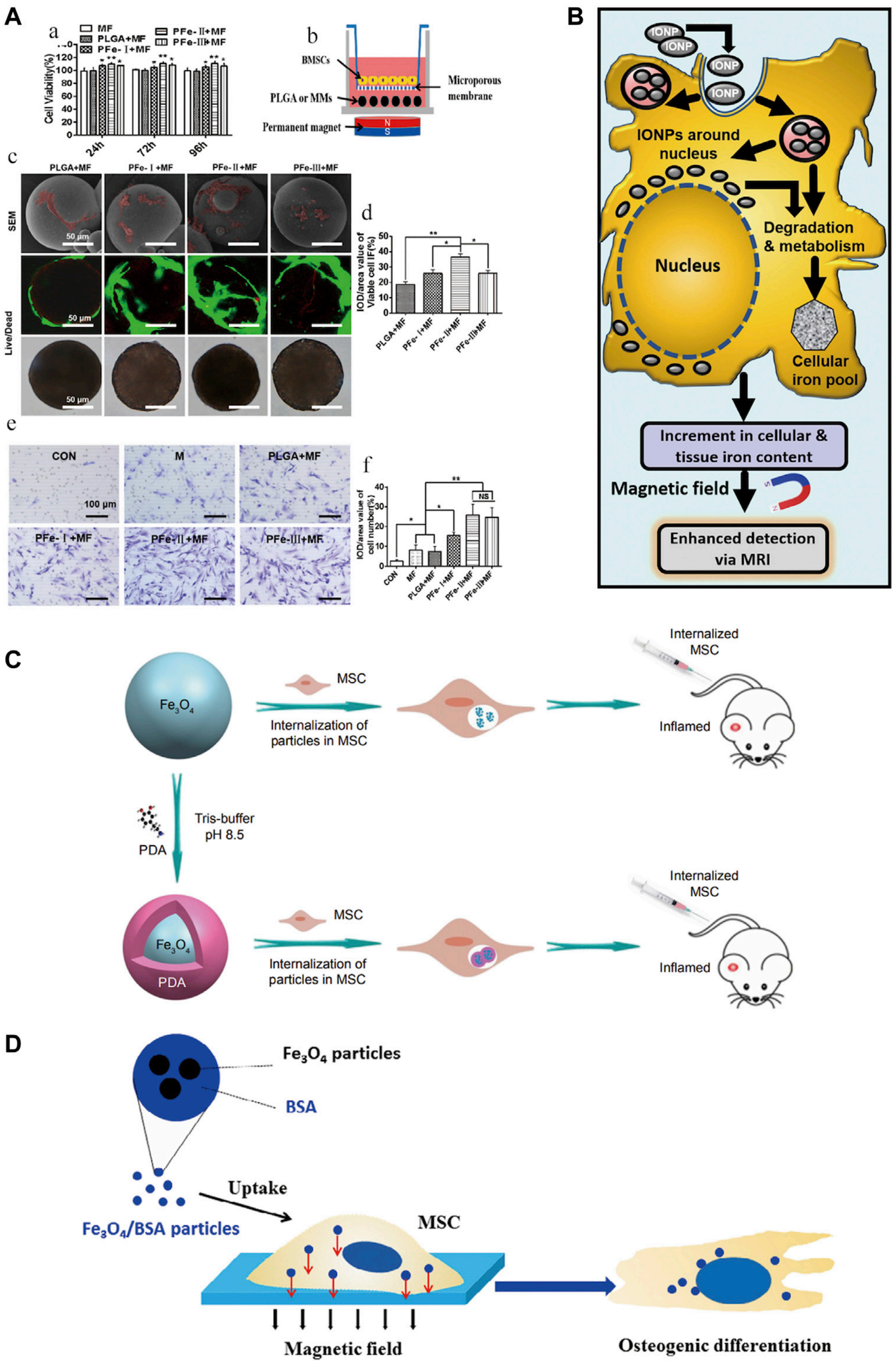

FIGURE 8
Role of IONPs on stem cells. **(A)** Promotion of stem cell migration (Zhao et al., 2021); **(B)** stem cell labeling (Mehta, 2022); **(C)** promotion of stem cell homing (Li et al., 2019); **(D)** promotion of stem cell differentiation (Jiang et al., 2016).

microgels that can effectively promote the adhesion, proliferation, and osteogenesis of BMSCs, providing a new idea for repairing large bone defects. Liu et al. (Liu et al., 2022) also designed functional spheroids containing MSCs to create a 3D cell-directed microenvironment for the bone repair of large defects, resulting in excellent osteogenesis, angiogenesis, and bone regeneration of MSCs. For cells expanded *in vitro*, a stable cell phenotype should be maintained, targeting SCs to specific sites, promoting differentiation and proliferation of SCs to osteoblasts at the site of injury, maintaining local cell stability, and reducing cell loss at the defect site, all of which are necessary for bone defect repair.

Stem cells differentiation

The differentiation of SCs is influenced by many factors, of which magnetic conditions are an important one. Ruchita et al. (Shelat et al., 2020) used L-lysine-functionalized IONPs to interfere with bone marrow mesenchymal stem cells (BMSCs) and showed efficacy in promoting *in situ* cartilage regeneration and its ability to label cells and act as a contrast agent. Driven by a magnetic field, carbon quantum dot (CD)-doped SPION can also differentiate MSCs into bone and cartilage for osteochondral regeneration (Das et al., 2019). Uptake of bovine serum albumin (BSA) (Fe_3O_4/BSA) particles loaded with IONPs also significantly enhanced osteogenic differentiation of MSCs under a constant static magnetic field (Jiang et al., 2016). Low-temperature atmospheric nitrogen plasma positively affects the behaviour of MSCs cultured on bone scaffolds containing IO-loaded silica nanoparticle catalysts, improving SCs behavior and promoting the value-added and osteogenic differentiation (Przekora et al., 2020). IONPs can directly promote the differentiation of SCs. However, current research tends to package and combine IONPs to strengthen this impact.

Stem cells migration and homing

SCs labeled by IOPNs can migrate and home to specific sites in response to magnetic fields. It has been disclosed that the presence of SPIONs confers special magnetic properties to PLGA microspheres, which greatly promote the proliferation, migration, and osteogenic differentiation of BMSCs under the influence of external magnetic fields (Zhao et al., 2021). Moreover, the combination of pulsed electromagnetic fields (PEMF) and SPIONs were synergistic role in promoting the directional migration and osteogenic differentiation of BMSCs (Wu et al., 2018). A further finding was that silica-encapsulated IONPs promoted migration while retaining the proliferation and differentiation capacity of BMSCs and that the labeled BMSCs were more viable and migrated better, but their osteogenic potential was not affected (Yao et al., 2020). *In vitro* magnetic targeting system was used to attract rabbit BMSCs. This technique significantly facilitated the penetration of IONPs-labelled cells into porous hydroxyapatite ceramics transplanted into rabbit ulnar bone defects and promoted bone formation (Chen et al., 2010). IONPs enhance the homing potential of MSCs to the site of injury and have no negative impact on MSCs function; furthermore, MSCs-loaded nanoparticles exhibit good homing and anti-inflammatory capacity in the absence of external magnetic field intervention (Li et al., 2019). The combination of IONPs with MSCs has special magnetic effects and pro-osteogenic differentiation potential, which indicates the great ability of the two to merge for bone regeneration.

Stem cell tracking

IONPs can be used as nuclear magnetic resonance (NMR) contrast agents for cell tracking (Hua et al., 2015). Currently, the commonly used MRI contrast agent is gadolinium, but its toxicity has raised the level of concern. When searching for an effective alternative without significant toxic effects, IONPs-labelled MSCs were found to show positive results both *in vitro* and *in vivo* (Mehta, 2022). Similarly, in a sheep tendinitis model treated with MSCs labeled with IONPs, cells were still detectable in MRI 7 days after surgery (Scharf et al., 2015). The magnetic effect mediated by IONPs is a crucial tool for SCs tracking and a wide range of applications. It has great potential as a magnetic particle imaging (MPI) tracer advancing SCs therapy (Wang et al., 2020).

Targeted drug delivery

Targeted drug delivery is an important feature of IONPs (Figure 9), and IONPs complexes are commonly used as carriers for controlled drug release (Prodan et al., 2013). For instance, IONPs have been found to stimulate the corresponding drug delivery systems for targeted drug delivery in arthritis (Zhang et al., 2022). To enhance the anti-osteoporosis effect, the investigators synergized IONPs with alendronate, and the combination substantially improved bone mineral density and microarchitecture compared to the same dose of alendronate (Zheng et al., 2022). Merging bisphosphonate (Bis) and IONPs and incorporating them into osteoblasts, this composite magnetic nanoparticle has the significant anti-osteoporotic potential (Lee et al., 2016). Guo et al. (2021) constructed a PLGA-based drug delivery system, co-loaded with 17β-estradiol (E2) and iron oxide (Fe_3O_4) and modified with alendronate for the remote targeting of estradiol in the treatment of post-ovariectomy osteoporosis in rats, which achieved good efficacy and magnetically remote targeted drug release. Besides, IONPs can be loaded with various cytokines, genes, and targets to reach the site of bone defects for the purpose

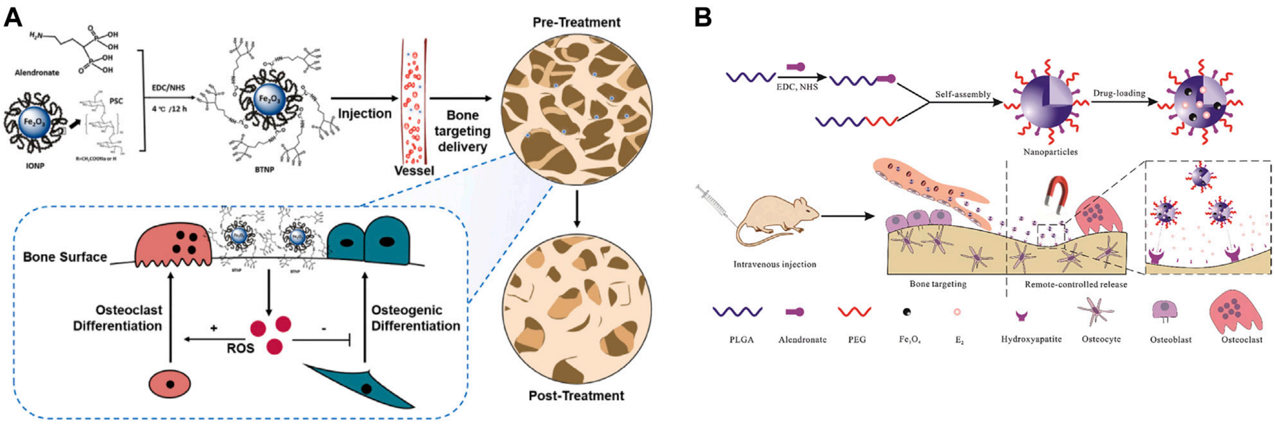

FIGURE 9
IONPs can be used for drug delivery. **(A)** Delivery of alendronate to osteoporosis (Zheng et al., 2022); **(B)** Remote controlled bone-targeted delivery of estradiol to treat ovariectomy-induced osteoporosis in rats (Guo et al., 2021).

of targeting and promoting bone regeneration. Jiang et al. (Chiang et al., 2018) developed magnetic gelatin nanocapsules containing transforming growth factor (TGF)-β1 consisting of hexanoic anhydride grafted gelatin and IONPs and achieved magnetic enrichment of loaded cells through combined treatment with magnetically induced stimulation and TGF-β1. Fan et al. (2014) developed a magnetic IONPs-encapsulated biopolymer nanogel consisting of chitosan and heparin via specific nucleobase pairing for Bone morphogenetic protein 2 (BMP-2) delivery, which plays an important role in cartilage and bone regeneration. For this purpose, Sahmani et al. (2020) generated a specific biomimetic scaffold with drug delivery capacity, a porous scaffold for biomedical use, prepared from hydroxyapatite and IONPs and loaded with gelatin, in which ibuprofen was incorporated to achieve excellent pain relief at the specified site. Researchers (Wang et al., 2021) have developed IONPs containing HA and raloxifene (R-IONPs-HA), which exhibit superior biocompatibility, antibacterial activity, and osteoinduction, and have great potential for fracture repair and infection prevention. Specific composite platforms are also being investigated for targeted drug delivery (Pistone et al., 2014). It is evident that the targeted delivery of IONPs is being refined and matured, and multiple compound platforms loaded with drugs have been investigated, showing a good ability to promote osteochondral regeneration.

The role of the scaffolds

In bone tissue engineering exploration, scaffolds are the most used modality because they can retain specific structural and mechanical properties while loading other factors, particles, and materials, as well as being biocompatible and offering outstanding advantages in maintaining the normal physiological structure of bone and maintaining good weight-bearing and force-bearing functions. The design of delivery platforms plays a crucial role in the activation of bone regeneration as they provide a suitable environment for cell adhesion and growth while providing a beneficial platform for delivery strategies (Bi et al., 2020). Simple biodegradable polymeric materials or ceramics have been investigated as bone tissue engineering scaffolds, but these materials have significant limitations, including insufficient mechanical strength. In contrast, nanoparticle-modified composite scaffolds offer significant promise for promoting bone regeneration. The nanomaterials incorporated into polymeric scaffolds are divided into organic and materials, and they can provide sufficient surface area and mechanical properties required for support, as well as cell adhesion, differentiation, and integration (Kim and Fisher, 2007). The scaffolds currently in use mainly consist of organic materials (lipids, liposomes, dendrimers and polymers, chitosan, gelatin, collagen) or inorganic nano-biomaterials (silica, bioceramics, bioglass, hydroxyapatite) fused (Navarro et al., 2008; Virlan et al., 2016; Kumar et al., 2020). Xia et al. (2018a) mixes IONPs with calcium phosphate cement to create a scaffold that promotes osteoinduction and bone regeneration, adheres to SCs, and promotes osteogenic differentiation. In contrast, thermoplastic polyurethane (TPU) and PLA polymers doped with IONPs exhibited significant osteogenic differentiation of MSCs in response to external magnetic fields (Marycz et al., 2020). Hydrogels have excellent biocompatibility and adjustable mechanical properties, promising biomaterials for replacing extracellular matrix (ECM) and organ regeneration (Hu et al., 2015; Huang et al., 2017a; Xue et al., 2019). Han et al. (Han et al.,

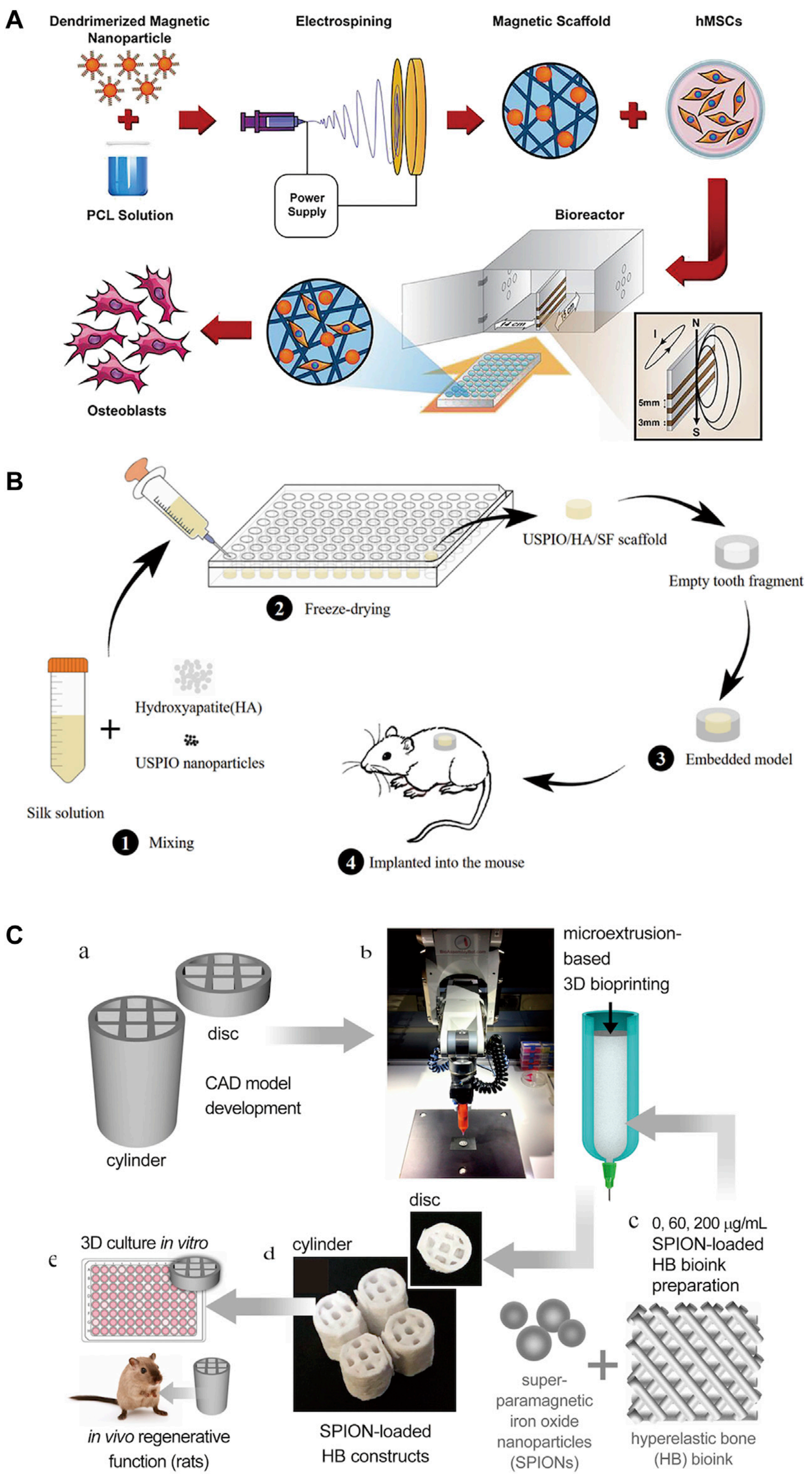

FIGURE 10
Three common methods for constructing scaffolds for IONPs. **(A)** Electrostatic spinning technique (Khalili et al., 2022); **(B)** freeze-drying technique (Zhang W. et al., 2019b); and **(C)** 3D printing technique (Shokouhimehr et al., 2021).

2021b) developed a tunable hydrogel for the 3D culture of dental pulp stem cells (DPSCs), through which DPSCs could aggregate and generate spheroids enriched with $CD146^+$ cell subpopulations, which exhibited significant osteogenic differentiation in response to the intervention of IONPs.

The mainstream methods currently used to synthesize scaffolds containing IONPs are electrospinning techniques, freeze drying and three-dimensional (3D) printing (Figure 10).

Electrospinning technology is a well-established scaffold fabrication method with many critical advantages, including its simple nature, high surface area to volume ratio, potential to release drugs and antimicrobial agents, controlled fiber diameter, high porosity, and permeability (Mortimer and Wright, 2017). To promote the fruitful differentiation of MSCs, a researcher prepared magnetic polycaprolactone (PCL) nanofiber scaffolds by adding third-generation dendrimer-modified SPIONs (G3-SPIONs) during electrospinning, which demonstrated promising results with favorable cytocompatibility and cell adhesion (Khalili et al., 2022). Although electrospinning technology is simple to handle and easy to control the surface properties of the support, it still has the disadvantage of low yield and low strength (Singh et al., 2014; Li et al., 2018b).

The freeze-drying technique contains both freezing and drying steps and is one of the most commonly used methods to enhance the stability of scaffolds (Rahman et al., 2010; Hassanajili et al., 2019). It is currently used as a common method for producing scaffolds in bone regeneration research. Freeze-dried scaffolds have a unique structure with the required porosity and pore interconnections for the selective movement of small molecules and closely resemble the natural bone extracellular matrix, making them optimal for bone tissue engineering studies (Singh and Dasgupta, 2022). Lu et al. (Lu et al., 2020) successfully prepared gadolinium-hyaluronic acid (Gd-HA) nanoparticles (NPs) by a simple freeze-drying method as a novel MRI contrast agent for the accurate detection of cartilage damage without toxic side effects. Wu Zhang et al. (2019b) used a combination of freeze-drying monthly physical mixing methods to prepare ultra-small superparamagnetic iron oxide (USPOI)-labeled hydroxyapatite (HA)/silk fibroin (SF) scaffolds loaded with dental pulp stem cells (DPSCs), which were physically stable and significantly promoted pulp tissue repair and regeneration. Azam et al. (Hajinasab et al., 2018) also applied freeze-drying methods to fabricate a 3D nanocomposite scaffold consisting of gelatin and hydroxyapatite (GEL/HA) loaded with Fe_3O_4 nanoparticles, which has great potential for drug loading and bone replacement. The flexibility of the freeze-drying technique can be seen to provide important support for the study of bone regeneration scaffolds.

3D printing methods allow the precise, reproducible, and large-scale manufacture of complex scaffold systems with tunable structural and physicomechanical properties (Filardo et al., 2019; Serpooshan and Guvendiren, 2020). 3D printing technology for bone tissue engineering also allows for specific geometric design of defective bone areas (Trombetta et al., 2017; Tomov et al., 2019). The manipulation of computer-aided design (CAD) models for printing scaffolds permits precise adjustment of the porosity, size, and geometric design of the graft to closely correspond to the target bone defect (Moreno Madrid et al., 2019). 3D printing technology offers good stability, 3D spatial structure, and high efficiency, but materials are more restricted and expensive (Zhao et al., 2014). Shokouhimehr et al. (2021) 3D printed a new generation of hyperelastic bone (HB) implants loaded with SPIONs applying a bio-ink consisting primarily of HA to scaffolds and studied their therapeutic effect on large non-healing fractures, demonstrating great potential for bone regeneration. The three scaffold fabrication methods and components are shown in Table 2.

The role of the composite scaffolds

Tissue engineering is a method of reconstructing functional tissue at the site of damage, usually including cells, growth factors, and 3D biodegradable scaffolds. With the addition of IONPs to the tissue project, it will contain four main components (Figure 11). Its complex construction is of great importance in promoting bone regeneration. In order to strengthen the effectiveness of the bone repair, extend the synergistic effect and reduce the deficiencies possessed by a single scaffold, researchers are now primarily developing composite scaffolds to reach the desired goal (Figure 12). Researchers combined aminopropyltriethoxysilane (APTES)-modified nanohydroxyapatite (nHAp) with IONPs to develop composites that significantly enhanced osteoblast activity and reduced inflammatory responses and osteoclastogenesis (Marycz et al., 2022). By coating core-shell structured HA on SPIONs (SPIO@HA), Li et al. (Li M. et al., 2021) discovered it could target osteoclastogenesis and osteogenesis. A multifunctional scaffold of filamentous protein/hydroxyapatite scaffold combined with ultra-small SPIONs (USPIO) doped with BMSCs promotes osteogenic differentiation of SCs and allows for osteogenic differentiation non-invasive monitoring of bone regeneration by quantitative MRI (Liu Q. et al., 2020). Moreover, oleic acid-modified IONPs (IO-OA NPs) and PLGA were used to produce homogeneous magnetic nanocomposites, which showed good mechanical properties and enhanced osteogenic differentiation (Hao et al., 2019). In addition, calcium phosphate cement (CPC) scaffolds doped with IONPs on SCs utilizing an external static magnetic field (SMF) have great osteoinductivity, which may be related to the physical forces generated by the magnetic field and the cell-intrinsic action of the magnetic nanoparticles released from the scaffold (Xia et al., 2019a). The relevant modification of the surface of IONPs and their subsequent application to composite scaffolds is also a way of extending their efficacy.

TABLE 2 Fabrication type and research of scaffolds.

Manufacturing method	Coating	Magnetic field type	Cell type	Synthetic method	Nanoparticle type	Magnetic field intensity (emu/g)	Scaffolds proportion	References
Electrospinning techniques	PCL	PEMF	ADMSCs	Coprecipitation	G3-SPIONs	57.75	495 ± 144 nm	Khalili et al. (2022)
Electrospinning techniques	PCL	EMF	MC3T3-E1 cells	Coprecipitation	SPIONs	71	No application	Singh et al. (2014)
Freeze-drying technique	HA/SF	No application	DPSCs	Feeeze-drying	USPIO	No application	0.025 mg/ml USPIO and 5 mg/ml HA/SF	Wu Zhang et al. (2019b)
Freeze-drying technique	GEL-HA	EMF	L929 cells	Feeeze-drying	Fe_3O_4 nanoparticles	49.6	No application	Hajinasab et al. (2018)
3D printing methods	HA	No application	C3H10T12 cells and HBO cells	3D printing	SPIONs	No application	SPION concentration between 60 and 200 μ g/ml	Shokouhimehr et al. (2021)

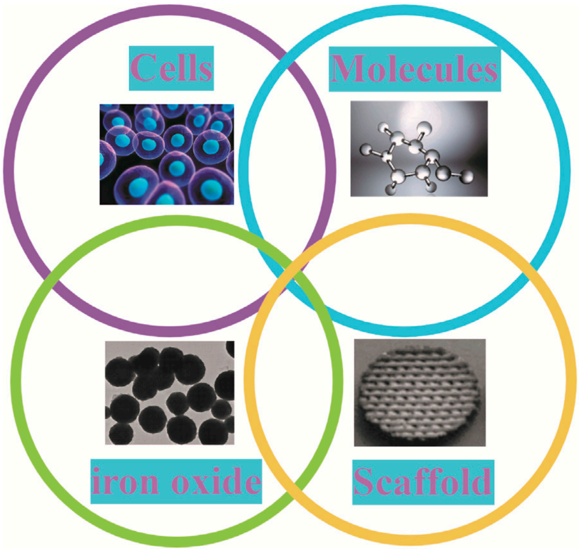

FIGURE 11
Components of tissue engineering in IONPs. When IONPs are applied to tissue engineering, this body has four main components: cells, molecules, IO and scaffold.

Kartogenin (KGN), an emerging stable non-protein compound that promotes the differentiation of BMSCs into chondrocytes, was transplanted onto the surface of modified USPIO and then made into a fibrin nanocrystal/dextran hydrogel, which showed enhanced cartilage regeneration (Yang et al., 2019).

Bone tissue-engineered scaffolds alone have many drawbacks, including lack of osteoinduction and low mechanical strength. To circumvent these limitations, the option of composite scaffolds is necessary. Hu et al. (Hu et al., 2021) used a poly (lactic acid-ethanolic acid copolymer)/polycaprolactone/β-tricalcium phosphate (PPT) scaffold, incorporating IONPs into a porous electromimetic scaffold for long-term release, and this composite scaffold was optimized to further enhance osteogenic capacity. The low mechanical strength of the scaffold can be regulated by various preparation techniques, of which electrostatic spinning is one of the most applied (Schiffman and Schauer, 2008; Jun et al., 2018). Chen et al. (2018) reported magnetic PLGA/PCL scaffolds made by electrostatic spinning technology and layer-by-layer assembly of SPIONs, which exhibit excellent biocompatibility, adjustable stiffness, physical sensing, and stimulus responsiveness. Estévez et al. (2022) were the first to combine type I collagen and SPIONs to design magnetic and biocompatible electrostatic spinning scaffolds, showing that the electrostatic spinning structures containing SPIONs could retain the magnetic properties of the nanoparticles alone and that these collagen scaffolds could promote the proliferation, adhesion, and viability of osteoblasts and HBMSCs.

3D printing technology for composite scaffolds is another commonly used method whose versatility makes it increasingly important in bone regeneration. The study found that IONPs-rich PLGA copolymer scaffolds prepared through the layer-by-layer assembly by 3D printing technology promoted cell adhesion and enhanced osteogenesis of rat BMSCs (Han L. et al., 2021). Saraiva's group (Saraiva et al., 2021) used 3D printing to create a polylactic acid platform loaded with HA, IONPs, and an antibiotic (minocycline) with tunable properties and a multi-stimulus response. The platform was discovered to regulate the anti-biofilm dose and strengthen the ability of bone tissue regeneration. Utilizing 3D printing technology, porous titanium aluminium vanadium (Ti6Al4V, pTi)

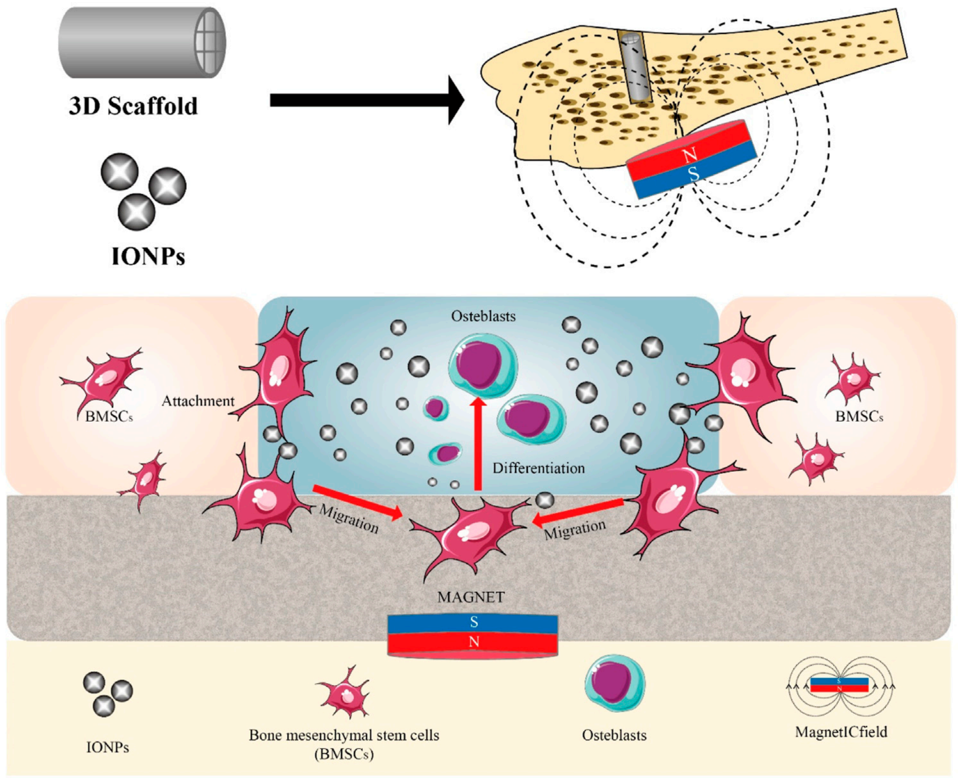

FIGURE 12
Application of composite scaffold in bone regeneration. IONPs are mostly found in the form of scaffolds in the treatment of bone defects. To enhance their efficacy, scaffolds can contain a variety of components that promote osteogenic differentiation of stem cells under the influence of a magnetic field.

scaffolds can reconstruct large bone defects (especially in load-bearing areas). Nevertheless, the lack of osteogenic properties limits its use in clinical practice. To address this dilemma, a researcher co-deposited IONPs and polydopamine (PDA) on the surface of 3D printed pTi scaffolds, a novel magnetic coating that improved the adhesion, proliferation, and osteogenic differentiation of HBMSCs (Huang et al., 2020). Wang et al. (2018) synthesized biodegradable shape memory polyurethane (PU) as the main component of a 3D printing ink for manufacturing bone scaffolds and added SPIONPs and polyethylene oxide (PEO) or gelatin to the 3D printing ink to promote osteogenic induction, shape fixation and increase printability. This composite scaffold with its shape memory properties, biodegradability, and osteogenic effect, has the potential to become a bone substitute. Petretta et al. (2021) prepared a polycaprolactone-based (PCL) scaffold with HA and SPIONs (PCL-HAp-1% SPION) by 3D printing to improve the healing efficiency of bone and inoculated the scaffold with MSCs.

The construction of composite scaffolds gives new ideas for bone regeneration, while the addition of drug loading after the platform has been established can achieve certain therapeutic effects for specific bone diseases. As Schneider et al. (Schneider et al., 2021) used citric acid (MG@CA) coated magnetic iron oxide nanoparticles (MNPs) as a raw material for the treatment of bone diseases to construct a magnetic nanoplatform, adding raloxifene (Ral), curcumin (Cur), and methylene blue (MB) for the symptomatic treatment of bone diseases.

Application of iron oxide nanoparticles in pathological bone defects

Mild bone injuries have some ability to heal themselves, but beyond a certain point, bone defects usually fail to reconstruct themselves. For this type of bone defect that does not heal on its own, pathological bone defects such as osteoporosis (Bai et al., 2020; Li et al., 2022a; Li et al., 2022b), rheumatoid arthritis (Liu et al., 2021), infections (Taylor and Webster, 2011) and tumors (Kesse et al., 2020) are the main causes. In contrast, IONPs have been extensively investigated in pathological bone defects. Several studies have demonstrated that IONPs can positively regulate bone metabolism *in vitro* and *in vivo*, and that they have favorable bone targeting, bone regeneration and biocompatibility properties. For instance, Zheng et al. (2022) revealed that IONPs can alleviate osteoporosis induced by ovariectomized mice (OVX) by scavenging reactive oxygen species, promoting osteogenic differentiation of BMSCs and inhibiting osteoclastogenesis *in vitro*. Krzysztof et al. (Marycz et al., 2022) combined aminopropyltriethoxysilane (APTES) modified nHAp with IO nanoparticles and demonstrated *in vitro* that this biomaterial promotes osteoblast viability and RUNX-2 expression, reduces osteoclast metabolism and inflammation, and can be used for healing of osteoporotic fractures. Another study produced a SPIO with a core-shell structure coated with HA (SPIO@HA), which was used to target osteoclastogenesis and osteogenesis. The results revealed that the material greatly prevented bone loss in OVX mice and that their mechanism may be related to TRAF6-p62-CYLD, TGF-β, PI3K-AKT and calcium signalling pathways (Li et al., 2021a). Moreover, IONPs can be used for drug delivery in the presence of magnetic fields, bone targeting for osteoporosis (Guo et al., 2021).

Rheumatoid arthritis (RA) is a systemic immune disease that is primarily characterised by joint inflammation accompanied by progressive bone and joint destruction, which can cause significant bone defects (Takeuchi et al., 2021). Magnetic nanoparticles, particularly IONPs, have been documented to be an important tool for the treatment and diagnosis of rheumatoid arthritis by targeting local lesions with additional magnetic fields and avoiding systemic side effects (Liu et al., 2021). IONPs are an effective nanoplatform for targeted drug delivery, stimulus-responsive drug release, MRI diagnostics, photothermal therapy, and magnetothermal therapy in RA treatment, and could also contribute to the development of new magnetic materials (Wu and Shen, 2019). Duan et al., (2014) synthesized polyethyleneimine-functionalized superparamagnetic iron oxide nanoparticles (PEI-SPION) *in vitro* and demonstrated through *in vivo* and *in vitro* experiments that PEI-SPION can be used for systemic siRNA delivery to strengthen the therapeutic effect of RA with the intervention of an external magnetic field. Furthermore, Carneiro et al. (2020) constructed gold-coated SPIO (AuSPION) for the treatment of arthritic rats by intraperitoneal injection and found that AuSPION inhibited joint inflammation and edema, redox imbalance and cytokine expression under the influence of an external magnetic field.

Infection is another major challenge for bone regeneration, but this has been made viable with the intervention of nanotechnology. Studies have indicated that SPIONs have good antimicrobial activity, magnetic properties, and bone regeneration properties, which could be used in the development of new drugs for the treatment of bone defects associated with orthopaedic infections (Taylor and Webster, 2011). Wang et al. (2021) used IONPs (R-IONPs-HA) containing HA and raloxifene for fracture repair and infection prevention which showed good biocompatibility, antibacterial activity and osteoinductive effects. Taylor et al. (Taylor and Webster, 2009) demonstrated in an *in vitro* study that SPION significantly inhibited the growth of *Staphylococcus* epidermidis and at the same concentration significantly enhanced osteoblast function, offering hope for bone repair after infection. Wei et al. (2021) synthesized IONPs-sHA-strontium@collagen (IONSs-HA-SR@C) using a co-precipitation method and evaluated its effect on the differentiation and proliferation of MC3T3-E1 cells and their morphological changes as well as its antibacterial activity by *in vitro* experiments. The results clearly indicate that IONSs-HA-SR@C has promising biocompatibility, bone growth promoting ability and antibacterial activity. It is evident that IONPS has great potential for bone repair and anti-infection.

The incorporation of IONPs into multifunctional biomaterials for the treatment of tumors and post-tumour bone defects has led to a number of advances and breakthroughs due to their thermal, magnetic targeting, bone healing and pro-tumour cell apoptosis properties. Pang et al. (2021) synthesized a bone-targeted SPIO that, when delivered to bone, inhibits flavoproteinase, thereby inhibiting bone resorption by osteoclasts and invasion by breast cancer cells, effectively protecting against breast cancer-induced osteolysis. Khodaei et al. (2022) developed a method for the delivery of curcumin by SPIONs-based magnetothermal nanocarriers, in which the release of curcumin was coordinated by temperature. *In vitro* results showed that the temperature could be stabilised at 41°C by alternating magnetic fields, and that curcumin and heat therapy could kill MG-63 osteosarcoma cells and achieve good anti-bone tumour effects. Not only that, IONPs can promote bone regeneration for the repair of bone defects after tumour surgery. Sasikala et al. (2022) developed a piezoelectric magnetic nanoparticle (PMNP) that can regulate cell behaviour and fate under ultrasound (US), magnetic field (MF) and light-responsive conditions to achieve superior bone regeneration and bone transformation after bone tumour surgery. Vergnaud et al. (2022) designed superparamagnetic bioactive nanoparticles with an IO core (γ-Fe2O3) wrapped in a bioactive glass (SiO2-CaO) shell, which demonstrated *in vitro* experiments its non-toxic, bone healing and thermal therapeutic properties for direct or combined scaffolding of bone defects after bone tumour resection. It is apparent that IONPs have a great platform and opportunity in the treatment of pathological bone defects and have now gained great traction.

Mechanism of iron oxide nanoparticles in bone regeneration

The rational use of IONPs can better promote bone regeneration. Previous studies have focused on the construction

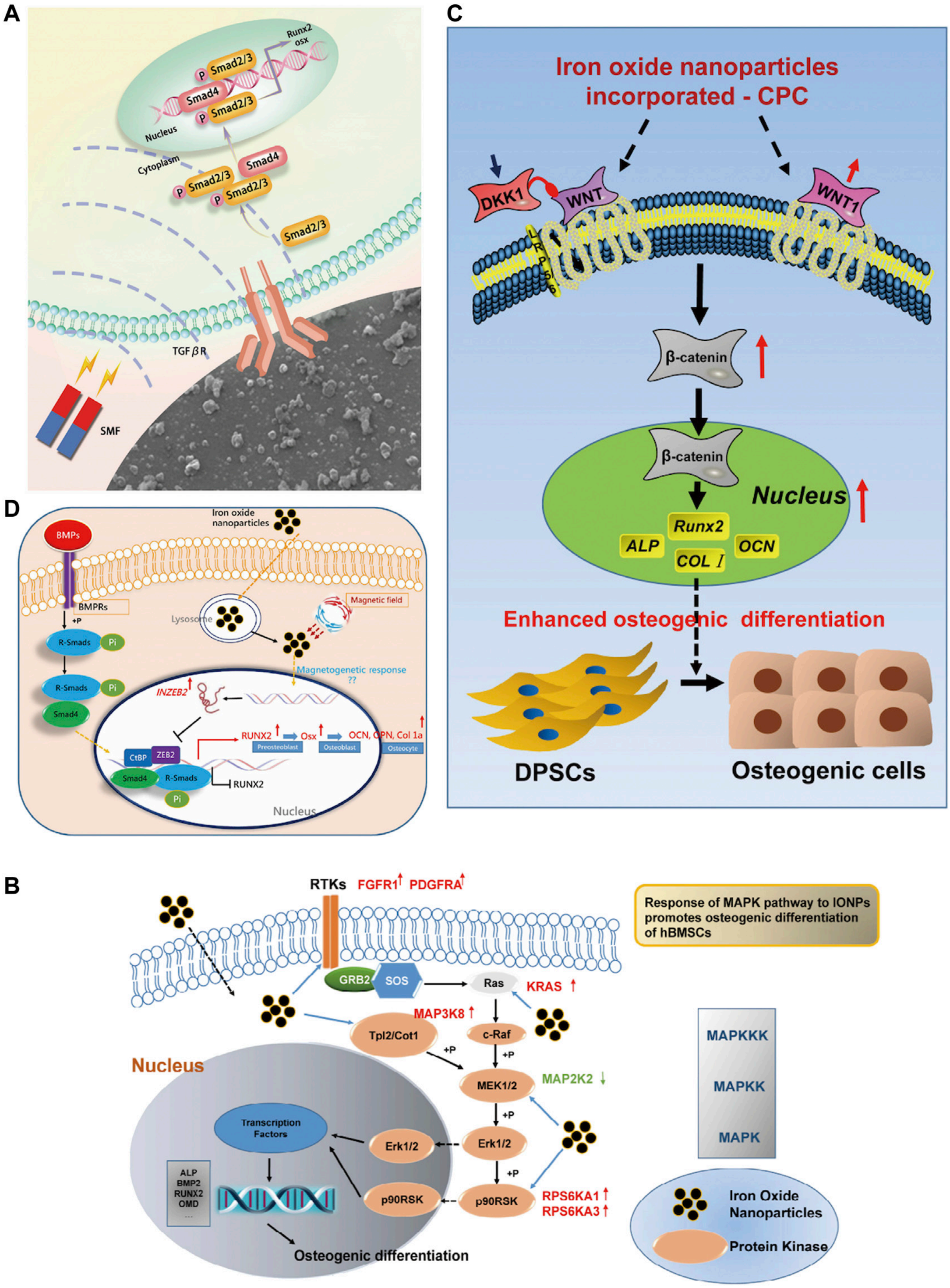

FIGURE 13
Mechanism of IONPs in the treatment of bone defects. **(A)** In the action of SMF, the Fe3O4/PDA@pTi scaffold regulates cellular function via the TGFβ-Smads signaling pathway (Huang et al., 2020); **(B)** IONPs promote osteogenic differentiation of HBMSCs through the MAPK pathway when they enter the cells (Wang et al., 2016); **(C)** IONPs + CPC can promote osteogenic differentiation of HDPSCs through the WNT signalling pathway (Xia et al., 2019b); **(D)** IONPs promote osteogenic differentiation of MSCs through the INZEB2 and BMP/Smads signaling pathways (Wang et al., 2017).

of scaffolds, the selection of composite materials, and the integrated use of SCs and drugs but neglected their specific mechanisms. In recent years, with the development of molecular biology, the study of the mechanism has gradually applied to the field of materials; the results found that IONPs promote bone regeneration with a variety of factors and signaling pathways related (Figure 13). Proteomic analysis revealed that magnetic iron oxide/polydopamine coating (Fe_3O_4/PDA) promotes osteogenesis by upregulating the TGFβ-Smads pathway in a static magnetic field (Huang et al., 2020). Heat therapy is beneficial in stimulating bone regeneration. Wang et al. (2022) constructed nanoparticle-hydrogel composites by embedding Arg-Gly-Asp (RGD)-coated core-shell structured magnetic iron oxide nanoparticles (MION) (CoFe2O4@MnFe2O4) in agarose with significant magnetothermal effects. Under mild magnetothermal treatment, the expression of HSP90 was upregulated in preosteoblasts and endothelial cells, activating the PI3K/Akt pathway in preosteoblasts, thus significantly promoting osteogenesis and biomineralization; meanwhile, the cobalt in CoFe2O4@MnFe2O4 upregulated the expression of the angiogenesis-related gene HIF-1 α, further promoting the formation of new blood vessels at the injury site. Zhuang et al. (2018) incorporated IONPs into mineralized collagen coatings (MC) to promote osteogenic differentiation by initiating mechanotransduction pathways and upregulating integrin α1, integrin β1 and RhoA under static magnetic fields. Jia et al. (2019) synthesized mesoporous silica-coated magnetic (Fe_3O_4) nanoparticles (M-MSN), which exhibited excellent biocompatibility and promoted osteogenic differentiation of MSCs *in vitro* via the Wnt/β-catenin pathway. In healing osteoporosis, IONPs can inhibit osteoclastogenesis by modulating the TRAF6-p62-CYLD signaling complex (Liu et al., 2020a). Yu et al. (2020) synthesized Fe_2O_3@PSC nanoparticles using the biopolysaccharide-based antioxidant polyglucose-sorbitol-carboxymethyl ether (PSC) as a precursor and found that it scavenged reactive oxygen species from MC3T3-E1 and Raw 264. cells by activating the Akt-GSK-3β-β-catenin pathway, inhibiting MAPK and NF-κB pathways ultimately promoting osteoblast differentiation. IONPs, in combination with SCs or biomaterials, will exhibit multiple functions. It was discovered to promote osteogenic differentiation of hBMSCs via the MAPK pathway (Wang et al., 2016). Jiang et al. (2016) prepared bovine serum albumin (BSA) particles loaded with IONPs (Fe_3O_4/BSA) and found that they significantly promoted the expression of alkaline phosphatase, type I collagen, and osteocalcin at the mRNA and protein levels in MSCs under static magnetic fields. The microbiota influences the process of bone repair. By constructing a rat palatal bone model, Jia et al. (2021) found that 3D printed SPION/PLGA could have a significant antibacterial effect and could alter the oral microbiota while treating palatal bone defects. Lu et al. (2018) prepared magnetic $SrFe_{12}O_{19}$ nanoparticle-modified mesoporous bioglass (BG)/chitosan (CS) porous scaffolds (MBCS) with excellent bone regeneration and anti-tumor functions. The magnetic field generated by MBCS can promote the expression of osteogenic genes such as OCN, COL1, Runx2, and ALP by activating the BMP-2/Smad/Runx2 pathway; it can also perform photothermal conversion to promote apoptosis of tumour cells, so it is used for tumor-associated bone defects. The combination of IONPs, MSCs, and biomaterials to build a composite system is the mainstay of bone regeneration research, and some breakthroughs have been made in their mechanisms. Duan et al. (2020) constructed a human umbilical cord mesenchymal stem cell-super magnetic iron oxide nanoparticles (NPs)@polydopamine (SCIOPs) system, which was found to inhibit osteoblast apoptosis, enhance osteoblast proliferation and promote bone repair through the Akt/Bcl-2/Bad/caspase-3 signaling pathway in the presence of a magnetic field and SCs homing ability. Xia et al. (2019b) added IONPs powder to CPC powder to fabricate CPC-IONP scaffolds and investigated the effect of the novel composite on bone matrix formation and osteogenesis of human dental pulp stem cells (hDPSCs). The results indicate that the osteogenic behavior of hDPSCs may be driven by CPC-IONP via the WNT signaling pathway. The mechanism by which IONPs promote bone repair has also been explored from the perspective of RNA. It was found to upregulate lncRNA INZEB2, regulating ZB2 expression and the BMP/Smads pathway (Wang et al., 2017). As nanomaterials are increasingly used in bone regeneration, it is essential to understand their biological effects (Table 3). The ongoing exploration of their molecular mechanisms may provide a theoretical basis and biological evidence for regenerative medicine.

Hot spots and trends in iron oxide nanoparticles for bone regeneration

A bibliometric approach was employed to investigate the hotspots and trends in IONPs on bone regeneration. We searched the Web of science core database for 631 relevant primary literature and, after limiting the language of the literature to English, eventually obtained 629 publications for inclusion in the study. The literature was imported into the Carrot2 clustering analysis tool to identify the current mainstream research directions. A burst analysis of the involved literature was also carried out using Citespace software to identify hot spots and trends in recent years. The results obtained from the Carrot2 analysis revealed that the main directions of research clustering are Mesenchymal Stem Cells, Magnetic Cells, Cells Labeled, Human, Superparamagnetic Iron Oxide, and Scaffolds (Figure 14). Burst analysis disclosed that IONPs were initially applied as magnetic resonance imaging contrast agents and transfection agents and then steadily moved towards magnetic resonance and *in vivo* tracking. After incorporating stem cells into the field, IONPs tend to be focused on migration, cell labeling, transplantation, and drug delivery. The increasing use of biomaterials has led to the development of IONPs from *in vivo* tracking to *in vitro* studies. Recent years have seen a shift towards the scaffold,

TABLE 3 Key elements of the study on the mechanism of IONPs for bone defects.

Compound component	Experimental method	Animal model	Cell type	Magnetic properties	Signaling pathway	References
Fe_3O_4/PDA	*In vivo* and *in vitro*	Rabbit model of femoral epicondyle defect	hBMSCs	SMF	TGFβ-Smads signaling pathway	Huang et al. (2020)
IONPs(Feraheme)	*In vivo* and *in vitro*	Ovariectomized (OVX) mice	RAW264.7 macrophages, bone marrow monocytes (BMMS), osteoclasts	No application	Inhibit RANK signaling pathway by regulating TRAF6-p62-CYLD signaling complex	Li Liu et al. (2020)
IONPs-PSC	*In vitro*	No application	hBMSCs	No application	MAPK signaling pathway	Wang et al. (2016)
Fe_3O_4/BSA	*In vitro*	No application	rBMSCs	SMF(1T)	Alkaline phosphatase (ALP) activity, calcium deposition, type I collagen and osteocalcin	Jiang et al. (2016)
SPION@ PDA NPs (Fe_3O_4)	*In vivo* and *in vitro*	Rats were injected with 20 mg/kg/d methylprednisolone in the muscle above the femoral head for 3 days (rat femoral head necrosis model)	HU-MSCs	SMF	Akt/Bcl-2/Bad/caspase-3 signaling pathway	Duan et al. (2020)
IONP-CPC (Fe_2O_3)	*In vitro*	No application	hDPSCs	No application	Wnt/β-catenin signaling pathway	Xia et al. (2019b)
IONPs-PSC	*In vitro*	No application	hBMSCs	No application	BMP/Smad signaling pathway	Wang et al. (2017)
IONP-Exos (Fe_3O_4)	*In vivo* and *in vitro*	Anterior cruciate ligament resection model in rats	hBMSCs, NIH3T3 fibroblasts	SMF	miR-21-5p/ SMAD7 signaling pathway	Xiang-Dong Wu et al. (2022)
M-MSNs (Fe_3O_4)	*In vivo* and *in vitro*	Rat tibia DO model	rBMSCs	No application	Wnt/β-catenin signaling pathway	Jia et al. (2019)
IOP-MC	*In vitro*	No application	MC3T3-E1 cells, rBMSCs	SMF	Mechanotransduction signaling pathway (integrin α1, integrin β1 and RhoA)	Zhuang et al. (2018)
MBCS ($SrFe_{12}O_{19}$)	*In vivo* and *in vitro*	Bilateral critical-sized calvarial-defect models in rat	hBMSCs, MG-63 cells	SMF	BMP-2/Smad/ Runx2 signaling pathway	Lu et al. (2018)

bone tissue engineering, osteogenic differentiation, hydroxyapatite, and composite scaffold (Figure 15). The results of the thematic clustering reveal that the research literature in this area focuses on three main blocks of research: stem cell research, cell marker research, and research on scaffolds. Based on the analysis of the strongest citation bursts of keywords, the development of this study can be divided into three main periods. In the early stages, research in this field concentrated on MRI and diagnostic aspects of disease; in the middle stages, it focused on the labeling of SCs and *in vivo* tracking; the current hotspots and trends are in scaffold research, regenerative tissue engineering of bone and osteogenesis, and the transformation of the scaffold from a single component at the beginning to a composite scaffold. It is worth mentioning that HA is the main inorganic component of bone and its excellent biocompatibility, osteoconductivity and osteoinductivity, binding similarity, and high porosity make it an important area of interest for bone regeneration research (Ramesh et al., 2018; Gomes et al., 2019). Its effects are primarily in the coating of IO, the construction of scaffolds, and the delivery of drugs (Khajuria et al., 2018). However, HA has certain drawbacks, as its fragility reduces the mechanical properties of the material, and its demonstrated difficulty in modification makes the nanoparticles prone to agglomeration (Jegatheeswaran and Sundrarajan, 2015; Alaribe et al., 2016). To address these issues, nHAp can be combined with polymers to strengthen their mechanical properties, biocompatibility, and biofunctionability, eventually improving overall regeneration (Song et al., 2016).

Concluding remarks—future perspectives

Although bone has the potential to heal itself, larger bone defects are irreversible; it is a serve health problem and how to promote bone regeneration remains a clinical challenge.

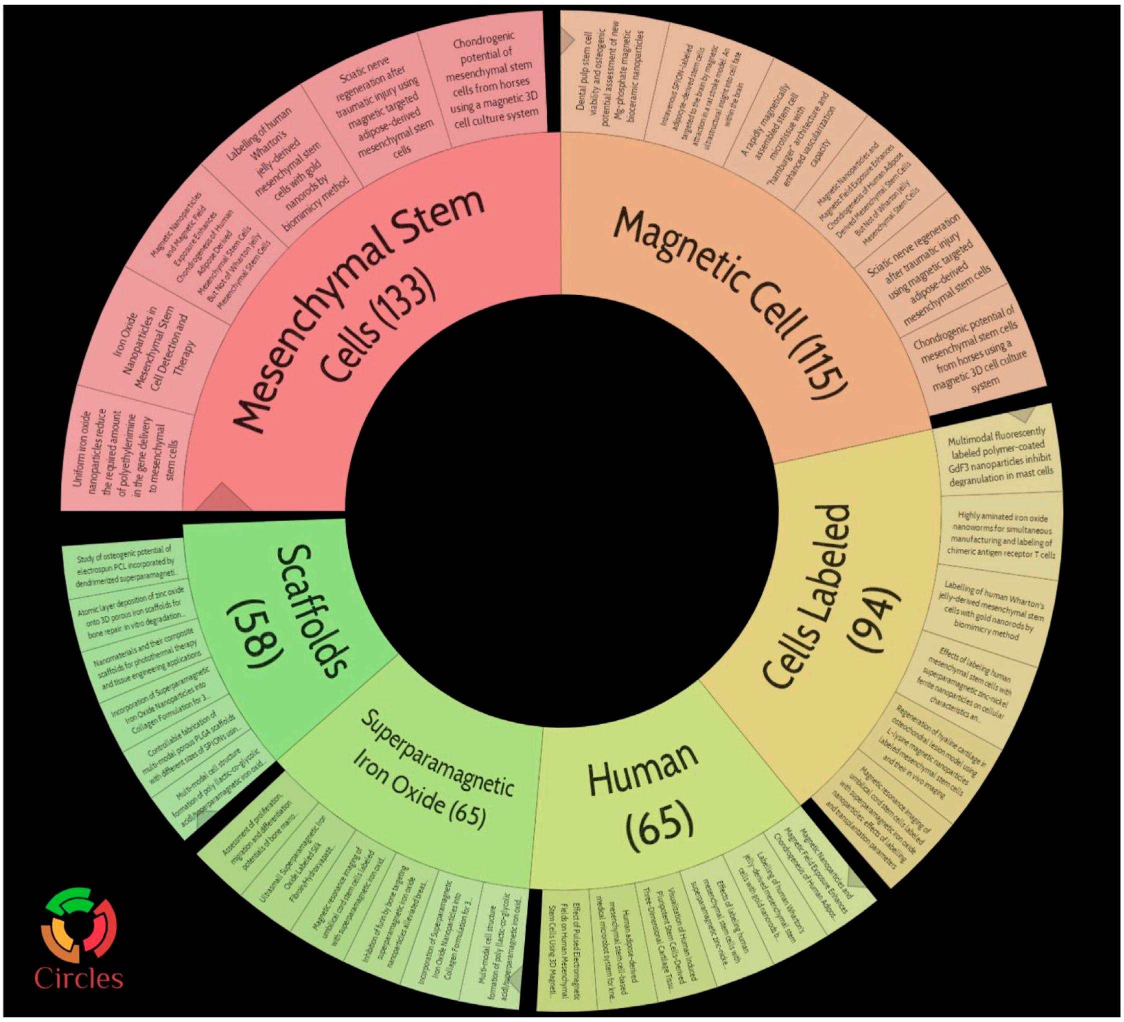

FIGURE 14
Pie chart of topic clustering in carrot2. The main directions of research clustering are Mesenchymal Stem Cells, Magnetic Cells, Cells Labeled, Human, Superparamagnetic Iron Oxide, and Scaffolds.

IONPs are an important member of the nanoparticle class because their magnetic properties give them unique advantages in bone repair, including stimulating osteogenic differentiation, cell labeling, drug delivery, molecular activation, and SCs homing. The powerful effect of IONPs is inseparable from their coating. The external coating reduces the toxicity of IO and improves the overall biocompatibility and mechanical properties of the IONPs. Additionally, the external modification of the coating with cytokines, drugs, and targets can also give IONPs a targeted therapeutic effect. The bone regenerative effect of IONPs is also influenced by external magnetic fields, which can be remotely controlled to induce various biological responses. IONPs are now regularly used in combination with SCs and scaffolds to achieve good bone regeneration results. It promotes migration, adsorption, homing, labeling, and osteogenic differentiation of SCs and confers a magnetic effect on the scaffold. In composite scaffolds, good biocompatibility, mechanical properties, resorbability, osteoconductivity, and osteoinductivity are essential for bone regeneration. Although some scholars have initiated to explore the specific mechanisms by which IONPs treat bone defects, the interactions between magnetic fields, cells, and nanoparticles in composite scaffolds are still not sufficiently understood. Although basic research has identified the crucial role of bone morphogenetic proteins, vascular endothelial growth factor, osteocalcin, and collagen in bone regeneration, there is still a need to further explore and elucidate their therapeutic mechanisms. The bibliometric analysis also identified hotspots and trends in promoting

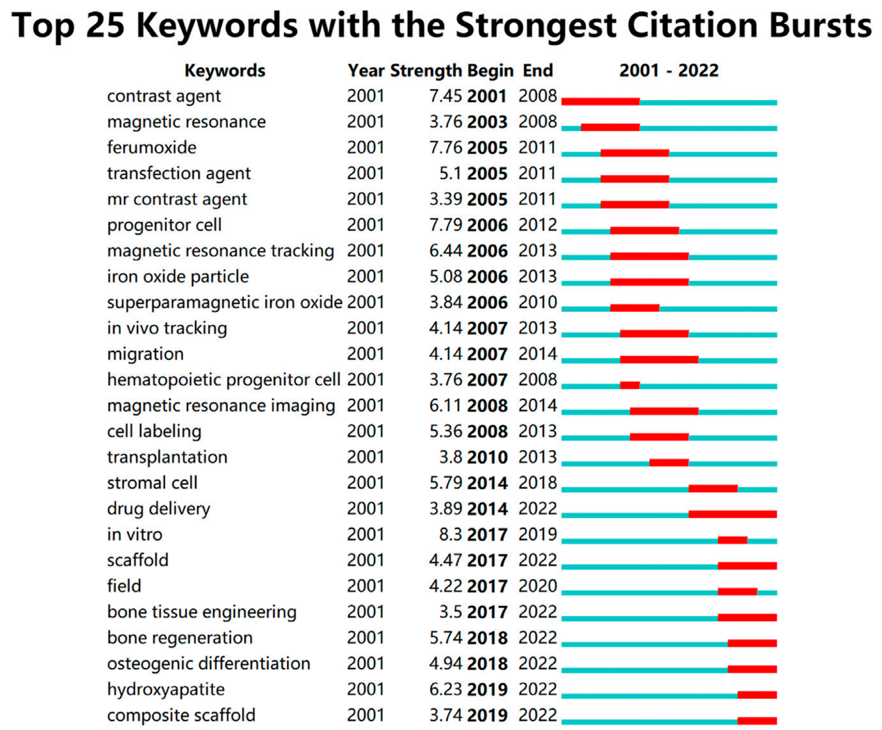

Keywords	Year	Strength	Begin	End
contrast agent	2001	7.45	**2001**	2008
magnetic resonance	2001	3.76	**2003**	2008
ferumoxide	2001	7.76	**2005**	2011
transfection agent	2001	5.1	**2005**	2011
mr contrast agent	2001	3.39	**2005**	2011
progenitor cell	2001	7.79	**2006**	2012
magnetic resonance tracking	2001	6.44	**2006**	2013
iron oxide particle	2001	5.08	**2006**	2013
superparamagnetic iron oxide	2001	3.84	**2006**	2010
in vivo tracking	2001	4.14	**2007**	2013
migration	2001	4.14	**2007**	2014
hematopoietic progenitor cell	2001	3.76	**2007**	2008
magnetic resonance imaging	2001	6.11	**2008**	2014
cell labeling	2001	5.36	**2008**	2013
transplantation	2001	3.8	**2010**	2013
stromal cell	2001	5.79	**2014**	2018
drug delivery	2001	3.89	**2014**	2022
in vitro	2001	8.3	**2017**	2019
scaffold	2001	4.47	**2017**	2022
field	2001	4.22	**2017**	2020
bone tissue engineering	2001	3.5	**2017**	2022
bone regeneration	2001	5.74	**2018**	2022
osteogenic differentiation	2001	4.94	**2018**	2022
hydroxyapatite	2001	6.23	**2019**	2022
composite scaffold	2001	3.74	**2019**	2022

FIGURE 15
Top 25 keywords with the strongest citation bursts. This research focuses on three main blocks of research: stem cell research, cell marker research, and research on scaffolds. Based on the analysis of the strongest citation bursts of keywords, the development of this study can be divided into three main periods. In the early stages, research in this field concentrated on MRI and diagnostic aspects of disease; in the middle stages, it focused on the labeling of SCs and *in vivo* tracking; the current hotspots and trends are in scaffold research, regenerative tissue engineering of bone and osteogenesis, and the transformation of the scaffold from a single component at the beginning to a composite scaffold.

bone regeneration by IONPs from MRI, cell labeling to *in vitro* experiments, composite scaffolds, bone tissue engineering, and hydroxyapatite. Later studies can further experiment with innovations in tissue engineering based on HA combined with IONPs, and adding other organic or inorganic material components, adding cytokines or pharmaceutical components to better accomplish the purpose of bone regeneration. It is worth mentioning that although IONPs are relatively safe for use in bone regeneration, their toxicity is influenced by some factors, and specific toxicological studies and refined interpretation protocols are areas that we will need to explore further at a later stage.

Author contributions

NW and YX: conceptualization, methodology, investigation, writing-original draft. ZX and ZM: conceptualization, datum analysis. RD and XL: writing-review and editing. XL and RK: Writing and revising, supervision.

Funding

This work was funded by the Natural Science Foundation of Jiangsu Province (BK20220464), National Natural Science Foundation of China (81772356), Project of National Clinical Research Base of Traditional Chinese Medicine in Jiangsu Province (JD2022SZXMS07) and Jiangsu Province Cadre Health Care Project (BJ19030). We sincerely thank Mr Zhanpeng Yan of the clinical research room of integrated traditional Chinese and Western medicine in the Affiliated Hospital of Integrated Traditional Chinese and Western Medicine, Nanjing University of Chinese Medicine for his guidance and help in writing this article.

Acknowledgments

We sincerely thank Mr Zhanpeng Yan of the clinical research room of integrated traditional Chinese and Western medicine in the Affiliated Hospital of Integrated Traditional Chinese and Western Medicine, Nanjing

University of Chinese Medicine for his guidance and help in writing this article.

Conflict of interest

The authors declare that the research was conducted in the absence of any commercial or financial relationships that could be construed as a potential conflict of interest.

Publisher's note

References

Accomasso, L., Gallina, C., Turinetto, V., and Giachino, C. (2016). Stem cell tracking with nanoparticles for regenerative medicine purposes: An overview. *Stem Cells Int.* 2016, 1–23. doi:10.1155/2016/7920358

Alaribe, F. N., Manoto, S. L., and Motaung, S. (2016). Scaffolds from biomaterials: Advantages and limitations in bone and tissue engineering. *Biologia* 71 (4), 353–366. doi:10.1515/biolog-2016-0056

Albarqi, H. A., Wong, L. H., Schumann, C., Sabei, F. Y., Korzun, T., Li, X. N., et al. (2019). Biocompatible nanoclusters with high heating efficiency for systemically delivered magnetic hyperthermia. *Acs Nano* 13 (6), 6383–6395. doi:10.1021/acsnano.8b06542

Arami, H., Khandhar, A., Liggitt, D., and Krishnan, K. M. (2015). *In vivo* delivery, pharmacokinetics, biodistribution and toxicity of iron oxide nanoparticles. *Chem. Soc. Rev.* 44 (23), 8576–8607. doi:10.1039/c5cs00541h

Bai, H. T., Zhao, Y., Wang, C. Y., Wang, Z. H., Wang, J. C., Liu, H., et al. (2020). Enhanced osseointegration of three-dimensional supramolecular bioactive interface through osteoporotic microenvironment regulation. *Theranostics* 10 (11), 4779–4794. doi:10.7150/thno.43736

Bardestani, A., Ebrahimpour, S., Esmaeili, A., and Esmaeili, A. (2021). Quercetin attenuates neurotoxicity induced by iron oxide nanoparticles. *J. Nanobiotechnology* 19 (1), 327. doi:10.1186/s12951-021-01059-0

Bhavani, P., Rajababu, C. H., Arif, M. D., Reddy, I. V. S., and Reddy, N. R. (2017). Synthesis of high saturation magnetic iron oxide nanomaterials via low temperature hydrothermal method. *J. Magnetism Magnetic Mater.* 426, 459–466. doi:10.1016/j.jmmm.2016.09.049

Bi, X., Li, L., Mao, Z., Liu, B., Yang, L., He, W., et al. (2020). The effects of silk layer-by-layer surface modification on the mechanical and structural retention of extracellular matrix scaffolds. *Biomater. Sci.* 8 (14), 4026–4038. doi:10.1039/d0bm00448k

Bobo, D., Robinson, K. J., Islam, J., Thurecht, K. J., and Corrie, S. R. (2016). Nanoparticle-based medicines: A review of FDA-approved materials and clinical trials to date. *Pharm. Res.* 33 (10), 2373–2387. doi:10.1007/s11095-016-1958-5

Carneiro, M. F. H., Machado, A. R. T., Antunes, L. M. G., Souza, T. E., Freitas, V. A., Oliveira, L. C. A., et al. (2020). Gold-coated superparamagnetic iron oxide nanoparticles attenuate collagen-induced arthritis after magnetic targeting. *Biol. Trace Elem. Res.* 194 (2), 502–513. doi:10.1007/s12011-019-01799-z

Česen Mazič, M., Girandon, L., Kneževič, M., Avčin, S. L., and Jazbec, J. (2018). Treatment of severe steroid-refractory acute-graft-vs.-host disease with mesenchymal stem cells-single center experience. *Front. Bioeng. Biotechnol.* 6, 93. doi:10.3389/fbioe.2018.00093

Chen, H., Sun, J., Wang, Z., Zhou, Y., Lou, Z., Chen, B., et al. (2018). Magnetic cell-scaffold interface constructed by superparamagnetic IONP enhanced osteogenesis of adipose-derived stem cells. *ACS Appl. Mat. Interfaces* 10 (51), 44279–44289. doi:10.1021/acsami.8b17427

Chen, S., Chen, X., Geng, Z., and Su, J. (2022). The horizon of bone organoid: A perspective on construction and application. *Bioact. Mat.* 18, 15–25. doi:10.1016/j.bioactmat.2022.01.048

Chen, Y., Bose, A., and Bothun, G. D. (2010). Controlled release from bilayer-decorated magnetoliposomes via electromagnetic heating. *ACS Nano* 4 (6), 3215–3221. doi:10.1021/nn100274v

Chen, Y., Geng, J. Q., Zhuang, Y. X., Zhao, J., Chu, L. Q., Luo, X. X., et al. (2016). Preparation of the chitosan grafted poly (quaternary ammonium)/Fe3O4 nanoparticles and its adsorption performance for food yellow 3. *Carbohydr. Polym.* 152, 327–336. doi:10.1016/j.carbpol.2016.06.114

Chiang, C. S., Chen, J. Y., Chiang, M. Y., Hou, K. T., Li, W. M., Chang, S. J., et al. (2018). Using the interplay of magnetic guidance and controlled TGF-β release from protein-based nanocapsules to stimulate chondrogenesis. *Int. J. Nanomedicine* 13, 3177–3188. doi:10.2147/ijn.S156284

Clark, S. M., Prilliman, S. G., Erdonmez, C. K., and Alivisatos, A. P. (2005). Size dependence of the pressure-induced gamma to alpha structural phase transition in iron oxide nanocrystals. *Nanotechnology* 16 (12), 2813–2818. doi:10.1088/0957-4484/16/12/013

Coccini, T., De Simone, U., Roccio, M., Croce, S., Lenta, E., Zecca, M., et al. (2019). *In vitro* toxicity screening of magnetite nanoparticles by applying mesenchymal stem cells derived from human umbilical cord lining. *J. Appl. Toxicol.* 39 (9), 1320–1336. doi:10.1002/jat.3819

Cotin, G., Heinrich, B., Perton, F., Kiefer, C., Francius, G., Mertz, D., et al. (2022). A confinement-driven nucleation mechanism of metal oxide nanoparticles obtained via thermal decomposition in organic media. *Small* 18, e2200414. doi:10.1002/smll.202200414

Dadfar, S. M., Roemhild, K., Drude, N. I., von Stillfried, S., Knüchel, R., Kiessling, F., et al. (2019). Iron oxide nanoparticles: Diagnostic, therapeutic and theranostic applications. *Adv. Drug Deliv. Rev.* 138, 302–325. doi:10.1016/j.addr.2019.01.005

Daldrup-Link, H. E. (2017). Ten things you might not know about iron oxide nanoparticles. *Radiology* 284 (3), 616–629. doi:10.1148/radiol.2017162759

Daneshmandi, S., Karimi, M. H., and Pourfathollah, A. A. (2017). TGF-β engineered mesenchymal stem cells (TGF-β/MSCs) for treatment of Type 1 diabetes (T1D) mice model. *Int. Immunopharmacol.* 44, 191–196. doi:10.1016/j.intimp.2017.01.019

Das, B., Girigoswami, A., Dutta, A., Pal, P., Dutta, J., Dadhich, P., et al. (2019). Carbon nanodots doped super-paramagnetic iron oxide nanoparticles for multimodal bioimaging and osteochondral tissue regeneration via external magnetic actuation. *ACS Biomater. Sci. Eng.* 5 (7), 3549–3560. doi:10.1021/acsbiomaterials.9b00571

Dasari, A., Xue, J. Y., and Deb, S. (2022). Magnetic nanoparticles in bone tissue engineering. *Nanomaterials* 12 (5), 757. doi:10.3390/nano12050757

Dhivya, S., Ajita, J., and Selvamurugan, N. (2015). Metallic nanomaterials for bone tissue engineering. *J. Biomed. Nanotechnol.* 11 (10), 1675–1700. doi:10.1166/jbn.2015.2115

Duan, J. L., Dong, J. L., Zhang, T. T., Su, Z. Y., Ding, J., Zhang, Y., et al. (2014). Polyethyleneimine-functionalized iron oxide nanoparticles for systemic siRNA delivery in experimental arthritis. *Nanomedicine* 9 (6), 789–801. doi:10.2217/nnm.13.217

Duan, L., Zuo, J., Zhang, F., Li, B., Xu, Z., Zhang, H., et al. (2020). Magnetic targeting of HU-MSCs in the treatment of glucocorticoid-associated osteonecrosis of the femoral head through akt/bcl2/bad/caspase-3 pathway. *Int. J. Nanomedicine* 15, 3605–3620. doi:10.2147/ijn.S244453

Estévez, M., Montalbano, G., Gallo-Cordova, A., Ovejero, J. G., Izquierdo-Barba, I., González, B., et al. (2022). Incorporation of superparamagnetic iron oxide nanoparticles into collagen formulation for 3D electrospun scaffolds. *Nanomater. (Basel)* 12 (2), 181. doi:10.3390/nano12020181

Fan, M., Yan, J., Tan, H., Miao, Y., and Hu, X. (2014). Magnetic biopolymer nanogels via biological assembly for vectoring delivery of biopharmaceuticals. *J. Mat. Chem. B* 2 (47), 8399–8405. doi:10.1039/c4tb01106f

Fazzalari, N. L. (2011). Bone fracture and bone fracture repair. *Osteoporos. Int.* 22 (6), 2003–2006. doi:10.1007/s00198-011-1611-4

Ferrage, L., Bertrand, G., Lenormand, P., Grossin, D., and Ben-Nissan, B. (2017). A review of the additive manufacturing (3DP) of bioceramics: Alumina, zirconia

(PSZ) and hydroxyapatite. *J. Aust. Ceram. Soc.* 53 (1), 11–20. doi:10.1007/s41779-016-0003-9

Ferreira, R. V., Silva-Caldeira, P. P., Pereira-Maia, E. C., Fabris, J. D., Cavalcante, L. C. D., Ardisson, J. D., et al. (2016). Bio-inactivation of human malignant cells through highly responsive diluted colloidal suspension of functionalized magnetic iron oxide nanoparticles. *J. Nanopart. Res.* 18 (4), 92. doi:10.1007/s11051-016-3400-7

Filardo, G., Petretta, M., Cavallo, C., Roseti, L., Durante, S., Albisinni, U., et al. (2019). Patient-specific meniscus prototype based on 3D bioprinting of human cell-laden scaffold. *Bone Jt. Res.* 8 (2), 101–106. doi:10.1302/2046-3758.82.Bjr-2018-0134.R1

Gao, J. Y., Cai, S. M., Wang, Z. J., Li, D., Ou, M. Y., Zhang, X. L., et al. (2022). The optimization of ligature/bone defect-induced periodontitis model in rats. *Odontology*. doi:10.1007/s10266-022-00715-7

Ghosh, S., More, P., Derle, A., Kitture, R., Kale, T., Gorain, M., et al. (2015). Diosgenin functionalized iron oxide nanoparticles as novel nanomaterial against breast cancer. *J. Nanosci. Nanotechnol.* 15 (12), 9464–9472. doi:10.1166/jnn.2015.11704

Gomes, D. S., Santos, A. M. C., Neves, G. A., and Menezes, R. R. (2019). A brief review on hydroxyapatite production and use in biomedicine. *Cerâmica* 65 (374), 282–302. doi:10.1590/0366-69132019653742706

Grayson, W. L., Bunnell, B. A., Martin, E., Frazier, T., Hung, B. P., and Gimble, J. M. (2015). Stromal cells and stem cells in clinical bone regeneration. *Nat. Rev. Endocrinol.* 11 (3), 140–150. doi:10.1038/nrendo.2014.234

Guo, X. M., Li, W., Luo, L. H., Wang, Z. H., Li, Q. P., Kong, F. F., et al. (2017). External magnetic field-enhanced chemo-photothermal combination tumor therapy via iron oxide nanoparticles. *ACS Appl. Mat. Interfaces* 9 (19), 16581–16593. doi:10.1021/acsami.6b16513

Guo, Y., Liu, Y., Shi, C., Wu, T., Cui, Y., Wang, S., et al. (2021). Remote-controllable bone-targeted delivery of estradiol for the treatment of ovariectomy-induced osteoporosis in rats. *J. Nanobiotechnology* 19 (1), 248. doi:10.1186/s12951-021-00976-4

Hajinasab, A., Saber-Samandari, S., Ahmadi, S., and Alamara, K. (2018). Preparation and characterization of a biocompatible magnetic scaffold for biomedical engineering. *Mater. Chem. Phys.* 204, 378–387. doi:10.1016/j.matchemphys.2017.10.080

Han, L., Guo, Y., Jia, L., Zhang, Q., Sun, L., Yang, Z., et al. (2021a). 3D magnetic nanocomposite scaffolds enhanced the osteogenic capacities of rat bone mesenchymal stem cells *in vitro* and in a rat calvarial bone defect model by promoting cell adhesion. *J. Biomed. Mat. Res. A* 109 (9), 1670–1680. doi:10.1002/jbm.a.37162

Han, X., Tang, S., Wang, L., Xu, X., Yan, R., Yan, S., et al. (2021b). Multicellular spheroids formation on hydrogel enhances osteogenic/odontogenic differentiation of dental pulp stem cells under magnetic nanoparticles induction. *Int. J. Nanomedicine* 16, 5101–5115. doi:10.2147/ijn.S318991

Hankenson, K. D., Gagne, K., and Shaughnessy, M. (2015). Extracellular signaling molecules to promote fracture healing and bone regeneration. *Adv. Drug Deliv. Rev.* 94, 3–12. doi:10.1016/j.addr.2015.09.008

Hao, J., Bai, B., Ci, Z., Tang, J., Hu, G., Dai, C., et al. (2022). Large-sized bone defect repair by combining a decalcified bone matrix framework and bone regeneration units based on photo-crosslinkable osteogenic microgels. *Bioact. Mat.* 14, 97–109. doi:10.1016/j.bioactmat.2021.12.013

Hao, L., Li, L., Wang, P., Wang, Z., Shi, X., Guo, M., et al. (2019). Synergistic osteogenesis promoted by magnetically actuated nano-mechanical stimuli. *Nanoscale* 11 (48), 23423–23437. doi:10.1039/c9nr07170a

Harrison, R., Markides, H., Morris, R. H., Richards, P., El Haj, A. J., and Sottile, V. (2017). Autonomous magnetic labelling of functional mesenchymal stem cells for improved traceability and spatial control in cell therapy applications. *J. Tissue Eng. Regen. Med.* 11 (8), 2333–2348. doi:10.1002/term.2133

Hassanajili, S., Karami-Pour, A., Oryan, A., and Talaei-Khozani, T. (2019). Preparation and characterization of PLA/PCL/HA composite scaffolds using indirect 3D printing for bone tissue engineering. *Mater. Sci. Eng. C* 104, 109960. doi:10.1016/j.msec.2019.109960

Ho-Shui-Ling, A., Bolander, J., Rustom, L. E., Johnson, A. W., Luyten, F. P., and Picart, C. (2018). Bone regeneration strategies: Engineered scaffolds, bioactive molecules and stem cells current stage and future perspectives. *Biomaterials* 180, 143–162. doi:10.1016/j.biomaterials.2018.07.017

Hola, K., Markova, Z., Zoppellaro, G., Tucek, J., and Zboril, R. (2015). Tailored functionalization of iron oxide nanoparticles for MRI, drug delivery, magnetic separation and immobilization of biosubstances. *Biotechnol. Adv.* 33, 1162–1176. doi:10.1016/j.biotechadv.2015.02.003

Hou, S., Niu, X., Li, L., Zhou, J., Qian, Z., Yao, D., et al. (2019). Simultaneous nano- and microscale structural control of injectable hydrogels via the assembly of nanofibrous protein microparticles for tissue regeneration. *Biomaterials* 223, 119458. doi:10.1016/j.biomaterials.2019.119458

Hu, K., Sun, J., Guo, Z., Wang, P., Chen, Q., Ma, M., et al. (2015). A novel magnetic hydrogel with aligned magnetic colloidal assemblies showing controllable enhancement of magnetothermal effect in the presence of alternating magnetic field. *Adv. Mat.* 27 (15), 2507–2514. doi:10.1002/adma.201405757

Hu, S., Chen, H., Zhou, F., Liu, J., Qian, Y., Hu, K., et al. (2021). Superparamagnetic core-shell electrospun scaffolds with sustained release of IONPs facilitating *in vitro* and *in vivo* bone regeneration. *J. Mat. Chem. B* 9 (43), 8980–8993. doi:10.1039/d1tb01261d

Hu, S., Zhou, Y., Zhao, Y., Xu, Y., Zhang, F., Gu, N., et al. (2018). Enhanced bone regeneration and visual monitoring via superparamagnetic iron oxide nanoparticle scaffold in rats. *J. Tissue Eng. Regen. Med.* 12 (4), e2085–e2098. doi:10.1002/term.2641

Hua, P., Wang, Y. Y., Liu, L. B., Liu, J. L., Liu, J. Y., Yang, Y. Q., et al. (2015). *In vivo* magnetic resonance imaging tracking of transplanted superparamagnetic iron oxide-labeled bone marrow mesenchymal stem cells in rats with myocardial infarction. *Mol. Med. Rep.* 11 (1), 113–120. doi:10.3892/mmr.2014.2649

Huang, J., Liu, W., Liang, Y., Li, L., Duan, L., Chen, J., et al. (2018). Preparation and biocompatibility of diphasic magnetic nanocomposite scaffold. *Mater. Sci. Eng. C* 87, 70–77. doi:10.1016/j.msec.2018.02.003

Huang, Q., Zou, Y., Arno, M. C., Chen, S., Wang, T., Gao, J., et al. (2017). Hydrogel scaffolds for differentiation of adipose-derived stem cells. *Chem. Soc. Rev.* 46 (20), 6255–6275. doi:10.1039/c6cs00052e

Huang, Y. W., Cambre, M., and Lee, H. J. (2017). The toxicity of nanoparticles depends on multiple molecular and physicochemical mechanisms. *Int. J. Mol. Sci.* 18 (12), 2702. doi:10.3390/ijms18122702

Huang, Z., He, Y., Chang, X., Liu, J., Yu, L., Wu, Y., et al. (2020). A magnetic iron oxide/polydopamine coating can improve osteogenesis of 3D-printed porous titanium scaffolds with a static magnetic field by upregulating the TGFβ-smads pathway. *Adv. Healthc. Mat.* 9 (14), e2000318. doi:10.1002/adhm.202000318

Iacoviță, C., Fizeșan, I., Nitica, S., Florea, A., Barbu-Tudoran, L., Dudric, R., et al. (2021). Silica coating of ferromagnetic iron oxide magnetic nanoparticles significantly enhances their hyperthermia performances for efficiently inducing cancer cells death *in vitro*. *Pharmaceutics* 13 (12), 2026. doi:10.3390/pharmaceutics13122026

Ingber, D. E. (2006). Cellular mechanotransduction: Putting all the pieces together again. *FASEB J.* 20 (7), 811–827. doi:10.1096/fj.05-5424rev

Iyer, S. R., Xu, S., Stains, J. P., Bennett, C. H., and Lovering, R. M. (2017). Superparamagnetic iron oxide nanoparticles in musculoskeletal biology. *Tissue Eng. Part B Rev.* 23 (4), 373–385. doi:10.1089/ten.TEB.2016.0437

Jakob, F., Ebert, R., Ignatius, A., Matsushita, T., Watanabe, Y., Groll, J., et al. (2013). Bone tissue engineering in osteoporosis. *Maturitas* 75 (2), 118–124. doi:10.1016/j.maturitas.2013.03.004

Jang, J. H., Castano, O., and Kim, H. W. (2009). Electrospun materials as potential platforms for bone tissue engineering. *Adv. Drug Deliv. Rev.* 61 (12), 1065–1083. doi:10.1016/j.addr.2009.07.008

Jegatheeswaran, S., and Sundrarajan, M. (2015). PEGylation of novel hydroxyapatite/PEG/Ag nanocomposite particles to improve its antibacterial efficacy. *Mater. Sci. Eng. C* 51, 174–181. doi:10.1016/j.msec.2015.02.012

Jia, L., Yang, Z. K., Sun, L. X., Zhang, Q., Guo, Y., Chen, Y. L., et al. (2021). A three-dimensional-printed SPION/PLGA scaffold for enhanced palate-bone regeneration and concurrent alteration of the oral microbiota in rats. *Mater. Sci. Eng. C* 126, 112173. doi:10.1016/j.msec.2021.112173

Jia, Y. C., Zhang, P. L., Sun, Y. C., Kang, Q. L., Xu, J., Zhang, C. F., et al. (2019). Regeneration of large bone defects using mesoporous silica coated magnetic nanoparticles during distraction osteogenesis. *Nanomedicine Nanotechnol. Biol. Med.* 21, 102040. doi:10.1016/j.nano.2019.102040

Jiang, P., Zhang, Y., Zhu, C., Zhang, W., Mao, Z., and Gao, C. (2016). Fe(3) O(4)/BSA particles induce osteogenic differentiation of mesenchymal stem cells under static magnetic field. *Acta Biomater.* 46, 141–150. doi:10.1016/j.actbio.2016.09.020

Jun, I., Han, H. S., Edwards, J. R., and Jeon, H. (2018). Electrospun fibrous scaffolds for tissue engineering: Viewpoints on architecture and fabrication. *Int. J. Mol. Sci.* 19 (3), 745. doi:10.3390/ijms19030745

Kangari, P., Talaei-Khozani, T., Razeghian-Jahromi, I., and Razmkhah, M. (2020). Mesenchymal stem cells: Amazing remedies for bone and cartilage defects. *Stem Cell. Res. Ther.* 11 (1), 492. doi:10.1186/s13287-020-02001-1

Kesse, X., Adam, A., Begin-Colin, S., Mertz, D., Larquet, E., Gacoin, T., et al. (2020). Elaboration of superparamagnetic and bioactive multicore-shell nanoparticles (gamma-Fe2O3@SiO2-CaO): A promising material for bone cancer treatment. *ACS Appl. Mat. Interfaces* 12 (42), 47820–47830. doi:10.1021/acsami.0c12769

Khajuria, D. K., Kumar, V. B., Gigi, D., Gedanken, A., and Karasik, D. (2018). Accelerated bone regeneration by nitrogen-doped carbon dots functionalized with hydroxyapatite nanoparticles. *ACS Appl. Mat. Interfaces* 10 (23), 19373–19385. doi:10.1021/acsami.8b02792

Khalili, M., Keshvari, H., Imani, R., Sohi, A. N., Esmaeili, E., and Tajabadi, M. (2022). Study of osteogenic potential of electrospun PCL incorporated by dendrimerized superparamagnetic nanoparticles as a bone tissue engineering scaffold. *Polym. Adv. Technol.* 33 (3), 782–794. doi:10.1002/pat.5555

Khodaei, A., Jahanmard, F., Madaah Hosseini, H. R., Bagheri, R., Dabbagh, A., Weinans, H., et al. (2022). Controlled temperature-mediated curcumin release from magneto-thermal nanocarriers to kill bone tumors. *Bioact. Mat.* 11, 107–117. doi:10.1016/j.bioactmat.2021.09.028

Kim, K., and Fisher, J. P. (2007). Nanoparticle technology in bone tissue engineering. *J. Drug Target.* 15 (4), 241–252. doi:10.1080/10611860701289818

Kircher, M. F., Gambhir, S. S., and Grimm, J. (2011). Noninvasive cell-tracking methods. *Nat. Rev. Clin. Oncol.* 8 (11), 677–688. doi:10.1038/nrclinonc.2011.141

Kitture, R., and Ghosh, S. J. (2019). *Hybrid nanostructures for* in vivo *imaging.*

Kiyani, M. M., Moghul, N. B., Butt, M. A., Rehman, H., Masood, R., Rajput, T. A., et al. (2022). Anti-hyperuricemic effect of iron oxide nanoparticles against monosodium urate crystals induced gouty arthritis in BALB/c mice. *Biol. Trace Elem. Res.* 200 (4), 1659–1666. doi:10.1007/s12011-021-02769-0

Kolosnjaj-Tabi, J., Wilhelm, C., Clément, O., and Gazeau, F. (2013). Cell labeling with magnetic nanoparticles: Opportunity for magnetic cell imaging and cell manipulation. *J. Nanobiotechnology* 11, S7. doi:10.1186/1477-3155-11-s1-s7

Koons, G. L., Diba, M., and Mikos, A. G. (2020). Materials design for bone-tissue engineering. *Nat. Rev. Mat.* 5, 584–603. doi:10.1038/s41578-020-0204-2

Kowalczewski, C. J., and Saul, J. M. (2018). Biomaterials for the delivery of growth factors and other therapeutic agents in tissue engineering approaches to bone regeneration. *Front. Pharmacol.* 9, 513. doi:10.3389/fphar.2018.00513

Kumar, P., Saini, M., Dehiya, B. S., Sindhu, A., Kumar, V., Kumar, R., et al. (2020). Comprehensive survey on nanobiomaterials for bone tissue engineering applications. *Nanomater. (Basel)* 10 (10), 2019. doi:10.3390/nano10102019

Laurent, S., Forge, D., Port, M., Roch, A., Robic, C., Vander Elst, L., et al. (2008). Magnetic iron oxide nanoparticles: Synthesis, stabilization, vectorization, physicochemical characterizations, and biological applications. *Chem. Rev.* 108 (6), 2064–2110. doi:10.1021/cr068445e

Lee, H., Thirunavukkarasu, G. K., Kim, S., and Lee, J. Y. (2018). Remote induction of *in situ* hydrogelation in a deep tissue, using an alternating magnetic field and superparamagnetic nanoparticles. *Nano Res.* 11 (11), 5997–6009. doi:10.1007/s12274-018-2114-9

Lee, M. S., Su, C. M., Yeh, J. C., Wu, P. R., Tsai, T. Y., and Lou, S. L. (2016). Synthesis of composite magnetic nanoparticles Fe_3O_4 with alendronate for osteoporosis treatment. *Int. J. Nanomedicine* 11, 4583–4594. doi:10.2147/ijn.S112415

Li, M., Fu, S., Cai, Z., Li, D., Liu, L., Deng, D., et al. (2021). Dual regulation of osteoclastogenesis and osteogenesis for osteoporosis therapy by iron oxide hydroxyapatite core/shell nanocomposites. *Regen. Biomater.* 8 (5), rbab027. doi:10.1093/rb/rbab027

Li, X., Wei, J., Aifantis, K. E., Fan, Y., Feng, Q., Cui, F. Z., et al. (2016). Current investigations into magnetic nanoparticles for biomedical applications. *J. Biomed. Mat. Res. A* 104 (5), 1285–1296. doi:10.1002/jbm.a.35654

Li, X., Wei, Z., Lv, H., Wu, L., Cui, Y., Yao, H., et al. (2019). Iron oxide nanoparticles promote the migration of mesenchymal stem cells to injury sites. *Int. J. Nanomedicine* 14, 573–589. doi:10.2147/ijn.S184920

Li, Y., Chen, Z. W., and Gu, N. (2012). *In vitro* biological effects of magnetic nanoparticles. *Chin. Sci. Bull.* 57 (31), 3972–3978. doi:10.1007/s11434-012-5295-8

Li, Y. J., Chen, H., Wu, J., He, Q., Li, Y. T., Yang, W. B., et al. (2018). Preparation and characterization of APTES modified magnetic MMT capable of using as anisotropic nanoparticles. *Appl. Surf. Sci.* 447, 393–400. doi:10.1016/j.apsusc.2018.03.230

Li, Y., Ye, D. W., Li, M. X., Ma, M., and Gu, N. (2018). Adaptive materials based on iron oxide nanoparticles for bone regeneration. *Chemphyschem* 19 (16), 1965–1979. doi:10.1002/cphc.201701294

Li, Z., Du, T., Ruan, C., and Niu, X. (2021). Bioinspired mineralized collagen scaffolds for bone tissue engineering. *Bioact. Mat.* 6 (5), 1491–1511. doi:10.1016/j.bioactmat.2020.11.004

Li, Z. H., Bai, H. T., Wang, Z. H., Liu, Y. Z., Ren, M., Wang, X. G., et al. (2022a). Ultrasound-mediated rapamycin delivery for promoting osseointegration of 3D printed prosthetic interfaces via autophagy regulation in osteoporosis. *Mater. Des.* 216, 110586. doi:10.1016/j.matdes.2022.110586

Li, Z. H., Zhao, Y., Wang, Z. H., Ren, M., Wang, X. G., Liu, H., et al. (2022b). Engineering multifunctional hydrogel-integrated 3D printed bioactive prosthetic interfaces for osteoporotic osseointegration. *Adv. Healthc. Mat.* 11 (11), 2102535. doi:10.1002/adhm.202102535

Li, Z. Y., Ba, R. K., Wang, Z. F., Wei, J. H., Zhao, Y. M., and Wu, W. (2017). Angiogenic potential of human bone marrow-derived mesenchymal stem cells in chondrocyte brick-enriched constructs promoted stable regeneration of craniofacial cartilage. *Stem Cells Transl. Med.* 6 (2), 601–612. doi:10.5966/sctm.2016-0050

Liao, W., Lu, J. W., Wang, Q. J., Yan, S., Li, Y., Zhang, Y. B., et al. (2022). Osteogenesis of iron oxide nanoparticles-labeled human precartilaginous stem cells in interpenetrating network printable hydrogel. *Front. Bioeng. Biotechnol.* 10, 872149. doi:10.3389/fbioe.2022.872149

Lin, S., Lin, K. F., Lu, D. N., and Liu, Z. (2017). Preparation of uniform magnetic iron oxide nanoparticles by co-precipitation in a helical module microchannel reactor. *J. Environ. Chem. Eng.* 5 (1), 303–309. doi:10.1016/j.jece.2016.12.011

Liu, L., Jin, R., Duan, J., Yang, L., Cai, Z., Zhu, W., et al. (2020). Bioactive iron oxide nanoparticles suppress osteoclastogenesis and ovariectomy-induced bone loss through regulating the TRAF6-p62-CYLD signaling complex. *Acta Biomater.* 103, 281–292. doi:10.1016/j.actbio.2019.12.022

Liu, Q., Feng, L., Chen, Z., Lan, Y., Liu, Y., Li, D., et al. (2020). Ultrasmall superparamagnetic iron oxide labeled silk fibroin/hydroxyapatite multifunctional scaffold loaded with bone marrow-derived mesenchymal stem cells for bone regeneration. *Front. Bioeng. Biotechnol.* 8, 697. doi:10.3389/fbioe.2020.00697

Liu, X., Li, L., Gaihre, B., Park, S., Li, Y., Terzic, A., et al. (2022). Scaffold-free spheroids with two-dimensional heteronano-layers (2DHNL) enabling stem cell and osteogenic factor codelivery for bone repair. *ACS Nano* 16 (2), 2741–2755. doi:10.1021/acsnano.1c09688

Liu, Y., Cao, F. L., Sun, B. Q., Bellanti, J. A., and Zheng, S. G. (2021). Magnetic nanoparticles: A new diagnostic and treatment platform for rheumatoid arthritis. *J. Leukoc. Biol.* 109 (2), 415–424. doi:10.1002/jlb.5mr0420-008rr

Liu, Y. N., Liu, Y., Zheng, C. P., Huang, N., Chen, X., Zhu, X. F., et al. (2018). Ru nanoparticles coated with gamma-Fe2O3 promoting and monitoring the differentiation of human mesenchymal stem cells via MRI tracking. *Colloids Surfaces B Biointerfaces* 170, 701–711. doi:10.1016/j.colsurfb.2018.05.041

Loi, F., Córdova, L. A., Pajarinen, J., Lin, T. H., Yao, Z., and Goodman, S. B. (2016). Inflammation, fracture and bone repair. *Bone* 86, 119–130. doi:10.1016/j.bone.2016.02.020

Lopes, D., Martins-Cruz, C., Oliveira, M. B., and Mano, J. F. (2018). Bone physiology as inspiration for tissue regenerative therapies. *Biomaterials* 185, 240–275. doi:10.1016/j.biomaterials.2018.09.028

Lu, J. W., Yang, F., Ke, Q. F., Xie, X. T., and Guo, Y. P. (2018). Magnetic nanoparticles modified-porous scaffolds for bone regeneration and photothermal therapy against tumors. *Nanomedicine Nanotechnol. Biol. Med.* 14 (3), 811–822. doi:10.1016/j.nano.2017.12.025

Lu, R., Zhang, Y., Tao, H., Zhou, L., Li, H., Chen, T., et al. (2020). Gadolinium-hyaluronic acid nanoparticles as an efficient and safe magnetic resonance imaging contrast agent for articular cartilage injury detection. *Bioact. Mat.* 5 (4), 758–767. doi:10.1016/j.bioactmat.2020.05.009

Ma, B., Xie, J., Jiang, J., Shuler, F. D., and Bartlett, D. E. (2013). Rational design of nanofiber scaffolds for orthopedic tissue repair and regeneration. *Nanomedicine (Lond)* 8 (9), 1459–1481. doi:10.2217/nnm.13.132

Mahmoudi, M., Hofmann, H., Rothen-Rutishauser, B., and Petri-Fink, A. (2012). Assessing the *in vitro* and *in vivo* toxicity of superparamagnetic iron oxide nanoparticles. *Chem. Rev.* 112 (4), 2323–2338. doi:10.1021/cr2002596

Mahmoudi, M., Simchi, A., Imani, M., Shokrgozar, M. A., Milani, A. S., Häfeli, U. O., et al. (2010). A new approach for the *in vitro* identification of the cytotoxicity of superparamagnetic iron oxide nanoparticles. *Colloids Surfaces B Biointerfaces* 75 (1), 300–309. doi:10.1016/j.colsurfb.2009.08.044

Marin, E., Boschetto, F., and Pezzotti, G. (2020). Biomaterials and biocompatibility: An historical overview. *J. Biomed. Mat. Res. A* 108 (8), 1617–1633. doi:10.1002/jbm.a.36930

Martino, F., Perestrelo, A. R., Vinarsky, V., Pagliari, S., and Forte, G. (2018). Cellular mechanotransduction: From tension to function. *Front. Physiol.* 9, 824. doi:10.3389/fphys.2018.00824

Marycz, K., Alicka, M., Kornicka-Garbowska, K., Polnar, J., Lis-Bartos, A., Wiglusz, R. J., et al. (2020). Promotion through external magnetic field of osteogenic differentiation potential in adipose-derived mesenchymal stem cells:

Design of polyurethane/poly(lactic) acid sponges doped with iron oxide nanoparticles. *J. Biomed. Mat. Res.* 108 (4), 1398–1411. doi:10.1002/jbm.b.34488

Marycz, K., Kornicka-Garbowska, K., Patej, A., Sobierajska, P., Kotela, A., Turlej, E., et al. (2022). Aminopropyltriethoxysilane (APTES)-Modified nanohydroxyapatite (nHAp) incorporated with iron oxide (IO) nanoparticles promotes early osteogenesis, reduces inflammation and inhibits osteoclast activity. *Mater. (Basel)* 15 (6), 2095. doi:10.3390/ma15062095

McNeill, E. P., Zeitouni, S., Pan, S. M., Haskell, A., Cesarek, M., Tahan, D., et al. (2020). Characterization of a pluripotent stem cell-derived matrix with powerful osteoregenerative capabilities. *Nat. Commun.* 11 (1), 3025. doi:10.1038/s41467-020-16646-2

Mehta, K. J. (2022). Iron oxide nanoparticles in mesenchymal stem cell detection and therapy. *Stem Cell. Rev. Rep.* 1–28. doi:10.1007/s12015-022-10343-x

Meng, H. X., Chowdhury, T. T., and Gavara, N. (2021). The mechanical interplay between differentiating mesenchymal stem cells and gelatin-based substrates measured by atomic force microscopy. *Front. Cell. Dev. Biol.* 9, 697525. doi:10.3389/fcell.2021.697525

Mengesha, A., Hoerres, A., and Mahajan, P. (2022). Cytocompatibility of oleic acid modified iron oxide nanoparticles. *Mater. Lett.* 323, 132528. doi:10.1016/j.matlet.2022.132528

Migliorini, F., La Padula, G., Torsiello, E., Spiezia, F., Oliva, F., and Maffulli, N. (2021). Strategies for large bone defect reconstruction after trauma, infections or tumour excision: A comprehensive review of the literature. *Eur. J. Med. Res.* 26 (1), 118. doi:10.1186/s40001-021-00593-9

Mohammadi, M., Mousavi Shaegh, S. A., Alibolandi, M., Ebrahimzadeh, M. H., Tamayol, A., Jaafari, M. R., et al. (2018). Micro and nanotechnologies for bone regeneration: Recent advances and emerging designs. *J. Control. Release* 274, 35–55. doi:10.1016/j.jconrel.2018.01.032

Moise, S., Céspedes, E., Soukup, D., Byrne, J. M., El Haj, A. J., and Telling, N. D. (2017). The cellular magnetic response and biocompatibility of biogenic zinc- and cobalt-doped magnetite nanoparticles. *Sci. Rep.* 7, 39922. doi:10.1038/srep39922

Mondschein, R. J., Kanitkar, A., Williams, C. B., Verbridge, S. S., and Long, T. E. (2017). Polymer structure-property requirements for stereolithographic 3D printing of soft tissue engineering scaffolds. *Biomaterials* 140, 170–188. doi:10.1016/j.biomaterials.2017.06.005

Moreno Madrid, A. P., Vrech, S. M., Sanchez, M. A., and Rodriguez, A. P. (2019). Advances in additive manufacturing for bone tissue engineering scaffolds. *Mater. Sci. Eng. C* 100, 631–644. doi:10.1016/j.msec.2019.03.037

Mortimer, C. J., and Wright, C. J. (2017). The fabrication of iron oxide nanoparticle-nanofiber composites by electrospinning and their applications in tissue engineering. *Biotechnol. J.* 12 (7), 1600693. doi:10.1002/biot.201600693

Murphy, C. M., Haugh, M. G., and O'Brien, F. J. (2010). The effect of mean pore size on cell attachment, proliferation and migration in collagen-glycosaminoglycan scaffolds for bone tissue engineering. *Biomaterials* 31 (3), 461–466. doi:10.1016/j.biomaterials.2009.09.063

Navarro, M., Michiardi, A., Castaño, O., and Planell, J. A. (2008). Biomaterials in orthopaedics. *J. R. Soc. Interface* 5 (27), 1137–1158. doi:10.1098/rsif.2008.0151

Ou, L., Lan, Y., Feng, Z., Feng, L., Yang, J., Liu, Y., et al. (2019). Functionalization of SF/HAP scaffold with GO-PEI-miRNA inhibitor complexes to enhance bone regeneration through activating transcription factor 4. *Theranostics* 9 (15), 4525–4541. doi:10.7150/thno.34676

Ozbey, A., Karimzadehkhouei, M., Yalcin, S. E., Gozuacik, D., and Kosar, A. (2015). Modeling of ferrofluid magnetic actuation with dynamic magnetic fields in small channels. *Microfluid. Nanofluidics* 18 (3), 447–460. doi:10.1007/s10404-014-1442-7

Paik, S. Y. R., Kim, J. S., Shin, S. J., and Ko, S. (2015). Characterization, quantification, and determination of the toxicity of iron oxide nanoparticles to the bone marrow cells. *Int. J. Mol. Sci.* 16 (9), 22243–22257. doi:10.3390/ijms160922243

Pang, Y. C., Su, L., Fu, Y., Jia, F., Zhang, C. X., Cao, X. K., et al. (2021). Inhibition of furin by bone targeting superparamagnetic iron oxide nanoparticles alleviated breast cancer bone metastasis. *Bioact. Mater.* 6 (3), 712–720. doi:10.1016/j.bioactmat.2020.09.006

Pariti, A., Desai, P., Maddirala, S. K. Y., Ercal, N., Katti, K. V., Liang, X., et al. (2014). Superparamagnetic Au-Fe3O4 nanoparticles: One-pot synthesis, biofunctionalization and toxicity evaluation. *Mat. Res. Express* 1 (3), 035023. doi:10.1088/2053-1591/1/3/035023

Petretta, M., Gambardella, A., Desando, G., Cavallo, C., Bartolotti, I., Shelyakova, T., et al. (2021). Multifunctional 3D-printed magnetic polycaprolactone/hydroxyapatite scaffolds for bone tissue engineering. *Polym. (Basel)* 13 (21), 3825. doi:10.3390/polym13213825

Pistone, A., Iannazzo, D., Panseri, S., Montesi, M., Tampieri, A., and Galvagno, S. (2014). Hydroxyapatite-magnetite-MWCNT nanocomposite as a biocompatible multifunctional drug delivery system for bone tissue engineering. *Nanotechnology* 25 (42), 425701. doi:10.1088/0957-4484/25/42/425701

Prodan, A. M., Iconaru, S. L., Ciobanu, C. S., Chifiriuc, M. C., Stoicea, M., and Predoi, D. (2013). Iron oxide magnetic nanoparticles: Characterization and toxicity evaluation by *in vitro* and *in vivo* assays. *J. Nanomater.* 2018, 587021. doi:10.1155/2013/587021

Przekora, A., Audemar, M., Pawlat, J., Canal, C., Thomann, J. S., Labay, C., et al. (2020). Positive effect of cold atmospheric nitrogen plasma on the behavior of mesenchymal stem cells cultured on a bone scaffold containing iron oxide-loaded silica nanoparticles catalyst. *Int. J. Mol. Sci.* 21 (13), 4738. doi:10.3390/ijms21134738

Pucci, C., Degl'Innocenti, A., Belenli Gümüş, M., and Ciofani, G. (2022). Superparamagnetic iron oxide nanoparticles for magnetic hyperthermia: Recent advancements, molecular effects, and future directions in the omics era. *Biomater. Sci.* 10, 2103–2121. doi:10.1039/d1bm01963e

Radeloff, K., Radeloff, A., Ramos Tirado, M., Scherzad, A., Hagen, R., Kleinsasser, N. H., et al. (2020). Toxicity and functional impairment in human adipose tissue-derived stromal cells (hASCs) following long-term exposure to very small iron oxide particles (VSOPs). *Nanomater. (Basel)* 10 (4), 741. doi:10.3390/nano10040741

Rahman, Z., Zidan, A. S., and Khan, M. A. (2010). Risperidone solid dispersion for orally disintegrating tablet: Its formulation design and non-destructive methods of evaluation. *Int. J. Pharm. X.* 400 (1-2), 49–58. doi:10.1016/j.ijpharm.2010.08.025

Rajan, A., Sharma, M., and Sahu, N. K. (2020). Assessing magnetic and inductive thermal properties of various surfactants functionalised Fe(3)O(4) nanoparticles for hyperthermia. *Sci. Rep.* 10 (1), 15045. doi:10.1038/s41598-020-71703-6

Ramesh, N., Moratti, S. C., and Dias, G. J. (2018). Hydroxyapatite-polymer biocomposites for bone regeneration: A review of current trends. *J. Biomed. Mat. Res.* 106 (5), 2046–2057. doi:10.1002/jbm.b.33950

Ramimoghadam, D., Bagheri, S., and Hamid, S. B. A. (2014). Progress in electrochemical synthesis of magnetic iron oxide nanoparticles. *J. Magnetism Magnetic Mater.* 368, 207–229. doi:10.1016/j.jmmm.2014.05.015

Rasker, J. J. (1995). Rheumatology in general practice. *Rheumatology* 34 (6), 494–497. doi:10.1093/rheumatology/34.6.494

Safarova, Y., Umbayev, B., Hortelano, G., and Askarova, S. (2020). Mesenchymal stem cells modifications for enhanced bone targeting and bone regeneration. *Regen. Med.* 15 (4), 1579–1594. doi:10.2217/rme-2019-0081

Sahmani, S., Khandan, A., Saber-Samandari, S., and Mohammadi Aghdam, M. (2020). Effect of magnetite nanoparticles on the biological and mechanical properties of hydroxyapatite porous scaffolds coated with ibuprofen drug. *Mater. Sci. Eng. C* 111, 110835. doi:10.1016/j.msec.2020.110835

Saiz, E., Zimmermann, E. A., Lee, J. S., Wegst, U. G., and Tomsia, A. P. (2013). Perspectives on the role of nanotechnology in bone tissue engineering. *Dent. Mat.* 29 (1), 103–115. doi:10.1016/j.dental.2012.08.001

Salehiabar, M., Nosrati, H., Davaran, S., Danafar, H., and Manjili, H. K. (2018). Facile synthesis and characterization of L-aspartic acid coated iron oxide magnetic nanoparticles (IONPs) for biomedical applications. *Drug Res. (Stuttg).* 68 (5), 280–285. doi:10.1055/s-0043-120197

Saraiva, A. S., Ribeiro, I. A. C., Fernandes, M. H., Cerdeira, A. C., Vieira, B. J. C., Waerenborgh, J. C., et al. (2021). 3D-printed platform multi-loaded with bioactive, magnetic nanoparticles and an antibiotic for re-growing bone tissue. *Int. J. Pharm. X.* 593, 120097. doi:10.1016/j.ijpharm.2020.120097

Sasikala, A. R. K., Kaliannagounder, V. K., Alluri, N. R., Shrestha, B. K., Kim, S. J., Ali-Boucetta, H., et al. (2022). Development of self-powered multifunctional piezomagnetic nanoparticles for non-invasive post-surgical osteosarcoma theranogeneration. *Nano Energy* 96, 107134. doi:10.1016/j.nanoen.2022.107134

Scharf, A., Holmes, S., Thoresen, M., Mumaw, J., Stumpf, A., and Peroni, J. (2015). Superparamagnetic iron oxide nanoparticles as a means to track mesenchymal stem cells in a large animal model of tendon injury. *Contrast Media Mol. Imaging* 10 (5), 388–397. doi:10.1002/cmmi.1642

Schiffman, J. D., and Schauer, C. L. (2008). A review: Electrospinning of biopolymer nanofibers and their applications. *Polym. Rev.* 48 (2), 317–352. doi:10.1080/15583720802022182

Schneider, M. G. M., Azcona, P., Campelo, A., Massheimer, V., Agotegaray, M., and Lassalle, V. (2021). Magnetic nanoplatform with novel potential for the treatment of bone pathologies: Drug loading and biocompatibility on blood and bone cells. *IEEE Trans. Nanobioscience*. doi:10.1109/tnb.2021.3136525

Schreivogel, S., Kuchibhotla, V., Knaus, P., Duda, G. N., and Petersen, A. (2019). Load-induced osteogenic differentiation of mesenchymal stromal cells is caused by mechano-regulated autocrine signaling. *J. Tissue Eng. Regen. Med.* 13 (11), 1992–2008. doi:10.1002/term.2948

Schwartz, L., da Veiga Moreira, J., and Jolicoeur, M. (2018). Physical forces modulate cell differentiation and proliferation processes. *J. Cell. Mol. Med.* 22 (2), 738–745. doi:10.1111/jcmm.13417

Serpooshan, V., and Guvendiren, M. (2020). Editorial for the special issue on 3D printing for tissue engineering and regenerative medicine. *Micromachines (Basel)* 11 (4), 366. doi:10.3390/mi11040366

Shan, D. Y., Shi, Y. Z., Duan, S., Wei, Y., Cai, Q., and Yang, X. P. (2013). Electrospun magnetic poly(L-lactide) (PLLA) nanofibers by incorporating PLLA-stabilized Fe3O4 nanoparticles. *Mater. Sci. Eng. C* 33 (6), 3498–3505. doi:10.1016/j.msec.2013.04.040

Shelat, R., Bhatt, L. K., Paunipagar, B., Kurian, T., Khanna, A., and Chandra, S. (2020). Regeneration of hyaline cartilage in osteochondral lesion model using L-lysine magnetic nanoparticles labeled mesenchymal stem cells and their *in vivo* imaging. *J. Tissue Eng. Regen. Med.* 14 (11), 1604–1617. doi:10.1002/term.3120

Shen, W. B., Plachez, C., Chan, A., Yarnell, D., Puche, A. C., Fishman, P. S., et al. (2013). Human neural progenitor cells retain viability, phenotype, proliferation, and lineage differentiation when labeled with a novel iron oxide nanoparticle, Molday ION Rhodamine B. *Int. J. Nanomedicine* 8, 4593–4600. doi:10.2147/ijn.S53012

Shokouhimehr, M., Theus, A. S., Kamalakar, A., Ning, L., Cao, C., Tomov, M. L., et al. (2021). 3D bioprinted bacteriostatic hyperelastic bone scaffold for damage-specific bone regeneration. *Polym. (Basel)* 13 (7), 1099. doi:10.3390/polym13071099

Shokrollahi, H. (2017). A review of the magnetic properties, synthesis methods and applications of maghemite. *J. Magnetism Magnetic Mater.* 426, 74–81. doi:10.1016/j.jmmm.2016.11.033

Singh, R. K., Patel, K. D., Lee, J. H., Lee, E. J., Kim, J. H., Kim, T. H., et al. (2014). Potential of magnetic nanofiber scaffolds with mechanical and biological properties applicable for bone regeneration. *PLoS One* 9 (4), e91584. doi:10.1371/journal.pone.0091584

Singh, Y. P., and Dasgupta, S. (2022). Gelatin-based electrospun and lyophilized scaffolds with nano scale feature for bone tissue engineering application: Review. *J. Biomater. Sci. Polym. Ed.*, 1–55. doi:10.1080/09205063.2022.2068943

Sniadecki, N. J. (2010). Minireview: A tiny touch: Activation of cell signaling pathways with magnetic nanoparticles. *Endocrinology* 151 (2), 451–457. doi:10.1210/en.2009-0932

Song, B. T., Xu, Q., Wang, C. Y., Xu, S. C., and Zhang, H. X. (2016). Fabrication of polymer/drug-loaded hydroxyapatite particle composite fibers for drug sustained release. *J. Appl. Polym. Sci.* 133 (3). doi:10.1002/app.42871

Takeuchi, T., Yoshida, H., and Tanaka, S. (2021). Role of interleukin-6 in bone destruction and bone repair in rheumatoid arthritis. *Autoimmun. Rev.* 20 (9), 102884. doi:10.1016/j.autrev.2021.102884

Tang, C. L., Mahoney, J. L., McKee, M. D., Richards, R. R., Waddell, J. P., Louie, B., et al. (1998). Donor site morbidity following vascularized fibular grafting. *Microsurgery* 18 (6), 383–386. doi:10.1002/(sici)1098-2752(1998)18:6<383::aid-micr8>3.0.co;2-5

Taylor, E. N., and Webster, T. J. (2011). Multifunctional magnetic nanoparticles for orthopedic and biofilm infections. *Int. J. Nanotechnol.* 8 (1-2), 21–35. doi:10.1504/ijnt.2011.037168

Taylor, E. N., and Webster, T. J. (2009). The use of superparamagnetic nanoparticles for prosthetic biofilm prevention. *Int. J. Nanomedicine* 4, 145–152. doi:10.2147/ijn.s5976

Tevlin, R., McArdle, A., Atashroo, D., Walmsley, G. G., Senarath-Yapa, K., Zielins, E. R., et al. (2014). Biomaterials for craniofacial bone engineering. *J. Dent. Res.* 93 (12), 1187–1195. doi:10.1177/0022034514547271

Thrivikraman, G., Madras, G., and Basu, B. (2014). Intermittent electrical stimuli for guidance of human mesenchymal stem cell lineage commitment towards neural-like cells on electroconductive substrates. *Biomaterials* 35 (24), 6219–6235. doi:10.1016/j.biomaterials.2014.04.018

Tomov, M. L., Cetnar, A., Do, K., Bauser-Heaton, H., and Serpooshan, V. (2019). Patient-specific 3-dimensional-bioprinted model for *in vitro* analysis and treatment planning of pulmonary artery atresia in tetralogy of fallot and major aortopulmonary collateral arteries. *J. Am. Heart Assoc.* 8 (24), e014490. doi:10.1161/jaha.119.014490

Torgbo, S., and Sukyai, P. (2018). Bacterial cellulose-based scaffold materials for bone tissue engineering. *Appl. Mater. Today* 11, 34–49. doi:10.1016/j.apmt.2018.01.004

Trombetta, R., Inzana, J. A., Schwarz, E. M., Kates, S. L., and Awad, H. A. (2017). 3D printing of calcium phosphate ceramics for bone tissue engineering and drug delivery. *Ann. Biomed. Eng.* 45 (1), 23–44. doi:10.1007/s10439-016-1678-3

Usković, V., Huynh, E., Tang, S., Jovanović, S., and Wu, V. M. (2019). Colloids or powders: Which nanoparticle formulations do cells like more? *Colloids Surfaces B Biointerfaces* 181, 39–47. doi:10.1016/j.colsurfb.2019.05.019

Vangijzegem, T., Stanicki, D., and Laurent, S. (2019). Magnetic iron oxide nanoparticles for drug delivery: Applications and characteristics. *Expert Opin. Drug Deliv.* 16 (1), 69–78. doi:10.1080/17425247.2019.1554647

Ventola, C. L. (2012). The nanomedicine revolution: Part 1: Emerging concepts. *P Trans.* 37 (9), 512–525.

Vergnaud, F., Kesse, X., Jacobs, A., Perton, F., Begin-Colin, S., Mertz, D., et al. (2022). Magnetic bioactive glass nano-heterostructures: A deeper insight into magnetic hyperthermia properties in the scope of bone cancer treatment. *Biomater. Sci.* 10 (14), 3993–4007. doi:10.1039/d2bm00319h

Verma, G. S., Nirmal, N. K., Gunpal, D., Gupta, H., Yadav, M., Kumar, N., et al. (2021). Intraperitoneal exposure of iron oxide nanoparticles causes dose-dependent toxicity in Wistar rats. *Toxicol. Ind. Health* 37 (12), 763–775. doi:10.1177/07482337211058668

Virlan, M. J., Miricescu, D., Radulescu, R., Sabliov, C. M., Totan, A., Calenic, B., et al. (2016). Organic nanomaterials and their applications in the treatment of oral diseases. *Molecules* 21 (2), 207. doi:10.3390/molecules21020207

Volokhova, M., Shugai, A., Tsujimoto, M., Kubo, A. L., Telliskivi, S., Nigul, M., et al. (2022). Cubic iron core-shell nanoparticles functionalized to obtain high-performance MRI contrast agents. *Mater. (Basel)* 15 (6), 2228. doi:10.3390/ma15062228

Wagner, J. M., Reinkemeier, F., Wallner, C., Dadras, M., Huber, J., Schmidt, S. V., et al. (2019). Adipose-derived stromal cells are capable of restoring bone regeneration after post-traumatic osteomyelitis and modulate B-cell response. *Stem Cells Transl. Med.* 8 (10), 1084–1091. doi:10.1002/sctm.18-0266

Wang, G., Xu, W., Zhang, J., Tang, T., Chen, J., and Fan, C. (2021). Induction of bone remodeling by raloxifene-doped iron oxide functionalized with hydroxyapatite to accelerate fracture healing. *J. Biomed. Nanotechnol.* 17 (5), 932–941. doi:10.1166/jbn.2021.3068

Wang, L. T., Hu, P., Jiang, H., Zhao, J. H., Tang, J., Jiang, D. J., et al. (2022). Mild hyperthermia-mediated osteogenesis and angiogenesis play a critical role in magnetothermal composite-induced bone regeneration. *Nano Today* 43, 101401. doi:10.1016/j.nantod.2022.101401

Wang, Q., Chen, B., Cao, M., Sun, J., Wu, H., Zhao, P., et al. (2016). Response of MAPK pathway to iron oxide nanoparticles *in vitro* treatment promotes osteogenic differentiation of hBMSCs. *Biomaterials* 86, 11–20. doi:10.1016/j.biomaterials.2016.02.004

Wang, Q., Ma, X., Liao, H., Liang, Z., Li, F., Tian, J., et al. (2020). Artificially engineered cubic iron oxide nanoparticle as a high-performance magnetic particle imaging tracer for stem cell tracking. *ACS Nano* 14 (2), 2053–2062. doi:10.1021/acsnano.9b08660

Wang, Q. W., Chen, B., Ma, F., Lin, S. K., Cao, M., Li, Y., et al. (2017). Magnetic iron oxide nanoparticles accelerate osteogenic differentiation of mesenchymal stem cells via modulation of long noncoding RNA INZEB2. *Nano Res.* 10 (2), 626–642. doi:10.1007/s12274-016-1322-4

Wang, Y. J., Jeng, U. S., and Hsu, S. H. (2018). Biodegradable water-based polyurethane shape memory elastomers for bone tissue engineering. *ACS Biomater. Sci. Eng.* 4 (4), 1397–1406. doi:10.1021/acsbiomaterials.8b00091

Wasnik, S., Lakhan, R., Baylink, D. J., Rundle, C. H., Xu, Y., Zhang, J. T., et al. (2019). Cyclooxygenase 2 augments osteoblastic but suppresses chondrocytic differentiation of CD90(+) skeletal stem cells in fracture sites. *Sci. Adv.* 5 (7), eaaw2108. doi:10.1126/sciadv.aaw2108

Watanabe, Y., Harada, N., Sato, K., Abe, S., Yamanaka, K., and Matushita, T. (2016). Stem cell therapy: Is there a future for reconstruction of large bone defects? *Injury* 47, S47–S51. doi:10.1016/s0020-1383(16)30012-2

Wei, X. H., Zhang, X. K., Yang, Z., Li, L., and Sui, H. T. (2021). Osteoinductive potential and antibacterial characteristics of collagen coated iron oxide nanosphere containing strontium and hydroxyapatite in long term bone fractures. *Arabian J. Chem.* 14 (3), 102984. doi:10.1016/j.arabjc.2020.102984

Weinstein, S. L. (2016). The burden of musculoskeletal conditions. *J. Bone Jt. Surg.* 98 (16), 1331. doi:10.2106/jbjs.16.00595

Williams, D. F. (2008). On the mechanisms of biocompatibility. *Biomaterials* 29 (20), 2941–2953. doi:10.1016/j.biomaterials.2008.04.023

Woo, S., Kim, S., Kim, H., Cheon, Y. W., Yoon, S., Oh, J. H., et al. (2021). Charge-modulated synthesis of highly stable iron oxide nanoparticles for *in vitro* and *in vivo* toxicity evaluation. *Nanomater. (Basel)* 11 (11), 3068. doi:10.3390/nano11113068

Wu, L., and Shen, S. (2019). What potential do magnetic iron oxide nanoparticles have for the treatment of rheumatoid arthritis? *Nanomedicine* 14 (8), 927–930. doi:10.2217/nnm-2019-0071

Wu, L., Wen, W., Wang, X., Huang, D., Cao, J., Qi, X., et al. (2022). Ultrasmall iron oxide nanoparticles cause significant toxicity by specifically inducing acute oxidative stress to multiple organs. *Part. Fibre Toxicol.* 19 (1), 24. doi:10.1186/s12989-022-00465-y

Wu, S., Yu, Q., Sun, Y., and Tian, J. (2018). Synergistic effect of a LPEMF and SPIONs on BMMSC proliferation, directional migration, and osteoblastogenesis. *Am. J. Transl. Res.* 10 (5), 1431–1443.

Wu, X.-D., Kang, L., Tian, J., Wu, Y., Huang, Y., Liu, J., et al. (2022). Exosomes derived from magnetically actuated bone mesenchymal stem cells promote tendon-bone healing through the miR-21-5p/SMAD7 pathway. *Mat. Today Bio* 15, 100319. doi:10.1016/j.mtbio.2022.100319

Xia, Y., Chen, H., Zhang, F., Wang, L., Chen, B., Reynolds, M. A., et al. (2018a). Injectable calcium phosphate scaffold with iron oxide nanoparticles to enhance osteogenesis via dental pulp stem cells. *Artif. Cells Nanomed. Biotechnol.* 46, 423–433. doi:10.1080/21691401.2018.1428813

Xia, Y., Chen, H., Zhao, Y., Zhang, F., Li, X., Wang, L., et al. (2019a). Novel magnetic calcium phosphate-stem cell construct with magnetic field enhances osteogenic differentiation and bone tissue engineering. *Mater. Sci. Eng. C* 98, 30–41. doi:10.1016/j.msec.2018.12.120

Xia, Y., Guo, Y., Yang, Z., Chen, H., Ren, K., Weir, M. D., et al. (2019b). Iron oxide nanoparticle-calcium phosphate cement enhanced the osteogenic activities of stem cells through WNT/β-catenin signaling. *Mater. Sci. Eng. C* 104, 109955. doi:10.1016/j.msec.2019.109955

Xia, Y., Sun, J., Zhao, L., Zhang, F., Liang, X. J., Guo, Y., et al. (2018b). Magnetic field and nano-scaffolds with stem cells to enhance bone regeneration. *Biomaterials* 183, 151–170. doi:10.1016/j.biomaterials.2018.08.040

Xia, Y., Zhao, Y. T., Zhang, F. M., Chen, B., Hu, X. T., Weir, M. D., et al. (2019c). Iron oxide nanoparticles in liquid or powder form enhanced osteogenesis via stem cells on injectable calcium phosphate scaffold. *Nanomedicine Nanotechnol. Biol. Med.* 21, 102069. doi:10.1016/j.nano.2019.102069

Xie, Y. Y., Liu, W., Zhang, B., Wang, B., Wang, L. D., Liu, S., et al. (2019). Systematic intracellular biocompatibility assessments of superparamagnetic iron oxide nanoparticles in human umbilical cord mesenchyme stem cells in testifying its reusability for inner cell tracking by MRI. *J. Biomed. Nanotechnol.* 15 (11), 2179–2192. doi:10.1166/jbn.2019.2845

Xu, G., Hu, X., Han, L., Zhao, Y., and Li, Z. (2021). The construction of a novel xenograft bovine bone scaffold, (DSS)6-liposome/CKIP-1 siRNA/calcine bone and its osteogenesis evaluation on skull defect in rats. *J. Orthop. Transl.* 28, 74–82. doi:10.1016/j.jot.2021.02.001

Xue, H., Zhang, Z. H., Lin, Z., Su, J., Panayi, A. C., Xiong, Y., et al. (2022). Enhanced tissue regeneration through immunomodulation of angiogenesis and osteogenesis with a multifaceted nanohybrid modified bioactive scaffold. *Bioact. Mater.* 18, 552–568. doi:10.1016/j.bioactmat.2022.05.023

Xue, K., Wang, X., Yong, P. W., Young, D. J., Wu, Y. L., Li, Z. B., et al. (2019). Hydrogels as emerging materials for translational biomedicine. *Adv. Ther. (Weinh).* 2 (1), 1800088. doi:10.1002/adtp.201800088

Yang, C. Y., Hsiao, J. K., Tai, M. F., Chen, S. T., Cheng, H. Y., Wang, J. L., et al. (2011). Direct labeling of hMSC with SPIO: The long-term influence on toxicity, chondrogenic differentiation capacity, and intracellular distribution. *Mol. Imaging Biol.* 13 (3), 443–451. doi:10.1007/s11307-010-0360-7

Yang, H. Y., Wang, H., Wen, C. H., Bai, S., Wei, P. F., Xu, B., et al. (2022). Effects of iron oxide nanoparticles as T-2-MRI contrast agents on reproductive system in male mice. *J. Nanobiotechnology* 20 (1), 98. doi:10.1186/s12951-022-01291-2

Yang, W., Zhu, P., Huang, H., Zheng, Y., Liu, J., Feng, L., et al. (2019). Functionalization of novel theranostic hydrogels with kartogenin-grafted USPIO nanoparticles to enhance cartilage regeneration. *ACS Appl. Mat. Interfaces* 11 (38), 34744–34754. doi:10.1021/acsami.9b12288

Yang, Y., Chu, L., Yang, S., Zhang, H., Qin, L., Guillaume, O., et al. (2018). Dual-functional 3D-printed composite scaffold for inhibiting bacterial infection and promoting bone regeneration in infected bone defect models. *Acta Biomater.* 79, 265–275. doi:10.1016/j.actbio.2018.08.015

Yao, D., Liu, N. N., and Mo, B. W. (2020). Assessment of proliferation, migration and differentiation potentials of bone marrow mesenchymal stem cells labeling with silica-coated and amine-modified superparamagnetic iron oxide nanoparticles. *Cytotechnology* 72 (4), 513–525. doi:10.1007/s10616-020-00397-5

Yao, S., Lin, X., Xu, Y., Chen, Y., Qiu, P., Shao, C., et al. (2019). Osteoporotic bone recovery by a highly bone-inductive calcium phosphate polymer-induced liquid-precursor. *Adv. Sci. (Weinh).* 6 (19), 1900683. doi:10.1002/advs.201900683

Yi, H., Ur Rehman, F., Zhao, C., Liu, B., and He, N. (2016). Recent advances in nano scaffolds for bone repair. *Bone Res.* 4, 16050. doi:10.1038/boneres.2016.50

Yin, X.-Y., Wang, C.-C., Du, P., Wang, X.-S., Lu, Y.-C., Sun, Y.-W., et al. (2023). Muse cells decrease the neuroinflammatory response by modulating the proportion of M1 and M2 microglia *in vitro*. *Neural Regen. Res.* 18 (1), 213–218. doi:10.4103/1673-5374.343885

Ying, H., Ruan, Y., Zeng, Z., Bai, Y., Xu, J., and Chen, S. (2022). Iron oxide nanoparticles size-dependently activate mouse primary macrophages via oxidative stress and endoplasmic reticulum stress. *Int. Immunopharmacol.* 105, 108533. doi:10.1016/j.intimp.2022.108533

Yu, C., Geng, J., Zhuang, Y., Zhao, J., Chu, L., Luo, X., et al. (2016). Preparation of the chitosan grafted poly (quaternary ammonium)/Fe3O4 nanoparticles and its adsorption performance for food yellow 3. *Carbohydr. Polym.* 152, 327–336. doi:10.1016/j.carbpol.2016.06.114

Yu, P., Zheng, L., Wang, P., Chai, S., Zhang, Y., Shi, T., et al. (2020). Development of a novel polysaccharide-based iron oxide nanoparticle to prevent iron accumulation-related osteoporosis by scavenging reactive oxygen species. *Int. J. Biol. Macromol.* 165, 1634–1645. doi:10.1016/j.ijbiomac.2020.10.016

Zhang, M., Hu, W., Cai, C., Wu, Y., Li, J., and Dong, S. (2022). Advanced application of stimuli-responsive drug delivery system for inflammatory arthritis treatment. *Mat. Today Bio* 14, 100223. doi:10.1016/j.mtbio.2022.100223

Zhang, W., Gu, J., Li, K., Zhao, J., Ma, H., Wu, C., et al. (2019a). A hydrogenated black TiO(2) coating with excellent effects for photothermal therapy of bone tumor and bone regeneration. *Mater. Sci. Eng. C* 102, 458–470. doi:10.1016/j.msec.2019.04.025

Zhang, W., Zheng, Y., Liu, H., Zhu, X., Gu, Y., Lan, Y., et al. (2019b). A non-invasive monitoring of USPIO labeled silk fibroin/hydroxyapatite scaffold loaded DPSCs for dental pulp regeneration. *Mater. Sci. Eng. C* 103, 109736. doi:10.1016/j.msec.2019.05.021

Zhang, Y., Hu, J., Zhao, X., Xie, R., Qin, T., and Ji, F. (2019). Mechanically robust shape memory polyurethane nanocomposites for minimally invasive bone repair. *ACS Appl. Bio Mat.* 2 (3), 1056–1065. doi:10.1021/acsabm.8b00655

Zhang, Y., and Zhang, J. (2005). Surface modification of monodisperse magnetite nanoparticles for improved intracellular uptake to breast cancer cells. *J. Colloid Interface Sci.* 283 (2), 352–357. doi:10.1016/j.jcis.2004.09.042

Zhao, S., Zhu, M., Zhang, J., Zhang, Y., Liu, Z., Zhu, Y., et al. (2014). Three dimensionally printed mesoporous bioactive glass and poly(3-hydroxybutyrate-co-3-hydroxyhexanoate) composite scaffolds for bone regeneration. *J. Mat. Chem. B* 2 (36), 6106–6118. doi:10.1039/c4tb00838c

Zhao, Y. Z., Chen, R., Xue, P. P., Luo, L. Z., Zhong, B., Tong, M. Q., et al. (2021). Magnetic PLGA microspheres loaded with SPIONs promoted the reconstruction of bone defects through regulating the bone mesenchymal stem cells under an external magnetic field. *Mater. Sci. Eng. C* 122, 111877. doi:10.1016/j.msec.2021.111877

Zhao, Z., Li, M., Zeng, J., Huo, L., Liu, K., Wei, R., et al. (2022). Recent advances in engineering iron oxide nanoparticles for effective magnetic resonance imaging. *Bioact. Mat.* 12, 214–245. doi:10.1016/j.bioactmat.2021.10.014

Zheng, L., Zhuang, Z., Li, Y., Shi, T., Fu, K., Yan, W., et al. (2022). Bone targeting antioxidative nano-iron oxide for treating postmenopausal osteoporosis. *Bioact. Mat.* 14, 250–261. doi:10.1016/j.bioactmat.2021.11.012

Zhu, G., Zhang, T., Chen, M., Yao, K., Huang, X., Zhang, B., et al. (2021). Bone physiological microenvironment and healing mechanism: Basis for future bone-tissue engineering scaffolds. *Bioact. Mat.* 6 (11), 4110–4140. doi:10.1016/j.bioactmat.2021.03.043

Zhuang, J., Lin, S., Dong, L., Cheng, K., and Weng, W. (2018). Magnetically actuated mechanical stimuli on Fe(3)O(4)/mineralized collagen coatings to enhance osteogenic differentiation of the MC3T3-E1 cells. *Acta Biomater.* 71, 49–60. doi:10.1016/j.actbio.2018.03.009

frontiers | Frontiers in Bioengineering and Biotechnology

TYPE Original Research
PUBLISHED 02 September 2022
DOI 10.3389/fbioe.2022.927987

OPEN ACCESS

EDITED BY
Jun Pan,
Chongqing University, China

REVIEWED BY
Huiyu Zhou,
Ningbo University, China
Jia Yu,
Soochow University, China

*CORRESPONDENCE
Shang-Hsun Yang,
syang@mail.ncku.edu.tw
Yi-Ju Tsai,
yijutsai@mail.ncku.edu.tw

SPECIALTY SECTION
This article was submitted to Biomechanics,
a section of the journal
Frontiers in Bioengineering and Biotechnology

RECEIVED 25 April 2022
ACCEPTED 25 July 2022
PUBLISHED 02 September 2022

CITATION
Ching S-H, Chiu Y-C, Liao Y-C, Yang S-H and Tsai Y-J (2022), A new mouse model of ankle instability induced by multiple mechanical sprains with controlled inversion angle and speed.
Front. Bioeng. Biotechnol. 10:927987.
doi: 10.3389/fbioe.2022.927987

A new mouse model of ankle instability induced by multiple mechanical sprains with controlled inversion angle and speed

Shih-Hong Ching[1], Yen-Chun Chiu[2], Yu-Ching Liao[3], Shang-Hsun Yang[1,3]* and Yi-Ju Tsai[4,5]*

[1]Institute of Basic Medical Science, College of Medicine, National Cheng Kung University, Tainan, Taiwan, [2]Department of Orthopaedic Surgery, E-Da Hospital, I-Shou University, Kaohsiung, Taiwan, [3]Department of Physiology, College of Medicine, National Cheng Kung University, Tainan, Taiwan, [4]Department of Physical Therapy, College of Medicine, National Cheng Kung University, Tainan, Taiwan, [5]Institute of Allied Health Sciences, College of Medicine, National Cheng Kung University, Tainan, Taiwan

Ankle sprain occurs by a sudden and extreme inversion and plantarflexion at the ankle joint to cause ligamentous injuries. A portion of ankle sprain patients experience recurrent ankle sprains and develop chronic ankle instability (CAI). The present CAI animal models are single events with severe ligamentous injury using surgical transection of ligaments or manually overextending the ankle.

Purpose: To simulate the mechanical and recurrent sprain injuries in CAI patients, we established a new ankle instability model with multiple ankle injuries using a self-designed machine to sprain the ankle with a controlled inversion angle and speed.

Methods: Male C57BL/6J mice were used and respectively subjected to a sham operation, calcaneofibular ligament (CFL) transection, and mechanical ankle sprains. Three mechanical sprains were performed on the 13th and 185th day after the initial mechanical ankle sprain.

Results: The first mechanical sprain and CFL transection induced ankle injury as indicated by an average of a 62% decrease in ankle pressure pain threshold and a 114% increase in the ankle thickness compared with the contralateral untreated ankle. The second and third mechanical sprains induced recurrent ankle injuries. The foot slips during beam tests were increased after mechanical ankle sprains but not after CFL transection, indicating the induction of motor balance deficits. Multiple mechanical ankle sprains induced significant gait changes in longer duration of stance (an average of 194% increase), swing (134%), and step cycle (147%) compared with CFL transection or sham operation, and slower walking speed (78% reduction) and shorter step distance (91%) after the third sprain.

Conclusion: These results elucidate that multiple mechanical sprains, which induce recurrent ankle injuries, balance deficits, and gait changes, are a good model for investigating the mechanisms of CAI induced by recurrent sprain injuries.

KEYWORDS

lateral ankle sprain, ligamentous injury, animal model, chronic ankle instability, gait

Introduction

Ankle sprain is the most common sports injury, with a rate of 4.95 lateral ligament complex ankle sprains per 10,000 athlete-exposures (Roos et al., 2017). Lateral ankle sprain is the most common type among all ankle sprains (Garrick and Schelkun, 1997). When the ankle experiences an inversion and/or plantarflexion motion that exceeds physiological limits, ligaments on the lateral side of the ankle are often damaged, including the anterior talofibular ligament (ATFL), posterior talofibular ligament (PTFL), and calcaneofibular ligament (CFL). The severity of the lateral ankle sprain is often classified into grades I (mild), II (moderate), and III (severe), respectively, representing only stretching, partial, and complete rupture of one or more lateral ligaments (Tiemstra, 2012; Slater, 2018). An acute ankle sprain could result in pain, swelling, and loss of function. Residual symptoms after an acute ankle sprain affect 55%–72% of patients at 6–18 months (Gerber et al., 1998; Braun, 1999).

Although conservative treatments often lead to full functional recovery in most people, up to 26% of the patients continue to have recurrent ankle sprains, suggesting chronic instability of the ankle joint. Chronic ankle instability (CAI) is defined as the patient having recurrent lateral ankle sprains after the initial sprain and is characterized by a recurring giving way sensation (i.e., instability) of the ankle during walking or other activities (Hertel, 2002). Depending on different populations, up to 70% of patients suffering from lateral ankle sprain develop CAI (Fong et al., 2007; Swenson et al., 2009; Hiller et al., 2012). CAI has also been found to have a higher risk of developing post-traumatic osteoarthritis (Gribble et al., 2016; Liu et al., 2021; Li et al., 2022).

The common symptoms of CAI include balance deficits, decreased physical activity (Wikstrom et al., 2018), and recurrent injuries (Yeung et al., 1994). CAI includes mechanical instability, functional instability, or both. Mechanical instability is the measurable anatomical change, such as joint laxity, that causes ankle joint motion to exceed normal physiological limits (Tropp, 2002). Functional instability is the sensation of ankle joint instability and repetitive re-injuries. The impairment of proprioception, neuromuscular control, postural control, and strength are proposed to be involved in functional instability. However, the supporting evidence is still poor (Hertel, 2000; Tropp, 2002). Therefore, an appropriate animal model is urgently needed to study the underlying mechanisms and treatments for ankle instability.

Currently, two ankle sprain models have been developed. The first one is a mouse model by surgically transecting the CFL and ATFL (Kim et al., 2008; Kim et al., 2011; Hubbard-Turner et al., 2013; Wikstrom et al., 2015; Liu et al., 2021; Li et al., 2022). The second one is a rat model induced by manually overextending the ankle repeatedly in the plantarflexion and inversion directions (Koo et al., 2002). The ligament transection model is a single injury event with severe injury, which does not replicate the recurrent sprains seen in the CAI patients. The manual ankle sprain model was developed for investigating ankle sprain related pain. It is still unknown whether other CAI-related symptoms can be induced by this model or not (Koo et al., 2008). Furthermore, twisting the ankle manually may introduce inter-experimenter variability, while twisting the ankle joint 60 times in 1 minute does not match how ankle sprain injuries occur in humans. However, these two models do not fulfil the development of CAI by recurrent and mechanical sprains in humans and may also not be appropriate for studying whether incomplete ligamentous (mild and moderate) injuries are able to induce CAI.

In order to simulate mechanical and recurrent inversion sprains seen in CAI patients, it is crucial to develop a non-invasive (closed) lateral ankle sprain animal model that replicates the ankle sprain motion more faithfully, with lower intra- and inter-experimenter variations. We designed a machine that has a computer-controlled motor capable of rotating the mouse ankle joint in the inversion direction with precise control of rotation angle and speed. Using the self-designed machine, we developed a new mouse model of mechanical ankle sprain and demonstrated that two consecutive twists (117° of inversion at the speed of 1,500° per second) can induce an acute ankle sprain injury similar to that induced by CFL transection. We also further performed multiple sprains to investigate whether CAI could be induced.

Materials and methods

Animals

All experimental protocols were in accordance with the National Institutes of Health Guidelines for Animal Research and were approved by the National Cheng Kung University Institutional Animal Care and Use Committee (IACUC #109126). All efforts were made to ensure animal welfare. Male 8-week old C57BL/6J mice (body weight 18–22 g) were used and obtained from the animal facility of the Medical College, National Cheng Kung University, Tainan, Taiwan. The mice were housed in a 12/12-h light/dark cycle room at 22 ± 2°C and had free access to standard laboratory chow and water *ad libitum*. Twelve mice were divided into three groups, $n = 4$ for each group: the sham operation group, the CFL transection group, and the mechanical sprain group. Mice were randomly allocated into groups after the baseline measures were made.

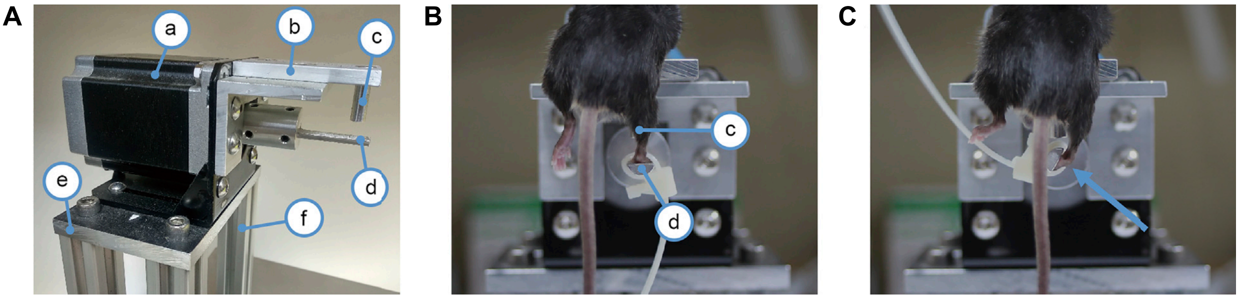

FIGURE 1
Device for mechanical ankle sprain. **(A)** photograph showing the device for spraining the ankle, a: a stepper motor, b: bed platform for the mouse, c: bed post for restraining the mouse shin to the machine, d: foot rest rod connected to the motor shaft for securing mouse foot to the motor, e: base plate to mount the motor, f: posts to support the motor. **(B)** photograph showing a mouse mounted on the ankle spraining machine. The right shin is held against the bed post (c) by the experimenter's hand (not shown) to restrict shin movement. The right paw is secured on the foot rest rod (d) by a cable tie. In photo **(B)**, the mouse foot is parallel to the floor and the mouse ankle has not yet been rotated. **(C)** photograph showing how much the motor shaft spins to sprain the ankle, it spins 117° in the inversion direction as indicated by an arrow.

Surgical injury model

For both the sham operation and CFL transection groups, mice were anesthetized in a chamber using 4% isoflurane and kept under anesthetization using a mask. Prior to the surgery operation, the lateral side of the right ankle was shaved and cleaned with 75% alcohol for both groups. A small incision was made longitudinally on the anterolateral side of the right ankle. Under the anatomical microscope, the CFL was transected using a purpose-made hook tool with sharpened edges (Kim et al., 2008; Wikstrom et al., 2018). After the operation was finished, the wound was sutured with polyamide monofilament (6/0, B. Braun Surgical, S.A. Rubi, Spain). Mice received subcutaneous injection of 5.0 mg·kg-1 Carprofen (Rimadyl; Zoetis, Parsippany, NJ), one injection per day for 3 days to prevent wound inflammation. For the sham operation group, the mice were anesthetized following the same procedure as the CFL transection group. The same incision as the CFL transection group was made, but no other surgical operations were performed. After the incision, the wound was sutured with the same procedure as the CFL transection group, following the same wound care protocol.

Mechanical sprain model

To establish a non-invasive (closed) lateral ankle sprain model, a device was designed and fabricated (Figure 1) that can restrain the mouse securely and precisely rotate the ankle joint in the inversion/eversion axis. A stepper motor (Figure 1Aa) is bolted on a heavy base (Figure 1Ae). The motor is powered by a 200W power supply and controlled by a computer-governed controller. A rod (Figure 1Ad) coupled to the motor shaft acted as the foot rest for securing the mouse foot in place. The rod was cut in half length-wise, thus, when the foot was resting on the foot rest, the rotation axis of the motor was able to come in line with the inversion/eversion axis of the ankle. A plate (Figure 1Ab) affixed on top of the motor acted as the bed platform to hold the mouse body. Above the foot rest rod, a bed post (Figure 1Ac) was affixed on the underside of the bed platform to provide an anchor point for restraining the mouse shin to the machine.

Mice were anaesthetized with inhalation of 4% isoflurane and then mounted on the bed platform, facing downwards. A cable tie was used to strap the mouse paw to the rod (foot rest) connected to the motor shaft. The mouse shin was held against the bed post by the experimenter's hand to restrict the shin's movement. After the mouse was strapped firmly in place, the right ankle joint was inverted in the inversion/eversion axis two times. A video was provided to demonstrate the condition of the mechanical sprain (Supplementary Video S1). The ankle was rotated to 117° of inversion at a speed of 1,500° per second. Based on previous studies of human ankle sprain kinematics (Fong et al., 2009; Kristianslund et al., 2011; Fong et al., 2012), we decided on a rotation speed of 1,500° per second. Our preliminary cadaver trials found that the mice have a much greater inversion range (an average of 90°) compared to humans (30°) (Norkin and White, 2016). To ensure that the mechanical sprains exceed the physiological limit of the ankle joint and accommodate the characteristics of the stepper motor of the device, 117° of inversion rotation was chosen for our study.

The measurement for ankle pain threshold

Pain at the joint site is one of the symptoms of ankle sprain. Pressure application measurement (PAM) was used to measure the ankle joint hypersensitivity to pressure (Barton et al., 2007). A 3 kg capacity load cell was used to measure how much force was applied. A load cell with a stainless rod (5 mm diameter) attached, acting as pressure point, was used to assert pressure on the mice's ankle. Mice were accustomed to being handled and restrained before the experiments. The intraperitoneal injection position was suited for measuring ankle joint hypersensitivity since the hind limbs were easily accessible. Following the measuring procedure provided by Barton et al. (2007), the load cell was used to apply force on the lateral side of the ankle joint across the joint with gradually increasing force. When mice showed withdrawal response with their legs or squealed, the load cell was released and the maximal force was recorded. Each mouse was measured three times at each time point and the average was shown.

The measurement for ankle swelling

Swelling at the ankle joint is another one of the primary symptoms of an ankle sprain. A handheld thickness gauge was used to measure the level of ankle swelling. Mice were trained to be handled and restrained before the experiment started. Each ankle joint was measured three times at each time point.

Beam test

The beam test is a commonly used test for assessing movement coordination (Luong et al., 2011). In brief, the beam is a transparent acrylic plate 1 m in length, 6 mm in width, 20 mm in height, and suspended 50 cm above the floor. A camera was used to capture footages of mice traversing the beam. Mice were trained for 3 days to get accustomed to the beam test before the experiment started. Mice traversed the beam three times for each time point. The speed of mice traversing the beam and the total number of hind foot slips were counted by two experimenters who were blind to the grouping.

Footprint assay

The footprint assay is based on the optical phenomenon of frustrated total internal reflection (FTIR) as previously described (Mendes et al., 2015). In brief, the footprint apparatus consists of a walkway, lights, a mirror, and a camera. The floor of the walkway was a 10 mm thick transparent acrylic panel. Two strips of blue light-emitting diodes (LEDs) were affixed to both sides of the floor acrylic to provide the light source for the FTIR. A mirror was located 45° underneath the floor panel to reflect the images of the underside of the floor panel towards the camera, which recorded the footage of mice's footprints traversing the walkway. The footprint assay was performed three times at each time point.

Recorded footages were loaded into the footprint analyzing program developed by Mendes et al. (2015). The program is capable of identifying footprint locations automatically and footprint parameters such as stance duration, swing duration, step cycle, step distance, foot size, and overall speed can be extracted. Since only the right hind limb was injured, the performance of the hind limbs was analyzed. Several gait cycles were recorded when a mouse traversed the walkway, and the average of each gait cycle was calculated. Stance duration was the duration of the stance phase of the gait cycle, while the swing duration was the the duration of swing phase of the gait cycle. A step cycle is the duration of each gait cycle. Step distance was the distance between the centroids of two sequential steps of the same paw. Foot size is the size of the lightened up area on the walkway for each paw. Overall speed is obtained from dividing the walkway length by the time the mouse takes to finish it, and can be treated as walking speed.

Statistical analysis

The data were analyzed and drawn in the GraphPad Prism 9.3 (GraphPad Software, San Diego, CA, United States), and represented as mean± standard error of means (S.E.M). The statistical significance was analyzed using a paired *t* test within the group, such as a comparison between the left untreated foot and the right treated foot, or a comparison before (baseline) and after the treatment. The statistical significance was analyzed using an unpaired *t* test between the independent groups, including a comparison between the sham group and the surgery group, or the sham group and the machine group, or the surgery group and the machine group.

Results

Mechanical ankle sprain induces pain on ankle

Hypersensitivity to pressure (pain) is a major indicator for ankle sprain injury. We evaluated whether the ankle sprain under the condition of 117° of inversion rotation and at a speed of 1,500° per second could induce pressure hypersensitivity on the injured ankle using PAM. Results showed that pressure threshold to induce foot withdrawal was decreased, indicating induction of pain on the injured ankles in all groups, with each group sustaining a different duration of decrease. (Figure 2A). The pressure threshold of the right treated foot was significantly reduced after the CFL transection (an average of 65 ± 3% reduction for D6–D9 or 42 ± 5% for D0–D9) and also after the first mechanical sprain (an average of 62 ± 5% for D3–D9 or 63 ± 3% for D0–D9), respectively, compared with the contralateral (untreated) left foot or corresponding pretreatment baseline on the right foot (Figure 2A). These results demonstrated that the induction of pressure

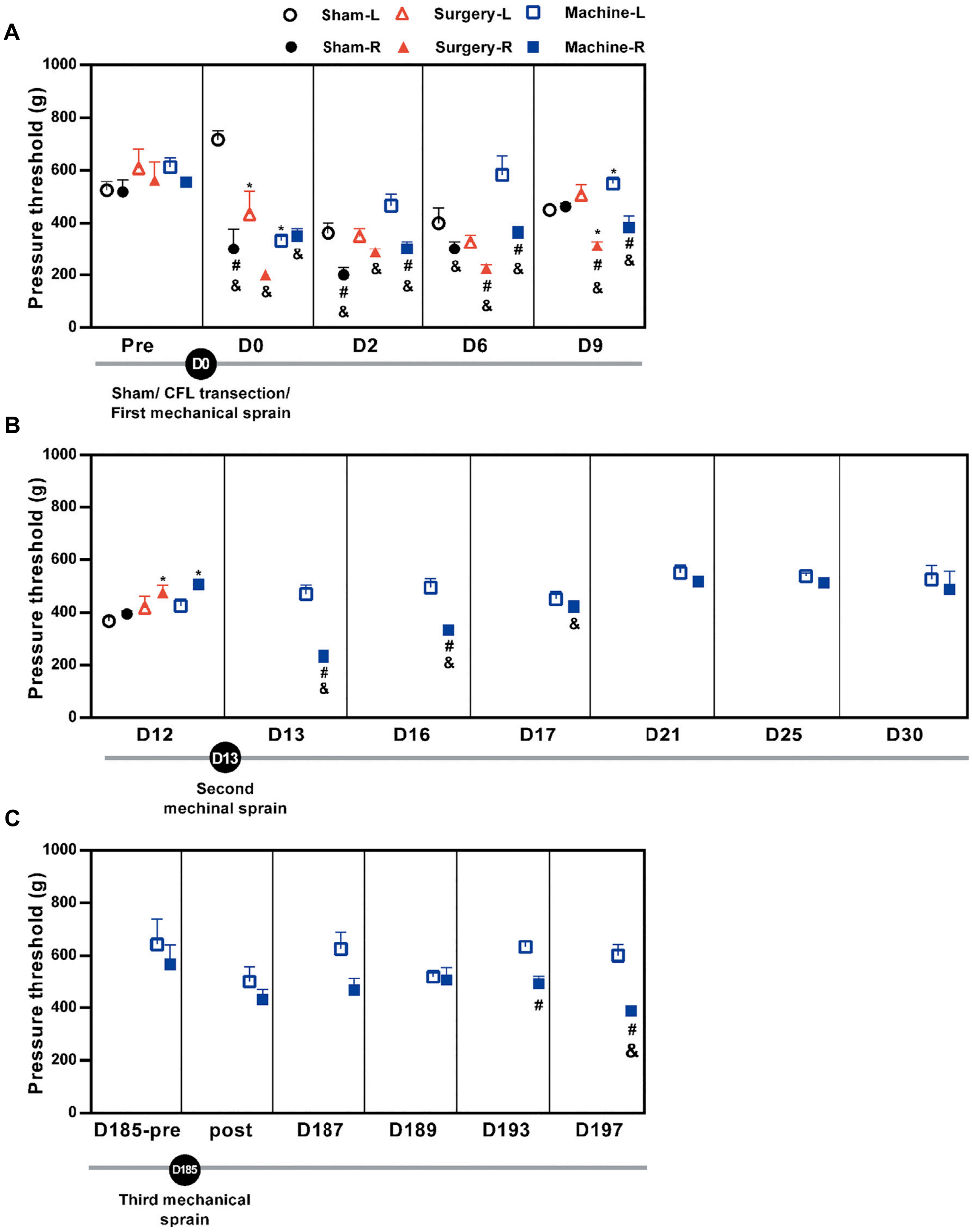

FIGURE 2
Changes in the pressure pain threshold after mechanical ankle sprains. The ankle pain threshold was measured using PAM on the indicated day. The pain threshold is shown **(A)** after the sham operation or the CFL transection or the first mechanical ankle sprain on day 0 (D0), **(B)** after the second mechanical ankle sprain on the 13th day (D13), and **(C)** before (D185-pre) and after (post) the third mechanical ankle sprain on the 185th day (D185). Values are mean ± SEM, $n = 4$. The statistical significance was analyzed using paired *t* test within the group (# and &) or unpaired *t* test between groups (*). *$p < 0.05$ compared with corresponding sham group; #$p < 0.05$ compared with corresponding left untreated foot (L); & $p < 0.05$ compared with the corresponding right treated foot (R) of pretreatment (pre) baseline on the 12th day (D12) in **(B)** and pretreatment baseline on the 185th day (D185-pre) in **(C)**.

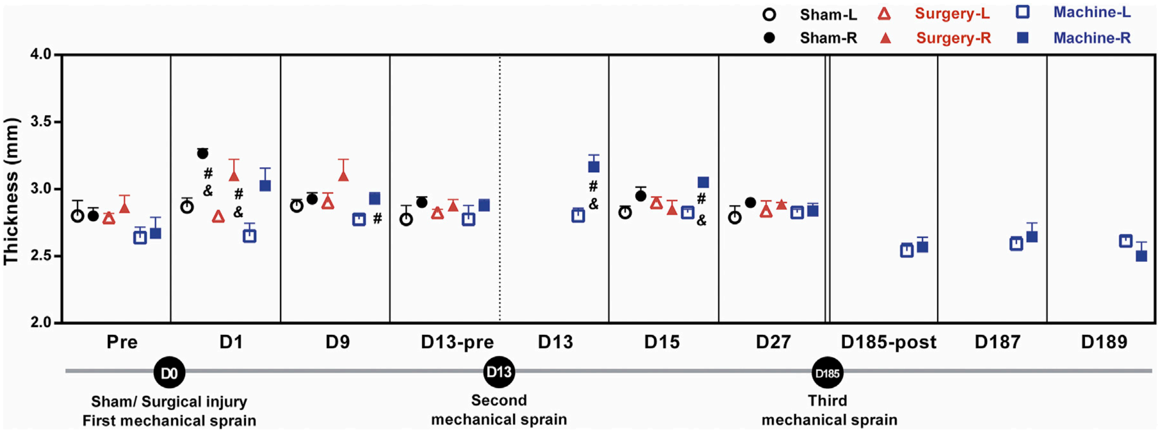

FIGURE 3
Changes in ankle thickness after mechanical ankle sprains. The level of ankle swelling was measured using a thickness gauge on the indicated day after sham operation or CFL transection or three times of mechanical ankle sprains. The statistical significance was analyzed using paired *t* test, #$p < 0.05$ compared with corresponding left untreated foot (L) and & $p < 0.05$ compared with the corresponding right foot (R) of pretreatment (pre) baseline or before the second mechanical sprain (D13-pre) on the 13th day (D13).

hypersensitivity by a single mechanical sprain was similar to that induced by CFL transection. In the sham operation group, decreased pressure threshold was found only immediately (D0) and on the second day (D2) after the sham operation. Moreover, results showed that pressure hypersensitivity on the injured side reappeared on the 13th day (D13, 51% reduction of pressure threshold vs. the contralateral left foot and 46% vs. the right foot of baseline on the D12), D16 (67% and 66%), and D17 (93% and 83%, Figure 2B). The third mechanical sprain also induced a significant decrease in pressure threshold on the 193th (78% reduction vs. the contralateral left foot and 87% vs. the injured right foot of baseline on the D185-pre) and 197th day (65% and 68%, Figure 2C). These results showed that a single mechanical ankle sprain is successful in inducing a similar pressure hypersensitivity caused by surgical CFL transection and that recurrent ankle sprain injuries can be developed by multiple mechanical sprains.

Swollen ankle is found after mechanical ankle sprain

One of the major symptoms of ankle sprain-induced inflammation is ankle swelling; the swelling was evaluated by measuring the ankle thickness with a thickness gauge. Results showed that ankle thickness in the treated right side increased significantly on the 1st day (D1) only after the sham operation (3.27 ± 0.03 mm) and CFL transection groups (3.2 ± 0.08 mm), respectively, compared with the contralateral uninjured side (2.87 ± 0.06 and 2.8 ± 0.00), or compared to the injured side on the baseline before the treatment (2.8 ± 0.06 and 2.86 ± 0.09, Figure 3). The first mechanical sprain induced an increasing trend in ankle thickness on D1 (3.03 ± 0.13 on the sprained ankle vs. 2.65 ± 0.09 on the un-sprained ankle, $p = 0.14$) and a significant increase on D9 (2.93 ± 0.04 on the sprained ankle vs. 2.77 ± 0.02 on the un-sprained ankle). These results indicated that in comparison with an acute ankle swelling induced by CFL transection, a single mechanical sprain induces a prolonged effect on the ankle swelling. Moreover, a swollen ankle reoccurred after the second mechanical sprain as shown by a significant increase in sprained ankle thickness compared to the un-sprained side (3.16 ± 0.07 mm vs. 2.80 ± 0.06 mm on the D13 and 3.05 ± 0.03 mm vs. 2.82 ± 0.03 mm on the D15) or compared to the injured side before the second sprain (2.87 ± 0.05 mm). However, the third mechanical sprain on the 185th day did not induce a significant increase in the thickness of the sprained ankle. The results demonstrated that in contrast to the one-time injury induced by CFL transection, the repeated mechanical sprains within 2 weeks were able to induce a recurrent ankle swelling but could not reproduce the swelling symptoms 6 months after the initial sprain.

Mechanical ankle sprain induces impairment of motor coordination

We performed the beam test to examine motor coordination after repeated mechanical ankle sprains. Results showed that after the first mechanical ankle sprain, the number of foot slips had a brief upward trend on the sprained side (4.67 ± 1.53 vs. 1.25 ± 0.75 on the un-sprained side, $p = 0.18$) on the 4th day. The sham operation did not induce an increase in foot slips on the treated side. CFL transection induced a significant increase in foot slips of the injured side compared with the un-injured side

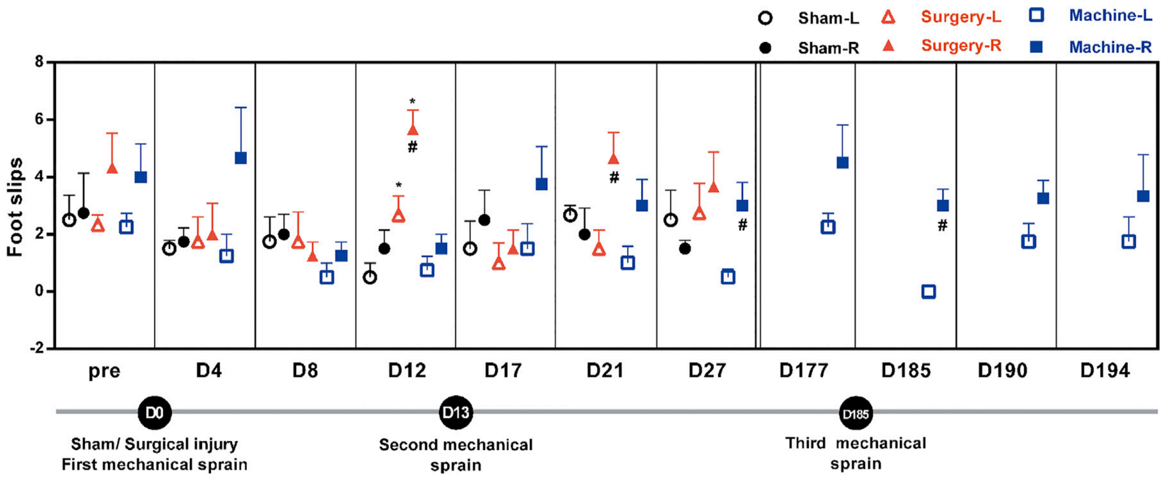

FIGURE 4
Effect of mechanical ankle sprains on motor balance and coordination. The number of hind foot slips were measured using a beam test on the indicated day to evaluate motor balance and coordination after sham operation, CFL transection, and three mechanical sprains. Total number of foot slips were counted in three tests at each time point. Values are mean ± SEM, $n = 4$. #$p < 0.05$ compared with corresponding left untreated foot (L) using paired t test. *$p < 0.05$ compared with sham operation group using unpaired t test.

(5.67 ± 0.57 vs. 2.66 ± 0.66 on the D12 and 4.66 ± 0.76 vs. 1.5 ± 0.64 on the D21, Figure 4). After the second mechanical sprain on the 13th day (D13), an increasing trend of foot slips was persistently found from D17 to D177, with a significantly higher number of slips on the 27th day (3.67 ± 0.57 vs. 0.33 ± 0.28 on D27) compared to the un-sprained side. Moreover, after the third mechanical sprain, a significantly higher number of foot slips on the sprained side was reproduced (3 ± 0.5 vs. 0 ± 0 on the un-sprained side) and continually found until the end of the experiment. These results demonstrated that repeated mechanical ankle sprains induced a long-term balance deficit.

Abnormal gait parameters are found after mechanical ankle sprain

Alterations in gait pattern can be seen in CAI patients. Gait parameters were analyzed using the footprint assay. Results showed a significant decrease in stance duration on the injured side in the CFL transection group (an average of 69 ± 3% decrease on the D14, D18, and D30) and the sham operation group (58% decrease on D24; 50% on D30) when compared to the corresponding pretreatment baseline (0.094 ± 0.006 s in CFL transection group and 0.116 ± 0.011 s in sham group, Figure 5A). For the mechanical sprain group, a significant decrease in stance duration was only found on the 180th day (56% reduction) when compared with the pre-treatment baseline. On the contrary, in comparison to the CFL transection group and the sham operation group, the first and second mechanical sprain induced a significantly longer stance duration on the sprained side (an average of 155 ± 7% increase on D1 and D5; 194 ± 20% on D14 to D30 compared with the CFL transection group; 168 ± 0% on D14 and D30 compared with the sham group, Figure 5A). In comparison with the baseline on the 180th day (0.065 ± 0.005 s), the third mechanical ankle sprain recurrently and significantly induced a longer stance duration (146% increase on D190 and 142% on D194, Figure 5A). In addition, the swing duration was also significantly longer in mice after the first and the second mechanical sprain than in mice treated with CFL transection (117% increase on D1 and an average of 128 ± 4% for D14 to D30, Figure 5B). However, the swing duration (Figure 5B) and step cycle (Figure 5C) in the CFL transection or the sham operation group showed no significant changes compared to the corresponding pre-treatment baseline. Moreover, the results demonstrated that the duration of step cycle was significantly longer (117% longer on D5 and 119% on D14) after the first and second mechanical sprains compared with the pre-injured baseline (0.273 ± 0.01 s) or compared with the CFL transection group (an average of 146% ± 6% longer for D1 to D30). After the third mechanical sprain, the step cycle also significantly increased on the 190th day (123% increase) compared with the baseline on the 180th day (0.224 ± 0.01 s) before the third mechanical sprain (Figure 5C). These results demonstrate that multiple mechanical sprains induce a gait change of longer step cycle due to increase in stance and swing duration.

In the mechanical sprain group, after the first and second mechanical sprains, step distance was found unaffected for the initial 30 days until a significant 120% increase on the 180th day compared with the pre-treatment baseline (72.8 ± 2.1 mm,

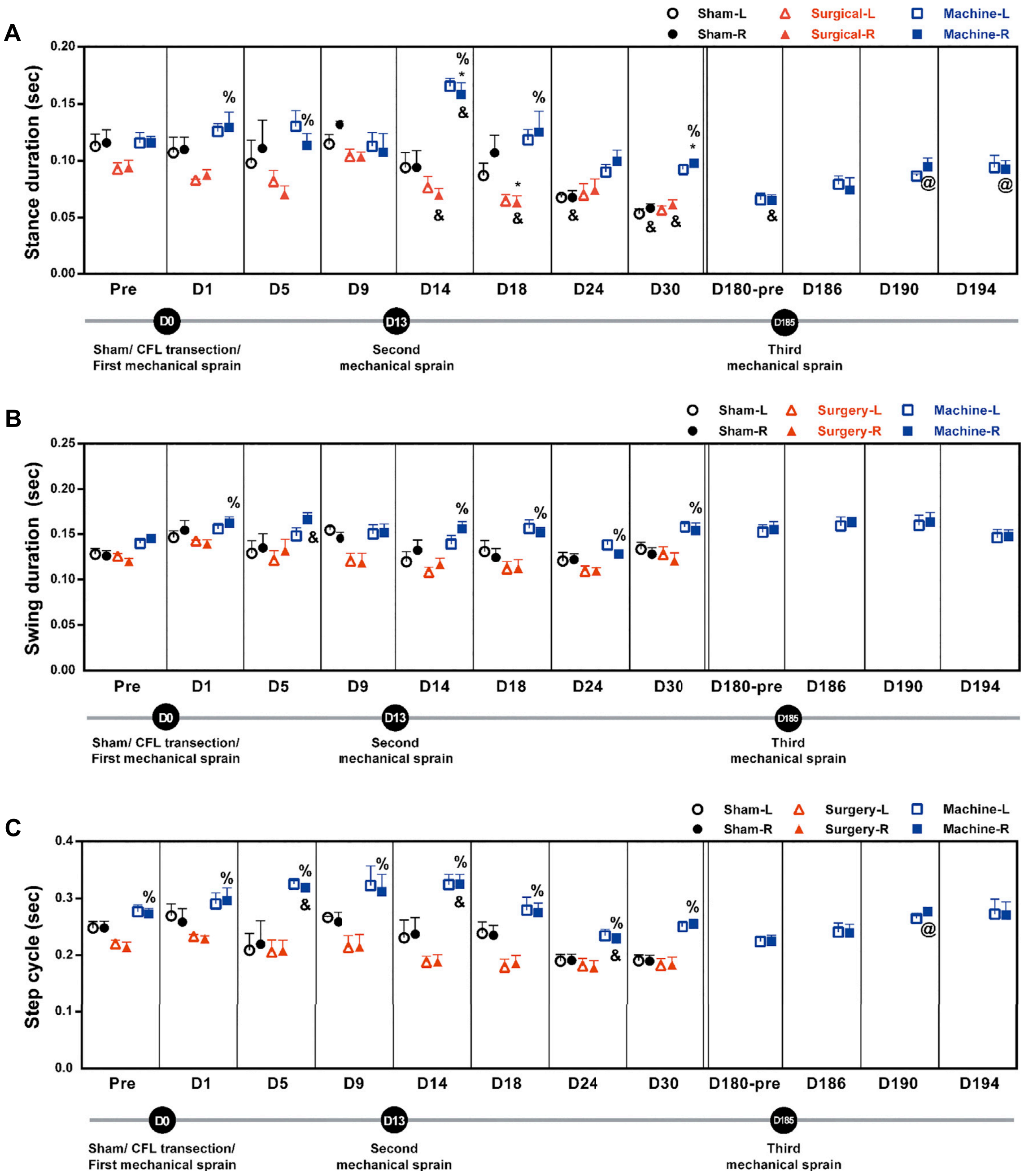

FIGURE 5
Mechanical ankle sprains induces gait abnormalities in stance duration, swing duration, and step cycle. Footprint was measured and analyzed on days indicated on the graphs after sham operation, CFL transection, and three mechanical ankle sprains to obtain gait parameters including stance duration **(A)**, swing duration **(B)** and step cycle **(C)**. Values are mean ± SEM, *n* = 4. The statistical significance was analyzed using unpaired *t* test (* and %) or paired *t* test (@ and &). *$p < 0.05$ compared with the corresponding right foot (R) of the sham operation group; % $p < 0.05$ compared with the corresponding right injured foot of the surgical transection group; & $p < 0.05$ compared with the corresponding pretreatment (pre) baseline; @ $p < 0.05$ compared with the pretreatment baseline of the third mechanical ankle sprain on the 180th day (D180-pre).

Figure 6A). The longer step distance was also found after the CFL transection and sham operation. However, the third mechanical sprain significantly induced a decrease in step distance (an average of 91 ± 0% decrease for D186 to D194) when compared with the baseline level on the 180th day (87.2 ± 0.9 mm, Figure 6A). These results indicate that the third, but not the first and second, mechanical ankle sprain induces a gait change of shorter step length.

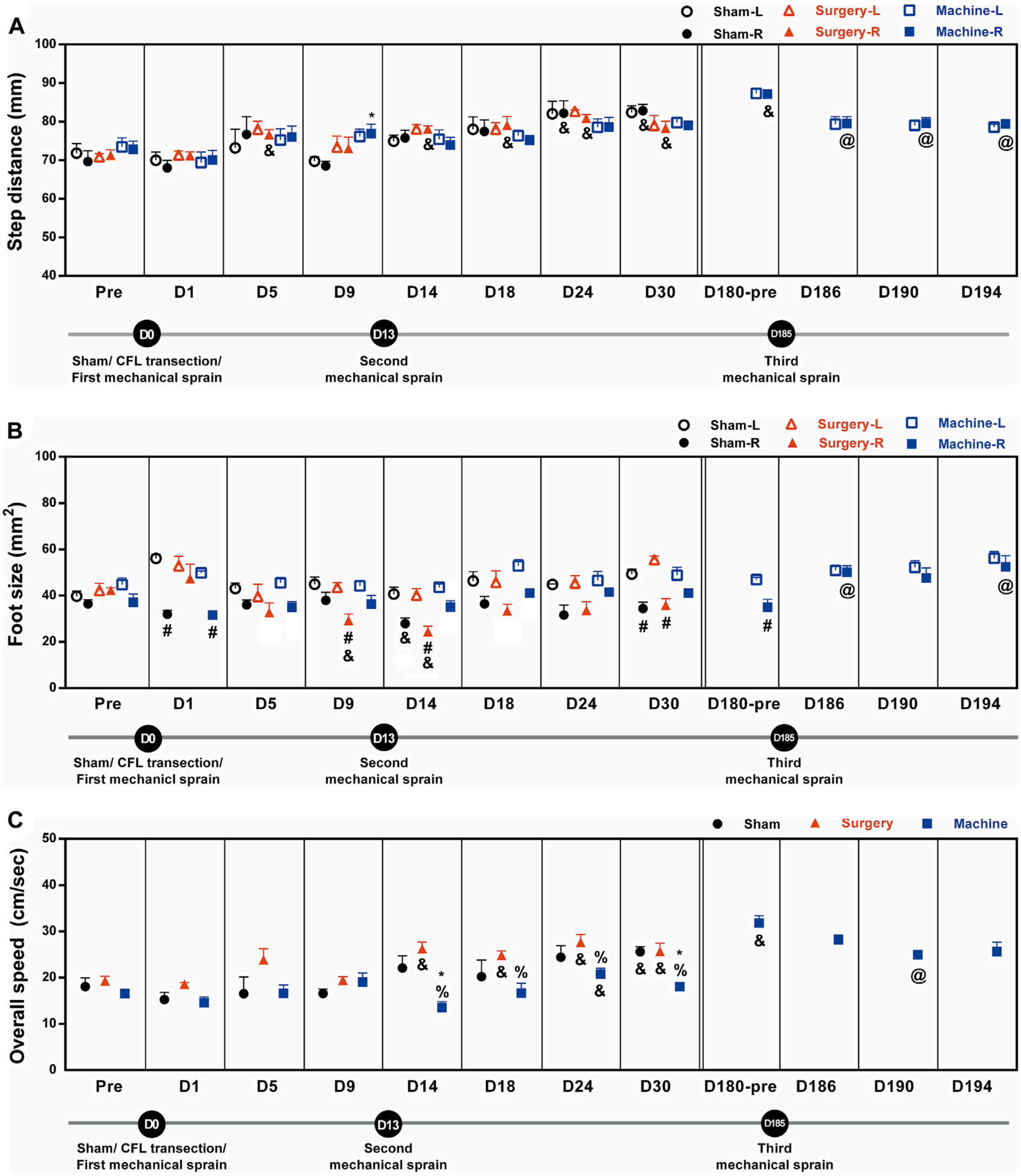

FIGURE 6

Mechanical ankle sprains induces gait abnormalities in step distance, foot size, and overall speed. Footprint was measured and analyzed on the days indicated on the graphs after sham operation, CFL transection, and three mechanical ankle sprains to obtain gait parameters including step distance **(A)**, foot size **(B)**, and overall speed **(C)**. Values are mean ± SEM, $n = 4$. The statistical significance was analyzed between groups using un-paired *t* test (* and %) or within group using paired *t* test (#, @, and &) $^*p < 0.05$ compared with right foot (R) of sham operation group; % $p < 0.05$ compared with the right injured foot of the surgical transection group; #$p < 0.05$, a significant difference between the right injured and the left untreated foot (L) in each group; & $p < 0.05$ compared with the corresponding pretreatment (pre) baseline; @ $p < 0.05$ compared with the pretreatment baseline of the third mechanical ankle sprain on the 180th day (D180-pre).

The foot sizes on the injured sides were significantly smaller than those on the uninjured sides after sham operation (57% reduction on D1; 64% on D30), CFL transection (an average of 64 ± 2% reduction on D9, D14, and D30), and the first mechanical sprain (64% on D1, Figure 6B). In addition, after the second mechanical sprain, the foot size was unaffected until a significant 80% reduction was found on the 180th day (D180). However, the smaller foot size on the sprained side was not found after the third mechanical sprain.

The overall walking speed increased significantly after CFL transection (an average of 135 ± 3% increase for D14 to D30) and after sham operation (142% increase on the 30th day) as compared with the corresponding pre-treatment baseline level (Figure 6C). After the first and second mechanical sprains, the overall speed was not changed for the initial 30 days until a significant 192% increase on the 180th day compared with the pretreatment baseline (16.6 ± 0.7 cm/s, Figure 6C). On the contrary, in comparison with the CFL transection or sham operation mice, the overall speed decreased significantly in mice after the second, but not the first, mechanical ankle sprain (an average of 66 ± 5% decrease vs. CFL transection for D14 to D30 and 67 ± 6% on D14 and D30 vs. sham operation). Moreover, the slow speed re-occurred after the third mechanical ankle sprain, a 78% decrease on the D190 compared with the baseline level on the 180th day (31.8 ± 1.6 cm/s, Figure 6C). These results demonstrated that the repeated mechanical ankle sprains induces a gait change of slower walking speed in contrast to faster walking speed in the CFL transection group.

Discussion

We demonstrated a new mouse model for ankle sprain induced by mechanical wrenching of the ankle with controlled rotation angle and speed. We found that a single mechanical sprain induces ankle injury, which is similar to the effect of surgical CFL transection on ankle tenderness. Moreover, the second mechanical ankle sprain 2 weeks later induces more pronounced responses in ankle tenderness and swelling, higher beam slips, and abnormal gait. Regardless of pain and swelling, the symptoms of ankle instability, balance deficits, and abnormal gait are reproduced after the third mechanical sprain 6 months later. This mechanical sprain model can induce multiple ankle injuries and is very suitable for investigating the molecular mechanisms and treatments of ankle instability with recurrent injuries.

We first demonstrated that the ankle is twisted to 117° of inversion at a speed of 1,500° per second, two at a time. The model was able to induce an effect similar to that of the surgical CFL transection on pressure hypersensitivity and swollen ankle in mice. In addition, the ligament injury-induced hypersensitivity and swelling can be reproduced when the second mechanical ankle sprain occurs 2 weeks later; while the surgical group did not show deficits in hypersensitivity or swelling at this time point, ankle swelling was seen in the mechanical sprain mice, indicating that inflammatory edema was induced by mechanical and non-invasive ankle sprain, which is contrary to the ligament transection model that has potential additional inflammation and swelling caused by the open wound of surgery operation. The results are consistent with the swollen ankles found in humans after suffering from an ankle sprain (Delahunt et al., 2018).

In terms of the severity of ligament injury for an ankle sprain, previous studies have shown that the surgical CFL or the ATFL transection model is a grade III injury owing to the complete rupture of one or more ankle ligaments, which is different from the CAI predictor of grade II lateral ankle ligament injury (Pourkazemi et al., 2014). In the mechanical sprain model, we found that the sprain injury-induced tenderness and swelling recovered 12 and 4 days after the first and second mechanical sprain, respectively. Since ankle injuries are recoverable, the mechanical sprain condition used in the present study may be considered to induce a strain of lateral ligaments without rupture, which is known to be classified as a grade I ankle injury (Slater, 2018). Moreover, when the third mechanical sprain was performed 6 months later, it induced a delayed ankle tenderness but did not result in ankle swelling. We hypothesized that the two previous mechanical sprains may have induced laxity in the ankle ligaments, leading to ankle joint laxity; therefore the third sprain using the same twisting condition was not sufficient to result in the same notable changes in pain threshold and ankle thickness seen in the previous two sprains. Previous studies have shown in patients suffering CAI, the recurrent sprains result in unstable ankle joint due to the induction of joint laxity (Al-Mohrej and Al-Kenani, 2016). Although the hypothesis still needs to be further examined using CT scan or other histology examination methods, unstable ankle caused by loose ligaments can be supported by our results showing that significant balance defects and gait changes are found after the second and third, but not the first mechanical ankle sprain.

In the beam tests, our results demonstrate that the increased number of slips on the sprained foot are found after the first and second sprain, and persistently occurs after the third sprain, 6 months later. However, the increased foot slips in the injured ankle are only found on days 12 and 21 after CFL transection. These results are consistent with the finding that increased number of foot slips were found in the earlier periods of 3 days and 1 week after CFL transection and that mice with ATFL and CFL transection have more foot slips than sham operation and CFL transection mice (Hubbard-Turner et al., 2013; Wikstrom et al., 2015). Since persistent higher number of foot slips were found after the second and third mechanical sprain, we propose that the repeated mechanical sprains used in this study result in long-term balance defects by inducing injuries of multiple ankle ligaments. Considering the induction of balance defects as one of the major symptoms of CAI (Hertel, 2002), the results and the following abnormal gaits supports the fact that our model of recurrent mechanical ankle sprain is able to induce CAI.

The gait changes in the mechanical sprain group included a significant increase in the stance duration and step cycle (Figure 5), whereas a decrease in the step distance and overall walking speed (Figure 6), were found after each mechanical sprain as compared with the CFL transection or sham operation group. These findings further support the results that repeated mechanical ankle sprain-induced injuries of multiple ankle ligaments lead to a decrease in the step distance and walking speed because smaller step lengths and slower running speeds were found in the wheel after the transection of two ligaments (ATFL and CFL), but not limited to CFL (Hubbard-Turner et al., 2013; Hubbard-Turner et al., 2015; Wikstrom et al., 2018). Furthermore, previous results from human studies demonstrate that individuals with ankle sprains have slow walking speed and shorter step length (Punt et al., 2015). On the contrary, in both the sham operation and CFL transection groups, the stance duration decreased but the step distance and overall walking speed increased from the 14th to 30th day when compared with the pretreatment baseline. Moreover, these gait changes are also found in the mechanical sprain of mice on the 180th day, but not found in the period between the 1st and 30th day after the first and second mechanical ankle sprain. Since no footprint assay was performed in the period between the 30th day (no gait changes) and the 180th day (significant gait changes) after the first mechanical sprain, we rule out a training effect of footprint assay as the reason behind gait changes on the 180th day in the mechanical sprain group. In addition, the gait changes found in both the sham operation and CFL transection groups are comparable and also found on the 180th day in the mechanical sprain group, suggesting that the shorter stance duration, longer step distance, and faster walking speed found in all groups may be normal physiological responses. Previous results support the suggestion, showing that a longer step length is observed along with age in all the groups of sham, CFL-only, and ATFL/CFL transections (Hubbard-Turner et al., 2013; Wikstrom et al., 2015).

In addition, decreased foot size in treated side of paws was found in all groups; a persistent decrease in both sham operation and CFL transection group as well as a transient decrease in the mechanical sprain group after the first and second mechanical sprain (Figure 6B). One study demonstrated that a smaller foot print area (foot size) of the affected side of the paws was found after unilateral intracerebral hemorrhage using a similar footprint camera system used in this study (Liu et al., 2013). These findings support that the decreased foot size may be associated with the injured ankle. However, the third mechanical sprain did not induce a smaller foot size (Figure 6B) in the sprained ankle, which may be due to the ankle laxity being unable to support the foot as discussed.

The limitation of the present study is that it is hard to directly evaluate the severity of the ligamentous injuries induced by mechanical ankle sprains. For example, it is difficult to isolate the tiny CFL or ATFL and also hard to get the longitudinal section of both ligaments from the ankle samples for the examination of ligament injuries using histological staining, such as HE and collagen staining. In addition, the mechanical sprains in this study may not induce complete ligamentous tears, which is also difficult to observe using the micro-CT. One previous report demonstrated that talus displacement was still not observed from micro-CT images in the mice with CFL and ATFL transection (Liu et al., 2021). However, the limitations may be overcome by changing the experimental animals into rats and modifying the device for the rats based on the experiences of the present study. Moreover, the measurement to detect the ankle joint range of motion or mobility needs to be done urgently to elucidate the ankle laxity and functional ankle instability induced by multiple mechanical ankle sprains in the present mouse CAI model.

In conclusion, we established a new model of lateral ankle sprain using a self-designed machine with a precise control of inversion angle and speed. Our model of multiple mechanical ankle sprains can induce recurrent injuries, long-term balance deficits, and gait changes, which simulate the major characteristics of ankle instability in humans (Hertel, 2002). Moreover, the advantage of this model is that the inversion angle, speed, and times and intervals of sprains can be manipulated and controlled. Therefore, this model can be used to further study the ankle instability induced by various ankle biomechanics of sprains, which may simulate the multiform of CAI in humans. On the other hand, the mechanical sprain-induced CAI model is distinguished by surgical transection of ligaments and may also be applied for investigating the incomplete ligamentous (mild to moderate) injuries induced by CAI. This mouse model is also applied to knockout and transgenic mice to study the potential molecular mechanisms involved in ankle instability, such as nociceptors, mechanoreceptors, and proprioceptors.

Data availability statement

The raw data supporting the conclusion of this article will be made available from the corresponding author on reasonable request.

Ethics statement

All experimental protocols were in accordance with the National Institutes of Health Guidelines for Animal Research and were approved by the National Cheng Kung University

Institutional Animal Care and Use Committee (IACUC #109126). All efforts were made to ensure animal welfare.

Author contributions

The authors confirm contribution to the paper as follows: study conception and design: S-HC, Y-JT, and S-HY; data collection: S-HC and Y-CL; analysis and interpretation of results: S-HC, Y-CL, Y-JT, and S-HY; draft manuscript preparation: S-HC, Y-JT, S-HY, and Y-CC. All authors reviewed the results and approved the final version of the manuscript.

Funding

This study was supported by grants from the Ministry of Science and Technology in Taiwan (Grant Nos. MOST 108-2314-B-006 -079 -MY3 and MOST 109-2410-H-006 -069 -MY2) for S-HY and Y-JT, respectively.

Conflict of interest

The authors declare that the research was conducted in the absence of any commercial or financial relationships that could be construed as a potential conflict of interest.

Publisher's note

Supplementary material

The Supplementary Material for this article can be found online at: https://www.frontiersin.org/articles/10.3389/fbioe.2022.927987/full#supplementary-material

References

Al-Mohrej, O. A., and Al-Kenani, N. S. (2016). Chronic ankle instability: current perspectives. *Avicenna J. Med.* 6 (4), 103–108. doi:10.4103/2231-0770.191446

Barton, N. J., Strickland, I. T., Bond, S. M., Brash, H. M., Bate, S. T., Wilson, A. W., et al. (2007). Pressure application measurement (PAM): a novel behavioural technique for measuring hypersensitivity in a rat model of joint pain. *J. Neurosci. Methods* 163 (1), 67–75. doi:10.1016/j.jneumeth.2007.02.012

Braun, B. L. (1999). Effects of ankle sprain in a general clinic population 6 to 18 months after medical evaluation. *Arch. Fam. Med.* 8 (2), 143–148. doi:10.1001/archfami.8.2.143

Delahunt, E., Bleakley, C. M., Bossard, D. S., Caulfield, B. M., Docherty, C. L., Doherty, C., et al. (2018). Clinical assessment of acute lateral ankle sprain injuries (ROAST): 2019 consensus statement and recommendations of the international ankle consortium. *Br. J. Sports Med.* 52 (20), 1304–1310. doi:10.1136/bjsports-2017-098885

Fong, D., Ha, S., Mok, K-M., Chan, C., and Chan, K. C. (2012). Kinematics analysis of ankle inversion ligamentous sprain injuries in sports: five cases from televised tennis competitions. *Am. J. Sports Med.* 40, 2627–2632. doi:10.1177/0363546512458259

Fong, D. T., Chan, Y. Y., Mok, K. M., Yung, P. S., and Chan, K. M. (2009). Understanding acute ankle ligamentous sprain injury in sports. *BMC Sports Sci. Med. Rehabil.* 1, 14. doi:10.1186/1758-2555-1-14

Fong, D. T-P., Hong, Y., Chan, L-K., Yung, P. S-H., and Chan, K-M. (2007). A systematic review on ankle injury and ankle sprain in sports. *Sports Med.* 37 (1), 73–94. doi:10.2165/00007256-200737010-00006

Garrick, J. G., and Schelkun, P. H. (1997). Managing ankle sprains. *Phys. Sportsmed.* 25 (3), 56–68. doi:10.1080/00913847.1997.11440201

Gerber, J. P., Williams, G. N., Scoville, C. R., Arciero, R. A., and Taylor, D. C. (1998). Persistent disability associated with ankle sprains: a prospective examination of an athletic population. *Foot Ankle Int.* 19 (10), 653–660. doi:10.1177/107110079801901002

Gribble, P. A., Bleakley, C. M., Caulfield, B. M., Docherty, C. L., Fourchet, F., Fong, D. T. P., et al. (2016). Evidence review for the 2016 international ankle consortium consensus statement on the prevalence, impact and long-term consequences of lateral ankle sprains. *Br. J. Sports Med.* 50 (24), 1496–1505. doi:10.1136/bjsports-2016-096189

Hertel, J. (2002). Functional anatomy, pathomechanics, and pathophysiology of lateral ankle instability. *J. Athl. Train.* 37 4, 364–375.

Hertel, J. (2000). Functional instability following lateral ankle sprain. *Sports Med.* 29 (5), 361–371. doi:10.2165/00007256-200029050-00005

Hiller, C. E., Nightingale, E. J., Raymond, J., Kilbreath, S. L., Burns, J., Black, D. A., et al. (2012). Prevalence and impact of chronic musculoskeletal ankle disorders in the community. *Arch. Phys. Med. Rehabil.* 93 (10), 1801–1807. doi:10.1016/j.apmr.2012.04.023

Hubbard-Turner, T., Wikstrom, E. A., Guderian, S., and Turner, M. J. (2013). Acute ankle sprain in a mouse model. *Med. Sci. Sports Exerc.* 45 (8), 1623–1628. doi:10.1249/mss.0b013e3182897d25

Hubbard-Turner, T., Wikstrom, E. A., Guderian, S., and Turner, M. J. (2015). An acute lateral ankle sprain significantly decreases physical activity across the lifespan. *J. Sports Sci. Med.* 14 (3), 556–561.

Kim, H. Y., Wang, J., Chung, K., and Chung, J. M. (2008). A surgical ankle sprain pain model in the rat: effects of morphine and indomethacin. *Neurosci. Lett.* 442 (2), 161–164. doi:10.1016/j.neulet.2008.06.074

Kim, J. H., Kim, H. Y., Chung, K., and Chung, J. M. (2011). Electroacupuncture reduces the evoked responses of the spinal dorsal horn neurons in ankle-sprained rats. *J. Neurophysiol.* 105 (5), 2050–2057. doi:10.1152/jn.00853.2010

Koo, S., Park, Y. I., Lim, K-s., Chung, K., and Chung, J. M. (2002). Acupuncture analgesia in a new rat model of ankle sprain pain. *Pain* 99, 423–431. doi:10.1016/s0304-3959(02)00164-1

Koo, S. T., Lim, K. S., Chung, K., Ju, H., and Chung, J. M. (2008). Electroacupuncture-induced analgesia in a rat model of ankle sprain pain is mediated by spinal alpha-adrenoceptors. *Pain* 135 (1-2), 11–19. doi:10.1016/j.pain.2007.04.034

Kristianslund, E., Bahr, R., and Krosshaug, T. (2011). Kinematics and kinetics of an accidental lateral ankle sprain. *J. Biomech.* 44 (14), 2576–2578. doi:10.1016/j.jbiomech.2011.07.014

Li, J., Chen, Z., Cheng, Y., Gao, C., Gu, X., et al. (2022). Ligamentous injury-induced ankle instability causing posttraumatic osteoarthritis in a mouse model. *BMC Musculoskelet. Disord.* 23 (1), 223. doi:10.1186/s12891-022-05164-5

Liu, P., Chen, K., Wang, S., Hua, C., Zhang, H., and Yu, J. (2021). A mouse model of ankle-subtalar joint complex instability induced post-traumatic osteoarthritis. *J. Orthop. Surg. Res.* 16 (1), 541. doi:10.1186/s13018-021-02683-0

Liu, Y., Ao, L. J., Lu, G., Leong, E., Liu, Q., Wang, X. H., et al. (2013). Quantitative gait analysis of long-term locomotion deficits in classical unilateral striatal intracerebral hemorrhage rat model. *Behav. Brain Res.* 257, 166–177. doi:10.1016/j.bbr.2013.10.007

Luong, T. N., Carlisle, H. J., Southwell, A., and Patterson, P. H. (2011). Assessment of motor balance and coordination in mice using the balance beam. *J. Vis. Exp.* 49, 2376. doi:10.3791/2376

Mendes, C. S., Bartos, I., Márka, Z., Akay, T., Márka, S., and Mann, R. S. (2015). Quantification of gait parameters in freely walking rodents. *BMC Biol.* 13, 50. doi:10.1186/s12915-015-0154-0

Norkin, C. C., and White, D. J. (2016). *Measurement of joint motion: A guide to goniometry*. F.A. Davis Company.

Pourkazemi, F., Hiller, C. E., Raymond, J., Nightingale, E. J., and Refshauge, K. M. (2014). Predictors of chronic ankle instability after an index lateral ankle sprain: A systematic review. *J. Sci. Med. Sport* 17 (6), 568–573. doi:10.1016/j.jsams.2014.01.005

Punt, I. M., Ziltener, J. L., Laidet, M., Armand, S., and Allet, L. (2015). Gait and physical impairments in patients with acute ankle sprains who did not receive physical therapy. *PM&R* 7 (1), 34–41. doi:10.1016/j.pmrj.2014.06.014

Roos, K. G., Kerr, Z. Y., Mauntel, T. C., Djoko, A., Dompier, T. P., and Wikstrom, E. A. (2017). The epidemiology of lateral ligament complex ankle sprains in national collegiate athletic association sports. *Am. J. Sports Med.* 45 (1), 201–209. doi:10.1177/0363546516660980

Slater, K. (2018). Acute lateral ankle instability. *Foot Ankle Clin.* 23 (4), 523–537. doi:10.1016/j.fcl.2018.07.001

Swenson, D. M., Yard, E. E., Fields, S. K., and Dawn Comstock, R. (2009). Patterns of recurrent injuries among US high school athletes, 2005-2008. *Am. J. Sports Med.* 37 (8), 1586–1593. doi:10.1177/0363546509332500

Tiemstra, J. (2012). Update on acute ankle sprains. *Am. Fam. Physician* 85, 1170–1176.

Tropp, H. (2002). Commentary: functional ankle instability revisited. *J. Athl. Train.* 37 (4), 512–515.

Wikstrom, E. A., Hubbard-Turner, T., Guderian, S., and Turner, M. J. (2018). Lateral ankle sprain in a mouse model: lifelong sensorimotor dysfunction. *J. Athl. Train.* 53 (3), 249–254. doi:10.4085/1062-6050-365-16

Wikstrom, E. A., Hubbard-Turner, T., Woods, S., Guderian, S., and Turner, M. J. (2015). Developing a mouse model of chronic ankle instability. *Med. Sci. Sports Exerc.* 47 (4), 866–872. doi:10.1249/mss.0000000000000466

Yeung, M. S., Chan, K. M., So, C. H., and Yuan, W. Y. (1994). An epidemiological survey on ankle sprain. *Br. J. Sports Med.* 28 (2), 112–116. doi:10.1136/bjsm.28.2.112

frontiers | Frontiers in Bioengineering and Biotechnology

TYPE Original Research
PUBLISHED 07 September 2022
DOI 10.3389/fbioe.2022.973389

OPEN ACCESS

EDITED BY
Damien Lacroix,
The University of Sheffield,
United Kingdom

REVIEWED BY
Feng Li,
Qingdao University of Science and Technology, China
Fancheng Chen,
Zhongshan Hospital, Fudan University, China

*CORRESPONDENCE
Jiantao Li,
lijiantao618@163.com
Wei Zhang,
bszw@hotmail.com

†These authors have contributed equally to this work and share first authorship

SPECIALTY SECTION
This article was submitted to Biomechanics,
a section of the journal
Frontiers in Bioengineering and Biotechnology

RECEIVED 20 June 2022
ACCEPTED 18 August 2022
PUBLISHED 07 September 2022

CITATION
Zeng C, Ren X, Xu C, Hu M, Li J and Zhang W (2022), Stability of internal fixation systems based on different subtypes of Schatzker II fracture of the tibial plateau: A finite element analysis.
Front. Bioeng. Biotechnol. 10:973389.
doi: 10.3389/fbioe.2022.973389

Stability of internal fixation systems based on different subtypes of Schatzker II fracture of the tibial plateau: A finite element analysis

Chuyang Zeng[1†], Xiaomeng Ren[1†], Cheng Xu[2†], Mengmeng Hu[1], Jiantao Li[2]* and Wei Zhang[1]*

[1]Senior Department of Orthopedics, The Fourth Medical Center of PLA General Hospital, Beijing, China, [2]National Clinical Research Center for Orthopedics, Sports Medicine and Rehabilitation, Beijing, China

Background: Schaztker II fracture is the most common type of the tibial plateau fractures (TPF). There has been a large number of cadaveric biomechanical studies and finite element simulation studies to explore the most stable fixation methods for this type of fracture, which were based on a single fracture morphology. But differences among fracture morphologies could directly affect the stability of internal fixation systems. In this sense, we verified the stability of existing internal fixation modalities by simulating Schatzker II fractures with different fracture morphologies.

Objectives: To compare the stability of different filler types combined with locked compression plate/screw in different subtypes of Schatzker II TPF.

Methods: Four subtypes of Schatzker II were created based on 3D map of TPF. Each of the subtypes was fixed with LCP/screw or LCP/screw combined with different fill types. Stress distribution, displacement distribution, and the load sharing capacity of the filler were assessed by applying the maximum load during gait. In addition, repeated fracture risks of depressed fragment were evaluated regarding to the ultimate strain of bone.

Results: The stress concentration of the implant in each scenario was located on the screw at the contact site between the plate and the screw, and the filler of the defect site significantly reduced the stress concentration of the implant (Subtype A: Blank group 402.0 MPa vs. Experimental group 315.2 ± 5.5 MPa; Subtype C: Blank group 385.0 MPa vs. Experimental group 322.7 ± 12.1 MPa). Displacement field analysis showed that filler significantly reduced the reduction loss of the depressed fragment (Subtype A: Blank group 0.1949 mm vs. Experimental group 0.174 ± 0.001 mm; Subtype C: 0.264 mm vs. 0.253 ± 0.002 mm). Maximum strain was in subtype C with the value of 2.3% ± 0.1% indicating the greatest possibility of failure risk. And with the increase of its modulus, the bearing capacity of filler increased.

Conclusion: The existence of filler at the defect site can effectively reduce the stress concentration of the implant and the reduction loss of the collapsed block, thus providing good stability for Schatzker II fracture. In subtype A fracture, the modulus of filler presented the slightest influence on the stability, followed by subtype C, while the stability of subtype B was most influenced by the modulus of filler. Therefore, it is necessary to evaluate the preoperative patient imaging data adequately to select the appropriate stiffness of the filler.

KEYWORDS

tibial plateau fracture, finite element, biomechanics, Schatzker II fracture, stability, fracture morphology

Introduction

Schatzker II split depression fractures are the most common type of TPF, accounting for 35% of the fractures (Elsoe et al., 2015). According to the AO recommendations, the goal of TPF treatment is anatomic reduction of the articular surface, the proper alignment of the lower extremity, stable fixation and reducing the risk of post-traumatic osteoarthritis (Júnior et al., 2009). Non-angular stable plate had been a standard method for this type of fracture. However, motion between fragments due to non-angular stability is likely to be the main cause of secondary reduction loss after surgery. Thereafter, angular stable plate was largely used. A matched retrospective cohort study by Prall et al. (2020) showed that angular stable plate significantly improved fracture stability. Other studies have also demonstrated the good performance of angular stable plate used in TPF (Trenholm et al., 2005; Lee et al., 2007). However, range 21%–58% of patients experienced early osteoarthritis and poor functional outcome was reported (Rademakers et al., 2007; Manidakis et al., 2010; Mattiassich et al., 2014).

Schatzker II of TPF split fracture is characterized by the lateral tibia plateau with associated depression of the articular surface, which need fixation augmentation of filler to fill the intraosseous void and to provide mechanical support for the articular surfaces. Numerous biomechanical and clinical studies on the benefits of fillers had been publish (Russell and Leighton, 2008). A systematic review by Goff et al. (2013) compared the effects of various types of fillers from the perspective of radiological evaluation, and showed that the secondary collapse rates (step-off above 2 mm) of the articular surface from high to low were calcium sulfate cement, biotype bone substitutes (allograft, demineralized bone matrix, and xenogeneic bone), hydroxyapatite, and calcium phosphate cement. Trenholm et al. (2005) demonstrated experimentally in cadaveric bone that augmentation with a-BSM bone substitute provided good stability compared with cancellous. Belaid et al. (2018) demonstrated that cement augmentation can improve implant stability and reduce the risk of re-collapse of collapsed fragment by means of finite element analysis. Aubert et al. (2021) also yielded similar conclusions as Belaid et al. (2018), affirming the good mechanical stability obtained by bone cement filling the defect site.

All of the above studies, although comparing the effects of different types of fillers, were simulated or experimentally performed under one fracture morphology alone and did not consider the morphological diversity of Schatzker II fractures themselves. The variety of fracture morphology may directly affect the stability of internal fixation methods. This study intends to compare the stability differences of different types of fillers in the treatment of different subtypes of Schatzker II fractures by finite element analysis, so as to provide value guidance for clinical practice.

Materials and methods

Geometry of studied structures

The tibial model was derived from the CT data of the lower extremities of a healthy adult female (female, 65 years, 75 Kg). The CT scan (slice thickness: 1.0 mm) was performed on a 64-slicer CT scanner (Siemens AG, Erlangen, Germany). The data archived from Picture Archiving and Communication Systems (PACS) were imported into Mimics (version 21.0, Materialize, Belgium), and the semi-automatic segmentation method based on the region growing algorithm was used to obtain the geometric shapes of cortical bone and cancellous bone. Then the preliminary model was imported into Geomagic Wrap (version 2017,3D Systems, United States) for smooth processing. Finally, the processed geometric models are imported into Unigraphic NX (version 10.0, Siemens PLM software, United States) for geometric shape split to construct the fracture model. The study was approved by the Institutional Review Board of our hospital (S2020-114-04).

The fracture model was established based on Zhang et al.'s 3D Mapping of Hundreds of patients with TPF (Yao et al., 2020). It consisted of four parts: tibia shaft, separated fragment, depressed fragment and defect site (Figure 1). By changing the size of the fragment to represent the diversities of fracture morphology, four different fracture subtypes were obtained from four different fragment types. Subtype A was a type in which the size of the collapsed fragment was relatively large, so that screws can directly penetrate the collapsed fragment, and

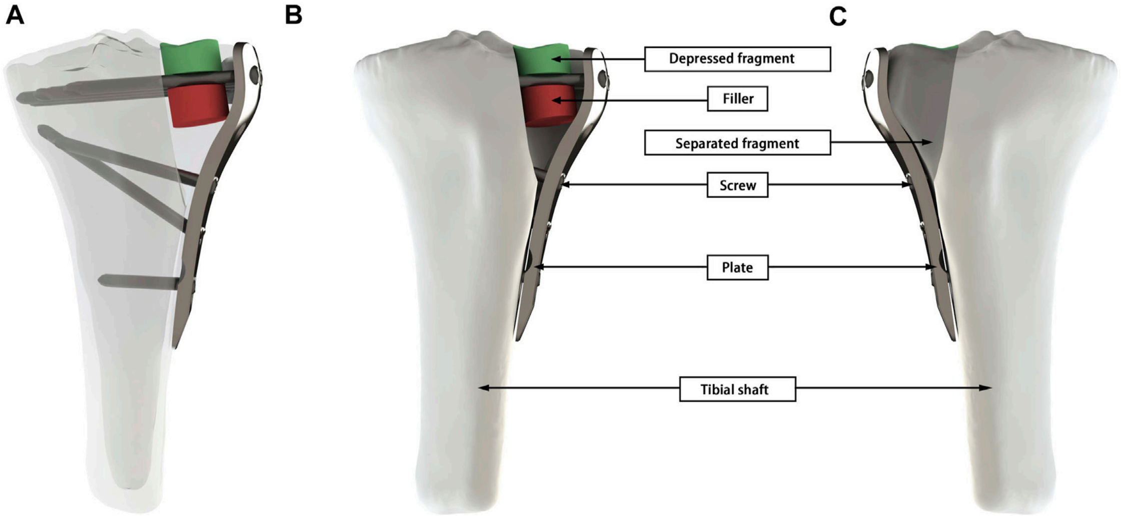

FIGURE 1
A geometric model of Schatzker II fracture was presented using Subtype C as an example. **(A)** Overall 3D view of the working conditions. **(B)** The frontal view of the tibial, shows the depressed fragment, filler, screw, plate, and tibial shaft. **(C)** The mirror view of **(A)** shows the separated fragment.

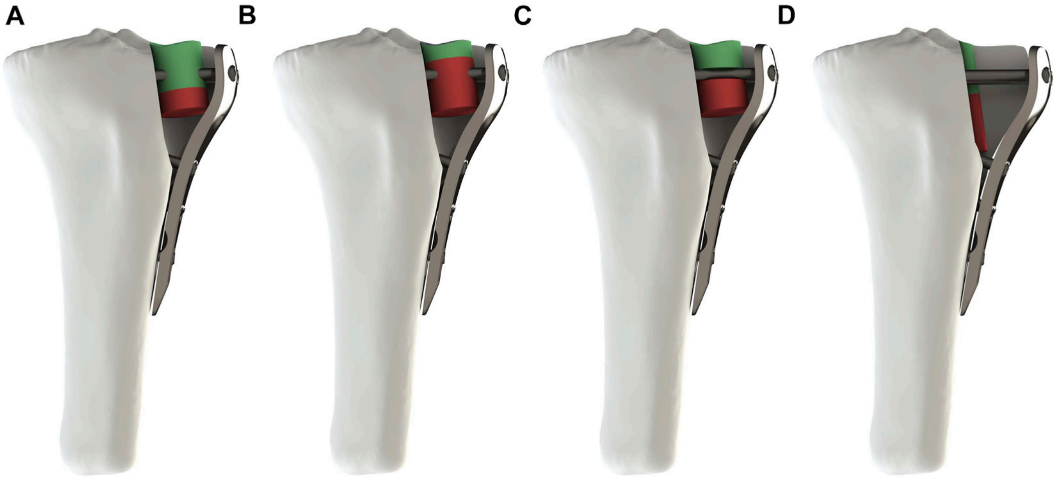

FIGURE 2
Four subtypes of fracture after assembly. **(A–D)** respectively represented Subtypes. **(A)** The screw penetrated the depressed fragment. **(B)** The screw penetrated the filler. **(C)** The screw was located between the depressed fragment and the filler. **(D)** The screw was not in contact with the depressed fragment and the filler.

this subtype occurred mostly in young people with better bone quality (Figure 2A). Subtype B was a type of relatively large defect area, which was more common in osteoporotic patients, and screws were often able to penetrate the filler in the defect area during treatment (Figure 2B). Subtype C belonged to the borderline type, and the position of the screw was between the collapsed block and the defect area, which appeared in a few cases (Figure 2C). Subtype D represented a type in which the screw was not in contact with the fracture fragment and it was an occasionally common type (Figure 2D). The implant was selected as a proximal tibial lateral LCP (SDJP-A 039; length 81 mm, width 11 mm, thickness 3.7 mm; AKEC, China) and eight unicortical locking screws (diameter 3.5 mm, AKEC, China). The screw threads were removed so as to improve the calculation efficiency, which didn't affect the simulation of locking function of locking screws. Simplified cylindrical filler

TABLE 1 Parameters of the FE models.

Nodes/elements of	Subtype A	Subtype B	Subtype C	Subtype D
Tibial shaft	45404/237308	45404/237308	45404/237308	57135/300659
Screw	16577/64040	16577/64040	16577/88514	16577/64040
Fragment	10293/41939	7733/30730	7724/30696	8923/39485
Plate	6311/23071	6311/23071	6311/23071	6311/23071
Filler	318/1055	2746/11770	438/1789	205/659

TABLE 2 Material properities.

	Young modulus [MPa]	Poisson's ration	References
Cortical bone	$E_3 = 12847$	$\upsilon_{12} = 0.381$	Belaid et al. (2018)
	$E_2 = 7098$	$\upsilon_{13} = 0.172$	
	$E_1 = 6498$	υ_{23}-0.167	
	$G_{12} = 2290$	$\upsilon_{21} = 0.396$	
	$G_{13} = 2826$	$\upsilon_{31} = 0.376$	
	$G_{23} = 3176$	$\upsilon_{32} = 3.346$	
Trabecular bone	$E_3 = 370.6$	$\upsilon_{12} = 0.381$	
	$E_2 = 123.4$	$\upsilon_{13} = 0.104$	
	$E_1 = 123.4$	$\upsilon_{23} = 0.104$	
	$G_{12} = 44.84$	$\upsilon_{21} = 0.381$	
	$G_{13} = 58.18$	$\upsilon_{31} = 0.312$	
	$G_{23} = 58.18$	$\upsilon_{32} = 0.312$	
Titanium alloy plate and screw	$E = 110000$	$\upsilon = 0.3$	
PEEK	$E = 2800$	$\upsilon = 0.3$	Kang et al. (2021)
FCB	$E = 1500$	$\upsilon = 0.3$	Nagasao et al. (2002)
AFHP	$E = 2500$	$\upsilon = 0.3$	van Gestel et al. (2019)
3DPT-1	$E = 600$	$\upsilon = 0.3$	[a]
3DPT-2	$E = 6000$	$\upsilon = 0.3$	[b]
3DPT-3	$E = 60000$	$\upsilon = 0.3$	

[a] 3D Printed block of a certain porosity.

[b] Theoretical test value.

was selected for the subchondral defect, and the material types included: polyether-ether-ketone (PEEK), fibula cancellous bone (FCB), allogenic femoral head particles (AFHP), 3D printed porous titanium (3DPT) and blank group (BG) of nothing filler. 3DPT were given three different elastic moduli. The four fracture subtypes after fixation were shown in Figure 2. Four fracture subtypes combined with seven filling methods resulted in 26 simulation scenarios, because there was no substantial comparison between the blank group of subtype B and D and the corresponding experimental group.

Material properties of each structure

We used Hypermesh software (version 2019; Altair; United States) to mesh geometric models and to allocate material properties. The different parts of the proximal tibial fracture model were meshed using quadratic tetrahedral elements as recommended in the literature (Polgar et al., 2001). To attain a fine meshing with a great convergence, a set of simulations was computed by increasing the degree of relevance until displacement values did not change by more than 1% (Belaid et al., 2018). The resulting mesh was quadratic tetrahedral elements with a mean size of 2 mm. The number of mesh was showed in Table 1.

We assigned cortical and cancellous bone separately to the corresponding elastic, homogeneous and orthotropic properties (Amini et al., 2015). The material properties of the other structures are assumed isotropic linear elasticity. Table 2 shows the material properties of all constructs as well as relevant literature sources.

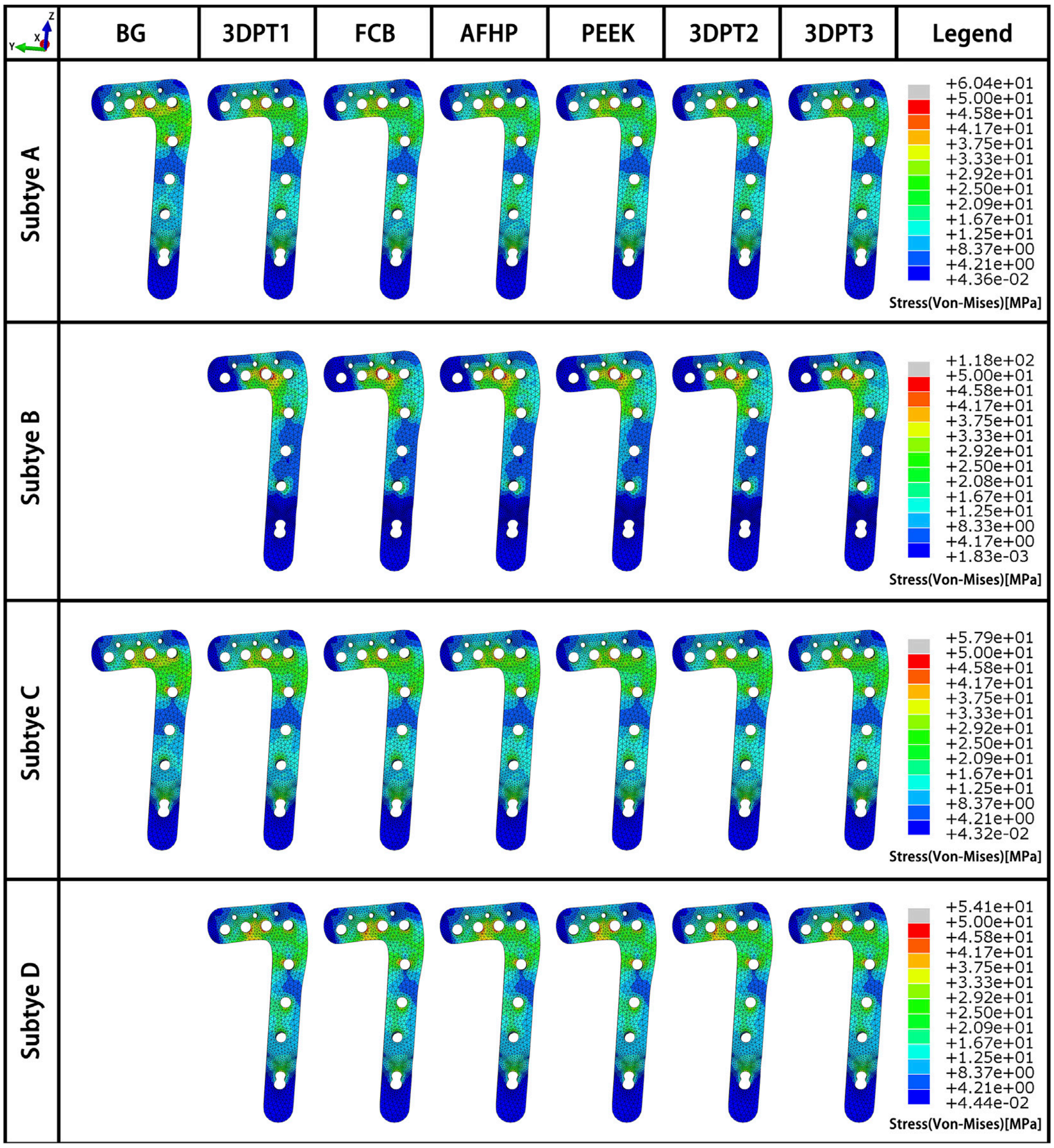

FIGURE 3
Stress fields (von Mises) in plate in a medial-lateral perspective for the 26 simulated scenarios. The maximum stress values in the plate for each subtype were presented in Figure 5B.

Boundary conditions and loading

Abaqus/CAE (version 2019, United States) was used to define the boundary conditions and to perform simulations. In each scenario, the maximum load during gait was simulated. It was defined as 3 times the patient's body weight (Taylor et al., 2004). The total load of 2250 N was divided between the medial (1417.5 N) and lateral condyles (832.5 N) (Zhao et al., 2007). The resulting surfaces approximately corresponded to 403 and 374 mm^2 in the lateral and medial condyle, respectively (Poh et al., 2012). Nodes at the distal end of the model were fixed in all degrees of freedom. The loading conditions were the same for all the models.

The contact between screws and bone was assumed to be fully ensured and the interface was considered perfectly bounded. Considering the fluid microenvironment in which the fragment was located after surgery, we defined the contact between the fragment as frictionless and the friction coefficient between the bone and the substitute as 0.2 (Simon et al., 2003).

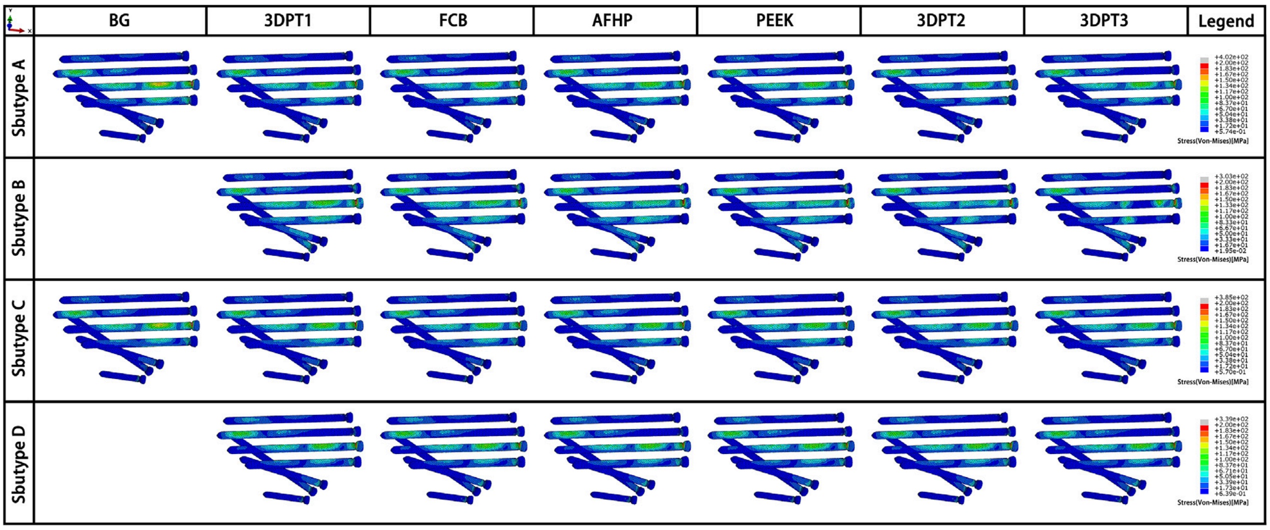

FIGURE 4
Stress fields (von Mises) in screw in an oblique downward view for the 26 simulated scenarios. The maximum stress values in the screw for each subtype were presented in Figure 5A.

Result analysis

Stress distribution (von Mises) of plate and screws was computed to predict the weak area of the implant. Strain distribution and reduction loss of the depressed fragment were output to assess the stability of implant and the risk of secondary subsidence. Strain value greater than 2% is considered to bone failure according to Perren's strain theory (Perren, 2002). Reduction loss was expressed as the maximum axial displacement of the depressed fragment (Aubert et al., 2021).

Results

Stress distribution fields of plate and screw were, respectively, presented in Figures 3, 4 for the twenty-six scenarios. In all scenarios, the change of plate, screws and bone was within the elastic deformation range of corresponding material. Additionally, the maximum stress was concentrated on the screw. In Subtype A, the peak stress of the blank group was 402.0 MPa, and the average peak stress distribution of the experimental group was 315.2 ± 5.5 MPa; in subtype B, the medial stress value of the test group was 278.8 ± 19.3 MPa; in subtype C, similar to the subtype A, the blank group showed the maximum stress, about 385.0 MPa, and the average peak stress of the experimental group was between 322.7 ± 12.1 MPa; in subtype D, the stress concentration in the filled group was 337.7 ± 0.7 MPa, though the stiffness value of the filler was 100 times the span. As for the plate, the maximum stress in subtype A was 60.4 MPa, and the average value of other group in this subtype was 50.9 ± 0.6 MPa. In subtype B, the mean of stress value is 107.3 ± 5.6 MPa. In subtype C, the maximum was 57.9 MPa and the average was 51.0 ± 1.1 MPa. In subtype D, the average was 54.1 ± 0.1 MPa. The trend of stress in screw and plate were showed in Figures 5A,B. The slope between BG and 3DPT1 groups was significantly higher than that of the experimental groups, especially in the A and C fracture subtypes.

The displacement fields of the depressed fragment were presented in Figure 6. Consistent with the peak stress, the blank groups in subtype A and C performed the maximum, and they were 0.195 and 0.264 mm respectively. The averages in the experimental groups of subtype A and C were 0.174 ± 0.001 mm and 0.253 ± 0.002 mm correspondingly. The mean values in the Subtype B and Subtype D were 0.253 ± 0.002 mm and 0.151 ± 0.002 mm. The trend of the reduction loss of the depressed fragment was showed in Figure 5C. It was the same as the change trend of peak stress.

The variation of the load of the supports' surface was showed in Figure 5D. The values were 134.2, 148.5, 153.6, 154.4, 159.2, 164.6 N respectively in subtype A. They were 629.5, 642.2, 646.8, 647.4, 652.7, 661.0 N correspondingly in subtype B. In subtype C, the values from bottom to top were 43.2, 59.1, 69.3, 71.3, 82.1, 94.0 N. In subtype D, the values were 13.0, 13.9, 14.1, 14.1, 14.3, 14.5 N respectively. Invariably, the surface load increased with increasing stiffness values.

The strain fields of the depressed fragment were presented in Figure 7. We recorded all internal fixed scenarios with strain greater than 2%. All the scenarios in Subtype C were included, the values were 2.3% all. Besides, the blank group in Subtype A achieve a strain of 2.2% which exceed the limit strain of the bone-

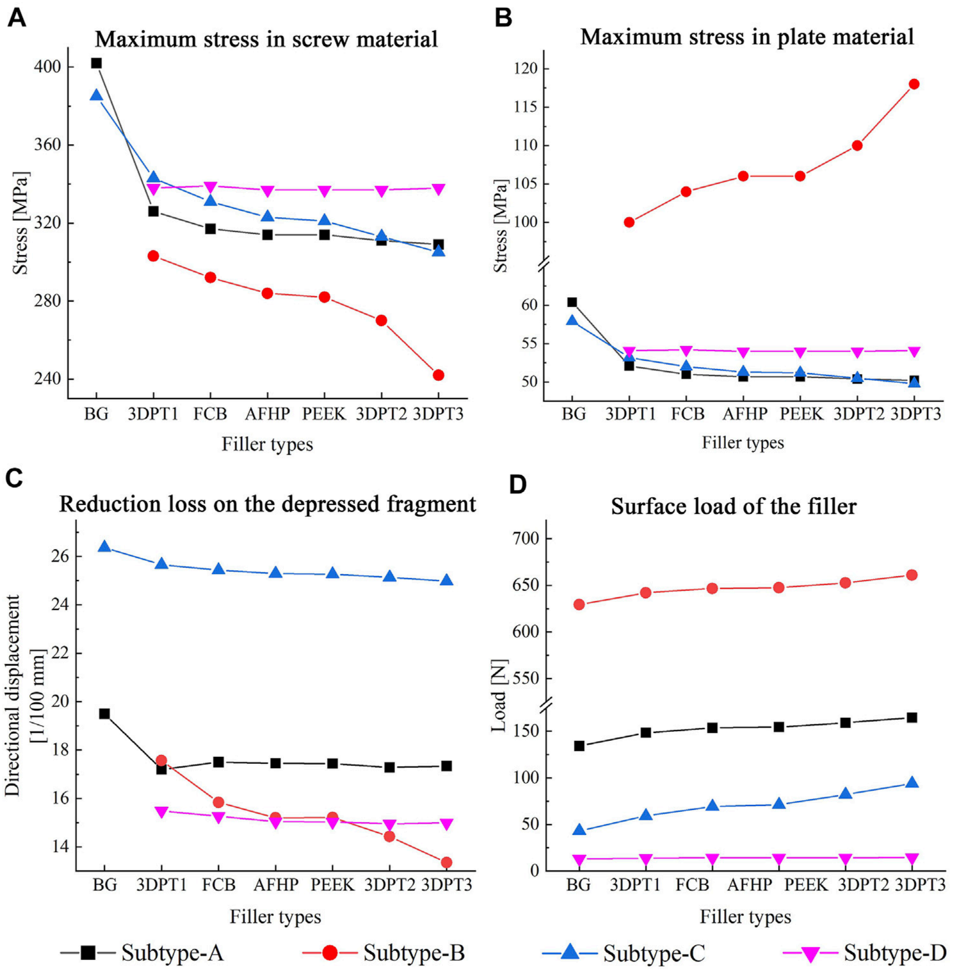

FIGURE 5
Maximum value and variation trend of screw material stress and plate material stress **(A,B)**, reduction loss on the depressed fragment expressed as directional displacement **(C)**, and the surface load of the filler **(D)**.

2%. The above data indicated that Subtype C fracture was a fracture type with a high risk of failure.

Discussion

Morphological diversity of fracture

Fracture is defined as the interruption of the continuity and integrity of a bone under a certain external force. The occurrence of TPF is mainly due to axial compression and valgus violence of the knee joint. In the past, the classification of tibial plateau fracture is mainly based on the injury mechanism and the position of fracture line, which enables the majority of scholars to have an intuitive understanding of tibial plateau fracture and provides efficient communication methods. To some extent, this macro classification provides a reference for treatment and has clinical guiding significance. However, studies on biomechanical problems only using traditional classification often have limitations. Belaid et al. indicated that the screw did not contact with the bone cement but passed through the collapsed block in the Schatzker II fracture. Kevin et al. indicated that the screw did not contact with the collapsed bone but passed through the bone cement. This fully demonstrates the actual existence of morphological variability in Schatzker II fractures. Therefore, the conclusion of the above two researchers only reflect the stability of specific Schatzker II fracture morphology, and its guiding significance for the macroscopic treatment of Schatzker II fracture is limited. We are trying the new morphology-based classification method to get better results to serve the clinical practice.

As shown in Figures 5A–C, in experimental group of subtype A, the slope of the curve of elastic modulus and implant stress and reduction loss was the minimum, followed by the curve of subtype C and subtype B. This reflected that the stiffness of filler presented the

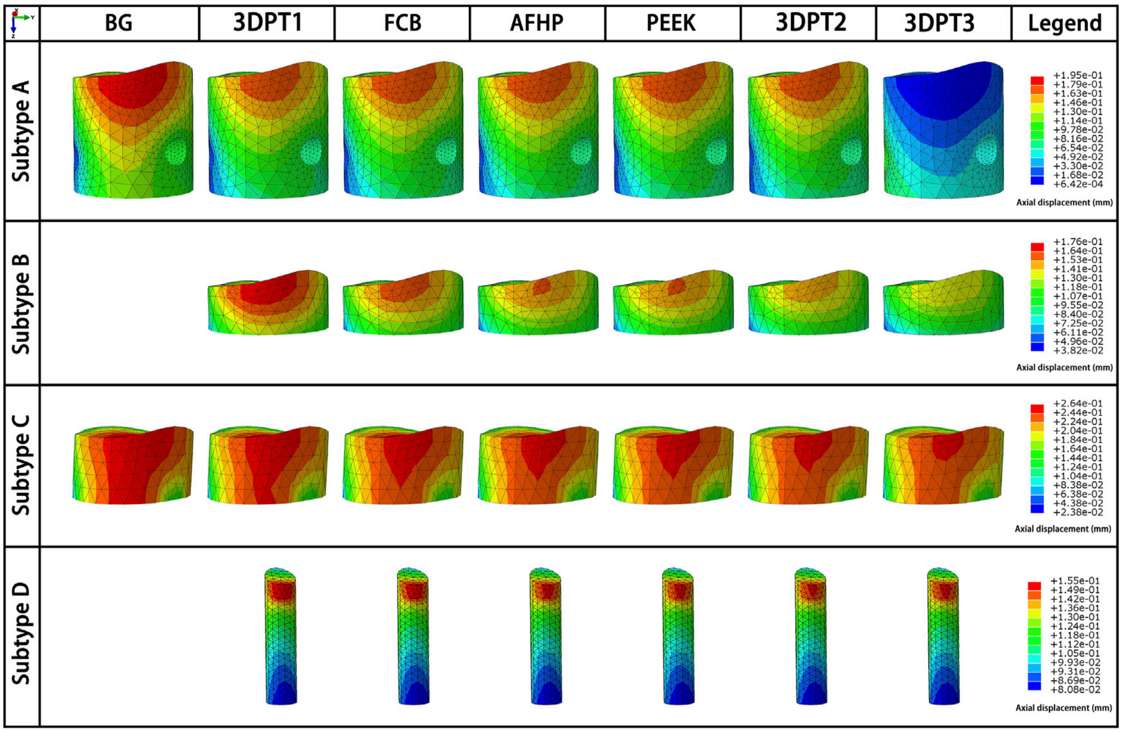

FIGURE 6
Directional displacement fields of the depressed fragment from the perspective of maximum displacement of the corresponding scenario.

slightest influence on the stability of subtype A fracture, while the stiffness of filler showed the greatest influence on the stability of subtype B fracture. This variation suggested that the morphologic diversity of fractures did affect the stability of the internal fixation system. When the screw penetrated through the depressed block, all the stress of the structure is transferred to the implant through the depressed fragment, resulting in a large number of stress shielding to the filling structure below, so the stiffness of the filling has the minimal influence on the stress of the implant. On the contrary, in subtype B, the intersection of the screw and the implant enabled the applied load to be successfully transferred to the implant and adjacent filler, making the implant-filler the main carrier of stress bearing, leading to the maximum influence of the stiffness of the implant on the stress of the implant. Similarly, the middle position of screws in subtype C determined the middle slope of the curve. In addition, as shown in Figures 5A,C, there is a noticeable difference between the blank group and the 3DPT1 group in subtype A and subtype C, which was larger than the difference between 3DPT1 and 3DPT3, indicating that the presence or absence of filler had a higher impact on stress concentration than the increase of filler modulus.

Angular-stability plate and structural filler

The principle of treatment of TPF is anatomical reduction and rigid fixation. Absolute stabilization is the primary principle of articular surface treatment, with which direct healing of metaphyseal cancellous bone can be achieved (McBride-Gagyi and Lynch, 2020). For the fracture site, compression force promotes the remodeling and combination of the fragments, and shear force aggravates the separation of the blocks, which leads to delayed union or nonunion of the fracture. As one of the most important joints in the human body, the treatment of knee fractures must require maximal restoration of structure and function.

The classical principle of treatment of tibial plateau fractures was to use a synthesis plate and several screws with autograft of the defect site (Júnior et al., 2009). In recent years, with the extensive spread of minimally invasive concept, two lag screw fixation combined with bone cement filling has been advocated by many scholars (Vendeuvre et al., 2013; Kfuri and Schatzker, 2018). Corresponding finite element simulations and cadaveric mechanical studies seemed to confirm the stability of the above methods, but the unicity of the experimental model does not indicate that the above treatment modalities can provide greater clinical benefits. In contrast, angle-stable plates have gradually replaced non-angle-stable plates due to their strong shear resistance, especially in the treatment of fractures involving the articular surface. A large number of controlled clinical studies have confirmed the good benefits of angle-stable plates in the treatment of TPF (Nikolaou et al., 2011; Prall et al., 2021).

Filling of the defect site is an eternal topic in orthopedics, and how to achieve a balance between biological activity and mechanical

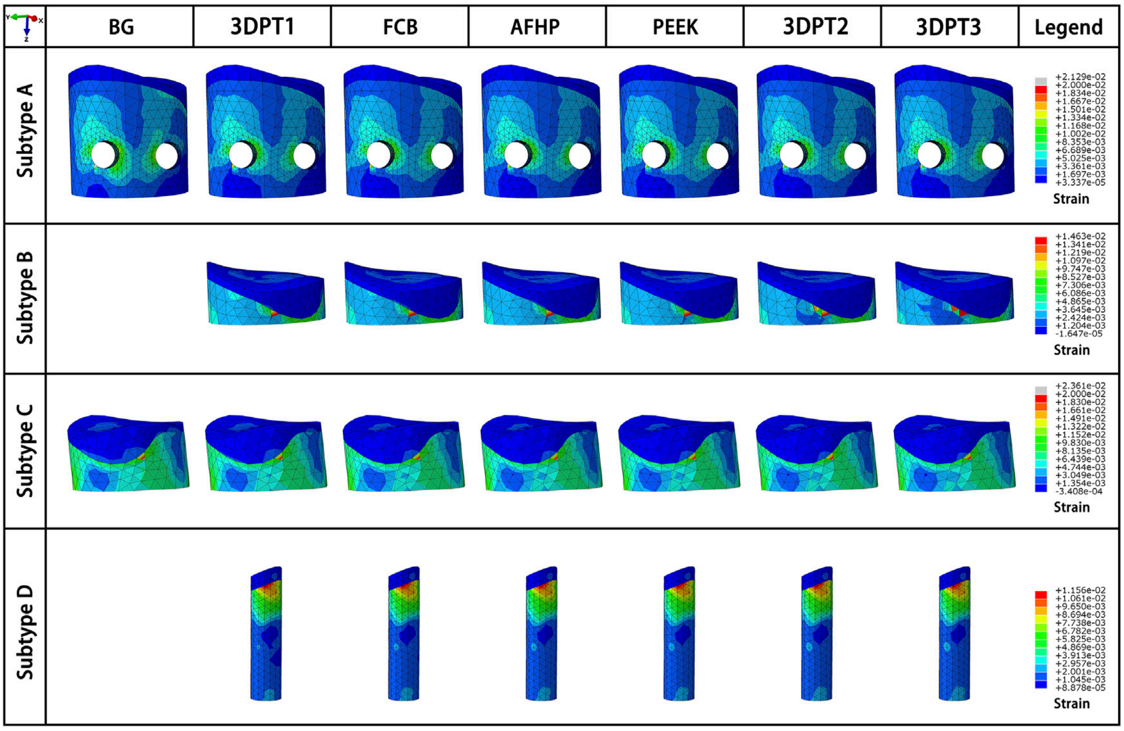

FIGURE 7
Strain fields of the depressed fragment from the perspective of maximum strain of the corresponding scenario.

stability has always been a problem to be solved all the time. In the early stage, we have proposed the internal support theory to reconstruct and repair the empty shell structure in view of the compression collapse in metaphysis (Li et al., 2020). The theory indicated that the compression collapse of metaphysis is due to the collapse effect of complex violence on cancellous. Traditional therapy failed to reconstruct the collapsed structure, resulting in the voids that transform the solid structure into a shell structure. The traditional plate-screw fixation system relies on the raft support of external screws to achieve fixation. The shell structure is supported by surface, which has poor mechanical strength and cannot be effectively fixed. In addition, hollow physical space is formed inside the empty shell, which cannot form bone. As a result, the fixation strength cannot be improved with the extension of postoperative time, which further increases the occurrence of postoperative failure. The present study is introduced to compare the different types of internal support in the void of Schatzker II TPF and got a meaningful result. PEEK, FCB, AFHP and 3DPT are all proven types of materials with good biological activity, differing in stiffness values. Whether a large change in stiffness values can have a significant effect on the stability of internal fixation has not been concluded in previous finite element studies. The results of our data showed that the filling or not of the defect site was the main factor affecting the structural stability, and the change in stiffness value of 100 times did not significantly affect the structural stability (Figures 5A–C). However, it is undeniable that an increase in stiffness value increases the ability of the filler to share the load (Figure 5D).

Different filler type

There are three main treatment methods for subchondral bone defects: autologous bone, allogeneic bone and bone substitutes. Autologous bone is of great osteogenesis, but the disadvantage is greater surgical trauma and long-term postoperative pain for the patient. Allografts have been used as a natural substitute to fill the bone defect, but disadvantages like transmission of diseases, rejection reactions, nonunion, graft resorption, and limitations of donor have been reported. Bone substitutes have been studied for decades in the field of bone tissue engineering, and the current consensus is that porous structures can provide scaffolds for osteoblasts to grow into bone. With the rapid development of 3D printing technology, it is no longer difficult to fabricate structures with specific porosity from specific material powders. 3D printing technology has been successfully applied in the treatment of large bone defects, and we expect that this technology will also play a full role in the treatment of smaller bone defects in the epiphysis. Therefore, FCB, AFHP, PEEK, and 3DPT were used as representatives of bone substitutes to carry out this study. In addition, according to the 3D fracture map of the tibial plateau created by Zhang et al. (Yao et al., 2020), fracture lines in the collapse area of the tibial plateau are similar to the original shape, so we simplified the collapsed bone and filling into a cylinder.

Impact on surgery and rehabilitation

Our conclusion suggested that the position of the screw in relation to the bone fragment is an important factor affecting stability. The intersection of screws and fragments is ideal for surgery and is usually achieved in patients with good bone quality tibial plateau fractures. The coexistence of thin subchondral bone with a large subchondral defect, namely subtype C mentioned in this article, epitomizes the majority of patients and is a challenge for surgical treatment. The granular form of the implant is characterized by an inability to obtain a strong connection between the screw and the implant, which amounts to a failure to fill the defective area-the screw is suspended, as in the blank group in subtype C, and the risk of systemic failure is greatly increased. Our structural filler solves this problem to a certain extent, and reduces the peak stress concentration in the plate and screw. Therefore, in the surgical treatment of Schatzker II fractures, it is crucial to flexibly vary the screw placement to achieve a firm interlocking fixation while avoiding the levitating effect of the screws. This principle also applies to the surgical treatment of fractures in other parts of the body.

In addition, this study, which set up a scenario of normal postoperative walking, showed that satisfactory displacement and strain were achieved with all subtypes of the internal support system, except for subtype C. This suggested that it was mechanically safe for the patient to perform normal functional walking exercises immediately after surgery when an effective internal support system was achieved. Therefore, if possible, we recommend that functional exercise of the limb be performed as soon as possible after surgery.

Limitations and validity

This study has some limitations. The soft tissues, menisci and ligament were neglected. The bone was considered homogeneous. We assumed a lower coefficient of friction (μ = 0.2), to take into account the *in vivo* environment (blood, marrow). This was motivated by the measured values of the coefficient of friction between bone and smooth implant were in the range of 0.28–0.44 (Rancourt et al., 1990; Shirazi-Adl et al., 1993). All these factors could nonetheless constitute a significant contribution influencing the biomechanical model. In addition, the models had been tested for static load while the displacement may be caused by repetitive loading during mobilization and can be simulated in a cyclic loading protocol.

Simulation analysis based on human bone cannot directly verify the validity of the results, but our results are similar to those of D Belaid and Kevin et al. regarding Schatzker type II fracture, the stability of defect filling is much higher than that of blank group, and filling can reduce the stress concentration on the plate and screw. In addition, further validation through similar cadaveric biomechanical studies and animal experiments is required.

Conclusion

The existence of filler at the defect site can effectively reduce the stress concentration of the implant and the reduction loss of the collapsed block, thus providing good stability for Schatzker II fracture. In subtype A fracture, the modulus of filler presented the slightest influence on the stability, followed by subtype C, while the stability of subtype B was most influenced by the modulus of filler. Therefore, it is necessary to evaluate the preoperative patient imaging data adequately to select the appropriate stiffness of the filler.

Data availability statement

The raw data supporting the conclusion of this article will be made available by the authors, without undue reservation.

Ethics statement

Written informed consent was obtained from the individual(s) for the publication of any potentially identifiable images or data included in this article.

Author contributions

Conceptualization: WZ, JL, and XR; methodology: XR, CZ, and CX; software: JL, CX, CZ, and MH; validation: CZ, CX, XR, and MH; resources: WZ, JL, CZ, XR, CX, and MH; writing—original draft preparation: CZ, CX, and XR; writing—review and editing: WZ, JL, CZ, XR, and CX; supervision: WZ and JL; project administration: XR, CZ, and CX. All authors have read and agreed to the published version of the manuscript.

Funding

This work was supported by The 13th Five-year Plan for Key Discipline Construction Project of PLA (A350109).

Conflict of interest

The authors declare that the research was conducted in the absence of any commercial or financial relationships that could be construed as a potential conflict of interest.

Publisher's note

References

Amini, M., Nazemi, S. M., Lanovaz, J. L., Kontulainen, S., Masri, B. A., Wilson, D. R., et al. (2015). Individual and combined effects of OA-related subchondral bone alterations on proximal tibial surface stiffness: A parametric finite element modeling study. *Med. Eng. Phys.* 37 (8), 783–791. doi:10.1016/j.medengphy.2015.05.011

Aubert, K., Germaneau, A., Rochette, M., Ye, W., Severyns, M., Billot, M., et al. (2021). Development of digital twins to optimize trauma surgery and postoperative management. A case study focusing on tibial plateau fracture. *Front. Bioeng. Biotechnol.* 9, 722275. doi:10.3389/fbioe.2021.722275

Belaid, D., Vendeuvre, T., Bouchoucha, A., Bremand, F., Breque, C., Rigoard, P., et al. (2018). Utility of cement injection to stabilize split-depression tibial plateau fracture by minimally invasive methods: A finite element analysis. *Clin. Biomech. (Bristol, Avon.* 56, 27–35. doi:10.1016/j.clinbiomech.2018.05.002

Elsoe, R., Larsen, P., Nielsen, N. P. H., Swenne, J., Rasmussen, S., and Ostgaard, S. E. (2015). Population-based epidemiology of tibial plateau fractures. *Orthopedics* 38 (9), e780–e786. doi:10.3928/01477447-20150902-55

Goff, T., Kanakaris, N. K., and Giannoudis, P. V. (2013). Use of bone graft substitutes in the management of tibial plateau fractures. *Injury* 44 (1), S86–S94. doi:10.1016/S0020-1383(13)70019-6

Júnior, M. K., Fogagnolo, F., Bitar, R. C., Freitas, R. L., Salim, R., and Jansen Paccola, C. A. (2009). Tibial plateau fractures. *Rev. Bras. Ortop. (English Ed.* 44 (6), 468–474. doi:10.1016/s2255-4971(15)30142-7

Kang, J., Zhang, J., Zheng, J., Wang, L., Li, D., and Liu, S. (2021). 3D-printed PEEK implant for mandibular defects repair - a new method. *J. Mech. Behav. Biomed. Mater.* 116, 104335. doi:10.1016/j.jmbbm.2021.104335

Kfuri, M., and Schatzker, J. (2018). Revisiting the Schatzker classification of tibial plateau fractures. *Injury* 49 (12), 2252–2263. doi:10.1016/j.injury.2018.11.010

Lee, J. A., Papadakis, S. A., Moon, C., and Zalavras, C. G. (2007). Tibial plateau fractures treated with the less invasive stabilisation system. *Int. Orthop.* 31 (3), 415–418. doi:10.1007/s00264-006-0176-x

Li, J., Li, Z., Wang, M., Zhang, H., Liang, Y., and Zhang, W. (2020). Fixation augmentation using titanium cage packing with xenograft in the treatment of tibial plateau fractures. *Injury* 51 (2), 490–496. doi:10.1016/j.injury.2019.10.025

Manidakis, N., Dosani, A., Dimitriou, R., Stengel, D., Matthews, S., and Giannoudis, P. (2010). tibial plateau fractures: Functional outcome and incidence of osteoarthritis in 125 cases. *Int. Orthop.* 34 (4), 565–570. doi:10.1007/s00264-009-0790-5

Mattiassich, G., Foltin, E., Scheurecker, G., Schneiderbauer, A., Kröpfl, A., and Fischmeister, M. (2014). Radiographic and clinical results after surgically treated tibial plateau fractures at three and twenty two years postsurgery. *Int. Orthop.* 38 (3), 587–594. doi:10.1007/s00264-013-2174-0

McBride-Gagyi, S. H., and Lynch, M. E. (2020). "Biomechanical principles of fracture healing," in *Essential Biomechanics for orthopedic trauma A case-based guide: A case-based guide*. Editors B. D. Crist, J. Borrelli, and E. J. Harvey, Jr (Cham: Springer International Publishing), 3–15.

Nagasao, T., Kobayashi, M., Tsuchiya, Y., Kaneko, T., and Nakajima, T. (2002). Finite element analysis of the stresses around endosseous implants in various reconstructed mandibular models. *J. Cranio-Maxillofacial Surg.* 30 (3), 170–177. doi:10.1054/jcms.2002.0310

Nikolaou, V. S., Tan, H. B., Haidukewych, G., Kanakaris, N., and Giannoudis, P. V. (2011). Proximal tibial fractures: Early experience using polyaxial locking-plate technology. *Int. Orthop.* 35 (8), 1215–1221. doi:10.1007/s00264-010-1153-y

Perren, S. M. (2002). Evolution of the internal fixation of long bone fractures. The scientific basis of biological internal fixation: Choosing a new balance between stability and biology. *J. Bone Jt. Surg.* 84 (8), 1093–1110. doi:10.1302/0301-620x.84b8.0841093

Poh, S.-Y., Yew, K.-S. A., Wong, P.-L. K., Koh, S.-B. J., Chia, S.-L., Fook-Chong, S., et al. (2012). Role of the anterior intermeniscal ligament in tibiofemoral contact mechanics during axial joint loading. *Knee* 19 (2), 135–139. doi:10.1016/j.knee.2010.12.008

Polgar, K., Viceconti, M., and O'Connor, J. J. (2001). A comparison between automatically generated linear and parabolic tetrahedra when used to mesh a human femur. *Proc. Inst. Mech. Eng. H.* 215 (1), 85–94. doi:10.1243/0954411011533562

Prall, W. C., Kusmenkov, T., Rieger, M., Haasters, F., Mayr, H. O., Böcker, W., et al. (2021). Radiological outcome measures indicate advantages of precontoured locking compression plates in elderly patients with split-depression fractures to the lateral tibial plateau (AO41B3). *Geriatr. Orthop. Surg. Rehabil.* 12, 1–9. doi:10.1177/21514593211043967

Prall, W. C., Rieger, M., Fürmetz, J., Haasters, F., Mayr, H. O., Böcker, W., et al. (2020). Schatzker II tibial plateau fractures: Anatomically precontoured locking compression plates seem to improve radiological and clinical outcomes. *Injury* 51 (10), 2295–2301. doi:10.1016/j.injury.2020.07.012

Rademakers, M. V., Kerkhoffs, G. M. M. J., Sierevelt, I. N., Raaymakers, E. L. F. B., and Marti, R. K. (2007). Operative treatment of 109 tibial plateau fractures: Five- to 27-year follow-up results. *J. Orthop. Trauma* 21 (1), 5–10. doi:10.1097/bot.0b013e31802c5b51

Rancourt, D., Shirazi-Adl, A., Drouin, G., and Paiement, G. (1990). Friction properties of the interface between porous-surfaced metals and tibial cancellous bone. *J. Biomed. Mat. Res.* 24 (11), 1503–1519. doi:10.1002/jbm.820241107

Russell, T. A., and Leighton, R. K. (2008). Comparison of autogenous bone graft and endothermic calcium phosphate cement for defect augmentation in tibial plateau fractures. A multicenter, prospective, randomized study. *J. Bone Jt. Surgery-American Volume* 90 (10), 2057–2061. doi:10.2106/JBJS.G.01191

Shirazi-Adl, A., Dammak, M., and Paiement, G. (1993). Experimental determination of friction characteristics at the trabecular bone/porous-coated metal interface in cementless implants. *J. Biomed. Mat. Res.* 27 (2), 167–175. doi:10.1002/jbm.820270205

Simon, U., Augat, P., Ignatius, A., and Claes, L. (2003). Influence of the stiffness of bone defect implants on the mechanical conditions at the interface--a finite element analysis with contact. *J. Biomechanics* 36 (8), 1079–1086. doi:10.1016/s0021-9290(03)00114-3

Taylor, W. R., Heller, M. O., Bergmann, G., and Duda, G. N. (2004). Tibio-femoral loading during human gait and stair climbing. *J. Orthop. Res.* 22 (3), 625–632. doi:10.1016/j.orthres.2003.09.003

Trenholm, A., Landry, S., McLaughlin, K., Deluzio, K. J., Leighton, J., Trask, K., et al. (2005). Comparative fixation of tibial plateau fractures using alpha-BSM, a calcium phosphate cement, versus cancellous bone graft. *J. Orthop. Trauma* 19 (10), 698–702. doi:10.1097/01.bot.0000183455.01491.bb

van Gestel, N. A. P., Gabriels, F., Geurts, J. A. P., Hulsen, D. J. W., Wyers, C. E., van de Bergh, J. P., et al. (2019). The implantation of bioactive glass granules can contribute the load-bearing capacity of bones weakened by large cortical defects. *Mater. (Basel, Switz.* 12 (21), 3481. doi:10.3390/ma12213481

Vendeuvre, T., Babusiaux, D., Brèque, C., Khiami, F., Steiger, V., Merienne, J. F., et al. (2013). Tuberoplasty: Minimally invasive osteosynthesis technique for tibial plateau fractures. *Orthop. Traumatology Surg. Res.* 99 (4), S267–S272. doi:10.1016/j.otsr.2013.03.009

Yao, X., Zhou, K., Lv, B., Wang, L., Xie, J., Fu, X., et al. (2020). 3D mapping and classification of tibial plateau fractures. *Bone & Jt. Res.* 9 (6), 258–267. doi:10.1302/2046-3758.96.BJR-2019-0382.R2

Zhao, D., Banks, S. A., Mitchell, K. H., D'Lima, D. D., Colwell, C. W., and Fregly, B. J. (2007). Correlation between the knee adduction torque and medial contact force for a variety of gait patterns. *J. Orthop. Res.* 25 (6), 789–797. doi:10.1002/jor.20379

frontiers | Frontiers in Bioengineering and Biotechnology

TYPE Original Research
PUBLISHED 09 September 2022
DOI 10.3389/fbioe.2022.950839

Patient-specific numerical investigation of the correction of cervical kyphotic deformity based on a retrospective clinical case

Tianchi Wu[1,2†], Hongyu Chen[3,4,5†], Yu Sun[3,4,5], Tian Xia[3,4,5], Feifei Zhou[3,4,5*] and William W. Lu[1,2]

[1]Department of Orthopaedics and Traumatology, The University of Hong Kong, Hong Kong, Hong Kong SAR, China, [2]Shenzhen Institutes of Advanced Technology, Chinese Academy of Science, Shenzhen, China, [3]Department of Orthopaedics, Peking University Third Hospital, Beijing, China, [4]Engineering Research Center of Bone and Joint Precision Medicine, Beijing, China, [5]Beijing Key Laboratory of Spinal Disease Research, Beijing, China

OPEN ACCESS

EDITED BY
Damien Lacroix,
The University of Sheffield,
United Kingdom

REVIEWED BY
Jeremie Oliver,
National Institutes of Health (NIH),
United States
Harvinder Singh Chhabra,
Indian Spinal Injuries Centre, India

*CORRESPONDENCE
Feifei Zhou,
zhoufeifei@bjmu.edu.cn

†These authors have contributed equally to this work and share first authorship

SPECIALTY SECTION
This article was submitted to Biomechanics,
a section of the journal
Frontiers in Bioengineering and Biotechnology

RECEIVED 23 May 2022
ACCEPTED 12 August 2022
PUBLISHED 09 September 2022

CITATION
Wu T, Chen H, Sun Y, Xia T, Zhou F and Lu WW (2022), Patient-specific numerical investigation of the correction of cervical kyphotic deformity based on a retrospective clinical case.
Front. Bioeng. Biotechnol. 10:950839.
doi: 10.3389/fbioe.2022.950839

Little research has been reported on evaluating the safety of the fixation construct in cervical kyphosis correction. In this study, we proposed a principal-strain criterion to evaluate the safety of the fixation construct and validated the modeling method against a retrospective case of anterior cervical discectomy fusion (ACDF). From C2 to T2 vertebra bodies, fixation instruments were reconstructed and positioned as per postoperative computed tomography (CT) scans. Head weight (HW) and various moments estimated from isometric strength data were imposed onto the C2. The postoperative stability of non-surgical segments, deformations surrounding the screw trajectories, and contact slipping on zygapophysial joints were analyzed. The model was validated against the reality that the patient had a good fusion and deformity correction. The ACDF restricted the range of motions (ROMs) of cervical segments and lent stability to vertebra fusion, no failure was found in the finite element (FE) model of cervical vertebrae. The deformation surrounding the screw trajectories were concentrated to the lateral sides of trajectories, recommending that the shape of the anterior cervical plate conforming to the curvature of the vertebra and screws fully inserted into vertebrae reduced the deformation concentration around the screw trajectories.

KEYWORDS
patient-specific, numerical investigation, kyphosis correction, principal strain, range of motion

1 Introduction

Cervical kyphotic deformity alters the normal functioning of the cervical spine, reducing the quality of life (Tang et al., 2012). Anterior-only approaches, posterior-only approaches, or 360° and 540° reconstructions are normal surgical options to correct the deformity (Nottmeier et al., 2009), among which, the anterior approach is of importance in correcting the kyphosis (Ebot et al., 2020). However, Park et al. (2019) conducted a retrospective cohort study on discectomy and found that multi-level fusion was significantly associated with the increased risk of screw failure ($p < 0.01$). Screw loosening and plate migration in the anterior cervical discectomy fusion (ACDF) is not rare (Ning et al., 2008; Guo et al., 2021), even though hardware failure attributed to ACDF was demonstrated only 0.1%–0.9% in the United States (Epstein, 2019). Many clinical case reports revealed that screw loosening and anterior cervical plate migration happened in ACDF (Azadarmaki and Soliman, 2014; Nathani et al., 2015; Wójtowicz et al., 2015; Fryer et al., 2019; Ansari et al., 2020). Screw loosening in ACDF is one of the most dangerous complications in cervical anterior plating fixation, which may lead to severe consequences such as esophageal perforation and bone nonunion (Ning et al., 2008; Hershman et al., 2017; Fryer et al., 2019). Therefore, prompt recognition and effective foreseeing of the potential pharyngoesophageal perforation would be pretty helpful in reducing the mortality and morbidity.

Previous clinical research and biomechanical research studies help make decisions but not to improve surgical approaches. Furthermore, few studies stated a detailed FE modeling strategy from a numerical computation and biomechanical perspective for reference and few proposed a practical criterion to evaluate the biomechanical outcomes of the ACDF. Researchers reported an in-silico analysis of the cervical-related surgery and concluded various treatment suggestions based on the reduced Von Mises stress of joint facets or endplates, restricted ROMs, etc. (Ng and Teo, 2001; Li et al., 2017; Ouyang et al., 2019, 2020; Zhou et al., 2022), while limited investigations demonstrated the effective in-silico method to predict the surgical outcomes of deformity correction. Moreover, in most existing in-silico studies, the modeling method and the computational consideration have not been stated clearly, which may leave confusion for replication.

In the present investigation, a finite element analysis (FEA) and the principal–strain based criterion were proposed to capture the biomechanical response and damage evaluation of ACDF, as well as computational, biomechanical, and anatomical explanations of the modeling strategy, providing a numerical solution for surgeons to improve the surgical approach and determine instrument configuration.

2 Finite element model

2.1 Modeling strategy and material properties

In the present investigation, the computed tomography (CT) data of a 13-year-old patient suffering from cervical kyphosis were obtained, as well as the configuration of the cervical instruments used in the ACDF surgery. Preoperative moment-balanced traction was performed to stretch and relax the anterior muscles for 4 days; photo and X-ray were taken before and after the moment-balanced traction (Figures 1A–C). Three cervical spacers of two heights, a four-level ventral plate, and eight variable-angle screws were implanted to the C2–C5 vertebra bodies to correct the kyphosis to a Cobb angle of 0°, details are listed in Table 1. The cervical ventral plate is manufactured by Depuy Synthes (Raynham, MA, United States) and the cervical ventral plate and fixation screws are from Medtronic (Memphis, TN, United States), as shown in Figure 2. Anterior longitudinal ligaments from C2 to C5 were resected due to the placement of the implant. A three-month follow-up demonstrated that the postoperative Cobb angle of C2–C5 was maintained at −3.3° (Figure 1D) compared with the preoperative C2–C5 Cobb angle of −53.2° (Figure 1B).

During the reconstruction of the cervical–thoracic spine (from C2 to T2), preoperative CT scans were put into a 3D slicer (http://www.slicer.org) to perform the geometrical reconstruction of each vertebra, in which the trabecular bone was identified via a seed-growing method. The cortical layer will be built when mapping the mesh. Then, the cervical instruments were put into the exact positions as per postoperative CT scans, followed by the positional adjustment of the reconstructed vertebrae. Boolean operations allow the model to consider the grinding manipulation on the endplates of vertebra bodies. Thus, the postoperative spine-implant system was acquired. Geometries were then transferred to Hypermesh 2020 (Altair Technologies, Inc., CA, United States) and Jung and Bhutta, 2022 (Abaqus, Inc., Providence, RI, United States) to do the mesh work and perform the finite element (FE) analysis.

Following the representation of the trabecular bone volume, a layer of triangular prism elements was offset from the outer surface, corresponding to the cortex of each vertebra, 0.28 mm thickness for the cervical vertebrae and 0.24 mm for the thoracic vertebrae (Ritzel et al., 1997) (Figure 3). Intervertebral discs (IVDs) were reshaped based on the superior and inferior surfaces of the adjacent vertebral bodies, in which the anatomic structure including the inner nucleus pulposus and outer anulus were reconstructed, shown in Figure 4. Nucleus pulposus (NP) covers a total of 25 %–50 % of the area of the superior and inferior surfaces and accounts for 40 %–50 % of the intervertebral disc volume (Farfan et al., 1970; Pooni et al., 1986; Oegema, 1993; Iatridis et al., 1996; Nachemson, 2014; Perey, 2014). Typical architectures of IVDs were reconstructed for

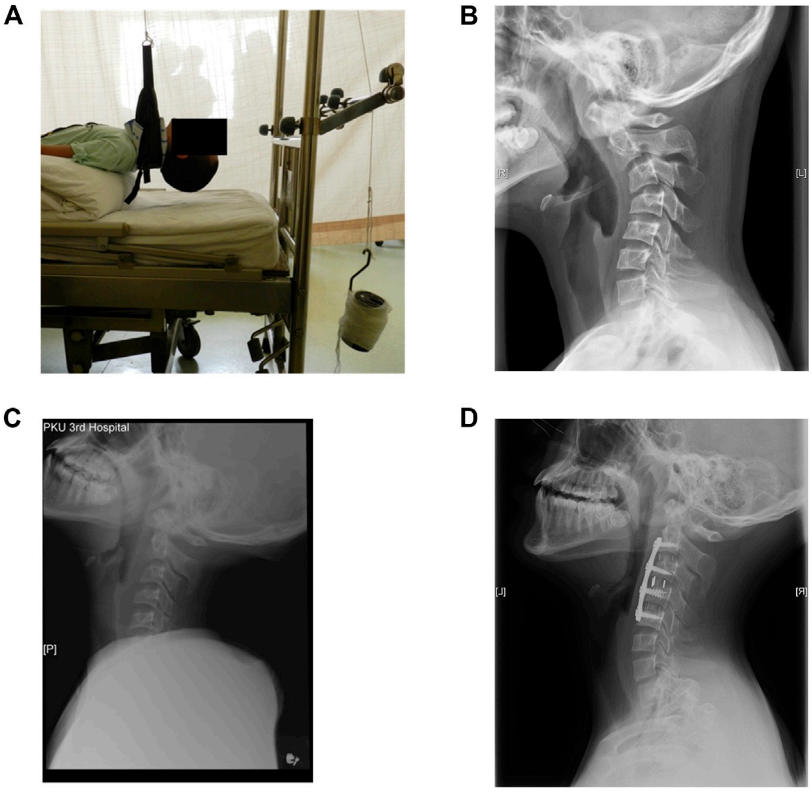
[redacted]

FIGURE 1
(A) Photo of the preoperative moment-balanced traction, **(B)** lateral view of preoperative cervical X-ray, C2–C5 Cobb angle was −53.2°, **(C)** X-ray after the moment-balanced traction, **(D)** lateral view of cervical spine at three-month follow-up, Cobb angle of C2–C5 was −3.3°.

TABLE 1 Implant configuration in the ACDF surgery. Intervertebral disc (IVD).

	Dimension (mm)	Material	Applied location	Product catalog
Lordosis cervical spacer	8 mm (Height, standard, lordosis)	PEEK	C2-C3 IVD, C3-C4 IVD	Depuy Synthesis Cervios
Lordosis cervical spacer	7 mm (Height, standard, lordosis)	PEEK	C4-C5 IVD	Depuy Synthesis Cervios
Fixed-angle screws	4.0 × 15.0 (D × L)	Titanium	C2, C3, C4 and C5	Atlantis Vision Elite
Anterior cervical plate	55 mm (total length)	Titanium	C2, C3, C4 and C5	Atlantis Vision Elite

simplification, although IVDs in the cervical spine lack a concentric anulus fibrosus around their entire perimeter (Mercer and Bogduk, 1999). Superior and inferior surfaces on NP and anulus fibrosus (AF) were tied onto the inferior surface of the superior vertebra and the superior surface of the inferior vertebra, respectively, forcing all translational and rotational degrees of freedom (DOFs) to be the same. Linear elastic mechanical properties of NP and AF were defined to level down the non-linearity of the FE model (Table 2) (Ng and Teo, 2001).

The linear elastic material model was defined to describe the biomechanical behavior of the trabecular bone and cortical bone, which was evaluated through a phantom-less bone mineral density (BMD) measurement (Liu et al., 2022); then, BMD was converted to Young's modulus as per Eq. 1 (Keyak et al., 1997), allowing a patient-specific and BMD-dependent analysis. The mechanical properties of the cortical bone were obtained from existing literature studies, since the cortex layer in CT cannot be computed to obtain the BMD given the thickness was about 0.3 mm. The curvature of the cervical spine and the force transition path shaped a non-uniform BMD distribution—BMD of the central vertebra body and exterior vertebra body are significantly different (Anderst et al., 2011; Feng et al., 2021). Therefore, BMD was

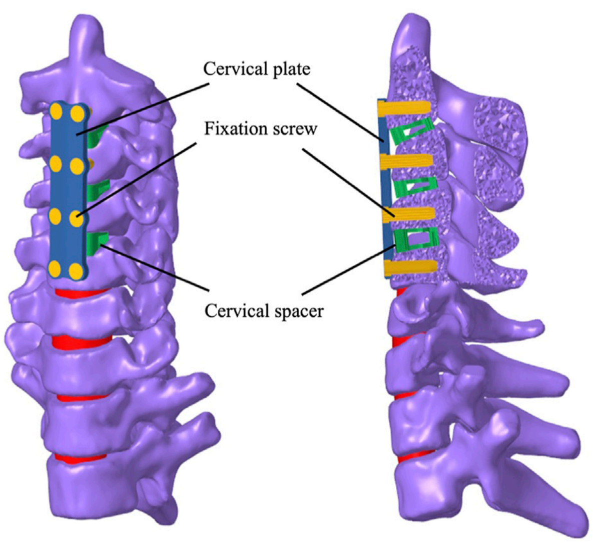

FIGURE 2
Schematics of the instrument configurations used in the ACDF surgery.

measured separately in the central vertebra body and exterior vertebra body.

$$\begin{cases} E = 0.001\,(BMD = 0.00) \\ E = 33900 \times \left(\dfrac{BMD}{1000}\right)^{2.2} (0.00 < BMD < 0.27mg/cc) \\ E = 5407 \times BMD + 469\,(0.27mg/cc \leq BMD \leq 0.60mg/cc) \\ E = 10200 \times \left(\dfrac{BMD}{1000}\right)^{2.01} (0.60mg/cc \leq BMD) \end{cases} \tag{1}$$

Modified quadratic tetrahedral elements (C3D10M) and quadratic triangular prism elements (C3D15) were used to map the vertebral bodies. Geometry-editing tools, including edge toggling and edge combining, were employed to clean the geometry and acquire an optimum mesh, though mild topographical deviation might be introduced. A hexahedron mesh mixed with prism mesh was created for screws, meshes of cervical plates, and spacers were mapped through delicate geometry partitions and symmetrical mesh generation. To minimize the numerical deviation brought by the mesh density, element aspect ratio, volume skewness, and tetrahedral collapse indices were inspected following the mesh mapping; Table 3 lists mesh quality indices for every vertebra. Convergence studies were conducted for every vertebra and IVD individually, and the final mesh size for vertebrae was set to 0.8–1.2 mm, and 0.8–1.5 mm for surgical instruments. Node equivalence between the bones and instruments were performed to avoid errors affected by the interpolation of node–node variables in node–node constraints theoretically.

Several truss elements were incorporated to represent major connective tissues. The posterior longitudinal ligament (PLL), anterior longitudinal ligament (ALL), interspinal ligament (ISL), supraspinal ligament (SSL), intertransverse ligament (ITL), and ligamentum flavum (LF) were built to simulate the force transition. Partial SSL was taken into consideration, as the remaining SSL were attached on ISL; miss-representation would import an extra system error to the numerical analysis. Only one truss element (T3D2) was mapped for every unit in each ligament, of which only the tension load would be effective and no moment being transited. Figure 5 illustrates both the attachment of ligaments and the graphical representation in the FE model, the transverse area of each ligament and mechanical properties are listed in Table 4 (Shirazi-Adl et al., 1984; Lu et al., 1996).

Joint facets within C2–C5 were difficult to identify due to the deformity of exterior vertebra bodies; cervical spacers and a

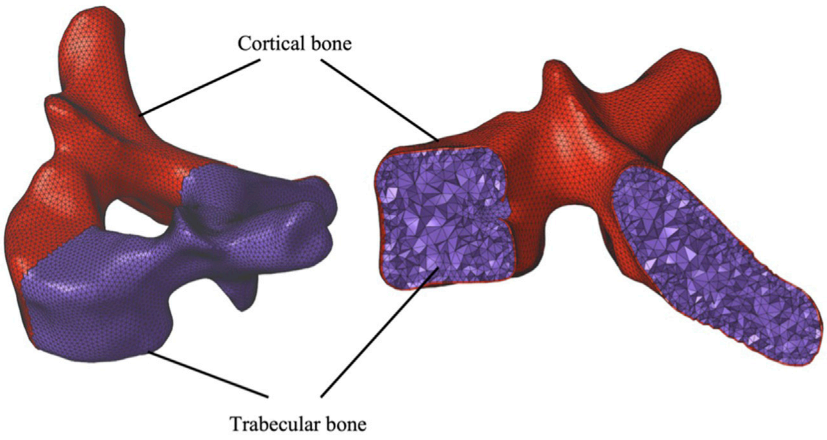

FIGURE 3
Segmentation of the trabecular bone and cortical bone in the vertebra.

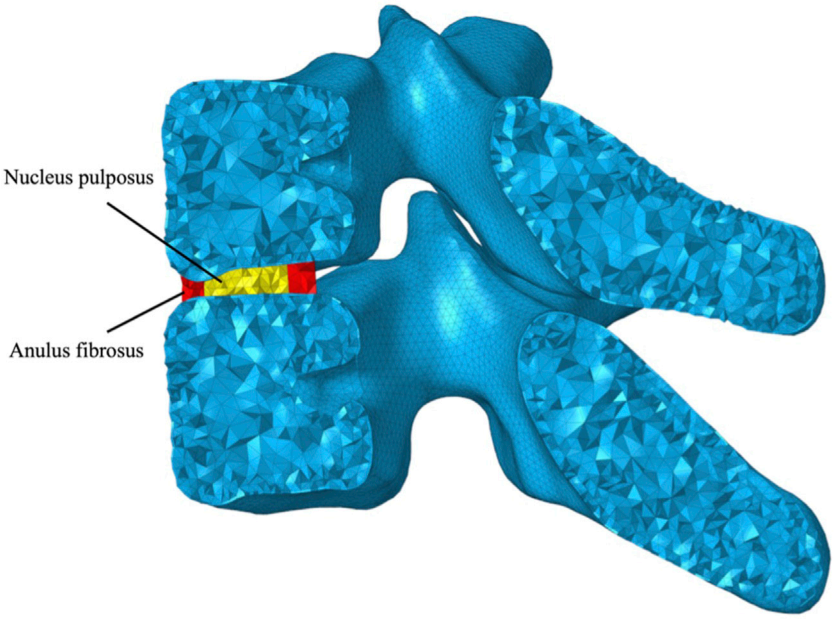

FIGURE 4
Graphical representation of the intervertebral disc (IVD) consisting of nucleus pulposus (NP) and anulus fibrosus (AF).

TABLE 2 Mechanical properties of the bones, IVD components, and implants in the FE model.

		BMD (mg/cc)	Young's modulus (MPa)	Poisson's ratio
C2 trabecular	Central vertebra body	200.4	403.10	0.30
	Exterior vertebra body	135.2	182.75	
C3 trabecular	Central vertebra body	242.1	589.43	
	Exterior vertebra body	99.7	99.08	
C4 trabecular	Central vertebra body	319.2	1,027.46	
	Exterior vertebra body	185.9	346.62	
C5 trabecular	Central vertebra body	301.3	914.93	
	Exterior vertebra body	251.5	636.33	
C6 trabecular	Central vertebra body	262.6	694.04	
	Exterior vertebra body	141.8	201.13	
C7 trabecular	Central vertebra body	229.1	527.53	
	Exterior vertebra body	124.7	155.34	
T1 trabecular	Central vertebra body	165.7	275.07	
	Exterior vertebra body	55.1	30.08	
T2 trabecular	Central vertebra body	187.4	352.26	
	Exterior vertebra body	140.4	197.16	
Cortical bone			1,000	0.30
Nucleus pulposus			1.0	0.49
Anulus fibrosus			3.4	0.40
PEEK			4,000	0.35
Titanium			110,000	0.30

TABLE 3 Mesh quality inspection criterion and the percentage of fair-quality element.

	Jacobian less than 0.7	Volume skew higher than 0.95	Tetra collapse higher less 0.1
C2	0.00% (min 0.65)	0.00% (max 0.89)	0.00% (min 0.12)
C3	0.00% (min 0.71)	0.00% (max 0.89)	0.00% (min 0.10)
C4	0.00% (min 0.65)	0.00% (max 0.90)	0.00% (min 0.10)
C5	0.00% (min 0.67)	0.00% (max 0.89)	0.00% (min 0.10)
C6	0.10% (min 0.61)	0.00% (max 0.89)	0.00% (min 0.10)
C7	0.00% (min 0.69)	0.00% (max 0.89)	0.00% (min 0.10)
T1	0.00% (min 0.55)	0.00% (max 0.89)	0.00% (min 0.10)
T2	0.00% (min 0.65)	0.00% (max 0.89)	0.00% (min 0.11)

cervical plate were placed and would carry most loads; besides, the reconstructed gap between the cervical articular processes was uneven in every joint. Therefore, the cartilage layers were excluded in the proposed FE model. Surface-to-surface, small-sliding contacts were set at the contacting area with a 0.07 friction coefficient and no penetration behavior was allowed, covering from the C5–C6 segment to T1–T2 segment. The finite-sliding contacting method was excluded considering the huge computational burden.

The head weight (HW) of the patient was 7.83% estimated by the averaging head weight percentage of human body weight (Ramachandran et al., 2016). Anatomically, HW will be transited through the occipital condyle to massa lateralis of C1, then loaded onto C2. Thus, a 30.7 N gravity load was applied onto both sides of the cartilage facets next to the odontoid process in C2. The present model neglects all muscles surrounding the cervical and cervical-thoracic segments, torque under different motions were estimated according to an isometric-strength experiment to simulate the daily cervical motion postoperatively (Kauther et al., 2012). The motion of the entire upper body was excluded (flexion, extension, and lateral flexion) in the present investigation, only the motion in cervical columns was considered, since the acceleration of the entire

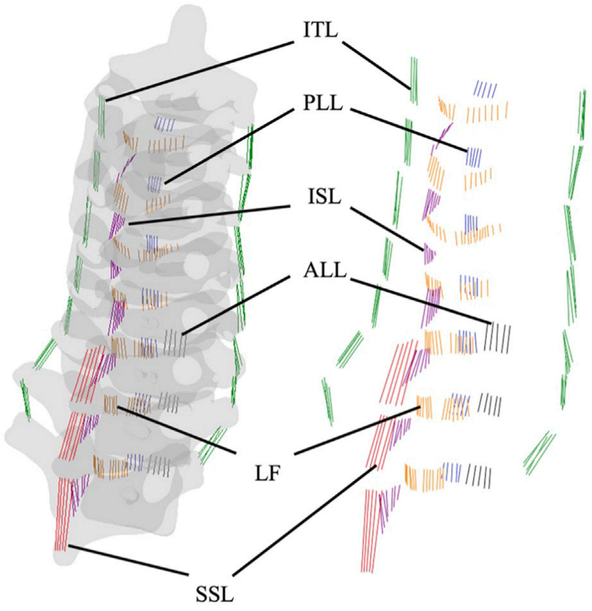

FIGURE 5
Anatomical schematics of ligaments and truss elements in the FEA model.

TABLE 4 Cross-section area of every ligament and mechanical property.

	Young's modulus (MPa)	Poisson's ratio	Cross-section area (mm^2)
Anterior longitudinal ligament (ALL)	20	0.3	38
Posterior longitudinal ligament (PLL)	70		20
Interspinal ligament (ISL)	28		35.5
Supraspinal ligament (SSL)	28		35.5
Intertransverse ligament (ITL)	50		10
Ligamentum flavum (LF)	50		60

TABLE 5 Torque applied under different loading conditions.

	Isometric cervical strength (Kauther et al., 2012) (Nmm/kg)	Applied torque (Nmm)
Flexion	418	1,308
Extension	683	2,138
Lateral flexion	542	1,696
Rotation	208	651

upper body cannot be estimated. Applied torque values are listed in Table 5, which were calculated by multiplying HW by the isometric cervical strength. The torque was applied on the spinous processus, and kinematic-based coupling was utilized to minimize the undesired deformation caused by the applied torque in C2.

The aforementioned FE configuration led to a computational time of less than 150 mins with a workstation of an i7-10700K (3.79 GHz) processor with 78 GB RAM in use.

2.2 Failure criterion

Principal strain was utilized to determine whether the bone was unable to bear the shear force or compression force caused by the fixation screws. If the tension principal strain (maximum component) in one bone element reaches 1.5 %, or the compression principal strain (minimum component) meets −2.0 % (Soyka et al., 2016), then that element is regarded as broken. The strain limit used here was taken from the study toward lumbar vertebrae, since the BMD in the present study is much higher than in the lumbar segments in Rene's research. The damage index of every bone element is defined as the maximum of the ratio between the element principal strains ($\varepsilon_{1,i}$ or $\varepsilon_{3,i}$) and the corresponding principal strain threshold ($\varepsilon_{t,t}$ or $\varepsilon_{c,t}$), i.e.,

$$D_i = max\left(\frac{\varepsilon_{1,i}}{\varepsilon_{t,t}}, \frac{\varepsilon_{3,i}}{\varepsilon_{c,t}}\right) \tag{2}$$

2.3 Validation

The proposed FE model was validated against the retrospective medical data of the patient directly and indirectly. The four-month postoperative CT images showed that the purchase of the fixation screws was good; no screw loosening or spacer subsidence was observed. After seventeen months, the surgery outcomes were good till the numerical investigation was performed. Inspecting the damage indices in the central vertebra body of each vertebra, bone elements surrounding the screw trajectories, and cage-contacting facet were all below the threshold of one under all four loading conditions, maintaining good fixation and forming a good fusion.

As small-sliding contacts were utilized to include joint slipping, contact slipping was examined thoroughly to determine the reasonability of small-sliding. The largest slip motion in slave nodes was below 0.8 mm, only three slave nodes (about 0.00%) displaced larger than the length of the element and reached 1.2 mm. No contact chattering and large node adjustments were found in the analysis according to the analysis log.

Computed damage indices showed good consistency with the surgical outcomes, calling for the acceptance of the proposed FE model's outputs and modeling strategy. Valuable insight to the influence of the cervical implant is discussed, as well as the biomechanical response toward various loadings in the following sections.

3 Results

3.1 Postoperative cervical stability

Most studies of the lower cervical spine have addressed flexion and extension movements, for these are the cardinal movements exhibited by these segments (Anatomy, Head and Neck, Neck Movements—StatPearls—NCBI Bookshelf). As shown in Figure 6, the range of motions (ROMs) of the non-surgical segments in the flexion, extension, and lateral flexion show a declining trend, especially in the extension motion (around 40% decrease), while an increasing trend is seen in the axial rotation.

ROMs of the C5–C6 segment under flexion, extension, lateral flexion, and axial rotation were 4.4°, 9.8°, 5.5°, and 0.7°, respectively; ROMs of the C6–C7 segment, 3.5°, 6.2°, 4.6°, and 0.7°, respectively; ROMs of the C7–T1 segment, 2.6°, 3.4°, 3.4°, and 2.0°, respectively; and ROMS of the T1–T2 segment, 1.6°, 1.2°, 1.5° and 2.7°, respectively.

Compared with the experimental results of asymptomatic subjects, computed ROMs of the C5–C6 segment and the C6–C7 segment in flexion–extension are below the mean ROM obtained from the literature, despite that Yu et al. (2019) recorded a 9.2 ± 4.3° in the C6–C7 joint (Figure 7A).

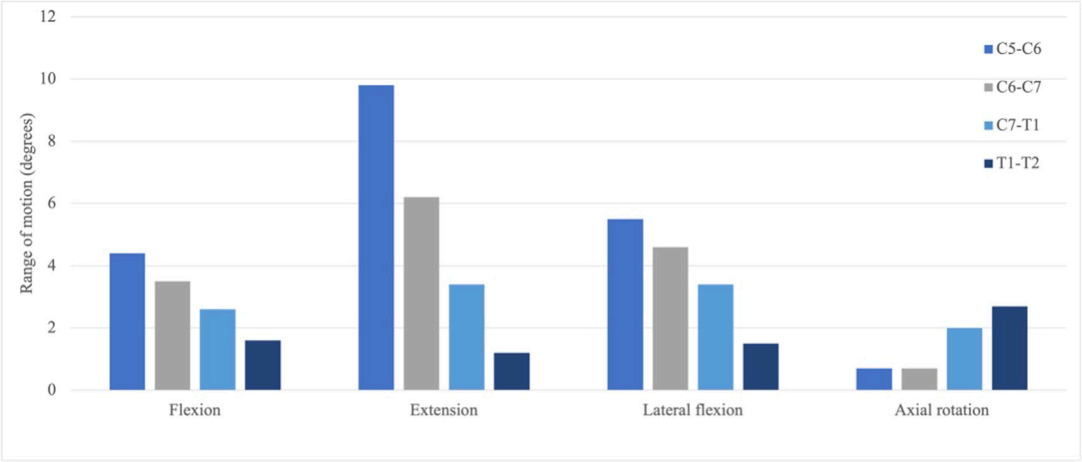

FIGURE 6
ROM of the intact joints under different loading scenarios.

The ROM in the flexion–extension of the C7–T1 segment in the present study falls into the mid of Zhou et al. (2020) and Anderst et al. (2015), 6.0°, 4.1°, and 8.3°, respectively. The decreasing percentage of the ROM in the present study is 32% and 38%, while Zhou captured 28% and 67% decrease percentages, and Anderst saw 20% and 47% decrease percentages. Figure 8 demonstrates a restricted lateral–flexion motion after the ACDF. The computed ROMs acquired the same lateral flexion at 1.4°, while the experimental results exhibited nearly the same ROMs for C5–C6 and C6–C7 segments; the C5–C6 segment flexed slightly smaller than the C6–C7 segment in experiments (Figure 7B). When the neck was subjected to an axial-rotation load, the computed ROMs of the C5–C6 segment moves little in contrast to the largest rotation measured in experiments, as shown in Figure 7C.

3.2 Mechanical response of bone

The absolute-maximum principal strain and deformation around the screw trajectories in four types of motion are exhibited below, where C2 always has the largest deformation among the four motions. Notably, the largest deformation in every trajectory concentrated to the segment on the anterior section where the short length of the point to the screw tip (Figure 8) screw-plowing is happening in cervical spine fixation.

3.2.1 C2

The largest compression and tension deformation were observed in the upper half of the anterior section, where the largest deformations of 1.4710 με (1.47%) and −1.6730 με (−1.67%) were recorded under the extension. Figure 9 gives the overall strain distribution in trajectories under every motion, including the absolute-maximum principal strain on nodes (figures outside box) and the principal strain in every bone element (figures inside box).

3.2.2 C3 and C4

Deformation on the trajectories in C3 and C4 are at the same level, slightly lower than in C5. In C3, maximum and minimum values in each element for flexion, extension, lateral flexion, and axial rotation are (689.2, −996 με), (1681, −4,114 με), (1,742, −1,889 με), and (1,923, −1,325 με), respectively; in C4, (675.6, −755.9 με), (1,421, −2,451 με), (1,211, −1,474 με), and (1,586, −1,054 με), respectively.

3.2.3 C5

Like C2, the strain concentrates to the segment on the anterior section of the trajectory due to the short length to screw tip planar; (1,840, −2,737 με) in flexion, (4,102, −2,925 με) in extension, (2,740, −3,545 με) in lateral flexion, and (1,717, −1,768 με) in axial rotation, respectively. Figure 10 shows such a strain pattern.

4 Discussion

4.1 Modeling method

Connective soft tissues in the human body are variables that depend on biological parameters, it is impossible to describe them accurately for individuals in clinical–biomechanical research. In the present FE investigation, the boundary conditions including the loads simulating the physical flexors and extensors were created based on existing well-designed biomechanical experiments

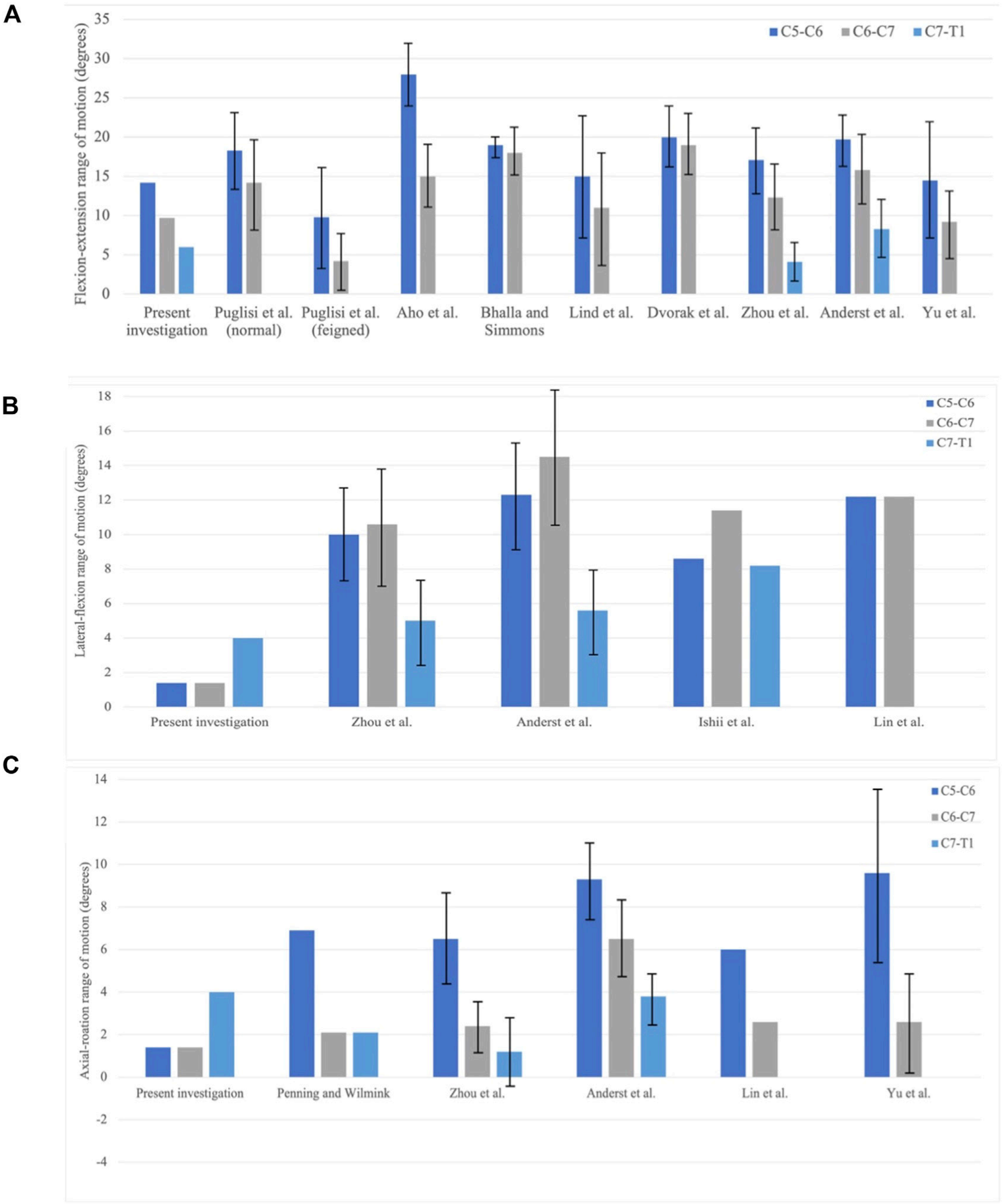

FIGURE 7
Comparison of the range of motion (ROM) in between the present investigation and experiment results. C5–C6, C6–C7, and C7–T1 joints are collected. **(A)** Flexion–extension; **(B)** lateral–flexion; and **(C)** axial rotation (Bogduk and Mercer, 2000; Puglisi et al., 2007).

and anatomical inspections. When applying the moment that forces the neck to do motion, the driving muscles are taken seriously, even though muscles are replaced with a moment. Anatomically speaking, the three main groups of cervical muscles surrounding the vertebral columns control the neck motion, which are the cervical flexors, the cervical extensors, and the sub-occipital muscles. The sub-occipital muscles dominate the motion in the cranio-cervical joint, thus they are skipped in the discussion section.

The cervical flexors consist of sternocleidomastoid (SCM) and anterior scalenes (AS); the SCM travels obliquely across the side of the neck and inserts at the skull (Robinson and Anderson, 2005; Gray and Grimsby, 2012) and the AS origins from the cervical vertebrae C3–C6. The AS functions as a contracting

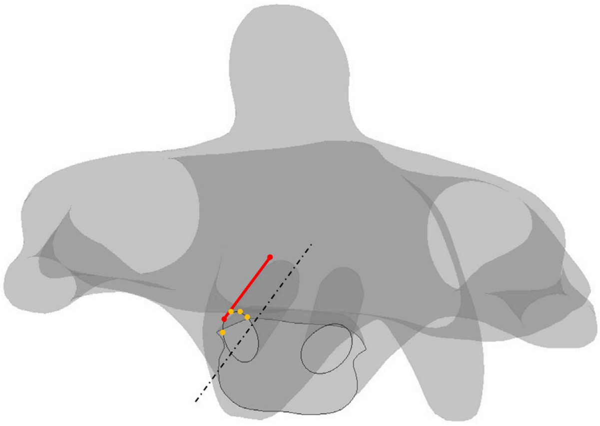

FIGURE 8
Schematics of screw plowing in the cervical screw fixation. Lines in dash form are for the reference, points in orange are on the trajectory, the line in red represents the shortest length from the anterior section to the posterior section.

motor that allows the neck to bend forward, flexing laterally and rotating; however, to the best of the author's knowledge, motion contribution of every vertebra (C3–C6) is unclear and makes the model unable to replicate the contracting effect of the AS. The deep flexor muscles mainly refer to the longus colli and longus capitus. The longus colli is regarded as a weak flexor, the longus capitus controls the cranio-cervical flexion and supports the cervical lordosis anteriorly (Falla et al., 2004; Jull et al., 2008). Consequently, the deep cervical flexors are excluded in the FE model.

The extensor group is described as having four layers (Schomacher and Falla, 2013): first layer, levator scapulae and upper trapezius; second layer, splenius capitus and cervicis; third layer, semispinalis capitus; and fourth layer, semispinalis cervicis and multifidus. The extensor group controls the flexion, extension, lateral flexion, and rotation of the neck (Cleland et al., 2015).

Hence, the moment that forces the neck to move was applied onto C2 and was coupled to a large sum of mesh nodes around the spinous process, distributing the moment to partial C2. Such a load-applying method is inherently flawed as only C2 was subjected to the load yet no more direct load was applied onto the lower cervical vertebrae. Various loading conditions are applied to perform the FE analysis in the previous research. Ouyang et al. (2020) applied a physiological compression of about 7.5 kg and 1,000 Nm moment on the superior endplate of the C3 vertebra in the intact model, then applied the movement angle acquired in the intact model to the ACDF model (Ouyang et al., 2020). The 1,000 Nm moment in their research kept the same magnitude as the load applied in the Panjabi et al. (2001), allowing the comparison of ROMs between the *in silico* model and *in vitro* model. Zhang et al. (2006) forced the skull to move along various anatomical planes with a 1,000 Nm moment, while Li and Lewis (Li and Lewis, 2010) applied 1,000 Nm onto the superior surface of the C1 vertebra. In reported biomechanical experiments, Panjabi et al. (1991) loaded a 1,000 Nm moment to cervical spine segments, in which, the 1,000 Nm was able to cause physiological motions without any damage; Wheeldon et al. (2006) tested the cervical spine segments with 330, 500, 1,000, and 1,500 Nm under the flexion–extension motion. Various loading conditions resulted in motions in the direction of loading under within the elastic range, exposing the primary kinematics and biomechanical response (Moroney et al., 1988; Oda et al., 1991; Panjabi et al., 1991, 1994; Crawford et al., 1998; Wilke et al., 1998; Winkelstein and Myers, 2000, 2002). The moment calculated based on the isometric strength is varied under different motions, similar to the measurement in the Rezasoltani's experiment, the moment applied here is smaller than in Rezasoltani's measurement though (Rezasoltani et al., 2008). The reduced moment covered the daily activities of the neck and produced conservative FE outcomes. Furthermore, the fixation of T1 in the present FE model was slightly offset from the rotation axis defined in the isometric-strength measurement, minimizing the influence of the location of thoracic support (Rezasoltani et al., 2008). The proposed loading conditions incorporated physical information into the FE model and represented the capacity of muscles that maintain a constant length.

4.2 Strain-based failure criterion

As far as authors' knowledge reached, few studies implement the principal-strain method onto the evaluation of the clinical outcomes of deformity correction. The principal strain properly pictures the structural response of the corresponding complex loads and demonstrates the direction of the deformation. Strain, instead of stress, was utilized to define the damage extent of the bone as researchers demonstrated the strain and damage localization early on in the progress were important to bones' brittleness and the matrix failure of human compact bones were dependent on the local strain type (Boyce et al., 1998; Zioupos et al., 2008). On the other hand, stress cannot be measured directly; if the stress-based threshold was utilized, it may incorporate error of misestimation of Young's modulus. Typically, the FE method was based on the displacement of the mesh nodes; then the strain field was obtained *via* derivatives of the displacement field, resulting in a higher accuracy of the strain field compared with stress, especially in non-uniform material.

4.3 Range of motions and stability

The proposed FE model captured the ROM declines across vertebra segments, especially rapid drops of 40 %–50 % in the

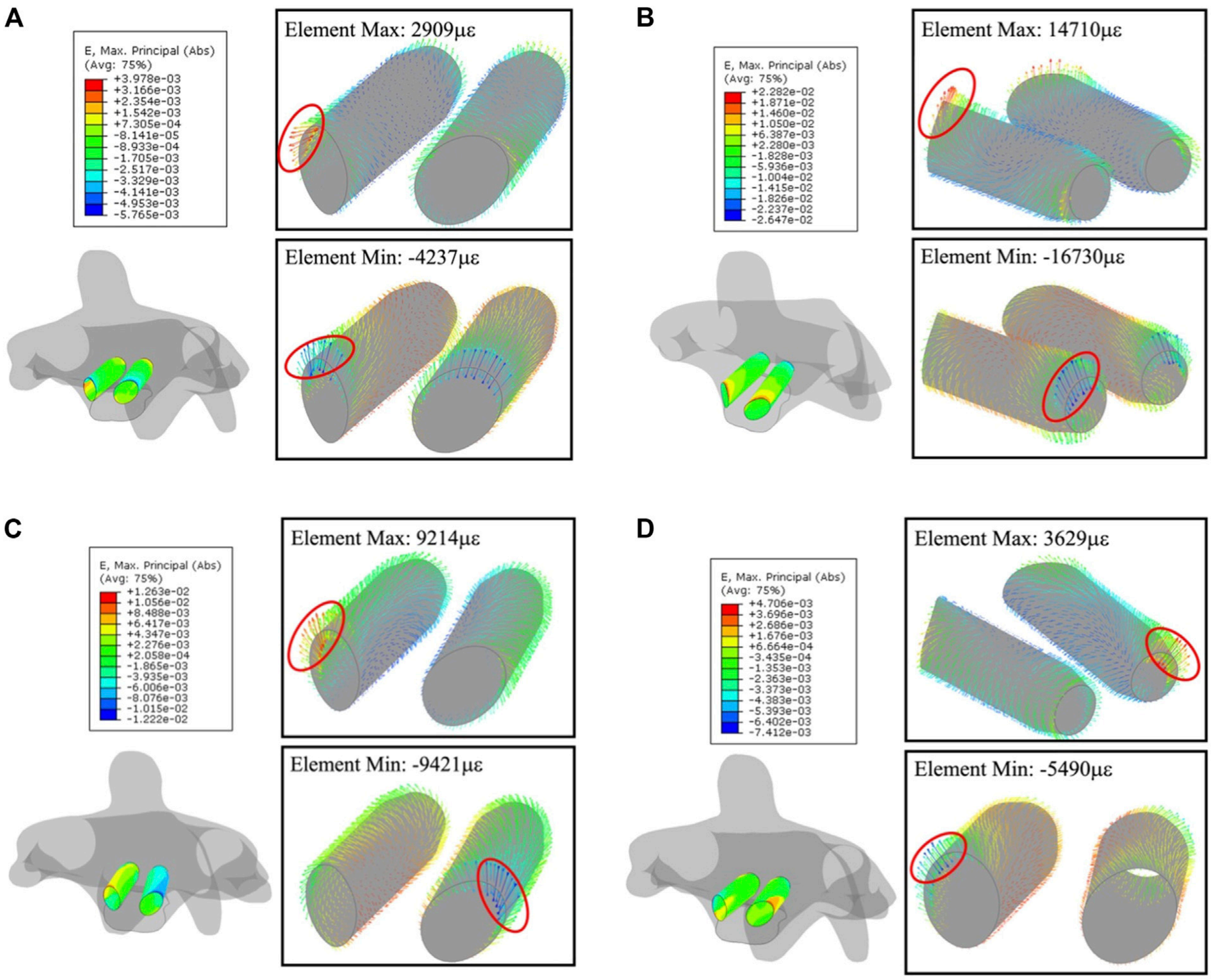

FIGURE 9
Principal-strain and deforming direction surrounding the trajectories in C2. **(A)** Flexion, **(B)** extension, **(C)** lateral flexion, and **(D)** axial rotation. Left figure in each motion is the strain on nodes, figures within the box display the strain in each element.

extension motion, showing an agreement with the FE outcomes obtained by Ouyang et al., 2019. The flexion and extension in normal individuals are complex and counter-intuitive, as described by Van Mameren (1988). Generally speaking, flexion begins from the lower cervical spine (C4–C7), in which the C6–C7 segment makes maximum contribution; then the C0–C4 block is involved and finally involves the lower cervical spine (C4–C7). Extension is initiated in the lower cervical spine (C4–C7) as well, the C4–C7 block then moves in the regular order of C4–C5, C5–C6, and C6–C7. However, in the proposed FE model, the ventral plate is fixed in the C2–C5 block, thus interrupting the order of contribution of individual segments, impacting the contribution of vertebra segments in flexion and extension motions.

The decreasing trending of the flexion–extension motion of C5–C6 and C6–C7 were also reported in existing biomechanical experiments (Aho et al., 1955; Lind et al., 1989; Puglisi et al., 2007; Anderst et al., 2015; Yu et al., 2019; Zhou et al., 2020). The ROMs in the present investigation were reduced by 40 %–50 % across vertebra junctions, a similar decreasing extent to the results in the feigned group in Puglisi's research (Puglisi et al., 2007) (Figure 7A). In their experiment, participants were asked to feign a 50 % restricted neck motion, no extra facility was utilized, and no pre-train was conducted though. Postoperative ROMs in the present investigation suggested that the placement of the ventral plate and intervertebral spacer constrained the ROM of the upper cervical vertebrae under flexion–extension. The ventral plate eliminated the relative motion on the processes; meanwhile, the spacer replaced the intervertebral disk, compromising the oblique between the normal of the intervertebral disk and the long axes of the vertebral bodies. Aforementioned restrictions in surgical

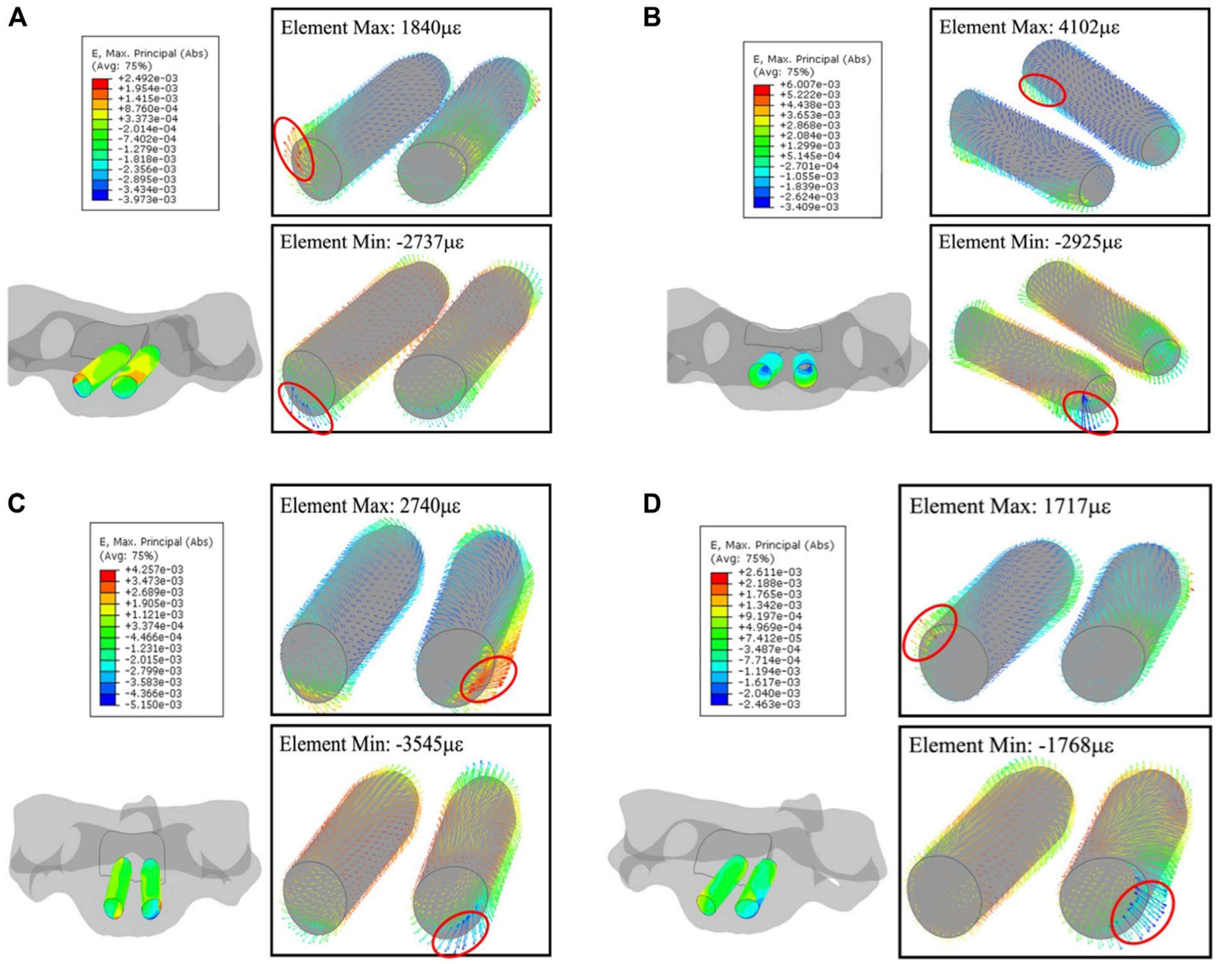

FIGURE 10
Principal-strain and deforming direction surrounding the trajectories in C5. **(A)** Flexion, **(B)** extension, **(C)** lateral flexion, and **(D)** axial rotation. The left figure in each motion is the strain on the nodes, figures within the box display the strain in each element.

junctions reduced the moment arm of HW, thus limiting the induced moment on non-surgical junctions.

The lateral-flexion and axial rotation were also restricted due to the ACDF. Therefore, stability is held to improve the segment fusion process and outcome. The restricting effect on flexion–extension ROM in T1–T2 cannot be determined, since the quantitative kinematics data of the cervical–thoracic segments are scarce.

4.4 Bone-implant interaction

In C2–C5, large deformations were found in C2 and C5 that are the superior and inferior fixed vertebrae. Furthermore, the deformation around the screws concentrated to the lateral side on the anterior section of the screw trajectory, where an uneven distribution of the distance from the ventral plate to vertebra body was observed. This gap between the ventral plate and bone will induce a moment, resulting in the repeated compression and extrusion on the anterior section of the screw trajectory. Daily activities of the neck will generate a complex loading history and may cause fatigue damage to the bone surrounding the screw trajectory, then the trajectory will be expanded, and screw loosening might happen after a long time. Researchers also demonstrated the excessive strain between the screw and bone interface and considered it as the primary cause for screw loosening (Schizas et al., 2009; Villa et al., 2014). Aycan and Demir (2020) reviewed the cyclic biomechanical experiments on pedicle screws and concluded that the pull-out performance of the screws generally decreased with the toggling effect, emphasizing the strain concentration in the bone–implant interface leading to the loss of the stabilization of fixation. The gap between plate and bones needs to be taken care in the ACDF surgery, and fixation screws should be fully inserted into vertebra bodies.

There are several limitations in the present FE investigation. The cartilage layer was neglected in the analysis, reducing the non-linearity of the relative motion and influencing the contacts between vertebra segments. This simplification introduced an error on the relative motion between two vertebra bodies. Secondly, the truss element was deployed to simulate the ligaments and mechanical properties of normal ligaments that were acquired from the literature; however, the subject in the FE model was diagnosed with kyphosis, anterior soft tissues might be stronger than normal, healthy people. Further work will include more clinical cases into the investigation and validate the proposed principal-strain based on the criterion against retrospective medical records (both successful deformity corrections and failed ones).

5 Conclusion

The present *in silico* study proposed a patient-specific method that can be used to inspect the safety of the fixation construct in the cervical spine and explained the modeling strategy in the perspective of mechanics, anatomy, and numerical computation, offering an explanation on the hardware migration. A principal-strain-based failure criterion was introduced to measure the bone failure in the cervical vertebrae body, meanwhile the pre-condition on how to use the criterion was elaborated. The proposed failure criterion of the bone demonstrated satisfying surgical outcomes and was validated against the retrospective inspection, though more clinical validation was needed. Furthermore, the gap between the ventral plate and bone (unsupported threads of the fixation screw) induced moment on the anterior section of the screw trajectory and might cause fatigue damage. Biomechanically, it is recommended that the ventral plate is bent to a conformed shape with the cervical vertebra to reduce the gap between the ventral plate and bone, and the fixation screws are always fully inserted into vertebrae.

Data availability statement

The datasets presented in this article are not readily available because requests to access the datasets should be directed to wuuuhku@connect.hku.hk.

Ethics statement

Written informed consent was obtained from the minor(s)' legal guardian/next of kin for the publication of any potentially identifiable images or data included in this article.

Author contributions

FZ, WL, and TW conceived and designed the study. YS and TX contributed to the acquisition of data. TW constructed, validated the FE model, and wrote the manuscript. HC helped interpret the results, provided the clinical and anatomical knowledge, and edited the manuscript. FZ and WL supervised the investigation and reviewed the manuscript. All authors have given final approval of the version to be published.

Funding

This work was partially supported by National Key Research and Development Program of China (2021YFB3800800), Hong Kong RGC grant (GRF 17101821) and BONES TECHNOLOGY R&D fund.

Conflict of interest

The authors declare that the research was conducted in the absence of any commercial or financial relationships that could be construed as a potential conflict of interest.

Publisher's note

References

Aho, A., Vartiainen, O., and Salo, O. (1955). Segmentary antero-posterior mobility of the cervical spine. *Ann. Med. Intern. Fenn.* 44, 287–299.

Anderst, W. J., Donaldson, W. F., Lee, J. Y., and Kang, J. D. (2015). Three-dimensional intervertebral kinematics in the healthy young adult cervical spine during dynamic functional loading. *J. Biomech.* 48, 1286–1293. doi:10.1016/j.jbiomech.2015.02.049

Anderst, W. J., Thorhauer, E. D., Lee, J. Y., Donaldson, W. F., and Kang, J. D. (2011). Cervical spine bone mineral density as a function of vertebral level and anatomic location. *Spine J.* 11, 659–667. doi:10.1016/j.spinee.2011.05.007

Ansari, D., Burley, H. E. K., Glinski, A., Elia, C., Chapman, J. R., and Oskouian, R. J. (2020). The new onset of dysphagia four years after anterior cervical discectomy and fusion: Case report and literature review. *Surg. Neurol. Int.* 11, 32. doi:10.25259/sni_46_2020

Aycan, F., and Demir, T. (2020). Toggling effect on pullout performance of pedicle screws: Review. *Int. Adv. Res. Eng. J.*, 4, 161–172. doi:10.35860/iarej.722229

Azadarmaki, R., and Soliman, A. M. S. (2014). Progressive dysphagia in a patient with a history of cervical spine fusion. *JAMA Otolaryngol. Head. Neck Surg.* 140, 675–676. doi:10.1001/jamaoto.2014.787

Bogduk, N., and Mercer, S. (2000). Biomechanics of the cervical spine. I: Normal kinematics. *Clin. Biomech. (Bristol, Avon.* 15, 633–648. doi:10.1016/s0268-0033(00)00034-6

Boyce, T. M., Fyhrie, D. P., Glotkowski, M. C., Radin, E. L., and Schaffler, M. B. (1998). Damage type and strain mode associations in human compact bone bending fatigue. *J. Orthop. Res.* 16, 322–329. doi:10.1002/jor.1100160308

Cleland, J., Koppenhaver, S., and Su, J. (2015). *Netter's orthopaedic clinical examination: An evidence-based approach*. Elsevier Health Sciences Available at : https://www.us.elsevierhealth.com/netters-orthopaedic-clinical-examination-9780323340632.html (Accessed February 2, 2022).

Crawford, N. R., Peles, J. D., and Dickman, C. A. (1998). The spinal lax zone and neutral zone. *J. Spinal Disord.* 11, 416–429. doi:10.1097/00002517-199810000-00009

Ebot, J., Foskey, S., Domingo, R., Nottmeier, E., J, E., S, F., et al. (2020). Kyphosis correction in patients undergoing a four-level anterior cervical discectomy and fusion. *Cureus* 12, e8826. doi:10.7759/cureus.8826

Epstein, N. E. (2019). A review of complication rates for anterior cervical diskectomy and fusion (ACDF). *Surg. Neurol. Int.* 10, 100. doi:10.25259/sni-191-2019

Falla, D., Bilenkij, G., and Jull, G. (2004). Patients with chronic neck pain demonstrate altered patterns of muscle activation during performance of a functional upper limb task. *Spine* 29, 1436–1440. doi:10.1097/01.brs.0000128759.02487.bf

Farfan, H. F., Cossette, J. W., Robertson, G. H., Wells, R. V., and Kraus, H. (1970). The effects of torsion on the lumbar intervertebral joints: The role of torsion in the production of disc degeneration. *J. Bone Jt. Surg.* 52, 468–497. doi:10.2106/00004623-197052030-00006

Feng, H., Ma, Y., Wang, S. J., Zhang, S., and Li, Z. (2021). The correlation of regional microstructure and mechanics of the cervical articular process in adults. *Materials* 14, 6409. doi:10.3390/ma14216409

Fryer, C., Tan, H. E., Bakmeedeniya, R., and Friedland, P. L. (2019). Late-Onset dysphagia from hardware migration after anterior cervical discectomy and fusion: An unusual cause and review of literature. *Clin. Med. Insights. Ear Nose Throat* 12, 117955061988113. doi:10.1177/1179550619881131

Gray, J. C., and Grimsby, O. (2012). Interrelationship of the Spine, Rib Cage, and Shoulder. *Neurologic Considerations*. 87–130. doi:10.1016/b978-1-4377-0740-3.00005-2

Guo, Z., Wu, X., Yang, S., Liu, C., Zhu, Y., Shen, N., et al. (2021). Anterior cervical discectomy and fusion using zero-P system for treatment of cervical spondylosis: A meta-analysis. *Pain Res. Manag.* 2021, 1–15. doi:10.1155/2021/3960553

Hershman, S. H., Kunkle, W. A., Kelly, M. P., Buchowski, J. M., Ray, W. Z., Bumpass, D. B., et al. (2017). Esophageal perforation following anterior cervical spine surgery: Case report and review of the literature. *Glob. Spine J.* 7, 28S–36S. doi:10.1177/2192568216687535

Iatridis, J. C., Weidenbaum, M., Setton, L. A., and Mow, V. C. (1996). Is the nucleus pulposus a solid or a fluid? Mechanical behaviors of the nucleus pulposus of the human intervertebral disc. *Spine* 21, 1174–1184. doi:10.1097/00007632-199605150-00009

Jull, G. A., O'Leary, S. P., and Falla, D. L. (2008). Clinical assessment of the deep cervical flexor muscles: The craniocervical flexion test. *J. Manip. Physiol. Ther.* 31, 525–533. doi:10.1016/j.jmpt.2008.08.003

Jung, B., and Bhutta, B. S. (2022). *Anatomy, head and neck, neck movements - StatPearls - NCBI*. Available at https://www.ncbi.nlm.nih.gov/books/NBK557555/#:~:text=Cervical%20flexion%3A%20bending%20the%20head,shoulder%20of%20the%20same%20side (Accessed May 19, 2022).

Kauther, M. D., Piotrowski, M., Hussmann, B., Lendemans, S., and Wedemeyer, C. (2012). Cervical range of motion and strength in 4, 293 young male adults with chronic neck pain. *Eur. Spine J.* 21, 1522–1527. doi:10.1007/s00586-012-2369-x

Keyak, J. H., Rossi, S. A., Jones, K. A., and Skinner, H. B. (1997). Prediction of femoral fracture load using automated finite element modeling. *J. Biomech.* 31, 125–133. doi:10.1016/s0021-9290(97)00123-1

Li, Y., and Lewis, G. (2010). Influence of surgical treatment for disc degeneration disease at C5–C6 on changes in some biomechanical parameters of the cervical spine. *Med. Eng. Phys.* 32, 595–603. doi:10.1016/j.medengphy.2010.02.009

Li, Y., Zhang, Z., Liao, Z., Mo, Z., and Liu, W. (2017). Finite element analysis of influence of axial position of center of rotation of a cervical total disc replacement on biomechanical parameters: Simulated 2-level replacement based on a validated model. *World Neurosurg.* 106, 932–938. doi:10.1016/j.wneu.2017.07.079

Lind, B., Sihlbom, H., Nordwall, A., and Malchau, H. (1989). Normal range of motion of the cervical spine. *Arch. Phys. Med. Rehabil.* 70, 692–695.

Liu, Z.-J., Zhang, C., Ma, C., Qi, H., Yang, Z.-H., Wu, H.-Y., et al. (2022). Automatic phantom-less QCT system with high precision of BMD measurement for osteoporosis screening: Technique optimisation and clinical validation. *J. Orthop. Transl.* 33, 24–30. doi:10.1016/j.jot.2021.11.008

Lu, Y. M., Hutton, W. C., and Gharpuray, V. M. (1996). Do bending, twisting, and diurnal fluid changes in the disc affect the propensity to prolapse? A viscoelastic finite element model. *Spine* 21, 2570–2579. doi:10.1097/00007632-199611150-00006

Mercer, S., and Bogduk, N. (1999). The ligaments and anulus fibrosus of human adult cervical intervertebral discs. *Spine* 24, 619–626. doi:10.1097/00007632-199904010-00002

Moroney, S. P., Schultz, A. B., Miller, J. A. A., and Andersson, G. B. J. (1988). Load-displacement properties of lower cervical spine motion segments. *J. Biomech.* 21, 769–779. doi:10.1016/0021-9290(88)90285-0

Nachemson, A. (2014). Lumbar intradiscal pressure: Experimental studies on post-mortem material. *Acta Orthop. Scand.* 31, 1–104. doi:10.3109/ort.1960.31.suppl-43.01

Nathani, A., Weber, A. E., Wahlquist, T. C., Graziano, G. P., Park, P., and Patel, R. D. (2015). Delayed presentation of pharyngeal erosion after anterior cervical discectomy and fusion. *Case Rep. Orthop.* 2015, 1–4. doi:10.1155/2015/173687

Ng, H.-W., and Teo, E.-C. (2001). Nonlinear finite-element analysis of the lower cervical spine (C4–C6) under axial loading. *J. Spinal Disord.* 14, 201–210. doi:10.1097/00002517-200106000-00003

Ning, X., Wen, Y., Xiao-Jian, Y., Bin, N., De-Yu, C., Jian-Ru, X., et al. (2008). Anterior cervical locking plate-related complications; prevention and treatment recommendations. *Int. Orthop.* 32, 649–655. doi:10.1007/s00264-007-0369-y

Nottmeier, E. W., Deen, H. G., Patel, N., and Birch, B. (2009). Cervical kyphotic deformity correction using 360-degree reconstruction. *J. Spinal Disord. Tech.* 22, 385–391. doi:10.1097/bsd.0b013e318180e672

Oda, T., Panjabi, M. M., and Crisco, J. J. (1991). Three-Dimensional translational movements of the upper cervical spine. *J. Spinal Disord.* 4, 411–419. doi:10.1097/00002517-199112000-00002

Oegema, T. R. (1993). Biochemistry of the intervertebral disc. *Clin. Sports Med.* 12, 419–438. doi:10.1016/s0278-5919(20)30404-x

Ouyang, P., Li, J., He, X., Dong, H., Zang, Q., Li, H., et al. (2020). Biomechanical comparison of 1-level corpectomy and 2-level discectomy for cervical spondylotic myelopathy: A finite element analysis. *Med. Sci. Monit.* 26, e919270–11. doi:10.12659/msm.919270

Ouyang, P., Lu, T., He, X., Gao, Z., Cai, X., and Jin, Z. (2019). Biomechanical comparison of integrated fixation cage versus anterior cervical plate and cage in anterior cervical corpectomy and fusion (accf): A finite element analysis. *Med. Sci. Monit.* 25, 1489–1498. doi:10.12659/msm.913630

Panjabi, M., Dvorak, J., and Crisco, J. (1991). Flexion, extension, and lateral bending of the upper cervical spine in response to alar ligament transections. *J. Spinal Disord.* 4, 157–167. doi:10.1097/00002517-199106000-00005

Panjabi, M. M., Crisco, J. J., Vasavada, A., Oda, T., Cholewicki, J., Nibu, K., et al. (2001). Mechanical properties of the human cervical spine as shown by three-dimensional load–displacement curves. *Spine* 26, 2692–2700. doi:10.1097/00007632-200112150-00012

Panjabi, M. M., Lydon, C., Vasavada, A., Grob, D., and Dvorak, J. J. C. (1994). On the understanding of clinical instability. *Spine* 19, 2642–2650. doi:10.1097/00007632-199412000-00008

Park, S., Lee, D.-H., Ha, J.-K., Hwang, S., Hwang, D., Cho, J. H., et al. (2019). How does screw migration or fracture after anterior cervical plate fixation affect the radiographic and clinical outcomes? *Clin. Spine Surg.* 32, 398–402. doi:10.1097/bsd.0000000000000844

Perey, O. (2014). Fracture of the vertebral end-plate in the lumbar spine: An experimental biomechanical investigation. *Acta Orthop. Scand.* 28, 1–101. doi:10.3109/ort.1957.28.suppl-25.01

Pooni, J., Hukins, D., Harris, P., Hilton, R., and Davies, K. (1986). Comparison of the structure of human intervertebral discs in the cervical, thoracic and lumbar regions of the spine. *Surg. Radiol. Anat.* 8, 175–182. doi:10.1007/bf02427846

Puglisi, F., Strimpakos, N., Papathanasiou, M., Kapreli, E., Bonelli, A., Sgambetterra, S., et al. (2007). Cervical spine segmental vertebral motion in healthy volunteers feigning restriction of neck flexion and extension. *Int. J. Leg. Med.* 121, 337–340. doi:10.1007/s00414-006-0111-0

Ramachandran, H. K., Vasudevan, D., Brahma, A. K., and Pugazhenthi, S. (2016). Estimation of mass moment of inertia of human body, when bending forward, for the design of A self-transfer robotic facility. *J. Eng. Sci. Technol.* 11, 166–176.

Rezasoltani, A., Ylinen, J., Bakhtiary, A.-H., Norozi, M., and Montazeri, M. (2008). Cervical muscle strength measurement is dependent on the location of thoracic support. *Br. J. Sports Med.* 42, 379–382. doi:10.1136/bjsm.2007.040709

Ritzel, H., Amling, M., Pösl, M., Hahn, M., and Delling, G. (1997). The thickness of human vertebral cortical bone and its changes in aging and osteoporosis: A histomorphometric analysis of the complete spinal column from thirty-seven autopsy specimens. *J. Bone Min. Res.* 12, 89–95. doi:10.1359/jbmr.1997.12.1.89

Robinson, J. K., and Anderson, E. R. (2005). *Surgery of the skin*. Part One Basic Surg Concepts. doi:10.1016/b978-0-323-02752-6.50006-7

Schizas, C., Tzinieris, N., Tsiridis, E., and Kosmopoulos, V. (2009). Minimally invasive versus open transforaminal lumbar interbody fusion: Evaluating initial experience. *Int. Orthop.* 33, 1683–1688. doi:10.1007/s00264-008-0687-8

Schomacher, J., and Falla, D. (2013). Function and structure of the deep cervical extensor muscles in patients with neck pain. *Man. Ther.* 18, 360–366. doi:10.1016/j.math.2013.05.009

Shirazi-Adl, S. A., Shrivastava, S. C., and Ahmed, A. M. (1984). Stress analysis of the lumbar disc-body unit in compression A three-dimensional nonlinear finite element study. *Spine* 9, 120–134. doi:10.1097/00007632-198403000-00003

Soyka, R. P. W., Helgason, B., Marangalou, J. H., Bergh, J. P. van den, Rietbergen, B. van, and Ferguson, S. J. (2016). The effectiveness of percutaneous vertebroplasty is determined by the patient-specific bone condition and the treatment strategy. *Plos One* 11, e0151680. doi:10.1371/journal.pone.0151680

Tang, J. A., Scheer, J. K., Smith, J. S., Deviren, V., Bess, S., Hart, R. A., et al. (2012). The impact of standing regional cervical sagittal alignment on outcomes in posterior cervical fusion surgery. *Neurosurgery* 71, 662–669. doi:10.1227/neu.0b013e31826100c9

Van Mameren, H. (1988). *Motion patterns in the cervical spine*. doi:10.26481/dis.19880616hm

Villa, T., Barbera, L. L., and Galbusera, F. (2014). Comparative analysis of international standards for the fatigue testing of posterior spinal fixation systems. *Spine J.* 14, 695–704. doi:10.1016/j.spinee.2013.08.032

Wheeldon, J. A., Pintar, F. A., Knowles, S., and Yoganandan, N. (2006). Experimental flexion/extension data corridors for validation of finite element models of the young, normal cervical spine. *J. Biomech.* 39, 375–380. doi:10.1016/j.jbiomech.2004.11.014

Wilke, H.-J., Wenger, K., and Claes, L. (1998). Testing criteria for spinal implants: Recommendations for the standardization of *in vitro* stability testing of spinal implants. *Eur. Spine J.* 7, 148–154. doi:10.1007/s005860050045

Winkelstein, B. A., and Myers, B. S. (2002). Importance of nonlinear and multivariable flexibility coefficients in the prediction of human cervical spine motion. *J. Biomech. Eng.* 124, 504–511. doi:10.1115/1.1504098

Winkelstein, B., and Myers, B. S. (2000). Experimental and computational characterization of three-dimensional cervical spine flexibility. *Stapp Car Crash J.* 44, 139–158. doi:10.4271/2000-01-sc11

Wójtowicz, P., Szafarowski, T., Migacz, E., and Krzeski, A. (2015). Recurrent laryngeal edema imitating angioedema caused by dislocated screw after anterior spine surgery. *Case Rep. Otolaryngol.* 2015, 1–3. doi:10.1155/2015/749463

Yu, Y., Li, J.-S., Guo, T., Lang, Z., Kang, J. D., Cheng, L., et al. (2019). Normal intervertebral segment rotation of the subaxial cervical spine: An invivo study of dynamic neck motions. *J. Orthop. Transl.* 18, 32–39. doi:10.1016/j.jot.2018.12.002

Zhang, Q. H., Teo, E. C., Ng, H. W., and Lee, V. S. (2006). Finite element analysis of moment-rotation relationships for human cervical spine. *J. Biomech.* 39, 189–193. doi:10.1016/j.jbiomech.2004.10.029

Zhou, C., Wang, H., Wang, C., Tsai, T.-Y., Yu, Y., Ostergaard, P., et al. (2020). Intervertebral range of motion characteristics of normal cervical spinal segments (C0-T1) during *in vivo* neck motions. *J. Biomech.* 98, 109418. doi:10.1016/j.jbiomech.2019.109418

Zhou, E., Huang, H., Zhao, Y., Wang, L., and Fan, Y. (2022). The effects of titanium mesh cage size on the biomechanical responses of cervical spine after anterior cervical corpectomy and fusion: A finite element study. *Clin. Biomech. (Bristol, Avon.* 91, 105547. doi:10.1016/j.clinbiomech.2021.105547

Zioupos, P., Hansen, U., and Currey, J. D. (2008). Microcracking damage and the fracture process in relation to strain rate in human cortical bone tensile failure. *J. Biomech.* 41, 2932–2939. doi:10.1016/j.jbiomech.2008.07.025

frontiers | Frontiers in Bioengineering and Biotechnology

TYPE Original Research
PUBLISHED 20 September 2022
DOI 10.3389/fbioe.2022.960090

Biomechanical analysis of sacroiliac joint motion following oblique-pulling manipulation with or without pubic symphysis injury

Jing Li[1], Yikai Li[2], Ruiyue Ping[1,3], Qing Zhang[4], Hai-Yun Chen[1,5]*, Dingkun Lin[1,5]* and Ji Qi[1,4,5,6]*

[1]Guangzhou University of Chinese Medicine, Guangzhou, China, [2]School of Traditional Chinese Medicine, Southern Medical University, Guangzhou, China, [3]Department of Dermatology, Guangdong Provincial Hospital of Chinese Medicine, Guangzhou, China, [4]Wang Jing Hospital of China Academy of Chinese Medical Sciences, Beijing, China, [5]Department of Orthopedics, Guangdong Provincial Hospital of Chinese Medicine, Guangzhou, China, [6]Postdoctoral Research Station, Guangdong Provincial Hospital of Chinese Medicine, Guangzhou, China

EDITED BY
Damien Lacroix,
University of Sheffield, United Kingdom

REVIEWED BY
Amaresh Vydyanathan,
Montefiore Medical Center,
United States
Hanno Steinke,
Leipzig University, Germany

*CORRESPONDENCE
Hai-Yun Chen,
drchygz@163.com
Dingkun Lin,
lindingkuntcm@126.com
Ji Qi,
haoruiml@163.com

SPECIALTY SECTION
This article was submitted to Biomechanics, a section of the journal Frontiers in Bioengineering and Biotechnology

RECEIVED 02 June 2022
ACCEPTED 22 August 2022
PUBLISHED 20 September 2022

CITATION
Li J, Li Y, Ping R, Zhang Q, Chen H-Y, Lin D and Qi J (2022), Biomechanical analysis of sacroiliac joint motion following oblique-pulling manipulation with or without pubic symphysis injury. *Front. Bioeng. Biotechnol.* 10:960090. doi: 10.3389/fbioe.2022.960090

Background: Oblique-pulling manipulation has been widely applied in treating sacroiliac joint (SIJ) dysfunction. However, little is known about the biomechanical mechanism of the manipulation. This study aims to analyze the SIJ motion under oblique-pulling manipulation, in comparison with compression and traction loads.

Methods/Study Design: A total of six specimens of embalmed human pelvis cadavers were dissected to expose the SIJ and surrounding ligaments. Through a servo-hydraulic testing system, biomechanical tests were performed on the stable pelvis and the unstable pelvis with pubic symphysis injury (PSI). A three-dimensional (3D) photogrammetry system was employed to determine the separation and nutation in three tests: axial compression (test A), axial traction (test B), and oblique-pulling manipulation (test C).

Results: After applying the testing loads, the range of nutation was no more than 0.3° (without PSI) and 0.5°(with PSI), separately. Except for test B, a greater nutation was found with PSI ($p < 0.05$). Under both conditions, nutation following test A was significantly greater than that of other tests ($p < 0.05$). SIJ narrowed in test A and separated in tests B and C, where the range of motion did not exceed 0.1 mm (without PSI) or 0.3 mm (with PSI) separately. Under both conditions, the separation of SIJ in test C was not as apparent as the narrowness of SIJ in test A ($p < 0.05$). Compared to SIJ, a more significant increasing displacement was found at the site of the iliolumbar ligament ($p < 0.05$). Nevertheless, when the force was withdrawn in all tests, the range of nutation and separation of SIJ nearly decreased to the origin.

Conclusion: Pubic symphysis is essential to restrict SIJ motion, and the oblique-pulling manipulation could cause a weak nutation and separation of SIJ. However, the resulting SIJ motion might be neutralized by regular standing and weight-bearing load. Also, the effect on SIJ seems to disappear at the end of manipulation. Therefore, the stretching and loosening of surrounding ligaments need to be paid more attention to.

KEYWORDS

oblique-pulling manipulation, sacroiliac joint, biomechanics, pubic symphysis injury, iliolumbar ligament, 3D photogrammetry

Introduction

The sacroiliac joint (SIJ) consists of two parts: the anterior synovial joint (intra-articular part) and the posterior syndesmosis (extra-articular part) (Gartenberg et al., 2021) (Standring, 2016). The SIJ follows a force closure model, characterized by the bony extensions protruding from both the sacral and iliac articular surfaces into the SIJ, forming a blunted, tight, interlocking structure that provides a high surface friction coefficient. This unique structure, combined with extensive ligamental stability, enables the SIJ to maintain vertical stability without additional forces from surrounding musculature (Vleeming and Schuenke, 2019). The primary stabilizers of the SIJ include the sacroiliac, sacrotuberous, and sacrospinous ligaments (Bertoldo et al., 2021). The thoracolumbar fascia connects the gluteus maximus muscle with the latissimus dorsi muscle and then continues with the deep fascia of the limbs (Vleeming et al., 2012; Stecco et al., 2013). Vleeming demonstrated how this aponeurotic structure anchors itself to other bone, muscular structures, and ligamentous in the sacroiliac region and forms a continuum with the lower limb fascia (Carvalho et al., 2013).

Sacroiliac joint dysfunction (SIJD) typically results from abnormal motion and malalignment of the joint. Abnormal motion includes hypo- or hyper-mobile SIJ. Increased secretion of estrogen and relaxation during pregnancy, as well as fetal growth pressure, may lead to hypermobility of the SIJ (Capobianco et al., 2015). In contrast, a sedentary lifestyle and pelvic fractures can cause joint fixation and hypo-mobility (Gartenberg et al., 2021). Although SIJD has been found to be the primary cause of lower back pain in 15%–40% of patients, it is constantly under diagnosed or overlooked and later under treated (Des Jarlais et al., 2004; Cusi, 2010; Grassi Dde et al., 2011; Graup et al., 2014; Buchanan et al., 2021). Standard physical therapy interventions can be employed to correct the underlying pathology and alleviate the symptoms of SIJD. Such interventions include manipulation, mobilization, sacroiliac belts, repetitive exercises, massage, aerobic conditioning, patient education, and electrotherapeutic modalities (Moyer et al., 2004; Huijbregts, 2008). Manipulation is a highly regarded treatment and is known to have a certain therapeutic effect on various diseases, including the treatment of SIJD (Tang et al., 2016). In particular, oblique-pulling manipulation is a simple, effective, and practical method for treating SIJD (Shokri et al., 2018). However, it is still controversial whether it can move the SIJ. Studies have speculated that the mechanism is to stretch and widen the joint space of the SIJ with the help of muscle strength to rotate the SIJ for the purpose of repositioning (Vleeming et al., 1990). Meanwhile, other studies support the opposite idea that the manipulation cannot move the SIJ as the joint is very stable. In addition, pubic symphysis plays an important role in maintaining the stability of SIJ, and the effects of oblique-pulling manipulation on SIJ with or without pubic symphysis injury (PSI) remain unknown.

Therefore, this study aimed to explore the SIJ motion under oblique-pulling manipulation compared to compression and traction loads, *via* biomechanical tests on adult cadaveric specimens.

Materials and methods

Ethics

All procedures performed in this study involving human participants followed the Declaration of Helsinki (as revised in 2013). The procedures were approved by the Ethics Committee of Guangdong Provincial Hospital of Chinese Medicine (BM 2022–059). The donors have dedicated their bodies for educational and research purposes to the local Institute of Anatomy prior to death, in compliance with local institutional and legislative requirements.

Materials

A total of six formalin-embalmed adult cadaveric pelvises were visually selected and examined by X-ray to rule out bone abnormalities such as tumor, fracture, dislocation, deformity, and severe osteoporosis. The three female and three male donors had a mean age of 42 years (range, 35–56 years). The specimens were approved and kept by the Department of Anatomy, Southern Medical University.

Specimen processing

Dissection was performed to expose the sacroiliac joint with intact ligaments, capsule, and pubic symphysis. The specimens were labeled after surface treatment with the imaging agent. Markers were placed on all of the pelvises as follows: two markers were aligned on the medial side of the SIJ and spaced 2 cm apart

FIGURE 1
Prepared pelvic cadaveric specimen and the three pairs of markers. **(A)** Medial point in the left and upper sacroiliac joint; **(B)** later point in the left and upper sacroiliac joint; **(C)** medial point in the left and lower sacroiliac joint; **(D)** lateral point in the left and lower sacroiliac joint; **(E)** left transverse process of the fifth lumbar vertebrae; **(F)** attaching point of the left iliolumbar ligament above the iliac crest.

at a distance of 1 cm from the joint line; two markers were aligned on the lateral side of the SIJ and spaced 2 cm apart at a distance of 1 cm from the joint line. Another two markers were placed on the attachment point of the iliolumbar ligament (IL) on the iliac crest and the costal process of the fifth lumbar vertebra separately. The aforementioned marking points were fixed by marking nails (Figure 1). In addition, the unstable condition with PSI was simulated by sectioning off the pubic symphysis.

Biomechanical protocol

All biomechanical tests were routinely conducted using the servo-hydraulic material testing system (Bose Electro Force 3520-AT; Bose, MN, United States). Also, the Win Test Digital software was used to control the applied load. During the experimental process, the room temperature was maintained at 20–25°C. To minimize the viscoelastic effect of the specimens, a small-scale loading/unloading pre-treatment of the specimens was performed prior to the experiment, as the previous study described (Wang et al., 2018). In turn, three kinds of biomechanical tests were performed on specimens under stable (SIJ without PSI) and unstable conditions (SIJ with PSI). Each test consisted of two sequential phases (loading phase and unloading phase), as follows:

- *Test A (compression)*: Once each pelvis was fixed to the machine, a progressive compression load of 300 N was applied at a rate of 20 mm/min to each specimen over the lumbar spine (L5) and the sacrum in the axial direction so as to simulate the equivalent of half of the weight of a 60-kg person (standing posture). Then the compression load was unloaded instantaneously.
- *Test B (traction)*: A progressive tensile load of 300 N was applied to each specimen at a rate of 20 mm/min in the axial direction. Then the tensile load was unloaded instantaneously.

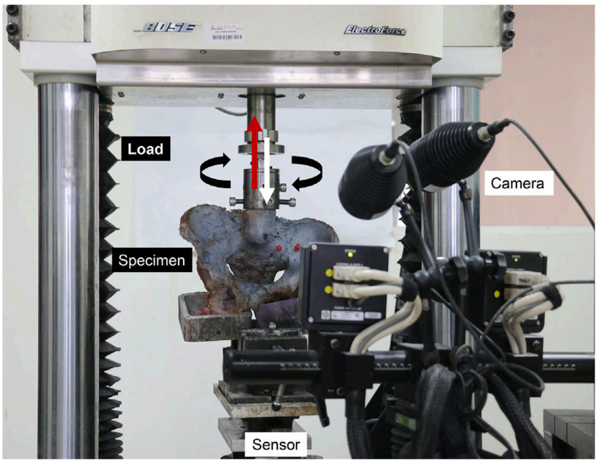

FIGURE 2
Process of biomechanical tests and the simultaneous noncontact optical 3D strain measurement.

- *Test C (oblique-pulling) (rotate to the left)*: In terms of clinical practice and related study, oblique-pulling manipulation was simulated as rotation and traction loading. First, the angle control mode was adopted with a pre-loading angle of 5° at a speed of 1°/sec. Then the maximum loading angle was 10° at a speed of 10°/sec. At the same time, 300 N was uploaded to simulate traction load along with rotation during the manipulation process. Finally, the rotation load was unloaded at the speed of 1°/sec until 0.

To record the separation and nutation of SIJ during the tests, a noncontact optical 3D strain measuring system (Aramis 3D camera 6 M, GOM, Braunschweig, Germany) was used to visualize the markers. For data acquisition, a frequency of four images/second was used. Through digital

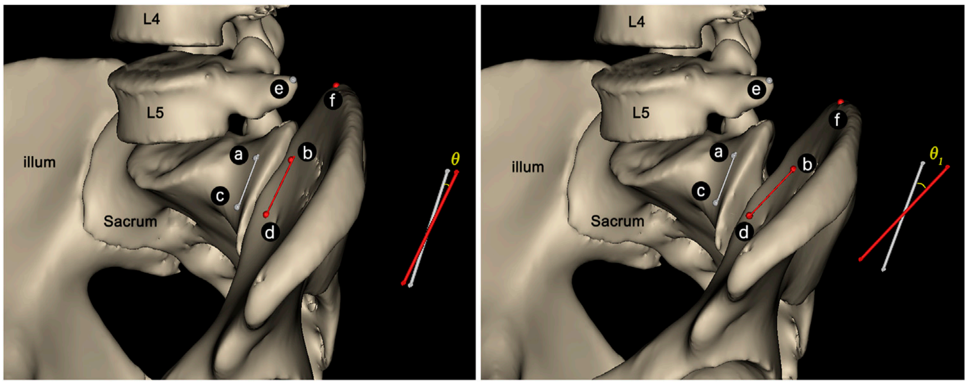

FIGURE 3
Sketch of θ angle between the line **(A,C)** and line **(B,D)**. The angle would increase to θ_1 along with the SIJ nutation **(C)**.

photogrammetry, the positions of these markers were calculated with a resolution of 2,448 × 2050 pixels and a precision error of 0.001 mm (Figure 2).

Mechanical data analysis

To reflect the separation of SIJ, the relative displacements during the loading phase were represented by L_{ab}, L_{cd}, and L_{ef}, respectively. Meanwhile, L_{ba}, L_{dc}, and L_{fe} represented the relative displacements during the unloading process, respectively. Detailed calculations were as follows: $L_{ab} = a_1b_1 – a_0b_0$, $L_{cd} = c_1d_1 – c_0d_0$, $L_{ef} = e_1f_1 – e_0f_0$, $L_{ba} = a_2b_2 – a_0b_0$, $L_{dc} = c_2d_2 – c_0d_0$, and $L_{fe} = e_2f_2 – e_0f_0$, where a_0b_0, c_0d_0, and e_0f_0 are the initial (no loading) distances between three pairs of markers; a_1b_1, c_1d_1, and e_1f_1 are the distances at the end of loading phase; and a_2b_2, c_2d_2, and e_2f_2 are the distances at the end of unloading phase. In addition, SIJ nutation was determined as the iliac rotations with respect to the sacrum.

Therefore, the angle between the line ac (from point a to point c) and line bd (from point b to point d) was defined as θ (Figure 3). The relative angular displacements during the loading phase ($\Delta\theta_1$) and unloading phase ($\Delta\theta_2$) were calculated as follows: $\Delta\theta_1 = \theta_1 – \theta_0$, $\Delta\theta_2 = \theta_2 – \theta_0$, where θ_0 is the initial angle, and θ_1 and θ_2 is the angle at the end of the loading phase, unloading phase, respectively.

Statistical analysis

Variables of the displacement and angle were expressed as mean ± standard deviation. ANOVA of random block design data was used to compare the differences in SIJ relative displacement and angular displacement under different loading conditions. A LSD-t test was used for multiple comparison between groups. An analysis was performed by SPSS software (version 20, IBM Corp). All statistical tests were two-sided, and the level of statistical significance was set at two-sided $p < 0.05$.

Results

Overall strain

During the loading phase, the uneven strain of pelvic specimens with stable SIJ became more and more evident over time, under three tests. The strain mainly concentrated upon the position of SIJ (Figure 4). In the contrast, during the unloading phase, the strain recovered to the origin state gradually (Figure 5). Despite the strain of pelvic specimen with unstable SIJ showing the same trend, the overall strain around SIJ seemed to be greater than the stable (Figures 6, 7).

Angular displacement of sacroiliac joint

During the loading phase, θ in three tests increased gradually, both on the stable and unstable SIJ. For the stable SIJ, the average $\Delta\theta_1$ produced by tests A, B, and C was 0.275°, 0.250°, and 0.098°, respectively. For the unstable SIJ, the $\Delta\theta_1$ produced by tests A and C were significantly greater than the stable condition ($p < 0.05$), with the average of 0.419° and 0.174°, respectively. However, the average $\Delta\theta_1$ produced by test B on the unstable SIJ was 0.165°, which was significantly lower than the stable condition. There was a significant difference in $\Delta\theta_1$ among three tests either ($p < 0.05$). For both stable and unstable SIJ conditions, $\Delta\theta_1$ produced by test A was significantly greater than that of the other two tests ($p < 0.05$). $\Delta\theta_1$ produced by test B was significantly greater than that of test C on stable SIJ ($p < 0.05$), without a significant difference on unstable SIJ ($p > 0.05$) (Table 1; Figure 8).

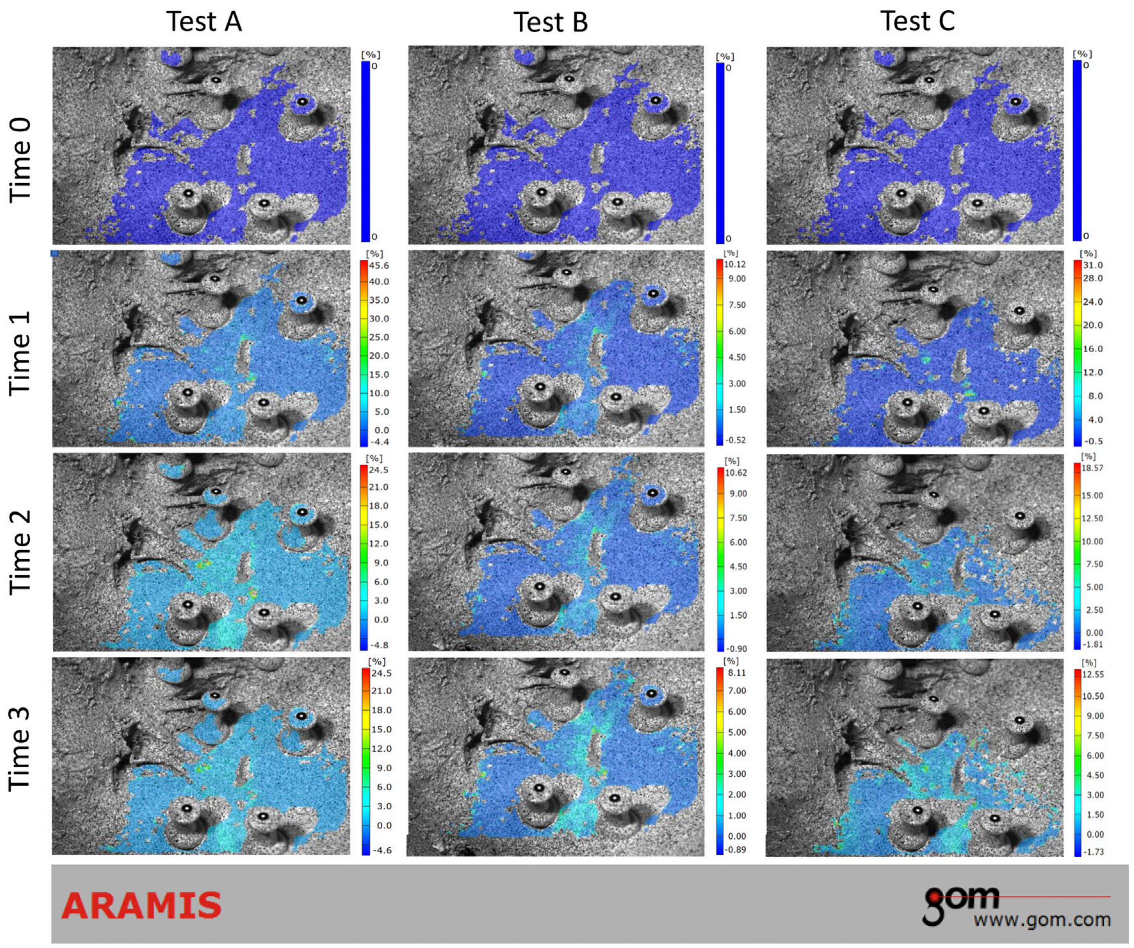

FIGURE 4
Strain trend of stable sacroiliac joint under three tests (loading phase). Time 0 showed the original condition without any load. Time 1 and 2 showed the process of loading. Time 3 showed the ending condition with loads.

During the unloading phase, θ in three tests decreased to the original angle gradually. The average $\Delta\theta_2$ produced by tests A, B, and C was 0.002°, 0.002°, and 0.005° for the stable SIJ and 0.007°, 0.003°, and 0.005°, respectively. No significant difference was found between stable and unstable SIJ ($p > 0.05$), or among three tests ($p > 0.05$) (Table 2; Figure 8).

Displacements of sacroiliac joint

During the loading phase, the distances of ab, cd, and ef in test B and test C increased gradually, both on the stable and unstable SIJ. In the contrast, the aforementioned distances showed a general decreasing trend. For the stable SIJ, L_{ab}, L_{cd}, and L_{ef} were 0.107 mm 0.087 mm, and 0.186 mm in test A; 0.036 mm, 0.013 mm, and 0.186 mm in test B; and 0.062 mm, 0.096 mm, and 0.220 mm in test C, respectively. No matter in which test, L_{ef} was significantly greater than L_{ab} and L_{cd} ($p < 0.05$). In the comparison among three tests, significant differences were found in L_{ab} and L_{cd} ($p < 0.05$), without L_{ef} ($p > 0.05$). In test A, L_{ab} and L_{cd} were significantly greater than test B ($p < 0.05$). In test B, L_{cd} was lower than test C ($p < 0.05$). For the unstable SIJ, L_{ab}, L_{cd}, and L_{ef} were 0.100 mm, 0.098 mm, and 0.216 mm in test A; 0.033 mm, 0.016 mm, and 0.183 mm in test B; 0.101 mm, 0.078 mm, and 0.259 mm in test C, respectively. In the three tests, L_{ef} was significantly greater than L_{ab} and L_{cd} ($p < 0.05$). In the comparison among three tests, significant differences were found in L_{ab}, L_{cd}, and L_{ef} ($p < 0.05$). In test A, L_{ab} and L_{cd} were significantly greater than test B ($p < 0.05$). In test B, L_{ab}, L_{cd}, and L_{ef} were lower than test C ($p < 0.05$). Moreover, compared to the stable SIJ, L_{ab} in test C was greater ($p < 0.05$); however, no significant difference was found in other displacements ($p > 0.05$) (Table 1; Figure 9).

During the unloading phase, the variation in distances showed the opposite trend. For the stable SIJ, L_{ba}, L_{dc}, and L_{fe}

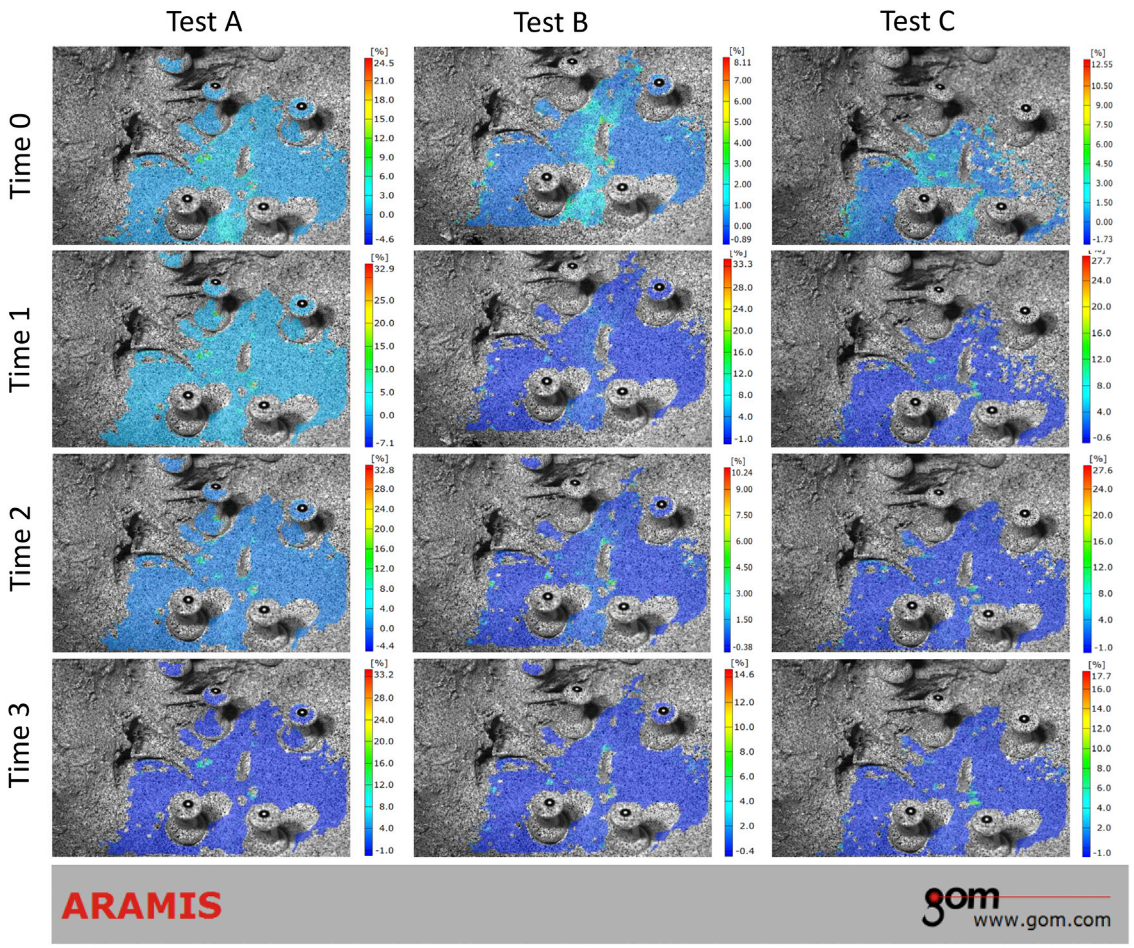

FIGURE 5
Strain trend of stable sacroiliac joint under three tests (unloading phase). Time 0 showed the original condition with the maximum load, which was the same as the ending condition during loading phase. Time 1 and 2 showed the process of unloading. Time 3 showed the ending condition without any load.

were 0.003 mm, 0.003 mm, and 0.002 mm in test A; 0.003 mm, 0.003 mm, and 0.002 mm in test B; 0.005 mm, 0.002 mm, and 0.002 mm in test C, respectively. For the unstable SIJ, L_{ba}, L_{dc}, and L_{fe} were 0.006 mm, 0.004 mm, and 0.005 mm in test A; 0.006 mm, 0.004 mm, and 0.002 mm in test B; 0.004 mm, 0.003 mm, and 0.003 mm in test C, respectively. No significant difference was found among three tests, or between the stable and the unstable SIJs ($p > 0.05$) (Table 2; Figure 9).

Discussion

The purpose of this study was to evaluate the current evidence on the magnitude of SIJ motion followed by oblique-pulling manipulation. In this study, the relative motion of the SIJ was observed by simulating the compression, traction, and oblique-pulling loads on human pelvic cadaveric specimens. The results revealed that the oblique-pulling manipulation could only cause a slight nutation of the stable SIJ. The relative angular displacement was as small as less than 0.2°, which was significantly less than the angular displacement under axial compression and traction loads. In the meantime, this study found that both the tensile and oblique-pulling loads widened the joint space of the normal SIJ, whereas the compression load narrowed the joint space of SIJ. The phenomenon is consistent with the anatomical features of SIJ. However, the widened joint space caused by the oblique-pulling load was not more than 0.2 mm, indicating that the oblique-pulling manipulation may separate SIJ to a very slight degree. Also, the differences in displacements proved that the oblique-pulling manipulation might have a better effect on SIJ in separation compared to traction therapy. Despite this, no

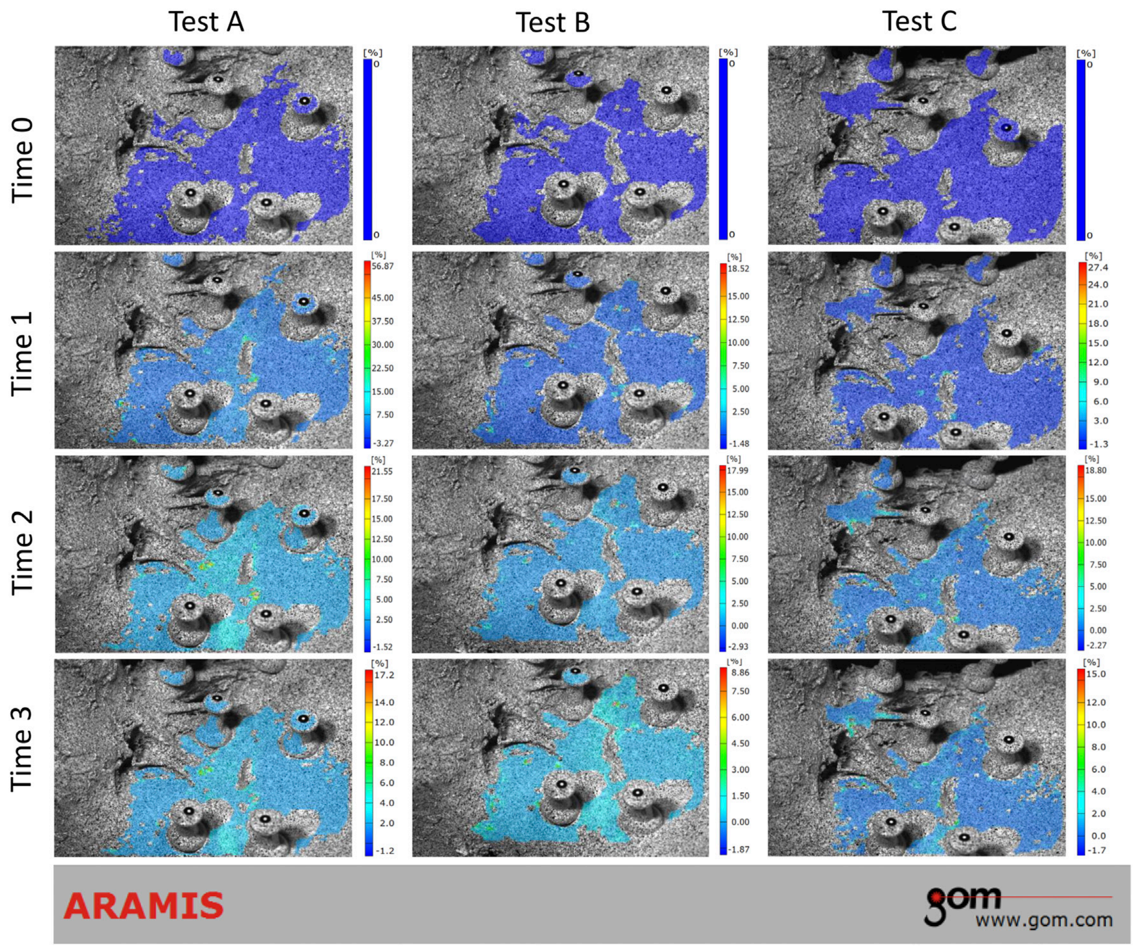

FIGURE 6
Strain trend of the unstable sacroiliac joint with injured pubic symphysis under three tests (loading phase). Time 0 showed the original condition without any load. Time 1 and 2 showed the process of loading. Time 3 showed the ending condition with loads.

significant difference was found, compared to the physiological compression load. That is, the separation of SIJ caused by oblique-pulling manipulation may recover due to the weight-bearing of the pelvis in the standing and sitting positions. Previously, it has been reported that the particularity of SIJ is that the range of motion (ROM) of the joint is minimal (Le Huec et al., 2019). The SIJ motion has been evaluated using different techniques, such as Doppler techniques, radio stereometric, ultrasound, and Roentgen stereophotogrammetric (Sturesson et al., 1989; Vlaanderen et al., 2005).

Studies have shown that ROM of the SIJ has a maximum rotation of about 1.5° in the axial direction, with 1.2° in males and 2.8° in females (Brunner et al., 1991; Kiapour et al., 2020), and a lateral bend of approximately 0.8° (Miller et al., 1987; Cardwell et al., 2021), and the rotation in different planes can be as small as 0.01°, not more than 3°(Sturesson et al., 1989; Sturesson et al., 2000; Foley and Buschbacher, 2006; Cho and Kwak, 2021). The minimum rotation angle is similar to the minimum rotation angle in this study (0.098°). Some cadaveric studies have shown that the average rotation of the sacrum around the *x*-axis is 3.2° (flexion + extension); fixation of only one iliac bone results in an average rotation of 6.2° (Miller et al., 1987; Sturesson et al., 2000). The angular motion of the SIJ has also been observed by sensors and computer techniques and found to be 9.0 ± 6.5° in the sagittal plane and 5.0 ± 3.9° in the transverse plane (Smidt et al., 1995). The level of motion in patients with SIJ pain never exceeds 1.6 mm in healthy individuals flattened 0.7 mm (Sturesson et al., 1989; H A C Jacob and Kissling, 1995), and the SIJ did not flatten more than 2 mm along the axis (Zheng et al., 1997; Kiapour et al., 2020). Therefore, most current studies conclude that the angular motion of the SIJ generally does not exceed 3°, with a displacement range of 0.3–7 mm (Walker, 1992). The angular displacement of the stable SIJ in this study ranged from 0.098° to 0.275°, with a translation range of 0.013–0.220 mm. Only if the

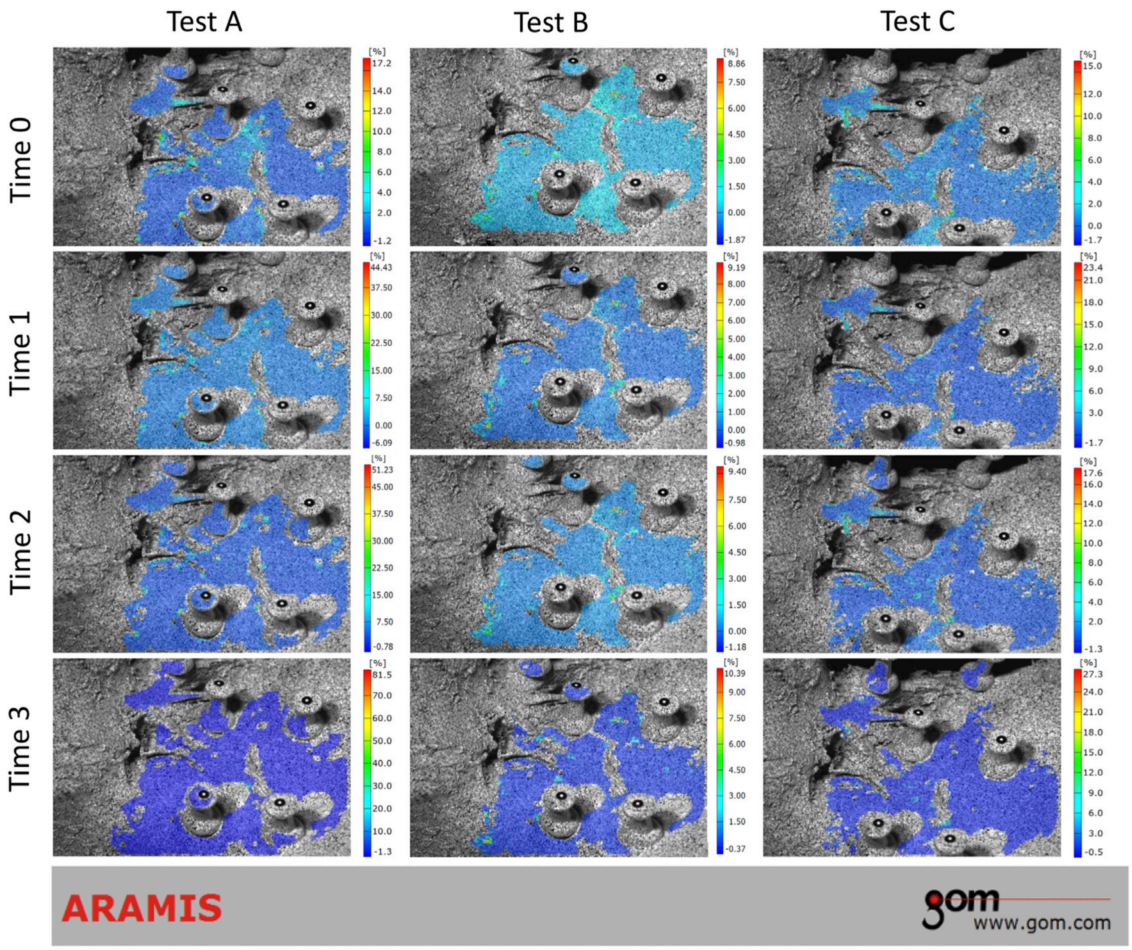

FIGURE 7
Strain trend of the unstable sacroiliac joint with injured pubic symphysis under three tests (unloading phase). Time 0 showed the original condition with the maximum load, which was the same as the ending condition during loading phase. Time 1 and 2 showed the process of unloading. Time 3 showed the ending condition without any load.

pubic symphysis diastasis occurred to simulate the unstable SIJ, ROM would increase with an angular range of 0.174°–0.419°, as well as a translation range of 0.016–0.259 mm. This finding proved the vital importance of pubic symphysis on the stability or mobility of SIJ again, as related studies have highlighted (Hammer et al., 2019; Ricci et al., 2020). Under this condition, it may become uneasy to realize the mobilization of SIJ with intact pubic symphysis, through oblique-pulling manipulation. Moreover, it has been reported that the mobility of the SIJ depends on a position of the joint and the load it is applied to. Increasing the load on the SIJ leads to a ventral inclination of the sacrum with stretching of dorsal ligaments, which shifts the bone position and interferes with its mobility (Tullberg et al., 1998) (de Toledo et al., 2020). Regarding the clinical procedure, oblique-pulling manipulation resembles high-velocity and low-amplitude thrust manipulation. As demonstrated in related studies, through the Roentgen stereophotogrammetric analysis, high-velocity, and low-amplitude thrust manipulation in the SIJ does not alter the position relationship between the sacrum and the ilium bone in healthy individuals (de Toledo et al., 2020). Although the analyzing method is different, the aforementioned results are consistent with our findings. Therefore, the mechanism of the oblique-pulling manipulation in treating SIJ dysfunction needs to be reconsidered.

Because of its importance in maintaining the joint mobility, ligament around SIJ has aroused far more concern, such as IL, sacrotuberous ligament (STL), and long dorsal sacroiliac ligament (LDL) (Vleeming et al., 1996) (van Wingerden et al., 1993) (de Toledo et al., 2020). STL showed extensive connections with the gluteus maximus muscle, long head of the biceps femoris muscle, and

TABLE 1 SIJ nutation and separation during the loading phase.

		N	Angular displacement $\Delta\theta_1$ (°)	Displacement				
				L_{ab} (mm)	L_{cd} (mm)	L_{ef} (mm)	F value	p value
Stable SIJ	Test A	6	$0.275 \pm 0.117^{a,d}$	$-0.107 \pm 0.048^{,b,c}$	$-0.087 \pm 0.025^{b,c}$	-0.186 ± 0.049	9.192	0.002
	Test B	6	0.250 ± 0.102^{d}	0.036 ± 0.024^{b}	$0.013 \pm 0.007^{b,d}$	0.186 ± 0.036^{a}	82.791	0.000
	Test C	6	0.098 ± 0.045^{a}	0.062 ± 0.043^{ab}	0.096 ± 0.027^{b}	0.220 ± 0.035	33.039	0.000
	F value		6.384	4.861	26.671	1.456	N/A	N/A
	p value		0.010*	0.024*	0.000*	0.264	N/A	N/A
Unstable SIJ	Test A	6	$0.419 \pm 0.118^{c,d}$	$-0.100 \pm 0.072^{b,c}$	$-0.098 \pm 0.066^{b,c}$	-0.216 ± 0.044	7.146	0.007
	Test B	6	0.165 ± 0.064	$0.033 \pm 0.019^{b,d}$	$0.016 \pm 0.006^{b,d}$	0.183 ± 0.037^{d}	86.926	0.000
	Test C	6	0.174 ± 0.054	0.101 ± 0.041^{b}	0.078 ± 0.025^{b}	0.259 ± 0.044	41.525	0.000
	F value		17.986	3.855	6.474	4.930	N/A	N/A
	p value		0.000*	0.045*	0.009*	0.023*	N/A	N/A

[a]$P < 0.05$ vs. unstable SIJ; [b]$P<0.05$ vs. L_{ef} ; [c]$P<0.05$ vs. Test B; [d]$P<0.05$ vs. Test C; *$p < 0.05$.

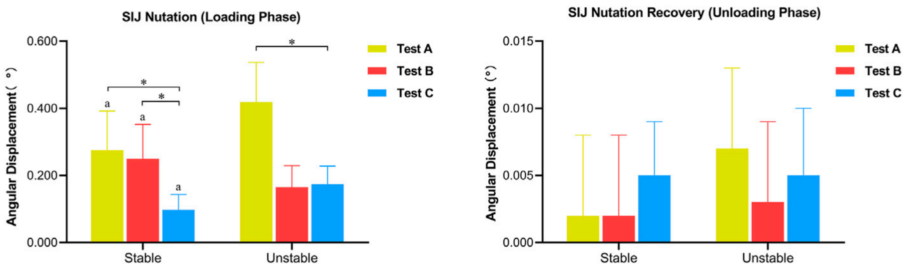

FIGURE 8
Differences in angular displacement of SIJ ([a]$P < 0.05$ vs. unstable SIJ; *$p < 0.05$).

TABLE 2 SIJ nutation and separation recovery during the unloading phase.

		N	Angular displacement $\Delta\theta_2$ (°)	Displacement				
				L_{ba} (mm)	L_{dc} (mm)	L_{fe} (mm)	F value	p value
Stable SIJ	Test A	6	0.002 ± 0.006	0.003 ± 0.005	0.003 ± 0.001	0.002 ± 0.002	0.309	0.819
	Test B	6	0.002 ± 0.006	0.003 ± 0.005	0.003 ± 0.001	0.002 ± 0.002	0.436	0.729
	Test C	6	0.005 ± 0.004	0.005 ± 0.002	0.002 ± 0.003	0.002 ± 0.003	1.991	0.148
	F value		0.688	0.193	1.199	0.659	N/A	N/A
	p value		0.518	0.826	0.329	0.532	N/A	N/A
Unstable SIJ	Test A	6	0.007 ± 0.006	0.006 ± 0.002	0.004 ± 0.004	0.005 ± 0.003	0.522	0.604
	Test B	6	0.003 ± 0.006	0.006 ± 0.002	0.004 ± 0.004	0.002 ± 0.003	2.149	0.151
	Test C	6	0.005 ± 0.005	0.004 ± 0.005	0.003 ± 0.001	0.003 ± 0.001	0.209	0.814
	F value		0.819	0.891	0.156	1.520	N/A	N/A
	p value		0.460	0.431	0.857	0.250	N/A	N/A

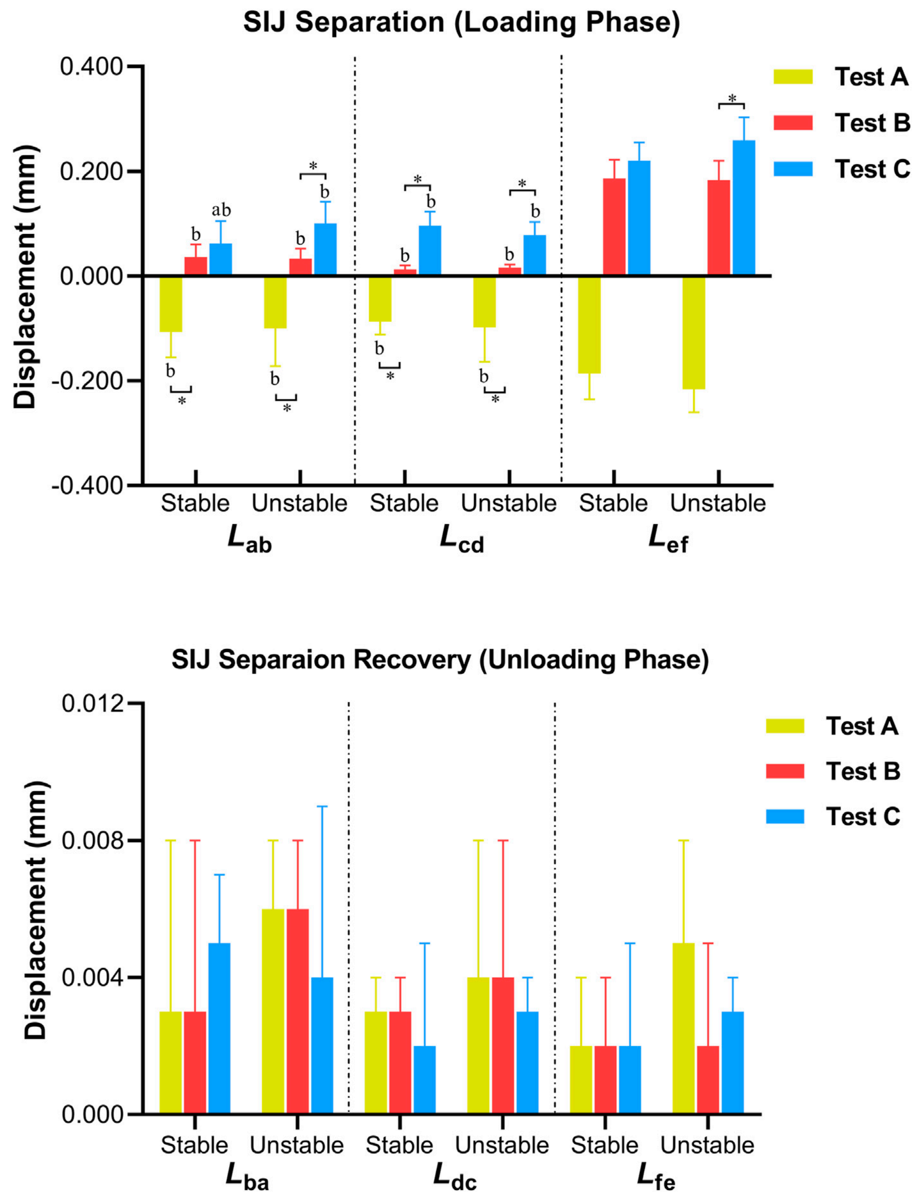

FIGURE 9
Differences in the displacement of SIJ ($^{a}P < 0.05$ vs. unstable SIJ; $^{b}P<0.05$ vs. L_{ef} ; $*p < 0.05$).

sacrospinous ligament but also has extensive connections to the iliococcygeus muscle on the anterior. It was shown that the incremental load of STL restricts the amount of nutation in the SIJ. LDL is closely related to the aponeurosis of the erector spinae muscle and the posterior layer of the thoracolumbar fascia (van Wingerden et al., 1993). Counternutation in the SIJ increases tension of the LDL, and the nutation slackens it. Therefore, the tension applied to the dorsal sacroiliac ligament, or the LDL appears to restrict the contrary movements in the SIJ. Both ligaments are partially connected (Vleeming et al., 1996) (van Wingerden et al., 1993). In this study, during the oblique-pulling, compression, and tensile tests, another important finding was that L_{ef} increased more obviously than the relative displacements at sites above and below the SIJ both on the stable and unstable joints. Taking the anatomical location into consideration, we focused on the biomechanical response of IL. IL, as an important primary source of low back pain (Sims and Moorman, 1996), originates from the fourth and fifth lumbar costal process to the iliac crest. Numerous studies have descriptions sketched the shape of IL. For example, Pool-Goudzwaard et al. characterized the ligament up to seven portions, especially including the sacroiliac part. This part originated on the sacrum and blended with the interosseous sacroiliac ligaments, with the length of 30.5 in women or 31.0 mm in men, the width of 12.7 mm in women or 14.5 mm in men, and the thickness of 1.6 mm in women or 1.5 mm in men (Pool-Goudzwaard et al., 2001). In addition, Hammer et al. described the minimal two parts of this ligament, mainly composed of the anterior part and the posterior part, with the length of 25–30 mm and the thickness of 4 mm (Hammer et al., 2010). Owing to the aforementioned characteristics, it has been described that IL restricts the movement of the SIJ, and the effect may be associated with the thickness, the length, and the angle between the insertion of the anterior and posterior parts. In the sagittal plane, the movement of SIJ performed as nutation. Previous biomechanical tests on embalmed pelvic specimens have found that the slope of the SIJ load-nutation curve would increase 28.1%, when the IL was totally cut. That is, injury to the ligament could result in increased up and down movement of the SIJ in sagittal plane, and this should be considered in patients presenting with symptoms related to this hypermobility (Pool-Goudzwaard et al., 2001; Pool-Goudzwaard et al., 2003). Therefore, we speculated that oblique-pulling manipulation might have a better effect of releasing and stretching on IL, and the effect is more apparent than the effects on SIJ itself. Studies have shown that the friction and coupling of the SIJ articular surfaces combined with the surrounding ligaments made the SIJ more stable (Snijders et al., 1993) (Cardwell et al., 2021).

To further explore the possible biomechanical effects of oblique-pulling manipulation on SIJ, in this study, the strain and relative motion of the SIJ were observed by simulating the loading of human pelvic specimens. Positive effects of manipulation may be promoting normal joint mobility, which may release articular or related soft tissue adhesions and synovial folds (Tullberg et al., 1998). There is evidence that manual therapy may refine the SIJ function by acting on nearby muscles (Behdad Hamidi-Ravari et al., 2014). Muscles generate strength, guide movements, and increase pelvic girdle stability (Vleeming et al., 2012). Previous studies on manipulation have lacked in-depth research on the immediate biomechanical effect on the joint when the force was withdrawn. In order to solve this problem, this study did not only observe nutation and separation of SIJ during the loading process but also measured them during the unloading process. The final results showed that the effect disappeared on the normal SIJ, when the force was withdrawn. The nutation and separation recovered nearly after withdrawing the loads, regardless of the stable or unstable joint. Since it was a transient effect, the weak effect on the SIJ produced by the oblique-pulling manipulation may not be sustainable. This is another reason to suspect that promoting joint mobility is not an essential mechanism of oblique-pulling manipulation for the treatment of SIJ dysfunction.

However, it should be mentioned that there are some limitations in the current study. First, formalin-embalmed specimens rather than fresh-frozen specimens were tested, because of financial constraints and considerations about the less ROM of SIJ. The fixation methods may decrease the biomechanical properties of soft tissue and bone may decrease, further resulting in few elongations seen in the tests. Second, no bone density scan was performed before test; thus, the effects of osteoporosis on the biomechanical response remain unknown. Third, the effects of loads on sacroiliac nodal ligament and posterior long sacroiliac ligament were not well investigated by 3D photogrammetry, owing to the complex and irregular posterior structure. Finally, as with other cadaver studies, muscle forces were not simulated. All of the issues need to be further investigated.

Conclusion

The oblique-pulling manipulation could cause the slight nutation and separation of SIJ; however, the resulting SIJ motion is not more than that of normal people standing and bearing weight. At the same time, the effect of the manipulation is transient, and the effect disappears after the force is removed. Manipulation has a weak effect on the motion of SIJ and thus triggering the SIJ may not be the primary mechanism of the oblique-pulling manipulation. The stretching and loosening of the ligaments around the SIJ by the oblique-pulling manipulation to achieve the therapeutic effect might be another mechanism of action of the manipulation.

Data availability statement

The raw data supporting the conclusions of this article will be made available by the authors, without undue reservation.

Ethics statement

The studies involving human participants were reviewed and approved by Ethics Committee of Guangdong Provincial Hospital of Traditional Chinese Medicine. The patients/participants provided their written informed consent to participate in this study.

Author contributions

JL: conceptualization, investigation, writing—original draft, and manuscript revision. YL, HC, and RP: data curation, visualization, and writing—original draft. HC: data curation and investigation. DL and JQ: supervision and writing—review and editing.

Funding

This work was supported by the Science and Technology Project of Guangdong Province [grant number 2020A1515110966]; Project of China Postdoctoral Science Foundation [grant number 2021M690757].

Conflict of interest

The authors declare that the research was conducted in the absence of any commercial or financial relationships that could be construed as a potential conflict of interest.

Publisher's note

References

Antonio, A., Wolfgang, W., Robert, R., Fullerton, B., and Carla, C. (2013). The anatomical and functional relation between gluteus maximus and fascia lata. *J. Bodyw. Mov. Ther.* 17 (4), 512–517. doi:10.1016/j.jbmt.2013.04.004

Bertoldo, D., Pirri, C., Roviaro, B., Stecco, L., Day, J. A., Fede, C., et al. (2021). Pilot study of sacroiliac joint dysfunction treated with a single session of fascial manipulation method: Clinical implications for effective pain reduction. *Medicina* 57 (7), 691. doi:10.3390/medicina57070691

Brunner, C., Kissling, R., and Jacob, H. A. (1991). The effects of morphology and histopathologic findings on the mobility of the sacroiliac joint. *Spine* 16 (9), 1111–1117. doi:10.1097/00007632-199109000-00017

Buchanan, P., Vodapally, S., Lee, D. W., Hagedorn, J. M., Bovinet, C., Strand, N., et al. (2021). Successful diagnosis of sacroiliac joint dysfunction. *Jpr* Vol. 14, 3135–3143. doi:10.2147/JPR.S327351

Capobianco, R., Cher, D., and Cher, S. S. (2015). Safety and effectiveness of minimally invasive sacroiliac joint fusion in women with persistent post-partum posterior pelvic girdle pain: 12-month outcomes from a prospective, multi-center trial. *Springerplus* 4, 570. doi:10.1186/s40064-015-1359-y

Cardwell, M. C., Meinerz, C. M., Martin, J. M., Beck, C. J., Wang, M., and Schmeling, G. J. (2021). Systematic review of sacroiliac joint motion and the effect of screw fixation. *Clin. Biomech.* 85, 105368. doi:10.1016/j.clinbiomech.2021.105368

Carvalho, A., Ré, Daniela, Lam, David, Cunha, Daniela Martins, Sena, Ilírian Buosi, and Bertolini, Gladson Ricardo Flor (2013). Efeito imediato da manipulação osteopática tibiotársica no equilíbrio estático de mulheres jovens. *Rev. Bras. Ciênc. Esporte* 35 (2), 455–467. doi:10.1590/S0101-32892013000200014

Cho, H. J., and Kwak, D. S. (2021). Movement of the sacroiliac joint: Anatomy, systematic review, and biomechanical considerations. *Proc. Inst. Mech. Eng. H.* 235 (3), 357–364. doi:10.1177/0954411920978021

Cusi, M. F. (2010). Paradigm for assessment and treatment of SIJ mechanical dysfunction. *J. Bodyw. Mov. Ther.* 14 (2), 152–161. doi:10.1016/j.jbmt.2009.12.004

de Toledo, D. F. A., Kochem, F. B., and Silva, J. G. (2020). High-velocity, low-amplitude manipulation (hvla) does not alter three-dimensional position of sacroiliac joint in healthy men: A quasi-experimental study. *J. Bodyw. Mov. Ther.* 24 (1), 190–193. doi:10.1016/j.jbmt.2019.05.020

Des Jarlais, D. C., Lyles, C., Crepaz, N., and Group, T. (2004). Improving the reporting quality of nonrandomized evaluations of behavioral and public health interventions: The TREND statement. *Am. J. Public Health* 94 (3), 361–366. doi:10.2105/ajph.94.3.361

Foley, B. S., and Buschbacher, R. M. (2006). Sacroiliac joint pain. *Am. J. Phys. Med. Rehabil.* 85 (12), 997–1006. doi:10.1097/01.phm.0000247633.68694.c1

Gartenberg, A., Nessim, A., and Cho, W. (2021). Sacroiliac joint dysfunction: Pathophysiology, diagnosis, and treatment. *Eur. Spine J.* 30 (10), 2936–2943. doi:10.1007/s00586-021-06927-9

Grassi, O., de Souza, M. Z., Ferrareto, S. B., Montebelo, M. I., and Guirro, E. C. (2011). Immediate and lasting improvements in weight distribution seen in baropodometry following a high-velocity, low-amplitude thrust manipulation of the sacroiliac joint. *Man. Ther.* 16 (5), 495–500. doi:10.1016/j.math.2011.04.003

Graup, S. d. A. B., de Araújo Bergmann, Mauren, and Bergmann, Gabriel Gustavo (2014). Prevalence of nonspecific lumbar pain and associated factors among adolescents in Uruguaiana, state of Rio Grande do Sul. *Rev. Bras. Ortop. (English Ed.* 49 (6), 661–667. doi:10.1016/j.rboe.2014.10.003

Hamidi-Ravari, Behdad, Tafazoli, Sharwin, Chen, Hamilton, and Perret, Danielle (2014). Diagnosis and current treatments for sacroiliac joint dysfunction: A review. *Curr. Phys. Med. Rehabil. Rep.* 2 (1), 48–54. doi:10.1007/s40141-013-0037-7

Hammer, N., Scholze, M., Kibsgård, T., Klima, S., Schleifenbaum, S., Seidel, T., et al. (2019). Physiological *in vitro* sacroiliac joint motion: A study on three-dimensional posterior pelvic ring kinematics. *J. Anat.* 234 (3), 346–358. doi:10.1111/joa.12924

Hammer, N., Steinke, H., Böhme, J., Stadler, J., Josten, C., and Spanel-Borowski, K. (2010). Description of the iliolumbar ligament for computer-assisted reconstruction. *Ann. Anat. - Anatomischer Anzeiger* 192 (3), 162–167. doi:10.1016/j.aanat.2010.02.003

Huijbregts, P. A. (2008). Evidence-based diagnosis and treatment of the painful sacroiliac joint. *J. Man. Manip. Ther.* 16 (3), 153–154. doi:10.1179/jmt.2008.16.3.153

Jacob, H. A. C., and Kissling, R. O. (1995). The mobility of the sacroiliac joints in healthy volunteers between 20 and 50 years of age. *Clin. Biomech.* 10 (7), 352–361. doi:10.1016/0268-0033(95)00003-4

Kiapour, A., Joukar, A., Elgafy, H., Erbulut, D. U., Agarwal, A. K., and Goel, V. K. (2020). Biomechanics of the sacroiliac joint: Anatomy, function, biomechanics, sexual dimorphism, and causes of pain. *Int. J. Spine Surg.* 14 (1), S3–S13. doi:10.14444/6077

Le Huec, J. C., Tsoupras, A., Leglise, A., Heraudet, P., Celarier, G., and Sturresson, B. (2019). The sacro-iliac joint: A potentially painful enigma. Update on the diagnosis and treatment of pain from micro-trauma. *Orthop. Traumatology Surg. Res.* 105 (1), S31–S42. doi:10.1016/j.otsr.2018.05.019

Miller, J. A., Schultz, A. B., and Andersson, G. B. (1987). Load-displacement behavior of sacroiliac joints. *J. Orthop. Res.* 5 (1), 92–101. doi:10.1002/jor.1100050112

Moyer, C. A., Rounds, J., and Hannum, J. W. (2004). A meta-analysis of massage therapy research. *Psychol. Bull.* 130 (1), 3–18. doi:10.1037/0033-2909.130.1.3

Pool-Goudzwaard, A., Hoek van Dijke, G., Mulder, P., Spoor, C., Snijders, C., and Stoeckart, R. (2003). The iliolumbar ligament: Its influence on stability of the sacroiliac joint. *Clin. Biomech.* 18 (2), 99–105. doi:10.1016/s0268-0033(02)00179-1

Pool-goudzwaard, A. L., Kleinrensink, G. J., Snijders, C. J., Entius, C., and Stoeckart, R. (2001). The sacroiliac part of the iliolumbar ligament. *J. Anat.* 199 (4), 457–463. doi:10.1046/j.1469-7580.2001.19940457.x

Ricci, P. L., Maas, S., Gerich, T., and Kelm, J. (2020). Influence of pubic symphysis stiffness on pelvic load distribution during single leg stance. *Int. J. Numer. Meth Biomed. Engng* 36 (4), e3319. doi:10.1002/cnm.3319

Shokri, E., Kamali, F., Sinaei, E., and Ghafarinejad, F. (2018). Spinal manipulation in the treatment of patients with MRI-confirmed lumbar disc herniation and sacroiliac joint hypomobility: A quasi-experimental study. *Chiropr. Man. Ther.* 26, 16. doi:10.1186/s12998-018-0185-z

Sims, J. A., and Moorman, S. J. (1996). The role of the iliolumbar ligament in low back pain. *Med. Hypotheses* 46 (6), 511–515. doi:10.1016/s0306-9877(96)90123-1

Smidt, G. L., McQuade, K., Wei, S. H., and Barakatt, E. (1995). Sacroiliac kinematics for reciprocal straddle positions. *Spine* 20 (9), 1047–1054. doi:10.1097/00007632-199505000-00011

Snijders, C. J., Vleeming, A., and Stoeckart, R. (1993). Transfer of lumbosacral load to iliac bones and legs. *Clin. Biomech.* 8 (6), 295–301. doi:10.1016/0268-0033(93)90003-Z

Standring, S. (2016). *Gray's anatomy : The anatomical basis of clinical practice*. New York: Elsevier Limited.

Sturesson, B., Selvik, G., and Udén, A. (1989). Movements of the sacroiliac joints. *Spine* 14 (2), 162–165. doi:10.1097/00007632-198902000-00004

Sturesson, B., Uden, A., and Vleeming, A. (2000). A radiostereometric analysis of the movements of the sacroiliac joints in the reciprocal straddle position. *Spine* 25 (2), 214–217. doi:10.1097/00007632-200001150-00012

Tang, S., Qian, X., Zhang, Y., and Liu, Y. (2016). Treating low back pain resulted from lumbar degenerative instability using Chinese tuina combined with core stability exercises: A randomized controlled trial. *Complementary Ther. Med.* 25, 45–50. doi:10.1016/j.ctim.2016.01.001

Tullberg, T., Blomberg, S., Branth, B., and Johnsson, R. (1998). Manipulation does not alter the position of the sacroiliac joint. *Spine* 23 (10), 1124–1128. doi:10.1097/00007632-199805150-00010

van Wingerden, J. P., Vleeming, A., Snijders, C. J., and Stoeckart, R. (1993). A functional-anatomical approach to the spine-pelvis mechanism: Interaction between the biceps femoris muscle and the sacrotuberous ligament. *Eur. Spine J.* 2 (3), 140–144. doi:10.1007/BF00301411

Vlaanderen, E., Conza, N. E., Snijders, C. J., Bouakaz, A., and De Jong, N. (2005). Low back pain, the stiffness of the sacroiliac joint: A new method using ultrasound. *Ultrasound Med. Biol.* 31 (1), 39–44. doi:10.1016/j.ultrasmedbio.2004.09.014

Vleeming, A., Pool-Goudzwaard, A. L., Hammudoghlu, D., Stoeckart, R., Snijders, C. J., and Mens, J. M. (1996). The function of the long dorsal sacroiliac ligament. *Spine* 21 (5), 556–562. doi:10.1097/00007632-199603010-00005

Vleeming, A., Schuenke, M. D., Masi, A. T., Carreiro, J. E., Danneels, L., and Willard, F. H. (2012). The sacroiliac joint: An overview of its anatomy, function and potential clinical implications. *J. Anat.* 221 (6), 537–567. doi:10.1111/j.1469-7580.2012.01564.x

Vleeming, A., and Schuenke, M. (2019). Form and force closure of the sacroiliac joints. *PM&R.* 11 (1), S24–S31. doi:10.1002/pmrj.12205

Vleeming, A., Stoeckart, R., Volkers, A. C., and Snijders, C. J. (1990). Relation between form and function in the sacroiliac joint. *Spine* 15 (2), 130–132. doi:10.1097/00007632-199002000-00016

Walker, J. M. (1992). The sacroiliac joint: A critical review. *Phys. Ther.* 72 (12), 903–916. doi:10.1093/ptj/72.12.903

Wang, F., Zhang, J., Feng, W., Liu, Q., Yang, X., Zhang, H., et al. (2018). Comparison of human lumbar disc pressure characteristics during simulated spinal manipulation vs. spinal mobilization. *Mol. Med. Rep.* 18 (6), 5709–5716. doi:10.3892/mmr.2018.9591

Zheng, N., Watson, L. G., and Yong-Hing, K. (1997). Biomechanical modelling of the human sacroiliac joint. *Med. Biol. Eng. Comput.* 35 (2), 77–82. doi:10.1007/BF02534134

frontiers | Frontiers in Bioengineering and Biotechnology

TYPE Original Research
PUBLISHED 27 September 2022
DOI 10.3389/fbioe.2022.965295

OPEN ACCESS

EDITED BY
Bin Wang,
Chongqing Medical University, China

REVIEWED BY
Wai Leung Ambrose Lo,
The First Affiliated Hospital of Sun Yat-sen University, China
Chich-Haung Richard Yang,
Tzu Chi University, Taiwan

*CORRESPONDENCE
Yan Qi,
fuchankeyisheng@163.com

†These authors have contributed equally to this work and share first authorship

SPECIALTY SECTION
This article was submitted to Biomechanics,
a section of the journal
Frontiers in Bioengineering and Biotechnology

RECEIVED 09 June 2022
ACCEPTED 07 September 2022
PUBLISHED 27 September 2022

CITATION
Chang X-Q, Chen X-P, Shen Y-X, Wang K, Huang S-J, Qi Y and Niu W-X (2022), The deer play in Wuqinxi and four-point hand–knee kneeling positions for training core muscle function and spinal mobility.
Front. Bioeng. Biotechnol. 10:965295.
doi: 10.3389/fbioe.2022.965295

The deer play in Wuqinxi and four-point hand–knee kneeling positions for training core muscle function and spinal mobility

Xiao-Qian Chang[1,2†], Xin-Peng Chen[1,2†], Yi-Xin Shen[1,2], Kuan Wang[1], Shang-Jun Huang[1,2], Yan Qi[1,2*] and Wen-Xin Niu[1,2]

[1]Shanghai YangZhi Rehabilitation Hospital (Shanghai Sunshine Rehabilitation Center), School of Medicine, Tongji University, Shanghai, China, [2]Laboratory of Biomechanics and Rehabilitation Engineering, School of Medicine, Tongji University, Shanghai, China

The four-point kneeling exercise is a core stabilization exercise that provides the spine with dynamic stability and neuromuscular control. In the traditional Chinese exercise Wuqinxi, deer play is performed in a hand–foot kneeling (HFK) position, which is remarkably similar to the four-point hand–knee kneeling (HKK) position. However, the differences in spinal function promotion between these two positions are poorly understood. The aim of this study was to investigate muscle activation patterns and spinal kinematics during specific core stabilization training to provide evidence for selecting specific exercises. A total of 19 healthy adults were recruited to perform HFK and HKK. The rotation angle of the C7–T4 vertebra and the surface EMG signals of abdominal and lumbar muscles on both sides were collected. The paired *t*-test showed that the vertebral rotation angles were significantly higher during HKK than HFK, and the intra-group differences mainly occurred at the level of the thoracic vertebra. The muscle activation of both sides of the rectus abdominis and external oblique in HFK was significantly higher than in HKK when the upper limb was lifted ($p < 0.05$). The activation of the ipsilateral lumbar multifidus and erector spinae muscles was significantly higher during the HKK position than during HFK when the lower limb was lifted ($p < 0.05$). HFK provided more training for strengthening abdominal muscles, while HKK could be recommended for strengthening lumbar muscles and increasing spine mobility. These findings can be used to help physiotherapists, fitness coaches, and others to select specific core exercises and develop individualized training programs.

KEYWORDS

Wuqinxi exercise, core stabilization exercise, surface electromyography (EMG), vertebral rotation, core muscle stability

Introduction

Core stabilization exercise (CSE) is designed to promote the muscular co-activation patterns and the stability of the spinal structures (Essendrop et al., 2002; Brown and McGill, 2008; Oliva-Lozano and Muyor, 2020). It has been widely used in training programs to improve health and physical fitness as well as in clinical rehabilitation for the elderly (Areeudomwong and Buttagat, 2019; Ozsoy et al., 2019; Kim et al., 2020; Vera-Garcia et al., 2020). A well-trained core is essential for optimal performance and injury prevention (Cortell-Tormo et al., 2017).

Four-point kneeling exercise is regarded as a CSE that provides dynamic stability and neuromuscular control to the spine (O'Sullivan, 2000; Martuscello et al., 2013; Cortell-Tormo et al., 2017). It is a quadruped position, with the hip and knee at 90° flexion while maintaining abdominal hollowing (Stevens et al., 2007b; Pirouzi et al., 2013). To distinguish it from the other positions in this article, we call it the four-point hand–knee kneeling (HKK) position. Wuqinxi is a traditional Chinese fitness exercise (Huang, 2020) that is a set of exercises based on the typical movements of five animals: the tiger, deer, bear, ape, and bird (Guo et al., 2018). The positions between the five movements are quite different, and each movement is designed to promote a particular body function (Li et al., 2020; Chang et al., 2022). The deer play in Wuqinxi is played in a hand–foot kneeling (HFK) position, which is remarkably similar to the conventional core stabilization exercise, the four-point hand–knee kneeling (HKK) position. These quadruped positions provide relatively low-loaded and non-anti-gravity postures and could be appropriate choices for people with low back pain or spinal disorders starting a rehabilitation program.

Previous studies have shown that HKK and its variants could activate the abdominal and lumbar muscles, thereby enhancing lumbar spine stability (Sakulsriprasert et al., 2015). In the starting position, the electromyography (EMG) amplitudes of abdominal and lumbar muscles were generally lower than 20% (Chanthapetch et al., 2009; Park and Lee, 2010). HKK with the upper limb lifted had higher ipsilateral internal oblique and transversus abdominis muscle activation (Pirouzi et al., 2013). Another study found that the lower limb extension task in four-point kneeling provides both low joint loading and limited muscle activity, and this result suggested that changes in the limb position could have an effect on the core muscle activity pattern (Yu et al., 2022). Compared to HKK, the most distinctive feature of HFK is that the knee does not touch the ground. However, the differences in core muscle activity caused by the positions are not clear until now.

Spinal intervertebral joints are complex structures allowing motion in flexion–extension, lateral bending, and axial rotation. Spinal rotation has been proposed as a necessary motion for our everyday activities (Gombatto et al., 2015; Reitmaier and Schmidt, 2020). A previous study showed that an artificial restriction of spinal rotation resulted in significantly slower walking velocity and higher energy consumption in walking (Kumar, 2004). Moreover, both abdominal and dorsal muscles are involved in the development of axial torque (McGill. 1991). Kumar et al. (2002) also reported that the pre-rotated spine decreased force production significantly and increased EMG activity significantly. In the current study, we also measured the two quadruped positions with different limb extensions, which were unstable positions with asymmetrical body postures. Measuring spinal rotation is important for the evaluation of certain tasks involving asymmetrical body posture, which could provide not only information related to the rotation angles but also information about muscle activity patterns (Kouwenhoven et al., 2006; Fan et al., 2014).

Therefore, the purpose of this research was to investigate trunk muscle activation and spine kinematics to compare the differences between these two quadruped positions in training core muscle function and spinal mobility. It was hypothesized that physical demands differ between these two quadruped positions, which might be used in training for different spinal disorders. In this way, a normative database can be created, which is necessary to interpret the results of performing these exercises.

Materials and methods

Participants

A total of 19 healthy university students (12 males and 7 females) were recruited in this study according to the paired *t*-test, with a power of 0.80, an alpha level of 0.05, and an effect size of 0.68 (Kim, 2015). The sample size was calculated using G*Power software (v3.1.9.2) based on the pre-experiment in which the activation of the rectus abdominis was compared between these two different four-point kneeling exercises.

Their age was 21.8 ± 0.9 years, height was 169.9 ± 9.5 cm, weight was 61.9 ± 10.2 kg, and body mass index (BMI) was 21.3 ± 2.0 kg/m^2. All participants were free from musculoskeletal pain, neuromuscular disorders, or any form of joint or bone disease. Participants with BMI greater than 28 kg/m^2 were also excluded, aimed to decrease the EMG artifact due to adipose tissue lying between surface electrodes and tested muscles. All participants were informed about the purpose and content of the investigation and signed informed consent. Written informed consent was obtained from the individuals for the publication of any potentially identifiable images or data included in this article.

Experimental design

All participants performed HKK and HFK and their variants in random order. Each movement was performed 2 times and held for 10 s. Rest periods of 60 s were allowed between

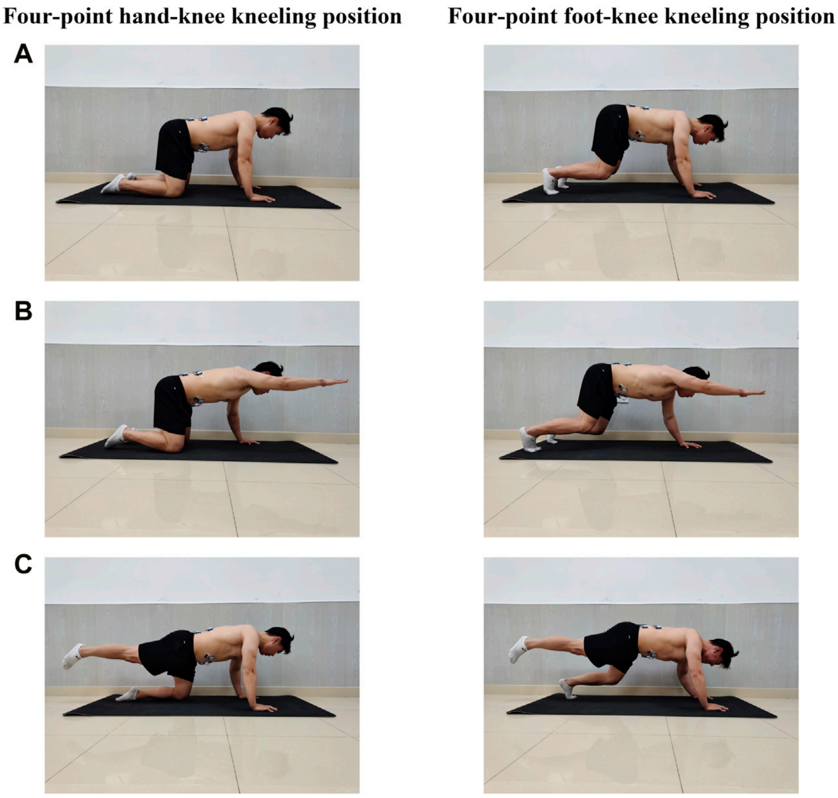

FIGURE 1
Core stabilization exercises in two positions. **(A)** Exercises in the starting position. **(B)** Exercisers with a single upper limb lifted; participants lifted their right or left upper limb parallel to the floor, respectively. **(C)** Exercisers with a single lower limb lifted; participants lifted their right or left lower limb parallel to the floor as possible, respectively.

repetitions of the movements, and a 2-min rest period was given between movements minimizing the possibility of residual fatigue (Bjerkefors et al., 2010a). Each participant was trained to perform movements in two positions, and this assured that they could correctly perform the movements. The two exercises and their variants were briefly described in the following paragraphs.

HKK in the starting position: participants were in the quadruped position with hips and shoulders flexion at approximately 90°. Their hips were directly above the knees, and their shoulders were above the hands. The spine was in a neutral position (Figure 1A). HKK with the right or left upper limb lifted: from the starting position, participants lifted their right or left upper limb parallel to the floor, respectively (Figure 1B). HKK with the right or left lower limb lifted: from the starting position, participants lifted their right or left lower limb parallel to the floor, respectively (Figure 1C).

HFK in the starting position: participants were in the quadruped position with hips, knees, and shoulders flexion > 90°, the knee joints did not touch the ground, and the spine was required to be in a neutral position as possible (Figure 1A). HFK with the right or left upper limb lifted: from the starting position, participants tried to lift the right or left upper limb parallel to the floor, respectively (Figure 1B). HFK with the right or left lower limb lifted: from the starting position, participants lifted their right or left lower limb as parallel to the floor as possible, respectively (Figure 1C).

Surface electromyography data acquisition and processing

The surface electromyography (sEMG) signal acquisition was performed using Noraxon TeleMyo DTS (Noraxon Inc., AZ, United States). The sampling rate was at 1,500 Hz. The bipolar self-adhesive Ag/AgCl surface electrodes, with a 20 mm inter-electrode distance, were placed in parallel to muscle fiber orientation after alcohol was used to cleanse each participant's skin to decrease skin impedance. EMG signals were collected from eight trunk muscles bilaterally: EO, ES, MF, and rectus abdominis (RA) (Table 1).

TABLE 1 Placement of surface electromyography electrodes and measurement of the maximum voluntary contraction of trunk muscles.

Muscle	Placement of electrodes	Maximum voluntary contraction test
Rectus abdominis	3 cm lateral to the umbilicus	Participants were in the supine position with knees bent and feet flat and were asked to flex against manual resistance at the shoulders
External oblique	15 cm lateral to the umbilicus	Participants were in the supine position with knees bent and feet flat and were asked to laterally bend and axially twist against manual resistance at the shoulders
Erector spinae	3 cm lateral to the L3 spinous process	Participants were in the prone position. Then, trunk extension was performed against manual resistance at the shoulders
Lumbar multifidus	3 cm lateral to the L5 spinous process	Test was the same as the test of the erector spinae muscle

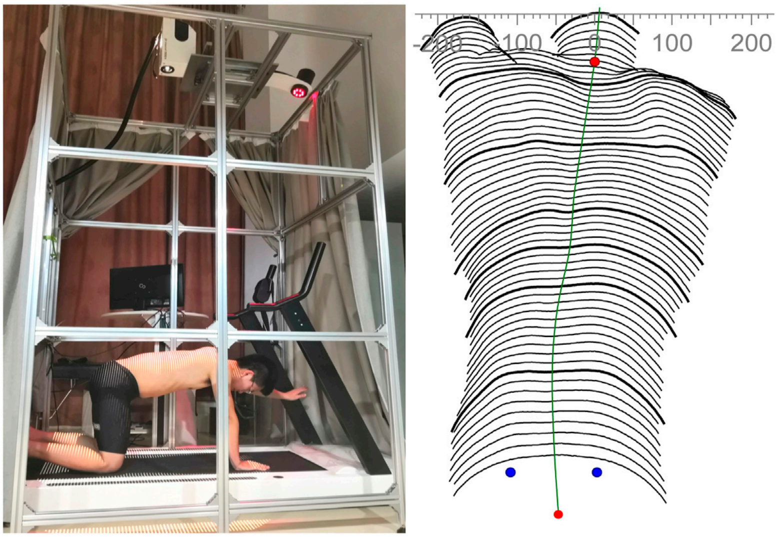

FIGURE 2
Modified Formetric 4D device (left panel) and computerized surface topography map of the participant's back (right panel). The distance between the camera and the participant's back is about 2 m.

To normalize the EMG data, the participants were instructed to perform a maximal voluntary contraction (MVC) test according to SENIAM recommendations (Hermens et al., 2000), and more details are given in Table 1. A total of two repetitions of the 5-s isometric MVC test were performed for each target muscle against manual resistance, with a 2-min rest between trials; the order of the test was randomly assigned. After the measurement of MVC, all participants randomly performed the HKK and HFK movements according to the procedure.

The raw EMG data were measured using automated programs written in MATLAB version R2018a (MathWorks, Inc., Natick, United States). During postprocessing, the first 3 s and the last 2 s data were discarded. The discarded EMG signal was quantified by digital full-wave rectifying and band-pass filtering (at 20–500 Hz) and smoothed with a root-mean-square (RMS) algorithm with a 100-millisecond moving window. The average EMG signal amplitude of each muscle during the MVC trials was regarded as representing 100% muscle activity, and then the average EMG data of each exercise were normalized to a percentage of the average of the MVC.

Kinematics data acquisition and processing

The Formetric 4D analysis system (DIERS International GmbH, Schlangenbad, Germany) was used to measure vertebral rotation, which is a radiation-free and contact-free method based on raster stereography (Drerup and Hierholzer, 1996). The process takes only seconds, unlike traditional spinal

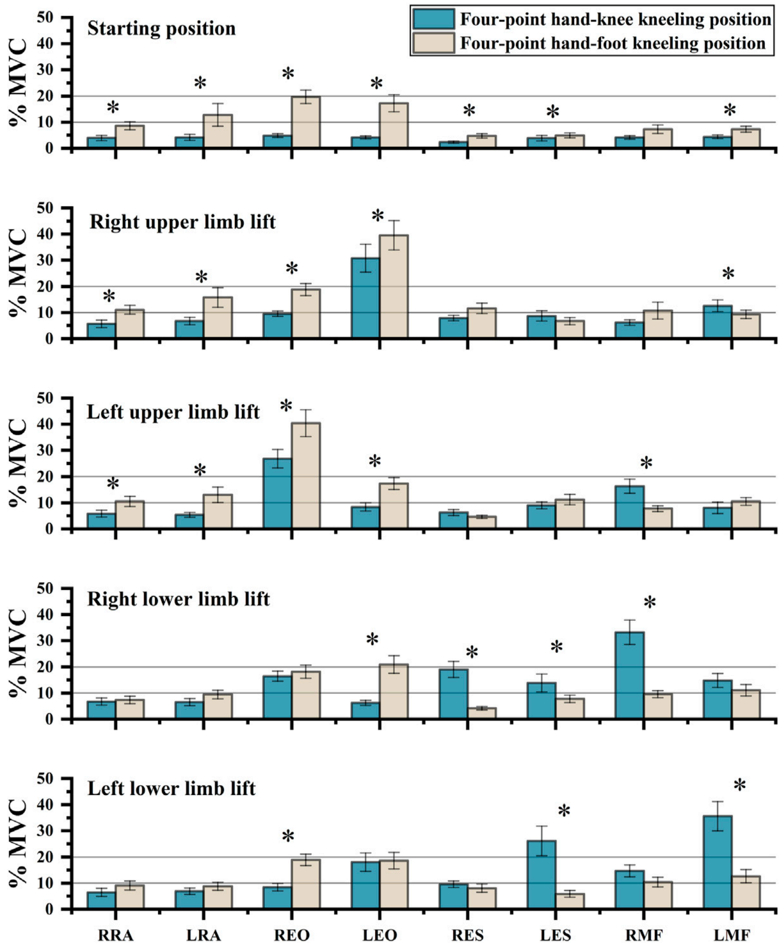

FIGURE 3
Comparison of sEMG values between the four-point hand–knee and hand–foot kneeling positions with the same limb lifted. RRA, right rectus abdominis; LRA, left rectus abdominis; REO, right external oblique; LEO, left external oblique; RES, right erector spinae; LES, left erector spinae; RMF, right lumbar multifidus; LMF, left lumbar multifidus. *: statistically significant, $p < 0.05$.

motion laboratory system measurement methods that require multiple markers to describe the limited number of spine segments' motion and need complex post-data processing (Papi et al., 2017; Ryan and Bruno, 2017).

Parallel light lines are projected onto the surface of the back and detected using a digital camera. From the distortion of the raster lines and with the help of a personal computer, the three-dimensional model of the spine was reconstructed. By a mathematical shape analysis, the frontal, the sagittal, and the transversal profile can be determined (Drerup and Hierholzer, 1994). The reliability and validity of the Formetric raster stereography device had been proved in previous studies (Betsch et al., 2011; Schroeder et al., 2015).

All parameters were measured using the function tool four-dimensional average (4D average). The duration of image acquisition was set at 6 s, and the frequency was set at 2 Hz. Moreover, the original design of equipment was to measure the spine in the standing position; we modified the equipment to fulfill the experiments. As shown in Figure 2, the distance between the camera and the participant's back was about 2 m, and the height of the camera could be fine-tuned to suit different participants. More details of the preparation are referred to Gipsman et al. (2014).

The collected data were processed by software automatically. The averages of the vertebral rotations were calculated, and the negative value and the positive value meant that the vertebra rotates to the left and right in the data set, respectively.

Statistical analysis

All the statistical analyses were performed using SPSS statistical software (version 20.0; Inc., Chicago, IL, United States), and statistical significance was accepted at $p <$

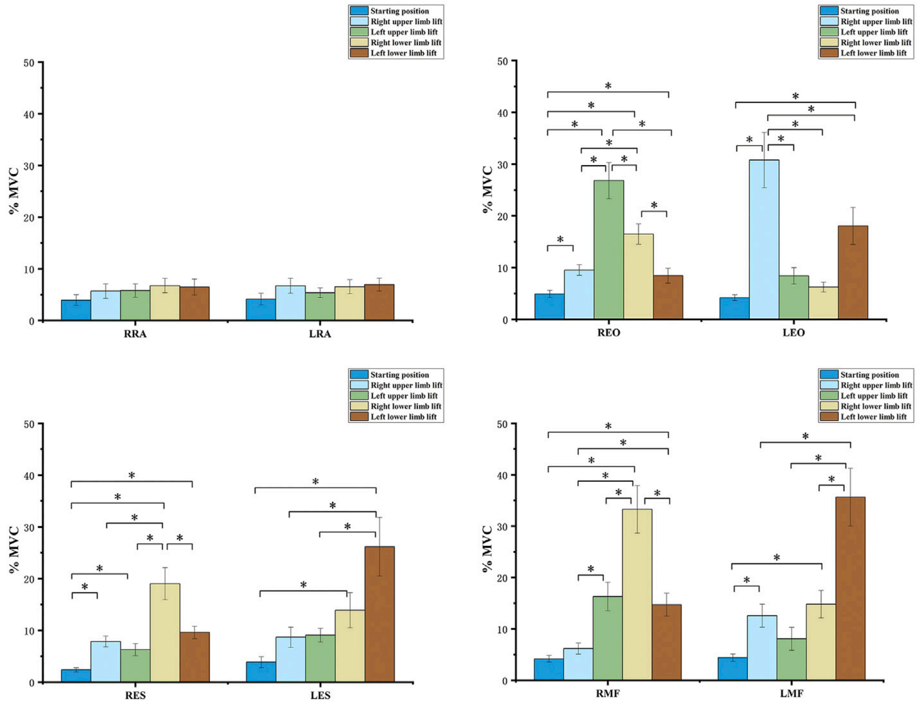

FIGURE 4
sEMG values and results of one-way ANOVA during the four-point hand–knee kneeling positions, respectively. The negative value meant the vertebra rotates to the left, and the positive value meant the vertebra rotates to the right; RRA, right rectus abdominis; LRA, left rectus abdominis; REO, right external oblique; LEO, left external oblique; RES, right erector spinae; LES, left erector spinae; RMF, right lumbar multifidus; LMF, left lumbar multifidus. *: statistically significant, $p < 0.05$.

0.05. The paired *t*-test was utilized to compare them between the two positions with the same limb lifted. The one-way ANOVA test with the Bonferroni correction was utilized to compare the muscle activity and vertebral rotation between five positions in both HKK and HFK, respectively.

Results

Muscle activity

The *t*-test showed the activation of the same muscle between HKK and HFK with the same limb lifted was statistically different (Figure 3). The activation of both sides of RA ($p < 0.05$), EO ($p < 0.001$), ES ($p < 0.05$), and left MF ($p = 0.009$) in HFK were higher than that in HKK in the starting position. The activation of both sides of RA and EO in HFK was higher than that in HKK when the upper limb was lifted ($p < 0.05$), while the activation of contralateral MF was higher in HKK than in HFK when the upper limb was lifted ($p < 0.05$). The activation of ipsilateral MF and ES in HKK was higher than that in HFK when the lower limb was lifted ($p < 0.05$), while the activation of EO muscles was higher in HFK than in HKK when the contralateral lower limb was lifted ($p < 0.05$).

The one-way ANOVA test for comparing the five exercises in the HKK position showed significant differences in the muscle activation of most trunk muscles ($p < 0.001$), except the left RA ($p = 0.076$) (Figure 4). During exercises in the HFK position, statistically significant differences were found in the activation of the muscles ($p < 0.05$), except for the left RA ($p = 0.161$) and right MF ($p = 0.263$) (Figure 5).

Vertebral rotation

The vertebral rotation between two positions with the same limb lift was compared (Figure 6). The results showed that the difference was mainly at T8 and above ($p < 0.05$) when the lower limb was lifted, while the difference existed at T7–T10 during exercises with the upper limb lifted ($p < 0.05$). Moreover, the exercises in the HKK position had a greater vertebral rotation angle than those in the HFK position, unless the right upper limb was lifted, although the rotation might be in a different direction.

The rotation angle of each vertebra from C7 to L4 for each exercise in the HKK and HFK positions is displayed in Figure 7. In HKK, the results showed that the thoracic vertebral rotation (from T1 to T7) was significantly larger when the left lower limb

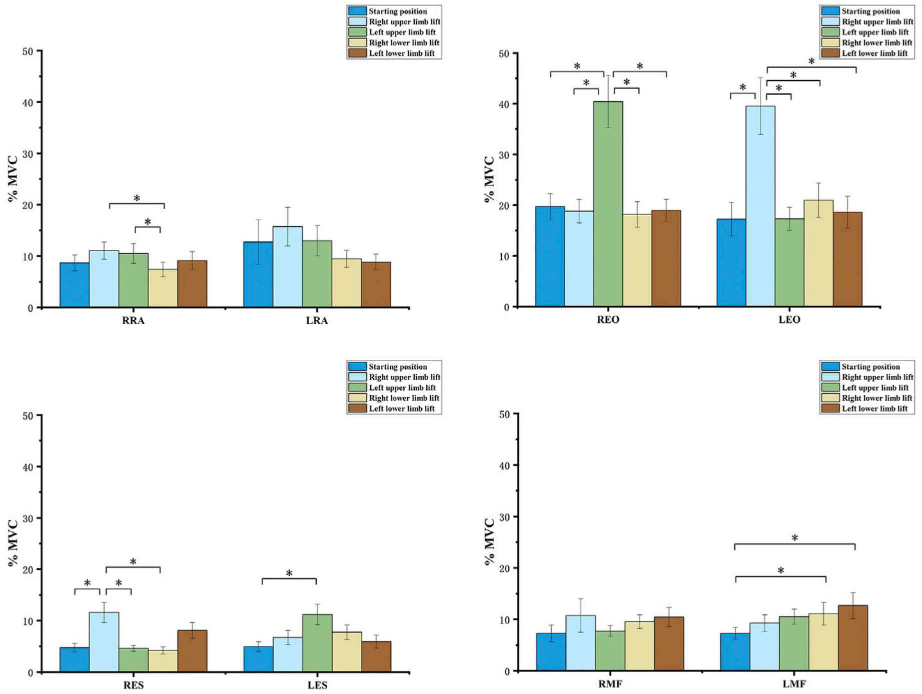

FIGURE 5
sEMG values and results of one-way ANOVA during the four-point hand–foot kneeling positions, respectively. The negative value meant the vertebra rotates to the left, and the positive value meant the vertebra rotates to the right. RRA, right rectus abdominis; LRA, left rectus abdominis; REO, right external oblique; LEO, left external oblique; RES, right erector spinae; LES, left erector spinae; RMF, right lumbar multifidus; LMF, left lumbar multifidus. *: statistically significant, $p < 0.05$.

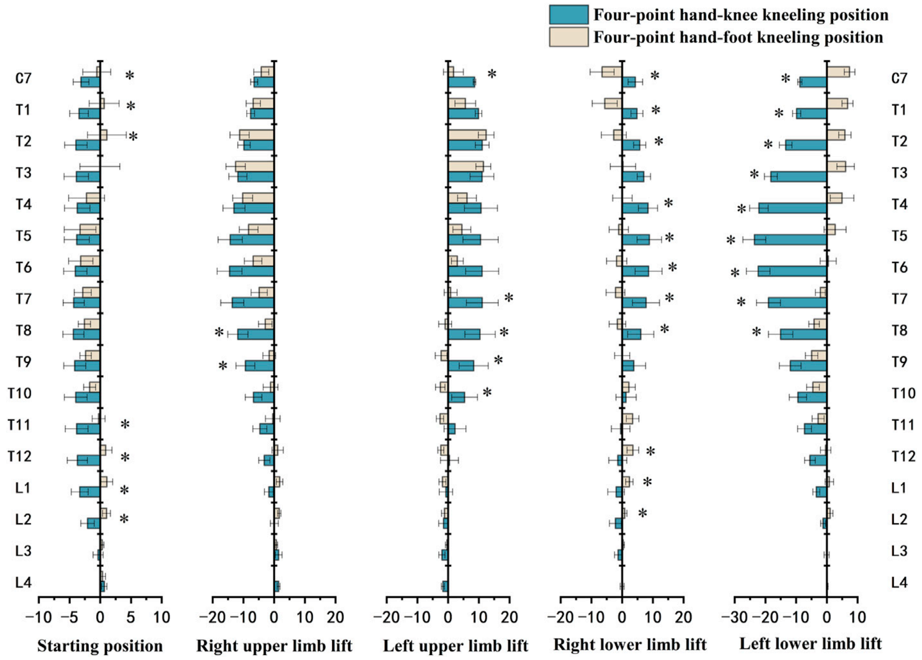

FIGURE 6
Comparison of vertebral rotation (°) between the four-point hand–knee and hand–foot kneeling positions. The negative value meant the vertebra rotates to the left; the positive value meant the vertebra rotates to the right. *: statistically significant, $p < 0.05$.

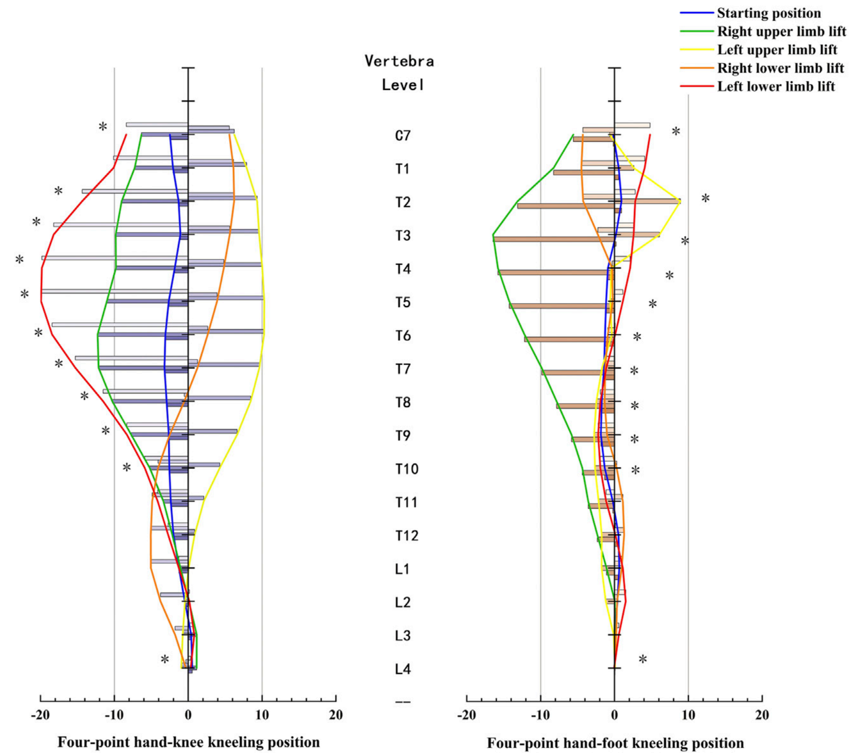

FIGURE 7
Vertebra rotation and results of one-way ANOVA during the four-point hand–knee kneeling positions and four-point hand–foot kneeling positions, respectively. *: statistically significant, *p* < *0.05*.

was lifted than in the starting position ($p < 0.05$), and the thoracic vertebra (from T1 to T8) showed the opposite rotation direction when the left upper limb was lifted and the left lower limb was lifted. However, there were no significant differences in the lumbar spinal rotation (from L1 to L3) between positions with different limbs lifted in both HKK and HFK.

Discussion

The purpose of this study was to quantify muscle activation and spine kinematics during movements in HKK and HFK to compare the differences between these two quadruped positions in training core muscle function and spinal mobility. The muscle activity data in HKK were consistent with some earlier results (Beith et al., 2001; Stevens et al., 2007b; Pirouzi et al., 2013). Furthermore, our study provided comprehensive comparisons of bilateral muscle activation in two four-point kneeling positions with specific limb lift.

According to the classification of muscle activation, the relative EMG levels (%MVC) were classified into high (>20% MVC), moderate (10%–20% MVC), and low (<10% MVC) muscle activity (Stevens et al., 2007b). In the starting position, all muscle activation was low (<10% MVC) during HKK. Only one study showed that the activation of all muscles was less than 10% in the HKK position (Stevens et al., 2007a). This result was in line with our study. The activation of the RA, EO, ES, and left MF was higher during HFK than during HKK in the starting position and with the upper limb lifted. Previous studies have indicated that abdominal trunk muscle strength decreases with chronic low back pain (Cho et al., 2014; Cruz-Díaz et al., 2017). Moreover, Kato et al. (2019) found that abdominal muscle training could effectively improve transversus abdominis muscle activation in patients with chronic low back pain and was associated with pain and function improvement. HFK in the starting position and with the left limb lifted could provide more training for strengthening abdominal muscles and might be used for people with chronic low back pain caused by abdominal muscle weakness.

The ES and MF had higher activity during HKK than during HFK with the ipsilateral lower limb lifted. A previous study showed that HKK with the right lower limb lifted had higher activity of the right EO and MF muscles and lower activity of the RA, which was consistent with our results (Stevens et al., 2007b). The ES and MF were thought to play an important role in the active stabilization and movement of the spine (Sadeghi et al., 2019; Kouwijzer et al., 2020). Previous studies showed that people with low back pain were found to have smaller multifidus muscles with a significant amount of intramuscular fat infiltration (Seyedhoseinpoor et al., 2021). Considering the high activation of ES and MF (>20% MVC) during HKK with the lower limb lifted, it could be used to strengthen ES and MF in particular.

The findings of the present study also revealed that the muscle activation was closely related to the uplifted limb, and the relationship was affected by whether the knee touched the ground. Analyzing the moderate and high activated muscles during exercises, we could conclude the following: the EO and MF muscles had a higher muscle activity during HKK with the contralateral upper limb or the ipsilateral lower limb lifted, and the EO muscle activation was higher during HFK with the contralateral upper limb lifted. HKK with the lower limb lifted had a highly activated ipsilateral ES muscle. Based on these results, we suggested the specific variant could strengthen specific muscles.

The results showed that the rotation angle of the thoracic spine in HKK with the lower limb lifted was significantly larger than that in HFK, and the results also showed that the rotation angles of T7–T10 in HKK with the upper limb lifted were significantly larger than those in HFK. A previous study focused on spine motion during axial rotation activities also showed the greatest degree of axial rotation of the upper thoracic spine in comparison with the other spinal segments (Sung et al., 2012). Yang et al. (2015) pointed out that motion reduction of the thoracic segments caused excessive movements of the lumbar spine *via* compensatory mechanisms. The abnormal movements of the lumbar spine led to the instability that develops in the facet joints, which eventually causes pain in the lower back (Panjabi, 1992). However, the results showed that little rotation angles of the lumbar were observed in HKK and HFK because the high activation of the trunk muscle led to intervertebral joint stiffness, which restricted the axial rotation (Lee et al., 2006; Graham and Brown, 2014; Inoue et al., 2020).

The vertebral rotation was also closely related to the uplifted limb in different positions. For example, in HKK and HFK, the thoracic spine rotated oppositely to the side of the uplifted upper limb. However, the direction of the thoracic rotation was on the same side of the raised lower limb in HKK, while that in HFK was on the opposite. Recently, some studies also showed that thoracic mobilization exercises had positive outcomes in relieving pain and functional disability in patients with chronic low back pain (Divya et al., 2020; Kostadinović et al., 2020). In our research, HKK with limbs lifted increased thoracic mobilization and reduced lumbar hypermobility, which might be used in low back pain management.

In the starting position, the rotation angles of T11–L2 during HKK were significantly larger than those during HKF. However, there were no significant differences in most thoracic rotation angles between HKK and HFK, and relatively little rotation angles were shown in both HKK and HFK. Because the body weight is supported by two knees (feet) and two hands in the starting position, which is a stable posture, the neutral spine position could be easily achieved (Pirouzi et al., 2013). Also, previous studies showed that trunk muscles activated less when in the starting position than when the limbs were lifted. (Stevens et al., 2007b; Chanthapetch et al., 2009). This result was in line with our findings in muscle activation. Thus, it was a suitable choice for people at the beginning of rehabilitation programs for low back pain or spinal disorders due to the little physical demands needed.

Limitations

There are some limitations to this study. First, all the participants recruited were young healthy subjects. Further studies need to take people with low back pain or the elderly into consideration. Second, the beneficial effects need to be identified by long-term intervention based on two kinds of four-point kneeling positions.

Conclusion

The exercises in both four-point hand–knee kneeling positions could train core muscle and spinal mobility and could be suitable choices for people with low back pain or spinal disorders. The exercises in the HFK (deer play) position could provide more training for strengthening abdominal muscles, while the exercises in the HKK position with the lower limber lifted could be recommended for strengthening lumbar muscles. HKK and its variants were presumably suitable for increasing spine mobility. The findings in this study can be used to help physiotherapists, fitness coaches, and others to select specific exercises and develop individualized training programs.

Data availability statement

The raw data supporting the conclusion of this article will be made available by the authors, without undue reservation.

Ethics statement

The studies involving human participants were reviewed and approved by the Ethics Committee of Shanghai Yangzhi Rehabilitation Hospital (2020-074). The patients/participants provided their written informed consent to participate in this study.

Author contributions

X-QC, X-PC, YQ, and W-XN conceptualized this study. X-PC, X-QC, KW, and S-JH designed the methodology for the study. X-PC, X-QC, and Y-XS participated in data acquisition and data curation. X-PC, X-QC, Y-XS, and S-JH analyzed and interpreted the data. X-QC and X-PC drafted the manuscript. YQ and W-XN critically revised the manuscript for content.

Funding

This work was supported by the National Natural Science Foundation of China (31900942) and the Shanghai Administration of Sports (21Q002).

Conflict of interest

The authors declare that the research was conducted in the absence of any commercial or financial relationships that could be construed as a potential conflict of interest.

Publisher's note

References

Areeudomwong, P., and Buttagat, V. (2019). Comparison of core stabilisation exercise and proprioceptive neuromuscular facilitation training on pain-related and neuromuscular response outcomes for chronic low back pain: A randomised controlled trial. *Malays. J. Med. Sci.* 26 (6), 77–89. doi:10.21315/mjms2019.26.6.8

Beith, I. D., Synnott, R. E., and Newman, S. A. (2001). Abdominal muscle activity during the abdominal hollowing manoeuvre in the four point kneeling and prone positions. *Man. Ther.* 6 (2), 82–87. doi:10.1054/math.2000.0376

Betsch, M., Wild, M., Jungbluth, P., Hakimi, M., Windolf, J., Haex, B., et al. (2011). Reliability and validity of 4D rasterstereography under dynamic conditions. *Comput. Biol. Med.* 41 (6), 308–312. doi:10.1016/j.compbiomed.2011.03.008

Bjerkefors, A., Ekblom, M. M., Josefsson, K., and Thorstensson, A. (2010a). Deep and superficial abdominal muscle activation during trunk stabilization exercises with and without instruction to hollow. *Man. Ther.* 15 (5), 502–507. doi:10.1016/j.math.2010.05.006

Brown, S. H., and McGill, S. M. (2008). How the inherent stiffness of the *in vivo* human trunk varies with changing magnitudes of muscular activation. *Clin. Biomech. (Bristol, Avon.* 23 (1), 15–22. doi:10.1016/j.clinbiomech.2007.08.011

Chang, X. Q., Wang, K., Chen, X. P., Wang, L. J., and Niu, W. X. (2022). A comparative study of the muscle activation and co-contraction patterns of trunk muscles in four-point hand-knee and hand-foot kneeling positions. *J. Med. Biomech.* 18, 2021. in press[in Chinese]. doi:10.3390/ijerph182312804

Chanthapetch, P., Kanlayanaphotporn, R., Gaogasigam, C., and Chiradejnant, A. (2009). Abdominal muscle activity during abdominal hollowing in four starting positions. *Man. Ther.* 14 (6), 642–646. doi:10.1016/j.math.2008.12.009

Cho, K. H., Beom, J. W., Lee, T. S., Lim, J. H., Lee, T. H., and Yuk, J. H. (2014). Trunk muscles strength as a risk factor for nonspecific low back pain: A pilot study. *Ann. Rehabil. Med.* 38 (2), 234–240. doi:10.5535/arm.2014.38.2.234

Cortell-Tormo, J. M., García-Jaén, M., Chulvi-Medrano, I., Hernández-Sánchez, S., Lucas-Cuevas Á, G., and Tortosa-Martínez, J. (2017). Influence of scapular position on the core musculature activation in the prone plank exercise. *J. Strength Cond. Res.* 31 (8), 2255–2262. doi:10.1519/jsc.0000000000001689

Cruz-Díaz, D., Bergamin, M., Gobbo, S., Martínez-Amat, A., and Hita-Contreras, F. (2017). Comparative effects of 12 weeks of equipment based and mat Pilates in patients with chronic low back pain on pain, function and transversus abdominis activation. A randomized controlled trial. *Complement. Ther. Med.* 33, 72–77. doi:10.1016/j.ctim.2017.06.004

DivyaParveen, A., Nuhmani, S., Ejaz Hussain, M., and Hussain Khan, M. (2020). Effect of lumbar stabilization exercises and thoracic mobilization with strengthening exercises on pain level, thoracic kyphosis, and functional disability in chronic low back pain. *J. Complement. Integr. Med.* 18 (2), 419–424. doi:10.1515/jcim-2019-0327

Drerup, B., and Hierholzer, E. (1996). Assessment of scoliotic deformity from back shape asymmetry using an improved mathematical model. *Clin. Biomech. (Bristol, Avon.* 11 (7), 376–383. doi:10.1016/0268-0033(96)00025-3

Drerup, B., and Hierholzer, E. (1994). Back shape measurement using video rasterstereography and three-dimensional reconstruction of spinal shape. *Clin. Biomech. (Bristol, Avon.* 9 (1), 28–36. doi:10.1016/0268-0033(94)90055-8

Essendrop, M., Andersen, T. B., and Schibye, B. (2002). Increase in spinal stability obtained at levels of intra-abdominal pressure and back muscle activity realistic to work situations. *Appl. Ergon.* 33 (5), 471–476. doi:10.1016/s0003-6870(02)00028-5

Fan, J.-Z., Liu, X., and Ni, G.-X. (2014). Angular velocity affects trunk muscle strength and EMG activation during isokinetic axial rotation. *Biomed. Res. Int.* 2014, 623191–623198. doi:10.1155/2014/623191

Gipsman, A., Rauschert, L., Daneshvar, M., and Knott, P. (2014). Evaluating the reproducibility of motion analysis scanning of the spine during walking. *Adv. Med.* 2014, 1–9. doi:10.1155/2014/721829

Gombatto, S. P., Brock, T., DeLork, A., Jones, G., Madden, E., and Rinere, C. (2015). Lumbar spine kinematics during walking in people with and people without low back pain. *Gait Posture* 42 (4), 539–544. doi:10.1016/j.gaitpost.2015.08.010

Graham, R. B., and Brown, S. H. M. (2014). Local dynamic stability of spine muscle activation and stiffness patterns during repetitive lifting. *J. Biomech. Eng.* 136 (12), 121006. doi:10.1115/1.4028818

Guo, Y., Xu, M., Wei, Z., Hu, Q., Chen, Y., Yan, J., et al. (2018). Beneficial effects of Qigong Wuqinxi in the improvement of health condition, prevention, and treatment of chronic diseases: Evidence from a systematic review. *Evidence-Based Complementary Altern. Med.* 2018, 1–40. doi:10.1155/2018/3235950

Hermens, H. J., Freriks, B., Disselhorst-Klug, C., and Rau, G. (2000). Development of recommendations for SEMG sensors and sensor placement procedures. *J. Electromyogr. Kinesiol.* 10 (5), 361–374. doi:10.1016/s1050-6411(00)00027-4

Huang, X. (2020). Qi, return to bodily experience: A new perspective of qi and qigong experience research. *Chin. Med. Cult.* 3 (4), 216–219. doi:10.4103/cmac.cmac_19_20

Inoue, N., Orías, A. A. E., and Segami, K. (2020). Biomechanics of the lumbar facet joint. *Spine Surg. Relat. Res.* 4 (1), 1–7. doi:10.22603/ssrr.2019-0017

Kato, S., Murakami, H., Demura, S., Yoshioka, K., Shinmura, K., Yokogawa, N., et al. (2019). Abdominal trunk muscle weakness and its association with chronic low back pain and risk of falling in older women. *BMC Musculoskelet. Disord.* 20 (1), 273. doi:10.1186/s12891-019-2655-4

Kim, J., Ko, J., Lim, J., Choi, H., Seo, K., Lee, S., et al. (2020). Effects of a four-week core stability exercise on functional movement and balance in people with mild lower-limb discomfort. *Monten. J. Sports Sci. Med.* 9 (2), 13–20. doi:10.26773/mjssm.200903

Kim, T. K. (2015). T test as a parametric statistic. *Korean J. Anesthesiol.* 68 (6), 540–546. doi:10.4097/kjae.2015.68.6.540

Kostadinović, S., Milovanović, N., Jovanović, J., and Tomašević-Todorović, S. (2020). Efficacy of the lumbar stabilization and thoracic mobilization exercise program on pain intensity and functional disability reduction in chronic low back pain patients with lumbar radiculopathy: A randomized controlled trial. *J. Back Musculoskelet. Rehabil.* 33 (6), 897–907. doi:10.3233/BMR-201843

Kouwenhoven, J.-W. M., Vincken, K. L., Bartels, L. W., and Castelein, R. M. (2006). Analysis of preexistent vertebral rotation in the normal spine. *Spine* 31 (13), 1467–1472. doi:10.1097/01.brs.0000219938.14686.b3

Kouwijzer, I., van der Meer, M., and Janssen, T. W. J. (2020). Effects of trunk muscle activation on trunk stability, arm power, blood pressure and performance in wheelchair rugby players with a spinal cord injury. *J. Spinal Cord. Med.* 11 (9), 605–613. doi:10.1080/10790268.2020.1830249

Kumar, S., Narayan, Y., and Garand, D. (2002). Isometric axial rotation of the human trunk from pre-rotated postures. *Eur. J. Appl. Physiol.* 87 (1), 7–16. doi:10.1007/s00421-002-0590-8

Kumar, S. (2004). The ergonomics society – the society lectures 2003. *Ergonomics* 47 (4), 370–415. doi:10.1080/0014013032000157940

Lee, P. J., Rogers, E. L., and Granata, K. P. (2006). Active trunk stiffness increases with co-contraction. *J. Electromyogr. Kinesiol.* 16 (1), 51–57. doi:10.1016/j.jelekin.2005.06.006

Li, M., Wang, K., Niu, W., and Zhang, S. (2020). A Musculoskeletal modeling of hand-foot crawling with different heights. *J. Bionic Eng.* 17 (3), 591–599. doi:10.1007/s42235-020-0047-y

Martuscello, J. M., Nuzzo, J. L., Ashley, C. D., Campbell, B. I., Orriola, J. J., and Mayer, J. M. (2013). Systematic review of core muscle activity during physical fitness exercises. *J. Strength Cond. Res.* 27 (6), 1684–1698. doi:10.1519/JSC.0b013e318291b8da

McGill, S. M. (1991). Electromyographic activity of the abdominal and low back musculature during the generation of isometric and dynamic axial trunk torque: Implications for lumbar mechanics. *J. Orthop. Res.* 9 (1), 91–103. doi:10.1002/jor.1100090112

O'Sullivan, P. B. (2000). Lumbar segmental 'instability': Clinical presentation and specific stabilizing exercise management. *Man. Ther.* 5 (1), 2–12. doi:10.1054/math.1999.0213

Oliva-Lozano, J. M., and Muyor, J. M. (2020). Core muscle activity during physical fitness exercises: A systematic review. *Int. J. Environ. Res. Public Health* 17 (12), 4306. doi:10.3390/ijerph17124306

Ozsoy, G., Ilcin, N., Ozsoy, I., Gurpinar, B., Buyukturan, O., Buyukturan, B., et al. (2019). The effects of myofascial release technique combined with core stabilization exercise in elderly with non-specific low back pain: A randomized controlled, single-blind study. *Clin. Interv. Aging* 14, 1729–1740. doi:10.2147/CIA.S223905

Panjabi, M. M. (1992). The stabilizing system of the spine. Part I. Function, dysfunction, adaptation, and enhancement. *J. Spinal Disord.* 5 (4), 383–389. doi:10.1097/00002517-199212000-00001

Papi, E., Koh, W. S., and McGregor, A. H. (2017). Wearable technology for spine movement assessment: A systematic review. *J. Biomech.* 64, 186–197. doi:10.1016/j.jbiomech.2017.09.037

Park, D., and Lee, H. (2010). Activation of abdominal muscles during abdominal hollowing in four different positions. *J. Phys. Ther. Sci.* 22 (2), 203–207. doi:10.1589/jpts.22.203

Pirouzi, S., Emami, F., Taghizadeh, S., and Ghanbari, A. (2013). Is abdominal muscle activity different from lumbar muscle activity during four-point kneeling? *Iran. J. Med. Sci.* 38 (4), 327–333.

Reitmaier, S., and Schmidt, H. (2020). Review article on spine kinematics of quadrupeds and bipeds during walking. *J. Biomech.* 102, 109631. doi:10.1016/j.jbiomech.2020.109631

Ryan, N., and Bruno, P. (2017). Analysis of 3D multi-segment lumbar spine motion during gait and prone hip extension. *J. Electromyogr. Kinesiol.* 33, 111–117. doi:10.1016/j.jelekin.2017.02.005

Sadeghi, S., Quinlan, K., E Eilertson, K., G Billy, G., Bible, J., Sions, M., et al. (2019). Changes in shear modulus of the lumbar multifidus muscle during different body positions. *J. Biomech. Eng.* 141 (8), 081003. doi:10.1115/1.4043443

Sakulsriprasert, P., Eak-udchariya, P., and Jalayondeja, W. (2015). Muscle activity of abdominal and back muscles during six starting positions in untrained individuals. *J. Med. Assoc. Thai* 98 (5), 125–130.

Schroeder, J., Reer, R., and Braumann, K. M. (2015). Video raster stereography back shape reconstruction: A reliability study for sagittal, frontal, and transversal plane parameters. *Eur. Spine J.* 24 (2), 262–269. doi:10.1007/s00586-014-3664-5

Seyedhoseinpoor, T., Taghipour, M., Dadgoo, M., Sanjari, M. A., Takamjani, I. E., Kazemnejad, A., et al. (2021). Alteration of lumbar muscle morphology and composition in relation to low back pain: A systematic review and meta-analysis. *Spine J.* 22, 660–676. doi:10.1016/j.spinee.2021.10.018

Stevens, V. K., Coorevits, P. L., Bouche, K. G., Mahieu, N. N., Vanderstraeten, G. G., and Danneels, L. A. (2007a). The influence of specific training on trunk muscle recruitment patterns in healthy subjects during stabilization exercises. *Man. Ther.* 12 (3), 271–279. doi:10.1016/j.math.2006.07.009

Stevens, V. K., Vleeming, A., Bouche, K. G., Mahieu, N. N., Vanderstraeten, G. G., and Danneels, L. A. (2007b). Electromyographic activity of trunk and hip muscles during stabilization exercises in four-point kneeling in healthy volunteers. *Eur. Spine J.* 16 (5), 711–718. doi:10.1007/s00586-006-0181-1

Sung, P. S., Park, W. H., and Kim, Y. H. (2012). Three-dimensional kinematic lumbar spine motion analyses of trunk motion during axial rotation activities. *J. Spinal Disord. Tech.* 25 (3), E74–E80. doi:10.1097/BSD.0b013e3182404b87

Vera-Garcia, F. J., Irles-Vidal, B., Prat-Luri, A., García-Vaquero, M. P., Barbado, D., and Juan-Recio, C. (2020). Progressions of core stabilization exercises based on postural control challenge assessment. *Eur. J. Appl. Physiol.* 120 (3), 567–577. doi:10.1007/s00421-020-04313-9

Yang, S.-R., Kim, K., Park, S.-J., and Kim, K. (2015). The effect of thoracic spine mobilization and stabilization exercise on the muscular strength and flexibility of the trunk of chronic low back pain patients. *J. Phys. Ther. Sci.* 27 (12), 3851–3854. doi:10.1589/jpts.27.3851

Yu, X., Ma, L., He, R., Zhao, J., and Wang, S. (2022). Research on the protection of extensor and flexor muscles in the waist and back of competitive athletes. *Biomed. Res. Int.* 2022, 1–8. doi:10.1155/2022/7378953

Frontiers in Bioengineering and Biotechnology

TYPE Original Research
PUBLISHED 27 September 2022
DOI 10.3389/fbioe.2022.858488

EDITED BY
Jun Pan,
Chongqing University, China

REVIEWED BY
Uriel Zapata,
EAFIT University, Colombia
Joshua W. Giles,
University of Victoria, Canada

*CORRESPONDENCE
Jia Jiang,
jessicajj19@hotmail.com
Jinzhong Zhao,
jzzhao@sjtu.edu.cn

†These authors have contributed equally to this work

SPECIALTY SECTION
This article was submitted to Biomechanics,
a section of the journal Frontiers in Bioengineering and Biotechnology

RECEIVED 20 January 2022
ACCEPTED 18 August 2022
PUBLISHED 27 September 2022

CITATION
Wang L, Kang Y, Jin H, Wang M, Wei Y, Gao H, Shi D, Yu S, Xie G, Jiang J and Zhao J (2022), Relationship between the progression of posterosuperior rotator cuff tear size and shoulder abduction function: A cadaveric study via dynamic shoulder simulator.
Front. Bioeng. Biotechnol. 10:858488.
doi: 10.3389/fbioe.2022.858488

Relationship between the progression of posterosuperior rotator cuff tear size and shoulder abduction function: A cadaveric study *via* dynamic shoulder simulator

Liren Wang[1,2†], Yuhao Kang[1,2†], Haocheng Jin[1,2], Mingqi Wang[2,3], Yiyao Wei[2,3], Haihan Gao[4], Dingyi Shi[4], Suiran Yu[5], Guoming Xie[1], Jia Jiang[1,2,6*] and Jinzhong Zhao[1,2,6*]

[1]Department of Sports Medicine, Shanghai Jiao Tong University Affiliated Sixth People's Hospital, Shanghai, China, [2]Regenerative Sports Medicine and Translational Youth Science and Technology Innovation Workroom, Shanghai Jiao Tong University School of Medicine, Shanghai, China, [3]School of Basic Medical Science, Fudan University, Shanghai, China, [4]Shanghai Jiao Tong University School of Medicine, Shanghai, China, [5]School of Mechanical Engineering, Shanghai Jiao Tong University, Shanghai, China, [6]Regenerative Sports Medicine Lab of the Institute of Microsurgery on Extremities, Shanghai Jiao Tong University Affiliated Sixth People' Hospital, Shanghai, China

Posterosuperior rotator cuff tear (PSRCT) is one of the most common shoulder disorders in elderly people's daily life; however, the biomechanical relationship between PSRCT and shoulder abduction function is still controversial. In this study, a total of twelve freshly frozen cadaveric shoulders were included and tested in five conditions: intact rotator cuff, 1/3 PSRCT, 2/3 PSRCT, entire PSRCT, and global RCT. In each condition, extra load (0%, 45%, and 90% failure load) was sequentially added to the distal humerus, and the function of the remaining rotator cuff was mainly evaluated *via* the middle deltoid force (MDF) required for abduction. It is found that the peak MDF is required for abduction did not differ among the three PSRCT conditions (1/3 PSRCT: 29.30 ± 5.03 N, $p = 0.96$; 2/3 PSRCT: 29.13 ± 9.09 N, $p = 0.98$; entire PSRCT: 28.85 ± 7.12 N, $p = 0.90$) and the intact condition (29.18 ± 4.99 N). However, the peak MDF significantly differed between the global RCT (76.27 ± 4.94 N, $p < 0.01$) and all PSRCT and intact conditions. Under 45% failure load, the MDF of the entire PSRCT and global tear conditions were significantly increased compared with another status. With the 90% failure load, only the 1/3 PSRCT condition maintained the same shoulder function as the intact rotator cuff. These biomechanical testing jointly suggested that the weight-bearing ability of the shoulder significantly decreased as PSRCT progressed.

KEYWORDS

shoulder stimulator, rotator cuff tear, abduction function, biomechanics, deltoid

Introduction

Posterosuperior rotator cuff tear (PSRCT) complaints are highly variable, with some patients exhibiting minimal symptoms and discomfort, while others exhibit pseudoparalysis or debilitating pain (Oh, et al., 2011; Rashid, et al., 2017). This controversy may result from the rotator cuff tear (RCT) size and the physical demand of individual patients (Keener, et al., 2017; Rizvi, et al., 2021). Mild PSRCT patients with minimal physical requirements might not notice any symptoms, while severe PSRCT patients with more physical demands suffer greatly in daily life (Kim, et al., 2019; Kwon, et al., 2019; Keener, et al., 2020). The former may respond favorably to non-operative treatment, and surgical intervention may be more suited for the latter. However, no biomechanical studies have tested these hypotheses. Therefore, it is unclear if a significant functional impediment would be observed in an originally compensable PSRCT shoulder under increased extra load; this information would be informative for determining suitable clinical treatment options.

To investigate the biomechanical relationship between PSRCT and shoulder function, a suitable biomechanical testing system is indispensable. The most commonly used biomechanical testing system is Instron. However, the machine only gets primary testing results, such as stiffness, number of cycles to failure, and maximum load rage at failure, which do not reflect the dynamic process of shoulder abduction (van der Meijden, et al., 2013). In addition, only uniaxial force could be applied to the muscle or tendon unit in this kind of machine, which is an oversimplification of the shoulder. Recently established biomechanical testing systems have made much improvement. In order to make the biomechanical testing platform closer to the clinical environment, some researchers have added a mechanical arm to the biomechanical testing system (Wellmann, et al., 2011). Through the mechanical arm, the shoulder can be put into a specific position to simulate the activities of the human shoulder joint. Moreover, the researcher can control the glenohumeral joint flexion and internal rotation activities by fixing the scapula and humerus, so as to detect the relatively complex biomechanical results including forward–backward translation and maximum internal rotation. Baumgartner et al. (2014) made a metal mechanical biomechanical testing system. They used an electric linear driver to simulate the force exerted by the deltoid, supraspinatus, infraspinatus/teres minor, and subscapularis, and transmitted it to the metal humerus through a cable pulley system, thus simulating the force exerted by the rotator cuff on the humerus. By equipping the metal machinery with sensors, the system can output accurate biomechanical results, including the force of each rotator cuff muscle and the glenohumeral contact force. Mihata et al. (2016) established a static biomechanical testing system, which would apply precise force on the deltoid, supraspinatus, infraspinatus, teres minor, and subscapularis to stimulate abduction motion when the glenohumeral joint angle was fixed at a certain angle (Mihata, et al., 2016). In this testing system, the shoulder index in each injured or repaired condition could be compared by evaluating the acromial contact area or glenohumeral contact force. Nevertheless, this is still a static biomechanical testing system, not reflecting the dynamic change of the shoulder. Thus, it is essential to establish a dynamic shoulder abduction stimulator that is able to reflect the active process of shoulder motion in order to precisely determine the biomechanical difference in each shoulder condition.

In this study, we explored the relationship between functional impediments of the shoulder and RCT size under extra load using a previously established dynamic shoulder abduction simulator. *Via* this machine, the tendinous insertions of the deltoid (anterior, middle, and posterior), infraspinatus/teres minor, supraspinatus, and subscapularis were dynamically loaded through a pneumatic actuator, which allows dynamic shoulder abduction from 0° to 90° (Video 1). We hypothesized that as the extra load increased, shoulder abduction impediments would be observed in a medium PSRCT, which was previously believed to be compensable.

Materials and methods

Specimen preparation and testing measurements

This study was reviewed by the Science and Research Development of the Shanghai Sixth People's Hospital, which concluded that no institutional review was necessary for this research. Cadaver shoulders (donated for medical research from the tissue bank of our university; six males and six females; aged between 54–68 years) without the signs of abnormality or preexisting pathological findings, including a full-thickness RCT, osteoarthritis, or fatty infiltration, detected *via* computed tomography and gross visual examination, were used. The cadaver shoulders were thawed overnight before the experiment. Tendinous insertions of the rotator cuff and deltoid on the humerus were reserved. Other tissue was removed while the coracoacromial ligament and capsule were carefully retained. After preparation, each specimen was mounted on a previously validated biomechanical testing system (Figure 1) (Wang L. et al., 2021). To perform active dynamic evaluation, the tendinous insertion of the anterior deltoid, middle deltoid, posterior deltoid, superior and inferior subscapularis, superior and inferior supraspinatus, infraspinatus, as well as teres minor were attached to a specific actuator, prior to load application, as reported previously. Customized plates and nails were used to imitate physiological muscle force vectors without friction. Subsequently, we simulated active dynamic abduction from 0° to 90°, using scapular rotation, and adjusted to a 2:1 glenohumeral-to-scapulothoracic ratio.

Testing model setup

Each specimen received dynamic glenohumeral abduction from 0° to 90° during our investigation. Shoulder muscle load distribution

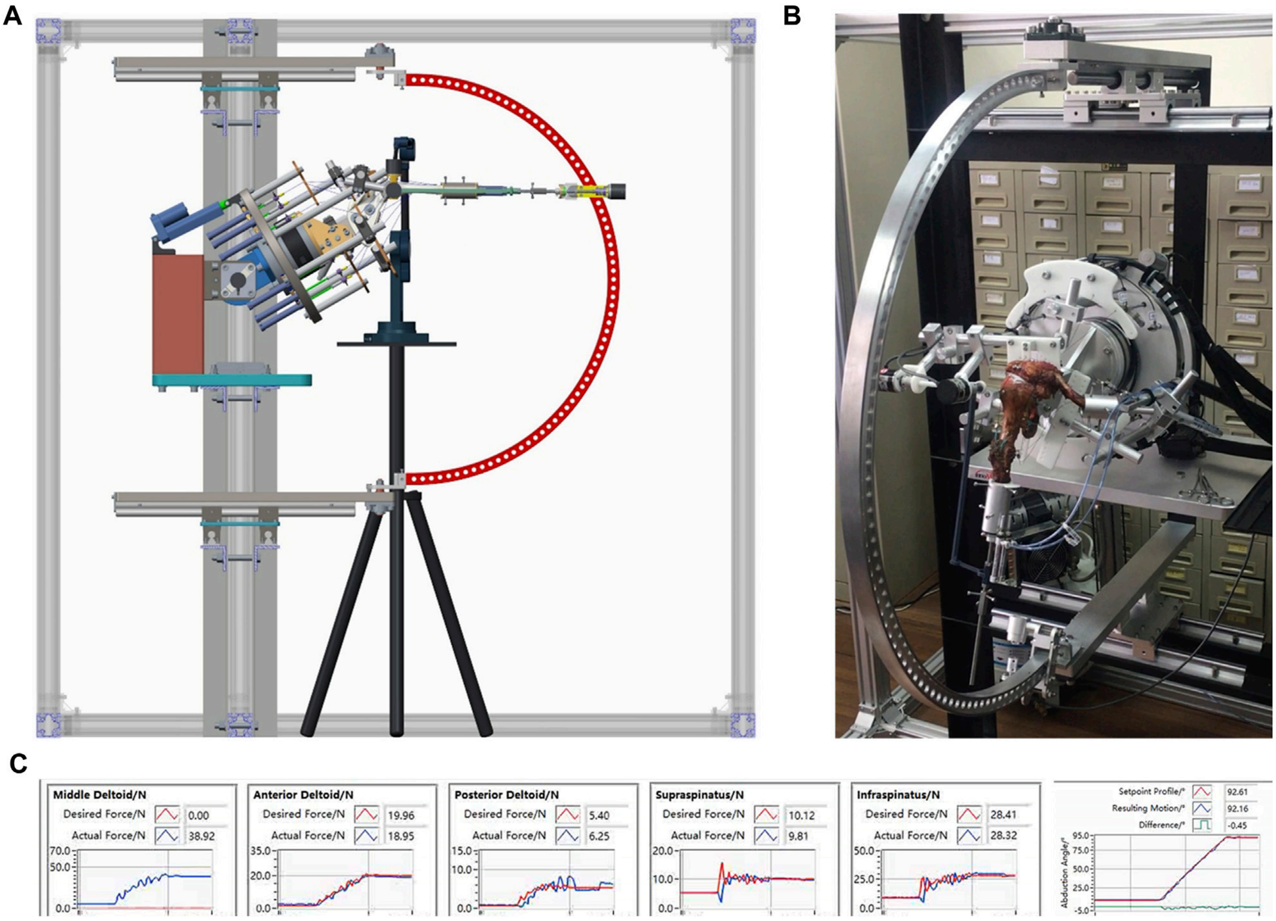

FIGURE 1
(A) Schematic and **(B)** actual experimental setup of the dynamic experimental shoulder biomechanics system, which allows 0°–60° glenohumeral abduction; **(C)** Dynamic mechanical detection of muscle force stimulation.

was assessed *via* load on the middle deltoid (supporting information). Peak middle deltoid force (MDF) referred to the peak value of MDF during shoulder dynamic abduction. Stable MDF referred to the value of MDF when the shoulder abduction angle is stabilized at 90°. Peak subacromial contact pressure (SACP) referred to the peak value of subacromial contact pressure during shoulder dynamic abduction recorded by a pressure measurement system (Fujifilm, Tokyo: measurement accuracy: 0.25 mPa). Average SACP referred to the average value of subacromial contact pressure during shoulder dynamic abduction recorded by pressure measurement system (Fujifilm, Tokyo: measurement accuracy: 0.25 mPa). Subacromial contact area (SACA) referred to the subacromial contact area during shoulder dynamic abduction recorded by a pressure measurement system (Fujifilm, Tokyo). Subacromial contact force (SACF) referred to the cumulative subacromial contact force during shoulder dynamic abduction recorded by a pressure measurement system (Fujifilm, Tokyo). Peak glenohumeral contact force (GHCF) referred to the peak value of GHCF during shoulder dynamic abduction. Stable GHCF referred to the value of GHCF when the shoulder abduction angle is stabilized at 90°. The value of GHCF was previously used to evaluate the shoulder stability on different rotator cuff injuries or repairing conditions *via* a static shoulder biomechanical testing system when the force applied to the shoulder is constant (Mihata, et al., 2012; Mihata, et al., 2016). However, in this dynamic biomechanical testing system, the force applied to the shoulder has significant differences in different rotator cuff injury conditions. To eliminate this difference, we used the GHCF/MDF ratio to represent the shoulder stability on different rotator cuff injuries or repairing conditions.

Simulation of abduction failure

In biomechanical studies, it is indeed possible to make the shoulder complete 0–90° abduction with extra loading by increasing

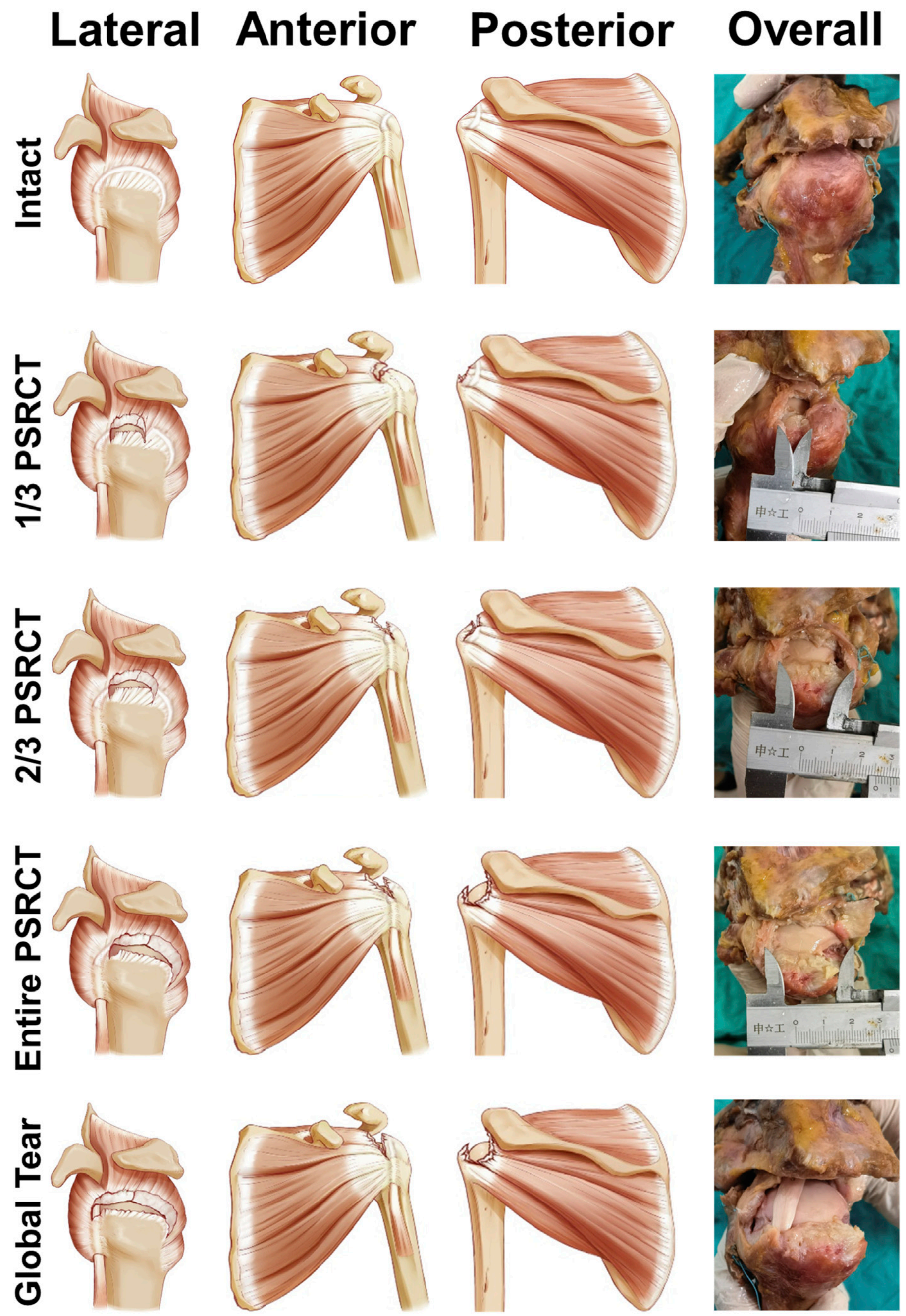

FIGURE 2
Schematic graph of the testing conditions.

the force of the middle deltoid. However, if the increased force applied by the middle deltoid exceeds the threshold of normal deltoid in the human body, the 0–90° abduction can only be completed on the biomechanical machine, not in the human body. Therefore, the threshold of middle deltoid force is very important. In previous biomechanical studies, the failure load of the middle deltoid was usually set to 80 N. (Cline et al., 2021; Denard, et al., 2022; Tibone, et al., 2022). According to these suggestions, when installing the electric actuators matching the middle deltoid, we specially selected the electric actuators with a maximum range of 100 N. *Via* this electric actuator, when the biomechanical machine cannot complete 0–90° abduction, it means that the normal shoulder joint may not be able to complete the abduction of the shoulder joint in this certain situation, which is determined as a failure state in this study. In this condition, the maximal extra load was recorded as 100% failure load. In this study, 0, 45, and 90% failure loads were individually added to each shoulder on the distal humerus to stimulate daily activities as an empty hand, medium, and heavy upper extremity weight-bearing, respectively.

Experimental conditions

In total, 15 conditions (five PSRCT conditions with three loads each) were tested (Figure 2). Intact rotator cuff shoulder was recorded as condition 1. Then, PSRCT was created from the anterior insertion of the supraspinatus with sequentially enlarged sizes to establish three PSRCT models: the anterior one-third (1/3 PSRCT, condition 2), anterior and middle one-third (2/3 PSRCT, condition 3), and entire posterior–superior rotator cuff (entire PSRCT, condition 4). The rotator cuff part of the teres minor and the subscapularis lying above the rotation center of the humeral head was torn as a global tear control (global tear, condition 5). For each condition, 0, 45, and 90% failure loads were individually added to the distal humerus to examine the function of shoulder abduction.

Statistical analysis

The average of three measurements from each parameter was used for data analyses. To test differences in the peak MDF, stable MDF, average SACP, peak SACP, SACA, SACF, stable GHCF/MDF ratio, and peak GHCF/MDF ratio, two-way ANOVA analysis was performed. When a significant difference in interaction was observed, a simple effect analysis was performed. *p*-value of <0.05 was considered significant.

To reach 80% power based on the mean and standard deviation of the first four specimens, three specimens were required for stable MDF and the peak GHCF/MDF ratio, three specimens were required for SACA and the GHCF/MDF ratio, seven specimens were required for peak SACP, nine specimens were required for average SACP, ten specimens were required for peak MDF, and eleven specimens were required for SACF. Totally, twelve cadaveric specimens were used.

Results

Stimulation of pseudoparalysis in the biomechanical testing system

Clinically, pseudoparalysis patients suffer from a limited abduction angle. However, in a biomechanical testing system, with enough force and fulcrum, an arm can always abduct to a certain angle. Nevertheless, the deltoid is increasingly required to complete the abduction angle. Thus, instead of the maximum abduction degree, the MDF required for the abduction was considered the most important factor for evaluating pseudoparalysis in the current biomechanical testing system. Figure 3 presents the dynamic change between MDF abduction and the shoulder abduction angle. The minimum MDF required for abduction with 100% failure load less than 90° was 87.58 ± 7.17 N (95% confidence interval [CI]: 83.03–92.14 N), which was significantly increased compared with that for the 0% failure load condition (29.18 ± 4.99 N, 95% CI: 26.01–32.36 N).

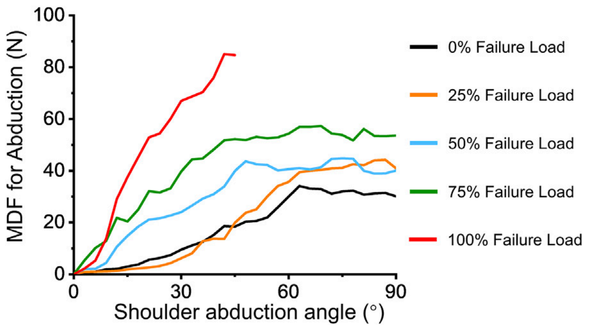

FIGURE 3
Effect of extra loading on MDF during abduction.

Effect of rotator cuff tear on middle deltoid force during abduction

Figure 4 presents the MDF curve of the intact and other RCT conditions under variable loading. For the 0% failure load condition (Table 1), the peak and stable MDFs in the global tear condition were significantly increased compared with those in the intact, 1/3 PSRCT, 2/3 PSRCT, and entire PSRCT conditions. For the 45% failure load condition (Table 1), the peak and stable MDFs in the entire PSRCT and global tear conditions were significantly increased compared with those in the intact, 1/3 PSRCT, and 2/3 PSRCT conditions. For the 90% failure load (Table 1), the peak and stable MDFs in the 2/3 PSRCT, entire PSRCT, and global tear conditions were significantly increased compared with those in the intact and 1/3 PSRCT conditions.

Effect of rotator cuff tear on the subacromial contact pressure, area, and force during abduction

As is shown in Figure 5, for the 0% failure load (Table 2), peak and average SACPs, SACA, and SACF in the global tear condition were significantly increased compared with those in the intact, 1/3 PSRCT, 2/3 PSRCT, and entire PSRCT condition. For the 45% failure load (Table 2), the peak and average SACPs, SACA, and SACF in the entire PSRCT and global tear condition

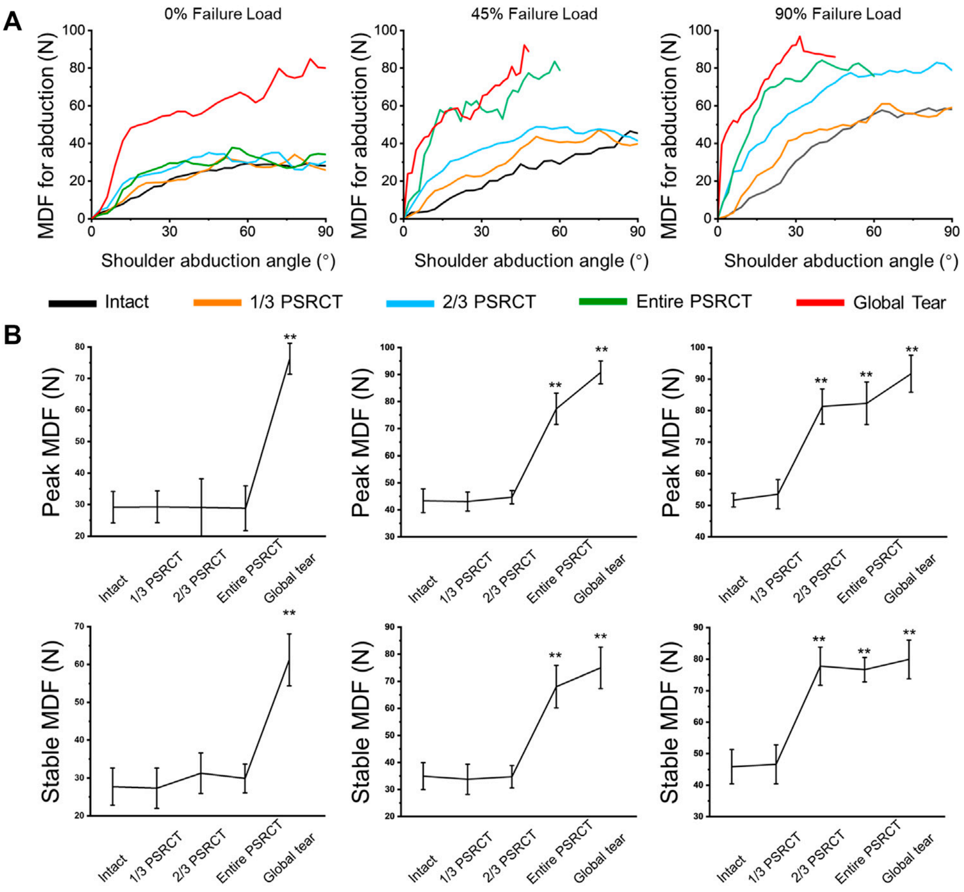

FIGURE 4
Effect of RCT on MDF during abduction. **(A)** The MDF curves of the intact, 1/3, 2/3, entire, and global tear conditions under 0, 45, and 90% failure loads. **(B)** The peak and stable MDFs during 60° glenohumeral abduction. MDF, middle deltoid force. **, a significant difference compared with the intact condition, $p < 0.01$.

TABLE 1 Effect of RCT on MDF during abduction.

	0% Failure load (N)		45% Failure load (N)		90% Failure load (N)	
	Peak	**Stable**	**Peak**	**Stable**	**Peak**	**Stable**
Intact	29.18 ± 4.99	27.71 ± 4.93	43.35 ± 4.39^{a}	34.91 ± 4.98^{a}	51.66 ± 2.17^{a,b}	45.84 ± 5.45^{a,b}
1/3 PSRCT	29.30 ± 5.03	27.28 ± 5.33	43.09 ± 3.52^{a}	33.77 ± 5.59^{a}	53.52 ± 4.64^{a,b}	46.62 ± 6.21^{a,b}
2/3 PSRCT	29.13 ± 8.14	31.25 ± 5.38	44.68 ± 2.46^{a}	37.20 ±4.02^{a}	81.31 ± 5.57^{a,b,**}	77.77 ± 6.04^{a,b,**}
entire PSRCT	28.85 ± 7.12	29.88 ± 3.81	77.32 ± 5.81^{a,**}	68.00 ± 7.84^{a,**}	82.31 ± 6.74^{a,**}	76.65 ± 3.86^{a,b,**}
global tear	76.27 ± 4.94**	61.22 ± 6.88**	90.77 ± 4.23^{a,**}	74.95 ± 7.65^{a,**}	91.67 ± 5.85^{a,**}	79.90 ± 6.14^{a,**}

MDF: middle deltoid force; RCT: rotator cuff tear. ^{a}significant difference compared with 0% failure load, $p < 0.05$; ^{b}significant difference compared with 45% failure load, $p < 0.05$; **significant difference compared with the intact condition, $p < 0.01$.

were significantly increased compared with those in the intact, 1/3 PSRCT, and 2/3 PSRCT conditions. For the 90% failure load (Table 2), the peak and average SACPs, SACA, and SACF in the 2/3 PSRCT, entire PSRCT, and global tear conditions were significantly increased compared with those in the intact and 1/3 PSRCT conditions.

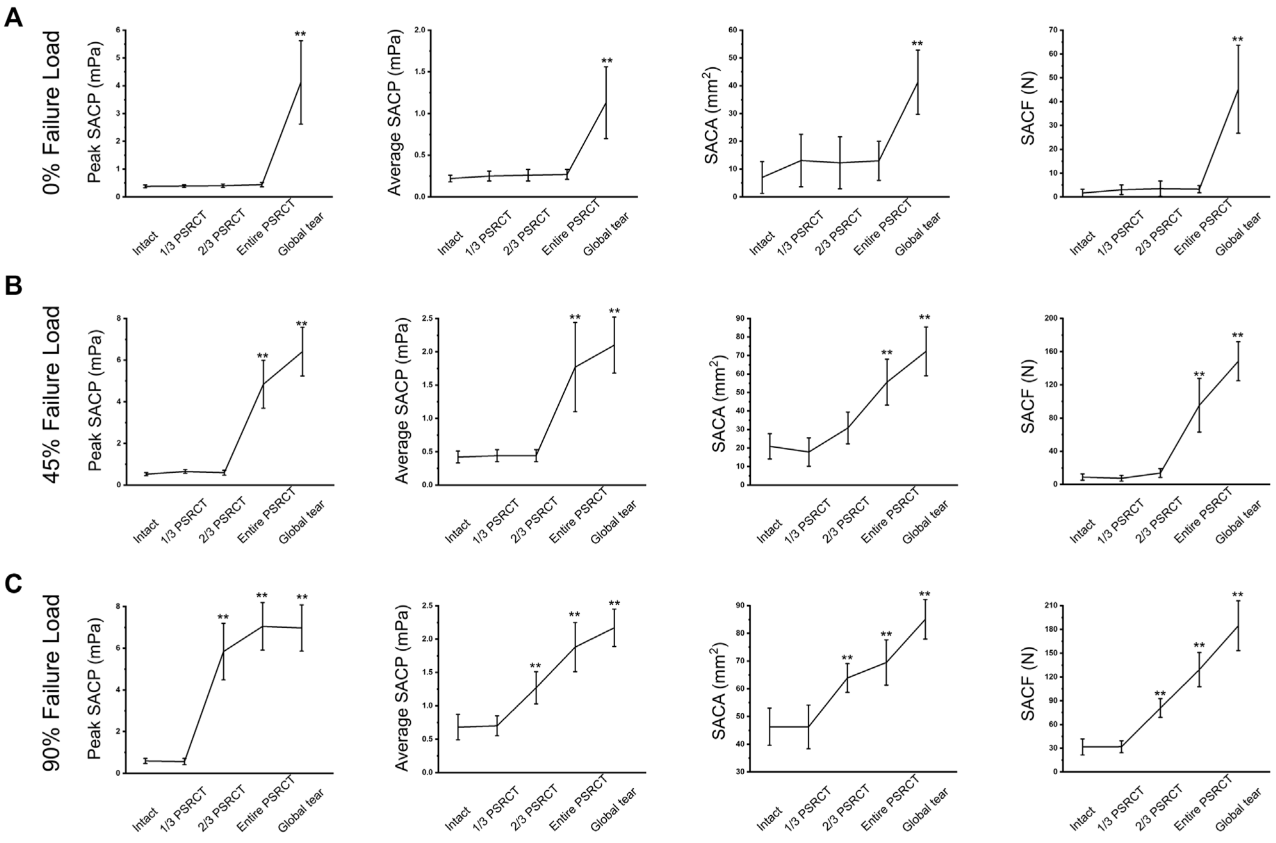

FIGURE 5
Effect of RCT on the peak and average SACPs, SACA, and SACF under **(A)** 0, **(B)** 45, and **(C)** 90% failure loads during abduction. SACP, subacromial contact pressure; SACA, subacromial contact area; SACF, subacromial contact force. **, a significant difference compared with the intact condition, $p < 0.01$.

TABLE 2 Effect of RCT on the subacromial contact pressure, area, and force during abduction.

	0% Failure Load (N)				45% Failure Load (N)				90% Failure Load (N)			
	Peak SACP (MPa)	Average SACP (MPa)	SACA (mm^2)	SACF (N)	Peak SACP (MPa)	Average SACP (MPa)	SACA (mm^2)	SACF (N)	Peak SACP (MPa)	Average SACP (MPa)	SACA (mm^2)	SACF (N)
Intact	0.38 ± 0.05	0.22 ± 0.04	7.00 ± 5.73	1.62 ± 1.60	0.52 ± 0.07 mPa^{a}	0.42 ± 0.11^{a}	20.92 ± 6.84^{a}	8.91 ± 3.88^{a}	0.59 ± 0.12^{a,b}	0.68 ± 0.19^{a,b}	46.33 ± 6.70^{a,b}	31.59 ± 10.08^{a,b}
1/3 PSRCT	0.40 ± 0.06	0.25 ± 0.06	13.08 ± 9.46	2.98 ± 2.05	0.65 ± 0.09^{a}	0.44 ± 0.09^{a}	17.83 ± 7.65	7.48 ± 3.41^{a}	0.56 ± 0.15^{a,b}	0.70 ± 0.15^{a,b}	46.25 ± 7.90^{a,b}	31.81 ± 7.56^{a,b}
2/3 PSRCT	0.40 ± 0.06	0.26 ± 0.07	12.25 ± 9.37	3.43 ± 3.22	0.59 ± 0.12^{a}	0.44 ± 0.09^{a}	30.83 ± 8.59^{a}	13.79 ± 5.28^{a}	5.84 ± 1.36^{a,b,**}	1.27 ± 0.24^{a,b,**}	63.92 ± 5.20^{a,b,**}	80.76 ± 11.83^{a,b,**}
entire PSRCT	0.44 ± 0.08	0.27 ± 0.06	12.98 ± 7.03	3.22 ± 1.51	4.84 ± 1.15^{a,**}	1.77 ± 0.67^{a,**}	55.58 ± 12.41^{a,**}	95.42 ± 32.33^{a,**}	7.05 ± 1.14^{a,b,**}	1.88 ± 0.37^{a,**}	69.50 ± 8.17^{a,b,**}	129.24 ± 21.52^{a,b,**}
global tear	4.12 ± 1.50**	1.13 ± 0.43**	41.28 ± 11.56**	45.19 ± 18.49**	6.41 ± 1.17^{a,**}	2.10 ± 0.43^{a,**}	72.25 ± 13.14^{a,**}	148.43 ± 23.54^{a,**}	6.97 ± 1.11^{a,**}	2.17 ± 0.28^{a,**}	85.08 ± 7.15^{a,b,**}	184.60 ± 31.44^{a,b,**}

RCT: rotator cuff tear; SACA: subacromial contact area; SACF: subacromial contact force; SACP: subacromial contact pressure. ^{a}significant difference compared with 0% Failure Load, $p < 0.05$; ^{b}significant difference compared with 45% Failure Load, $p < 0.05$; **significant difference compared with the intact condition, $p < 0.01$.

TABLE 3 Effect of RCT on the GHCF/MDF ratio.

	0% Failure Load (N)		45% Failure Load (N)		90% Failure Load (N)	
	Peak	Stable	Peak	Stable	Peak	Stable
Intact	2.19 ± 0.12	2.55 ± 0.29	2.11 ± 0.22	2.74 ± 0.41	1.80 ± 0.06^{a,b}	2.09 ± 0.23^{a,b}
1/3 PSRCT	2.14 ± 0.14	2.73 ± 0.19	2.11 ± 0.17	2.69 ± 0.25	1.80 ± 0.07^{a,b}	1.99 ± 0.13^{a,b}
2/3 PSRCT	2.14 ± 0.15	2.69 ± 0.38	2.13 ± 0.17	2.49 ± 0.19	1.46 ± 0.06^{a,**}	1.41 ± 0.10^{a,**}
entire PSRCT	2.17 ± 0.15	2.48 ± 0.32	1.32 ± 0.15^{a,**}	1.41 ± 0.07^{a,**}	1.37 ± 0.07^{a,**}	1.34 ± 0.06^{a,**}
global tear	1.43 ± 0.11**	1.60 ± 0.30**	1.22 ± 0.09^{a,**}	1.39 ± 0.04^{a,**}	1.35 ± 0.08^{a,**}	1.22 ± 0.06^{a,b,**}

GHCF: glenohumeral contact force; MDF: middle deltoid force; RCT: rotator cuff tear. ^{a}significant difference compared with 0% Failure Load, *p* < 0.05; ^{b}significant difference compared with 45% Failure Load, *p* < 0.05; **significant difference compared with the intact condition, *p* < 0.01.

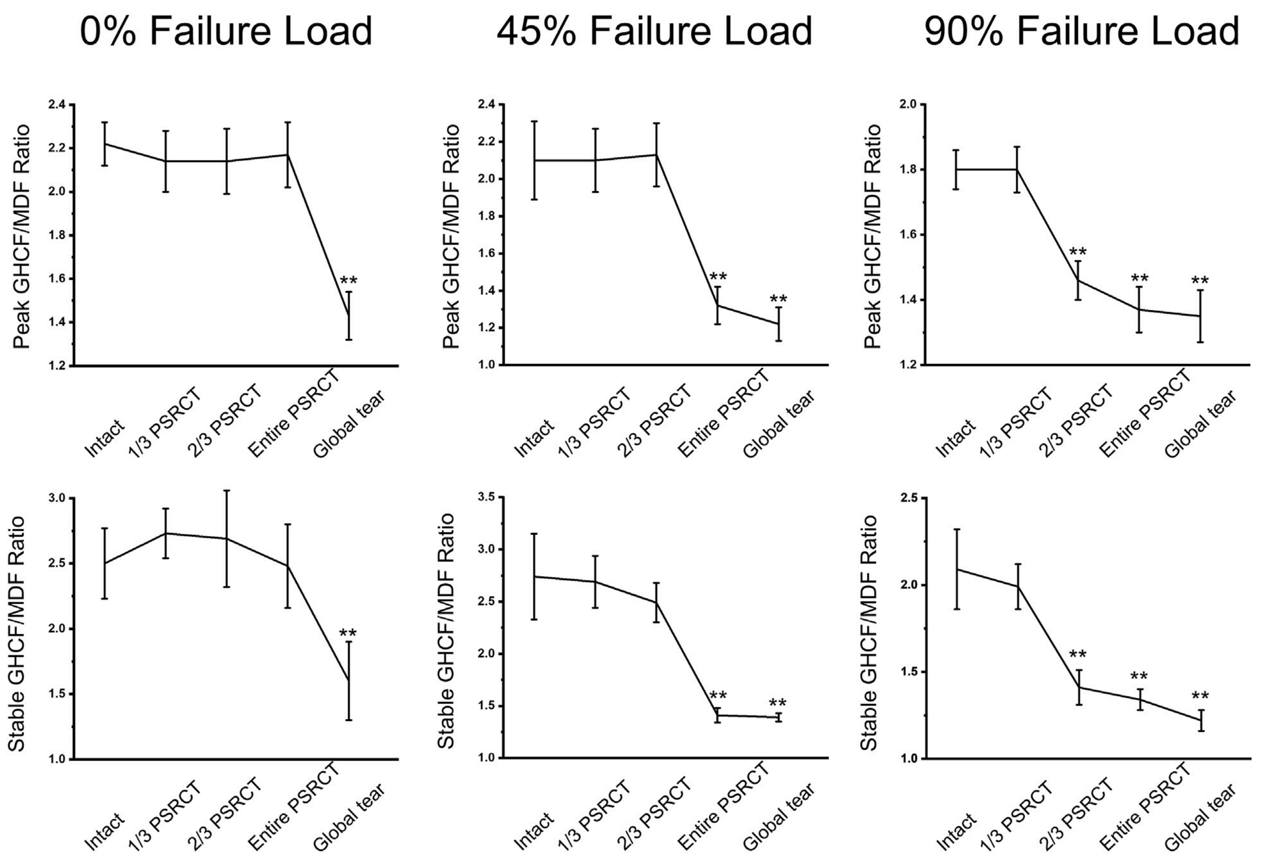

FIGURE 6
Effect of RCT on the peak and stable GHCF/MDF ratios under 0, 45, and 90% failure loads during abduction. MDF, middle deltoid force. **, a significant difference compared with the intact condition, *p* < 0.01.

Effect of rotator cuff tear on the glenohumeral contact force/middle deltoid force ratio

The GHCF/MDF ratio is used to evaluate shoulder stability based on a study (Figure 6) (Wang L. R. et al., 2021). For the 0% failure load (Table 3), the peak and stable GHCF/MDF ratios in the global tear condition were significantly decreased compared with those in the intact, 1/3 PSRCT, 2/3 PSRCT, and entire PSRCT conditions. For the 45% failure load, the peak and stable GHCF/MDF ratios in the entire PSRCT and global tear conditions were significantly decreased compared with those in the intact, 1/3 PSRCT, and 2/3 PSRCT conditions. For the 90% failure load, the peak and stable GHCF/MDF ratios in the 2/3 PSRCT, entire PSRCT, and global tear conditions were significantly decreased compared with those in the intact and 1/3 PSRCT conditions.

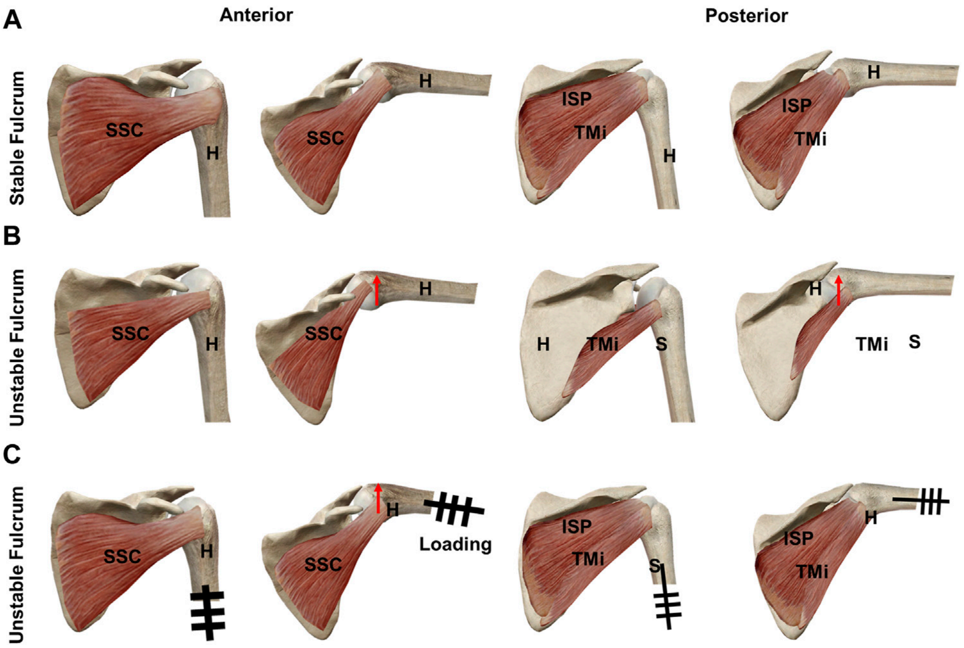

FIGURE 7
Schematic graphs of the superior migration of the humeral head and fulcrum during abduction: **(A)** RCT with remnant rotator cuff tissue above the equatorial line of the humeral head at 0° and 60° glenohumeral abduction, **(B)** 0° and 60° glenohumeral abduction of MRCT without remnant rotator cuff tissue above the equatorial line of the humeral head, and **(C)** RCT with remnant rotator cuff tissue above the equatorial line of the humeral head with extra loading at 0° and 60° glenohumeral abduction. H: humerus; ISP: infraspinatus; RCT: rotator cuff tear; S: scapular; SSC: subscapularis; TMi: teres minor.

Discussion

Our biomechanical findings indicated that as PSRCT progressed, the weight-bearing ability of the shoulder became significantly impaired. There was a significant increase in the peak and stable MDFs, peak and average SACPs, SACA, and SACF with extra loading compared with the empty hand condition. Furthermore, there was a significant decrease in shoulder stability in high–weight-bearing conditions with larger tears, indicated by decreased peak and stable GHCF/MDF ratios. Taken together, these results suggested that when there is some remaining rotator cuff attachment above the equatorial line of the humeral head, active abduction is not affected by the PSRCT without extra loading, regardless of the tear size. However, with the extra load, the MDF significantly increases, resulting in the dysfunction of the remnant rotator cuff attachment above the equatorial line of the humeral head. Thus, the humeral head inevitably shifts upwards, significantly impairing the glenohumeral abduction function.

Recent studies have investigated whether a critical RCT stage contributed to the functional impediments of shoulder abduction function. Oh et al. (2011) suggested that the entire detachment of supraspinatus was the critical RCT stage causing significantly decreased abduction capability and increased anterior-posterior humeral head shift. The impeded shoulder function deteriorated when the infraspinatus was subsequently detached. However, Dyrna F et al. (2018) investigated biomechanical differences in deltoid force after posterior-superior and anterior-superior massive RCTs (MRCTs) in a cadaveric model using a sub dynamic testing system and found that the mean force generated by anterior, middle, and posterior deltoids significantly increased in anterior-superior MRCT but not in posterior-superior MRCT. Yoon TH et al. (2019) enrolled 108 MRCT patients and found that the patients with subscapularis and teres minor integrity experienced significantly decreased incidences of conventional treatment failure compared with patients lacking integrity of one or both muscles. Currently, the relationship between the abduction limitation and global RCT is under review. Ernstbrunner et al. (2021) reviewed 50 RCT patients and found that without extra loading, the shoulder abduction function only deteriorated when the degree of global tear extension reached 225 ± 14°. These contract biomechanical findings might be because PSRCT might partly impair the rotator cuff function compared with native uninjured shoulder, which can be detected in intricate biomechanical testing. However, the whole glenohumeral dynamic abduction remained unchanged without bearing extra loading.

Clinically, MRCT patients always complain about heavy lifting limitations in daily life. However, the abduction strength is also important in the Constant–Murley Score (Hirschmann, et al., 2010; Roy, et al., 2010). Our biomechanical results suggested that the loss of muscle tone resulted in a limited abduction ability for carrying heavy things and increased the required MDF for abduction. This biomechanical phenomenon might be explained by the fulcrum theory. Burkhart et al. (1992) suggested that the glenohumeral fulcrum is classified into stable and unstable fulcrums depending on the severity of RCT. The unstable fulcrum was commonly caused by MRCT and clinically characterized as the decreased interface between the humeral head position and acromion on magnetic resonance images or radiographs (de Oliveira Franca et al., 2016; Denard, et al., 2018) which was believed to play a critical role in glenohumeral function (Kozono, et al., 2018a; Kozono, et al., 2018b). The shift from a stable to an unstable fulcrum represented a significant alternation of the normal biomechanical status and was correlated with impaired abduction function. However, because the decreased interface between the humeral head position and the acromion is not easy to record in dynamic biomechanical testing, the SACP, SACA, and SACF were used to represent the fulcrum status. The increased SACP, SACA, and SACF indicated increased contact between the humerus and acromion, suggesting a shift to an unstable fulcrum. The present study demonstrated that the glenohumeral fulcrum remained stable in the 1/3 PSRCT, 2/3 PSRCT, and entire PSRCT conditions. However, as the extra load added on the distal humerus increased, the remnant rotator cuff above the equatorial line of the humeral head gradually became inadequate for stabilizing the humeral head. Consequently, the humeral head migrated proximally and hit the acromion, increasing SACP, SACA, and SACF and forming a newly unstable fulcrum (Figure 7). We hypothesized that unlike the stable fulcrum, the newly formed unstable fulcrum would result in significantly increased MDF during the abduction, as previously suggested.

The present study indicated a negative relationship between the PSRCT and shoulder function without extra loading and a positive correlation between the tear size and shoulder abduction limitations as the extra load increased. Thus, RCT treatment should be matched with the physical demand of the patient (Kweon, et al., 2015; Kim, et al., 2018; Ramme, et al., 2019; Merlet, et al., 2021). For most young patients with sports needs, a surgical repair to restore the rotator cuff integrity is inevitable to guarantee the quality of life after injury (Klouche, et al., 2016; Azzam, et al., 2018; Rossi, et al., 2019). However, for some elderly patients with medium or entire PSRCT who only require daily life movements, such as hair brushing, conservative treatment with an analgesic might be adequate.

There were some limitations to our study. First, only deltoid, supraspinatus, infraspinatus, subscapularis, and teres minor were loaded during our humeral abduction experiments. Other muscles, including the pectoralis major, latissimus dorsi, and teres major, should be included in future dynamic biomechanical studies. Second, this biomechanical testing system was based on a pneumatic loading machine. Third, in this study, the relative force ratio of each group of muscles was consistent during the 0–90° shoulder abduction, in the state of rotator cuff intact, injury, and repairing, which may not be identical to the clinical situation. Forth, resulting from the limitation of feedback speed of the biomechanical testing system, the profile of the MDF during 0–90° shoulder abduction is not smooth enough, which might affect the reliability of the conclusion. Fifth, the dynamic muscle loading protocol in this biomechanical testing system was based on normal shoulder conditions, which are different compared with RCT conditions and might influence the biomechanical results.

Data availability statement

The raw data supporting the conclusion of this article will be made available by the authors, without undue reservation.

Author contributions

LW: Investigation, methodology, data curation, formal analysis, and writing and original draft. YK: Investigation, methodology, data curation, formal analysis, writing—original draft, and funding acquisition. HJ: Investigation, visualization, and formal analysis. MW: Investigation and formal analysis. YW: Investigation, visualization, and formal analysis. HG: Investigation and formal analysis. DS: Resources. SY: Investigation, methodology, and data curation. GX: Investigation, methodology, and data curation. JJ: Conceptualization, supervision, writing—review and editing, and project administration. JZ: Funding acquisition, conceptualization, supervision, writing—review and editing, and project administration.

Funding

This work was supported by the National Natural Science Foundation of China (Grant nos 81902186, 81671920, 31972923, 81871753, and 81772341), National Key Research and Development Program of China (Grant nos 2018YFC1106200, 2018YFC1106201, and 2018YFC1106202), and Technology Support Project of Science and Technology Commission of Shanghai Municipality of China (Grant nos 19441901700, 19441901701, 19441901702, 18441902800, 21S31908500, and 19441902500). The authors would like to thank Dr. Thay Q. Lee for his help in the design of this testing system.

Conflict of interest

The authors declare that the research was conducted in the absence of any commercial or financial relationships that could be construed as a potential conflict of interest.

Publisher's note

References

Azzam, M. G., Dugas, J. R., Andrews, J. R., Goldstein, S. R., Emblom, B. A., and Cain, E. L., Jr (2018). Rotator cuff repair in adolescent athletes. *Am. J. Sports Med.* 46 (5), 1084–1090. doi:10.1177/0363546517752919

Baumgartner, D., Tomas, D., Gossweiler, L., Siegl, W., Osterhoff, G., and Heinlein, B. (2014). Towards the development of a novel experimental shoulder simulator with rotating scapula and individually controlled muscle forces simulating the rotator cuff. *Med. Biol. Eng. Comput.* 52 (3), 293–299. doi:10.1007/s11517-013-1120-z

Burkhart, S. S. (1992). Fluoroscopic comparison of kinematic patterns in massive rotator cuff tears. A suspension bridge model. *Clin. Orthop. Relat. Res.* 284 (284), 144–152.

Cline, K. E., Tibone, J. E., Ihn, H., Akeda, M., Kim, B. S., McGarry, M. H., et al. (2021). Superior capsule reconstruction using fascia lata allograft compared with double- and single-layer dermal allograft: A biomechanical study. *Arthrosc. J. Arthrosc. Relat. Surg.* 37 (4), 1117–1125. doi:10.1016/j.arthro.2020.11.054

de Oliveira Franca, F., Godinho, A. C., Ribeiro, E. J., Falster, L., Burigo, L. E., and Nunes, R. B. (2016). Evaluation of the acromiohumeral distance by means of magnetic resonance imaging umerus. *Rev. Bras. Ortop.* 51 (2), 169–174. doi:10.1016/j.rboe.2016.01.008

Denard, P. J., Brady, P. C., Adams, C. R., Tokish, J. M., and Burkhart, S. S. (2018). Preliminary results of arthroscopic superior capsule reconstruction with dermal allograft. *Arthrosc. J. Arthrosc. Relat. Surg.* 34 (1), 93–99. doi:10.1016/j.arthro.2017.08.265

Denard, P. J., Park, M. C., McGarry, M. H., Adamson, G., and Lee, T. Q. (2022). Biomechanical assessment of a V-shaped semitendinosus allograft anterior cable reconstruction for irreparable rotator cuff tears. *Arthrosc. J. Arthrosc. Relat. Surg.* 38 (3), 719–728. doi:10.1016/j.arthro.2021.07.031

Dyrna, F., Kumar, N. S., Obopilwe, E., Scheiderer, B., Comer, B., Nowak, M., et al. (2018). Relationship between deltoid and rotator cuff muscles during dynamic shoulder abduction: A biomechanical study of rotator cuff tear progression. *Am. J. Sports Med.* 46 (8), 1919–1926. doi:10.1177/0363546518768276

Ernstbrunner, L., El Nashar, R., Favre, P., Bouaicha, S., Wieser, K., and Gerber, C. (2021). Chronic pseudoparalysis needs to Be distinguished from pseudoparesis: A structural and biomechanical analysis. *Am. J. Sports Med.* 49 (2), 291–297. doi:10.1177/0363546520969858

Hirschmann, M. T., Wind, B., Amsler, F., and Gross, T. (2010). Reliability of shoulder abduction strength measure for the Constant-Murley score. *Clin. Orthop. Relat. Res.* 468 (6), 1565–1571. doi:10.1007/s11999-009-1007-3

Keener, J. D., Aleem, A. W., Chamberlain, A. M., Sefko, J., and Steger-May, K. (2020). Factors associated with choice for surgery in newly symptomatic degenerative rotator cuff tears: A prospective cohort evaluation. *J. Shoulder Elb. Surg.* 29 (1), 12–19. doi:10.1016/j.jse.2019.08.005

Keener, J. D., Skelley, N. W., Stobbs-Cucchi, G., Steger-May, K., Chamberlain, A. M., Aleem, A. W., et al. (2017). Shoulder activity level and progression of degenerative cuff disease. *J. Shoulder Elb. Surg.* 26 (9), 1500–1507. doi:10.1016/j.jse.2017.05.023

Kim, H. J., Kim, J. Y., and Rhee, Y. G. (2019). When do patients return to previous daily activity after arthroscopic rotator cuff repair? *Clin. Orthop. Relat. Res.* 477 (2), 403–413. doi:10.1097/corr.0000000000000554

Kim, Y. S., Lee, H. J., Kim, J. H., and Noh, D. Y. (2018). When should we repair partial-thickness rotator cuff tears? Outcome comparison between immediate surgical repair versus delayed repair after 6-month period of nonsurgical treatment. *Am. J. Sports Med.* 46 (5), 1091–1096. doi:10.1177/0363546518757425

Klouche, S., Lefevre, N., Herman, S., Gerometta, A., and Bohu, Y. (2016). Return to sport after rotator cuff tear repair: A systematic review and meta-analysis. *Am. J. Sports Med.* 44 (7), 1877–1887. doi:10.1177/0363546515598995

Kozono, N., Okada, T., Takeuchi, N., Hamai, S., Higaki, H., Shimoto, T., et al. (2018a). Dynamic kinematics of the glenohumeral joint in shoulders with rotator cuff tears. *J. Orthop. Surg. Res.* 13 (1), 9. doi:10.1186/s13018-017-0709-6

Kozono, N., Okada, T., Takeuchi, N., Hamai, S., Higaki, H., Shimoto, T., et al. (2018b). *In vivo* dynamic acromiohumeral distance in shoulders with rotator cuff tears. *Clin. Biomech. (Bristol, Avon.* 60, 95–99. doi:10.1016/j.clinbiomech.2018.07.017

Kweon, C., Gagnier, J. J., Robbins, C. B., Bedi, A., Carpenter, J. E., and Miller, B. S. (2015). Surgical versus nonsurgical management of rotator cuff tears: Predictors of treatment allocation. *Am. J. Sports Med.* 43 (10), 2368–2372. doi:10.1177/0363546515593954

Kwon, J., Kim, S. H., Lee, Y. H., Kim, T. I., and Oh, J. H. (2019). The rotator cuff healing index: A new scoring system to predict rotator cuff healing after surgical repair. *Am. J. Sports Med.* 47 (1), 173–180. doi:10.1177/0363546518810763

Merlet, M. C., Guinet, V., Rousseau, T., van Rooij, F., Saffarini, M., Dujardin, F., et al. (2021). Arthroscopic side-to-side repair of massive rotator cuff tears maintains adequate functional improvement at 12 to 14 Years' follow-up. *Am. J. Sports Med.* 49 (2), 298–304. doi:10.1177/0363546520985224

Mihata, T., McGarry, M. H., Kahn, T., Goldberg, I., Neo, M., and Lee, T. Q. (2016). Biomechanical effect of thickness and tension of fascia lata graft on glenohumeral stability for superior capsule reconstruction in irreparable supraspinatus tears. *Arthrosc. J. Arthrosc. Relat. Surg.* 32 (3), 418–426. doi:10.1016/j.arthro.2015.08.024

Mihata, T., McGarry, M. H., Pirolo, J. M., Kinoshita, M., and Lee, T. Q. (2012). Superior capsule reconstruction to restore superior stability in irreparable rotator cuff tears: A biomechanical cadaveric study. *Am. J. Sports Med.* 40 (10), 2248–2255. doi:10.1177/0363546512456195

Oh, J. H., Jun, B. J., McGarry, M. H., and Lee, T. Q. (2011). Does a critical rotator cuff tear stage exist?: A biomechanical study of rotator cuff tear progression in human cadaver shoulders. *J. Bone Jt. Surg.* 93 (22), 2100–2109. doi:10.2106/jbjs.j.00032

Ramme, A. J., Robbins, C. B., Patel, K. A., Carpenter, J. E., Bedi, A., Gagnier, J. J., et al. (2019). Surgical versus nonsurgical management of rotator cuff tears: A matched-pair analysis. *J. Bone Jt. Surg.* 101 (19), 1775–1782. doi:10.2106/jbjs.18.01473

Rashid, M. S., Cooper, C., Cook, J., Cooper, D., Dakin, S. G., Snelling, S., et al. (2017). Increasing age and tear size reduce rotator cuff repair healing rate at 1 year. *Acta Orthop.* 88 (6), 606–611. doi:10.1080/17453674.2017.1370844

Rizvi, S. M. T., Bishop, M., Lam, P. H., and Murrell, G. A. C. (2021). Factors predicting frequency and severity of postoperative pain after arthroscopic rotator cuff repair surgery. *Am. J. Sports Med.* 49 (1), 146–153. doi:10.1177/0363546520971749

Rossi, L. A., Atala, N., Bertona, A., Tanoira, I., Bongiovanni, S., Maignon, G., et al. (2019). Return to sports after *in situ* arthroscopic repair of partial rotator cuff tears. *Arthrosc. J. Arthrosc. Relat. Surg.* 35 (1), 32–37. doi:10.1016/j.arthro.2018.07.037

Roy, J. S., MacDermid, J. C., and Woodhouse, L. J. (2010). A systematic review of the psychometric properties of the Constant-Murley score. *J. Shoulder Elb. Surg.* 19 (1), 157–164. doi:10.1016/j.jse.2009.04.008

Tibone, J. E., Mansfield, C., Kantor, A., Giordano, J., Lin, C. C., Itami, Y., et al. (2022). Human dermal allograft superior capsule reconstruction with graft length determined at glenohumeral abduction angles of 20° and 40° decreases joint translation and subacromial pressure without compromising range of motion: A cadaveric biomechanical study. *Arthrosc. J. Arthrosc. Relat. Surg.* 38 (5), 1398–1407. doi:10.1016/j.arthro.2021.11.007

van der Meijden, O. A., Wijdicks, C. A., Gaskill, T. R., Jansson, K. S., and Millett, P. J. (2013). Biomechanical analysis of two-tendon posterosuperior rotator cuff tear repairs: Extended linked repairs and augmented repairs. *Arthrosc. J. Arthrosc. Relat. Surg.* 29 (1), 37–45. doi:10.1016/j.arthro.2012.07.012

Wang, L., Kang, Y., Xie, G., Cai, J., Chen, C., Yan, X., et al. (2021). Incomplete rotator cable did not cause rotator cuff dysfunction in case of rotator cuff tear: A biomechanical study of the relationship between rotator cable integrity and rotator cuff function. *Arthrosc. J. Arthrosc. Relat. Surg.* 37 (8), 2444–2451. doi:10.1016/j.arthro.2021.03.051

Wang, L. R., Kang, Y. H., Xie, G. M., Cai, J. Y., Chen, C. A., Yan, X. Y., et al. (2021). Incomplete rotator cable did not cause rotator cuff dysfunction in case of rotator cuff tear: A biomechanical study of the relationship between rotator cable integrity and rotator cuff function. *Arthroscopy* 37 (8), 2444–2451. doi:10.1016/j.arthro.2021.03.051

Wellmann, M., Bobrowitsch, E., Khan, N., Patzer, T., Windhagen, H., Petersen, W., et al. (2011). Biomechanical effectiveness of an arthroscopic posterior bankart repair versus an open bone block procedure for posterior shoulder instability. *Am. J. Sports Med.* 39 (4), 796–803. doi:10.1177/0363546510389991

Yoon, T. H., Kim, S. J., Choi, C. H., Yoon, S. P., and Chun, Y. M. (2019). An intact subscapularis tendon and compensatory teres minor hypertrophy yield lower failure rates for non-operative treatment of irreparable, massive rotator cuff tears. *Knee Surg. Sports Traumatol. Arthrosc.* 27 (10), 3240–3245. doi:10.1007/s00167-019-05403-8

frontiers | Frontiers in Bioengineering and Biotechnology

TYPE Original Research
PUBLISHED 29 September 2022
DOI 10.3389/fbioe.2022.965009

EDITED BY
Damien Lacroix,
The University of Sheffield,
United Kingdom

REVIEWED BY
Björn Rath,
Klinikum Wels-Grieskirchen, Austria
Wei Chai,
Chinese PLA General Hospital, China

*CORRESPONDENCE
Yumin Zhang,
Zym2666@163.com

†These authors have contributed equally to this work

SPECIALTY SECTION
This article was submitted
to Biomechanics,
a section of the journal
Frontiers in Bioengineering
and Biotechnology

RECEIVED 09 June 2022
ACCEPTED 08 September 2022
PUBLISHED 29 September 2022

CITATION
Wen P, Zhang Q, Sun X, Zhang B, Ma T and Zhang Y (2022), Exploring the relationship between bearing extrusion and postoperative persistent pain in Oxford unicompartmental knee arthroplasty: A trajectory measurement study. *Front. Bioeng. Biotechnol.* 10:965009. doi: 10.3389/fbioe.2022.965009

Exploring the relationship between bearing extrusion and postoperative persistent pain in Oxford unicompartmental knee arthroplasty: A trajectory measurement study

Pengfei Wen[1†], Qidong Zhang[2†], Xiaowei Sun[2†], Binfei Zhang[1], Tao Ma[1] and Yumin Zhang[1]*

[1]Department of Joint Surgery, Honghui Hospital, Xi'an Jiaotong University, Xi'an, China, [2]Department of Orthopaedic Surgery, China-Japan Friendship Hospital, Beijing, China

Objective: The aim of the study is to explore the relationship between the extrusion of the meniscus bearing and postoperative persistent pain of Oxford unicompartmental knee arthroplasty.

Methods: Patients undertaking Oxford UKA from January 2019 to June 2020 were retrospectively analyzed. Intraoperatively, the displacement and movement trajectory of the meniscus bearing was recorded by the specially designed gridding mold of the tibial component. The k-means clustering analysis was applied based on the incidence of postoperative persistent knee pain and the bearing extrusion distance. The intraoperative meniscus bearing movement trajectories were analyzed between the two groups and the patients' clinical outcomes and radiographic assessments.

Results: The k-means clustering analysis indicated that the extrusion of the bearing of 5 mm was the grouping standard. There were 27 patients with 30 knees in the extrusion group and 58 patients with 68 knees in the non-extrusion group. The proportion of optimal bearing movement trajectories in the extrusion group was significantly lower than that in the non-extrusion group ($p < 0.05$). Postoperative persistent knee pain occurred in six cases (6.1%), with four and two cases in the extrusion and non-extrusion groups, respectively. The incidence of postoperative persistent knee pain in the extrusion group was higher than that of the non-extrusion group ($p < 0.05$). Radiographic assessment showed that the continuity of the femoral and tibial components in the extrusion group was greater than that in the non-extrusion group ($p < 0.05$). However, there were no differences in pre- and postoperative HKAA, the varus/valgus degree of both femoral and tibial components, and the flexion/extension angles of the femoral component, and the tibial slope also showed no statistical difference ($p > 0.05$).

Conclusion: For Oxford mobile-bearing UKA, the extrusion of meniscus bearing over 5 mm may increase the incidence of postoperative persistent knee pain, while the improvement of the bearing movement trajectory can effectively reduce this complication.

KEYWORDS

unicompartmental knee arthroplasty (UKA), bearing extrusion, postoperative knee pain, bearing movement trajectory, VAS

1 Introduction

Unicompartmental knee arthroplasty (UKA) is an effective option for treating anteromedial knee osteoarthritis (KOA) (Ateş et al., 2021). In recent years, due to faster postoperative recovery and better functional outcomes (Bayoumi et al., 2022), UKA has received increasing attention among orthopedic surgeons. Although UKA has obvious mini-invasive advantage compared to total knee arthroplasty (TKA), it has always been criticized for its complication and revision rate, which are reportedly higher than those of TKA (Kazarian et al., 2020; Di Martino et al., 2021). In a recent study, it was found that the lifetime revision risk of UKA was two times as that of TKA across all age periods (Tay et al., 2022).

Among the reasons for UKA revision, unexplained knee pain is one of the most common reasons and accounts for 14%–23% of all the reasons (Baker et al., 2012; van der List et al., 2016; Dyrhovden et al., 2017; Vasso et al., 2018). Different authors have different opinions on the origin of unexplained knee pain after UKA (Simpson et al., 2009; Lyu et al., 2021). Overhang of the tibial component was reported as a reason for knee pain after UKA (Chau et al., 2009; Gudena et al., 2013). During the physical examination for patients with knee pain after UKA, with the knee motion from flexion to extension, doctors can usually touch the extrusion of the meniscus bearing at the medial joint space and feel the tenderness at the same time. Therefore, the bearing extrusion may also lead to pain due to soft tissue impingement. This phenomenon has also been reported previously (Jung et al., 2009). However, the relationship between bearing extrusion and persistent pain after UKA is still unknown. The aim of this study is to explore the relationship between bearing extrusion and postoperative outcomes of Oxford UKA.

2 Materials and methods

We retrospectively reviewed all the cases of medial Oxford UKA from January 2019 to June 2020 in our hospital. The inclusion criteria included the following: 1) medial KOA; 2) no pain or tenderness in the lateral compartment; 3) no sign of infection in the surgical site and the whole body; 4) the varus deformity and flexion contracture were less than 15°; and 5) the function of the knee ligaments was good. Patients who fit either of the following conditions were excluded from the study: 1) KOA involved lateral compartment; 2) inflammation arthritis; and 3) incomplete clinical and radiological record. The study was approved by the ethics committee and was in accordance with the Declaration of Helsinki. All the patients included in the studies have signed the informed consent.

2.1 General information

In total, from January 2019 to June 2020, there were 162 UKAs of 137 patients being conducted in our hospital. Due to the COVID-19 epidemic, 64 UKAs of 52 patients were

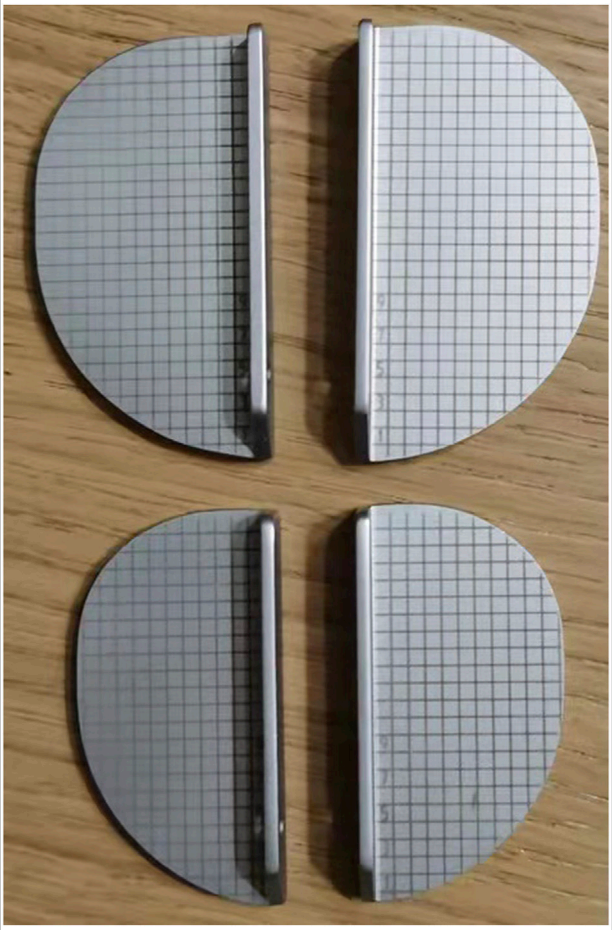

FIGURE 1
Gridding mold of the tibial component; the interval was 2 mm.

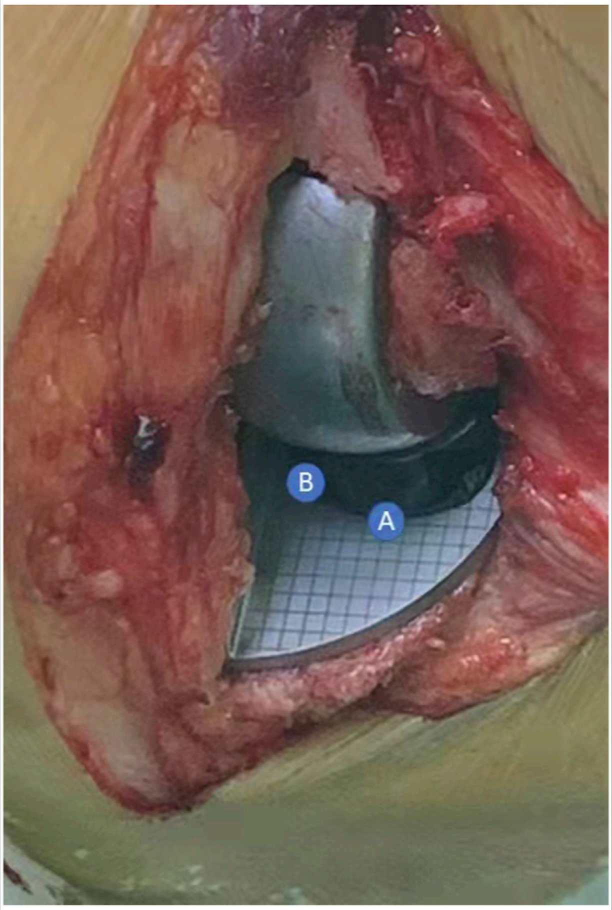

FIGURE 2
In 90° knee flexion, recording the coordinate of the anterior corner **(A point)** and anterolateral corner **(B point)** as the location of the meniscus bearing. The location of the meniscus bearing in other angles (90°, 60°, 45°, 30°, 20°, and 0°) was recorded in the same way and finally formed the movement trajectory.

excluded for incomplete follow-up. Finally, the study enrolled 98 UKAs of 85 patients.

2.2 Surgical technique

All of the surgeries were performed by an experienced senior surgeon. The surgical procedure followed the surgical techniques of Oxford partial knee microplasty instrumentation (Zimmer). A thigh tourniquet was installed, and the thigh was positioned on the adjustable support, with about 30° hip flexion and knee freedom. With 90° knee flexion, a medial parapatellar incision was made from the medial edge of the patella to a 1.5 cm distal to the tibial plateau. The subcutaneous tissue was dissected, and the joint capsule was incised to expose the medial knee compartment. The size of the medial femoral condyle was measured with a femoral sizing spoon and connected with the tibial extramedullary positioning rod through a G-clamp. The tibial osteotomy direction was adjusted with a 7° posterior slope, fixed with a tibial saw guide, and the tibial plateau resection was performed. A hole was drilled in the intramedullary canal of the femur and an intramedullary positioning rod was inserted and then connected, and the femoral intramedullary rod was fixed with the femoral drill guide by a tuning fork. Two positioning holes on the distal medial femur condyle were drilled, the osteotomy device was inserted, and the posterior femoral condyle was resected. The flexion gap was measured and the femoral milling column was installed. After milling, the single-column prosthesis was installed. The gap tension at 20° and 90° of flexion was estimated according to the feeling of difficulty in inserting and pulling the inserts with bare hands. Depending on the gap tension, the femoral condyle was milled until the flexion and extension gaps are balanced. Osteophytes on the anterior and posterior femoral condyle are removed, the groove on the tibial plateau is cut with a toothbrush saw, and the trial implantation is installed. Then, the knee motion is checked and the

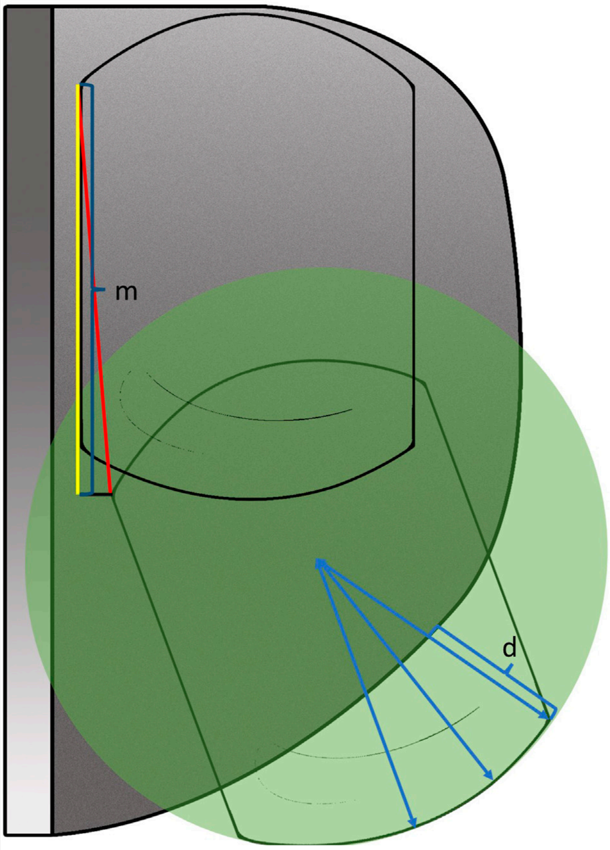

FIGURE 3
Diagram of the extrusion distance (d) and moving distance (m) of the meniscus bearing.

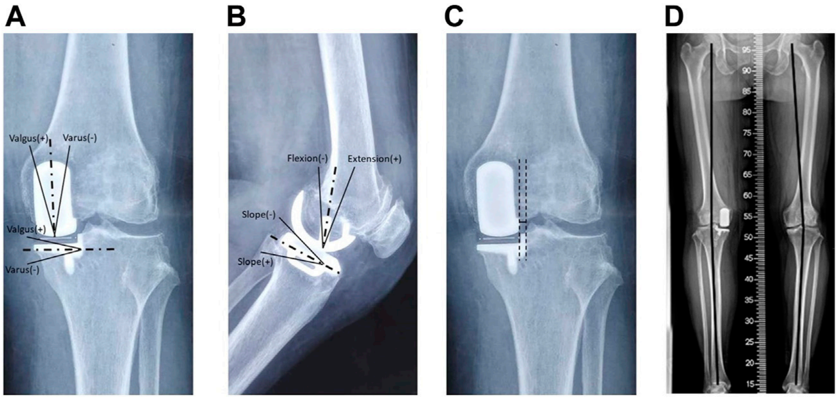

FIGURE 4
Radiological measures of the prosthesis after UKA. **(A)** Valgus/varus angle of femoral and tibial components on the antero-posterior view; **(B)** flexion/extension angle of the femoral component and slope of the tibial component; **(C)** adjacent degree between femoral and tibial components, a line is drawn vertical to the ground from the lateral edge of the femoral component, and the adjacent degree is measured as the horizontal distance between this line and the tibial vertical osteotomy line; **(D)** hip–knee–ankle angle (HKAA).

TABLE 1 Comparison of preoperative baseline characteristics of the two groups.

	Extrusion group (n = 27)	Non-extrusion group (n = 58)	p-value
Age (years)	66.85 ± 8.91	67.20 ± 9.63	0.721
Sex (M/F)	8/19	17/45	0.226
BMI(kg/m^2)	26.26 ± 3.62	27.36 ± 4.05	0.186
Follow-up time (months)	27.35 ± 1.31	26.67 ± 3.24	0.443

flexion–extension gap balance is evaluated by pulling and inserting the insert again. Finally, the prosthesis is installed and the incision is closed without placing drainage.

2.3 Outcome measures

2.3.1 Intraoperative measures

According to Kawaguchi's method (Kawaguchi et al., 2019), we used a specially designed gridding mold of the tibial component (Figure 1) to record the displacement and the movement trajectory of the meniscus bearing mold. Before placing the real prosthesis, the location of the anterior corner and anterolateral corner of the meniscus bearing from flexion to full extension (90°, 60°, 45°, 30°, 20°, and 0°) was recorded (Figure 2). After placing the real prosthesis product, the distance of the bearing extrusion relative to the tibial component was measured. The extrusion distance was defined as the distance of the medial edge of meniscus bearing beyond the medial edge of the tibial component. It was measured through the line connecting the circle center of the anterior arc and the anteromedial end of the meniscus bearing (Figure 3).

2.3.2 Clinical outcome assessment

The VAS score during walking was adopted for postoperative knee pain assessment. The clinical outcome was assessed by recording KSS clinical and functional scores of the preoperative and final follow-up.

2.3.3 Radiological measures

Patients commonly received preoperative and postoperative (within 5 days after UKA) X-ray examinations, including anteroposterior view, lateral view, Merchant view, and full-weight total length lower limb image. We measured the varus/valgus angle of the tibial and femoral components (Figure 4A), flexion/extension angle of the femoral component, and the slope of the tibial component (Figure 4B). We also measured the adjacent degree between the tibial and femoral components (Figure 4C). The hip–knee–ankle angle (HKAA) was measured on the full-weight bearing total length lower limb

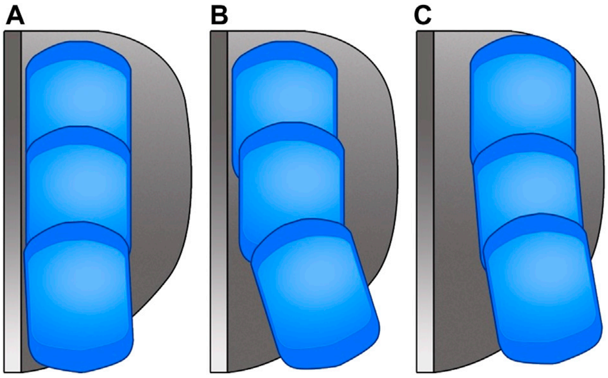

FIGURE 5
Diagram of the moving trajectory of the meniscus bearing. **(A)** Distance between the meniscus bearing and lateral wall of the tibial component is maintained stable within 2 mm during flexion/extension; **(B)** meniscus bearing is maintained close to the lateral wall of the tibial component during knee flexion and kept away from the lateral wall of the tibial component during knee extension, and the horizontal distance between the meniscus bearing and the lateral wall of the tibial component is over 2 mm in full extension; **(C)** meniscus bearing is consistently kept away from the lateral wall of the tibial component during knee flexion and knee extension. Type c was rarely seen in over study with only three cases.

image (Figure 4D). Two authors independently measured these outcomes, and the mean value was adopted as the result for statistical analysis.

2.4 Statistics

SPSS 23.0 software was used for statistical analysis. K-means rapid clustering analysis was adopted for grouping (Sun et al., 2021a), and the final grouping was determined according to the clustering results and data characteristics. Measurement data were represented as ($\bar{x} \pm s$). When the data were presented as normal distribution, the independent samples *t*-test was used to compare the two groups. Otherwise, the rank sum test was adopted. Fisher's exact test was adopted for enumeration data. The Mann–Whitney *U* test was used for comparing the rank data between the two groups. Statistical significance of the difference was defined as $p < 0.05$.

3 Results

The k-means clustering was determined according to the postoperative persistent knee pain and extrusion distance of meniscus bearing, and the k value was set as 2. Finally, the 98 UKAs were divided into two groups; the sum of squared Euclidean distances from each point to the centroid between groups is equal. After grouping, we found the unique feature of group 1 ($n = 30$) and group 2 ($n = 68$) was extrusion distance ≥5 mm and extrusion distance <5 mm, respectively. Therefore, we defined the extrusion distance of 5 mm as the threshold value for meniscus bearing extrusion. As a result, the extrusion group consisted of 30 knees of 28 patients, and the non-extrusion group consisted of 68 knees of 58 patients. The baseline characteristics included age, sex, BMI, and follow-up time, and no statistical difference was found in these indexes (Table 1).

3.1 Intraoperative measures

The extrusion distance of the extrusion group was significantly greater than that of the non-extrusion group ($p < 0.05$), whereas no statistical significance was found in the moving distance between the two groups ($p > 0.05$). Furthermore, the movement trajectories of meniscus bearing were divided into three types. As shown in Figure 5, type a was defined as the optimal trajectory and types b and type c were defined as the non-optimal trajectory. The ratio of the optimal trajectory in the extrusion group was significantly lower than that in the non-extrusion group ($p < 0.05$) (Table 2).

3.2 Clinical outcomes

All the 98 UKAs of the two groups were carried out well, and all the incisions healed smoothly, with no delayed healing or infection event occurring. In total, six cases (6.1%) complained postoperative persistent knee pain, four cases belonged to the extrusion group, and two cases were in the non-extrusion group. Conservative drug or local block treatment was applied to these cases; the effect of pain release was acceptable but sometimes relapsed. However, due to the satisfied knee function, no patients required revision surgery. The rate of postoperative persistent knee pain in the extrusion group was significantly higher than that in the non-extrusion group ($p < 0.05$). No statistical difference was found in preoperative VAS score and pre- and postoperative KSS clinical and functional scores between the two groups ($p > 0.05$). But, statistical difference was found in postoperative VAS score between the two groups ($p < 0.05$) (Table 3).

3.3 Radiological outcomes

In all the cases of the two groups, the postoperative HKAA significantly increased than that before UKA ($p < 0.05$), whereas no statistical difference was observed in the pre- and postoperative HKAA between the two groups ($p > 0.05$). For postoperative varus/valgus angle in femoral and tibial components, sagittal flexion/extension angle in the femoral

TABLE 2 Comparison of the intraoperative measures on the movement trajectory of the meniscus bearing between the two groups.

	Extrusion group (n = 30)	**Non-extrusion group (n = 68)**	***p*-value**
Extrusion distance (mm)	6.70 ± 1.02	2.97 ± 0.77	**<0.001**
Optimal trajectory (knees, %)	7 (23.33%)	66 (97.06%)	**<0.001**
Moving distance	8.57 ± 3.80	8.31 ± 4.14	0.571

TABLE 3 Comparison of the clinical outcomes between the two groups.

	Extrusion group (n = 30)	**Non-extrusion group (n = 68)**	***p*-value**
Postoperative persist pain (knees, %)	5 (16.67%)	2 (2.94%)	**0.027**
KSS clinical score			
Preoperative	55.24 ± 6.31	57.49 ± 7.97	0.191
Last follow-up	89.93 ± 6.63	91.83 ± 5.22	0.138
p-value	**<0.001**	**<0.001**	
KSS function score			
Preoperative	55.37 ± 6.02	52.93 ± 9.44	0.215
Last follow-up	87.26 ± 11.08	90.00 ± 5.61	0.109
p-value	**<0.001**	**<0.001**	
VAS score			
Preoperative	7.81 ± 1.14	8.07 ± 1.10	0.312
Last follow-up	0.90 ± 1.52	0.35 ± 1.02	**0.039**
p-value	**<0.001**	**<0.001**	

TABLE 4 Comparison of the radiological measures between the two groups.

	Extrusion group (n = 30)	**Non-extrusion group (n = 68)**	***p*-value**
HKAA (°)			
Preoperative	171.89 ± 4.31	172.51 ± 3.69	0.347
Last follow-up	177.38 ± 3.11	177.86 ± 2.35	0.772
p-value	**<0.001**	**<0.001**	
Postoperative varus/valgus degree of the femoral component (°)	1.21 ± 4.53	0.48 ± 2.51	0.630
Postoperative flexion/extension degree of the femoral component (°)	9.65 ± 2.75	9.58 ± 3.11	0.758
Postoperative varus/valgus degree of the tibial component (°)	−2.02 ± 2.51	−1.06 ± 2.26	0.142
Postoperative tibial component slope (°)	8.39 ± 2.61	7.54 ± 1.37	0.197
Postoperative adjacent degree between tibial and femoral components	7.56 ± 3.21	4.82 ± 1.83	**<0.001**

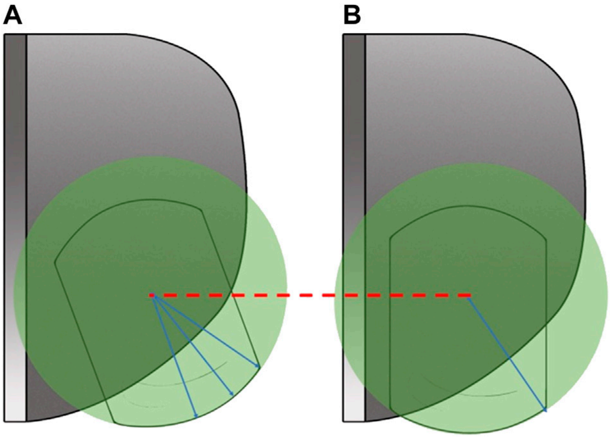

FIGURE 6
Compared to the optimal moving trajectory **(A)**, the non-optimal moving trajectory **(B)** may increase the extrusion distance and area of the meniscus bearing.

component, and the slope in the tibial component, no significant difference was presented between the two groups ($p > 0.05$). However, the adjacent degree between the tibial and femoral component was found to be significantly greater in the extrusion group than in the non-extrusion group ($p < 0.05$) (Table 4).

4 Discussion

Persistent knee pain after UKA is a confusing complication for joint arthroplasty surgeons and a common reason for revision (Baker et al., 2012; Grosu et al., 2014; van der List et al., 2016). In recent years, many authors from different countries have reported this complication during the postoperative follow-up. Although the rate is quite different in different articles, the unhappy function and increasing revision rate resulting from this complication can lead to the declined satisfactory rates of UKA (van der List et al., 2016; Dyrhovden et al., 2017; Vasso et al., 2018). However, the reason for persistent knee pain after UKA has not yet reached a consensus, and some authors even directly named it as unexplained knee pain (Baker et al., 2012; Hama et al., 2015). Previous studies have reported some potential reasons for persistent knee pain after UKA, such as tibial component overhang (Simpson et al., 2009), overstuff of the medial knee compartment (Crawford et al., 2021), bursitis (Jung et al., 2009), and medial abrasion syndrome (Lyu et al., 2021). Meanwhile, according to the result in our study, the rate of postoperative persistent knee pain was 16.7% in the extrusion group and significantly higher than 2.94% in the extrusion group.

From the perspective of the prosthesis design of the Oxford UKA, slight meniscus bearing extrusion is common and unavoidable because the shape of the meniscus bearing is rectangle, whereas the tibial component has a distinct curving margin in the anterior edge. But in most situations, the meniscus bearing extrusion may not cause irritation to soft tissue around, which is quite different from tibial component overhang. Many studies have indicated that excessive coverage of the tibial component over 2 mm can cause impingement and stretching to medial collateral ligament (MCL) and may even further lead to serious complications like MCL loosening (Kim et al., 2014). The position of meniscus bearing extrusion is usually located in the anteromedial edge of the tibial plateau, and the local surrounding soft tissue is joint capsule and pes anserinus bursae. As they are not the main stabilization structures of the knee, slight meniscus bearing extrusion and soft tissue impingement may not lead to unhappy events. However, in previous literature, there were no criteria for the edge of meniscus bearing extrusion. Our study found meniscus bearing extrusion over 5 mm can lead to an increasing rate of persistent knee pain after UKA. Therefore, in medial Oxford UKA, the meniscus bearing extrusion should be controlled under 5 mm as possible.

So, what caused meniscus bearing over-extrusion in medial Oxford UKA? Previous studies have found that the meniscus bearing was maintained parallel to the lateral wall of the tibial component during the knee flexion from 60° to 90° and kept away from the lateral wall of the tibial component during the knee flexion from 0° to 60° (Kamenaga et al., 2019; Kawaguchi et al., 2019). If the meniscus bearing separates a certain distance from the lateral wall of the tibial component, the possibility of bearing rotation is increasing, especially with the stimulation of external force. Under this condition, the limitation to the meniscus bearing from the femoral component is loosening, which is regarded as the mechanism for bearing dislocation (Clarius et al., 2010; Bae et al., 2020; Sun et al., 2021). The bearing dislocation can be regarded as an extreme condition of over-extrusion. Therefore, we hold that the mal-tracking of the meniscus bearing is the primary cause for meniscus bearing over-extrusion. As is shown in Figure 6, with the center of the meniscus bearing in same anteroposterior displacement, the non-optimal movement trajectory can lead to increasing extrusion distance and area. According to Kawaguchi's classification to the movement trajectory of meniscus bearing, we analyzed and compared the trajectory between the two groups. The result showed that most trajectories in the extrusion group were non-optimal, and optimal trajectories occupied only 23.33%. By contrast, the rate of the optimal trajectory was up to 97.06% in the non-extrusion group, with statistical significance compared with the extrusion group ($p < 0.05$). Conversely, we further conducted a subgroup analysis for the 98 UKA cases, according to the optimal or non-optimal trajectory. The result showed the rate of postoperative persistent knee pain was only 2.74% in the optimal trajectory group, whereas it was up to 25% in the non-optimal trajectory group ($p < 0.05$). Moreover, the improper movement trajectory can also lead to rotation and dislocation of the meniscus bearing (Bae et al., 2020; Sun et al., 2021b). Therefore, we should pay sufficient attention to the movement trajectory of the meniscus bearing in Oxford UKA.

As the meniscus bearing is put between the femoral and tibial components to achieve the optimal bearing trajectory, the relative position between the femoral and tibial components is important. In detail, the key is the central aligning factor between the femoral and tibial components in the coronal plane. Previous studies also found over separation between the femoral and tibial components can increase the risk for bearing dislocation (Koh et al., 2016; Bae et al., 2020). In our study, we measured the adjacent degree to describe this meaning. The adjacent degree between the tibial and femoral components was found significantly greater in the extrusion group than in the non-extrusion group ($p < 0.05$). This indicated the central aligning between the femoral and tibial components in the extrusion group was superior to that of the non-extrusion group, which was in accordance to our theory. According to this concept, techniques for improving the movement trajectory of meniscus bearing in Oxford UKA have also been reported in recent years. Techniques like the kinematic alignment method with the extramedullary position technique of Zhang et al. (2020) and the modified tibial osteotomy technique introduced by Hiranaka et al. (2021) have all been proven to improve the movement trajectory of meniscus bearing.

There are also some limitations in our study. Due to the low rate of persistent knee pain after UKA, studies with larger samples or multi-center prospective studies are still required to get more accurate results and more convinced conclusions. In addition, the extrusion distance of meniscus bearing was measured manually using a disinfected ruler. The limited surgery time also cannot allow repeated measures by different observers. As a result, the system error is unavoidable.

5 Conclusion

In medial Oxford UKA, meniscus bearing extrusion over 5 mm may lead to an increasing rate of postoperative persistent knee pain. The over-extrusion may be due to the mal-tracking of the meniscus bearing. To reduce the rate of postoperative persistent knee pain, surgeons should pay sufficient attention to improve the movement trajectory of the meniscus bearing in Oxford UKA.

Data availability statement

The original contributions presented in the study are included in the article/Supplementary Material; further inquiries can be directed to the corresponding author.

Ethics statement

The studies involving human participants were reviewed and approved by the ethics committee of Honghui Hospital, Xi’an Jiaotong University. The patients/participants provided their written informed consent to participate in this study.

Author contributions

All authors listed have made a substantial, direct, and intellectual contribution to the work and approved it for publication.

Funding

This work was supported by the Youth Cultivation Project of Xi’an Health Commission (Program No. 2020qn18), the Key Research and Development Program of Shaanxi Province (Program No. 2022SF-237), and the Capital Health Research and Development of Special (Grant Number 2020-2-4067).

Conflict of interest

The authors declare that the research was conducted in the absence of any commercial or financial relationships that could be construed as a potential conflict of interest.

Publisher’s note

References

Ateş, Y., Akdoğan, M., and Atilla, H. A. (2021). Which knee replacement do the patients forget? Unicondylar or total knee arthroplasty. *Acta Orthop. Traumatol. Turc.* 55, 417–421. doi:10.5152/j.aott.2021.20173

Bae, J. H., Kim, J. G., Lee, S. Y., Lim, H. C., and In, Y. (2020). Epidemiology of bearing dislocations after mobile-bearing unicompartmental knee arthroplasty: Multicenter analysis of 67 bearing dislocations. *J. Arthroplasty* 35, 265–271. doi:10.1016/j.arth.2019.08.004

Baker, P. N., Petheram, T., Avery, P. J., Gregg, P. J., and Deehan, D. J. (2012). Revision for unexplained pain following unicompartmental and total knee replacement. *J. Bone Jt. Surg.* 94, e126. doi:10.2106/jbjs.k.00791

Bayoumi, T., van der List, J. P., Ruderman, L. V., Zuiderbaan, H. A., Kerkhoffs, G., and Pearle, A. D. (2022). Successful same-day discharge in 88% of patients after unicompartmental knee arthroplasty: A systematic review and meta-analysis. *Knee Surg. Sports Traumatol. Arthrosc.*, 1–17. doi:10.1007/s00167-022-07094-0

Chau, R., Gulati, A., Pandit, H., Beard, D., Price, A., Dodd, C., et al. (2009). Tibial component overhang following unicompartmental knee replacement--does it matter. *Knee* 16, 310–313. doi:10.1016/j.knee.2008.12.017

Clarius, M., Hauck, C., Seeger, J. B., Pritsch, M., Merle, C., and Aldinger, P. R. (2010). Correlation of positioning and clinical results in Oxford UKA. *Int. Orthop.* 34, 1145–1151. doi:10.1007/s00264-009-0881-3

Crawford, D. A., Lapsley, L., Hurst, J. M., Morris, M. J., Lombardi, A. V., and Berend, K. R. (2021). Impact of polyethylene thickness on clinical outcomes and survivorship in medial mobile-bearing unicondylar knee arthroplasty. *J. Arthroplasty* 36, 2440–2444. doi:10.1016/j.arth.2021.02.062

Di Martino, A., Bordini, B., Barile, F., Ancarani, C., Digennaro, V., and Faldini, C. (2021). Unicompartmental knee arthroplasty has higher revisions than total knee arthroplasty at long term follow-up: A registry study on 6453 prostheses. *Knee Surg. Sports Traumatol. Arthrosc.* 29, 3323–3329. doi:10.1007/s00167-020-06184-1

Dyrhovden, G. S., Lygre, S., Badawy, M., Gothesen, O., and Furnes, O. (2017). Have the causes of revision for total and unicompartmental knee arthroplasties changed during the past two decades. *Clin. Orthop. Relat. Res.* 475, 1874–1886. doi:10.1007/s11999-017-5316-7

Grosu, I., Lavand'homme, P., and Thienpont, E. (2014). Pain after knee arthroplasty: An unresolved issue. *Knee Surg. Sports Traumatol. Arthrosc.* 22, 1744–1758. doi:10.1007/s00167-013-2750-2

Gudena, R., Pilambaraei, M. A., Werle, J., Shrive, N. G., and Frank, C. B. (2013). A safe overhang limit for unicompartmental knee arthroplasties based on medial collateral ligament strains: An *in vitro* study. *J. Arthroplasty* 28, 227–233. doi:10.1016/j.arth.2012.05.019

Hama, S., Hamada, D., Goto, T., Tsutsui, T., Tonogai, I., Suzue, N., et al. (2015). Revision total knee arthroplasty for unexplained pain after unicompartmental knee arthroplasty: A case report. *J. Med. Invest.* 62, 261–263. doi:10.2152/jmi.62.261

Hiranaka, T., Tanaka, T., Okimura, K., Fujishiro, T., Shigemoto, R., Araki, S., et al. (2021). Manipulation of tibial component to ensure avoidance of bearing separation from the vertical wall of tibial component in Oxford unicompartmental arthroplasty. *Clin. Orthop. Surg.* 13, 123. doi:10.4055/cios20277

Jung, K. A., Lee, S. C., and Hwang, S. H. (2009). Pseudomeniscal synovial impingement after unicondylar knee arthroplasty. *Orthopedics* 32, 361. doi:10.3928/01477447-20090501-05

Kamenaga, T., Hiranaka, T., Takayama, K., Tsubosaka, M., Kuroda, R., and Matsumoto, T. (2019). Adequate positioning of the tibial component is key to avoiding bearing impingement in Oxford unicompartmental knee arthroplasty. *J. Arthroplasty* 34, 2606–2613. doi:10.1016/j.arth.2019.05.054

Kawaguchi, K., Inui, H., Taketomi, S., Yamagami, R., Nakazato, K., Shirakawa, N., et al. (2019). Intraoperative mobile-bearing movement in Oxford unicompartmental knee arthroplasty. *Knee Surg. Sports Traumatol. Arthrosc.* 27, 2211–2217. doi:10.1007/s00167-018-5064-6

Kazarian, G. S., Barrack, T. N., Okafor, L., Barrack, R. L., Nunley, R. M., and Lawrie, C. M. (2020). High prevalence of radiographic outliers and revisions with unicompartmental knee arthroplasty. *J. Bone Jt. Surg.* 102, 1151–1159. doi:10.2106/JBJS.19.01277

Kim, G. H., Park, B. Y., Bae, T. Y., Song, K. Y., and In, Y. (2014). Implant overhang after unicompartmental knee arthroplasty: Oxford prosthesis versus miller-galante II prosthesis. *Knee Surg. Relat. Res.* 26, 82–87. doi:10.5792/ksrr.2014.26.2.82

Koh, I. J., Kim, J. H., Jang, S. W., Kim, M. S., Kim, C., and In, Y. (2016). Are the Oxford(®) medial unicompartmental knee arthroplasty new instruments reducing the bearing dislocation risk while improving components relationships? A case control study. *Orthop. Traumatology Surg. Res.* 102, 183–187. doi:10.1016/j.otsr.2015.11.015

Lyu, S. R., Hsu, C. C., and Hung, J. P. (2021b). Medial abrasion syndrome: A neglected cause of persistent pain after knee arthroplasty. *J. Orthop. Surg. Res.* 16, 61. doi:10.1186/s13018-020-02191-7

Simpson, D. J., Price, A. J., Gulati, A., Murray, D., and Gill, H. (2009a). Elevated proximal tibial strains following unicompartmental knee replacement--a possible cause of pain. *Med. Eng. Phys.* 31, 752–757. doi:10.1016/j.medengphy.2009.02.004

Sun, X., Hernigou, P., Zhang, Q., Zhang, N., Wang, W., Chen, Y., et al. (2021). Sensor and machine learning-based assessment of gap balancing in cadaveric unicompartmental knee arthroplasty surgical training. *Int. Orthop.* 45, 2843–2849. doi:10.1007/s00264-021-05176-1

Sun, X., Liu, P., Lu, F., Wang, W., Guo, W., and Zhang, Q. (2021). Bearing dislocation of mobile bearing unicompartmental knee arthroplasty in east asian countries: A systematic review with meta-analysis. *J. Orthop. Surg. Res.* 16, 28. doi:10.1186/s13018-020-02190-8

Tay, M. L., Young, S. W., Frampton, C. M., and Hooper, G. J. (2022). The lifetime revision risk of unicompartmental knee arthroplasty. *Bone Jt. J.* 104-B, 672–679. doi:10.1302/0301-620X.104B6.BJJ-2021-1744.R1

van der List, J. P., Zuiderbaan, H. A., and Pearle, A. D. (2016). Why do medial unicompartmental knee arthroplasties fail today. *J. Arthroplasty* 31, 1016–1021. doi:10.1016/j.arth.2015.11.030

Vasso, M., Antoniadis, A., and Helmy, N. (2018). Update on unicompartmental knee arthroplasty: Current indications and failure modes. *EFORT Open Rev.* 3, 442–448. doi:10.1302/2058-5241.3.170060

Zhang, Q., Wang, W., Liu, Z., Yue, D., Cheng, L., Wang, B., et al. (2020). A novel extramedullary technique to guide femoral bone preparation in mobile unicompartmental knee arthroplasty based on tibial cut and overall alignment. *J. Orthop. Surg. Res.* 15, 92. doi:10.1186/s13018-020-01598-6

Zimmer, B. *Oxford partial knee*microplasty instrumentation surgical technique. Available at: https://www.zimmerbiomet.com/content/dam/zimmer-biomet/medical-professionals/000-surgical-techniques/knee/oxford-partial-knee-microplasty-instrumentation-surgical-technique.pdf (Accessed August 20, 2022).

frontiers | Frontiers in Bioengineering and Biotechnology

TYPE Original Research
PUBLISHED 10 October 2022
DOI 10.3389/fbioe.2022.957435

Biomechanical effects of medial meniscus radial tears on the knee joint during gait: A concurrent finite element musculoskeletal framework investigation

Sentong Wang[1]*, Kazunori Hase[2]*, Shunsuke Kita[3,4] and Shinya Ogaya[5]

[1]Human-Mechanical System Laboratory, Graduate School of Systems Design, Tokyo Metropolitan University, Hachioji, Japan, [2]Human-Mechanical System Laboratory, Faculty of Systems Design, Tokyo Metropolitan University, Hachioji, Japan, [3]Biomechanics of Exercise and Sports in Physical Therapy Laboratory, Graduate Course of Health and Social Services, Saitama Prefectural University, Koshigaya, Japan, [4]Department of Rehabilitation, Soka Orthopedics Internal Medicine, Saitama, Japan, [5]Biomechanics of Exercise and Sports in Physical Therapy Laboratory, Department of Physical Therapy, Saitama Prefectural University, Koshigaya, Japan

The biomechanical variation in the knee during walking that accompanies medial meniscal radial tears stemming from knee osteoarthritis (OA) has not been explored. This study introduced a finite element musculoskeletal model using concurrent lower limb musculoskeletal dynamics and knee joint finite element analysis in a single framework and expanded the models to include knees with medial meniscal radial tears and total medial meniscectomy. The radial tears involved three locations: anterior horn, midbody, and posterior horn with grades of 33%, 50%, and 83% of the meniscus width. The shear and hoop stresses of the tear meniscus and tibial cartilage contact load, accompanying tears, and postmeniscectomy were evaluated during the stance phase of the gait cycle using the models. In the 83% width midbody tear group, shear stress at the end of the tear was significantly greater than in the intact meniscus and other tear groups, and the maximum shear stress was increased by 310% compared to the intact meniscus. A medial meniscus radial tear has a much smaller effect on the tibial cartilage load (even though in the 83% width tear, the cartilage/total load ratio increased by only 9%). However, the contact force on the tibial cartilage with total postmeniscectomy was increased by 178.93% compared with a healthy intact meniscus, and the peak contact pressure after meniscectomy increased from 11.94 to 12.45 MPa to 17.64 and 13.76 MPa, at the maximum weight acceptance and push-off, respectively. Our study shows that radial tears with larger medial meniscus widths are prone to high stress concentrations at the end of the tears, leading to the potential risk of complete meniscal rupture. Furthermore, although the tears did not change the cartilage load distribution, they disrupted the circumferential stress-transmitting function of the meniscus, thus greatly increasing the likelihood of the onset of knee OA. The significant increase in the tibial cartilage load with total postmeniscectomy indicates a potential risk of OA flare-ups. This study contributes to a better understanding of meniscal tear-

EDITED BY
Jun Pan,
Chongqing University, China

REVIEWED BY
Tammy Haut Donahue,
University of Memphis, United States
Ginu Unnikrishnan,
BlueHalo, United States
Andreas Martin Seitz,
Ulm University Medical Center,
Germany

*CORRESPONDENCE
Sentong Wang,
sentongwang@gmail.com
Kazunori Hase,
kazunori.hase@tmu.ac.jp

SPECIALTY SECTION
This article was submitted to Biomechanics, a section of the journal Frontiers in Bioengineering and Biotechnology

RECEIVED 31 May 2022
ACCEPTED 26 September 2022
PUBLISHED 10 October 2022

CITATION
Wang S, Hase K, Kita S and Ogaya S (2022), Biomechanical effects of medial meniscus radial tears on the knee joint during gait: A concurrent finite element musculoskeletal framework investigation.
Front. Bioeng. Biotechnol. 10:957435.
doi: 10.3389/fbioe.2022.957435

induced OA biomechanical changes during human activities and offers some potential directions for surgical guidance of meniscectomies and the prophylaxis and treatment of OA.

KEYWORDS

meniscus tear, finite element, musculoskeletal model, gait, knee, osteoarthritis

Introduction

A meniscus tear is the most common damage associated with the meniscus, and it more commonly occurs on the medial compartment than on the lateral compartment (Fox et al., 2012). Moreover, radial tears are not uncommon in young patients (<50 years), often caused from trauma or degenerative processes (Terzidis et al., 2006; Howell et al., 2014), and can occur anywhere on either meniscus, anterior horn, posterior horn, or midbody (Fox et al., 2012). A meniscus tear can significantly affect the functions of the meniscus, such as shock absorption and load transmission, resulting in abnormal kinematics and redistribution of load on the knee (Kurosawa et al., 1980; Fox et al., 2015). The occurrence of these abnormal kinematics and mechanics often leads to increased cartilage wear or knee osteoarthritis (OA) changes (Felson, 2013). A large proportion of radial tears of the meniscus are considered irreparable, because they occur mostly in the white zone that lacks a blood supply (Scotti et al., 2013), so meniscectomy is often used to relieve pain and instability in the knee (Rao et al., 2015). However, meniscectomies have been reported to induce an increased risk of the progress of knee OA (Roemer et al., 2016). Hence, the biomechanical impact of meniscus radial tears and resultant meniscectomies on the knee joint needs to be investigated. Because activity-related radial tears are the most common (Terzidis et al., 2006), it is crucial to study the effects of radial tears on the kinematics and mechanics of the knee during human activities such as walking.

Previously, some researchers have used implantable pressure-sensitive film to study the contact mechanics between the torn menisci and articular cartilages in cadaveric knees in a knee machine that simulates walking (Bedi et al., 2010; Bedi et al., 2012; Gilbert et al., 2014). These works aimed to analyze the mechanical effect of the meniscus tears on the knee joint during human activities using an *in vitro* knee simulating apparatus. However, the *in vivo* knee physiological motion and loading pattern during activities were hard to replicate, and the contraction activity of muscles that act as “motors” for joint motion cannot be reproduced in cadavers. Moreover, the use of these sensors can severely alter meniscus translation and deformation, resulting in errors in predictions of the joint kinematics and contact mechanics (Hu et al., 2019). Thus, the kinematics and mechanics effects of meniscus tears on the knee during human activity are difficult to study using an *in vitro* approach.

Currently, a computational approach, the finite element (FE) method, has been proven to provide detailed geometric representations of torn menisci and can explain the stress alterations of menisci and load redistribution on the knee that accompanies meniscus tears (Kedgley et al., 2019; Li et al., 2019; Zhang et al., 2019). However, these studies cannot investigate the effect of meniscus tears on the knee during natural human activities, such as walking, because knee biomechanics were predicted based on simplified assumed loads and boundary conditions, such as fixed compressive load and flexion angles (Kedgley et al., 2019; Li et al., 2019; Zhang et al., 2019). In addition, muscles that produce the force that causes joint movement were not considered in biomechanical analysis of the knee (Mononen et al., 2013). Therefore, the biomechanical effect of the meniscus tears in the actual physiological conditions on the knee during human activities is still unclear.

This study aimed to elucidate 1) the stress alterations on the meniscus resulting from radial tears of the medial meniscus and 2) the effect of the tears and total medial meniscectomy on the knee biomechanics during the stance phase of the gait cycle. In the above discussion, we pointed out the problems of previous gait analyses using FE models: the inability to maintain a realistic representation of the knee joint tissue deformation and motion under natural physiological conditions. Therefore, we applied our previously developed finite element musculoskeletal (FEMS) model using a single concurrent framework combining the entire lower limb musculoskeletal dynamics and knee joint FE analysis, which has been proven to describe natural knee biomechanics during the gait (Wang et al., 2021; Wang et al., 2022), to clarify the biomechanical effect of tears on the knee during gait.

Methods

Subject experiments

A healthy male participant (age 29 years, height 175 cm, weight 80 kg) participated in the gait measurement. The participant was thoroughly informed about the purpose, methods, and caveats of the experiment. The experiment was approved by the research ethics committee of the Tokyo Metropolitan University. A straight, approximately 10-m-long walkway was prepared for the gait experiment. The participant was verbally instructed to “walk at a comfortable pace” with his preferred gait during the experiment. The marker-based motion

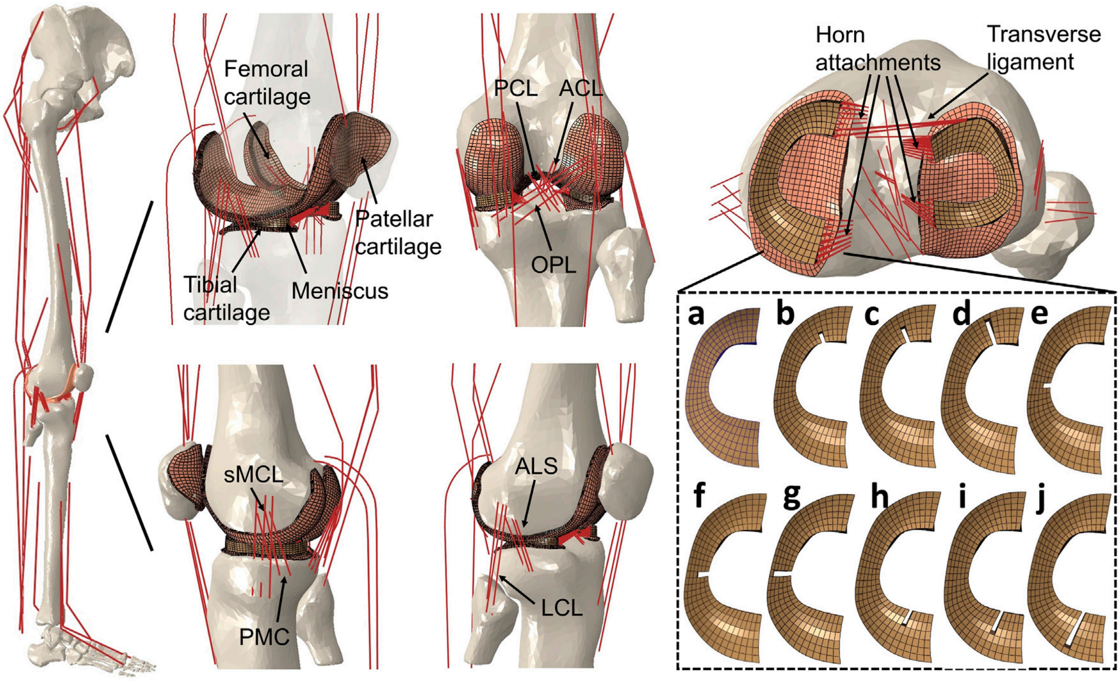

FIGURE 1
Right lower limb finite element musculoskeletal models containing knees with an intact healthy meniscus **(A)**; a medial meniscus with radial tears in the anterior horn involving three grades with widths of **(B)** 33%, **(C)** 50%, and **(D)** 83%; midbody with widths of **(E)** 33%, **(F)** 50%, and **(G)** 83%; and posterior horns with widths of **(H)** 33%, **(I)** 50%, and **(J)** 83%. A model without medial meniscus, equivalent to total meniscectomy, was also prepared (not shown). The lower limb finite element musculoskeletal model includes a 12-DOF knee joint, along with 20 muscles, ligaments (ACL, anterior cruciate ligament; PCL, posterior cruciate ligament; MCL, medial collateral ligament; PMC, posteromedial capsule; LCL, lateral collateral ligament; ALS, anterolateral structure; OPL, oblique popliteal ligament; transverse ligament), cartilage, the meniscus, and meniscus horn attachments.

trajectories (100-Hz sampling frequency, Vicon Nexus, Oxford Metrics Ltd., Oxford, United Kingdom) and ground reaction force (1000-Hz sampling frequency, TF-4060-D force plate, Tec Gihan Co., Ltd., Kyoto, Japan) were synchronously collected during a single stance phase.

Finite element musculoskeletal model

A FEMS model of the right lower limb, including a healthy knee with FE analysis previously developed in ABAQUS/Explicit (SIMULIA, Providence, RI, United States) (Figure 1), was used in the study. The modeling approach of the FEMS framework (Figure 2) of the lower limb has been discussed and validated previously (Wang et al., 2021; Wang et al., 2022) but is summarized below. The FEMS model included the geometry of all right lower limb bones and the articular cartilages and meniscus of the knee, which were segmented manually and reconstructed from computed tomography and magnetic resonance imaging scans (Figure 1). The femoral, tibial, and patellar bones were meshed using rigid triangular shell elements, and the cartilage and meniscus were defined using elastic eight-node hexahedral elements. A spherical joint with three degrees of freedom (DOF) was used to represent the hip, joints with six DOFs represented the tibiofemoral and patellofemoral joints, and a hinge joint at the ankle with one DOF were included in the FEMS model of the right lower limb, as shown in Figure 1. The anterior cruciate ligament, posterior cruciate ligament, medial collateral ligament, posteromedial capsule, lateral collateral ligament, anterolateral structure, and oblique popliteal ligament cross tibiofemoral joint were modeled as nonlinear spring bundles with a force-strain relationship (Abdel-Rahman and Hefzy, 1998):

$$f_i = \begin{cases} 0 & \varepsilon_i \leq 0 \\ {}^1k_i\,(l_i - {}^0l_i)^2 & 0 < \varepsilon_i \leq 2^l\varepsilon \\ {}^2k_i\,[l_i - (1 + {}^l\varepsilon)^0 l_i] & 2^l\varepsilon < \varepsilon_i \end{cases} \tag{1}$$

where f_i is the force sustained by the ith ligament, l_i is the current length of the ith ligament, ${}^0l_i$ is the slack length of the ith ligament, ${}^l\varepsilon$ is the strain assumed to be constant at 0.03, and ${}^1k_i$ and ${}^2k_i$ are the stiffness coefficients of the spring elements representing the ith ligament for the nonlinear and the linear regions, respectively. The values of the material properties of the

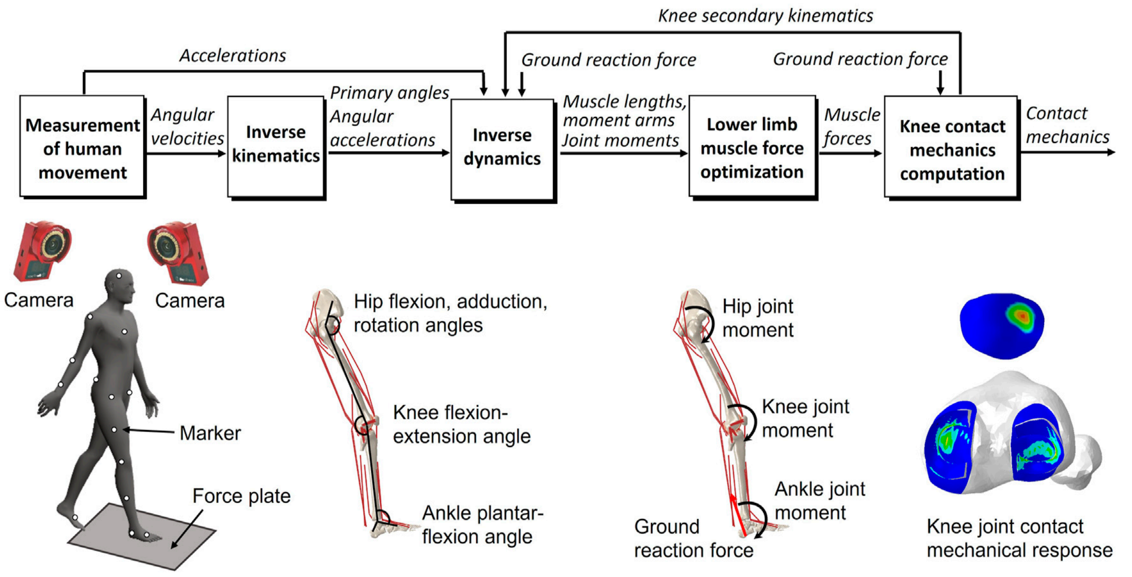

FIGURE 2
Overview of the dynamic gait simulation. Marker positions were input into the inverse kinematics to predict the joint primary angles (lumbar flexion–extension, hip joint 3-DOF rotations, knee joint flexion–extension, and ankle dorsiflexion–plantarflexion). The joint primary angles on each joint and ground reaction force measured from the force plate were input into the inverse dynamics to predict the muscle lengths, muscle moment arms, and right lower limb joint moments. The static optimization of the muscle force was performed with the joint moments, the muscle lengths, and the muscle moment arms as inputs to predict the muscle force. The knee contact mechanics were computed from the muscle forces and the ground reaction force to predict the knee joint secondary kinematics and contact mechanics. The predicted knee secondary kinematics were fed back to a new inverse dynamics analysis, and the muscle force optimization and knee contact mechanics were again computed.

TABLE 1 Stiffness parameters of ligaments.

Ligament	Ligament bundle	Number of bundles	$^{1}k(\mathrm{N\,mm^{-2}})$	$^{2}k(\mathrm{N\,mm^{-1}})$
ACL	anterior	2	22.48	83.15
	posterior	2	26.27	83.15
PCL	anterior	2	31.26	125.00
	posterior	2	19.29	60.00
MCL	anterior	1	10.00	91.25
	oblique	1	5.00	27.86
	deep	1	5.00	21.07
PMC		3	12.00	52.59
LCL		3	10.00	72.22
ALS		3	5.00	19.00
OPL		3	3.00	21.42

nonlinear spring elements are listed in Table 1 (Abdel-Rahman and Hefzy, 1998; Yu et al., 2001).

The FEMS model included 20 representative one-dimensional linear element muscles on the lower limb: the gluteus maximus (3 units), iliopsoas, pectineus, rectus femoris, vastus medialis, vastus intermedius, vastus lateralis, semimembranosus, semitendinosus, biceps femoris (short and long heads), gastrocnemius (medial and lateral heads), soleus, tibialis (anterior and posterior), extensor halluces longus, and extensor digitorum longus. The wrapping between the muscles and femoral and tibial bone was considered in the model to represent the muscle paths (Ali et al., 2016). The mechanical properties of the muscles were represented using a Hill-type dynamic model containing a contractile element (active fiber force-length property) in parallel with a passive elastic element (passive fiber force-length property) (Zajac, 1989).

Modeling of the meniscus with radial tears and meniscectomy

Modeling with FEMS, including knees with radial tears of the medial meniscus in the anterior horn, posterior horn, and midbody segment and without the medial meniscus (describing total meniscectomy), was an extension of the previously developed FEMS model with intact menisci. The medial meniscal model had radial tears in the anterior horn, midbody, and posterior horn involving three grades: 1) one-third width (33%), 2) one-half width (50%), and 3) five-sixths width (83%). These were created by partially removing the mesh from an intact medial meniscus (Figure 1). The intact and torn menisci were defined to be transversely isotropic with radial and axial moduli of 20 MPa and a circumferential modulus of 140 MPa (Donahue et al., 2002). The in-plane and out-of-plane Poisson's ratios were 0.2 and 0.3, respectively (Donahue et al., 2002; Yao et al., 2006). The articular cartilage was considered as a linear elastic isotropic material with an elastic modulus of 5 MPa and a Poisson's ratio of 0.46 (Li et al., 2001). It should be noted that to exclude the biomechanical effect of biological changes of tissue properties in the knee, only changes in the geometry of the meniscus tears were considered; in other words, the material property changes of tissues after tearing were not considered. The contact behaviors were defined with a coefficient of friction of 0.04 (McCann et al., 2009) for all contact pairs in the intact knee and knees with meniscus tear models: the femoral cartilage–medial and lateral meniscus, femoral cartilage–medial and lateral tibial cartilages, femoral cartilage–patellar cartilage, and between the meniscus and tibial cartilages on the medial and lateral sides. In the total meniscectomy model, the medial meniscus was resected, and the contact behavior of cartilage and the medial meniscus was not included.

The anterior transverse ligament connecting the anterior convex margin of the lateral meniscus to the anterior end of the medial meniscus was modeled as multiple linear spring elements with a stiffness of 12.5 N/mm (Donahue et al., 2003). The four meniscal horn attachments were assumed as multiple linear spring elements firmly connecting the meniscal horn faces and the tibial bone (Figure 1). The spring constants were calculated from Young's modulus reported for the horn attachments (Hauch et al., 2009):

$$k_{hp} = \frac{E}{n_h l_{hp}} a_h \tag{2}$$

where h indicates the meniscal horn; p indicates the linear spring, where k_{hp} is the pth spring stiffness for the hth meniscal horn; l_{hp} is the pth spring length of the hth meniscal horn; E is Young's modulus of the meniscal horn; a_h is the hth horn face area; and n_h is the number of spring elements for the hth meniscal horn. The spring length of each spring element was calculated from the insertions of the spring at the node of the horn face and the node of the tibial attachments.

Concurrent finite element musculoskeletal framework for gait analysis

The gait analysis considering lower limb motion achieved through inverse kinematics, inverse dynamics, muscle force optimization, and FE analysis on the knee, using inertial measurement unit sensors or motion capture system has been described previously (Wang et al., 2021; Wang et al., 2021; Wang et al., 2022) but is briefly presented below. In the study, considering that measurement accuracy was more important than measurement convenience, the gait analysis was performed using a motion capture system and force plate, generally regarded as the gold standard for motion analysis, instead of inertial measurement sensor units. An inverse kinematics analysis was used to derive the primary angles (hip joint flexion–extension, internal–external rotation, and abduction–adduction angles; knee joint flexion-extension angle; and ankle joint dorsiflexion–plantarflexion angle) of joints from marker trajectories measured in a human gait experiment. These primary joint angles and the measured ground reaction force were input to the inverse dynamics analysis to determine the joint moments, muscle lengths, and muscle moment arms. The muscle lengths and muscle moment arms were input to a static optimization algorithm to estimate the muscle forces by satisfying an equilibrium equation of the joint moment, and the muscle forces were optimized by minimizing the sum of the cube of the muscular activation s_m as follows (Hase and Yamazaki, 2002):

$$\mathbf{M}_j(\theta_j, e_s) = \sum_m \left[\mathbf{r}_{jm}(\theta_j, e_s) \times \mathbf{f}_{jm}(s_m)\right] \tag{3}$$

$$C = \min \sum_m s_m^3 \tag{4}$$

where j indicates the joint, m indicates the muscle, s indicates the knee secondary kinematics, $\mathbf{M}_j(\theta_j, e_s)$ is the moment of the jth joint, θ_j is the primary angle of the jth joint, e_s is the secondary kinematics of the knee joint (note that the hip and ankle joints only include primary angles) for the sth degree of freedom, and $\mathbf{r}_{jm}(\theta_j, e_s)$ is the moment arm vector for the jth joint. With each muscular activation considered as a variable, the force of the mth muscle can be expressed as a function $\mathbf{f}_{jm}(s_m)$ of the activation about the jth joint. In addition, the muscular activations were constrained to be in the range of zero to one (inclusive).

The static optimization method was performed by implementing subroutines written in MATLAB (R2018b, MathWorks, MA, United States) using the interior-point method, which combines concurrent FE contact analysis on the knee joint in ABAQUS/Explicit at 16 evenly distributed time

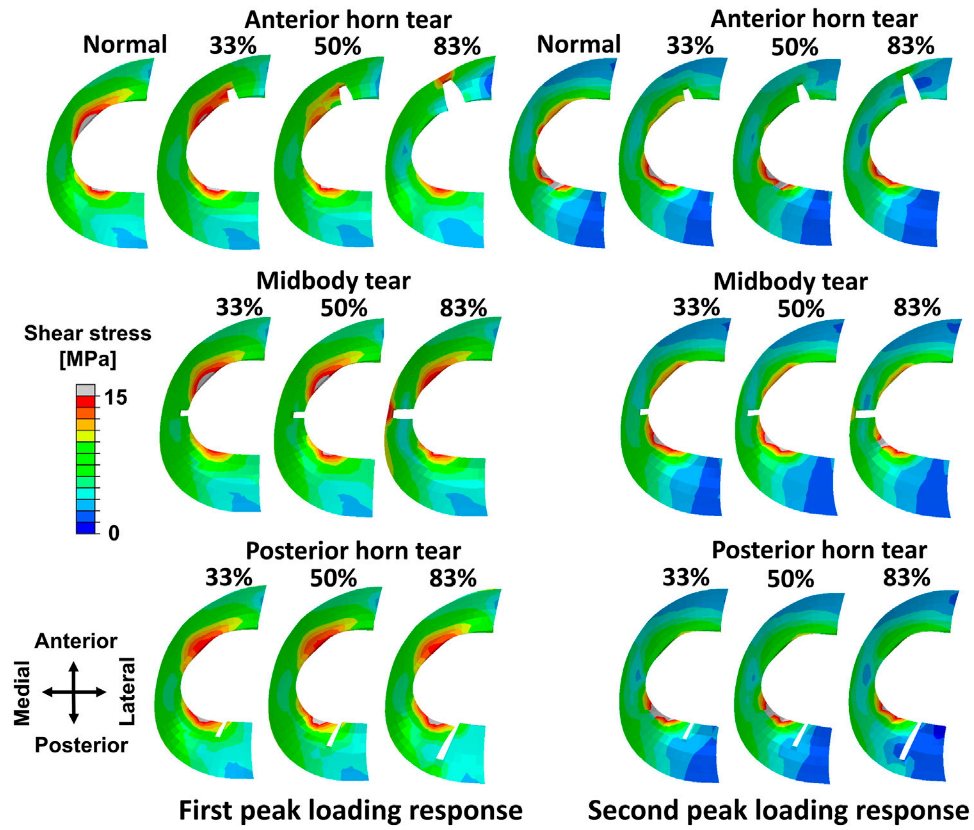

FIGURE 3
Results of shear stress distribution on the medial meniscus involving a healthy knee and a knee with radial tears in the medial meniscus during the maximum weight acceptance and push-off.

points (0%, 6.67%, 13.33%, 20%, 26.67%, 33.33%, 40%, 46.67%, 53.33%, 60%, 66.67%, 73.33%, 80%, 86.67%, 93.33%, and 100% of the stance phase) during one stance phase. The secondary kinematics of the knee, which were determined entirely from the interaction of the joint contact mechanics, muscle forces, and ligament restraint, were fed back to a new inverse dynamics analysis updating muscle lengths and muscle moment arms until the stability of optimization was ensured with the convergence criteria for equilibrium in the joint moment. The FEMS models containing an intact knee joint, damaged knee joints with meniscal tears, and a joint without a meniscus were used to perform the optimization procedures, separately, under the same input condition (marker position and ground reaction force).

Results

The peak shear stress, occurred on the white zone of the medial meniscus in the intact meniscus during the maximum weight acceptance of the stance phase (1st peak of the vertical ground reaction force) (Figure 3). The shear stress distribution of the meniscus changed as the anterior horn tear widened, shear stress in the anterior horn tear increased significantly, and the peak shear stress occurred at the end (deepest portion of tear near the side of the red zone) of the 83% tear. The changes in shear stress distribution that occurred on the medial meniscus with the midbody tear were not observed at widths of 33% and 50%. Tears of the posterior horn did not alter the shear stress distribution on the meniscus during the maximum weight acceptance. During the push-off at the stance phase (2nd peak of the vertical ground reaction force), changes in the shear stress on the medial meniscus were barely observed at three locations with tears.

High shear stress was observed at the ends of meniscal anterior horn tears, including all three grades compared to the intact meniscus, except during the terminal stance (50%–70% stance phase) (Figure 4A). In the 83% midbody tear group, the shear stress located at the end of the tear was significantly more prominent than that in the intact meniscus and other tear groups, and the maximum shear stress at the 90% stance phase was increased by 310% compared to the intact meniscus (Figure 4B). Alterations in the ends of the meniscal posterior horn tear groups were not detected during the stance phase (Figure 4C).

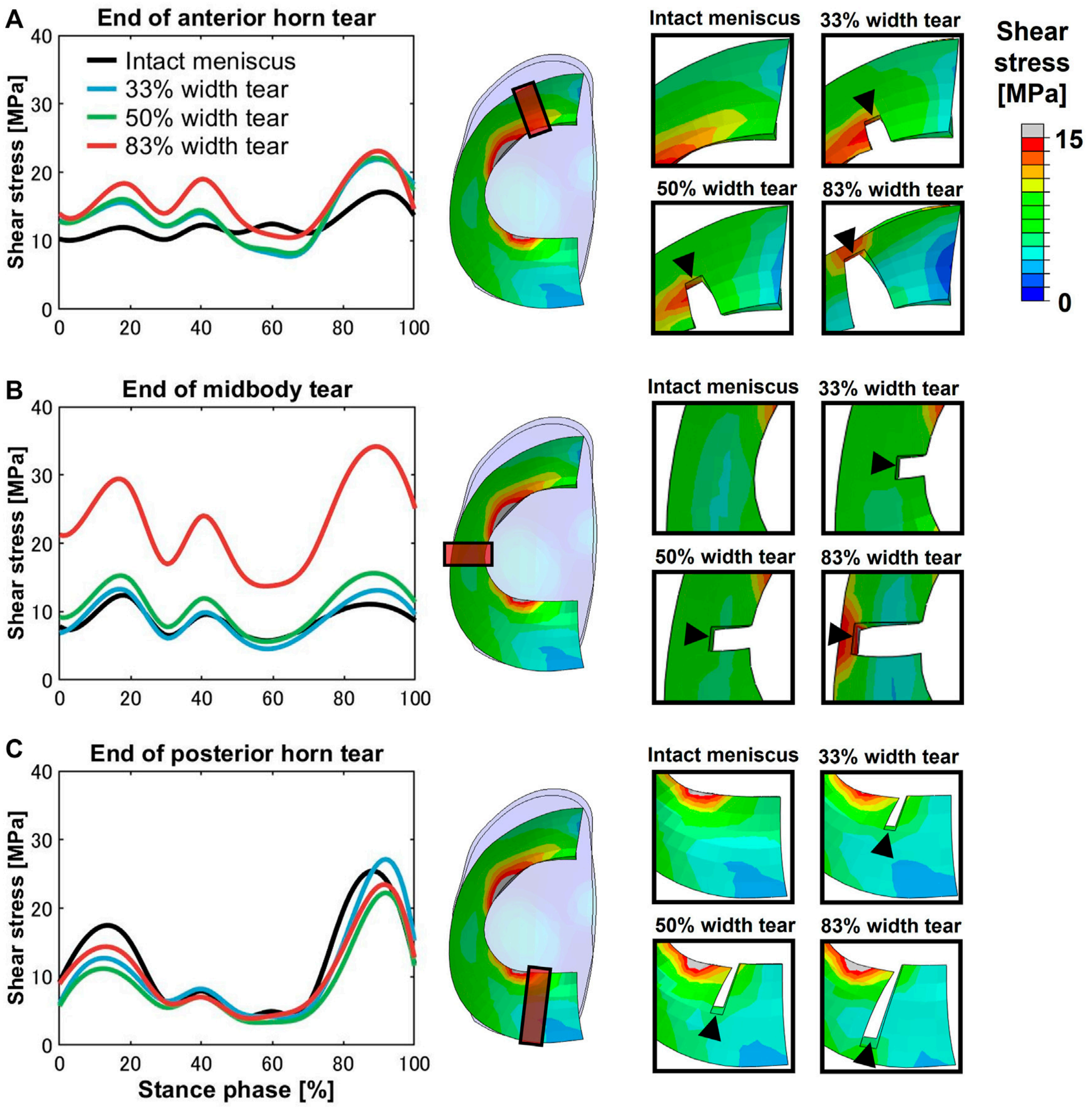

FIGURE 4
Shear stress differences on an intact meniscus and a meniscus with a medial radial tear at the ends of the tears. The left subfigures show the magnitude of stress at the **(A)** anterior horn, **(B)** midbody, and **(C)** posterior horn, involving an intact meniscus and 33%, 50%, and 83% width tears during the stance phase of the gait cycle. The right subfigures indicated the tear locations (orange box) at the anterior horn, midbody, and posterior horn and enlarged views of the tear locations.

The tibial cartilage contact forces were hardly affected by radial tears in the medial meniscus (Figures 5A–C). The ratio of the medial meniscus contact force to the whole medial contact force was 0.61 on average in the intact meniscus; that is, the tibial cartilage shared 39% of the total medial load, which illustrates the essential function of the medial meniscus in load sharing. An insignificant increase in the load shared by the tibial cartilage to the total medial side was observed with tears (Figures 5E,F), consistent with previous experimental *in vitro* results (Walker et al., 2015). However, after meniscectomy, the maximum contact force on the medial tibial cartilage was 3.6 times the bodyweight, compared to 2.17 times in the intact healthy knee. The contact pressure distributions on the medial tibial cartilages in the intact, torn, and meniscectomy knees are shown in Figure 6 at the maximum weight acceptance and push-off. The peak contact pressure on the tibial cartilage increased after meniscectomy to 17.64 MPa and 13.76 MPa, compared with the healthy knee (11.94 MPa and 12.45 MPa) at the maximum weight acceptance and push-off, respectively.

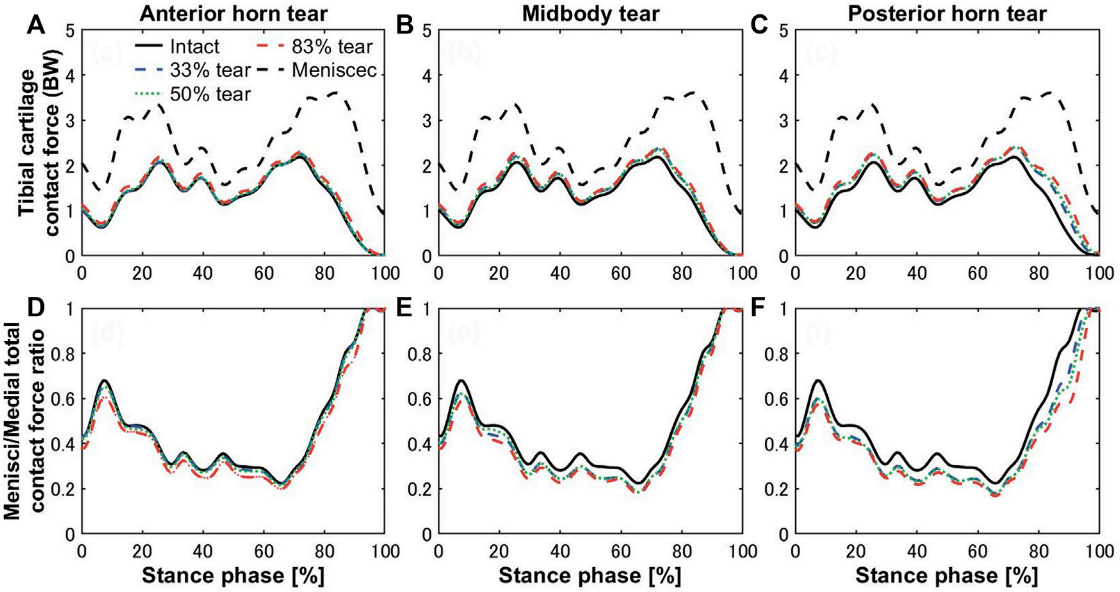

FIGURE 5
Contact forces on medial tibial cartilages of the intact knee (black solid curves) compared with total meniscectomy (black dashed curves) and **(A)** anterior horn, **(B)** midbody, and **(C)** posterior horn tears with widths of 33% (blue dashed curve), 50% (green dotted curve), and 83% (red dashed curve) during the stance phase of the gait cycle. The lower panels show the ratios of the medial meniscal contact forces to total knee joint contact forces on the medial side with tears in the **(D)** anterior horn, **(E)** midbody, and **(F)** posterior horn.

Discussion

In this study, models of the lower limb with a medial meniscus having radial tears and without a medial meniscus were developed based on a previously developed FEMS model (Wang et al., 2021; Wang et al., 2022), which has been proven to describe realistic knee biomechanics during the gait cycle. The predicted knee biomechanics results of the model containing an intact knee were compared with experimental *in vivo* and *in vitro* results (Kozanek et al., 2009; Bergmann et al., 2014; Gilbert et al., 2014; Clément et al., 2018) and proven to be reliable. We evaluated the knee biomechanical changes after meniscus tears and total meniscectomy using the models.

The anterior horn with intact meniscus bore stable shear stress with an average value of 12.27 MPa (Figure 4A) from the knee during the stance phase of the gait, compared with 6.72 MPa (Zhang et al., 2019) and 15.34 MPa (Zhang et al., 2019) predicted by other finite element simulation during slight flexion. However, some investigators also reported smaller results of less than 4 MPa (Li et al., 2019; Li et al., 2020); these differences might be due to the definition of the geometry, material properties, and contact behavior of the knee joint. In the medial meniscus, the mobility of the anterior horn was most prominent (Thompson et al., 1991; Vedi et al., 1999), and there was basically no obvious fluctuation in the shear stress of the anterior horn in the intact knee during the stance phase (Figure 4A), which may suggest that the anterior horn plays a role in stabilizing load transmission, but only during knee extension. As shown in Figure 7A, circumferential tensile stress occurred in the anterior horn of the intact meniscus, which showed a uniform decreasing trend from the inner circumference to the outer circumference. The shear stresses that accompanied the tear increased significantly at the ends of the anterior horn tears (Figure 4A); this was due to the destruction of the circumferential collagen fibers on the inner circumference, which results in the transfer of the load to the tear and produces more significant circumferential stress (Figure 7A). When the 83% width tear occurs, the changing trend of the circumferential tensile stress from the inner to the outer circumference changes from a uniform decrease to a gradual increase. Especially, the stress at the end of the tear increases extremely, and all the tear areas were stretched, which may lead to further tearing or complete rupture. On the intact meniscus, the average shear stress experienced by the midbody was 8.77 MPa, which is less than 12.27 MPa for the anterior horn and 11.54 MPa for the posterior horn. The anterior and posterior horns carry the anteroposterior shear forces applied to the femur, while the midbody primarily provides stability against medial subluxation by the midbody of the meniscus through hoop stress transmission (Hwang et al., 2012). The midbody of the intact meniscus exhibited a uniform hoop tensile stress trend that increases from the inner circumference to the outer circumference, as shown in Figure 7B. Therefore, the higher

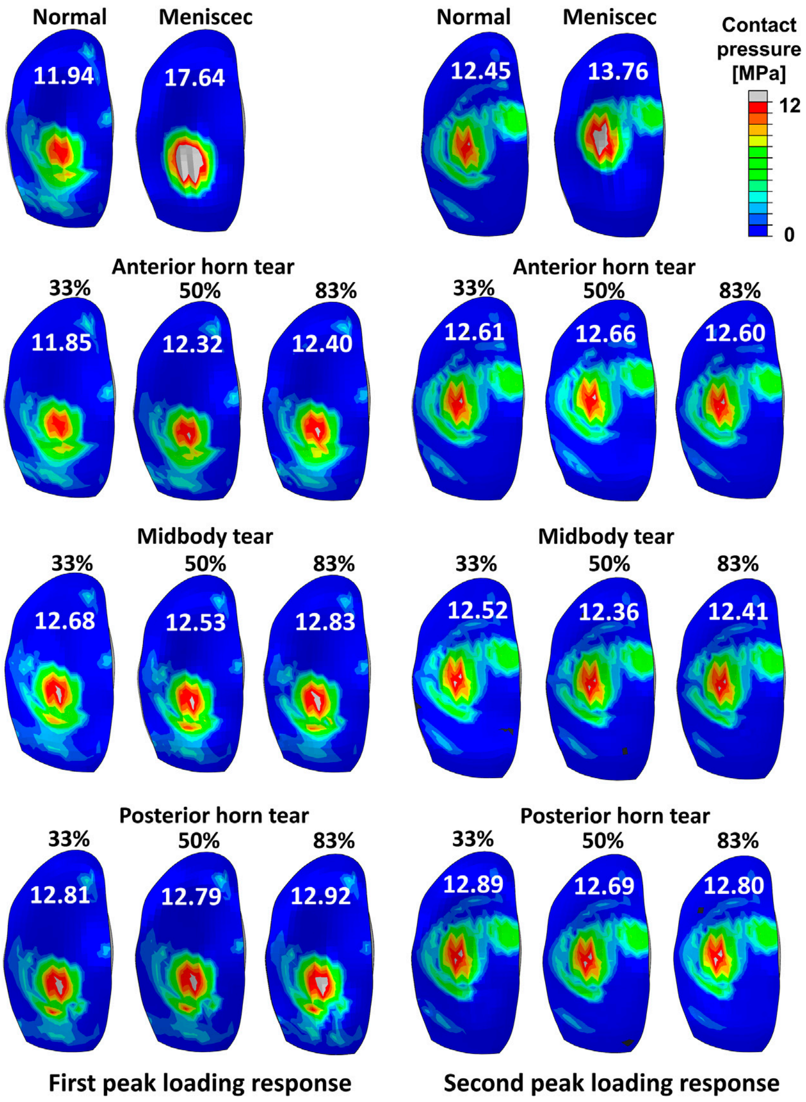

FIGURE 6
Results of the contact pressure distribution and resultant peak values (white words) occurring on the medial tibial cartilage obtained by a healthy intact knee, total meniscectomy knee, and radial tears during the maximum weight acceptance and push-off.

hoop stress from the outer circumference can make the meniscus firmly lock onto the medial femoral condyle (Figure 7A). The tears with widths of 33% and 50% hardly affected changes in the midbody shear stress distribution (Figures 3, 4B). However, substantial stress concentrations were detected at the end of the 83% midbody tear (Figure 4B), which may mean that longer tears at the midbody severely disrupt more circumferential fibers and hoop stress transmission, causing an increase in stress. Stresses reached the experimentally measured failure stress range of 20–170 MPa (Kohn et al., 1992). We observed that the hoop tensile stress in the tear region was replaced by compressive stress as the tear increased, resulting in the need for extremely high tensile stress at the tear to maintain circumferential stress transmission, as shown in Figure 7B. The observed compressive stress was favorable for compressing the tear surfaces together, resulting in a stable tear and possibly more favorable healing conditions. However, a study reported that five of the six radial tears had no evidence of healing and one had become longer (Weiss et al., 1989). Henning et al. (1988) suggested that only shallow radial tears do not require treatment because they heal spontaneously or remain asymptomatic. Our observations contradict these conclusions from clinical reports. This may be because the defined isotropic material models cannot accurately calculate the stresses within a fibrillar tissue such as the meniscus, and a fibril-reinforced material model, which can represent fluid pressure and site-

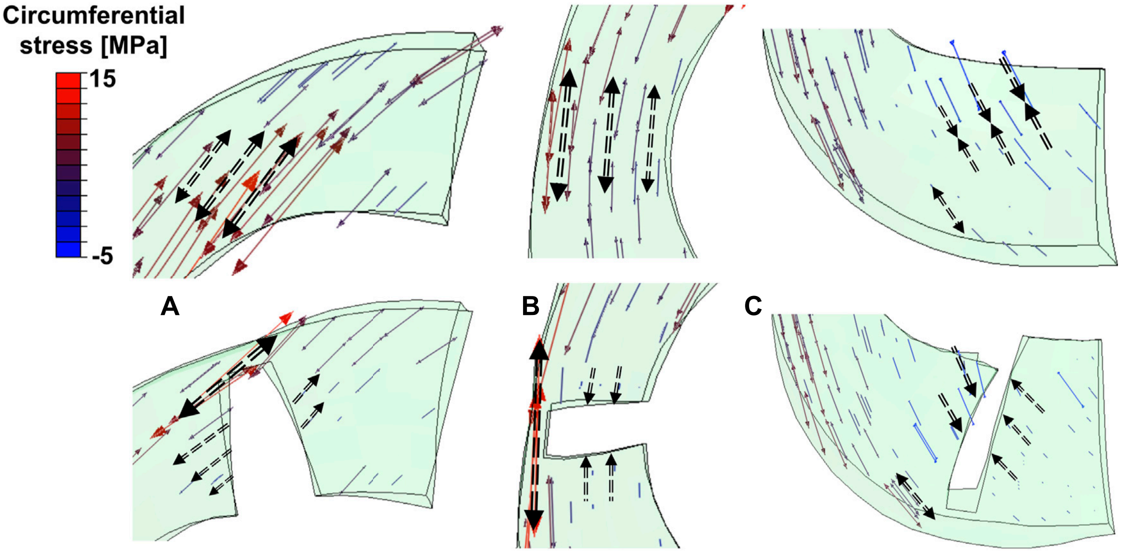

FIGURE 7
Tensor plots of circumferential stress for the **(A)** anterior horn, **(B)** midbody, and **(C)** posterior horn with 83% width tears. The color changes from blue to red represent the stress variation from small (negative, compressive stress) to large (positive, tensile stress) on the tensor plot. Dashed arrows indicated circumferential stress in tensile or compressive directions. Thicker longer arrows represent higher magnitudes.

specific collagen fiber orientation, should be used for accurate simulations (Klets et al., 2016). Even so, this finding could indicate that alongside vascularity, biomechanics may play an essential role in healing for nonoperative treatment or postoperative meniscal repair. The translation is significant in the anterior horn and small in the posterior horn of the medial meniscus. Therefore, stress readily accumulated at the junction of the middle and the posterior portions of the medial meniscus (Figure 3), consistent with the results reported in other studies (Bin et al., 2004). The posterior horn of the intact meniscus carried a high percentage of the load overall, with shear stress reaching a peak of 25.16 MPa at higher flexion angles during preswing, compared with 17.08 MPa for the anterior horn and 10.98 for the midbody during the same gait phase. The low translation of the posterior horn of the medial meniscus is a potential mechanism for meniscal tears, with a resultant "trapping" of the fibrocartilage between the femoral condyle and the tibial plateau during high flexion (Fox et al., 2012), possibly contributing to the high circumferential compressive stress distribution. As shown in Figure 7C, the tears did not change the hoop compressive stress distribution, and the stress that occurred at the tear surfaces caused them to be compressed together. Apart from vascularity, this may explain why radial tears in this region are most amenable to healing (Belzer and Cannon, 1993). In the addition, the slackness of the meniscus horn attachment also affects the loading of the meniscus horn. Guess et al. (2016) showed that increased meniscal extrusion occurs with laxity of the attachment, and increased laxity results in loss of meniscal function. In contrast, simulating an overly stiff meniscus horn attachment might lead to an overloading of the meniscal horns, and the study provides important guidance for related research on meniscus modeling.

Bergmann group has conducted measurements of the *in vivo* tibiofemoral joint contact loads, which are 2.61 body weight (Kutzner et al., 2010) and 3.98 body weight (Dreyer et al., 2022), respectively, using instrumented implants. These studies directly measured the knee joint load of multiple patients and performed statistical analysis. Although these measurement results are not natural knee data, and due to the material properties of the total knee arthroplasty prosthesis, prosthesis geometry, and interprosthesis contact, the represented behavior varies widely from natural or removed meniscal knees. However, they can be used as a quantitative reference to properly verify the accuracy of our prediction results. The peak contact forces of 4.42 BW (Navacchia et al., 2019) and 4.02 BW (Hume et al., 2019) during the gait cycle were predicted by the Shelburne group using a finite element knee model without a meniscus. As far as we know, the joint contact force is generally accepted as being between two and 4.5 BW (Kumar et al., 2013; Bergmann et al., 2014; Richards et al., 2018; Hume et al., 2019; Shu et al., 2022). In general, the results predicted by computational models are usually greater than those predicted by *in vivo* experiments (Kutzner et al., 2010; Esrafilian et al., 2020; Wang et al., 2022). The role of the meniscus in sharing knee joint loading on the medial side was most significant during the loading response (0%–20% stance phase) and preswing (80%–100% stance phase) (Figure 5E,F). The ratio of the medial meniscus contact force to the whole medial contact force was 0.57 and

0.78 on average on the intact meniscus during the loading response and preswing, respectively. The trends of increased cartilage load caused by tearing were not apparent, compared with the ratio of meniscus–medial total contact force on the intact meniscus, which increased by 2.6%, 5.1%, and 7.7% on average in the anterior horn, midbody, and posterior horn tear groups, respectively, during the stance phase. Of these, even though the presence of an 83% width tear of the posterior horn during the preswing resulted in the most significant increase in cartilage load, the cartilage/total load ratio increased by only 9%. The findings suggested that medial meniscus radial tears have lesser influence on the tibial cartilage loading (Figure 5), consistent with previous experimental results (Bedi et al., 2010; Bedi et al., 2012), however, some studies have also concluded that meniscal tears lead to increased cartilage loading (Zhang et al., 2015; Sukopp et al., 2021). Previously, investigators have pointed out that meniscal tears in a healthy knee may ultimately lead to the occurrence of knee OA due to the loss of much of the meniscal functionality, such as circumferential stress transmission (Englund et al., 2009). According to results from previous case-control studies, OA is more likely to occur in the knee with meniscus tears without arthropathy than in knees with intact menisci, suggesting that meniscal tears occur before any visible cartilage changes (Englund et al., 2009). The cartilage loads were not significantly increased by the meniscal tears, but OA may begin to occur as tears result in loss of most of the meniscus function, which requires extreme vigilance. Therefore, the evaluation of meniscal function in addition to mechanical evaluation of cartilage is critical.

The peak contact pressure was 12.45 MPa on a healthy knee in our model. The results might be acceptable, compared with other computational studies, which reported results of 7.9 (Park et al., 2019), 13.0 (Halonen et al., 2017), and 15 MPa (Kłodowski et al., 2016). Bedi et al. (2010) reported maximum contact pressures of 7.4 ± 0.6 MPa and 6.4 ± 1.1 MPa (Bedi et al., 2012) in vitro studies on a cadaver knee joint with film contact pressure sensors to simulate gait conditions. Our calculated maximum contact pressures were high compared to these *in vitro* experiment results. However, with *in vitro* experiments, the contraction activity of muscles cannot be reproduced in cadavers, which may have resulted in the measurement of relatively small contact loads. Moreover, the use of these sensors can severely alter meniscus translation and deformation, possibly resulting in prediction errors of the contact mechanics. The maximum peak contact pressure on the tibial cartilage increased to 17.64 MPa after meniscectomy, which indicated a risk of cartilage damage (Kempson et al., 1971). The contact force on the tibial cartilage after total meniscectomy was increased by 178.93% compared with the intact meniscus knee (Figure 5). The magnitude of the peak contact pressure on the tibial cartilage with total meniscectomy greatly increased, and the contact distribution was significantly altered compared to the intact and tear meniscus groups. Previous research reported that radial tears extending to the periphery result in a loss of hoop tension, which has been described as functionally equivalent to a total meniscectomy (Allaire et al., 2008). Therefore, total meniscectomy is the mainstream treatment for long radial tears. However, despite the benefits of short-term pain relief, meniscectomy resulted in a substantial cartilage load that may increase the risk of OA progression; in other words, the effect on the knee biomechanics can be much worse than the meniscus tear itself. Our finding demonstrated that although tears can disrupt the meniscal circumferential stress transfer function, even wider meniscal radial tears have little effect on cartilage loading, whereas meniscectomy has a significant effect on the cartilage load. Therefore, we emphasize the importance of meniscal preservation whenever feasible, including consideration of meniscus repair or the implantation of an artificial meniscus.

This study had some limitations. First, the FEMS lower limb model and gait data were not from the same subject. The most accurate computational analysis of knee mechanics requires subject-specific model geometry and human motion data. Second, only one subject participated in the gait measurement experiment. Due to individual differences, the generalizability of our findings may be affected by random individual traits. However, using the same walking pattern of the same subject as input data while only changing the meniscus tear model eliminates the influence of the walking pattern itself on changes in joint load; the effects of meniscal tears can be directly evaluated. Therefore, we decided to perform the analysis using the data of one trial with one subject without considering the walking pattern and the subject's own gait variation. In addition, analysis using the same gait measurement data was also beneficial for eliminating the influence of different gait patterns themselves in meniscal tear patients on changes in joint load. Third, the ligaments were simplified as one-dimensional elastic elements to reduce the computational expense. However, because wrapping and realistic soft tissue contact are not included in the model, the effect of the medial collateral ligament and oblique popliteal ligament contacting the medial meniscus could not be represented, which may have implications for meniscal mechanical prediction. Fourth, to exclude the influence of mesh conditions, we did not reconstruct and remesh the geometries of the menisci with tears; instead, these were created by partially removing the mesh from an intact medial meniscus. However, this modelling was unable to replicate a more realistic meniscus with tears geometry and may lead in errors in predictions of the joint contact mechanics. In addition, the division of the mesh was based on experience in the study; however, to identify the optimum mesh size, a mesh convergence analysis should be conducted. A final limitation was that the articular cartilages were defined as linear elastic isotropic material, whereas a biphasic fibril-reinforced material might better approximate the representation of cartilage's dynamic response (Brindle et al., 2001). However, studies have also shown that the properties of linear elastic materials can accurately mimic the overall behavior of cartilage (Bell et al., 2009).

Conclusion

In this study, FEMS models of the lower limb, including knees with radial tears of the medial meniscus and total medial meniscectomy, were developed and used to investigate the effects of radial meniscal tears and total meniscectomy on the meniscal stress changes and biomechanical redistribution on the knee. Our research demonstrated that wider radial tears of the medial meniscus are prone to high-stress concentrations at the end of the tears, leading to the potential risk of developing complete meniscal ruptures. In addition, although the tears did not cause changes in cartilage load distribution, they disrupted the circumferential stress transmitting function of the meniscus; thus, knee OA may begin to develop. Significantly increased load on the tibial cartilage with the postmeniscectomy model indicated potential risks for the onset of OA. Therefore, surgical procedures such as meniscectomy should be applied conservatively; that is, excessive removal of meniscal tissue should be avoided. The modeling may provide a potential clinical tool for surgical decisions for patients with meniscus and other soft tissue injures, including more accurate pathology analysis and treatment of OA. Overall, the FEMS is expected to provide doctors with a reference for diagnosis.

Data availability statement

The original contributions presented in the study are included in the article/supplementary material, further inquiries can be directed to the corresponding authors.

Ethics statement

The studies involving human participants were reviewed and approved by The research ethics committee of the Tokyo Metropolitan University. The patients/participants provided their written informed consent to participate in this study. Written informed consent was obtained from the individual(s) for the publication of any potentially identifiable images or data included in this article.

Author contributions

This paper was conceptualized by SW, KH, SK, and SO. The methodology was developed by SW, KH, and SO. Subject motion data acquisition and analysis were carried out by SW and SK. Resources were arranged by KH and SO. The original draft was prepared by SW. All authors have read and agreed to the published version of the manuscript.

Funding

Supported in part by the Japan Society for the Promotion of Science [Grant-in-Aid for Scientific Research (B) 19H03970] (No. 50452199; Funder ID: 10.13039/501100001691).

Acknowledgments

We would like to express our gratitude to the Nagoya Orthopedic Surgery and Artificial Joint Clinic for providing medical images of patients.

Conflict of interest

The authors declare that the research was conducted in the absence of any commercial or financial relationships that could be construed as a potential conflict of interest.

Publisher's note

References

Abdel-Rahman, E. M., and Hefzy, M. S. (1998). Three-dimensional dynamic behaviour of the human knee joint under impact loading. *Med. Eng. Phys.* 20, 276–290. doi:10.1016/S1350-4533(98)00010-1

Ali, A. A., Shalhoub, S. S., Cyr, A. J., Fitzpatrick, C. K., Maletsky, L. P., Rullkoetter, P. J., et al. (2016). Validation of predicted patellofemoral mechanics in a finite element model of the healthy and cruciate-deficient knee. *J. Biomech.* 49, 302–309. doi:10.1016/j.jbiomech.2015.12.020

Allaire, R., Muriuki, M., Gilbertson, L., and Harner, C. D. (2008). Biomechanical consequences of a tear of the posterior root of the medial meniscus. Similar to total meniscectomy. *J. Bone Jt. Surgery-American Volume* 90, 1922–1931. doi:10.2106/JBJS.G.00748

Bedi, A., Kelly, N. H., Baad, M., Fox, A. J. S., Brophy, R. H., Warren, R. F., et al. (2010). Dynamic contact mechanics of the medial meniscus as a function of radial tear, repair, and partial meniscectomy. *J. Bone Jt. Surgery-American Volume* 92, 1398–1408. doi:10.2106/JBJS.I.00539

Bedi, A., Kelly, N. H., Sc, B., Baad, M., Fox, A. J. S., Sc, M., et al. (2012). Dynamic contact mechanics of radial tears of the lateral meniscus: Implications for treatment. *Arthrosc. J. Arthrosc. Relat. Surg.* 28, 372–381. doi:10.1016/j.arthro.2011.08.287

Bell, J. S., Winlove, C. P., Smith, C. W., and Dehghani, H. (2009). Modeling the steady-state deformation of the solid phase of articular cartilage. *Biomaterials* 30, 6394–6401. doi:10.1016/j.biomaterials.2009.08.026

Belzer, J. P., and Cannon, W. D. (1993). Meniscus tears: Treatment in the stable and unstable knee. *J. Am. Acad. Orthop. Surg.* 1, 41–47. doi:10.5435/00124635-199309000-00006

Bergmann, G., Bender, A., Graichen, F., Dymke, J., Rohlmann, A., Trepczynski, A., et al. (2014). Standardized loads acting in knee implants. *PLoS ONE* 9, 86035. doi:10.1371/journal.pone.0086035

Bin, S., Kim, J., and Shin, S. (2004). Radial tears of the posterior horn of the medial meniscus. *Arthrosc. J. Arthrosc. Relat. Surg.* 20, 373–378. doi:10.1016/j.arthro.2004.01.004

Brindle, T., Nyland, J., and Johnson, D. L. (2001). The meniscus: Review of basic principles with application to surgery and rehabilitation. *J. Athl. Train.* 36, 160–169.

Clément, J., Toliopoulos, P., Hagemeister, N., Desmeules, F., Fuentes, A., and Vendittoli, P. A. (2018). Healthy 3D knee kinematics during gait: Differences between women and men, and correlation with X-ray alignment. *Gait Posture* 64, 198–204. doi:10.1016/j.gaitpost.2018.06.024

Donahue, T. L. H., Hull, M. L., Rashid, M. M., and Jacobs, C. R. (2002). A finite element model of the human knee joint for the study of tibio-femoral contact. *J. Biomech. Eng.* 124, 273–280. doi:10.1115/1.1470171

Donahue, T. L. H., Hull, M. L., Rashid, M. M., and Jacobs, C. R. (2003). How the stiffness of meniscal attachments and meniscal material properties affect tibio-femoral contact pressure computed using a validated finite element model of the human knee joint. *J. Biomech.* 36, 19–34. doi:10.1016/s0021-9290(02)00305-6

Dreyer, M. J., Trepczynski, A., Nasab, S. H. H., Kutzner, I., Schütz, P., Weisse, B., et al. (2022). European Society of Biomechanics S.M. Perren Award 2022: Standardized tibio-femoral implant loads and kinematics. *J. Biomech.* 141, 111171. doi:10.1016/j.jbiomech.2022.111171

Englund, M., Guermazi, A., and Lohmander, S. L. (2009). The role of the meniscus in knee osteoarthritis: A cause or consequence? *Radiol. Clin. North Am.* 47, 703–712. doi:10.1016/j.rcl.2009.03.003

Esrafilian, A., Stenroth, L., Mononen, M. E., Tanska, P., Avela, J., and Korhonen, R. K. (2020). EMG-assisted muscle force driven finite element model of the knee joint with fibril-reinforced poroelastic cartilages and menisci. *Sci. Rep.* 10, 3026. doi:10.1038/s41598-020-59602-2

Felson, D. T. (2013). Osteoarthritis as a disease of mechanics. *Osteoarthr. Cartil.* 21, 10–15. doi:10.1016/j.joca.2012.09.012

Fox, A. J. S., Bedi, A., and Rodeo, S. A. (2012). The basic science of human knee menisci structure, composition, and function. *Sports Health.* 4, 340–351. doi:10.1177/1941738111429419

Fox, A. J. S., Wanivenhaus, F., Burge, A. J., Warren, R. F., and Rodeo, S. A. (2015). The human meniscus: A review of anatomy, function, injury, and advances in treatment. *Clin. Anat.* 28, 269–287. doi:10.1002/ca.22456

Gilbert, S., Chen, T., Hutchinson, I. D., Choi, D., Voigt, C., Voigt, C., et al. (2014). Dynamic contact mechanics on the tibial plateau of the human knee during activities of daily living. *J. Biomech.* 47, 2006–2012. doi:10.1016/j.jbiomech.2013.11.003

Guess, T. M., Razu, S., Jahandar, H., and Stylianou, A. (2016). Predicted loading on the menisci during gait: The effect of horn laxity. *J. Biomech.* 48, 1490–1498. doi:10.1016/j.jbiomech.2015.01.047

Halonen, K. S., Dzialo, C. M., Mannisi, M., Venäläinen, M. S., de Zee, M., and Andersen, M. S. (2017). Workflow assessing the effect of gait alterations on stresses in the medial tibial cartilage - combined musculoskeletal modelling and finite element analysis. *Sci. Rep.* 7, 17396. doi:10.1038/s41598-017-17228-x

Hase, K., and Yamazaki, N. (2002). Computer simulation study of human locomotion with a three-dimensional entire-body neuro-musculo-skeletal model (I. Acquisition of normal walking). *JSME Int. J. Ser. C* 45, 1040–1050. doi:10.1299/jsmec.45.1040

Hauch, K. N., Oyen, M. L., Odegard, G. M., and Donahue, T. L. H. (2009). Nanoindentation of the insertional zones of human meniscal attachments into underlying bone. *J. Mech. Behav. Biomed. Mat.* 2, 339–347. doi:10.1016/j.jmbbm.2008.10.005

Henning, C. E., Clark, J. R., Lynch, M. A., Stallbaumer, R., Yearout, K. M., and Vequist, S. W. (1988). Arthroscopic meniscus repair with a posterior incision. *Instr. Course Lect.* 37, 209–221.

Howell, R., Kumar, N. S., Patel, N., and Tom, J. (2014). Degenerative meniscus: Pathogenesis, diagnosis, and treatment options. *World J. Orthop.* 5, 597–602. doi:10.5312/wjo.v5.i5.597

Hu, J., Xin, H., Chen, Z., Zhang, Q., Peng, Y., and Jin, Z. (2019). The role of menisci in knee contact mechanics and secondary kinematics during human walking. *Clin. Biomech. (Bristol, Avon.* 61, 58–63. doi:10.1016/j.clinbiomech.2018.11.009

Hume, D. R., Navacchia, A., Rullkoetter, P. J., and Shelburne, K. B. (2019). A lower extremity model for muscle-driven simulation of activity using explicit finite element modeling. *J. Biomech.* 84, 153–160. doi:10.1016/j.jbiomech.2018.12.040

Hwang, S. H., Jung, K. A., Lee, W. J., Yang, K. H., Lee, D. W., Carter, A., et al. (2012). Morphological changes of the lateral meniscus in end-stage lateral compartment osteoarthritis of the knee. *Osteoarthr. Cartil.* 20, 110–116. doi:10.1016/j.joca.2011.11.005

Kedgley, A. E., Saw, T., Segal, N. A., Hansen, U. N., Bull, A. M. J., and Masouros, S. D. (2019). Predicting meniscal tear stability across knee-joint flexion using finite-element analysis. *Knee Surg. Sports Traumatol. Arthrosc.* 27, 206–214. doi:10.1007/s00167-018-5090-4

Kempson, G. E., Spivey, C. J., Swanson, S. A. V., and Freeman, M. A. R. (1971). Patterns of cartilage stiffness on normal and degenerate human femoral heads. *J. Biomech.* 4, 597–608. doi:10.1016/0021-9290(71)90049-2

Klets, O., Mononen, M. E., Tanska, P., Nieminen, M. T., Korhonen, R. K., and Saarakkala, S. (2016). Comparison of different material models of articular cartilage in 3D computational modeling of the knee: Data from the Osteoarthritis Initiative (OAI). *J. Biomech.* 16, 3891–3900. doi:10.1016/j.jbiomech.2016.10.025

Kłodowski, A., Mononen, M. E., Kulmala, J. P., Valkeapää, A., Korhonen, Rk, Avela, J., et al. (2016). Merge of motion analysis, multibody dynamics and finite element method for the subject-specific analysis of cartilage loading patterns during gait: Differences between rotation and moment-driven models of human knee joint. *Multibody Syst. Dyn.* 37, 271–290. doi:10.1007/s11044-015-9470-y

Kohn, D., Wirth, C. J., Plitz, G. R. W., Maschek, H., Erhardt, W., Wülker, N., et al. (1992). Medial meniscus replacement by a tendon autograft. experiments in sheep. *J. Bone Jt. Surg. Br. volume* 74, 910–917. doi:10.1302/0301-620X.74B6.1447257

Kozanek, M., Hosseini, A., Liu, F., Van de Velde, S. K., Gill, T. J., Rubash, H. E., et al. (2009). Tibiofemoral kinematics and condylar motion during the stance phase of gait. *J. Biomech.* 43, 1877–1884. doi:10.1016/j.jbiomech.2009.05.003

Kumar, D., Manal, K. T., and Rudolph, K. S. (2013). Knee joint loading during gait in healthy controls and individuals with knee osteoarthritis. *Osteoarthr. Cartil.* 21, 298–305. doi:10.1016/j.joca.2012.11.008

Kurosawa, H., Fukubayashi, T., and Nakajima, H. (1980). Load-bearing mode of the knee joint physical behavior of the knee joint with or without menisci. *Clin. Orthop. Relat. Res.* 149, 283–290. doi:10.1097/00003086-198006000-00039

Kutzner, I., Heinlein, B., Graichen, F., Bender, A., Rohlmann, A., Halder, A., et al. (2010). Loading of the knee joint during activities of daily living measured *in vivo* in five subjects. *J. Biomech.* 43, 2164–2173. doi:10.1016/j.jbiomech.2010.03.046

Li, G., Lopez, O., and Rubash, H. (2001). Variability of a three-dimensional finite element model constructed using magnetic resonance images of a knee for joint contact stress analysis. *J. Biomech. Eng.* 123, 341–346. doi:10.1115/1.1385841

Li, L., Yang, L., Zhang, K., Zhu, L., Wang, X., and Jiang, Q. (2020). Three-dimensional finite-element analysis of aggravating medial meniscus tears on knee osteoarthritis. *J. Orthop. Transl.* 20, 47–55. doi:10.1016/j.jot.2019.06.007

Li, L., Yang, X., Yang, L., Zhang, K., Shi, J., Zhu, L., et al. (2019). Biomechanical analysis of the effect of medial meniscus degenerative and traumatic lesions on the knee joint. *Am. J. Transl. Res.* 11, 542–556. eCollection 2019.

McCann, L., Ingham, E., Jin, Z., and Fisher, J. (2009). Influence of the meniscus on friction and degradation of cartilage in the natural knee joint. *Osteoarthr. Cartil.* 17, 995–1000. doi:10.1016/j.joca.2009.02.012

Mononen, M. E., Jurvelin, J. S., and Korhonen, R. K. (2013). Effects of radial tears and partial meniscectomy of lateral meniscus on the knee joint mechanics during the stance phase of the gait cycle—A 3D finite element study. *J. Orthop. Res.* 31, 1208–1217. doi:10.1002/jor.22358

Navacchia, A., Hume, D. R., Rullkoetter, P. J., and Shelburne, K. B. (2019). A computationally efficient strategy to estimate muscle forces in a finite element musculoskeletal model of the lower limb. *J. Biomech.* 84, 94–102. doi:10.1016/j.jbiomech.2018.12.020

Park, S., Lee, S., Yoon, J., and Chae, S. (2019). Finite element analysis of knee and ankle joint during gait based on motion analysis. *Med. Eng. Phys.* 63, 33–41. doi:10.1016/j.medengphy.2018.11.003

Rao, A. J., Erickson, B. J., Cvetanovich, G. L., Yanke, A. B., and Cole, B. J. (2015). The meniscus-deficient knee. *Orthop. J. Sports Med.* 3, 232596711561138. doi:10.1177/2325967115611386

Richards, D. P., Barber, F. A., and Herbert, M. A. (2008). Meniscal tear biomechanics: Loads across meniscal tears in human cadaveric knees. *Orthopedics* 31, 347–350. doi:10.3928/01477447-20080401-32

Richards, R. E., Andersen, M. S., Harlaar, J., and van den Noort, J. C. (2018). Relationship between knee joint contact forces and external knee joint moments in patients with medial knee osteoarthritis: Effects of gait modifications. *Osteoarthr. Cartil.* 26, 1203–1214. doi:10.1016/j.joca.2018.04.011

Roemer, F. W., Kwoh, C. K., Hannon, M. J., Hunter, D. J., Eckstein, F., Grago, J., et al. (2016). Partial meniscectomy is associated with increased risk of incident radiographic osteoarthritis and worsening cartilage damage in the following year. *Eur. Radiol.* 27, 404–413. doi:10.1007/s00330-016-4361-z

Scotti, C., Hirschmann, M. T., Antinolfi, P., Martin, I., and Peretti, G. M. (2013). Meniscus repair and regeneration: Review on current methods and research potential. *Eur. Cell. Mat.* 26, 150–170. doi:10.22203/ecm.v026a11

Shu, L., Yamamoto, K., Yoshizaki, R., Yao, J., Takashi, S., and Sugita, N. (2022). Multiscale finite element musculoskeletal model for intact knee dynamics. *Comput. Biol. Med.* 141, 105023. doi:10.1016/j.compbiomed.2021.105023

Sukopp, M., Schall, F., Hacker, S. P., Ignatius, A., Dürselen, L., and Seitz, A. M. (2021). Influence of menisci on tibiofemoral contact mechanics in human knees: A systematic review. *Front. Bioeng. Biotechnol.* 9, 765596. doi:10.3389/fbioe.2021.765596

Terzidis, L. P., Christodoulou, A., Ploumis, A., Givissis, P., Natsis, K., and Koimtzis, M. (2006). Meniscal tear characteristics in young athletes with a stable knee: Arthroscopic evaluation. *Am. J. Sports Med.* 34, 1170–1175. doi:10.1177/0363546506287939

Thompson, W. O., Thaete, F. L., Fu, F. H., and Dye, S. F. (1991). Tibial meniscal dynamics using three-dimensional reconstruction of magnetic resonance images. *Am. J. Sports Med.* 19, 210–216. doi:10.1177/036354659101900302

Vedi, V., Williams, A., Tennant, S. J., Spouse, E., Hunt, D. M., and Gedroyc, W. M. (1999). Meniscal movement. An *in-vivo* study using dynamic MRI. *J. Bone Jt. Surg. Br. volume* 81, 37–41. doi:10.1302/0301-620x.81b1.0810037

Walker, P. S., Arno, S., Bell, C., Salvadore, G., Borukhov, I., and Oh, C. (2015). Function of the medial meniscus in force transmission and stability. *J. Biomech.* 48, 1383–1388. doi:10.1016/j.jbiomech.2015.02.055

Wang, S., Cai, Y., Hase, K., Uchida, K., Kondo, D., Saitou, T., et al. (2021). Estimation of knee joint angle during gait cycle using inertial measurement unit sensors: A method of sensor-to-clinical bone calibration on the lower limb skeletal model. *J. Biomech. Sci. Eng.* 17, 21-00196–00196. doi:10.1299/jbse.21-00196

Wang, S., Hase, K., and Ota, S. (2022). A computationally efficient lower limb finite element musculoskeletal framework directly driven solely by inertial measurement unit sensors. *J. Biomech. Eng.* 144, 051011. doi:10.1115/1.4053211

Wang, S., Hase, K., and Ota, S. (2021). Development of a lower limb finite element musculoskeletal gait simulation framework driven solely by inertial measurement unit sensors. *Biomechanics* 1, 293–306. doi:10.3390/biomechanics1030025

Wiess, C. B., Lundberg, M., Hamberg, P., DeHaven, K. E., and Gillquist, J. (1989). Non-operative treatment of meniscal tears. *J. Bone Jt. Surg.* 71, 811–822. doi:10.2106/00004623-198971060-00003

Yao, J., Snibbe, J., Maloney, M., and Lerner, A. L. (2006). Stresses and strains in the medial meniscus of an ACL deficient knee under anterior loading: A finite element analysis with image-based experimental validation. *J. Biomech. Eng.* 128, 135–141. doi:10.1115/1.2132373

Yu, C., Walker, P. S., and Dewar, M. E. (2001). The effect of design variables of condylar total knees on the joint forces in step climbing based on a computer model. *J. Biomech.* 34, 1011–1021. doi:10.1016/s0021-9290(01)00060-4

Zajac, F. E. (1989). Muscle and tendon: Properties, models, scaling, and application to biomechanics and motor control. *Crit. Rev. Biomed. Eng.* 17, 359–411.

Zhang, A. L., Miller, S. L., Coughlin, D. G., Lotz, J. C., and Feeley, B. T. (2015). Tibiofemoral contact pressures in radial tears of the meniscus treated with all-inside repair, inside-out repair and partial meniscectomy. *Knee* 22, 400–404. doi:10.1016/j.knee.2015.05.008

Zhang, K., Li, L., Yang, L., Shi, J., Zhu, L., Liang, H., et al. (2019). Effect of degenerative and radial tears of the meniscus and resultant meniscectomy on the knee joint: A finite element analysis. *J. Orthop. Transl.* 18, 20–31. doi:10.1016/j.jot.2018.12.004

Zhang, K., Li, L., Yang, L., Shi, J., Zhu, L., Liang, H., et al. (2019). The biomechanical changes of load distribution with longitudinal tears of meniscal horns on knee joint: A finite element analysis. *J. Orthop. Surg. Res.* 14, 237. doi:10.1186/s13018-019-1255-1

Frontiers in Bioengineering and Biotechnology

TYPE Original Research
PUBLISHED 10 January 2023
DOI 10.3389/fbioe.2022.969636

Identification of optimal surgical plan for treatment of extraocular muscle damage in thyroid eye disease patients based on computational biomechanics

Byeong Cheol Jeong[1], Chiseung Lee[2,3,4], Jungyul Park[4,5]* and Dongman Ryu[6]*

[1]Department of Biomedical Engineering, Graduate School, Pusan National University, Busan, South Korea, [2]Department of Convergence Medicine, School of Medicine, Pusan National University, Busan, South Korea, [3]Department of Biomedical Engineering, School of Medicine, Pusan National University, Busan, South Korea, [4]Biomedical Research Institute, Pusan National University Hospital, Busan, South Korea, [5]Department of Ophthalmology, School of Medicine, Pusan National University Hospital, Busan, South Korea, [6]Medical Research Institute, Pusan National University, Busan, South Korea

OPEN ACCESS

EDITED BY
Jun Pan,
Chongqing University, China

REVIEWED BY
Jeongho Lee,
University of California, Berkeley, United States
Guibing Li,
Hunan University of Science and Technology, China

*CORRESPONDENCE
Jungyul Park,
✉ ophjyp@naver.com
Dongman Ryu,
✉ rdm.bme@gmail.com

SPECIALTY SECTION
This article was submitted to Biomechanics, a section of the journal Frontiers in Bioengineering and Biotechnology

RECEIVED 15 June 2022
ACCEPTED 28 December 2022
PUBLISHED 10 January 2023

CITATION
Jeong BC, Lee C, Park J and Ryu D (2023), Identification of optimal surgical plan for treatment of extraocular muscle damage in thyroid eye disease patients based on computational biomechanics.
Front. Bioeng. Biotechnol. 10:969636.
doi: 10.3389/fbioe.2022.969636

This study replicated the behavior of intraorbital tissue in patients with thyroid eye disease (TED) based on finite element analysis for general orbital decompression risk evaluation in thyroid eye disease patients. The orbit and intraorbital tissues of thyroid eye disease patients who underwent orbital decompression were modeled as finite element models. The stress was examined at specific locations of the removed orbital wall of a thyroid eye disease patient with undergone orbital decompression, and its variation was analyzed as a function of the shape and dimension (to be removed). As a result, in orbital decompression surgery which removes the orbital wall in a rectangular shape, the stress at the orbital wall decreased as the width and depth of the removed orbital wall increased. In addition, in the case of orbital decompression, it can be seen that the chamfered model compared to the non-chamfered model (a form of general orbital decompression) have the stress reduction rate from 11.08% to 97.88%. It is inferred that if orbital decompression surgery considering the chamfered model is performed on an actual thyroid eye disease patient, it is expected that the damage to the extraocular muscle caused by the removed orbital wall will be reduced.

KEYWORDS

thyroid eye disease, orbital decompression, hypertrophy, inferior rectus muscle, recurrence, finite element analysis

1 Introduction

Thyroid eye disease (TED) is an autoimmune disease characterized by lymphocyte infiltration in the orbit, including the extraocular muscle (EOM) and fat. In TED, the thyrotropin receptor antibodies (TRAbs) activate the immunological cascade in combination with the thyroid stimulating hormone receptor (TSH-R) on orbital fibroblasts, and they result in infiltration of activated B and T lymphocytes as well as fibrocytes that develop into myofibroblasts or adipocytes. The hydrophilic hyaluronic acid accumulation in the connective tissue and EOM can cause edema. Furthermore, the activation of periocular fibroblasts, which are known to be progenitor fat cells, can lead to the enlargement of orbital fat tissue (Gontarz-Nowak et al., 2020).

The TED has a worldwide prevalence rate of .1%–.3%, and has been reported to occur in approximately 40% of patients with Graves' disease (Noth et al., 2001; Bartalena and Tanda, 2009; Mohyi and Smith, 2018). As the orbital inflammation progresses, swelling of the EOM and fat, increasing intraorbital pressure (IOP), proptosis, compressive optic neuropathy, and visual loss may occur (Fichter et al., 2012; Jefferis et al., 2018). Several treatment strategies are available, including highdose glucocorticoid therapy, orbital radiation therapy, and teprotumumab treatment, which is a novel insulin-like growth factor-1 receptor (IGF-1R) antibody (Bartalena et al., 1991; Mohyi and Smith, 2018). Surgical treatments are a multistage approach, and 20%–30% of TED patients are offered this option after the disease stabilizes. Orbital decompression is the first stage in sequential surgical treatment and is performed in inactive TED patients with severe proptosis, exposure keratopathy, facial disfigurement, persistent prolonged congestion, and high IOP (Ismailova et al., 2018). When vision is threatened by compressive optic neuropathy, emergent orbital decompression may be needed, even in the active TED phase (Wang et al., 2019). Despite these treatments, there is a possibility of disease recurrence owing to various reasons such as thyroid hormone instability, continuous smoking (Genere and Stan, 2019), and in some cases, orbital surgery itself, which can reactivate inflammation, exacerbate ophthalmopathy, postoperative motility disturbances, and cause EOM regrowth (Wenz et al., 1994; Alsuhaibani et al., 2011; Fichter et al., 2012; Wang et al., 2019).

Hu et al. (2010) observed a significant increase in medial rectus (MR) muscle volume and inferior rectus (IR) muscle mean volume postoperatively in TED patients who underwent orbital decompression surgery. Some hypotheses were suggested to explain the observed outcomes, such as the mild inflammatory reaction or the hydrostatic pressure changes due to the expanded orbital volume during surgery. However, the etiologies of these postoperative volumetric changes, motility disturbances, and disease reactivation are unclear (Wenz et al., 1994). Animal experiments or finite element analysis (FEA) can be used to identify and solve these problems indirectly. In particular, *in silico* methods using FEA have been extensively used for years to investigate disease mechanisms in other organs and in eye-related research. Baillargeon et al. (2014) mimicked a computer biomechanism-based cardiac model to extract pressure-volume relationships and conducted comparative studies with clinical observations. Schutte et al. (2016) simulated the rotation of the eyeball and EOM displacement due to torsion using the FEA technique and then analyzed the intraorbital eye behavior. Norman et al. (2011) proved the correlation between the sclera on the optic nerve head side and glaucoma. In addition, Fisher et al. (2021) conducted a gaze-evoked deformation study of optic nerve head deformities in TED patients. Although these studies on the eyeball and optic nerve behavior have been conducted using FEA, research on surgical orbital decompression has been limited. In addition, absolute standards for the location and method of orbital wall removal and the size or shape of the bone to be removed have not been quantitatively established in clinical studies. Thus, surgeries are based on the practicing clinicians' experience.

Therefore, in this study, the behavior of EOM hypertrophy, which is one of the key contributors to elevated IOP, was simulated using the finite element method. An FEA technique was proposed to analyze the removed orbital wall's location, size, and shape. Particular, this study focused on the IR muscle, which is one of the most common muscles affected in TED (Yoo et al., 2009), and examined the stress value of the orbital wall according to the hypertrophy of this muscle. TED can be classically divided into three types: type I (lipogenic), type II (myogenic), and type III (lipogenic + myogenic) (Hiromatsu et al., 2000). Among these types, type II is characterized by a hypertrophy of the EOM, which may result in restrictive myopathy. According to studies on the differential involvement of orbital fat and EOM, there were high cases of increased muscle volume while having a normal fat volume in patients with TED-related diseases (Forbes et al., 1986; Wiersinga et al., 2013). Therefore, this study hypothesized that the recurring EOM hypertrophy after surgery could cause reinflammation between the orbital wall and EOM. A series of computational simulations for pre- and post-operative EOM hypertrophy were performed to examine the stress variation from EOM hypertrophy. Theses stress results are overestimated to consider the safety in clinical applications. Furthermore, the location of the removed orbital wall was identified considering the maximum stress value, and the effects of the type and dimension of the removed orbital wall were examined.

2 Materials and methods

2.1 Analysis of major orbital dimensions based on magnetic resonance imaging

This study considered only TED patients having EOM variations. The major dimensions were measured based on the patient's right orbit to examine the EOM variations in the TED-affected left orbit. The finite element model used in the series simulation was derived from medical images of a female patient in her 70s with moderate-to-severe, active TED at the initial diagnosis. The patient was treated with intravenous methylprednisolone, recommended by Bartalena et al. (2016). The patient was controlled for thyroid dysfunction in the Department of Endocrinology. The magnetic resonance image was acquired when TED was inactive, and no further progression of the disease for a year was confirmed. T1-weighted spin-echo images with a field of view (FOV) = 180 mm × 220 mm, matrix = 320 × 203, and slice thickness = 2.0 mm were acquired for magnetic resonance imaging (MRI). In addition, FOV/matrix was employed to establish pixel size. Coronal pictures were taken in 1 mm consecutive segments covering the entire orbit for the volume analysis. MRI were performed with the patient supine, and a stable head posture was achieved with adjustable head support. The patient underwent an MRI scan for 25–30 min with eyes closed and in a comfortable position. In addition, the numerical values of the intraorbital tissue were measured on the coronal, sagittal, and axial planes of the image. The study was conducted in accordance with the Declaration of Helsinki, and approved by the Institutional Review Board of Pusan National University Hospital (IRB No. 2104-018-102). All the patients voluntarily signed the informed written consent. Written consent to publish data containing personally identifiable information was also obtained.

As shown in Figure 1A, a straight line is drawn in the cross-sectional MRI image of the patient by connecting the end points of the zygomatic and maxillary bones. Another straight line is drawn perpendicular to this straight line, passing through the central point of the eyeball to measure proptosis. Comparing the proptosis dimensions of the two orbits confirmed that the proptosis in the TED orbit is 2.32 mm. Straight lines are drawn in the four azimuthal directions based on the center point of the eyeball in the sagittal

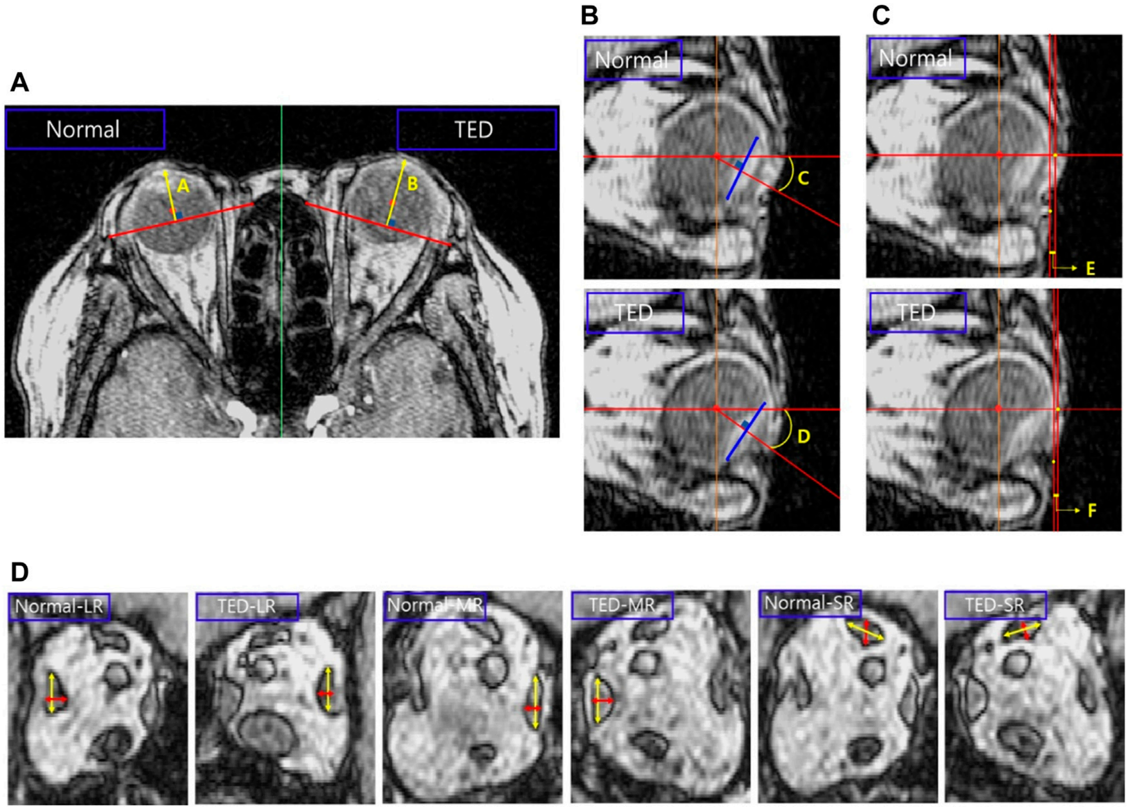

FIGURE 1
Analysis of major dimensions in the thyroid eye disease (TED) orbit and normal orbit based on magnetic resonance imaging (MRI). **(A)** Proptosis measurement. **(B)** Eye rotation measurement. **(C)** Distance measurement between the ocular and skin end point. **(D)** Thickness and width measurements in the extraocular muscle (EOM) except for the inferior rectus (IR) muscle.

TABLE 1 Dimensions measured in Figure 1.

Variables	A	B	C	D	E	F
Dimension	14.91 mm	17.23 mm	25.97°	32.81°	1.06 mm	.77 mm
	LR		**MR**		**SR**	
	Normal	**TED**	**Normal**	**TED**	**Normal**	**TED**
Thickness (mm)	3.60	3.73	3.43	3.69	3.78	3.84
Width (mm)	8.18	8.11	9.50	8.97	7.97	7.87

plane of the patient's MRI image, and a blue line is formed by connecting both ends of the eyeball lens, as in Figure 1B. After drawing a straight line in which the generated blue line is perpendicular to the eyeball center, the angle is measured. A comparison of the eye rotation dimensions of both orbits confirmed 6.84° eyeball rotation in the TED-affected orbit. Figure 1C shows straight lines perpendicular to the endpoint of the eyeball and lower skin in the patient's sagittal plane. The measured distance between the two straight lines confirmed that the skin protruded by .29 mm in the TED-affected orbit. In addition, the distance in the TED orbit decreased by more than 27.36% compared to that in the normal orbit. Moreover, in Figures 1B, C, the measurements are in the sagittal plane corresponding to the lateral side of the zygomatic arch. Figure 1D shows the thickness and width measurements of the midpoints of each EOM in the coronal plane of the patient. In the TED orbit, the thickness and width loss rates are 7.58% and 5.58% in the MR muscle, −3.61% and .86% in the lateral rectus muscle, and −1.59% and 1.25% in the superior rectus muscle, respectively, compared with the normal orbit. Overall, the thickness of all EOMs increased, and the width decreased in the TED orbit compared with the normal orbit. In addition, all measurements in Figure 1 were repeated five times. The average values derived are listed in Table 1. These dimensions were used to select the load condition in the computerized IR hypertrophy and elevated IOP analyses.

2.2 Modeling and material properties

This study modeled the eyeball, orbit, EOM, optic nerve, skin, and fat as a finite element model using Mimics (version 19.0, Materialize, Leuven, Belgium), as shown in Figure 2A. The finite element model simulation, based on the patient's medical image and the method proposed by Yiyi et al. (2005), offered a more precise simulation than the existing modeling method using MRI and computed tomography (CT) images. As shown in Figure 2B, the length and angle of the orbital medial wall (axial, coronal, and sagittal planes) and hypertrophied muscle dimensions obtained using the finite element model and medical image is compared to verify the model reliability. In the case of EOM, four rectus muscles are expressed, but in the case of the

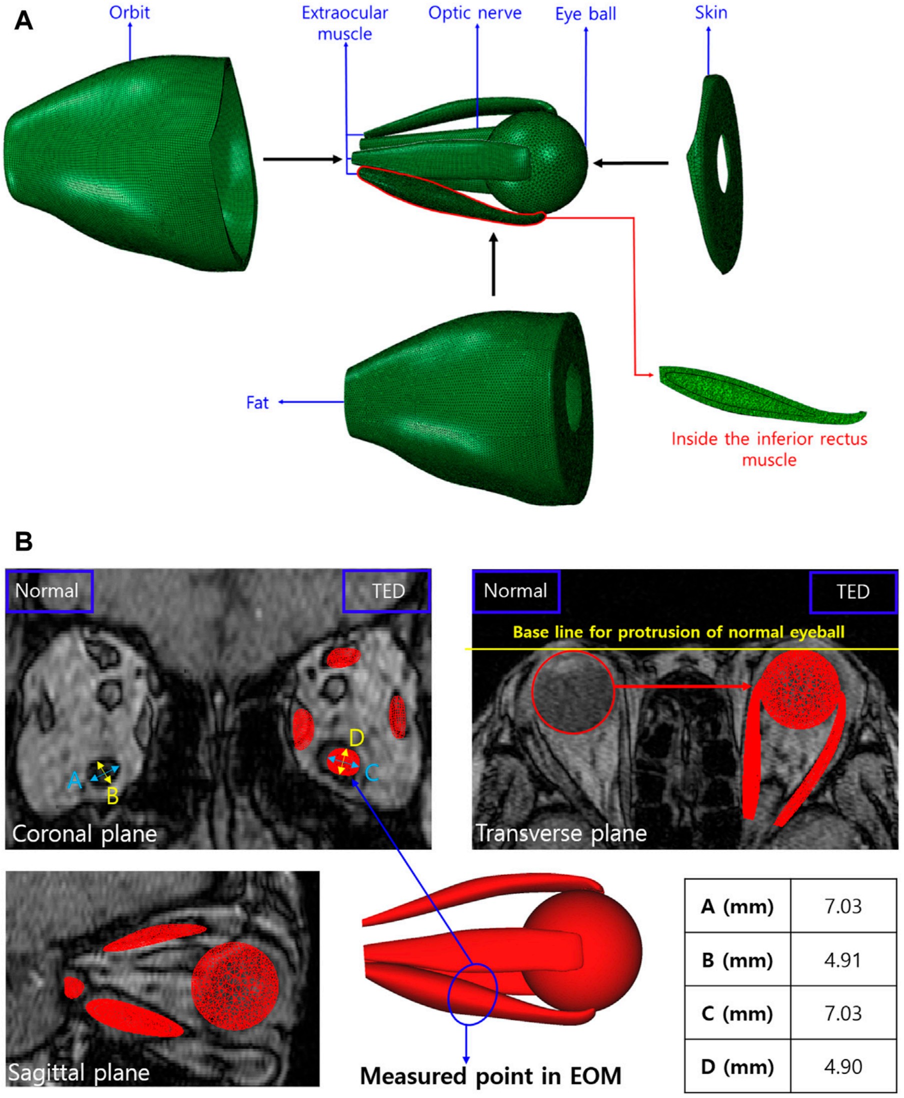

FIGURE 2
(A) Finite element model of orbit and intraorbital tissue. **(B)** Validation between the medical image and finite element model.

TABLE 2 Material properties of finite element models.

Variables	Fat	EOMs	Optic nerve	Orbital wall	Eye ball	Skin
E (MPa)	.047	.09	5.5	14,500	14,500	1
ν	.49	0.4	.47	.35	0.3	.45
ρ (kg/m³)	999	1,600	1,012	1,610	—	—

two oblique muscles, there is a model limitation in the expression, and they are excluded. In addition, a model resembling the IR shape is placed inside the IR, as shown in Figure 2A, for simulating the enlarged IR. When a load condition is applied only to the inner or outer parts of the IR, the actual hypertrophied IR shape could not be derived; thus, load conditions were applied to both parts simultaneously for analysis. Finally, ABAQUS (version 6.14, Dassault Systèmes, SIMULIA, United States) was used to perform three-dimensional FEA, and the finite element model consisted of 901,542 solid elements (C3D8R).

Table 2 lists the material properties for the elastic modulus (E), Poisson's ratio (ν), and density (ρ) of each tissue applied in the FEA of TED patients. The fat surrounding the eye was assumed as nearly incompressible "soft" human tissue with ν = .49 (Power et al., 2002). In the literature on EOM, information on human material properties is lacking, and the material property values were estimated based on the

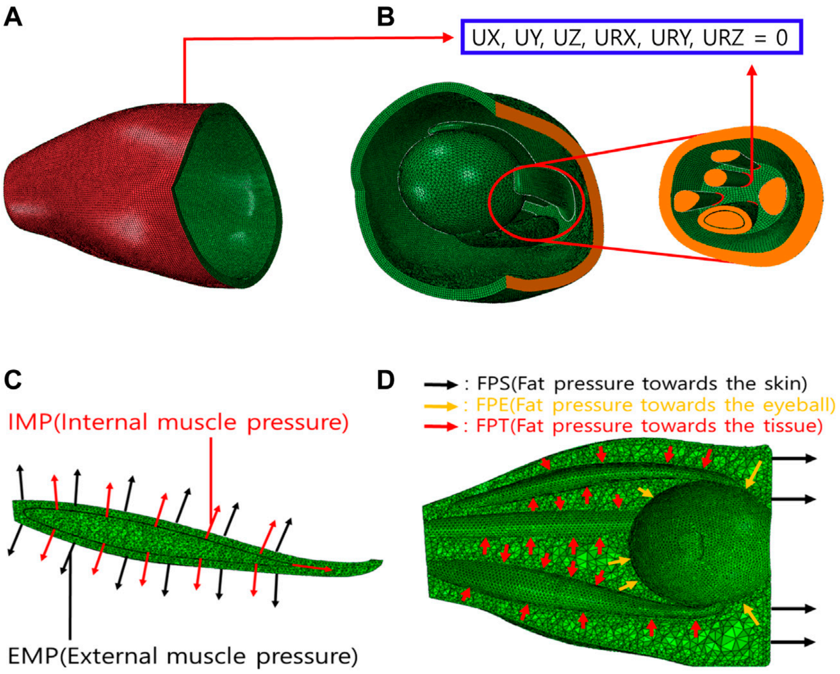

FIGURE 3
Boundary and load conditions of finite element model. **(A)** Orbital outer wall boundary conditions for movement restriction. **(B)** Boundary conditions of intraorbital. **(C)** Loading conditions of IR hypertrophy. **(D)** Loading conditions of elevated intraorbital pressure (IOP).

tensile test results of the bovine EOM (Power et al., 2002; Schutte et al., 2006). The material properties that changed owing to IR hypertrophy were also based on literature (Barin et al., 2019). In FEA, the eyeball was set as a rigid body because only the proptosis and eye rotation measurements were significant, with no stress requirement. In addition, the material properties of the orbital wall, optic nerve, and skin investigated are listed in Table 2, based on existing studies (Cirovic et al., 2006; Geng et al., 2018).

2.3 Boundary and loading conditions

Figure 3 shows the boundary and load conditions of the finite element model. The orbital movement is restricted by securing the orbital outer wall (Figure 3A), and the degrees of freedom from the axial direction and rotation are restricted to the surface behind the orbital inner wall and that where the ocular and optic nerves begin (Figure 3B). The load condition is applied at two positions perpendicular to the IR surface (Figure 3C). Hypertrophy is simulated by generating internal and external muscle pressure (IMP and EMP) on the internal and external IR surfaces, respectively. In addition, fat pressure toward the skin (FPS), eyeball (FPE), and tissue (FPT) are generated to simulate IOP (Figure 3D). On average, the IOP of an adult is 3–6 mmHg (Kratky et al., 1990). In this study, the maximum value was set at 6 mmHg (equivalent to 800 Pa).

In addition, simulations were conducted under various loading conditions to simulate IR muscle hypertrophy and elevated IOP in TED patient's. The results were validated based on the patient's EOM hypertrophy, eye rotation, and proptosis values, as shown in Figure 4. First, IR hypertrophy was simulated by applying 45 and 300 MPa loads to the IMP and EMP. In FPE, which is most influenced by elevated IOP, simulations were conducted under a single loading condition, increasing from 100 to 500 kPa (interval: 50 kPa). The results under the loading condition of 100–400 kPa (interval: 50 kPa) were validated within the error range, set to +20% of the eye rotation and proptosis values measured by MRI. However, for more accurate simulation results, other complex loads such as FPS and FPT were considered. Second, 35 series simulations were conducted under FPE and FPS loading conditions ranging from 100 to 400 kPa (interval: 50 kPa) and 5–15 kPa (interval: 2.5 kPa), respectively. It was determined that the simulation results for the simultaneous FPE 300 kPa and FPS 5–15 kPa loading conditions were within the ±20% error range. Finally, 25 series simulations with loading conditions ranging from 5 to 15 kPa (interval: 2.5 kPa) of FPT to intraorbital tissues were performed, and cases within the ±5% error range were obtained.

2.4 FEA scenarios of orbital wall removal

The maximum stress point was identified at the optimal load conditions for the IR muscle hypertrophy and elevated IOP. Moreover, the orbital wall was removed (in rectangular or circular shapes), and a series FEA was performed. The results are given in Table 3. When the removed orbital wall is rectangular, a distance of 5 mm from the posterior surface of the orbital wall is assumed to be a risk area associated with the removal. Therefore, the posterior edge of the inner orbital wall is fixed at 8 mm to facilitate the removal of the rectangular orbital wall. Subsequently, the length of the orbital wall front edge and the depth of the rectangle to be removed were changed, and FEA was performed according to the presence or absence of chamfering. When the removed orbital wall was circular, the maximal stress point in the IR muscle hypertrophy and elevated IOP FEA was set as the circle's

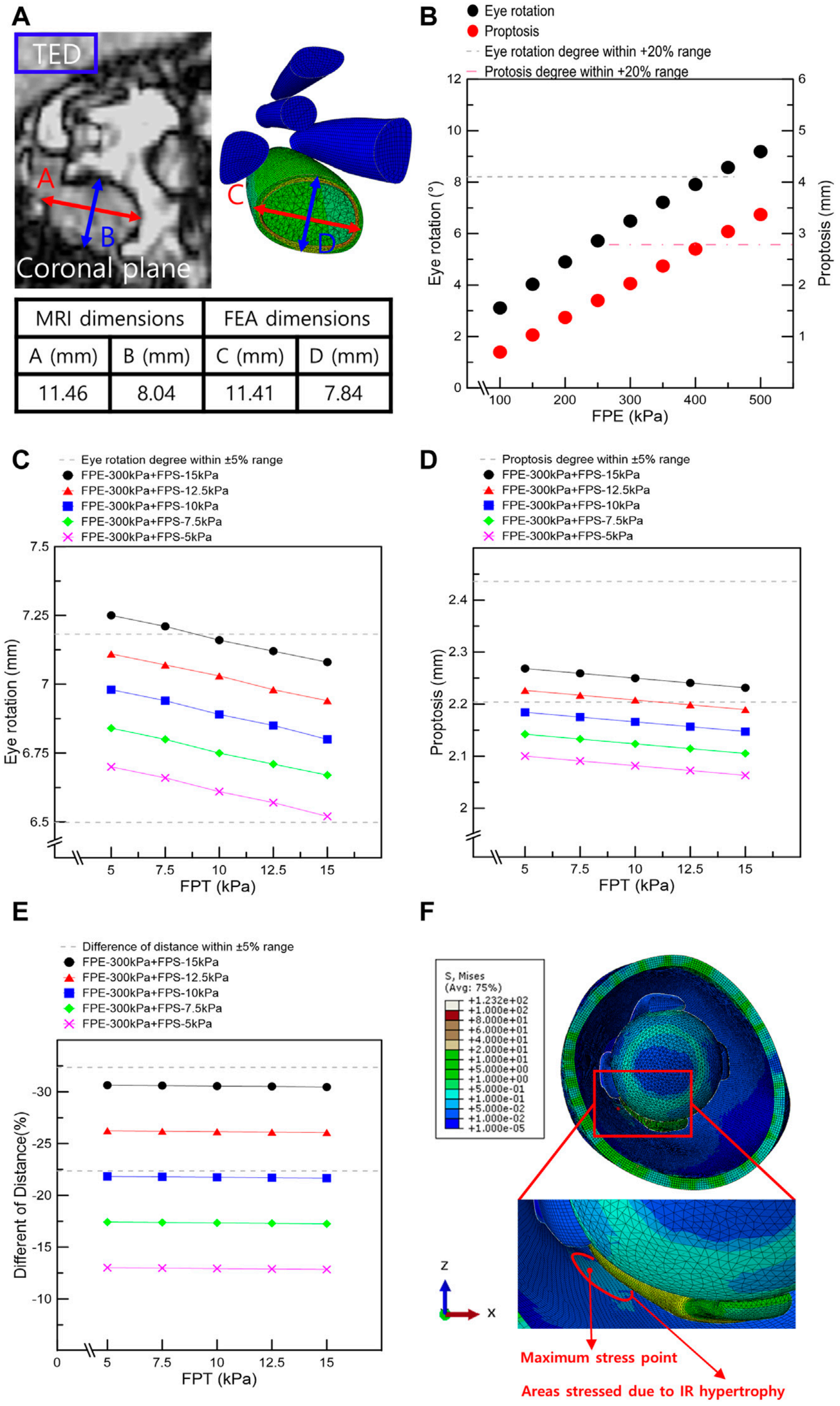

FIGURE 4
Results from finite element analysis of IR muscle hypertrophy and elevated IOP. **(A)** Thickness and width of IR in MRI image and finite element analysis of IR muscle hypertrophy. **(B)** Eye rotation and proptosis according to the load conditions of FPE. **(C)** Eye rotation responses according to the load conditions of fat pressure toward the skin eyeball (FPE), skin (FPS), and tissue (FPT). **(D)** Proptosis according to the load conditions of FPE, FPS, and FPT. **(E)** Distances between the ocular and skin endpoints according to the load conditions of FPE, FPS, and FPT. **(F)** Maximum stress point in FEA of IR hypertrophy and elevated IOP.

center point. Subsequently, FEA was performed according to the circle diameter and the presence or absence of a chamfer.

In addition, CT scans of four TED patients who had orbital decompression were evaluated to identify the volumetric changes and possible damage to EOM to assess the TED recurrence risk. The four male patients (aged 46–65) had their orbital floor and medial wall removed. The inclusion criteria were evidence of disease inactivity for at least 1 year, normal thyroid function, and normal thyroid-stimulating hormone receptor antibodies, including thyroid-stimulating antibodies. Modified NOSPECS classification scores

TABLE 3 Scenarios associated with orbital wall removal.

	Rectangular		
No.	Chamfering	Width (mm)	Depth (mm)
1	X	10	15–25 (Interval: 2)
2	X	12	15–25 (Interval: 2)
3	X	14	15–25 (Interval: 2)
4	O	10	15–25 (Interval: 2)
5	O	12	15–25 (Interval: 2)
6	O	14	15–25 (Interval: 2)
	Circular		
	Chamfering		**Diameter (mm)**
7	X		10–15 (Interval: 1)
8	O		10–15 (Interval: 1)

TABLE 4 Muscle loss rate in finite element analysis of inferior rectus (IR) muscle hypertrophy and the elevated IOP (based on FPE of 300 kPa).

			FPS-12.5 kPa			FPS-15 kPa		
		Base dimension before analysis	FPT 7.5 kPa	FPT 10 kPa	FPT 12.5 kPa	FPT 10 kPa	FPT 12.5 kPa	FPT 15 kPa
Thickness (mm)	LR	3.80	3.87	3.85	3.83	3.85	3.83	3.81
	MR	4.12	4.47	4.44	4.41	4.44	4.42	4.39
	SR	3.47	3.60	3.58	3.56	3.58	3.56	3.54
Width (mm)	LR	7.71	7.39	7.36	7.32	7.36	7.33	7.29
	MR	7.71	7.47	7.43	7.39	7.43	7.40	7.36
	SR	7.15	7.14	7.11	7.08	7.11	7.08	7.05
	Loss rate measured using MRI							
Thickness (%)	LR	−3.61	−1.79	−1.29	−.78	−1.37	−.87	−.37
	MR	−7.58	−8.39	−7.68	−6.97	−7.87	−7.16	−6.45
	SR	−1.59	−4.01	−3.38	−2.74	−3.43	−2.79	−2.16
Width (%)	LR	.86	4.09	4.57	5.04	4.47	4.95	5.42
	MR	5.58	3.14	3.64	4.14	3.54	4.04	4.55
	SR	1.25	.21	.65	1.09	.56	1.00	1.45

determined clinical severity, and the Clinical Activity Score (CAS) was used to assess the TED activity (Bartalena et al., 2016).

3 Results

3.1 Selection of orbit loading conditions based on IR muscle hypertrophy

Simulations were performed based on the above-mentioned scenarios to simulate the IR hypertrophy and elevated IOP in TED patients. Figure 4A shows the outcomes of the IR muscle hypertrophy as measured by the FEA and the IR muscle dimensions of the TED patient as measured using the CT. In addition, the aforementioned loading conditions were used to simulate IOP and IR muscle hypertrophy, and Figures 4B–E display the results as eye rotation, proptosis, and skin protrusion. Especially, Figure 4B shows the procedure for obtaining outcomes within a +20% error range during the initial selection phase for FPE loading conditions. Figures 4C–E also demonstrate the established results based on the medical information of TED patients and computational simulations; 69 scenarios were simulated with FPE, FPS, and FPT loading conditions. In Tables 4, 5, six scenarios had an error rate of less than 5% compared to the MRI-measured dimensions. In these six

TABLE 5 Main dimensions of IR hypertrophy and the elevated IOP simulation.

Case no.	FPE (kPa)	FPS (kPa)	FPT (kPa)	Distance difference between the eye and skin endpoint		IR thickness (mm)	IR width (mm)	Eye rotation (°)	Proptosis (mm)	Orbital wall stress (kPa)
				(mm)	(%)					
1	300	12.5	7.5	1.0319	−26.19	7.84	11.41	7.07 (Down)	2.22 (Protend)	117.44
2	300	12.5	10	1.0324	−26.15	7.84	11.41	7.03 (Down)	2.21 (Protend)	117.47
3	300	12.5	12.5	1.0330	−26.11	7.84	11.41	6.98 (Down)	2.20 (Protend)	117.50
4	300	15	10	.9709	−30.55	7.84	11.41	7.16 (Down)	2.25 (Protend)	117.09
5	300	15	12.5	.9714	−30.52	7.84	11.41	7.12 (Down)	2.24 (Protend)	117.12
6	300	15	15	.9721	−30.46	7.84	11.41	7.08 (Down)	2.23 (Protend)	117.15

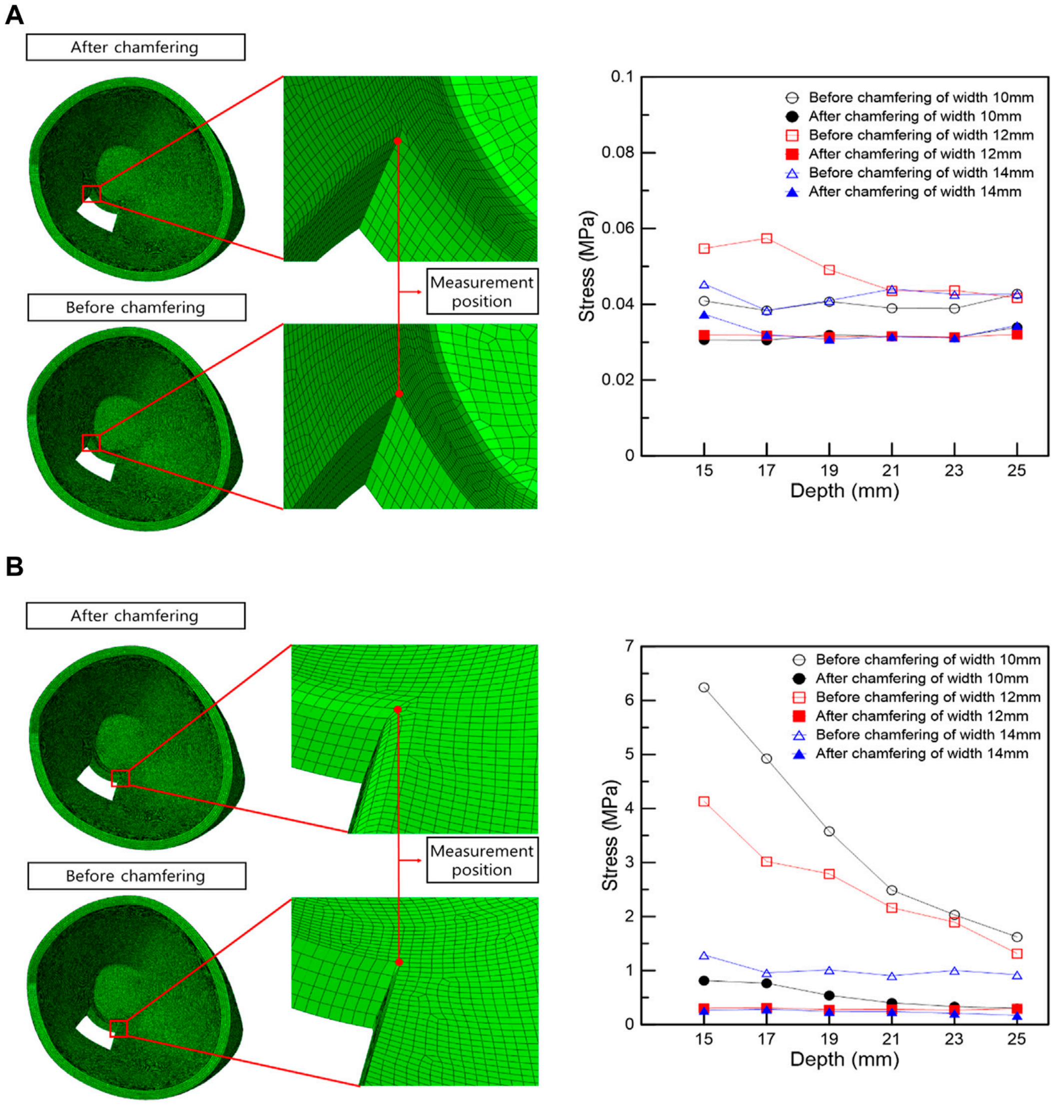

FIGURE 5
Stress measurement position and stress graph in the vertex following the rectangular removal of the orbital wall. **(A)** Left vertex. **(B)** Right vertex.

TABLE 6 Induced stress at left and right measurement positions following the removal of the orbital wall with a rectangular shape.

Depth (mm)	Width (mm)	Stress of left point (MPa)		Stress of right point (MPa)	
		Before chamfering	After chamfering	Before chamfering	After chamfering
15	10	.035326	.03062	6.24453	.813527
	12	.054737	.032	4.13248	.302808
	14	.04535	.03740	1.28819	.259452
17	10	.038368	.03053	4.92509	.764399
	12	.057419	.03179	3.02016	.307206
	14	.038398	.03199	.95818	.284504
19	10	.040739	.03198	3.57721	.538666
	12	.04911	.03143	2.79114	.276484
	14	.041005	.0308	1.01248	.241615
21	10	.038983	.03153	2.48868	.400518
	12	.043538	.0316	2.16375	.282113
	14	.044043	.03151	.90297	.238358
23	10	.038903	.03126	2.03128	.33216
	12	.035255	.03135	1.89548	.26846
	14	.090272	.03116	1.011	.20817
25	10	.042763	.03394	1.621	.300002
	12	.041728	.0321	1.31453	.2928
	14	.042743	.03444	.92155	.169208

scenarios, the same ranges of concentrated stresses were obtained from the inferomedial orbital strut to the rear one-third point (Figure 4F). In addition, in the six scenarios, the maximum stress in the region of concentrated stress was measured at the same point.

3.2 Stress distribution and trends in rectangular orbital wall removal

The optimal loading conditions were identified in the FEA of IR hypertrophy and elevated IOP in TED patients. Subject to the optimal load conditions, the range was set in a rectangular shape based on the maximum stress point in the orbit wall, the orbital wall was removed, and the surrounding stress was measured. Stress was measured at the left and right vertices of the inner corner of the orbit, which are common in rectangular orbital wall removal scenarios. Figure 5A shows that the stress before and after chamfering at the left vertex has no significant effect, depending on the removal depth and width. However, the FEA results before and after chamfering at the right vertex indicate a slight difference in stress.

In the right vertex, in Figure 5B, the stress decreased as the width and depth of the removed orbital wall increased, and the stress difference before and after chamfering was identified. In addition, the chamfered model analysis confirmed low-stress levels, regardless of the depth and width, in most cases. Therefore, in the right vertex, a large stress difference exists depending on chamfering rather than the depth or width removed, as shown in Table 6.

3.3 Stress distribution and trends following the circular orbital wall with removal

The maximum stress point in the FEA of IR hypertrophy and elevated IOP was at the circle center in circular orbital wall removal. Moreover, a circular orbital wall was removed owing to the increase in diameter before and after chamfering, and the surrounding stress was measured. The stress measurement position was divided along four directions, as shown in Figure 6A, and stress measurement was performed at three points by selecting the direction with a high-stress distribution rate. FEA of the orbital wall removal model before chamfering, as shown in Figures 6B–D, confirmed that point α had lower stress than the other points owing to the distance from the maximum hypertrophy point of the IR. In addition, at β and γ points, the stress decreases as the diameter increases. Accordingly, the high stress is measured when the removed orbital wall diameter is 11 mm.

As shown in Figure 7, when IR is hypertrophic, the positions of the β and γ points coincide with the point of maximum hypertrophy when the removed orbital wall is 11 mm in diameter, and the highest stress load is received. Compared to the model with 11 mm diameter, the load applied to the β and γ points was reduced as the diameter decreased or increased in models with diameters in the range of

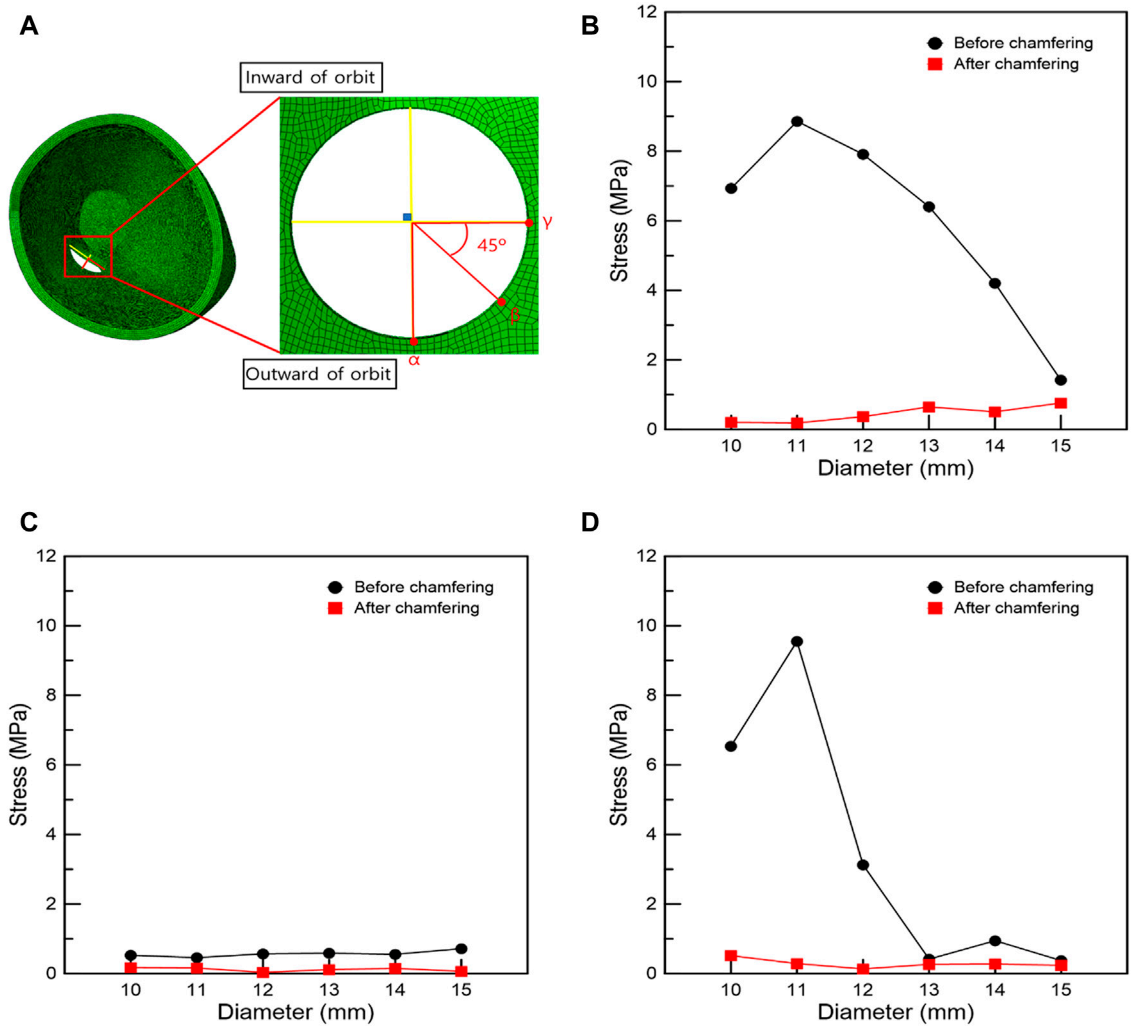

FIGURE 6
Stress measurement position and graphs associated with the circular removal of the orbital wall. **(A)** Stress measurement position. Stresses at positions **(B)** γ, **(C)** α, and **(D)** β.

10–15 mm. Therefore, it was confirmed that the IR stress was highest near the maximum hypertrophy point of the IR at β and γ points. In addition, in the chamfered orbital wall removal model analysis, the stress was lower than that before chamfering at α, β, and γ points, as shown in Table 7.

3.4 Computed tomographic analysis of patient datasets with removed orbital wall

The risk of damaging EOMs and recurrence of TED at the surgery site was evaluated using image analysis, as shown in Figure 8. Based on sagittal and axial CT images, Figure 8 shows the orbital tissues of the four patients whose orbital floor and the medial wall had been previously removed. As depicted in Figure 8, the EOM and surgical site's margin with a sharply sloping surface were observed. In other words, the space between the hypertrophied EOM and the margin of the surgical site is extremely narrow. Particularly, as a large quantity of EOM moves toward the decompression site, the EOM surface at the surgical site edge becomes compressed and sharper. After orbital decompression, the EOM and bone margin became contiguous, and the EOM underwent considerable morphological alteration.

4 Discussion

TED is an autoimmune inflammatory disease characterized by proptosis attributed to EOM. Accordingly, orbital decompression is required to remove the orbital wall and lower IOP. We simulated the IR hypertrophy and elevated IOP of TED patients and identified the maximum stress point of the orbital wall. Subsequently, FEA was performed based on the maximum stress point of the removed orbital wall according to the shape and size, and stress changes were confirmed.

First, we analyzed the MRI images of TED patients and constructed a three-dimensional finite element model; the IR model before hypertrophy was implemented by analyzing the IR

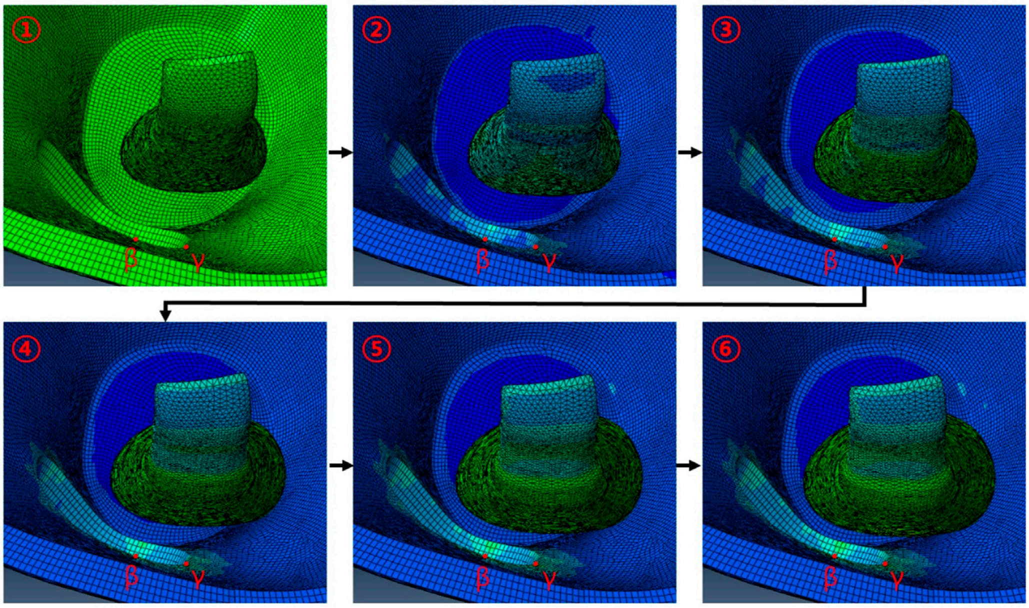

FIGURE 7
Behavior associated with IR hypertrophy in FEA following circular orbital wall removal of diameter 11 mm.

TABLE 7 Stress at α, β, and γ positions when removing the orbital wall in a circular shape.

Diameter (mm)	Stress at α point (MPa)		Stress at β point (MPa)		Stress at γ point (MPa)	
	Before chamfering	After chamfering	Before chamfering	After chamfering	Before chamfering	After chamfering
10	.528024	.1746	6.536398	.516669	6.935254	.207131
11	.459065	.159243	9.551042	.287233	8.859715	.187805
12	.567837	.035651	3.12807	.134126	7.912384	.370978
13	.58731	.114341	.41591	.2646	6.40473	.649128
14	.554781	.150457	.945533	.277382	4.206018	.507885
15	.71653	.064393	.37459	.23486	1.42209	.761282

dimension in the patient's normal orbit. In addition, a model similar to the IR shape was created inside IR to show the hypertrophic response of the IR muscle. When the load value was defined only inside or outside the IR muscle, the shape of the actual hypertrophic IR muscle could not be reproduced; thus, both loads were applied simultaneously. With only hypertrophic IR muscle, the eye rotation and proptosis could not be measured; therefore, the load condition was applied vertically to the surfaces associated with the intraorbital tissue, and IOP variations were simulated. The results confirmed that the thickness and width of the IR muscle, proptosis, eye rotation, distance from the skin and the eyeball endpoint, and the muscle's loss rate were associated with an error rate of ±5% according to the dimension measured on MRI image. In addition, the maximum stress point on the orbital wall owing to IR hypertrophy and elevated IOP was determined to be the location where clinical surgery was performed. The results confirm that the FEA of IR hypertrophy and elevated IOP performed in this study are reliable.

In the FEA of the IR hypertrophy and elevated IOP, orbital decompression was simulated by the rectangular orbital wall removal based on the maximum stress point. A distance of 5 mm anterior from the posterior orbital inner wall surface was assumed as a risk area for orbital wall removal. This is because when removal was attempted at the back of the orbital wall, it increased the damage risk to critical structures at the orbital apex, and it is difficult to access to the end of the orbital wall clinically. In addition, the stress at the inner vertex of the non-chamfered model, and that in the middle of the edge connected to the inner vertex in the chamfered model were measured to evaluate the stress trend according to the removed depth and width. This was set as the stress measurement location because it is the only location that remains the same even if the depth and width of the orbital wall to be removed in the rectangular orbital decompression

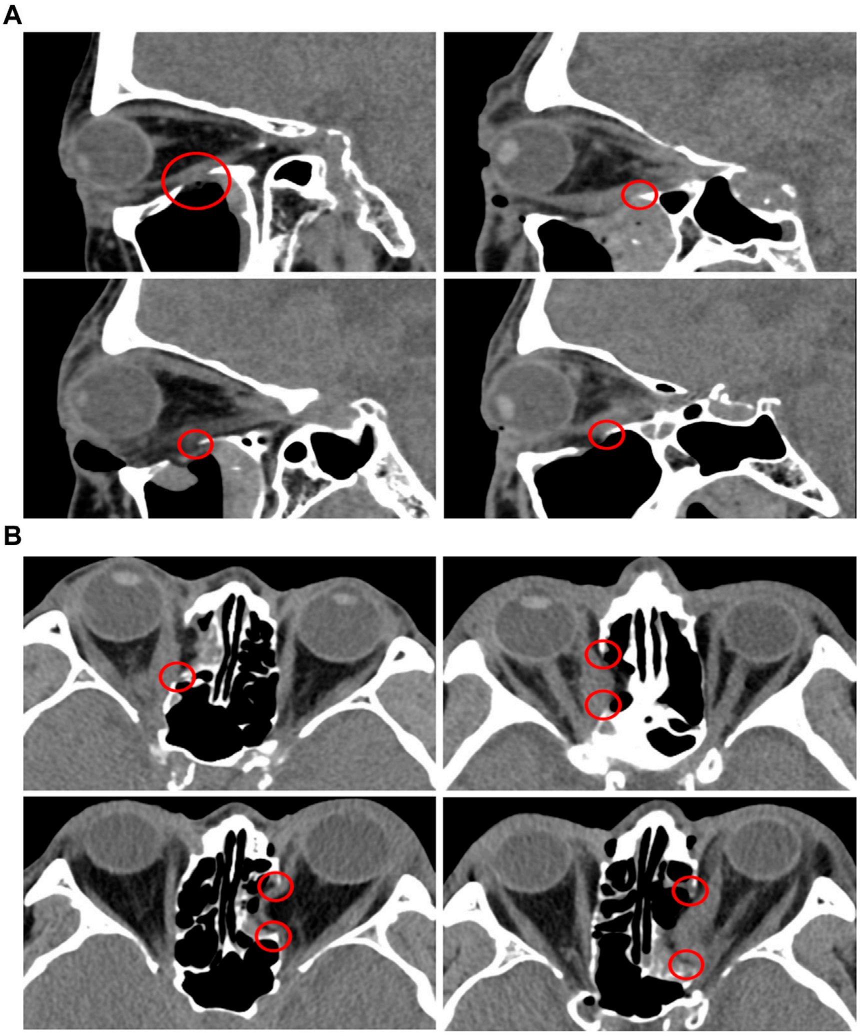

FIGURE 8
CT analysis of TED patients who underwent orbital decompression surgeries. **(A)** Sagittal plane. **(B)** Axial plane.

FEA changed. It was observed that the load decreased on the right vertex as the values of the removed depth and width increased, and large load stress was applied to the right vertex before chamfering compared with the post-chamfering state. However, in the left vertex, there was no significant difference in stress with depth and width, and similar stress was applied before and after chamfering. This is probably because the load transmission was weakened as the position of the hypertrophic IR was farther away.

Additionally, in the FEA of the IR hypertrophy and elevated IOP, orbital decompression was simulated in which the maximum stress point was set to the distal center, and the orbital medial wall was removed in a circular shape. Four orientations were set in the circle for circular orbital decompression, and three points were selected in the area with the highest generated stress to measure the stress. This is because measuring the stress at the same location as in the rectangular orbital decompression procedure with increasing diameter becomes challenging. As the distance from the hypertrophic IR increased, the load applied to the α position decreased, and a low-stress level was measured. The difference in stress before and after chamfering was insignificant. At β and γ points, the load decreased as the diameter increased. This was because it coincided with the point of maximal IR hypertrophy. Consequently, it was proved that when the removed circle diameter decreased or increased by more than 11 mm, it moved away from the point of maximum IR hypertrophy and resulted in low-load stress values. However, there was no decrease in the stress of the orbital wall with the increasing diameter after chamfering. These findings confirmed that the stress bands were similar. Hence, it was confirmed that the non-chamfered model was significantly affected by the hypertrophic IR muscle compared to the chamfered model, regardless of the removed orbital wall shape.

In addition, we analyzed the CT images of TED patients who underwent orbital decompression to understand TED recurrence risk. The removed margin of the orbital medial wall and margin of the orbital floor had a steep slope and were confirmed to be in close contact with the EOMs. Hu et al. (2010) reported that the volume of IR and MR increased after orbital decompression surgery. Therefore, it was concluded that inflammation was generated in IR and MR owing to the close contact between the bone edge and muscle, which is one of the causes of TED recurrence. There is a need for a method to minimize EOM damage to prevent TED recurrence, considering the significant level of damage caused.

In the non-chamfered orbit model, the shape of the bone margin removed during orbital decompression in actual surgery was similar.

Large stress was confirmed in the non-chamfered orbital wall based on the simulation of the orbital decompression through FEA. Therefore, we reaffirmed the concern that sharp edges severely damage the EOM. The chamfered orbital decompression is proposed as the first method to minimize EOM damage. The proposed method significantly reduces the stress applied to the orbital wall compared with that in non-chamfered orbital decompression. Therefore, when implementing orbital decompression and chamfering by drilling, the stress applied to the EOM is reduced, and the damage is minimized. However, there are cases wherein it is difficult to implement chamfering because the orbital wall is thin. Hence, another method is required to protect the sharp edges of the margin.

Therefore, we provide a method of incising the periorbita between the orbital wall and fat in a specific form to protect the sharp edges. Periorbita exists between the orbital wall and fat; as the periorbita provides suspension for the orbital contents not to prolapse even after orbital wall removal, the periorbital incision is the key procedure during orbital decompression surgery. Some methods are reported on periorbita incisions like complete removal of the periorbita after removing the orbital wall (Cubuk et al., 2018; Jefferis et al., 2018), the orbital sling procedure method that preserves the median part of the periorbita to keep the MR muscle intact (Metson and Samaha, 2002), and the method of making a parallel incision of the periorbita from the posterior to the anterior (Jimenez-Chobillon and Lopez-Oliver, 2010; Hernandez-Garcia et al., 2017). The exposure of bare bone without periorbital covering through the complete removal of periorbita does not protect the edge of the removed orbital wall and can damage the EOM. The orbital sling procedure might have some protective function but diminishes the extent of decompression. We propose a method in which the periorbita is incised in the II-shape in parallel from the posterior to the anterior direction, and incisions are made in the direction perpendicular to the incised line to perform H-shaped incision. Therefore, we conclude that the "H" shaped periorbita will cover both sides of the sharp edge of the removed orbital wall and minimize the EOM damage.

However, this study had several limitations. First, the inferior oblique muscle and superior oblique tendon exist in addition to the four rectus muscles inside the orbit, and various biological tissues, such as ligaments, septum, and lacrimal gland, are complexly located inside the orbit. Biological tissues, such as oblique muscles and tissues, were excluded from this analysis because the location and exact dimensions could not be determined from the MRI and CT data. It is believed that more accurate results can be obtained by simulating the oblique muscle and tendon. However, behavior inside the orbit of a TED patient can be efficiently simulated with the four rectus EOMs. Second, the material properties of the finite element model of the orbit and intraorbital tissues were assumed based on animal experiments because of the lack of experimental literature and information on human properties. Therefore, the accuracy of the FEA results can be further improved by obtaining the human material properties. However, there are ethical issues associated with the conduct of *in vivo* experiments. Therefore, in this study, the physical properties of the orbit and intraorbital tissues were applied using the results of published animal experimental studies. Third, the eyeball may be deformed by IR hypertrophy, considering that it has various structures and its inside is filled with vitreous and aqueous humor. However, this study focused on examining the contact stress of the orbital inner wall, excluding the eyeball, caused by EOM hypertrophy. If the deformation of other tissues, such as the eye, is considered, further results can be achieved besides the contact stress in the inner orbital wall. Finally, if image data is available prior to the patient's onset of thyroid eye disease, more accurate results for muscle growth variation can be obtained. However, because medical images were difficult to obtain prior to the onset of thyroid eye disease in this study, the main dimensions were measured based on the patient's contralateral orbit.

5 Conclusion

We simulated the orbit and intraorbital tissue of TED patients with enlarged IR muscle with a finite element model. In addition, an FEA was performed to assess the tissue responses in the orbit of TED patients based on the application of load conditions to the IR muscle and IOP. Thereafter, FEA of the tissue behavior in the orbit of a TED patient was performed after the orbital wall removal around the point of maximum stress on the orbital lining under the same conditions. The orbital wall stress at a specific point was measured according to the shape and location of the removed orbital wall. The main conclusions of this study are as follows.

- The hypertrophic load conditions of the IR muscle alone could not simulate the rotation and extrusion of the eye; the addition of IOP load conditions could simulate the intraocular tissue behavior of TED patients.
- The maximum stress point of the orbital wall was identified by the FEA of the IR hypertrophy and elevated IOP, and this point was applied for surgery.
- When the removed orbital wall has a rectangular shape, the difference in stress before and after chamfering was small at locations farther than the IR hypertrophy position. However, non-chamfered model analysis at a point close to the IR hypertrophy position confirmed that the applied stress decreased as the depth and width of the removed orbital wall increased.
- In chamfered model analysis with rectangular orbital wall removal, the stress decreased as the overall removal depth and width increased, but the stress width was not large. In addition, the orbital wall stress of the non-chamfered model with general orbital decompression formed a higher load than the orbital wall stress of the chamfered model.
- In the non-chamfered model with circular orbital wall removal, the stress of the orbital wall decreased as the diameter increased. However, the highest stress was measured at a specific diameter close to the maximum IR hypertrophy point. In the chamfered model, there was no difference in stress with the diameter of the removed circle.
- When the removed orbital wall had a circular shape, the stress of the non-chamfered model, with general orbital decompression, was significantly greater than that of the chamfered model.
- Therefore, we confirmed that the edge of the removed orbital wall, regardless of the removal type, generated significantly higher stress on the orbital wall in the case of the non-chamfered model (a form of general orbital decompression) than that in the chamfered model.
- Finally, if the edge of the orbital wall removed during orbital decompression was removed in a chamfering form, the EOM damage was expected to be minimal, preventing recurrence. If the orbital wall was thin and could not be removed in a

> chamfering form, the periorbita between the orbital wall and fat could be sectioned in an “H” shape. Moreover, the orbital wall of the sharp edge would be wrapped with the periorbita to prevent EOM damage.

Thus, if orbital decompression surgery is performed on a TED patient, the damage to the EOM caused by the removed orbital wall could be reduced. In addition, even if TED recurs, EOM damage can be minimized. Overall, the findings and inferences of this study can help treat TED in patients. Furthermore, only the hypertrophied IR in TED patients was considered, but in future studies, complex environmental conditions, including hypertrophied cases of other EOMs, will be included.

Data availability statement

The original contributions presented in the study are included in the article/Supplementary Material, further inquiries can be directed to the corresponding authors.

Ethics statement

The studies involving human participants were reviewed and approved by the Institutional Review Board of Pusan National University Hospital. The patients/participants provided their written informed consent to participate in this study.

Author contributions

BJ, CL, JP, and DR contributed to conceptualization and methodology and validation. BJ, JP, and DR contributed to original draft preparation, review, and editing. All authors contributed to manuscript revision, read, and approved the submitted version.

Funding

This study was supported by Biomedical Research Institute Grant (202000150001), Pusan National University Hospital.

Conflict of interest

The authors declare that the research was conducted in the absence of any commercial or financial relationships that could be construed as a potential conflict of interest.

Publisher’s note

References

Alsuhaibani, A. H., Carter, K. D., Policeni, B., and Nerad, J. A. (2011). Effect of orbital bony decompression for Graves’ orbitopathy on the volume of extraocular muscles. *Br. J. Ophthalmol.* 95, 1255–1258. doi:10.1136/bjo.2010.188946

Baillargeon, B., Rebelo, N., Fox, D. D., Taylor, R. L., and Kuhl, E. (2014). The living heart project: A robust and integrative simulator for human heart function. *Eur. J. Mech. A Solids* 48, 38–47. doi:10.1016/j.euromechsol.2014.04.001

Barin, F. R., de Sousa Neto, I. V., Vieira Ramos, G., Szojka, A., Ruivo, A. L., Anflor, C. T. M., et al. (2019). Calcaneal tendon plasticity following gastrocnemius muscle injury in rat. *Front. Physiol.* 10, 1098. doi:10.3389/fphys.2019.01098

Bartalena, L., Baldeschi, L., Boboridis, K., Eckstein, A., Kahaly, G. J., Marcocci, C., et al. (2016). The 2016 European thyroid association/European group on Graves’ orbitopathy guidelines for the management of Graves’ orbitopathy. *Eur. Thyroid. J.* 5, 9–26. doi:10.1159/000443828

Bartalena, L., Marocci, C., Bogazzi, F., Bruno-Bossio, G., and Pinchera, A. (1991). Glucocorticoid therapy of Graves’ ophthalmopathy. *Exp. Clin. Endocrinol. Diabetes* 97, 320–327. doi:10.1055/s-0029-1211086

Bartalena, L., and Tanda, M. L. (2009). Graves’ ophthalmopathy. *N. Engl. J. Med.* 360, 994–1001. doi:10.1056/NEJMcp0806317

Cirovic, S., Bhola, R. M., Hose, D. R., Howard, I. C., Lawford, P. V., Marr, J. E., et al. (2006). Computer modelling study of the mechanism of optic nerve injury in blunt trauma. *Br. J. Ophthalmol.* 90, 778–783. doi:10.1136/bjo.2005.086538

Cubuk, M. O., Konuk, O., and Unal, M. (2018). Orbital decompression surgery for the treatment of Graves’ ophthalmopathy: Comparison of different techniques and long-term results. *Int. J. Ophthalmol.* 11, 1363–1370. doi:10.18240/ijo.2018.08.18

Fichter, N., Guthoff, R. F., and Schittkowski, M. P. (2012). Orbital decompression in thyroid eye disease. *ISRN Ophthalmol.* 2012, 1–12. doi:10.5402/2012/739236

Fisher, L. K., Wang, X., Tun, T. A., Chung, H. W., Milea, D., and Girard, M. J. A. (2021). Gaze-evoked deformations of the optic nerve head in thyroid eye disease. *Br. J. Ophthalmol.* 105, 1758–1764. doi:10.1136/bjophthalmol-2020-318246

Forbes, G., Gorman, C. A., Brennan, M. D., Gehring, D. G., Ilstrup, D. M., and Earnest, F. (1986). Ophthalmopathy of Graves’ disease: Computerized volume measurements of the orbital fat and muscle. *Am. J. Neuroradiol.* 7, 651–656.

Genere, N., and Stan, M. N. (2019). Current and emerging treatment strategies for Graves’ orbitopathy. *Drugs* 79, 109–124. doi:10.1007/s40265-018-1045-9

Geng, X., Liu, X., Wei, W., Wang, Y., Wang, L., Chen, K., et al. (2018). Mechanical evaluation of retinal damage associated with blunt craniomaxillofacial trauma: A simulation analysis. *Transl. Vis. Sci. Technol.* 7, 16. doi:10.1167/tvst.7.3.16

Gontarz-Nowak, K., Szychlinska, M., Matuszewski, W., Stefanowicz-Rutkowska, M., and Bandurska-Stankiewicz, E. (2020). Current knowledge on Graves’ orbitopathy. *J. Clin. Med.* 10, 16. doi:10.3390/jcm10010016

Hernandez-Garcia, E., San-Roman, J. J., Gonzalez, R., Nogueira, A., Genol, I., Stoica, B., et al. (2017). Balanced (endoscopic medial and transcutaneous lateral) orbital decompression in Graves’ orbitopathy. *Acta Otolaryngol.* 137, 1183–1187. doi:10.1080/00016489.2017.1354394

Hiromatsu, Y., Yang, D., Bednarczuk, T., Miyake, I., Nonaka, K., and Inoue, Y. (2000). Cytokine profiles in eye muscle tissue and orbital fat tissue from patients with thyroid-associated ophthalmopathy. *J. Clin. Endocrinol. Metabolism* 85, 1194–1199. doi:10.1210/jcem.85.3.6433

Hu, W. D., Annunziata, C. C., Chokthaweesak, W., Korn, B. S., Levi, L., Granet, D. B., et al. (2010). Radiographic analysis of Extraocular Muscle volumetric changes in thyroid-related orbitopathy following orbital decompression. *Ophthalmic Plast. Reconstr. Surg.* 26, 1–6. doi:10.1097/IOP.0b013e3181b80fae

Ismailova, D. S., Belovalova, I. M., Grusha, Y. O., and Sviridenko, N. Y. (2018). Orbital decompression in the system of treatment for complicated thyroid eye disease: Case report and literature review. *Int. Med. Case Rep. J.* 11, 243–249. doi:10.2147/IMCRJ.S164372

Jefferis, J. M., Jones, R. K., Currie, Z. I., Tan, J. H., and Salvi, S. M. (2018). Orbital decompression for thyroid eye disease: Methods, outcomes, and complications. *Eye (Lond).* 32, 626–636. doi:10.1038/eye.2017.260

Jimenez-Chobillon, M. A., and Lopez-Oliver, R. D. (2010). Transnasal endoscopic approach in the treatment of Graves ophthalmopathy: The value of a medial periorbital strip. *Eur. Ann. Otorhinolaryngol. Head. Neck Dis.* 127, 97–103. doi:10.1016/j.anorl.2010.04.005

Kratky, V., Hurwitz, J. J., and Avram, D. R. (1990). Orbital compartment syndrome. Direct measurement of orbital tissue pressure: 1. Technique. *Can. J. Ophthalmol.* 25, 293–297.

Metson, R., and Samaha, M. (2002). Reduction of diplopia following endoscopic orbital decompression: The orbital sling technique. *Laryngoscope* 112, 1753–1757. doi:10.1097/00005537-200210000-00008

Mohyi, M., and Smith, T. J. (2018). 40 years of IGF1: IGF1 receptor and thyroid-associated ophthalmopathy. *J. Mol. Endocrinol.* 61, 29–43. doi:10.1530/JME-17-0276

Norman, R. E., Flanagan, J. G., Sigal, I. A., Rausch, S. M., Tertinegg, I., and Ethier, C. R. (2011). Finite element modeling of the human sclera: Influence on optic nerve head biomechanics and connections with glaucoma. *Exp. Eye Res.* 93, 4–12. doi:10.1016/j.exer.2010.09.014

Noth, D., Gebauer, M., Müller, B., Bürgi, U., Diem, P., and Burgi, U. (2001). Graves' ophthalmopathy: Natural history and treatment outcomes. *Swiss Med. Wkly.* 131, 603–609. doi:10.4414/smw.2001.09781

Power, E. D., Stitzel, J. D., Duma, S. M., Herring, I. P., and West, R. L. (2002). Investigation of ocular injuries from high velocity objects in an automobile collision. *SAE Int.* 111, 211–218. doi:10.4271/2002-01-0027

Schutte, S., van den Bedem, S. P., van Keulen, F., van der Helm, F. C., and Simonsz, H. J. (2006). A finite-element analysis model of orbital biomechanics. *Vis. Res.* 46, 1724–1731. doi:10.1016/j.visres.2005.11.022

Wang, Y., Patel, A., and Douglas, R. S. (2019). Thyroid eye disease: How A novel therapy may change the treatment paradigm. *Ther. Clin. Risk Manag.* 15, 1305–1318. doi:10.2147/tcrm.s193018

Wenz, R., Levine, M. R., Putterman, A., Bersani, T., and Feldman, K. (1994). Extraocular muscle enlargement after orbital decompression for Graves' ophthalmopathy. *Ophthalmic Plastic Reconstr. Surg.* 10, 34–41. doi:10.1097/00002341-199403000-00007

Wiersinga, W. M., Regensburg, N. I., and Mourits, M. P. (2013). Differential involvement of orbital fat and extraocular muscles in Graves' ophthalmopathy. *Eur. Thyroid. J.* 2, 14–21. doi:10.1159/000348246

Yiyi, Z., Guangzhi, W., Hui, D., and Yonghong, J. (2005). Finite element modeling and biomechanical analysis of eyeball and extraocular muscles. *Conf. Proc. IEEE Eng. Med. Biol. Soc.* 2005, 4978–4981. doi:10.1109/IEMBS.2005.1615592

Yoo, L., Kim, H., Gupta, V., and Demer, J. L. (2009). Quasilinear viscoelastic behavior of bovine Extraocular muscle tissue. *Invest. Ophthalmol. Vis. Sci.* 50, 3721–3728. doi:10.1167/iovs.08-3245

frontiers | Frontiers in Bioengineering and Biotechnology

TYPE Original Research
PUBLISHED 08 March 2023
DOI 10.3389/fbioe.2023.931202

EDITED BY
Damien Lacroix,
The University of Sheffield,
United Kingdom

REVIEWED BY
Maohua Lin,
Florida Atlantic University, United States
Ming Yang,
Army Medical University, China
Zhende Jiang,
Jilin University, China

*CORRESPONDENCE
Hao Liu,
✉ liuhao6304@126.com

†These authors have contributed equally to this work

SPECIALTY SECTION
This article was submitted to Biomechanics,
a section of the journal Frontiers in Bioengineering and Biotechnology

RECEIVED 28 April 2022
ACCEPTED 22 February 2023
PUBLISHED 08 March 2023

CITATION
Zhang X, Yang Y, Shen Y-W, Zhang K-R, Ma L-T, Ding C, Wang B-Y, Meng Y and Liu H (2023), Biomechanical performance of the novel assembled uncovertebral joint fusion cage in single-level anterior cervical discectomy and fusion: A finite element analysis.
Front. Bioeng. Biotechnol. 11:931202.
doi: 10.3389/fbioe.2023.931202

Biomechanical performance of the novel assembled uncovertebral joint fusion cage in single-level anterior cervical discectomy and fusion: A finite element analysis

Xiang Zhang†, Yi Yang†, Yi-Wei Shen, Ke-Rui Zhang, Li-Tai Ma, Chen Ding, Bei-Yu Wang, Yang Meng and Hao Liu*

Department of Orthopedics, Orthopedic Research Institute, West China Hospital, Sichuan University, Chengdu, China

Introduction: Anterior cervical discectomy and fusion (ACDF) is widely accepted as the gold standard surgical procedure for treating cervical radiculopathy and myelopathy. However, there is concern about the low fusion rate in the early period after ACDF surgery using the Zero-P fusion cage. We creatively designed an assembled uncoupled joint fusion device to improve the fusion rate and solve the implantation difficulties. This study aimed to assess the biomechanical performance of the assembled uncovertebral joint fusion cage in single-level ACDF and compare it with the Zero-P device.

Methods: A three-dimensional finite element (FE) of a healthy cervical spine (C2–C7) was constructed and validated. In the one-level surgery model, either an assembled uncovertebral joint fusion cage or a zero-profile device was implanted at the C5–C6 segment of the model. A pure moment of 1.0 Nm combined with a follower load of 75 N was imposed at C2 to determine flexion, extension, lateral bending, and axial rotation. The segmental range of motion (ROM), facet contact force (FCF), maximum intradiscal pressure (IDP), and screw–bone stress were determined and compared with those of the zero-profile device.

Results: The results showed that the ROMs of the fused levels in both models were nearly zero, while the motions of the unfused segments were unevenly increased. The FCF at adjacent segments in the assembled uncovertebral joint fusion cage group was less than that that of the Zero-P group. The IDP at the adjacent segments and screw–bone stress were slightly higher in the assembled uncovertebral joint fusion cage group than in those of the Zero-P group. Stress on the cage was mainly concentrated on both sides of the wings, reaching 13.4–20.4 Mpa in the assembled uncovertebral joint fusion cage group.

Abbreviations: ACDF, anterior cervical discectomy and fusion; ALL, anterior longitudinal ligament; FCF, facet contact force; FE, finite element; IDP, intradiscal pressure; PLL, posterior longitudinal ligament; ROM, range of motion.

Conclusion: The assembled uncovertebral joint fusion cage provided strong immobilization, similar to the Zero-P device. When compared with the Zero-P group, the assembled uncovertebral joint fusion cage achieved similar resultant values regarding FCF, IDP, and screw–bone stress. Moreover, the assembled uncovertebral joint fusion cage effectively achieved early bone formation and fusion, probably due to proper stress distributions in the wings of both sides.

KEYWORDS

finite element analysis, anterior cervical discectomy and fusion, assembled uncovertebral joint fusion cage, zero-P interbody fusion, bone fusion

Introduction

Anterior cervical discectomy and fusion (ACDF) is considered the gold standard surgical treatment for patients with cervical disc disease who have failed conservative treatments (Bohlman et al., 1993; Emery et al., 1998). Since its introduction by Cloward(1958) and Smith and Robinson (1958), the surgical technique has been continuously modified to improve fusion rates and clinical outcomes by optimizing the implant design and changing its materials (Hacker, 2000). Solid bone fusion after ACDF is one of the key indicators of achieving the expected clinical outcomes. As one of the most recommended fusion devices for ACDF, Zero-P devices use an integrated and low-profile plate design to reduce dysphagia rates and other plate-associated complications while maintaining satisfactory clinical outcomes (Barbagallo et al., 2013; Vanek et al., 2013; Chen et al., 2015). Previous studies have suggested that the fusion rates at 3 and 6 months after ACDF with Zero-P implant were 19.1% and 74.5%, respectively (He et al., 2020; Abudouaini et al., 2021a), but it did not achieve clinicians' desired results of a 90% fusion rate as early as possible (Vanek et al., 2013).

The uncovertebral joint, known as the Luschka joint, is a unique anatomical structure of the cervical spine. It is located on either side of the C3–C7 vertebral body, is formed by the anastomosis of the uncinate process on the posterolateral side of the lower vertebral body with the lower slope of the upper vertebral body, and has been shown to play an important role in limiting cervical lateral orientation and movement and maintaining cervical stability (Hartman, 2014). In our clinical practice, obvious bony fusion was often detected in the uncovertebral joint area during anterior intervertebral space release surgery on patients with old cervical fractures and dislocations. Additionally, heterotopic ossification was most significantly distributed at the uncovertebral joint during long-term follow-up after artificial cervical disc replacement (Tian et al., 2016). Furthermore, our previous clinical studies showed that the application of Zero-profile anchoring spacers (Zero-P, Johnson & Johnson) in ACDF with bone grafting in the uncovertebral joint area is safe and effective, with fusion rates of 16.7%, 63%, and 98.1% at 3, 6, and 12 months after the surgery when compared to control fusion rates of 2.5%, 33.3%, and 88.9%, respectively, indicating the great potential of accelerating fusion and improving fusion capacity (Liu. et al., 2020). In our prospective, randomized, controlled trial study, the fusion rate in the uncovertebral joint fusion group was found to be significantly higher than in the traditional interbody fusion group at 3 and 6 months after operation (3 months: 70% *vs* 10%, $p < 0.0001$; 6 months: 95% *vs* 65%, $p = 0.0177$, respectively) (Hao et al., 2022).

Therefore, we postulated that uncovertebral joint fusion might have potential advantages in cervical spine interbody fusion and designed a novel uncovertebral joint fusion cage. In our previous goat model research (Shen et al., 2021), 75.0% (9/12) of the goats in the uncovertebral joint fusion cage group were evaluated as achieving fusion at 12 weeks when compared to 41.7% (5/12) in the non-profile cage group. Additionally, the fusion grading scores of the uncovertebral joint fusion cage group were significantly higher than those of the non-profile cage group, both at 12 and 24 weeks ($p < 0.05$), without increasing serious complications during the 6 months of follow-up. Furthermore, in the goat experiment, initial stability biomechanical tests showed that the uncovertebral joint fusion cage had slightly better stability than the Zero-P device in the right and left lateral flexion and axial rotation and comparable stability to the Zero-P device in anterior flexion and posterior extension (Yang. et al., 2019). However, the existing uncovertebral joint fusion cage cannot be used to perform both inter–end plate bone grafting and uncinate joint bone grafting.

Due to the differences in the physiological state and osteogenesis ability of different patients, a single bone grafting area limits the improvement of fusion efficiency to a certain extent. Also, implantation difficulties hinder further development of the uncovertebral joint fusion cage. Therefore, we designed the assembled uncovertebral joint fusion cage to make the surgery easier. A double bone grafting path combining inter–end plate bone grafting and uncovertebral joint bone grafting was designed, which not only ensures a good biomechanical environment for osteogenesis but also combines the advantages of the two fusion ideas to make bone grafting safer and more effective. Specifically, we designed an assembled uncovertebral joint fusion cage comprising an intervertebral body support and uncovertebral joint fusion components on either side. The uncovertebral joint fusion components had upper and lower penetrating bone graft cavities, and the intervertebral support body or uncovertebral joint fusion components had an anatomical surface pattern. We printed the bone graft material or artificially filled and compacted it into the bone graft area before surgery, eliminating the need to implant decompressed bone or artificial bone particles into the uncovertebral joint fusion area through surgical forceps, thus reducing the risk of complications caused by dislodged bone graft particles, shortening surgery time, and making the operation easier. In addition, because of the split design, we could use 3D printing technology to individually print the intervertebral support body and the uncovertebral joint fusion components in reference to previous studies which focused on 3D-printed discs or fusion devices (Serra et al., 2016; Basgul et al., 2020; Li et al., 2021; Zhu et al., 2021) to achieve a good fit between the intervertebral support body, the uncovertebral joint fusion components, and the patient's vertebral space, thereby reducing the difficulty of surgical operation and improving the prosthesis–end plate fit.

However, a comprehensive finite element model has not yet been established to analyze its mechanical state. To the best of our knowledge, this is the first study to assess the biomechanical performance of the assembled uncovertebral joint fusion cage in single-level ACDF and compare it with the Zero-P device.

Materials and methods

Development of FE intact cervical spine model

A non-linear three-dimensional finite element (FE) model of the cervical spine segments (C2–C7) was developed and validated in our previous study (Rong et al., 2017). The model was constructed on the basis of computed tomography (CT) images from a young male volunteer without cervical degeneration (28 years, 165 cm, 65 kg), with a resolution of 0.75 mm and an interval of 0.69 mm from a CT scanner (SOMATOM Definition AS+, Siemens, Germany).

Generation of cervical spine model and instrument

The CT scans were imported into the Mimics 19.0 (Materialize Inc., Leuven, Belgium) software to reconstruct the geometric structure of the C2–C7 cervical vertebrae. The corresponding tissues were distinguished according to CT grayscale and exported to STL or Cloud point cloud format. The intervertebral disc geometries were constructed by filling the intervertebral space and connecting the adjacent vertebral bodies. Next, a preliminary geometric model was established, followed by denoising, paving, and smoothing to optimize the geometric structure of the model with the CATIA V5 R21 (Dassault Systèmes Corporation, Velizy-Villacoublay Cedex, France) and importing it into HyperMesh 12.0 (Altair, Troy, MI, United States) to prepare mesh division, such as the cervical spine, intervertebral disc, ligament, and other structural mesh. Last, the boundary conditions of the prepared model were set using ABAQUS 6.9.1 (Dassault Systèmes Corporation).

The cancellous bone regions of the vertebrae were set as solid elements. A 0.4-mm-thick shell consisting of the cortical bone and end plates covered the cancellous bone. The intervertebral disc was divided into the annulus fibrosus and nucleus pulposus with a volume ratio of 6:4. Annulus fibers surrounded the ground substance with an inclination to the transverse plane between 15° and 30,° accounting for approximately 19% of the entire annulus fibrosus volume (Denozière and Ku, 2006; Panzer and Cronin, 2009). The facet joint space was 0.5 mm and was covered by a cartilage layer with non-linear surface-to-surface contact. The ligamentous complex, which includes the anterior longitudinal ligament (ALL), posterior longitudinal ligament (PLL), ligamentum flavum, interspinous ligament, and capsular ligament, was developed using tension-only rod elements and was attached to the corresponding vertebrae. The Zero-P system (Synthes, Oberdorf, Switzerland), composed of the zero-profile titanium plate, polyetheretherketone (PEEK) cage, and two self-tapping screws in opposite directions, was adopted in this study. The primary dimensions (width, length, and height) were 13.6, 17.5, and 5 mm, respectively. The self-tapping screws were 16 mm long. Additionally, convergence analysis was performed to ensure that the maximum changes in the strain energy were <3% and showed that when the element size was between 0.1 and 1, the error stabilized at a minimum value, i.e., less than 3%, which is concordant with previous studies (Jones and Wilcox, 2008; Ayturk and Puttlitz, 2011; Zhang et al., 2022b). The material properties of the bone graft and newly formed bone were set as the cortical bone (Figure 1). The material properties and mesh types are listed in Table 1 (Denozière and Ku, 2006; Lee et al., 2011; Mo et al., 2017; Rong et al., 2017). The number of nodes and elements of the cervical spine model are shown in Table 2.

Boundary conditions

A tie connection was assigned between the intervertebral discs and adjacent vertebral bodies and between the insertion of ligaments to the bone. The facet joint was built as a non-linear three-dimensional contact problem using surface-to-surface elements. Frictionless contact was defined between the articular surfaces of the facet joints (Panzer and Cronin, 2009; Rong et al., 2017). The cancellous bone that filled the central cavity of the cage was defined as frictionless (Completo et al., 2015). A non-bonded contact was applied between the cage's supra- and infra-adjacent surfaces and the relevant vertebral surfaces with a contact friction coefficient of 0.3 (Galbusera et al., 2008). The graft–vertebrae and screw–vertebrae interfaces were defined as tie constraints to simulate rigid fusion and sufficient osseointegration. To simplify the model, shared nodes at the screw–plate interfaces were used, thus preventing relative motion between the components. The implant interfaces of the artificial cervical disc were defined as surface-to-surface sliding contact with a fraction coefficient of 0.07 (Li et al., 2018).

Biomechanical testing

The FE model of intact C2–C7 segments was fixed at the inferior end plate of C7. Follower loads of 75 N were used to simulate muscle force and head weight. A 1.0-N/m moment and 75-N follower load were applied to the odontoid of the C2 vertebrae to produce flexion, extension, lateral bending, and axial rotation (Rong et al., 2017; Wu et al., 2019; Wo et al., 2021; Lu et al., 2022). The ALL, PLL, nucleus pulposus, and annulus fibrosus were resected at C5/6, while the bilateral structures, such as uncinate processes, were preserved according to real surgical procedures. The range of motion (ROM) was defined as the rotation from the neutral position to the end position with a 1.0-N/m load. The ROM for each level was calculated on the basis of the relative motions of the markers of each vertebra in each motion mode (Panjabi et al., 2001).

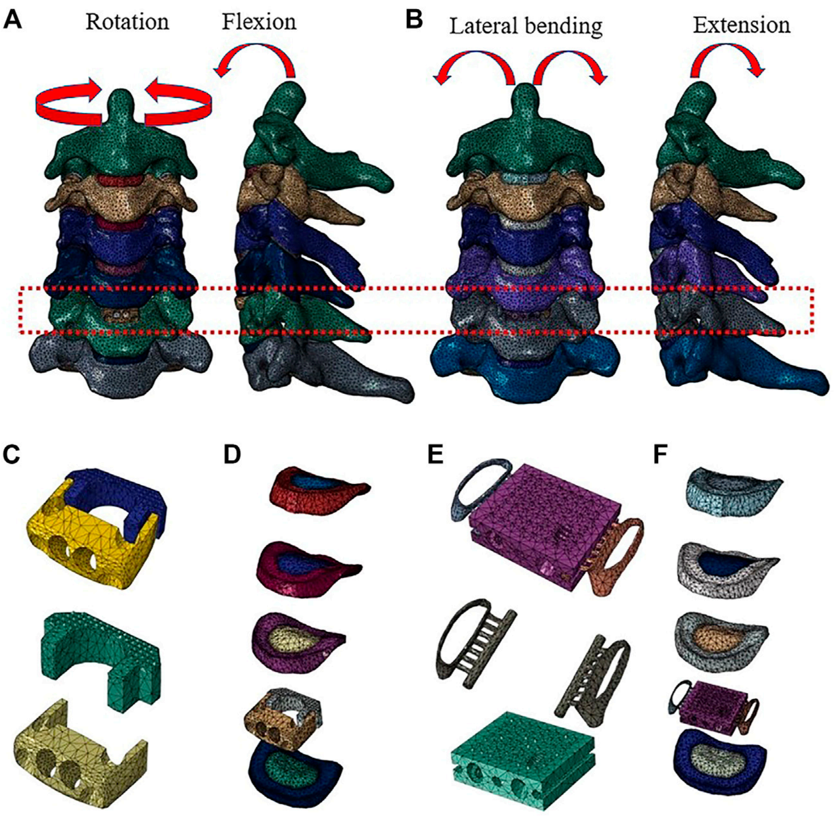

FIGURE 1
Finite element model of the C2–C7 cervical spine: **(A)** front view and sagittal view of the implanted Zero-P model, and **(B)** front view and sagittal view of the implanted assembled uncovertebral joint fusion cage model. **(C)** The Zero-P device (screws are not shown). **(D)** Intact intervertebral disk and the Zero-P device of the implanted Zero-P model. **(E)** The assembled uncovertebral joint fusion cage was composed of a body part, two wings, and screws (screws are not shown). **(F)** Intact intervertebral disk and the assembled uncovertebral joint fusion cage of the implanted assembled uncovertebral joint fusion cage model.

TABLE 1 Material properties and mesh types of the cervical finite element model.

Component	Young's modulus (MPa)	Poisson's ratio	Element type	Cross sections (mm^2)
Cortical bone	12,000	0.29	C3D4	—
Cancellous bone	450	0.29	C3D4	—
Nucleus pulpous	1.0	0.49	C3D4	—
Facet joint cartilage	10.4	0.4	C3D4	—
Annulus fibers	110	0.3	T3D2	—
Anterior longitudinal ligament	10	0.3	T3D2	6.0
Posterior longitudinal ligament	10	0.3	T3D2	5.0
Capsular ligament	10	0.3	T3D2	46.0
Interspinous ligament	1.5	0.3	T3D2	10.0
Supraspinous ligament	1.5	0.3	T3D2	5.0
Ligamentum flavum	1.5	0.3	T3D2	5.0
Cage (titanium)	1,10,000	0.3	C3D4	—
Screws	1,10,000	0.3	C3D4	—
Cage (PEEK)	3,600	0.3	C3D4	—

Note: C3D4, tetrahedron; T3D2, truss, tension-only.

TABLE 2 Number of elements and nodes for the cervical spine model.

	Element	Node
C2	63,892	96,991
C3	62,239	95,895
C4	60,707	93,960
C5	68,221	1,07,543
C6	59,809	94,578
C7	65,885	1,03,284
C2/3	11,400	20,170
C3/4	7,621	14,121
C4/5	9,818	17,721
C6/7	11,101	20,026
Anterior longitudinal ligament	135	136
Posterior longitudinal ligament	158	159
Capsular ligament	150	200
Ligamentum flavum	137	138
Interspinous ligament	92	98
Supraspinous ligament	280	290

According to the hybrid control proposed by Panjabi et al. (2001), the corresponding movement angles of all directions in the intact cervical model were applied to the ACDF surgical constructs. The ROM of each segment of the intact cervical spine model under all moments was compared with previously published data to validate the model. Based on our previous study and literature data, we chose the C5/6 level as the implanted level because it is the most frequently involved level in clinical practice (Bisson et al., 2011; Wang et al., 2013; Qizhi et al., 2016; Shi et al., 2016; Wu et al., 2017).

Results

Validation of the intact cervical spine model

As shown in Figure 2, the predicted segmental ROM of the present intact cervical spine model was within the standard deviation of the previous experimental data (Panjabi et al., 2001; Lee et al., 2016; Liu et al., 2016). The maximal intradiscal pressure of adjacent levels was consistent with *in vitro* experiments and previous finite element results (Welke et al., 2016; Zhou et al., 2021), and the facet contact force (FCF) of the model was also in agreement with the literature (Wu et al., 2019; Shen et al., 2022). All indicated that the present model was reliable in representing a healthy individual and could be used for further experiments.

Range of motion

The ROMs of each segment during flexion, extension, lateral bending, and axial rotation are shown in Figure 3. For all motions, the ROMs of the fused levels in the assembled uncovertebral joint fusion cage and Zero-P device models were nearly zero, and the ROMs of the unfused levels in all models were increased by 10.4%–73.2% for all motions when compared with the intact model. The unfused levels that exhibited increased motions fulfilled a compensatory function to maintain normal movement.

Facet contact force

Under the extension moment, FCF tended to decrease by 52.6% and 47.4% at the fused levels in the assembled uncovertebral joint fusion cage and Zero-P device group, respectively. When compared to the intact model, the maximum increase in the facet joint force in the superior adjacent and inferior adjacent segments of the assembled uncovertebral joint fusion cage group was 9.0% and 12.7% under the extension moment, respectively. Additionally, under the extension moment, the facet joint force in the Zero-P device group increased by 26.0% and 19.3% in the superior adjacent and inferior adjacent segments, respectively, when compared with the intact model (Figure 4).

Intradiscal pressure

Intradiscal pressure (IDP) measures at C2/3, C3/4, superior adjacent (C4/5), and inferior adjacent (C6/7) segments are shown in Figure 5. As expected, the intradiscal pressure at the adjacent levels in both groups was increased when compared with the intact model. The maximum increase of IDP measures was noted at the inferior adjacent (C6/7) segments under all motions in both models. Notably, the IDP measures in the adjacent segments of the assembled uncovertebral joint fusion cage model were comparable to that in the Zero-P group, only 0.061–0.121 Mpa higher (Figure 5). Stress contour diagrams in all movements in both the assembled uncovertebral joint fusion cage and the Zero-P device group are shown in Figure 6.

Maximum stress in the end plate–cage interface at the treatment level

A comparison of the maximum von Mises stress developed on the cage–end plate interfaces is shown in Figure 6. The maximum stress on the surface of the C6 superior and C5 inferior end plates of both surgical groups was compared with the intact model. Under flexion, extension, lateral bending, and axial rotation movements, the maximum stress in the C5 inferior end plate of the assembled uncovertebral joint fusion cage group was 1.435, 1.721, 2.009, and 2.575 Mpa, respectively, which is slightly higher than in the Zero-P group (1.189, 1.383, 1.598, and 2.011 Mpa, respectively). Under flexion, extension, lateral bending, and axial rotation, the maximum stress in the C6 superior end plate of the assembled uncovertebral joint fusion cage group was 1.479, 1.680, 1.880, and 2.413 Mpa, respectively, which is slightly higher than in the Zero-P group (1.220, 1.423, 1.633, and 1.936 Mpa, respectively) (Figure 7).

Maximum stress of the fusion cage

Stress contour diagrams in all movements in both surgical groups are shown in Figure 7. In the assembled uncovertebral

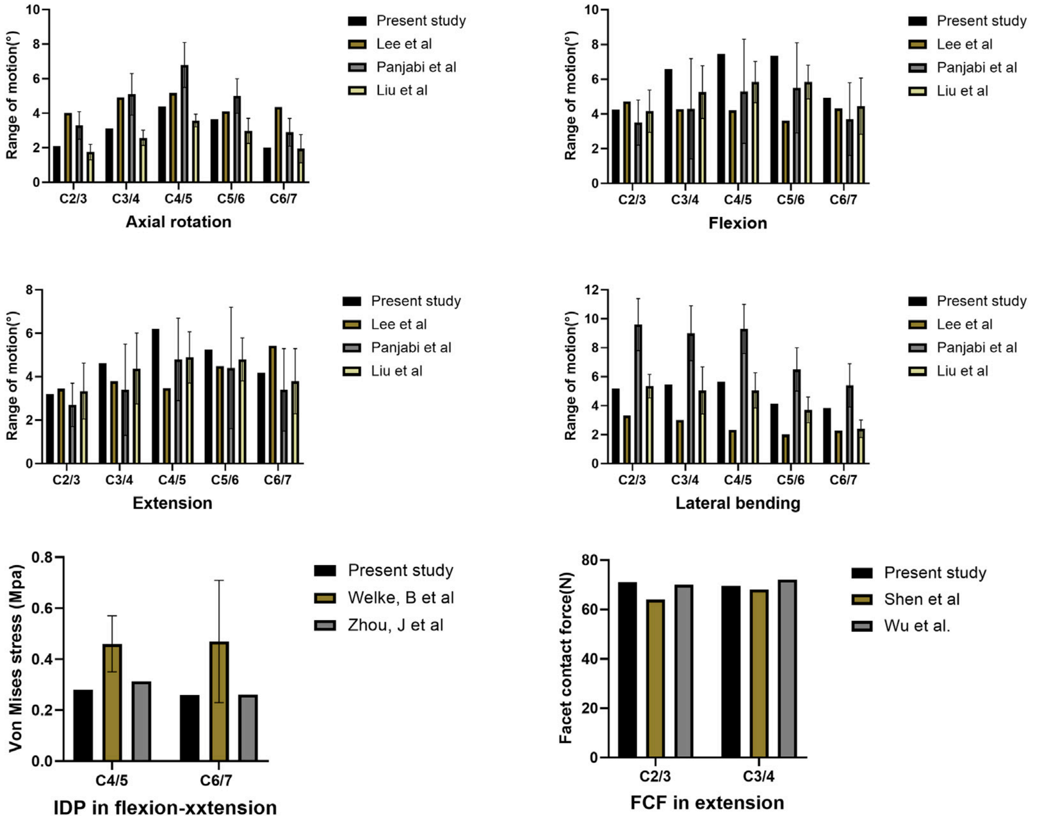

FIGURE 2
Comparison of the predicted ranges of motion (ROMs), intradiscal pressure (IDP), and facet contact force (FCF) with published literature.

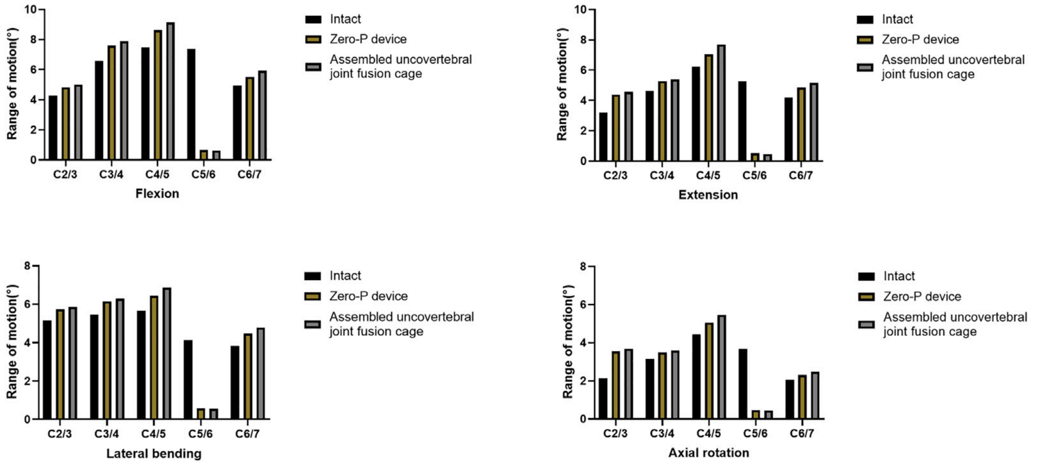

FIGURE 3
Range of motion (ROM) of three-dimensional finite element models of one-level anterior cervical discectomy and fusion using either the assembled uncovertebral joint fusion cage or Zero-P device.

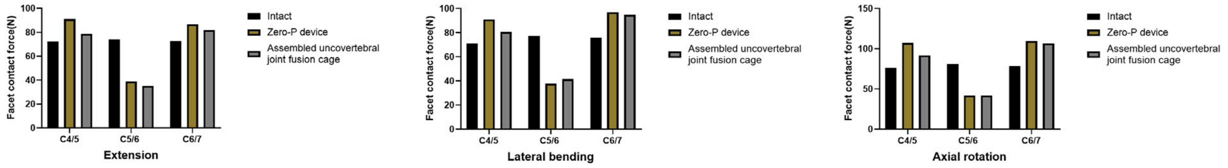

FIGURE 4
Facet contact force at the surgical and adjacent levels in extension, lateral bending, and axial rotation.

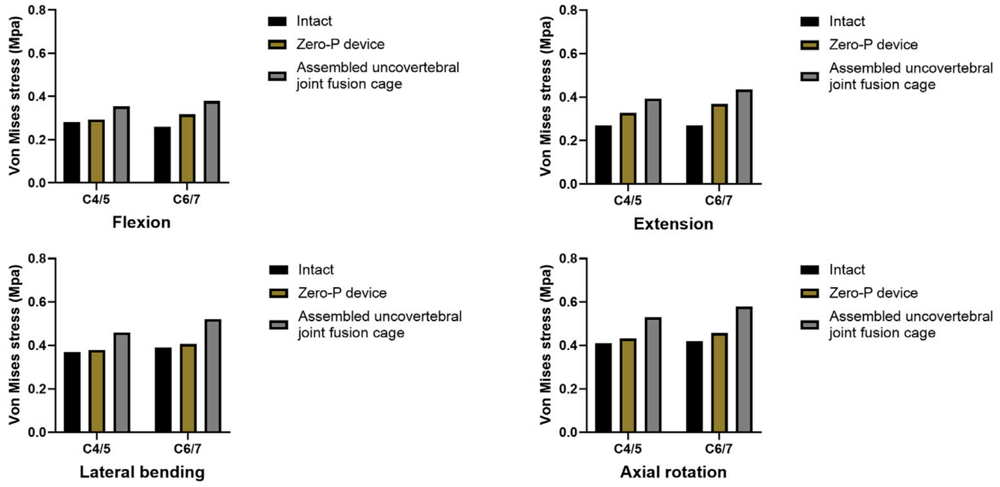

FIGURE 5
Intradiscal pressure in adjacent levels (the intact model *vs*. Zero-P device *vs*. the assembled uncovertebral joint fusion cage).

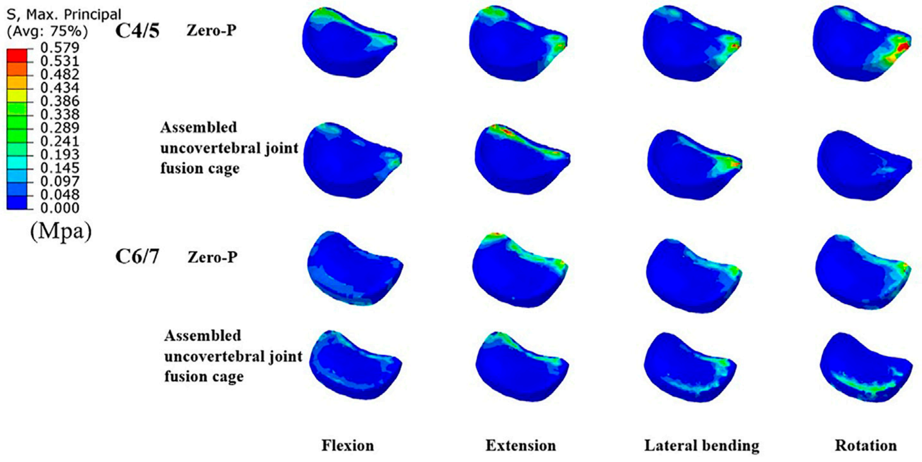

FIGURE 6
Cloud map of maximum Intradiscal pressure in adjacent levels (the comparisions between Zero-P device and the assembled uncovertebral joint fusion cage during flexion, extension, lateral bending and rotation).

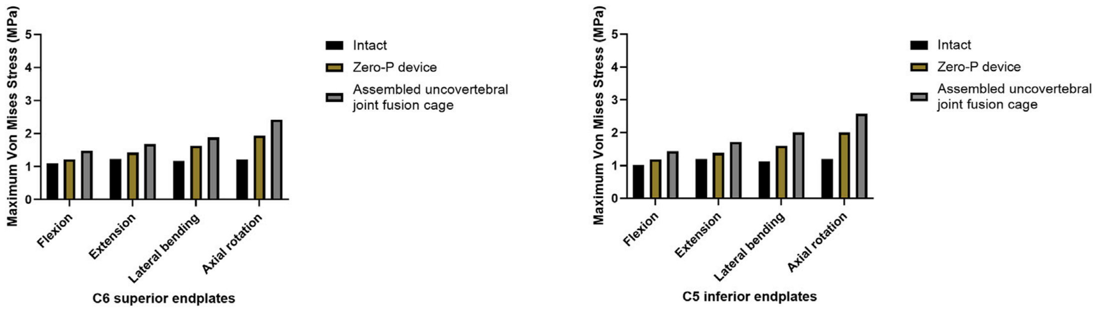

FIGURE 7
Maximum stress in the cage-endplate interface at surgical levels (the intact model *vs*. Zero-P device *vs*. the assembled uncovertebral joint fusion cage).

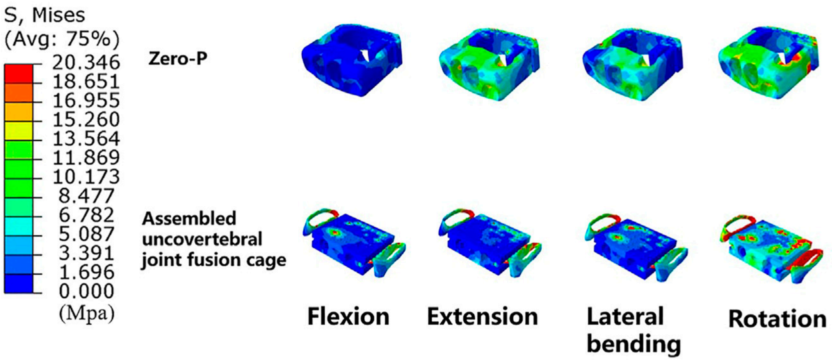

FIGURE 8
Cloud map of maximum stress of the fusion cage (Zero-P device *vs*. the assembled uncovertebral joint fusion cage).

joint fusion cage group, the stress was mainly concentrated in the wings on both sides, reaching 13.4–20.4 Mpa, whereas in the Zero-P group, it was concentrated in the anterior region of the Zero-P device, reaching 11.1–17.4 Mpa (Figure 8).

Discussion

This study assessed the biomechanical performance of the assembled uncovertebral joint fusion cage in single-level ACDF, which was then compared with that of Zero-P in terms of the range of motion, FCF, IDP, and stress in the end plate–cage interface and also explored the underlying mechanism by which the uncovertebral joint fusion accelerated bone fusion.

Construct stability

The results showed that the ROMs of the surgical segments in all movement directions decreased by 85.9%–91.6% postoperatively, which is consistent with the outcomes of previous literature (Hua et al., 2020b; Ke et al., 2021). Attributed to the anterior fixation and interbody fusion, sacrificed ROM at the fused segments mainly indicated strong immobilization (Gao et al., 2012; Song and Choi, 2014). Stulik et al. (2007) found that relatively loose internal fixation would lead to excessive relative movement between the bone graft and bone graft bed, easily resulting in the formation of pseudarthrosis. Vandamme et al. (2007) proposed that micromotion controlled within a certain small range can promote bone formation and the occurrence of bone integration. As shown in the results, slightly smaller ROMs of the fused segment in the assembled uncovertebral joint fusion cage group were achieved when compared with the Zero-P group, suggesting that the assembled uncovertebral joint fusion cage could provide strong immobilization, similar to the Zero-P device. Since the uncinate cage increased intervertebral stability at an early stage and limited excessive mobility, it might have effectively promoted the fusion of more parts of the intervertebral space, thus providing the basis for the assembled uncovertebral joint fusion cage with bone grafting in the inter–end plate and bilateral uncovertebral joint to promote bone fusion (Vandamme et al., 2007).

Due to the progressive enhancement of bony fusion at the inter–end plate and bilateral uncovertebral joint, the stiffness of the anterior column increased, which further improved the stability of the construct (Zhang et al., 2022b). It is worth noting that the ROMs of the unfused levels in all models increased by 10.4%–73.2% for all motions when compared to the intact model. The increased mobility of the unfused segment when compared to that of the normal group might be due to the loss of fusion of the fused segments and the compensation of the preserved normal cervical mobility. ACDF was of sacrificed ROM at the fused segments, while increased stress in the adjacent segment may be an important cause for developing adjacent segment degeneration (ASD) (Eck et al., 2002; Hua et al., 2020a; Ke et al., 2021). Considering that the ROM in the assembled uncovertebral joint fusion cage model achieved similar results to those after implantation with the Zero-P device, it is prudent to speculate that the assembled uncovertebral joint fusion cage did not significantly accelerate the degeneration of adjacent segments when compared with Zero-P. In general, the assembled uncovertebral joint fusion cage not only improves stability immediately after surgery but also has great potential for maintaining long-term stability after the operation.

Risks of degeneration at adjacent segments

Facet contact force (FCF) tended to decrease at the fused segments in both groups due to rigid fixation without relative motion. Under the extension, all unfused levels exhibited a substantial increase in FCF, which was consistent with the change in ROMs. Though stable segmental fixation is necessary for bony fusion, a stiff segment may result in increased FCF and IDP at adjacent levels, thus contributing to adjacent segments degeneration (Hilibrand and Robbins, 2004; Dickerman et al., 2009; Park et al., 2014; Kim et al., 2015; Hashimoto et al., 2019). Promisingly, the FCF increase inside the adjacent facet joints was lower in the assembled uncovertebral joint fusion cage group than in the Zero-P device group, indicating that the assembled uncovertebral joint fusion cage, to a certain degree, may have prevented the development of ASD. However, we noticed that the IDP at the adjacent levels in the assembled uncovertebral joint fusion cage group was greater than in the Zero-P device group, which might have been due to stronger fixation by the surgical segment and faster bone osseointegration after surgery provided in the assembled uncovertebral joint fusion cage when compared with the Zero-P device. Nevertheless, the IDP measures in the assembled uncovertebral joint fusion cage model were comparable to those in the Zero-P group and were only higher by 0.061–0.121 Mpa.

It could be seen from the intradiscal pressure nephograms that the stress distribution with the Zero-P device in ACDF was mainly concentrated at the margin of the intervertebral disc. Although disc stress in the assembled uncovertebral joint fusion cage group was slightly higher than that in the Zero-P group, no such degree of stress concentration was observed, suggesting that comparing only maximum stress values might not be an accurate assessment of the biomechanical disc stress changes in the adjacent segments (Figure 6). Thus, we could cautiously infer that the assembled uncovertebral joint fusion cage did not significantly affect the biomechanics of the adjacent segments when compared with the Zero-P device, but this should be confirmed in long-term follow-up. Additionally, the material properties of intervertebral discs in the FE models may influence the biomechanical results. Nishida et al. (2022), Nikkhoo et al. (2019), Gandhi et al. (2019), and Chen et al. (2022) developed an intervertebral disc model with hyperelastic material properties. Also, a lumbar disc geometry and the properties of disc annulus fibrosis described using a microstructure-based chemo-viscoelastic model have been constructed in some studies (Kandil et al., 2019; Khalaf and Nikkhoo, 2021). Ebrahimkhani et al. (2022) exploited a novel musculoskeletal finite element (MS-FE) spine model in which the intervertebral discs with the nucleus and annulus as a composite of the homogeneous matrix reinforced by collagen fiber networks was constructed. Therefore, it might be more realistic to analyze the biomechanics of adjacent discs through advanced models.

Cage subsidence

The concentration of high stress at the end plate–cage interface plays an important role in facilitating the penetration of the cage into the end plate and inducing cage subsidence (Chen et al., 2008; Lu et al., 2017). In this present study, end plate stress of both surgical groups was greater than that in the intact model. The outcomes of end plate stress show that the assembled uncovertebral joint fusion cage could still achieve promising results when compared with ACDF using the Zero-P device, though it was 0.246–0.560 Mpa higher. However, cage subsidence is a relatively uncommon postoperative complication in ACDF. Recent studies have demonstrated that ACDF using a Zero-P implant provides satisfactory clinical efficacy and acceptable safety, with a cage subsidence of 7.4%–13.58% at last follow-up (Li et al., 2017; Shen et al., 2018; Sun et al., 2020; Abudouaini et al., 2021b). Although subsidence of the cage had little influence on the clinical outcome in most patients, kyphosis, neurological deterioration, and instrumental complications might occur in some severe cases (Chen et al., 2016; Noordhoek et al., 2018; Oliver et al., 2018). Sun et al. (2021) determined the average stress of the end plate–cage interface from 0.9420 Mpa to 2.0423 Mpa in various fusion cages. Li et al. (2020) found that end plate stress peaks were the highest with the cage plate (0.6–2.4 MPa), followed by ACDF with the Zero-P device (0.5–2.3 MPa). Considering that end plate stress after the assembled uncovertebral joint fusion cage implantation was 1.435–2.575 Mpa, which is consistent with the abovementioned studies, it also supports that the assembled uncovertebral joint fusion cage may not increase the risk of end plate failure when compared with the Zero-P device.

In addition, great attention should be paid to the maximum stress that the end plate can withstand. Kwon et al. (2016) determined that the maximum peak loads at end plate failure for static and expandable spacers were 1764 N (±966 N) and 2284 N (±949 N), respectively. Zhang et al. (2008) determined that the average end plate failure load was 1,875 ± 1,023 N. Based on the abovementioned reference data, we calculated the stress threshold of the end plate, which was ~25.8 Mpa when the cage–end plate contact area was 31 mm^2. In addition, the assembled uncovertebral joint fusion cage seemed safe and may not cause end plate failure because the maximum stress at the end plate–cage interface was no more than 3 Mpa. However, current methods for making reasonable estimates of stress thresholds for subsidence are still limited and not individualized. Because the physiological curvature of the cervical spine is anteriorly convex and loads on the anterior spine are eccentric relative to the posterior spine (Zhang et al., 2022b), the failure loads were related to many factors, such as the applied high tensile strains (Fields et al., 2010), bone–end plate contact area or cage shape (Tan et al., 2005), and bone mineral density (BMD) or cage placement (Labrom et al., 2005). Lin et al. (2021, 2022) determined subsidence by measuring the distance that penetrated both the cage and screw into the end plate bone. Therefore, it is necessary to adopt a more rational and individual approach in estimating the maximum stress to failure loads, and we aim to perform relevant targeted optimizations in future studies. In our previous goat model research (Shen et al., 2021), no screw loosening, screw breakage, cage displacement, or subsidence was observed for the uncovertebral joint fusion cage during the 6 months of follow-up. In our prospective, randomized, controlled trial study, there were no cage subsidence and displacement, screw loosening, and fracture in the uncovertebral joint fusion cage group during the 6-month follow-up. Both studies indicated the safety and efficacy of the assembled uncovertebral joint fusion cage.

Osteogenesis promotion

Another important finding was that stress was mainly concentrated in the wings on both sides, reaching 13.4–20.4 Mpa in the assembled uncovertebral joint fusion cage group. It had been stated that if E signifies the typical peak strains of load-bearing bones, then healthy small and large load-bearing bones should satisfy this criterion: $2 \text{ MPa} < E < 20 \text{ MPa}$ (Frost, 2004). As mentioned above, the uncovertebral joint fusion cage effectively achieved early bone formation and fusion, probably due to proper distribution of stress concentration on both sides of the wings. This finding was clinically important because the bone graft area is located in the uncovertebral joint area on both sides of the assembled uncovertebral joint cage, which might receive proper stress stimulation to promote osteogenesis. However, simulation of the “sufficient osteointegration” stage was required. Our results have suggested greater stress in the uncovertebral joint area, which could also explain the increased speed and quality of bone healing with bone grafting in the uncovertebral joint area during the short term. The method of immediate postoperative testing of biomechanical properties was adopted in most studies (Wu et al., 2019; Huang et al., 2022; Liu et al., 2022; Lv et al., 2022; Zhang et al., 2022a). Considering that osseointegration is a long-term process, a longer dynamic observation of the stress distribution in the region of the uncovertebral joint is necessary.

FE analysis is a valuable method to predict trends after implantation in different cages, providing certain guidance for treatment. However, several limitations of the present study should be discussed. First, the FE model of the cervical spine was simplified to improve the efficiency of convergence in the FE study, which may not simulate the actual biomechanical environment, particularly for end plates at the implanted levels. Second, the FE model was constructed with a healthy cervical spine rather than a degenerative one, and only C5/6 (the most commonly involved one-level ACDF) was implanted for analysis. Thus, the model may not perfectly represent real-world clinical scenarios. However, the current study aimed to provide a trend instead of natural status. Several recent studies have adopted similar methods in developing the finite element spine model and reported acceptable results (Wu et al., 2019; Liang et al., 2022; Zhang et al., 2022b). Third, the geometry of the human spine varies among individuals, while the model of this present study was developed on the basis of the data from a single patient. Thus, the current modeling data should be interpreted with caution. Fourth, this study simplifies the musculoskeletal system, and the results under this ideal condition did not fully reflect the actual postoperative situation. Although this study aimed to provide a biomechanical reference for clinics, the manipulation of the muscular–ligamentous system in this finite analysis was based on previous literature (Fu et al., 2022; Huang et al., 2022; Shen et al., 2022; Zhang et al., 2022b). Last, linear elastic materials were adopted for the cervical vertebral body and intervertebral disc. In our study, the ligamentous complex, which includes anterior longitudinal ligaments (ALL), posterior longitudinal ligaments (PLL), capsular ligament (CL), ligamentum flavum (LF), interspinous ligaments (IL), and supraspinous ligament (SL), was established using non-linear tension-only truss elements. The facet joint was built as a non-linear three-dimensional contact problem using surface-to-surface contact elements. A face-to-face contact algorithm was used to define facet joint interaction, which was assumed with frictionless sliding contact. Also, we chose linear elastic materials for the vertebral body and intervertebral disc for good convergence in the calculating process. Although linear elastic materials may partially affect the biomechanical environment, the present study primarily focused on the changing trends following the implantation of a newly assembled uncovered vertebral joint fusion cage. The material properties should be re-assessed if the objective of the study changes. Analogously, several recent studies have adopted similar methods for developing a finite element cervical spine model and provided satisfactory results (He et al., 2021; Hua et al., 2020a; Hua et al., 2020b; Lin et al., 2021; Wo et al., 2021; Shen et al., 2022; Zhang et al., 2022b). Given that material properties such as hyperelastic, viscoelastic, or poroelastic materials within the intervertebral disc can result in better biomechanical predictions, a more realistic model has to be developed in future studies.

Conclusion

In conclusion, this study showed that the assembled uncovertebral joint fusion cage provided strong immobilization similar to the Zero-P device. Compared with the Zero-P group, the assembled uncovertebral joint fusion cage achieved similar resultant values regarding FCF, IDP, and stress in the end plate–cage interface. Altogether, the assembled uncovertebral joint fusion cage was non-inferior to the Zero-P device in terms of biomechanical properties. Moreover, the proper distribution of stress concentration in the wings on both sides may play an important role in achieving early bone formation and fusion of the assembled uncovertebral joint fusion cage.

Data availability statement

The original contributions presented in the study are included in the article/Supplementary Material; further inquiries can be directed to the corresponding author.

Author contributions

XZ and YY contributed to the design of the study. XZ drafted the manuscript with help from YY. Y-WS, K-RZ, L-TM, and CD helped in the statistical analyses. Statistical analyses were discussed with B-YW and YM. YY and HL contributed to the revision. All authors have read and approved the final manuscript.

Funding

This study was supported by the National Natural Science Foundation of China (82172522), Sichuan Province Science and Technology Support Program of China (No. 2020YFS0089), Sichuan Province Science and Technology Support Program of China (No. 2020YFS0077), Postdoctoral Research Project, West China Hospital, Sichuan University (No. 2019HXBH063), and the Postdoctoral Science Foundation of China (No. 2020M673240).

Acknowledgments

The authors thank the Home for Researchers editorial team (www.home-for-researchers.com) for their language editing service.

Conflict of interest

The authors declare that the research was conducted in the absence of any commercial or financial relationships that could be construed as a potential conflict of interest.

Publisher's note

References

Abudouaini, H., Huang, C., Liu, H., Hong, Y., Wang, B., Ding, C., et al. (2021a). Change in the postoperative intervertebral space height and its impact on clinical and radiological outcomes after ACDF surgery using a zero-profile device: A single-centre retrospective study of 138 cases. *BMC Musculoskelet. Disord.* 22, 543. doi:10.1186/s12891-021-04432-0

Abudouaini, H., Wu, T., Liu, H., Wang, B., Chen, H., Huang, C., et al. (2021b). Partial uncinatectomy combined with anterior cervical discectomy and fusion for the treatment of one-level cervical radiculopathy: Analysis of clinical efficacy and sagittal alignment. *BMC Musculoskelet. Disord.* 22, 777. doi:10.1186/s12891-021-04680-0

Ayturk, U. M., and Puttlitz, C. M. (2011). Parametric convergence sensitivity and validation of a finite element model of the human lumbar spine. *Comput. Methods Biomech. Biomed. Engin* 14, 695–705. doi:10.1080/10255842.2010.493517

Barbagallo, G. M., Romano, D., Certo, F., Milone, P., and Albanese, V. (2013). Zero-P: A new zero-profile cage-plate device for single and multilevel ACDF. A single institution series with four years maximum follow-up and review of the literature on zero-profile devices. *Eur. Spine J.* 6, S868–S878. doi:10.1007/s00586-013-3005-0

Basgul, C., Yu, T., Macdonald, D. W., Siskey, R., Marcolongo, M., and Kurtz, S. M. (2020). Does annealing improve the interlayer adhesion and structural integrity of FFF 3D printed PEEK lumbar spinal cages? *J. Mech. Behav. Biomed. Mater* 102, 103455. doi:10.1016/j.jmbbm.2019.103455

Bisson, E. F., Samuelson, M. M., and Apfelbaum, R. I. (2011). Intermediate segment degeneration after noncontiguous anterior cervical fusion. *Acta Neurochir. (Wien)* 153, 123–128. doi:10.1007/s00701-010-0832-1

Bohlman, H. H., Emery, S. E., Goodfellow, D. B., and Jones, P. K. (1993). Robinson anterior cervical discectomy and arthrodesis for cervical radiculopathy. Long-term follow-up of one hundred and twenty-two patients. *J. Bone Jt. Surg. Am.* 75, 1298–1307. doi:10.2106/00004623-199309000-00005

Chen, Y., Chen, D., Guo, Y., Wang, X., Lu, X., He, Z., et al. (2008). Subsidence of titanium mesh cage: A study based on 300 cases. *J. Spinal Disord. Tech.* 21, 489–492. doi:10.1097/bsd.0b013e318158de22

Chen, Y., Chen, H., Cao, P., and Yuan, W. (2015). Anterior cervical interbody fusion with the zero-P spacer: Mid-term results of two-level fusion. *Eur. Spine J.* 24, 1666–1672. doi:10.1007/s00586-015-3919-9

Chen, Y., Lü, G., Wang, B., Li, L., and Kuang, L. (2016). A comparison of anterior cervical discectomy and fusion (ACDF) using self-locking stand-alone polyetheretherketone (PEEK) cage with ACDF using cage and plate in the treatment of three-level cervical degenerative spondylopathy: A retrospective study with 2-year follow-up. *Eur. Spine J.* 25, 2255–2262. doi:10.1007/s00586-016-4391-x

Chen, S. H., Hsiao, C. K., Wang, C. W., Chen, H. H., and Zhong, Z. C. (2022). Biomechanical comparison between isobar and dynamic-transitional optima (dto) hybrid lumbar fixators: A lumbosacral finite element and intersegmental motion analysis. *Biomed. Res. Int.* 2022, 1–13. doi:10.1155/2022/8273853

Cloward, R. B. (1958). The anterior approach for removal of ruptured cervical disks. *J. Neurosurg.* 15, 602–617. doi:10.3171/jns.1958.15.6.0602

Completo, A., Nascimento, A., Ramos, A., and Simões, J. (2015). Failure analysis of C-5 after total disc replacement with ProDisc-C at 1 and 2 levels and in combination with a fusion cage: Finite-element and biomechanical models. *J. Neurosurg. Spine* 22, 639–646. doi:10.3171/2014.10.spine14217

Denozière, G., and Ku, D. N. (2006). Biomechanical comparison between fusion of two vertebrae and implantation of an artificial intervertebral disc. *J. Biomech.* 39, 766–775. doi:10.1016/j.jbiomech.2004.07.039

Dickerman, R. D., Reynolds, A. S., Zigler, J., and Guyer, R. (2009). Adjacent-segment degeneration. *J. Neurosurg. Spine* 10, 177. doi:10.3171/2008.10.spi16794l

Ebrahimkhani, M., Arjmand, N., and Shirazi-Adl, A. (2022). Adjacent segments biomechanics following lumbar fusion surgery: A musculoskeletal finite element model study. *Eur. Spine J.* 31, 1630–1639. doi:10.1007/s00586-022-07262-3

Eck, J. C., Humphreys, S. C., Lim, T. H., Jeong, S. T., Kim, J. G., Hodges, S. D., et al. (2002). Biomechanical study on the effect of cervical spine fusion on adjacent-level intradiscal pressure and segmental motion. *Spine (Phila Pa 1976)* 27, 2431–2434. doi:10.1097/00007632-200211150-00003

Emery, S. E., Bohlman, H. H., Bolesta, M. J., and Jones, P. K. (1998). Anterior cervical decompression and arthrodesis for the treatment of cervical spondylotic myelopathy. Two to seventeen-year follow-up. *J. Bone Jt. Surg. Am.* 80, 941–951. doi:10.2106/00004623-199807000-00002

Fields, A. J., Lee, G. L., and Keaveny, T. M. (2010). Mechanisms of initial endplate failure in the human vertebral body. *J. Biomech.* 43, 3126–3131. doi:10.1016/j.jbiomech.2010.08.002

Frost, H. M. (2004). A 2003 update of bone physiology and Wolff's Law for clinicians. *Angle Orthod.* 74, 3–15. doi:10.1043/0003-3219(2004)074<0003:AUOBPA>2.0.CO;2

Fu, G., Zhong, G., Yang, Z., Cheng, S., Ma, L., and Zhang, Y. (2022). Two cannulated screws provide sufficient biomechanical strength for prophylactic fixation in adult patients with an aggressive benign femoral neck lesion. *Front. Bioeng. Biotechnol.* 10, 891338. doi:10.3389/fbioe.2022.891338

Galbusera, F., Bellini, C. M., Costa, F., Assietti, R., and Fornari, M. (2008). Anterior cervical fusion: A biomechanical comparison of 4 techniques. Laboratory investigation. *J. Neurosurg. Spine* 9, 444–449. doi:10.3171/spi.2008.9.11.444

Gandhi, A. A., Grosland, N. M., Kallemeyn, N. A., Kode, S., Fredericks, D. C., and Smucker, J. D. (2019). Biomechanical analysis of the cervical spine following disc degeneration, disc fusion, and disc replacement: A finite element study. *Int. J. Spine Surg.* 13, 491–500. doi:10.14444/6066

Gao, R., Yang, L., Chen, H., Liu, Y., Liang, L., and Yuan, W. (2012). Long term results of anterior corpectomy and fusion for cervical spondylotic myelopathy. *PLoS One* 7, e34811. doi:10.1371/journal.pone.0034811

Hacker, R. J. (2000). A randomized prospective study of an anterior cervical interbody fusion device with a minimum of 2 years of follow-up results. *J. Neurosurg.* 93, 222–226. doi:10.3171/spi.2000.93.2.0222

Hao, L., Sheng, X., Yi, Y., Meng, Y., Wang, B., and Ding, C. (2022). Comparison of fusion effectiveness between anterior cervical uncovertebral joint fusion and conventional interbody fusion: A prospective, randomized, controlled trial study. *Chin. J. Spine Spinal Cord Chin.* 32, 410–417. doi:10.3969/j.issn.1004-406X.2022.05.05

Hartman, J. (2014). Anatomy and clinical significance of the uncinate process and uncovertebral joint: A comprehensive review. *Clin. Anat.* 27, 431–440. doi:10.1002/ca.22317

Hashimoto, K., Aizawa, T., Kanno, H., and Itoi, E. (2019). Adjacent segment degeneration after fusion spinal surgery-a systematic review. *Int. Orthop.* 43, 987–993. doi:10.1007/s00264-018-4241-z

He, J., Ding, C., Liu, H., Wu, T., Huang, K., Wang, B., et al. (2020). Is there a relationship between bony fusion after anterior cervical discectomy and fusion and heterotopic ossification after cervical disc arthroplasty in hybrid surgery? *Spine (Phila Pa 1976)* 45, E1653–e1660. doi:10.1097/brs.0000000000003687

He, T., Zhang, J., Yu, T., Wu, J., Yuan, T., Liu, R., et al. (2021). Comparative analysis of the biomechanical characteristics after different minimally invasive surgeries for cervical spondylopathy: A finite element analysis. *Front. Bioeng. Biotechnol.* 9, 772853. doi:10.3389/fbioe.2021.772853

Hilibrand, A. S., and Robbins, M. (2004). Adjacent segment degeneration and adjacent segment disease: The consequences of spinal fusion? *Spine J.* 4, 190–S194. doi:10.1016/j.spinee.2004.07.007

Hua, W., Zhi, J., Ke, W., Wang, B., Yang, S., Li, L., et al. (2020a). Adjacent segment biomechanical changes after one- or two-level anterior cervical discectomy and fusion using either a zero-profile device or cage plus plate: A finite element analysis. *Comput. Biol. Med.* 120, 103760. doi:10.1016/j.compbiomed.2020.103760

Hua, W., Zhi, J., Wang, B., Ke, W., Sun, W., Yang, S., et al. (2020b). Biomechanical evaluation of adjacent segment degeneration after one- or two-level anterior cervical discectomy and fusion versus cervical disc arthroplasty: A finite element analysis. *Comput. Methods Programs Biomed.* 189, 105352. doi:10.1016/j.cmpb.2020.105352

Huang, Z. B., Nie, M. D., Zhang, N. Z., Liu, S., Yuan, J. B., Lin, X. M., et al. (2022). Biomechanical evaluation of a short-rod technique for lumbar fixation surgery. *Front. Bioeng. Biotechnol.* 10, 959210. doi:10.3389/fbioe.2022.959210

Jones, A. C., and Wilcox, R. K. (2008). Finite element analysis of the spine: Towards a framework of verification, validation and sensitivity analysis. *Med. Eng. Phys.* 30, 1287–1304. doi:10.1016/j.medengphy.2008.09.006

Kandil, K., Zaïri, F., Derrouiche, A., Messager, T., and Zaïri, F. (2019). Interlamellar-induced time-dependent response of intervertebral disc annulus: A microstructure-based chemo-viscoelastic model. *Acta Biomater.* 100, 75–91. doi:10.1016/j.actbio.2019.10.005

Ke, W., Chen, C., Wang, B., Hua, W., Lu, S., Song, Y., et al. (2021). Biomechanical evaluation of different surgical approaches for the treatment of adjacent segment diseases after primary anterior cervical discectomy and fusion: A finite element analysis. *Front. Bioeng. Biotechnol.* 9, 718996. doi:10.3389/fbioe.2021.718996

Khalaf, K., and Nikkhoo, M. (2021). Comparative biomechanical analysis of rigid vs. flexible fixation devices for the lumbar spine: A geometrically patient-specific poroelastic finite element study. *Comput. Methods Programs Biomed.* 212, 106481. doi:10.1016/j.cmpb.2021.106481

Kim, H. J., Kang, K. T., Son, J., Lee, C. K., Chang, B. S., and Yeom, J. S. (2015). The influence of facet joint orientation and tropism on the stress at the adjacent segment after lumbar fusion surgery: A biomechanical analysis. *Spine J.* 15, 1841–1847. doi:10.1016/j.spinee.2015.03.038

Kwon, A. J., Hunter, W. D., Moldavsky, M., Salloum, K., and Bucklen, B. (2016). Indirect decompression and vertebral body endplate strength after lateral interbody spacer impaction: Cadaveric and foam-block models. *J. Neurosurg. Spine* 24, 727–733. doi:10.3171/2015.10.spine15450

Labrom, R. D., Tan, J. S., Reilly, C. W., Tredwell, S. J., Fisher, C. G., and Oxland, T. R. (2005). The effect of interbody cage positioning on lumbosacral vertebral endplate failure in compression. *Spine (Phila Pa 1976)* 30, E556–E561. doi:10.1097/01.brs.0000181053.38677.c2

Lee, S. H., Im, Y. J., Kim, K. T., Kim, Y. H., Park, W. M., and Kim, K. (2011). Comparison of cervical spine biomechanics after fixed- and mobile-core artificial disc replacement: A finite element analysis. *Spine (Phila Pa 1976)* 36, 700–708. doi:10.1097/brs.0b013e3181f5cb87

Lee, J. H., Park, W. M., Kim, Y. H., and Jahng, T. A. (2016). A biomechanical analysis of an artificial disc with a shock-absorbing core property by using whole-cervical spine finite element analysis. *Spine (Phila Pa 1976)* 41, E893–e901. doi:10.1097/brs.0000000000001468

Li, Z., Zhao, Y., Tang, J., Ren, D., Guo, J., Wang, H., et al. (2017). A comparison of a new zero-profile, stand-alone fidji cervical cage and anterior cervical plate for single and multilevel ACDF: A minimum 2-year follow-up study. *Eur. Spine J.* 26, 1129–1139. doi:10.1007/s00586-016-4739-2

Li, Y., Fogel, G. R., Liao, Z., Tyagi, R., and Liu, W. (2018). Prosthesis and hybrid strategy consideration for treating two-level cervical disc degeneration in hybrid surgery. *Spine (Phila Pa 1976)* 43, 379–387. doi:10.1097/brs.0000000000002316

Li, X. F., Jin, L. Y., Liang, C. G., Yin, H. L., and Song, X. X. (2020). Adjacent-level biomechanics after single-level anterior cervical interbody fusion with anchored zero-profile spacer versus cage-plate construct: A finite element study. *BMC Surg.* 20, 66. doi:10.1186/s12893-020-00729-4

Li, S., Huan, Y., Zhu, B., Chen, H., Tang, M., Yan, Y., et al. (2021). Research progress on the biological modifications of implant materials in 3D printed intervertebral fusion cages. *J. Mater Sci. Mater Med.* 33, 2. doi:10.1007/s10856-021-06609-4

Liang, W., Han, B., Hai, Y., Yang, J., and Yin, P. (2022). Biomechanical analysis of the reasonable cervical range of motion to prevent non-fusion segmental degeneration after single-level ACDF. *Front. Bioeng. Biotechnol.* 10, 918032. doi:10.3389/fbioe.2022.918032

Lin, M., Shapiro, S. Z., Doulgeris, J., Engeberg, E. D., Tsai, C. T., and Vrionis, F. D. (2021). Cage-screw and anterior plating combination reduces the risk of micromotion and subsidence in multilevel anterior cervical discectomy and fusion-a finite element study. *Spine J.* 21, 874–882. doi:10.1016/j.spinee.2021.01.015

Lin, M., Shapiro, S. Z., Engeberg, E. D., Tsai, C. T., and Vrionis, F. D. (2022). Finite element analysis of the effect of dynamic plating on two-level anterior cervical discectomy fusion biomechanics. *World Neurosurg.* 163, e43–e52. doi:10.1016/j.wneu.2022.02.032

Liu, Q., Guo, Q., Yang, J., Zhang, P., Xu, T., Cheng, X., et al. (2016). Subaxial cervical intradiscal pressure and segmental kinematics following atlantoaxial fixation in different angles. *World Neurosurg.* 87, 521–528. doi:10.1016/j.wneu.2015.09.025

Liu, H., Duan, Y.-C., and Rong, X. (2020). Effect of autogenous bone grafting in uncovertebral joint on early fusion after anterior cervical discectomy and fusion with the Zero-P device (Chinese). *Chin. BONE Jt. Surg.* 13, 1.doi:10.3969/j.issn.2095-9958.2020.05.02

Liu, B., Li, X., Qiu, W., Liu, Z., Zhou, F., Zheng, Y., et al. (2022). Mechanical distribution and new bone regeneration after implanting 3D printed prostheses for repairing metaphyseal bone defects: A finite element analysis and prospective clinical study. *Front. Bioeng. Biotechnol.* 10, 921545. doi:10.3389/fbioe.2022.921545

Lu, T., Liang, H., Liu, C., Guo, S., Zhang, T., Yang, B., et al. (2017). Effects of titanium mesh cage end structures on the compressive load at the endplate interface: A cadaveric biomechanical study. *Med. Sci. Monit.* 23, 2863–2870. doi:10.12659/msm.905466

Lu, X., Zou, F., Lu, F., Ma, X., Xia, X., and Jiang, J. (2022). How to reconstruct the lordosis of cervical spine in patients with hirayama disease? A finite element analysis of biomechanical changes focusing on adjacent segments after anterior cervical discectomy and fusion. *J. Orthop. Surg. Res.* 17, 101. doi:10.1186/s13018-022-02984-y

Lv, M. L., Ni, M., Sun, W., Wong, D. W., Zhou, S., Jia, Y., et al. (2022). Biomechanical analysis of a novel double-point fixation method for displaced intra-articular calcaneal fractures. *Front. Bioeng. Biotechnol.* 10, 791554. doi:10.3389/fbioe.2022.791554

Mo, Z., Li, Q., Jia, Z., Yang, J., Wong, D. W., and Fan, Y. (2017). Biomechanical consideration of prosthesis selection in hybrid surgery for bi-level cervical disc degenerative diseases. *Eur. Spine J.* 26, 1181–1190. doi:10.1007/s00586-016-4777-9

Nikkhoo, M., Cheng, C. H., Wang, J. L., Khoz, Z., El-Rich, M., Hebela, N., et al. (2019). Development and validation of a geometrically personalized finite element model of the lower ligamentous cervical spine for clinical applications. *Comput. Biol. Med.* 109, 22–32. doi:10.1016/j.compbiomed.2019.04.010

Nishida, N., Mumtaz, M., Tripathi, S., Kelkar, A., Kumaran, Y., Sakai, T., et al. (2022). Biomechanical analysis of laminectomy, laminoplasty, posterior decompression with instrumented fusion, and anterior decompression with fusion for the kyphotic cervical spine. *Int. J. Comput. Assist. Radiol. Surg.* 17, 1531–1541. doi:10.1007/s11548-022-02692-2

Noordhoek, I., Koning, M. T., Jacobs, W. C. H., and Vleggeert-Lankamp, C. L. A. (2018). Incidence and clinical relevance of cage subsidence in anterior cervical discectomy and fusion: A systematic review. *Acta Neurochir. (Wien)* 160, 873–880. doi:10.1007/s00701-018-3490-3

Oliver, J. D., Goncalves, S., Kerezoudis, P., Alvi, M. A., Freedman, B. A., Nassr, A., et al. (2018). Comparison of outcomes for anterior cervical discectomy and fusion with and without anterior plate fixation: A systematic review and meta-analysis. *Spine (Phila Pa 1976)* 43, E413–e422. doi:10.1097/brs.0000000000002441

Panjabi, M. M., Crisco, J. J., Vasavada, A., Oda, T., Cholewicki, J., Nibu, K., et al. (2001). Mechanical properties of the human cervical spine as shown by three-dimensional load-displacement curves. *Spine (Phila Pa 1976)* 26, 2692–2700. doi:10.1097/00007632-200112150-00012

Panzer, M. B., and Cronin, D. S. (2009). C4-C5 segment finite element model development, validation, and load-sharing investigation. *J. Biomech.* 42, 480–490. doi:10.1016/j.jbiomech.2008.11.036

Park, J., Shin, J. J., and Lim, J. (2014). Biomechanical analysis of disc pressure and facet contact force after simulated two-level cervical surgeries (fusion and arthroplasty) and hybrid surgery. *World Neurosurg.* 82, 1388–1393. doi:10.1016/j.wneu.2014.06.013

Qizhi, S., Lei, S., Peijia, L., Hanping, Z., Hongwei, H., Junsheng, C., et al. (2016). A comparison of zero-profile devices and artificial cervical disks in patients with 2 noncontiguous levels of cervical spondylosis. *Clin. Spine Surg.* 29, E61–E66. doi:10.1097/bsd.0000000000000096

Rong, X., Wang, B., Ding, C., Deng, Y., Chen, H., Meng, Y., et al. (2017). The biomechanical impact of facet tropism on the intervertebral disc and facet joints in the cervical spine. *Spine J.* 17, 1926–1931. doi:10.1016/j.spinee.2017.07.009

Serra, T., Capelli, C., Toumpaniari, R., Orriss, I. R., Leong, J. J., Dalgarno, K., et al. (2016). Design and fabrication of 3D-printed anatomically shaped lumbar cage for intervertebral disc (IVD) degeneration treatment. *Biofabrication 8* 8, 035001. doi:10.1088/1758-5090/8/3/035001

Shen, Y., Du, W., Wang, L. F., Dong, Z., and Wang, F. (2018). Comparison of zero-profile device versus plate-and-cage implant in the treatment of symptomatic adjacent segment disease after anterior cervical discectomy and fusion: A minimum 2-year follow-up study. *World Neurosurg.* 115, e226–e232. doi:10.1016/j.wneu.2018.04.019

Shen, Y. W., Yang, Y., Liu, H., Wu, T. K., Ma, L. T., Chen, L., et al. (2021). Preliminary results in anterior cervical discectomy and fusion with the uncovertebral joint fusion cage in a goat model. *BMC Musculoskelet. Disord.* 22, 628. doi:10.1186/s12891-021-04412-4

Shen, Y. W., Yang, Y., Liu, H., Qiu, Y., Li, M., Ma, L. T., et al. (2022). Biomechanical evaluation of intervertebral fusion process after anterior cervical discectomy and fusion: A finite element study. *Front. Bioeng. Biotechnol.* 10, 842382. doi:10.3389/fbioe.2022.842382

Shi, S., Zheng, S., Li, X. F., Yang, L. L., Liu, Z. D., and Yuan, W. (2016). Comparison of a stand-alone anchored spacer versus plate-cage construct in the treatment of two noncontiguous levels of cervical spondylosis: A preliminary investigation. *World Neurosurg.* 89, 285–292. doi:10.1016/j.wneu.2016.02.009

Smith, G. W., and Robinson, R. A. (1958). The treatment of certain cervical-spine disorders by anterior removal of the intervertebral disc and interbody fusion. *J. Bone Jt. Surg. Am. 40-a* 40, 607–624. doi:10.2106/00004623-195840030-00009

Song, K. J., and Choi, B. Y. (2014). Current concepts of anterior cervical discectomy and fusion: A review of literature. *Asian Spine J.* 8, 531–539. doi:10.4184/asj.2014.8.4.531

Stulik, J., Pitzen, T. R., Chrobok, J., Ruffing, S., Drumm, J., Sova, L., et al. (2007). Fusion and failure following anterior cervical plating with dynamic or rigid plates: 6-months results of a multi-centric, prospective, randomized, controlled study. *Eur. Spine J.* 16, 1689–1694. doi:10.1007/s00586-007-0451-6

Sun, B., Shi, C., Wu, H., Xu, Z., Lin, W., Shen, X., et al. (2020). Application of zero-profile spacer in the treatment of three-level cervical spondylotic myelopathy: 5-year follow-up results. *Spine (Phila Pa 1976)* 45, 504–511. doi:10.1097/brs.0000000000003312

Sun, J., Wang, Q., Cai, D., Gu, W., Ma, Y., Sun, Y., et al. (2021). A lattice topology optimization of cervical interbody fusion cage and finite element comparison with ZK60 and Ti-6Al-4V cages. *BMC Musculoskelet. Disord.* 22, 390. doi:10.1186/s12891-021-04244-2

Tan, J. S., Bailey, C. S., Dvorak, M. F., Fisher, C. G., and Oxland, T. R. (2005). Interbody device shape and size are important to strengthen the vertebra-implant interface. *Spine (Phila Pa 1976)* 30, 638–644. doi:10.1097/01.brs.0000155419.24198.35

Tian, W., Fan, M. X., Liu, Y. J., Han, X., Yan, K., Wang, H., et al. (2016). An analysis of paravertebral ossification in cervical artificial disc replacement: A novel classification based on computed tomography. *Orthop. Surg.* 8, 440–446. doi:10.1111/os.12286

Vandamme, K., Naert, I., Geris, L., Vander Sloten, J., Puers, R., and Duyck, J. (2007). The effect of micro-motion on the tissue response around immediately loaded roughened titanium implants in the rabbit. *Eur. J. Oral Sci.* 115, 21–29. doi:10.1111/j.1600-0722.2007.00416.x

Vanek, P., Bradac, O., Delacy, P., Lacman, J., and Benes, V. (2013). Anterior interbody fusion of the cervical spine with zero-P spacer: Prospective comparative study-clinical and radiological results at a minimum 2 years after surgery. *Spine (Phila Pa 1976)* 38, E792–E797. doi:10.1097/brs.0b013e3182913400

Wang, H. R., Li, X. L., Dong, J., Yuan, F. L., and Zhou, J. (2013). Skip-level anterior cervical discectomy and fusion with self-locking stand-alone PEEK cages for the treatment of 2 noncontiguous levels of cervical spondylosis. *J. Spinal Disord. Tech.* 26, E286–E292. doi:10.1097/bsd.0b013e31828679b3

Welke, B., Schwarze, M., Hurschler, C., Book, T., Magdu, S., and Daentzer, D. (2016). *In vitro* investigation of a new dynamic cervical implant: Comparison to spinal fusion and total disc replacement. *Eur. Spine J.* 25, 2247–2254. doi:10.1007/s00586-015-4361-8

Wo, J., Lv, Z., Wang, J., Shen, K., Zhu, H., Liu, Y., et al. (2021). Biomechanical analysis of cervical artificial disc replacement using cervical subtotal discectomy prosthesis. *Front. Bioeng. Biotechnol.* 9, 680769. doi:10.3389/fbioe.2021.680769

Wu, T., Wang, B., Ding, C., Meng, Y., Lou, J., Yang, Y., et al. (2017). Artificial cervical disc replacement with the prestige-LP prosthesis for the treatment of non-contiguous 2-level cervical degenerative disc disease: A minimum 24-month follow-up. *Clin. Neurol. Neurosurg.* 152, 57–62. doi:10.1016/j.clineuro.2016.11.015

Wu, T. K., Meng, Y., Liu, H., Wang, B. Y., Hong, Y., Rong, X., et al. (2019). Biomechanical effects on the intermediate segment of noncontiguous hybrid surgery with cervical disc arthroplasty and anterior cervical discectomy and fusion: A finite element analysis. *Spine J.* 19, 1254–1263. doi:10.1016/j.spinee.2019.02.004

Yang, Y., Luo, S., Liu, H., and Wu., T.-K., (2019). biomechanicalinitial stabilitytest of the uncovertebral joint fusion cage. *J. Pract. Orthop. Chin.* 25, 986–990. doi:10.13795/j.cnki.sgkz.2019.11.007

Zhang, X., Ordway, N. R., Tan, R., Rim, B. C., and Fayyazi, A. H. (2008). Correlation of ProDisc-C failure strength with cervical bone mineral content and endplate strength. *J. Spinal Disord. Tech.* 21, 400–405. doi:10.1097/bsd.0b013e318157d382

Zhang, J., Liu, Y., Han, Q., Zhang, A., Chen, H., Ma, M., et al. (2022a). Biomechanical comparison between porous Ti6Al4V block and tumor prosthesis UHMWPE block for the treatment of distal femur bone defects. *Front. Bioeng. Biotechnol.* 10, 939371. doi:10.3389/fbioe.2022.939371

Zhang, K. R., Yang, Y., Ma, L. T., Qiu, Y., Wang, B. Y., Ding, C., et al. (2022b). Biomechanical effects of a novel anatomic titanium mesh cage for single-level anterior cervical corpectomy and fusion: A finite element analysis. *Front. Bioeng. Biotechnol.* 10, 881979. doi:10.3389/fbioe.2022.881979

Zhou, J. M., Guo, X., Kang, L., Zhao, R., Yang, X. T., Fu, Y. B., et al. (2021). Biomechanical effect of C(5)/C(6) intervertebral reconstructive height on adjacent segments in anterior cervical discectomy and fusion - a finite element analysis. *Orthop. Surg.* 13, 1408–1416. doi:10.1111/os.13010

Zhu, M., Tan, J., Liu, L., Tian, J., Li, L., Luo, B., et al. (2021). Construction of biomimetic artificial intervertebral disc scaffold via 3D printing and electrospinning. *Mater Sci. Eng. C Mater Biol. Appl.* 128, 112310. doi:10.1016/j.msec.2021.112310

Frontiers in
Bioengineering and Biotechnology

Accelerates the development of therapies, devices, and technologies to improve our lives

A multidisciplinary journal that accelerates the development of biological therapies, devices, processes and technologies to improve our lives by bridging the gap between discoveries and their application.

Discover the latest Research Topics

See more →

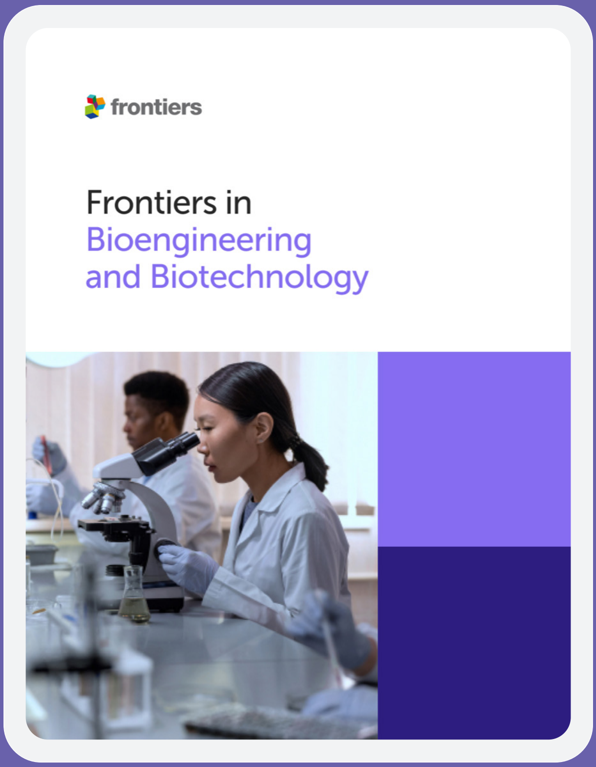

Frontiers

Avenue du Tribunal-Fédéral 34
1005 Lausanne, Switzerland
frontiersin.org

Contact us

+41 (0)21 510 17 00
frontiersin.org/about/contact